

**MICROMECHANICAL SENSOR FOR THE SPECTRAL  
DECOMPOSITION OF ACOUSTIC SIGNALS**

A Thesis  
Presented to  
The Academic Faculty

by

Michael S. Kranz

In Partial Fulfillment  
of the Requirements for the Degree  
Doctor of Philosophy in the  
School of Electrical and Computer Engineering

Georgia Institute of Technology  
May 2011

**COPYRIGHT 2011 BY MICHAEL S. KRANZ**

**MICROMECHANICAL SENSOR FOR THE SPECTRAL  
DECOMPOSITION OF ACOUSTIC SIGNALS**

Approved by:

Dr. Mark G. Allen, Advisor  
School of Electrical and Computer  
Engineering  
*Georgia Institute of Technology*

Dr. Thomas Michaels  
School of Electrical and Computer  
Engineering  
*Georgia Institute of Technology*

Dr. Jennifer Michaels  
School of Electrical and Computer  
Engineering  
*Georgia Institute of Technology*

Dr. W. Jud Ready  
School of Materials Science and  
Engineering  
*Georgia Institute of Technology*

Dr. Oliver Brand  
School of Electrical and Computer  
Engineering  
*Georgia Institute of Technology*

Date Approved: January 06, 2011

To my friends and family

## **ACKNOWLEDGEMENTS**

I wish to thank the sponsors of this work, Mr. Jim Holt and Dr. Tracy Hudson, of the U.S. Army Aviation and Missile Research, Development, and Engineering Center (AMRDEC), for their financial, programmatic, and technical support. I also wish to thank a number of individuals for their various technical expertise and for the long technical discussions. These include Dr. Phil Reiner, Mr. Andy Jenkins, Dr. Wayne Long, Dr. Paul Ashley, Mr. Scott Hill, and Dr. Al Killen. Furthermore, sincere appreciation is extended to Ms. Sharon Sanchez and Mr. Michael Allen for their microfabrication support. I also would like to thank Dr. Mark Allen for his technical expertise and project guidance as my thesis advisor. Finally, I would like to thank God for His strength and guidance through what has been, at least to this date, the most difficult time in my life.

# TABLE OF CONTENTS

	Page
<b>ACKNOWLEDGEMENTS.....</b>	<b>IV</b>
<b>LIST OF TABLES .....</b>	<b>VII</b>
<b>LIST OF FIGURES .....</b>	<b>VIII</b>
<b>LIST OF SYMBOLS AND ABBREVIATIONS.....</b>	<b>XVI</b>
SYMBOLS .....	XVI
ABBREVIATIONS.....	XVII
GREEK.....	XVII
<b>SUMMARY.....</b>	<b>XIX</b>
<b>CHAPTER 1 - INTRODUCTION .....</b>	<b>1</b>
1.1 STATEMENT OF PROBLEM.....	1
1.2 OBJECTIVES AND OVERVIEW.....	3
<b>CHAPTER 2 - PREVIOUS WORK .....</b>	<b>7</b>
2.1 SHOCK/IMPACT CHARACTERIZATION .....	7
2.2 SHOCK/IMPACT SENSORS .....	10
2.3 MECHANICAL SPECTRUM ANALYSIS .....	14
2.4 ACOUSTIC EMISSION SIGNAL PROCESSING.....	15
2.5 ENERGY HARVESTING .....	17
2.6 ELECTRET INTEGRATION WITH MEMS.....	18
2.7 MEMS-BASED CORONAS, PLASMAS, AND IN SITU CHARGING .....	24
<b>CHAPTER 3 - RESONANT ARRAY PROCESSING.....</b>	<b>28</b>
3.1 IMPACT SOURCE ANALYSIS .....	28
3.1.1 Ball-on-Rod Impact .....	29
3.1.2 Ball-on-Plate Impact.....	40
3.2 IMPACT CHARACTERIZATION .....	45
3.2.1 Ball-on-Rod Impact .....	45
3.2.2 Ball-on-Plate Impact.....	48
3.3 ARRAY RESPONSE ANALYSIS .....	53
3.3.1 Gaussian Pulse Frequency Content.....	55
3.3.2 Gaussian Pulse with Plate.....	71
3.4 RESONANT PROCESSING CONSIDERATIONS .....	82
<b>CHAPTER 4 - INTEGRATED ELECTRETS .....</b>	<b>84</b>
4.1 ELECTRET TYPE.....	85
4.1.1 Dipole Electret.....	85
4.1.2 Space-Charge Electret.....	90
4.2 SELECTION OF ELECTRET MATERIALS .....	95
4.2.1 Inorganic .....	95
4.2.2 Polymer.....	97
4.3 ELECTRET INTEGRATION IN MEMS.....	99
4.3.1 Wafer Bonding - Localized Heating.....	100
4.3.2 In Situ Charging Using MicroCorona.....	107
4.3.3 Microcorona Theoretical Analysis.....	112
4.4 ELECTRET ARRAY AND CHARGING GRID FABRICATION.....	123
4.5 ELECTRET MEASUREMENT TECHNIQUES.....	140
4.5.1 Remnant Voltage Measurement.....	140

4.5.2 Charging Current Measurement.....	143
4.6 ELECTRET CHARGING CURRENT.....	146
4.7 ELECTRET REMNANT VOLTAGE .....	155
4.8 INTEGRATED ELECTRET CONSIDERATIONS.....	161
<b>CHAPTER 5 - MEMS TRANSDUCER .....</b>	<b>164</b>
5.1 SENSOR DYNAMICS .....	164
5.2 SENSOR ELECTRICAL MODEL .....	168
5.3 READOUT ELECTRONICS.....	173
5.4 LASER MICROMACHINED TRANSDUCER ARRAY.....	177
5.5 MICROFABRICATED TRANSDUCER ARRAY .....	183
5.6 TRANSDUCER AND ELECTRONICS CONSIDERATIONS .....	198
<b>CHAPTER 6 - TRANSDUCER PROCESS DEVELOPMENT .....</b>	<b>201</b>
6.1 LASER MICROMACHINED TRANSDUCER ARRAY.....	202
6.2 MICROFABRICATED TRANSDUCER ARRAY .....	205
6.3 TRANSDUCER ASSEMBLY PROCESS .....	221
<b>CHAPTER 7 - SENSOR CHARACTERIZATION AND IMPACT TESTS .....</b>	<b>224</b>
7.1 TRANSDUCER CHARACTERIZATION AND FREQUENCY SCANS.....	224
7.2 BALL AND HAMMER DROP EXPERIMENTS .....	239
7.3 TEST SERIES .....	246
7.4 MEMS ARRAY ON ALUMINA DISC - BALL DROP .....	247
<b>CHAPTER 8 - CONCLUSION .....</b>	<b>265</b>
8.1 ELECTRET COMPARISON AND INTEGRATION .....	265
8.2 ARRAY PROCESSING BENEFITS AND CHALLENGES .....	268
8.3 FUTURE WORK .....	271
<b>APPENDIX A.    COUPLED RESONANCE TESTS.....</b>	<b>273</b>
<b>APPENDIX B.    TEST SERIES RESULTS .....</b>	<b>279</b>
B.1 SINGLE LASER MICROMACHINED DEVICE .....	279
B.2 LARGE PLATE RESULTS .....	280
B.3 SMALL PLATE RESULTS .....	292
B.4 LASER MICROMACHINED ARRAY ON STEEL CONE .....	302
B.5 1 <sup>ST</sup> MEMS ARRAY ON STEEL CONE - HAMMER DROP.....	305
B.6 2 <sup>ND</sup> MEMS ARRAY ON STEEL CONE - HAMMER DROP .....	308
B.7 3 <sup>RD</sup> MEMS ARRAY ON STEEL CONE - BALL DROP .....	324
B.8 4 <sup>TH</sup> MEMS ARRAY ON STEEL CONE - BALL AND SLUG DROP .....	332
<b>REFERENCES .....</b>	<b>340</b>
<b>VITA.....</b>	<b>343</b>
MICHAEL S. KRANZ .....	343

## LIST OF TABLES

	Page
Table 3.1: Material Properties of the Alumina Rod.....	33
Table 3.2: Material Properties for Ball Drop Sources .....	34
Table 3.3: Pulsewidths from Ball Drops of Different Materials.....	35
Table 3.4: Pulsewidth and -3dB Frequency for Stress Pulses .....	56
Table 4.1: Inorganic Electret Deposition Process.....	95
Table 4.2: CYTOP Test Process .....	110
Table 4.3: Metal Deposition Process .....	111
Table 4.4: Oxygen Plasma Undercut Process .....	111
Table 4.5: CYTOP Deposition Process Flow .....	124
Table 4.6: Charging Grid Patterning Process .....	125
Table 4.7: Charging Grid Metal Deposition Process .....	125
Table 4.8: CYTOP Etch Process.....	126
Table 4.9: Electret Charging Protocol .....	158
Table 5.1: Resonant Frequencies for Transducers in the Array.....	182
Table 5.2: Natural Frequencies for Array Element Designs.....	185
Table 5.3: Vibrational Frequencies for the Device Array.....	197
Table 5.4: Electrical Model Parameters.....	198
Table 6.1: Laser Cutting Process Parameters .....	204
Table 6.2: SU8 Coating Process .....	206
Table 6.3: SU8 Exposure Process.....	207
Table 6.4: Barrier and Seed Layer Deposition Steps.....	208
Table 6.5: Thick Photoresist Mold Formation.....	210
Table 6.6: Electroless Ni Plating Process .....	210
Table 6.7: Dice and Release Process .....	213
Table 6.8: Revised Cr Etch Process.....	216
Table 7.1: Natural Frequencies of Fabricated Sensors .....	237
Table 7.2: Test Series.....	246

## LIST OF FIGURES

	Page
Figure 1.1: Research Objectives, Questions, and Flow .....	5
Figure 2.1: Split-Hopkinson Bar [4] .....	8
Figure 2.2: Reverse Ballistic Air Gun.....	9
Figure 2.3: A MEMS-Based Inertial Sensor [5] .....	11
Figure 2.4: Common Configuration for Piezoelectric or Electret Active Films.....	12
Figure 2.5: Electret as a Voltage Bias.....	14
Figure 2.6: Typical Acoustic Emission Setup [18].....	16
Figure 2.7: Schematic Electret Condenser Microphone Operation [28].....	19
Figure 2.8: Typical Electret Microphone Assembly [29] .....	20
Figure 2.9: A MEMS-Based Electret Condenser Microphone [30] .....	21
Figure 2.10: Back-Lighted Thyratron (BLT) Electret Charging [30] .....	21
Figure 2.11: Patterned Electret with a Lateral Variation of the Electric Field [31].....	22
Figure 2.12: Patterned Electrets Realized with Patterned Films [31] .....	22
Figure 2.13: Patterned Electret Films Generate Current from Lateral Motion [32] .....	23
Figure 2.14: Electret Film Creates an Electrostatic Potential across an Air Gap. [33].....	23
Figure 2.15: Micro Corona Motor [34].....	25
Figure 2.16: Microplasma for <i>In Situ</i> Silicon Etching [35] .....	26
Figure 2.17: <i>In Situ</i> Soft X-Ray Charging of Electret [36].....	27
Figure 3.1: Mass Spring Impact on Face of Rod .....	30
Figure 3.2: Ball-on-Rod Impact Geometry.....	31
Figure 3.3: Stress Pulse Generated from Silicon Nitride Impact on Alumina Rod .....	35
Figure 3.4: Dependence of Pulwidth on Elastic Modulus of Ball .....	37
Figure 3.5: Dependence of $f_{3db}$ on Elastic Modulus of Ball .....	38
Figure 3.6: Dependence of $f_{3db}$ on Impact Velocity of Ball.....	39
Figure 3.7: Dependence of $f_{3db}$ on Ball Radius of Curvature .....	40
Figure 3.8: FEA of Ball Drop .....	42
Figure 3.9: Nodal Displacement - Teflon Ball Drop .....	43
Figure 3.10: Nodal Displacement - Steel Impact.....	44
Figure 3.11: Pulse Characterization Setup.....	46
Figure 3.12: Stress Pulses from A2 Steel on Multiple Tape Thicknesses .....	47
Figure 3.13: Stress Pulses from Silicon Nitride Ball on Multiple Tape Thicknesses.....	48
Figure 3.14: Pulse Characterization on Plate-Like Structure.....	50
Figure 3.15: Stress Pulses from Silicon Nitride Impact on Flattened Steel Cone .....	51
Figure 3.16: Stress Pulses from Silicon Nitride Impact on Alumina Disc .....	52
Figure 3.17: Stress Pulses Due to Impacts by ½ Inch Spheres of Different Materials .....	53
Figure 3.18: Schematic Representation of Impact on Array.....	54
Figure 3.19: Frequency Representation of Input Functions and Sensor Response.....	55
Figure 3.20: Frequency Spectrum of Impact Sources and Sensor Response.....	56
Figure 3.21: Pulse One Output Spectrum .....	57
Figure 3.22: Pulse Two Output Spectrum.....	58
Figure 3.23: Pulse Three Output Spectrum.....	58

Figure 3.24: Pulse Four Output Spectrum .....	59
Figure 3.25: Pulse Five Output Spectrum.....	59
Figure 3.26: Pulse Six Output Spectrum.....	60
Figure 3.27: Sensor Array Spectra (linear plot).....	61
Figure 3.28: Sensor Array Spectra (log-log plot) .....	62
Figure 3.29: Time Domain Simulation of 10-Element Sensor Array.....	63
Figure 3.30: Pulse One Output Waveform .....	64
Figure 3.31: Pulse Two Output Waveform.....	65
Figure 3.32: Pulse Three Output Waveform.....	66
Figure 3.33: Pulse Four Output Waveform.....	67
Figure 3.34: Pulse Five Output Waveform .....	68
Figure 3.35: Pulse Six Output Waveform.....	69
Figure 3.36: Sensor Array Output Spectra (linear plot).....	70
Figure 3.37: Sensor Array Output Spectra (log-log plot) .....	71
Figure 3.38: Frequency Response Representation of Source Functions, Sensor Array Response, and Plate Response .....	72
Figure 3.39: Pulse One Output Spectrum .....	73
Figure 3.40: Pulse Two Output Spectrum.....	73
Figure 3.41: Pulse Three Output Spectrum.....	74
Figure 3.42: Pulse Four Output Spectrum .....	74
Figure 3.43: Pulse Five Output Spectrum.....	75
Figure 3.44: Pulse Six Output Spectrum.....	75
Figure 3.45: Sensor Array Spectra (linear plot).....	76
Figure 3.46: Sensor Array Spectra (log-log plot) .....	77
Figure 3.47: Time Domain Block Diagram of Seven Element Sensor.....	78
Figure 3.48: Simulated Resonator Array Output Waveforms for Impacts on Teflon .....	79
Figure 3.49: Simulated Resonator Array Output Waveforms for Impacts on Steel .....	80
Figure 3.50: Comparison of Teflon (left) and Steel (right) Responses.....	81
Figure 4.1: Mass-Spring System with Electret Transducer .....	84
Figure 4.2: Process for Forming a Dipole Electret .....	86
Figure 4.3: FEA Model for High-K Dielectric Composite.....	87
Figure 4.4: Analytical Model for High-K Dielectric Application .....	87
Figure 4.5: Corona Discharge Apparatus [31].....	90
Figure 4.6: Physical Model of Space Charge Electret .....	92
Figure 4.7: Microneedle Array Charging Setups.....	96
Figure 4.8: MicroGrid Charging Setup.....	97
Figure 4.9: Point-to-Plane Charging Apparatus used for Polymer Electrets.....	99
Figure 4.10: Process Flow for Localized Heating .....	101
Figure 4.11: Fabricated Local Heaters.....	103
Figure 4.12: Temperatures Achieved by Local Heaters .....	104
Figure 4.13: Finite Element Model of Local Heaters .....	105
Figure 4.14: Process Flow for Fabrication of Releasable Diaphragms .....	106
Figure 4.15: Fabricated Releasable Diaphragms .....	106
Figure 4.16: <i>In Situ</i> Charging Process .....	108
Figure 4.17: Schematic of Microcorona Charging Approach.....	109
Figure 4.18: Microplasma Electrostatic Model .....	109

Figure 4.19: Electrostatic Simulation of MicroCorona.....	112
Figure 4.20: Electrostatic Simulation of Microgrid.....	113
Figure 4.21: Electrostatic Simulation of Microgrid (Close-Up).....	114
Figure 4.22: Electric Field Magnitude in Air Gap.....	115
Figure 4.23: Electric Field within Gap at -30V.....	116
Figure 4.24: Electric Field through Gap at a -30V Grid Potential.....	116
Figure 4.25: Electrostatic Simulation of Microgrid with 45 $\mu$ m Spacing.....	117
Figure 4.26: Electrostatic Simulation of Microgrid with 45 $\mu$ m Spacing (Close-Up).....	118
Figure 4.27: Electric Field Magnitude through Air Gap.....	119
Figure 4.28: Remnant Voltage from a Nonuniformly Charged Surface.....	120
Figure 4.29: Remnant Potential with a Floating Conductor.....	121
Figure 4.30: Remnant Potential with a Grounded Conductor.....	122
Figure 4.31: Process Flow for Electret and Charging Grid.....	123
Figure 4.32: Square Mesh MicroCorona Grid.....	127
Figure 4.33: Square Charging Grid Wafer Layout.....	128
Figure 4.34: 3x3 Matrix of Test Die.....	129
Figure 4.35: A Charging Grid with a Separation of 45 microns.....	130
Figure 4.36: Square Charging Grid with 10 Micron Spacing.....	131
Figure 4.37: Close-up of Charging Grid.....	132
Figure 4.38: Wafer with Circular Charging Areas.....	133
Figure 4.39: Variations of Die on Wafer.....	134
Figure 4.40: Square Microgrid Pattern.....	135
Figure 4.41: Microline pattern.....	135
Figure 4.42: Square Microgrid Chip with 30 Micron Spacing.....	136
Figure 4.43: Square Microgrid Pattern.....	137
Figure 4.44: SEM of Square Microgrid Pattern.....	137
Figure 4.45: Close-Up View of Square Microgrid Pattern.....	138
Figure 4.46: Chip with Microline Pattern.....	138
Figure 4.47: SEM of Microline Pattern.....	139
Figure 4.48: Close-up of Microline Pattern.....	139
Figure 4.49: Electrostatic Voltmeter Operation.....	141
Figure 4.50: Electrostatic Measurement Test Fixture.....	142
Figure 4.51: Schematic Diagram for Charging Current Measurement.....	143
Figure 4.52: Charging Current.....	144
Figure 4.53: Charging Circuit with Measurement of Charging Current.....	145
Figure 4.54: Filter Frequency Response for 60Hz Removal.....	146
Figure 4.55: Current vs. Time during Electret Charging Prior to Filtering.....	147
Figure 4.56: Current vs. Time during Electret Charging With Filtering.....	148
Figure 4.57: Charging Current through Electret Film.....	149
Figure 4.58: Charge Transfer as a Function of Time.....	150
Figure 4.59: Total Charge Transferred as a Function of Time.....	151
Figure 4.60: Voltage Input Waveform during Charging Cycle.....	152
Figure 4.61: Empirical Model of Various Electrical Discharge Regimes.....	153
Figure 4.62: Schematic Representation of Charging Process.....	154
Figure 4.63: Voltage across Sense Resistor during Charging Process.....	155
Figure 4.64: Remnant Voltage vs. Grid Spacing for Four Sets of Charging Grids.....	156

Figure 4.65: Average and Standard Deviation of Remnant Voltage .....	157
Figure 4.66: Single Die on Electret Wafer.....	158
Figure 4.67: 20 Micron Square Mesh Array.....	159
Figure 4.68: 20 Micron Line Array.....	159
Figure 4.69: 30 Micron Square Mesh Array.....	160
Figure 4.70: 30 Micron Line Array.....	160
Figure 5.1: Schematic Representation of Transducer.....	165
Figure 5.2: Transducer Transfer Function .....	167
Figure 5.3: Change in Capacitance vs. Frequency.....	170
Figure 5.4: Electrical Model of Single Element of Sensor .....	170
Figure 5.5: Voltage as a Function of Frequency.....	173
Figure 5.6: Transducer Readout Circuits .....	174
Figure 5.7: Response from Driven Sensor Element.....	176
Figure 5.8: Schematic of the Sensor including Sensor-to-Sensor Parasitic.....	176
Figure 5.9: Schematic of Laser Machined Sensor .....	177
Figure 5.10: Laser Machined Sensor Mode 1 .....	178
Figure 5.11: Laser Machined Sensor Mode 2 .....	178
Figure 5.12: Laser Machined Sensor Mode 3 .....	179
Figure 5.13: Laser Machined Sensor Mode 4 .....	179
Figure 5.14: Laser Machined Sensor Mode 5 .....	180
Figure 5.15: Laser Machined Sensor Mode 6 .....	180
Figure 5.16: Laser Machined Sensor Mode 7 .....	181
Figure 5.17: Laser Machined Sensor Mode 8 .....	181
Figure 5.18: Laser Machined Sensor Mode 9 .....	182
Figure 5.19: Schematic of Microfabricated Transducer Array Device.....	183
Figure 5.20: Microfabricated Array Charging Setup .....	184
Figure 5.21: Microfabricated Array Charging During Operation.....	184
Figure 5.22: Charging Grid Solid Model.....	186
Figure 5.23: Solid Model of Structure with SU8 and Thin Metal Layers .....	186
Figure 5.24: Solid Model of Wafer after Plating and Photoresist Strip.....	187
Figure 5.25: Solid Model of Released Structure.....	187
Figure 5.26: Microfabricated Transducer Array Wafer Layout.....	188
Figure 5.27: Test Matrix Layout.....	189
Figure 5.28: Microfabricated Transducer Array Layout.....	190
Figure 5.29: Single Transducer in the Array .....	191
Figure 5.30: Microfabricated Sensor Array Mode 1 .....	192
Figure 5.31: Microfabricated Sensor Array Mode 2 .....	192
Figure 5.32: Microfabricated Sensor Array Mode 3 .....	193
Figure 5.33: Microfabricated Sensor Array Mode 4 .....	193
Figure 5.34: Microfabricated Sensor Array Mode 5 .....	194
Figure 5.35: Microfabricated Sensor Array Mode 6 .....	194
Figure 5.36: Microfabricated Sensor Array Mode 7 .....	195
Figure 5.37: Microfabricated Sensor Array Mode 8 .....	195
Figure 5.38: Microfabricated Sensor Array Mode 9 .....	196
Figure 5.39: Microfabricated Sensor Array Mode 10.....	196
Figure 6.1: Laser Micromachined Sensor Array Process Flow .....	202

Figure 6.2: Laser Machined Mylar Utilized to Create Circular Cavities.....	203
Figure 6.3: Laser Machined Metal Diaphragms Adhered to the Mylar Surface .....	203
Figure 6.4: Laser Micromachined Transducer Array .....	204
Figure 6.5: SU8-Based Microfabrication Process for Electret Transducer Array .....	205
Figure 6.6: Image of Successful Metallization .....	208
Figure 6.7: Image of Unsuccessful Metallization Following Insufficient Post-Exposure Bake and SU8 Reflow.....	209
Figure 6.8: Electroless Ni Plated Structure.....	211
Figure 6.9: Stereoscope Image of Plated Structure.....	211
Figure 6.10: Incomplete Fill of Electroless Plating Mold.....	212
Figure 6.11: Opened Contact Pad for the Charging Grid .....	213
Figure 6.12: Fully Released Ni Structure Suspended Above Charging Grid .....	214
Figure 6.13: Stereomicroscope Image of Remaining “Skin” .....	215
Figure 6.14: Contact Pad Opening After Improved Cr Etch Process .....	216
Figure 6.15: Released Structure After Improved Cr Etch Process .....	217
Figure 6.16: Charging Grid Seen through Air Gap and the Clear SU8 .....	218
Figure 6.17: Full Released Device.....	219
Figure 6.18: SEM of the Edge of a Released Structure .....	220
Figure 6.19: SEM of Final Smallest Structure.....	220
Figure 6.20: Wired Sensor Array.....	222
Figure 6.21: Sensors Mounted on Large Aluminum Plate .....	223
Figure 7.1: Frequency Characterization Test.....	225
Figure 7.2: Microfabricated Array on PZT Driver .....	225
Figure 7.3: PZT Driver .....	226
Figure 7.4: Acoustic Frequency Sweep of Lowest Frequency Device.....	227
Figure 7.5: Improved Frequency Scan Apparatus .....	228
Figure 7.6: Frequency Response Sensor One .....	229
Figure 7.7: Frequency Response Sensor Two.....	229
Figure 7.8: Frequency Response Sensor Three.....	230
Figure 7.9: Frequency Response Sensor Four .....	231
Figure 7.10: Frequency Response Sensor Five.....	231
Figure 7.11: Frequency Response Sensor Six.....	232
Figure 7.12: Frequency Response Sensor Seven .....	232
Figure 7.13: Original First Mode Resonance.....	233
Figure 7.14: Original Second Mode Resonance .....	233
Figure 7.15: Original Third Mode Resonance .....	234
Figure 7.16: Fractured Sensor First Mode Resonance.....	234
Figure 7.17: Fractured Sensor Second Mode Resonance .....	235
Figure 7.18: Fractured Sensor Third Mode Resonance .....	235
Figure 7.19: Fractured Sensor Frequency Response.....	236
Figure 7.20: Frequency Sweep of an Intact Fourth Sensor.....	237
Figure 7.21: Fundamental Mode of Curved Structure .....	239
Figure 7.22: Schematic of Hammer Drop on Square Plate.....	240
Figure 7.23: Ball Drop Test .....	241
Figure 7.24: Single Laser Machined Transducer Element on a Steel Cone .....	242
Figure 7.25: Laser Machined Transducer Array on a Steel Cone.....	242

Figure 7.26: Microfabricated Transducer Array on a Steel Cone.....	243
Figure 7.27: Microfabricated Transducer Array on a Large Plate.....	243
Figure 7.28: Microfabricated Transducer Array on a Large Plate (Zoomed Out).....	244
Figure 7.29: Microfabricated Transducer Array on a Small Plate.....	244
Figure 7.30: Microfabricated Transducer Array on a Small Plate (Zoomed Out).....	245
Figure 7.31: Microfabricated Transducer Array on Small Alumina Disc .....	245
Figure 7.32: Modified Ball Drop Apparatus.....	248
Figure 7.33: Stress Pulses from Silicon Nitride Ball .....	249
Figure 7.34: Seven Sensor Array - Direct Si <sub>3</sub> N <sub>4</sub> Impact.....	250
Figure 7.35: Seven Sensor Array - Si <sub>3</sub> N <sub>4</sub> Impact - Five Tape Layers.....	252
Figure 7.36: Filtered Seven Sensor Array - Direct Si <sub>3</sub> N <sub>4</sub> Impact.....	253
Figure 7.37: Filtered Seven Sensor Array - Si <sub>3</sub> N <sub>4</sub> Impact - Five Tape Layers.....	254
Figure 7.38: Array Output from Silicon Nitride Impact and Multiple Tape Layers.....	255
Figure 7.39: Predicted Response for the Sensor Array.....	256
Figure 7.40: Stress Pulses from Different Ball Materials.....	257
Figure 7.41: Seven Sensor Array Impact - Teflon (left), Acrylic (right).....	258
Figure 7.42: Filtered Seven Sensor Array Impact - Teflon (left), Acrylic (right) .....	259
Figure 7.43: Array Spectrum from Acrylic and Teflon Ball Drops.....	260
Figure 7.44: Seven Sensor Array - Direct Stainless Steel Impact .....	261
Figure 7.45: Filtered Seven Sensor Array - Direct Stainless Steel Impact.....	262
Figure 7.46: Array Spectra from Four Different Materials.....	263
Figure A.1: Frequency Response of Sensor One when Resting on A Table .....	273
Figure A.2: Driven Sensor Array Attached to Large Thin Plate .....	274
Figure A.3: Sensor One Frequency Response on Large Alumina Plate.....	275
Figure A.4: Sensor Two Frequency Response on Large Alumina Plate .....	275
Figure A.5: Sensor Three Frequency Response on Large Alumina Plate .....	276
Figure A.6: Sensor Four Frequency Response on Large Alumina Plate .....	276
Figure A.7: Sensor Five Frequency Response on Large Alumina Plate.....	277
Figure A.8: Sensor Six Frequency Response on Large Alumina Plate .....	277
Figure B.1: Cross-section of Single Laser Machined Transducer .....	279
Figure B.2: Single Transducer Output.....	280
Figure B.3: First Mode of Large Plate .....	281
Figure B.4: Second Mode of Large Plate.....	281
Figure B.5: Laser Fabricated Array - Teflon Hammer on Large Plate.....	282
Figure B.6: Laser Fabricated Array - Teflon Hammer on Large Plate (Close-Up).....	283
Figure B.7: Microfabricated Array - Teflon Hammer on Large Plate.....	283
Figure B.8: Microfabricated Array - Teflon Hammer on Large Plate (Close-Up).....	284
Figure B.9: Laser Fabricated Array - Steel Hammer on Large Plate.....	285
Figure B.10: Laser Fabricated Array - Steel Hammer on Large Plate (Zoomed In) .....	285
Figure B.11: Microfabricated Array - Steel Hammer on Large Plate.....	286
Figure B.12: Microfabricated Array - Steel Hammer on Large Plate (Close-Up).....	286
Figure B.13: Seven Sensor Array - Steel Impact on Large Plate.....	287
Figure B.14: Seven Sensor Array - Steel Impact on Large Plate (second shot).....	288
Figure B.15: Seven Sensor Array - Teflon Impact on Large Plate.....	289
Figure B.16: Seven Sensor Array - Teflon Impact on Large Plate (second shot) .....	290
Figure B.17: Seven Sensor Array - Impact from a Stainless Steel Ball .....	291

Figure B.18: Scavenged Energy from Large Plate Impact .....	292
Figure B.19: First Excited Mode of Small Plate.....	293
Figure B.20: Second Excited Mode of Small Plate .....	293
Figure B.21: Laser Fabricated Array - Teflon Hammer on Small Plate.....	294
Figure B.22: Laser Fabricated Array - Teflon Hammer on Small Plate (Close-Up).....	295
Figure B.23: Microfabricated Array - Teflon Hammer on Small Plate.....	295
Figure B.24: Microfabricated Array - Teflon Hammer on Small Plate (Close-Up).....	296
Figure B.25: Laser Fabricated Array - Steel Hammer on Small Plate.....	297
Figure B.26: Laser Fabricated Array - Steel Hammer on Small Plate (Close-Up).....	297
Figure B.27: Microfabricated Array - Steel Hammer on Small Plate.....	298
Figure B.28: Microfabricated Array - Steel Hammer on Small Plate (Close-Up).....	298
Figure B.29: Seven Sensor Array - Steel Impact on Small Plate.....	299
Figure B.30: Seven Sensor Array - Teflon Impact on Small Plate.....	300
Figure B.31: Seven Sensor Array - Impact of Stainless Steel Ball.....	301
Figure B.32: Finite Element Analysis of Small Plate on Compliant Mounts.....	302
Figure B.33: Laser Machined Array with Steel Hammer Drop.....	303
Figure B.34: Laser Machined Array with Steel Hammer Drop (Close-Up).....	303
Figure B.35: Laser Machined Array with Teflon Hammer Drop .....	304
Figure B.36: Laser Machined Array with Teflon Hammer Drop .....	305
Figure B.37: Steel Hammer Impact on MEMS Array .....	306
Figure B.38: Steel Hammer Impact on MEMS Array (Close-Up) .....	306
Figure B.39: Teflon Hammer Impact on MEMS Array .....	307
Figure B.40: Teflon Hammer Impact on MEMS Array (Close-Up) .....	307
Figure B.41: Waveforms from Second Array with Teflon Impact.....	309
Figure B.42: Waveforms from Second Array with Steel Impact.....	310
Figure B.43: Sensor One Response to Four Impacts with Teflon .....	311
Figure B.44: Sensor One Response to Four Impacts with Steel .....	312
Figure B.45: Sensor Two Response to Four Impacts with Teflon.....	313
Figure B.46: Sensor Two Response to Four Impacts with Steel .....	314
Figure B.47: Sensor Three Response to Four Impacts with Teflon.....	315
Figure B.48: Sensor Three Response to Four Impacts with Steel .....	316
Figure B.49: Sensor Four Response to Four Impacts with Teflon .....	317
Figure B.50: Sensor Four Response to Four Impacts with Steel .....	318
Figure B.51: Side-by-Side Comparison of Sensor Response for Teflon Impact (left) and Steel Impact (right) - Shot One.....	319
Figure B.52: Side-by-Side Comparison of Sensor Response for Teflon Impact (left) and Steel Impact (right) - Shot Two .....	319
Figure B.53: Seven Sensor Output - Teflon Hammer Impact .....	320
Figure B.54: Band-Pass Filtered Response to Teflon Hammer Impact.....	321
Figure B.55: Seven Sensor Output - Steel Hammer Impact .....	322
Figure B.56: Band-Pass Filtered Response - Steel Hammer Impact .....	323
Figure B.57: Spectra from Teflon Impact (left) and Steel Impact (right).....	324
Figure B.58: Seven Sensor Array Output - Stainless Steel Ball Impact.....	325
Figure B.59: Band-Pass Filtered Response - Stainless Steel Ball Impact .....	326
Figure B.60: Spectrum Acquired from Stainless Steel Ball Impact .....	327
Figure B.61: Modified Ball Drop Setup .....	328

Figure B.62: Seven Sensor Array Output - Teflon Slug Impact.....	329
Figure B.63: Band-Pass Filtered Response - Teflon Slug Impact .....	330
Figure B.64: Band-Pass Filtered Response to Teflon Slug Impact .....	331
Figure B.65: Spectra from Teflon Impact (left) and Steel Impact (right).....	332
Figure B.66: Waveform from Teflon Impact.....	333
Figure B.67: Filtered Waveform from Teflon Impact .....	333
Figure B.68: Filtered Waveform from Teflon Impact (Close-Up) .....	334
Figure B.69: Waveform from Steel Impact .....	334
Figure B.70: Filtered Waveform from Steel Impact (Close-Up).....	335
Figure B.71: Teflon Spectra.....	335
Figure B.72: Steel Spectra .....	336
Figure B.73: Array Response to ½ Inch Stainless Steel Ball.....	337
Figure B.74: Array Response to ½ Inch Steel Rod.....	337
Figure B.75: Array Response to 2½ Inch Aluminum Rod .....	338
Figure B.76: Array Response to 2 Inch Teflon Rod .....	338
Figure B.77: Array Spectra from Multiple Impact Sources.....	339

## LIST OF SYMBOLS AND ABBREVIATIONS

### Symbols

$A$	Area
$b$	Damping Coefficient
$c$	Speed of Sound
$C$	Capacitance
$D$	Displacement Field
$E$	Elastic Modulus
$E$	Total Energy
$d_{33}$	Piezoelectric Constant
$f$	Frequency
$F$	Force
$g$	Acceleration Due to Gravity
$G$	Gain
$h$	Height
$I$	Current
$K$	Stiffness
$L$	Length
$m$	Mass
$P$	Pressure
$q$	Charge
$Q$	Charge
$u$	Local Particle Displacement
$r$	Radial Position
$R$	Radius of Curvature

$R$	Resistance
$t$	Time, Thickness
$T$	Temperature
$v$	Velocity
$V$	Volume
$V$	Voltage
$w$	Width
$W$	Electric Power
$x$	Linear Position
$z$	Vertical Displacement with Respect to Gravity

### **Abbreviations**

AF	Amorphous Film
ECM	Electret Condenser Microphone
FEA	Finite Element Analysis
FWHM	Full Width Half Maximum
PZT	Lead Zirconate Titanate
SU8	Photo-Definable Epoxy

### **Greek**

$\rho$	Resistivity, Density
$\epsilon_0$	Permittivity of Free Space
$\epsilon_r$	Relative Permittivity
$\sigma$	Stress, Surface Charge Density
$\epsilon$	Strain

$\alpha$	Approach
$\beta$	Local Displacement
$\nu$	Poisson's Ratio
$\omega$	Radial Frequency
$\Delta$	Delta or Difference

## SUMMARY

This research effort developed electret-biased MEMS-scale ultrasonic sensor arrays meant to discriminate between elastic waves generated by an impact with a hard material and elastic waves generated by impact with a soft material. The effort investigated two main technical areas; 1.) How to integrate electrets into MEMS fabrication processes so that sensor arrays could be easily realized, and 2.) How to use these sensor arrays to discriminate between elastic wave sources with different frequency content. The effort explored multiple electret materials, fabrication processes, and polarization techniques, leading to the development of an *in situ* electret charging process. It also explored multiple MEMS transducer designs, leading to placing actual sensor elements onto structures and capturing impact events.

The electret integration portion of the effort demonstrated an *in situ* charging process that allowed the entire MEMS fabrication to be completed prior to polarizing the electret film. The process was based on the fabrication of a micro-scale “charging grid” suspended a short distance above the electret material and separated by a charging gas. Energizing the grid with a high voltage led to ionization of the gas in the gap, and the migration of charge to the surface of the electret polymer. This process and the resulting performance of charged films were characterized. The process could be easily performed after entire device fabrication.

The MEMS sensor array portion of the effort built suspended metal resonant structures separated by an air gap above the electret film and charging grids. These structures were designed to respond at particular frequencies of interest in an ultrasonic system. After fabrication, devices were polarized and attached to test articles for impact tests. Waveforms captured from the impacts demonstrated how the resonant structures

can be employed to discriminate between the different impacts, and identified the challenges that exist in developing sensor arrays for impact scenario.

In summary, the effort resulted in a new technique for electret integration into MEMS devices, the demonstration of array processing of ultrasonic signals, and the micromechanical analysis of impact waveforms. The resulting device was able to discriminate between impacts with materials of differing acoustic impedance.

# CHAPTER 1 - INTRODUCTION

The objective of this research was to develop arrays of microfabricated capacitive resonant acoustic sensors, using electret materials as a permanent voltage bias, for the spectral decomposition of acoustic pulses such as those seen during impact events. Certain classes of problems exist that require determination of the spectral signature of an impact-, vibration-, or shock-induced pulse train in a low-power and small package. While micromechanical and nanomechanical structures have been investigated for decomposing acoustic and RF signals, these have been operated primarily in a mode in which the waveforms are multiple cycles in length. Likewise, even though energy harvesting from acoustic and other vibrational forms of energy has been demonstrated, the bulk of that work has used sinusoidal inputs. The work presented here, however, investigates nonsinusoidal inputs like those seen in impact and shock events. Furthermore, while electret-based biasing of capacitive sensors is widely employed, such as in the electret microphone, wafer-level fabrication of arrays has been challenging due to the charge-storage characteristics of the electret film. As the temperature of the film increases, the mobility of the charge and the polymer itself lead to recombination and charge dissipation. These temperatures are easily achieved in many MEMS processes. This work, therefore, investigated post-fabrication charging of electret films to overcome that challenge and to improve compatibility with standard wafer processing.

## 1.1 Statement of Problem

The problem addressed by this research is that of mechanical spectrum analysis of a broad band acoustic input signal, performing a processing function similar to that of the shock response spectrum (SRS) technique, and stems from three potential applications. All three applications require the ability to process broadband shock and acoustic pulses,

while two of them require extremely low-power operation. One application is in the determination of material hardness when being impacted by a projectile. The second application is the harvesting of energy from broadband shocks or vibrations, such as in personal computers powered by human walking or in vehicle health management sensors and smart structures. The third application is in the monitoring of expensive and/or critical equipment, such as rotating machinery and structural components, for signs of wear and fatigue.

The first application, impact classification, is most often found in the automotive and aerospace communities. Many impacting systems would be more effective, and more applicable to, multiple situations if they could classify certain properties of the materials involved in the impact. To achieve this functionality, the ability to determine, upon impact, whether the material being hit is soft or hard, whether or not it consists of multiple layers, whether it is coated with a harder material, and other characteristics, is required and currently lacking. If the capability existed to quickly analyze the shock signature generated at the time of impact, systems could adjust accordingly.

The second application involves the generation of electrical energy from shock and vibration sources in order to power such things as wireless sensor nodes and vehicle health monitoring systems. Federal agencies and services, DOT, the shipping industry, and multiple other organizations, are exploring the use of unattended sensor nodes, RFID, wireless sensors, and other systems to monitor the status and health of their inventory and assets. However, the lack of energy sources for these systems is hindering their implementation. The ideal energy source would be extremely small, have an indefinite lifetime, and could scavenge from multiple sources with multiple frequencies.

Therefore, a large body of work has been performed related to the harvesting of energy from the environment. In particular, the harvesting of energy from external vibrations has been investigated [1]. In many cases, investigations have focused on narrow band harvesting, where the harvesters are tuned to resonant frequencies that

match those vibrational frequencies seen in the environment. The difficulty is that the environment often has broadband vibrations and pulses. One example is scavenging energy from tire rotation. A device can harvest energy from the centripetal acceleration, but only for a short period of time. Investigators have looked at converting energy during the inertial pulse that accompanies the flattening of the tire when it contacts the road. The resulting pulse is broadband in nature, and broadband energy converters would therefore be beneficial in optimizing energy harvesting.

The third application is in the monitoring of equipment for fatigue and wear, and is of particular interest in rotating machinery and vibrating structural components. As bearings and other structures in rotating machinery wear, certain vibrational frequencies, pulses, and pulse trains, begin to develop. These vibrations can both power a sensing device and also provide signals that, when decomposed into their spectral content, can provide information as to the type, severity, and potential result of the wear. In addition, some machinery cannot be exposed to certain vibrational frequencies for extended periods of time without harm. Therefore, sensors are required to autonomously determine if external vibrations are beyond specifications for a particular piece of equipment.

In order to accomplish this function efficiently, the device must be able to decompose a broad spectral range. Furthermore, in order to compete with the traditional method of sampling an accelerometer output, followed by an FFT or other signal processing algorithm in a DSP, the device must perform the function using less power and taking up a smaller footprint. This would make the mechanical spectrum analysis function a better solution for unattended and extremely low power wireless sensor nodes.

## **1.2 Objectives and Overview**

The goal of this research was to develop approaches for realizing electret-biased MEMS arrays and utilizing them in an ultrasonic sensor array to characterize impact,

shock, and vibration signatures. This goal was achieved through meeting multiple objectives. The following bullets summarize the anticipated contributions of this effort to the state-of-the-art in active film technology and ultrasonic sensors.

- Provide new fabrication techniques for integrating polymer electret materials into MEMS devices. These techniques will contribute to enabling fully surface micromachined and batch-fabricated electret transducers, and also explore the limits of post-deposition charging of electret materials for MEMS.
- Realize resonant transducer arrays for detection and characterization of impact and other acoustic emissions, with similar performance to piezoelectric devices, but easier to integrate and potentially more survivable in high-shock applications.
- Demonstrate micromechanical processing of acoustic and vibration signals to reduce complexity and power consumption of monitoring systems.

In achieving those contributions, the following objectives were met:

- Determined characteristics of acoustic signals from analysis of applicable impact, shock, and vibration data
- Designed arrays of resonant structures for decomposing signals
- Selected, modeled, and developed processes for incorporating potential electret materials into the resonant structure arrays
- Developed charging techniques for activating the electret materials after fabrication and at wafer-level scales
- Developed readout circuits able to capture signals from the sensors arrays

The body of work follows the research flowchart shown in Figure 1.1, and is divided into eight chapters.

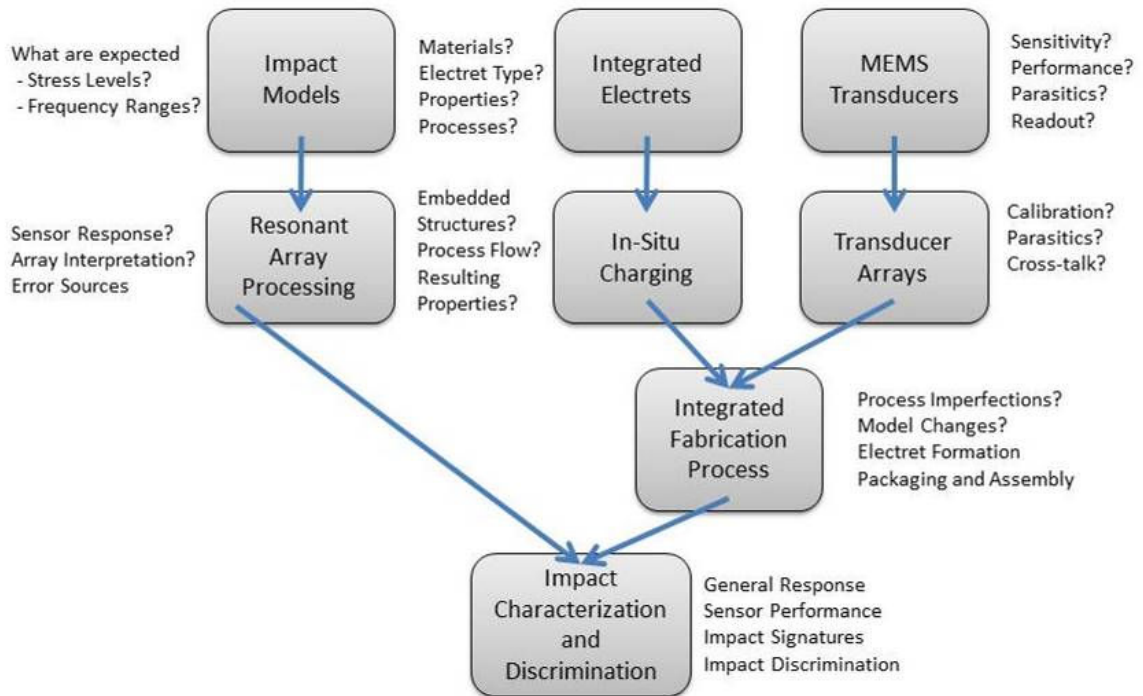


**Figure 1.1: Research Objectives, Questions, and Flow**

Chapter II consists of a literature review that looks at shock and vibration sensors and their applications. Electret films are reviewed in general, and specific charging techniques are reviewed based on their applicability. Industry standard electret fabrication processes are reviewed to establish techniques for achieving reliable charged films and consistent sensor bias. The general operation of vibration and acoustic emission sensors is reviewed as a backdrop for applications that would utilize sensor arrays. Finally, energy harvesting is reviewed as a potential non-sensor application. The goal of Chapter II is to organize existing data from currently employed shock and vibration sensors, utilizing electret transduction or otherwise, and to highlight successes and problems encountered during their fabrication and operation.

Chapter III discusses impact scenarios and develops requirements placed on the subcomponents of the sensors, and then presents mathematical models to predict resonant sensor array output as a function of design variables and impact stress pulses.

Chapter IV discusses electrets and their integration into MEMS devices, including the modeling of electret films, the analysis of charging systems, and the development of fabrication processes. The chapter also presents an *in situ* charging process using a micro-scale charging grid.

Chapter V discusses the design and response of individual resonant capacitive sensors and of sensor arrays based on these models. The purpose of this chapter is to detail design and engineering tools used in the development of the sensor array.

Chapter VI then details the fabrication processes for the sensor array. This chapter reviews similar fabrication literature, and then presents equipment and methods involved in the fabrication of the electret film. The integration of the film within the MEMS structure is critical to this dissertation, so design criteria, modes of failure, and limitations are covered.

Chapter VII presents results of characterization experiments and operational testing. The purpose of these chapters is to verify the operation of the sensor arrays. Chapter VIII then presents the established solutions to meet the goals of the problem statement.

## CHAPTER 2 - PREVIOUS WORK

This chapter discusses previous work in shock and impact sensors, energy harvesting based on piezoelectric and electret films, electret films and their charging processes, and microcorona and microplasma discharges.

### 2.1 Shock/Impact Characterization

The measurement and analysis of impact events and their associated shock and acoustic waveforms has been actively pursued over the past few decades. Motivation for from the Department of Defense (DoD) has been related to activities in armor and buried structure penetration, warhead fuzing, safe and arm devices, and impact detection. Interest in impact and shock sensing is also generated by the automotive and shipping industries, and is related to maintenance and safety concerns. The interest from these organizations has resulted in simulation tools, test and characterization tools, and sensor devices suitable for impact sensing.

Investigators in contact mechanics, acoustics, and high-velocity impact systems have developed nonlinear mechanical event simulations and codes for analyzing impact events. Many of these tools, such as Algor MES, ABAQUS, CTH, PRESTO, PRONTO, DYNA, have been developed for and applied to the cratering of planet surfaces after impact [2] and impact physics during munition engagement against armor [3]. In addition, these simulation tools are now being utilized to investigate the physics of automotive crashes and the effectiveness of pyrotechnic and explosive charges. These codes require materials data from actual impact events, and can then predict how structures will respond at time of impact.

To acquire the necessary data, impact tests are performed, with three primary tools being employed. These tools differ in the level of stress and strain-rate that can be

applied to the unit under test. The first tool is the split-Hopkinson bar (Figure 2.1) [4] designed to create specific shock waves in a specimen. A compressed gas launches one metal impact bar down a barrel where it impacts a second incident bar. The shock pulse travels down the bar, past strain gages that capture the incident and reflected pulses, and through an instrumented unit under test. After traveling through the specimen, the shock pulse traverses a second transmit bar, past a second strain gage that captures the transmitted pulse, and then launches a third momentum bar out the end of the apparatus. Hoppy Bars use strain gages to characterize the pulses. As strain gages have dropped in size, Hoppy Bars have been able to characterize ever narrower shock pulses. State-of-the-art silicon strain gages are less than 1mm in lateral dimension, allowing characterization of acoustic pulses with frequencies on the order of MHz, which may be necessary for impact signature detection in many geometries and velocities. These strain gages can be used in other systems for actual shock and impact sensing.

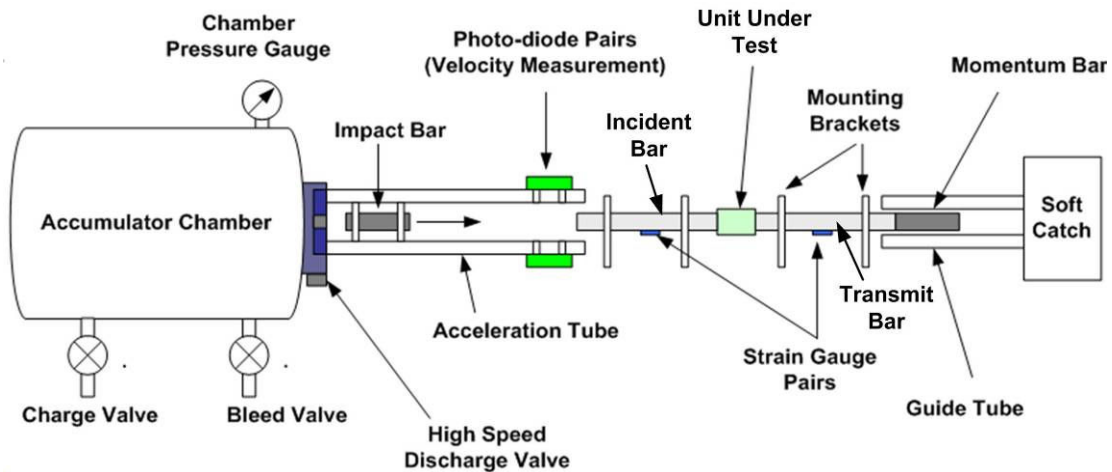


Figure 2.1: Split-Hopkinson Bar [4]

A second tool utilized in shock tests is a simple reverse ballistic air gun (Figure 2.2). It is similar to the Split-Hopkinson Bar except that there is no transmit bar. Instead, the unit under test is instrumented and is considered to be the “projectile”, while the

impact bar is the “target”. The air gun uses highly pressurized air to launch the “target” at a stationary “projectile”, hence the term “reverse ballistic” test. This reverse ballistic arrangement allows the projectile to be easily instrumented without worrying about telemetry systems, volume constraints, and independent power sources. Air gun tests have been used to collect a variety of data related to impact physics and impact sensors. Typical sensors characterized include mechanical g-switches, break wire sensors, and accelerometers.

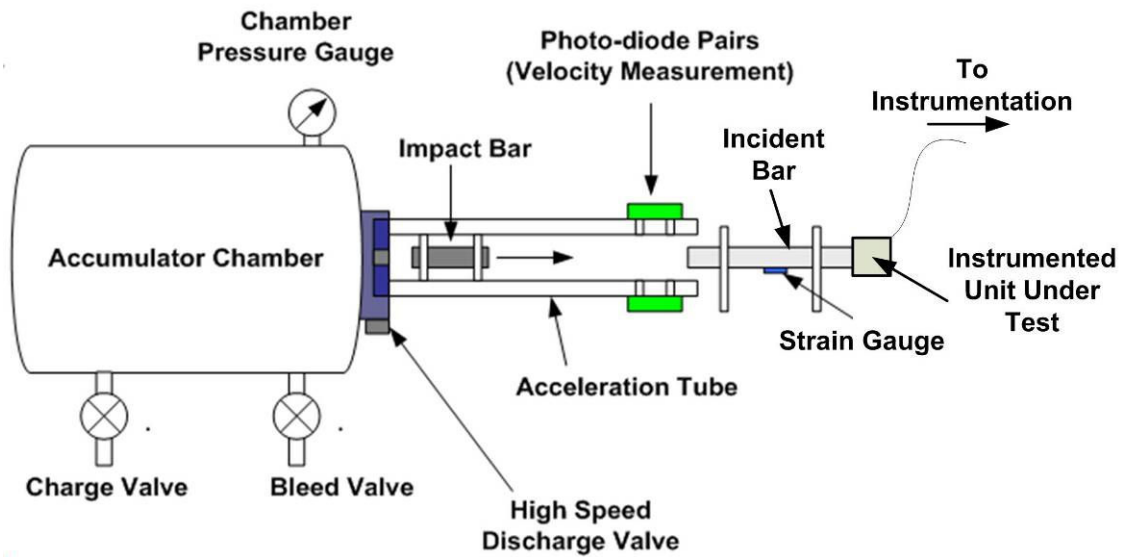


Figure 2.2: Reverse Ballistic Air Gun

The third tool, the drop tower, simply consists of an instrumented platform onto which a projectile is dropped in a controlled fashion from a specified height. Drop towers can be used to collect low velocity impact and shock data using similar sensor devices. An air gun can achieve an order of magnitude higher impact velocity, on the order of  $10^2$  m/s, than a drop tower, on the order of  $10^1$  m/s. A drop tower will typically be used to evaluate impact sensors such as large mechanical g-switches and MEMS accelerometers.

These testing tools are applied to a variety of state-of-the-art impact sensors and energy converters. Fundamentally, all of these sensors operate through the force of

impact causing a strain within the sensing element. The differences in the sensors rest in how the energy is converted into an electrical signal, and how the sensor alters the signal during that process.

## **2.2 Shock/Impact Sensors**

A current state-of-the-art inertial impact sensor, such as that employed in air bag systems and electronic fuzes, is the MEMS-based accelerometer, an example of which is shown in Figure 2.3 [5]. This device generally consists of a proof mass suspended by flexures that are calibrated to give a certain deflection under a given acceleration. State-of-the-art accelerometers for low-frequency applications are MEMS-based that use electrostatic [6], piezoelectric [7], or piezoresistive [8] readout schemes. The output of these devices is sampled by an A/D converter and the shock pulse analyzed for the information of interest, usually shock level, pulse width, power spectral density, and the shock response spectrum. Higher frequency accelerometers are also micromachined but rely more heavily on the output from a micromachined piezoelectric crystal. The bandwidth of these devices can be as high as 100 kHz, as demonstrated by recently available piezoresistive accelerometers, but subsequent signal processing reduces the overall system throughput, increases sensor size, and increases power consumption.

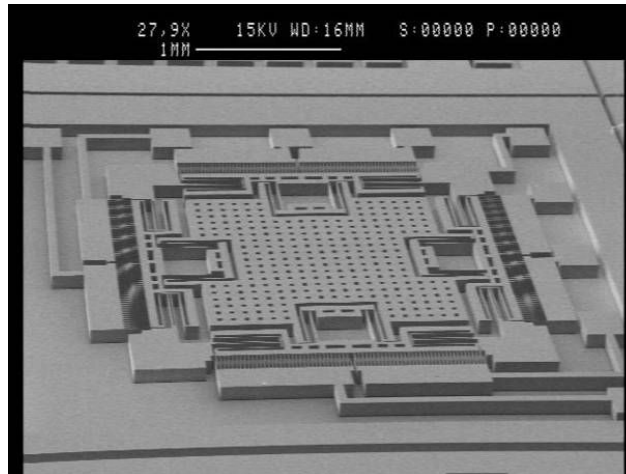


**Figure 2.3: A MEMS-Based Inertial Sensor [5]**

Piezoelectric strain gages and transducers are impact sensors that typically offer higher bandwidth measurements. These devices have also often been used in energy harvesting applications. However, they cannot easily measure low frequency events and require a high-impedance interface that is susceptible to noise. These devices, due to the unique nature of the piezoelectric material, are also often difficult to integrate with other supporting systems.

Piezoelectric strain gages can, however, be used as impact transducers with high bandwidths. These sensors are sensitive to the stress and strain experienced by a mechanical structure, rather than to inertial forces. The charge developed across a piezoelectric film, or the resistance of the silicon strain gage, is proportional to the pressure, or strain, across its surfaces, with this pressure being developed by the impact force. Silicon strain gages are available as small as 300 microns in width. Micromachined strain gages have been demonstrated that and are often integrated directly into other devices, such as pressure sensors and accelerometers, to measure the strain developed in those devices by the parameter being sensed. Quartz gages, and other gages fabricated from bulk piezoceramic, such as lead zirconate titanate (PZT), have been utilized in impact sensing systems, and are common transducers in acoustic emission systems.

These devices, however, do not survive some of the high-strain levels seen in high-speed impact scenarios.

Some applications do not require the continuous shock waveform measurement capability provided by accelerometers and piezoelectric materials. Instead, they only require knowledge that a specific shock threshold has been met. To address these applications, various g-switch mechanisms and devices have been demonstrated for impact sensing. MEMS shock sensors [9] have been demonstrated that do not utilize quiescent power, but that mechanically latch at predetermined shock levels. These devices have a small footprint and very little power consumption, but sacrifice information including spectral data.

The work presented in this thesis advances the state-of-the-art by realizing electret-biased sensors for acoustic emission and impact sensing. These polymer-based sensors are easier to integrate into sophisticated impact sensing systems, while providing performance levels similar to piezoelectric based transducers.

A common configuration for a piezoelectric or electret film uses parallel electrodes over a surface area,  $A$ , across which a stress,  $\sigma$ , is applied, leading to charge separation,  $q$ . The charge separation seen in piezoelectric films and electret films, respectively, under an applied stress as seen in Figure 2.4 is given by:

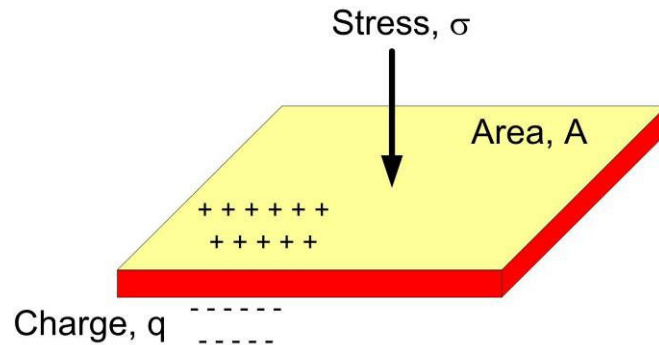


**Figure 2.4: Common Configuration for Piezoelectric or Electret Active Films**

$$q = d_{33} A \sigma \quad (1)$$

$$q = \frac{\epsilon V}{E t^2} A \sigma \quad (2)$$

In the piezoelectric film (1), the piezoelectric constant,  $d_{33}$ , predicts the film response of this configuration. For Aluminum Nitride (AlN) and Zinc Oxide piezoelectric films, the piezoelectric constants are 2.2 pC/N and 14.7 pC/N, respectively [10]. For a polymer electret (2), the equivalent sensitivity is defined by the dielectric constant of the film,  $\epsilon$ , the voltage the film is charged to,  $V$ , the bulk modulus of the dielectric material,  $E$ , and the thickness of the film,  $t$ . For an 18 $\mu$ m thick Teflon film charged to a surface potential of 600V, the equivalent sensitivity is 33 pC/N, which is comparable to that of piezoelectric materials. In addition, the strength of AlN is 2000 psi [11], compared to 3900 psi for Teflon [12]. At high levels of stress, AlN will shatter, whereas Teflon will plastically-deform, not necessarily representing failure of the sensing element. Furthermore, piezoceramic materials require sintering temperatures above 800°C for final processing. This makes integration with electronics and other MEMS structures difficult. Polymer electrets would only require a low-temperature cure of less than 200°C and a low-temperature corona charging step of less than 80°C.

Electret film sensors also allow a second configuration (Figure 2.5). The electret film possesses a large stable static voltage across its surfaces. It can therefore be utilized as a voltage bias in a capacitive sensor arrangement. This is how the electret is utilized in the electret microphone [29]. In this arrangement, as the top electrode of the capacitor moves, a current of

$$i = V_{bias} \frac{dC}{dt} \quad (3)$$

flows from the top electrode through a load, resulting in  $V_{out}$ . This arrangement is beneficial for many sensors because of the large static voltage that can be trapped on the electret. The large voltage contributes to a large sensitivity. It is also beneficial because no external power is required to maintain that bias voltage during sensor operation.

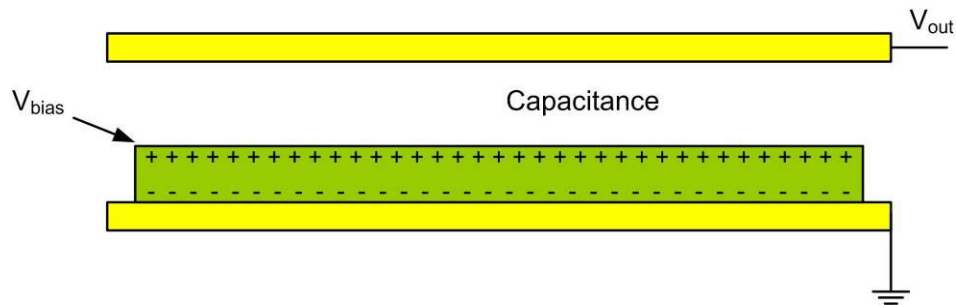


**Figure 2.5: Electret as a Voltage Bias**

In summary, certain applications exist in the fields of impact sensing and of energy harvesting that need the spectral and broadband information available from standard accelerometers and strain gages, but with the footprint and self powered nature of g-switches and piezoelectric sensors. Electret-biased sensor arrays can address some of these needs.

### **2.3 Mechanical Spectrum Analysis**

For impact and vibration measurements requiring spectral information, such as in condition monitoring systems looking for specific vibrational frequencies in malfunctioning equipment, researchers have investigated alternatives to the traditional sampled accelerometer and digital signal processor. The traditional approach, although very flexible in terms of spectral range and resolution, results in a device footprint and power consumption that can be too large for some space-constrained applications.

One alternative approach is mechanical spectral analysis, and employs a single mechanical resonator, or filter, to select one specific frequency within the shock and vibration event. To capture an entire spectrum of frequencies, an adjustment is made to the mechanical structure to alter its natural frequency such that it can be swept over the frequency range of interest. A device has been demonstrated in which a standard MEMS accelerometer with voltage feedback is operated with an extra AC signal present in the feedback [13]. This signal implements a voltage-controlled gain within the accelerometer and can be used to select a particular frequency in the incident shock and vibration signal. By sweeping this voltage, a spectral output can be achieved. Thus, spectral analysis can be realized in a very small footprint without the need for digital signal processing and its volume and power consumption.

An alternative approach to mechanical spectral analysis is that of an array of tuned mechanical resonators, each of which responds to a particular range of frequencies dependent on the quality factor of the structure [14],[15]. This is similar to the use of filter banks in electronic spectrum analyzers. By monitoring each detector within the tuned array, the spectral content within the vibration can be ascertained in parallel. This results in high signal-to-noise ratios and fast spectrum capture, but with sacrifices in functionality, flexibility, and footprint.

## **2.4 Acoustic Emission Signal Processing**

The processing of impact signatures has traditionally consisted of power spectral density and shock response spectrum calculations. The shock response spectrum is the output of an array of second-order systems, each with a different natural frequency, to the input source function. This approach has traditionally been performed through sampling an accelerometer or strain sensor, running that sampled waveform through a digital signal processor, and analyzing the resulting shock response spectrum. Signal processing has

primarily consisted of timing activities whereby specific impact events can be distinguished.

Acoustic emission technology has also traditionally employed a sampled transducer [16], with the resulting waveform processed in a digital signal processor, as seen in Figure 2.6, where a transducer converts elastic wave energy into electrical current that is then amplified, filtered, digitized, and processed in a computer or similar system [17]. One processing method used by conventional AE systems is to count the number of AE events above a specific threshold to acquire a measurement of the energy released by the event.

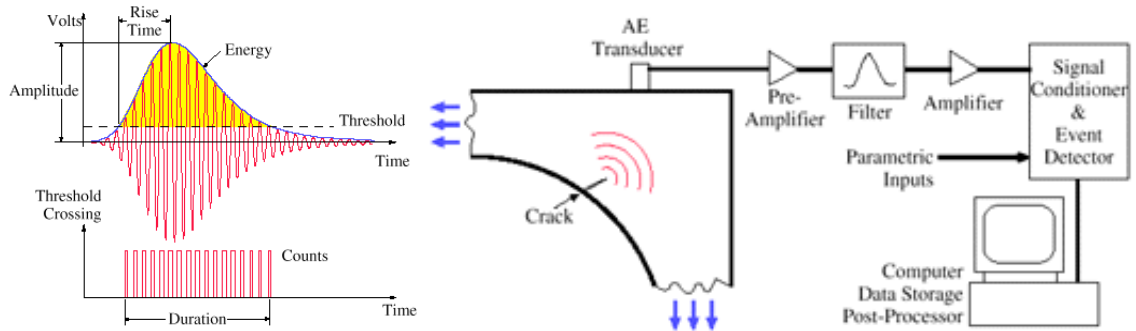


**Figure 2.6: Typical Acoustic Emission Setup [18]**

Multiple signal processing techniques have been applied to AE signatures to identify features of the source of the acoustic emission. In general, the output from the AE transducer is a convolution of the acoustic emission source function, propagation function, and transducer function. One goal of acoustic emission work has been to extract the source function and correlate it with a specific type and magnitude of acoustic emission event [19]. Both time-domain and frequency-domain deconvolution techniques have been applied to extract the source function [20]. Wavelet Transforms have also been applied to AE signals for identification of source characteristics [21].

These signal processing techniques have been applied to the identification of a wide variety of source functions. Buttle and Scruby [22] described using AE time-domain deconvolution techniques for the analysis of particle impacts to a structure, particularly impact angle and elasticity, for purposes of monitoring erosion. Carson and Mulholland [23] used AE techniques, and particularly acoustic emission spectra, in conjunction with impact models to perform particle sizing in chemical processing.

The work described in this thesis extends the state-of-the-art by developing the capability to perform spectral processing of acoustic signals using arrays of micromechanical structures. The objective is to determine impact source function characteristics without requiring sampling of a waveform and subsequent digital signal processing. In contrast to the previous work in mechanical spectrum analysis, this work performs the processing using arrays of frequency-selective transducers.

## **2.5 Energy Harvesting**

Previous work in energy harvesting is important for the research presented in this thesis because of the need to minimize power consumption for the mechanical spectrum analyzer for its intended applications in unattended sensor packages and other energy constrained systems. Energy harvesting has been investigated for power generation in wireless sensor nodes and other devices that operate in regimes in which changing or charging batteries is infeasible. Multiple energy harvesting schemes have been demonstrated, with the majority extracting energy from either solar power or external vibrations, and with the distinguishing characteristic being the method of energy transduction.

In general, a vibration scavenger consists of a large proof mass suspended through some means and allowed to couple with the external environment. The vibrations result in displacements of the proof mass against some restoring force. The work applied

against that force results in energy conversion. Vibration scavengers have been demonstrated using electrostatic, magnetostatic, and ferroelectric means.

A magnetic generator has been demonstrated [24] that utilizes a magnet suspended by a cantilever beam in such a way as to alter the magnetic flux through a nearby coil as the magnet moves. Piezoelectric generators [25] have been shown that utilize piezoelectric beams undergoing strain as a result of proof mass deflection. Electrostatic generators have also been demonstrated [26] in which charge is placed across a capacitor with one side of the capacitor being connected to the proof mass. The resulting motion creates a displacement current through a load. AS will be discussed later, Electrostatic energy harvesters have been also designed that use electrets, or permanently polarized dielectrics.

With some exceptions, these energy harvesters have been designed for steady-state sinusoidal vibration inputs. In particular, the energy conversion is maximized at the resonant frequency of the proof mass and suspension system, making them quasi-narrowband converters. In addition, the conversion efficiency for broadband pulse and shock inputs is not well characterized [27].

## **2.6 Electret Integration with MEMS**

Electrets are materials that have a quasi-permanent electrostatic polarization. The challenge with integrating these structures into MEMS devices is that a common charging method, corona-charging, requires access to the film, and as such, needs to be performed prior to MEMS fabrication. Most electrets are also polymer-based, and as such, need to be processed at low temperatures, thereby adding to the integration challenges.

Electret technology is widespread in the form of the electret condenser microphone (ECM) [28]. The electret microphone, Figure 2.7, typically consists of a thin metal diaphragm attached to a metal ring that has been separated from a back electrode

by a thin polymer electret spacer. The electret film provides a high electrostatic potential difference of typically 600V across the air gap between the diaphragm and back electrode. This electrostatic potential difference is much higher than that available in a normal battery-powered portable application, making the electret microphone two orders of magnitude more sensitive, for portable applications, than a simple capacitive microphone.

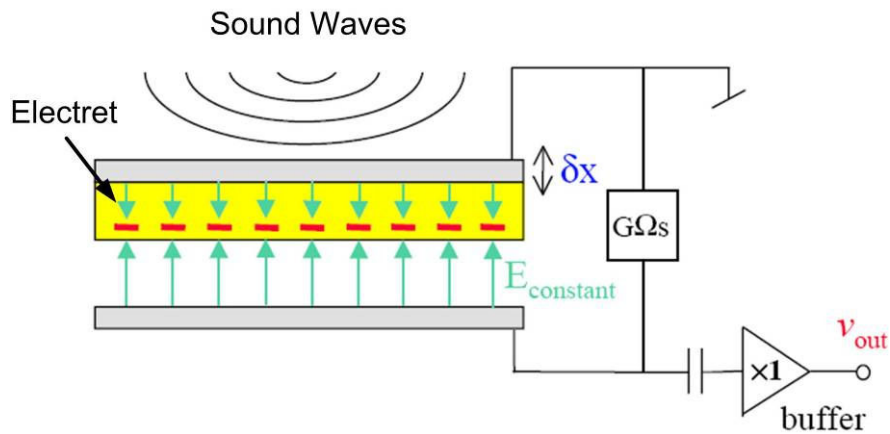


**Figure 2.7: Schematic Electret Condenser Microphone Operation [28]**

The electret in the ECM is a polymer ring stamped from sheet of polymer material that had previously been polarized through a corona-discharge. The components of the ECM; the electret, diaphragm, and back electrode, are distinct items assembled in the later production phases through a process, Figure 2.8 [29], of stacking, aligning, and crimping inside a metal canister or fixture that holds the stack in place. In the final assembly, a small transistor or other amplifier is soldered to the back electrode and pins are attached to the canister.

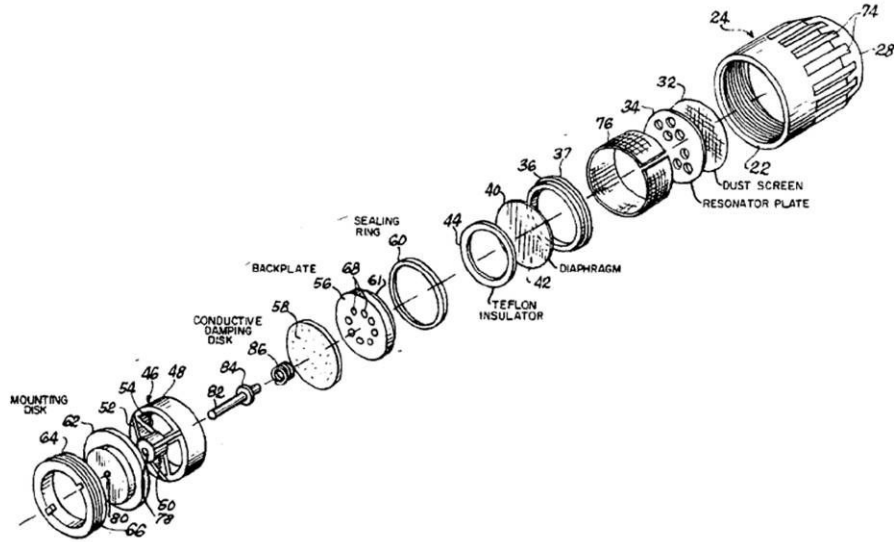


**Figure 2.8: Typical Electret Microphone Assembly [29]**

Recent work has demonstrated electret fabrication and machining processes in the development of a MEMS-based electret condenser microphone [30], Figure 2.9. The work used Teflon AF, an amorphous spin-castable Teflon material, as the electret material. The work fabricated the MEMS ECM in a fashion analogous to standard fabrication approaches, but with the smaller structures provided by microfabrication technology. The process flow was broken up into two major process sequences. One process sequence fabricated a MEMS diaphragm analogous to the metal diaphragm of the standard ECM. The second process sequence fabricated a back electrode with an integrated electret film, charged through a Back-Lighted Thyatron (BLT) process, Figure 2.10. The final step in the process consisted of a wafer bond to assemble the two components together into a functional device.

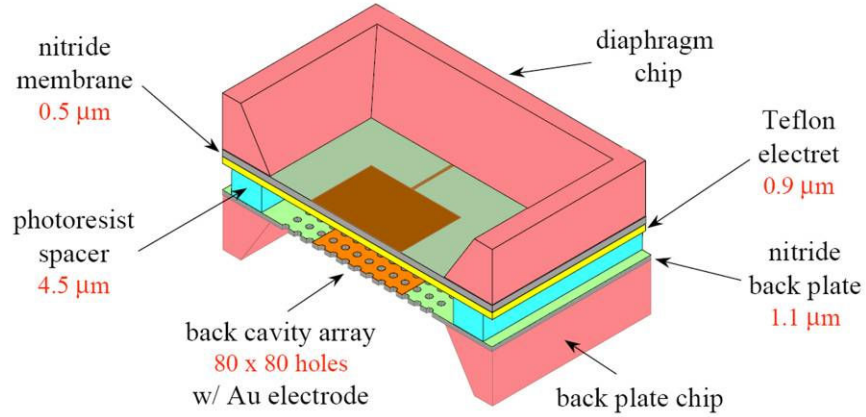


Figure 2.9: A MEMS-Based Electret Condenser Microphone [30]

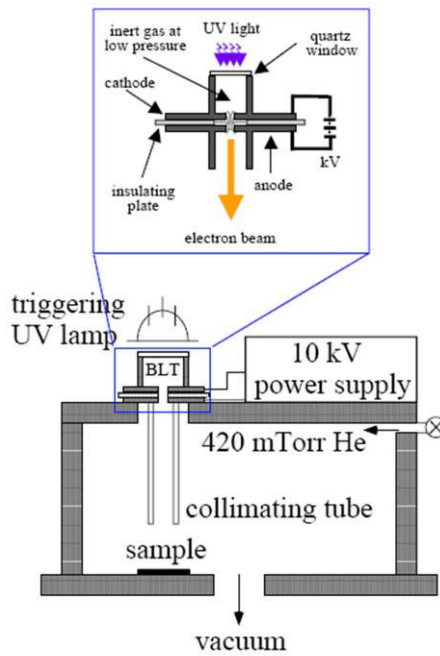
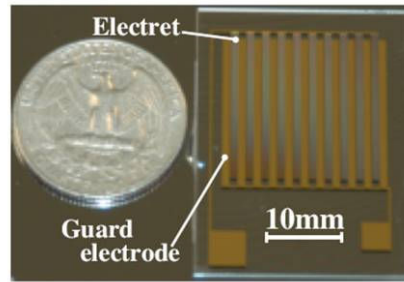


Figure 2.10: Back-Lighted Thyraton (BLT) Electret Charging [30]

Other recent electret developments are aimed at micromachining the electret materials to realize energy scavenging devices for long-term power production in low-power MEMS sensors and other devices. The electret in these cases provides a high electrostatic potential difference against which inertial forces developed from external vibrations can act and produce current, and hence power output. The large electrostatic

potential developed in an electret provides higher volumetric conversion efficiency than similar capacitive scavengers, and utilizes materials that are easier to integrate than piezoelectric-based energy scavengers.

The research in one energy scavenging device, Figure 2.11, focused on patterned electret material [31], [32] wherein the lateral variation of the electric field across the surface of the electret is coupled with vibrational motion to achieve power production. The device uses a Teflon-like polymer film, with the brand name of CYTOP, for the electret material. The film was charged through triode corona-charging techniques, as shown in Figure 2.12. Prior to charging, the CYTOP was patterned and etched to realize a varying electric field after charging. Motion against this electric field generates current in the moving electrode.



**Figure 2.11: Patterned Electret with a Lateral Variation of the Electric Field [31]**

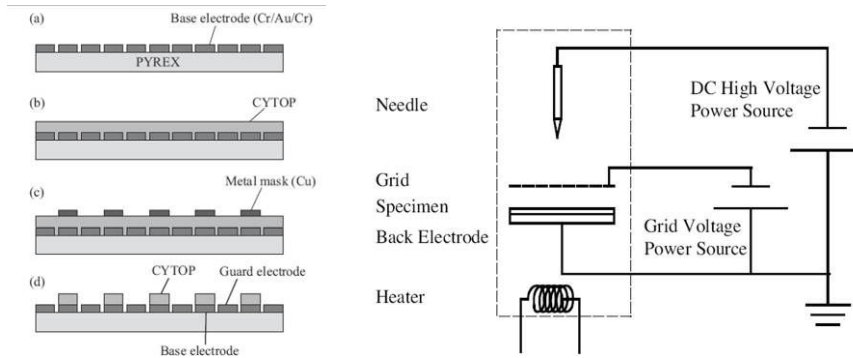


**Figure 2.12: Patterned Electrets Realized with Patterned Films [31]**

This previous work demonstrated the fabrication of the patterned electret, as well as measured surface charge densities. A fully assembled electret scavenger has not been demonstrated. However, for testing purposes, the fabricated electret was placed in close proximity to a counter electrode that was attached to a vibration stand, as shown in Figure 2.13. The current generated by the counter electrode was captured and used to predict the power generating performance of the electret film.

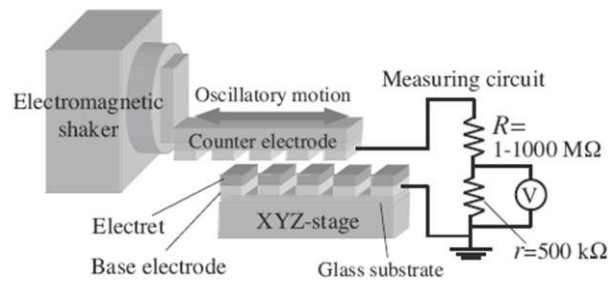


**Figure 2.13: Patterned Electret Films Generate Current from Lateral Motion [32]**

Other work has described and modeled an electret energy scavenger based on vibrational motion of a micromachined mass suspended above an electret film [33], as shown in Figure 2.14. The electret created a potential difference across two electrodes that would subsequently be in relative motion.

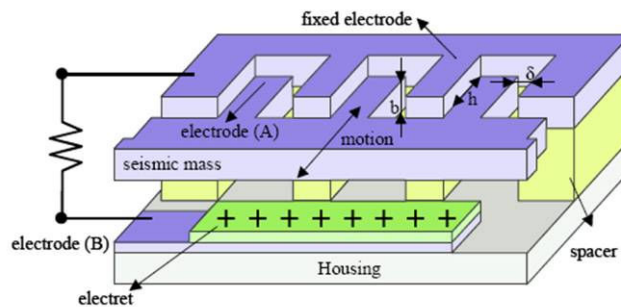


**Figure 2.14: Electret Film Creates an Electrostatic Potential across an Air Gap. [33]**

It was envisioned that integrating an inorganic Nitride/Oxide electret into this device, as opposed to the more common polymer electret structure, would allow a wafer-bonding approach to electret integration. The inorganic electret would then also directly serve as a bonding site for the wafer bonding steps.

The work presented here, however, aims at extending the integration of electret technology into MEMS by removing the need to perform wafer bonding as one of the final steps of assembly. This is beneficial because wafer bonding adds additional complexity to the overall process flow. Wafer bonding requires complex alignment steps as well as highly uniform pressures across the full wafer. In addition, for wafer bonding with electret features, a very low-temperature bonding process is required. Anodic and fusion bonds would result in electret discharge. Only low-temperature epoxy or polymer bonds could be employed, and these are typically weak and difficult to control.

Two methodologies for electret integration are explored in the work presented in this thesis. One methodology realizes electret films using *in situ* charging processes performed after device fabrication, thereby allowing the uncharged electret films to be integrated into the full process flow and charged after process completion. A second methodology uses electret films that maintain charge during fabrication steps so they can, again, be integrated into the full process flow.

## **2.7 MEMS-Based Coronas, Plasmas, and *In Situ* Charging**

Many current research efforts are investigating a variety of plasma and ionization processes and techniques for use at the microscale. There is a great variety of efforts in this area, with some being applicable to the problem of electret polarization within a MEMS device, and some efforts directly addressing the problem.

Researchers at the University of Texas [34] have explored micro corona discharges to create a torque on the rotor of a micro motor. In the motor (Figure 2.15), a

sharp stator electrode and a circular rotor form a point-to-plane electrode geometry similar to a standard corona discharge. The resulting corona ionizes the working gas and deposits charge on the surface of the rotor. That charge and the electric field lead to a repulsive force at the rotor surface, resulting in a torque. This work used a 1 micron tip diameter with a 50 micron gap to achieve corona formation.

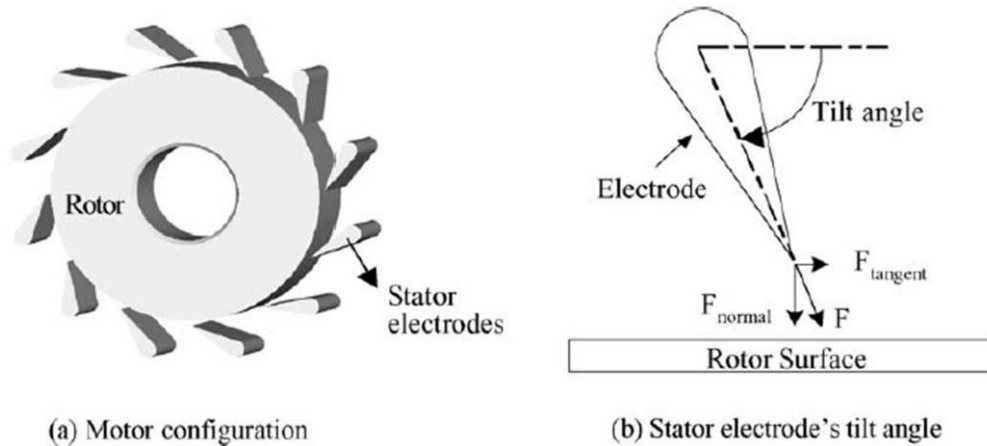


**Figure 2.15: Micro Corona Motor [34]**

Microcoronas and DC microplasma discharges have also been investigated by researchers for ionization of gaseous species in chemical analysis and for *in situ* etching processes and surface modification. Researchers at the University of Wisconsin have demonstrated *in situ* etching of silicon within a structure using a DC microplasma [35], and demonstrated up to 17 micron/min etch rates using  $\text{SF}_6$  as the working gas. In the device, two electrodes separated by a high strength dielectric are placed at a large voltage on the order of a 400V. The plasma is generated at the edge of the electrodes, thereby allowing the rest of the electrode to serve as a mask for the etching process. Figure 2.16 shows an electrode arrangement with a circular pattern in the center that leads to a circular etch into the underlying silicon substrate.

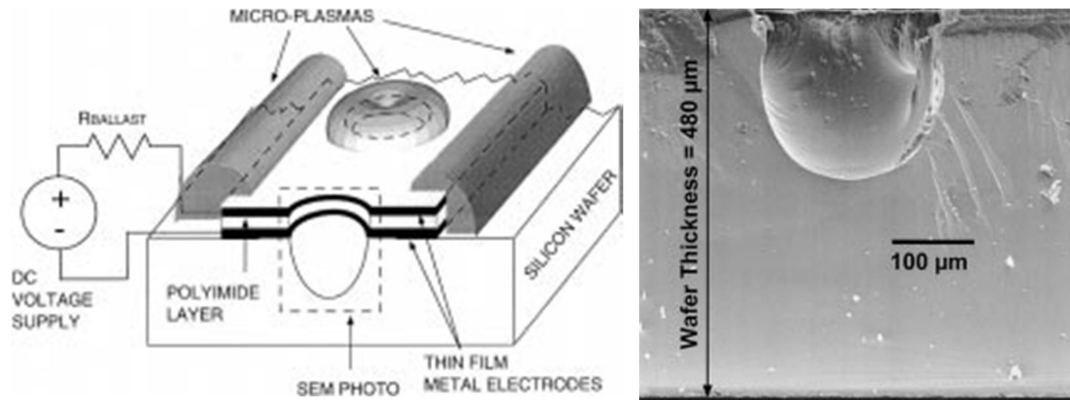


Figure 2.16: Microplasma for *In Situ* Silicon Etching [35]

Actual *in situ* polarization of electret material within a structure after fabrication has been demonstrated by the University of Tokyo using soft x-rays as the ionization source [36]. In the arrangement shown in Figure 2.17, an electret material is deposited on the vertical sidewall of a MEMS structure. The gap between the electrodes is filled with air that, upon being irradiated with soft x-rays, is ionized. The positive and negative species repel each other, leading to deposition of the charge on the vertical sidewalls. This process can be performed even through barrier materials as long as the soft x-rays can penetrate to the gap. Researchers have demonstrated surface potentials on the order of 100's of volts using this technique. The charging time is dependent on the x-ray flux, however, requiring strong sources of soft x-rays. However, the process has demonstrated the ability to charge vertical electrets within the MEMS structure, making it useful in a number of geometries.

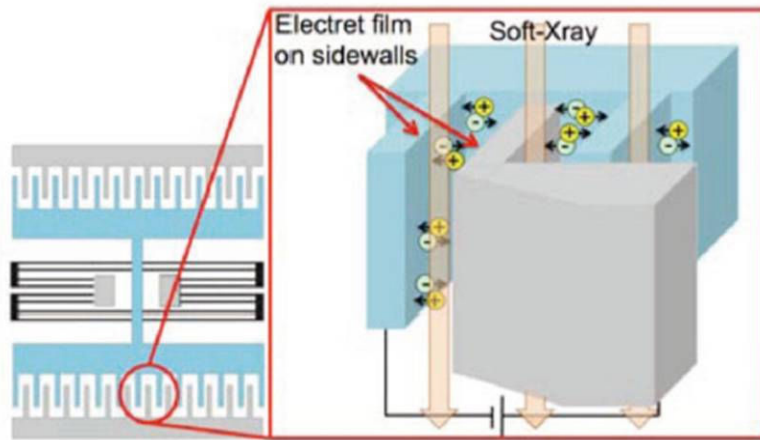


Figure 2.17: *In Situ* Soft X-Ray Charging of Electret [36]

The integrated electret work presented in this dissertation utilizes microplasma discharges such as those used in the micro motor, gas ionization, and *in situ* silicon etching described above to perform an *in situ* electret charging function similar to what was achieved using soft x-rays as the ionization source.

## **CHAPTER 3 - RESONANT ARRAY PROCESSING**

The research presented in this dissertation utilizes arrays of resonant microstructures in the analysis of acoustic and ultrasonic signals, and particularly those due to impacts between two materials of different stiffness. The analysis leads to methods for classifying the material impacting the sensor. This chapter discusses the physics of impacts, the characteristics of ultrasonic stress pulses developed from them, how to create idealized pulses in a test apparatus, the response of arrays of resonant structures to those pulses, and how to utilize that response in classifying the interacting materials.

### **3.1 Impact Source Analysis**

The objective of this research is to demonstrate an electret-biased sensor array in the processing of acoustic signals from impact events to classify the hardness of the material being impacted. Therefore, the stress pulses generated from an impact, as well as the responses from the array of sensors, need to be modeled and predicted.

This section presents idealized models for the stress pulses that are created during an impact scenario and that can be recreated with actual devices and test hardware in a controlled environment. This will allow prediction and interpretation of sensory array response, as well as verification that the final fabricated sensor array can sufficiently process acoustic data and provide a hardness classification for the impact. The impact geometry is based on ball-to-plane contacts, allowing the application of Hertzian contact theory to the prediction of stress pulses for different materials used in the impact [37]. This impact scenario is also simple to implement in a controlled laboratory environment and test apparatus for array characterization.

### 3.1.1 Ball-on-Rod Impact

Critical to the characterization and calibration of the transducer array response is the creation of known stress pulses with varying frequency content. Multiple methods exist for the creation of ultrasonic stress pulses. The Split-Hopkinson bar [4] is used to create very high strain rate pulses through the impact of rod face with rod face. This theoretically leads to infinitely fast rise times, with pulses that are square in nature, and with the amplitude of the pulses being related to the elastic moduli of the interacting materials. In practice, however, items such as Poisson's ratio, surface roughness, impact angle, and plastic deformation lead to smoothing of the shock pulse edges [39]. These items are hard to control at slower velocity impacts, leading to inconsistent pulse rise times. In addition, the desire was to create stress pulses that were Gaussian in nature.

To realize consistent pulses, this work used a conventional ball drop [38] as the primary source for stress pulses launched into the sensor array. The use of the ball drop realized approximately Gaussian shaped pulses that were consistent in nature. Using a ball drop reduced variations due to position and angle of impact because of the symmetrical nature of the spherical surface. In addition, since the risetime and pulsewidth of the ball drop is controlled by the radius of curvature and modulus of the interacting materials, different shaped stress pulses can be achieved in a controllable manner.

The stress pulse created by a ball drop has been analyzed in past work [39] and is heavily dependent on Hertzian contact theory and its assumptions. The key difference between ball-on-plane contact when compared to plane-on-plane contact is that the interaction area increases during the interaction, and is therefore more analogous to a mass-spring system impacting the planar surface (Figure 3.1), with the mass being that of the ball and the spring being that of the mutual deformation of the two surfaces. This leads to stress pulses of substantially longer time period than that of a rod of similar linear dimension. Plane-on-plane impact would be similar to the limiting case of Hertzian contact as the radius of curvature goes to infinity.

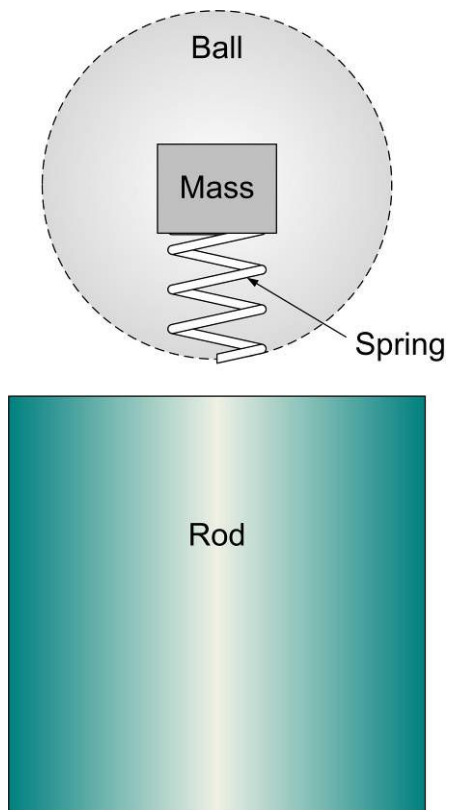


**Figure 3.1: Mass Spring Impact on Face of Rod**

The geometry for the derivation of ball-on-rod impact is shown in Figure 3.2.

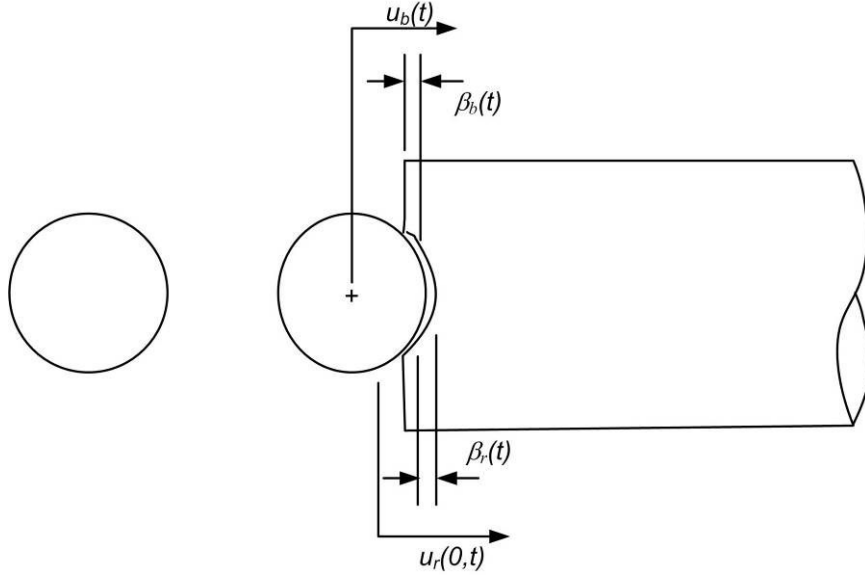


**Figure 3.2: Ball-on-Rod Impact Geometry**

In this arrangement,  $u_b$  refers to the displacement of the center of the ball, and  $u_r$  refers to the displacement of the rod.  $\beta_b$  and  $\beta_r$  are the local deformation of the ball and rod, respectively. In order for the surfaces to remain in contact,

$$u_r(0,t) + \beta_r(t) = u_b(t) - \beta_b(t) \quad (4)$$

must apply. The “approach”,  $\alpha$ , is then defined by

$$u_b(t) - u_r(0,t) = \beta_b(t) + \beta_r(t) = \alpha(t). \quad (5)$$

The differential equation governing the impact is

$$\frac{d^2\alpha}{dt^2} + \frac{Kc_o}{AE_r} \frac{d\alpha^{\frac{3}{2}}}{dt} + \frac{K}{m_b} \alpha^{\frac{3}{2}} = 0. \quad (6)$$

In this governing differential equation, in which wave effects within the ball are ignored, the coefficients are  $K$ ,  $c_o$ ,  $A_r$ ,  $E_r$ ,  $m_b$ :

$c_o$  = Speed of sound in rod

$A_r$  = Cross-sectional area of rod

$E_r$  = Elastic Modulus of rod material

$m_b$  = Mass of the ball

with

$$K = \frac{4}{3\pi} \frac{R^{\frac{1}{2}}}{k_r + k_b}, \quad (7)$$

and where  $R$  is the radius of curvature of the ball.  $K$  is then a function of

$$k_r = \frac{1 - \nu_r^2}{\pi E_r} \quad (8)$$

and

$$k_b = \frac{1 - \nu_b^2}{\pi E_b}, \quad (9)$$

where  $\nu_r$  and  $\nu_b$  are Poisson's Ratio for the rod and ball respectively, and  $E_r$  and  $E_b$  are the elastic moduli for the rod and ball respectively.

The initial conditions define the approach at time  $t = 0$  and the velocity at time  $t = 0$ , as

$$\alpha(0) = 0 \text{ and } \dot{\alpha}(0) = V_o. \quad (10)$$

The differential equation must be solved numerically for  $\alpha(t)$ . The contact force is then related to the approach by

$$F = -K\alpha^{\frac{3}{2}}, \quad (11)$$

and the propagated stress pulse is then given by

$$\sigma(x, t) = \frac{1}{A} F(c_o t - x) = E\varepsilon(c_o t - x). \quad (12)$$

The following tables list the material properties used in predicting the width of the stress pulse using the above relationships. It is this varying pulse width that is detected and processed by the MEMS sensor array, with shorter pulsewidths having higher frequency content than larger pulse widths. The various materials and radii of curvature were selected based on availability and the speed of sound propagation. The sensor array is ultimately attached to an Alumina flat disc, which is therefore used as the rod material in the above equations. Its properties are given in Table 3.1.

**Table 3.1: Material Properties of the Alumina Rod**

Property	Variable	Value
Elastic Modulus (GPa)	$E_r$	315.0
Poisson's Ratio	$\nu_r$	0.21
Density (kg/m <sup>3</sup> )	$\rho_r$	3690
Speed of Sound (m/s)	$c_o$	9240
Diameter (m)		0.019 (3/4" Diameter)
Area (m <sup>2</sup> )	$A_r$	$2.85 \times 10^{-4}$

Four different materials were selected for the balls. Their properties are listed in Table 3.2. These materials are selected for analysis so as to cover a range of frequencies.

**Table 3.2: Material Properties for Ball Drop Sources**

Property	Variable	Silicon Nitride	Stainless Steel	Acrylic	Teflon
Elastic Modulus (GPa)	$E_b$	345	200	3.5	0.5
Poisson's Ratio	$\nu_b$	0.24	0.285	0.37	0.3
Density (kg/m <sup>3</sup> )	$\rho_b$	3180	8055	1200	2200
Speed of Sound (m/s)	$c_o$	10416	4982	1708	478
Radius (m) (1/2" Diameter)	$R$	0.00635	0.00635	0.00635	0.00635
Drop Height (m)	$h$	0.625	0.625	0.625	0.625
Velocity (m/s)	$V_o$	3.5	3.5	3.5	3.5
Mass (g)	$m_b$	3.475	8.476	1.268	2.309

Through numerically solving the governing differential equations, a typical contact force is calculated for a 1/2" silicon nitride ball impact on an alumina plane, and shown in Figure 3.3. The stress pulse is Gaussian-like, not truly Gaussian. The other material sources lead to similar shaped stress pulses, but with different amplitudes and pulsewidths.

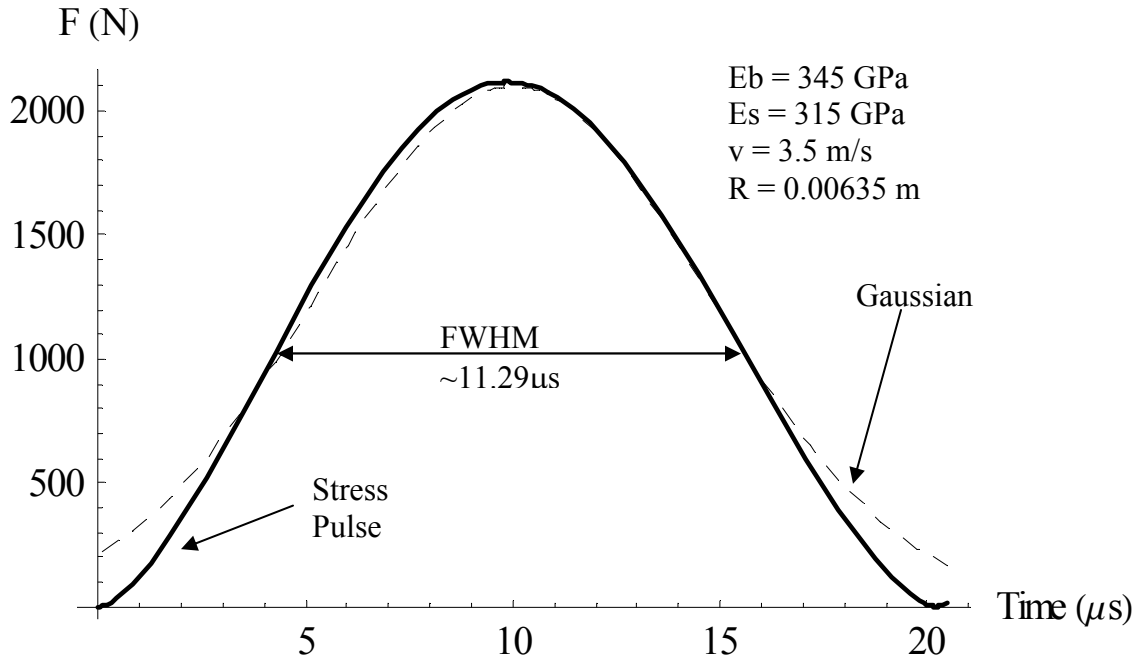


**Figure 3.3: Stress Pulse Generated from Silicon Nitride Impact on Alumina Rod**

Stress pulse waveforms were calculated for the other materials using the above parameters, and led to the calculation of the full width half max (FWHM) pulsewidths listed in Table 3.3.

**Table 3.3: Pulsewidths from Ball Drops of Different Materials**

<b>Material</b>	<b>E (GPa)</b>	<b>FWHM (μs)</b>
Silicon Nitride	345	11.29
Type 302 Stainless Steel	200	18.14
Acrylic	3.5	33.78
Teflon	0.5	74.79

These waveforms are the idealized source functions that will be applied to the sensor array after fabrication. A few features need to be noted regarding these impacts and the dependence on the materials, geometries, and velocities involved in the interaction. Most notably, the duration of the stress pulse, which determines its maximum

frequency content, is very sensitive to the elastic modulus of the two materials. This is beneficial to impact discrimination. However, the radius of curvature of each material involved in the impact also plays a significant role, as does the velocity of impact. Therefore, these characteristics of the impact need to be either controlled, measured, or removed.

For a Gaussian stress pulse, which the ball drop stress pulses approximate, the Fourier Transform is also Gaussian. For a Gaussian stress pulse described by

$$f(t) = Ae^{\frac{-t^2}{2\sigma^2}}, \quad (13)$$

the Full Width Half Maximum (FWHM) of the pulse is

$$t_{FWHM} = 2\sqrt{2\ln 2}\sigma \approx 2.3548\sigma. \quad (14)$$

The non-unitary angular frequency Fourier Transform of the pulse is then

$$f(x) = A\sigma\sqrt{2\pi}e^{-\frac{1}{2}\sigma^2\omega^2}. \quad (15)$$

Finally, the -3dB point, where the spectrum is half of its maximum, is given by

$$\omega_{3dB} = \frac{2\sqrt{2\ln 2}}{\sigma} \approx \frac{2.3548}{\sigma} \quad (16)$$

Figure 3.4 and Figure 3.5 show the pulsewidth dependence on the elastic modulus of the ball for a radius of curvature of ½ inch and a velocity of 3.5m/s. Potential materials

used in this work are also plotted in the figure. However, since this figure assumes a constant density of  $3180 \text{ kg/m}^3$  while varying elastic modulus, the pulsewidths for a particular material will not necessarily lie directly on the plot.

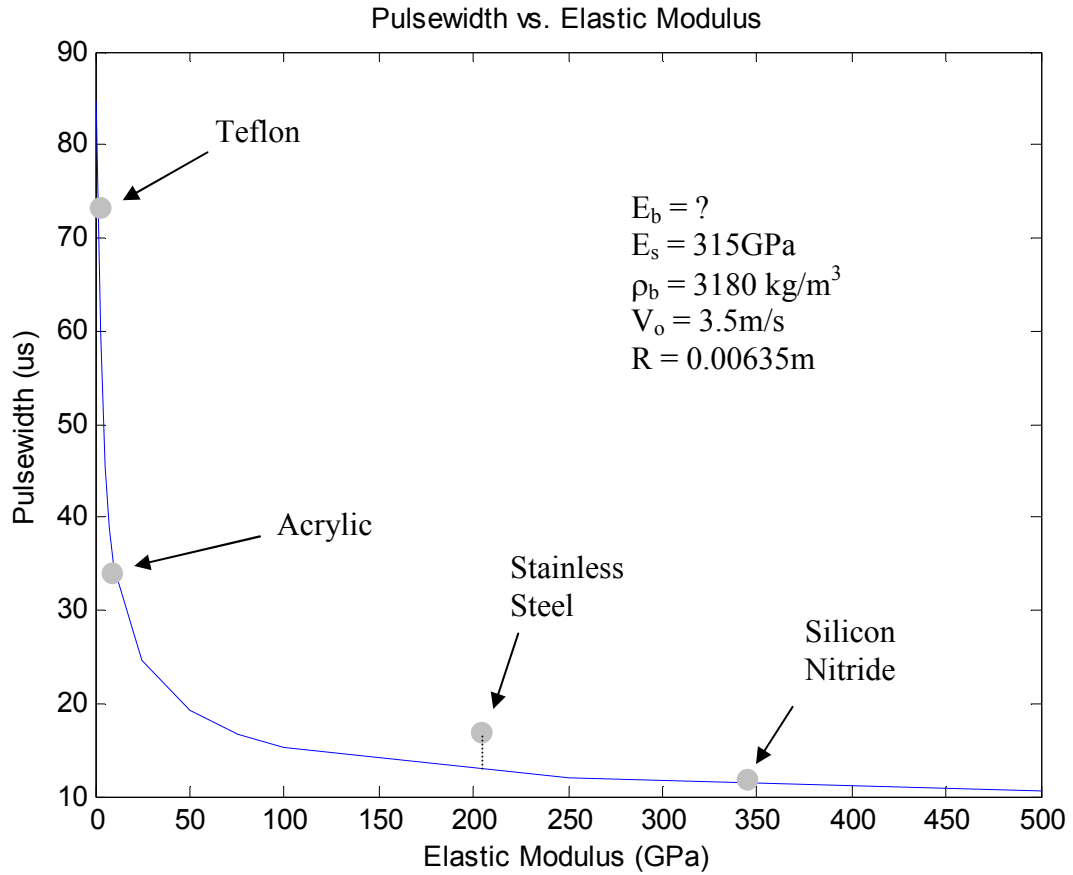
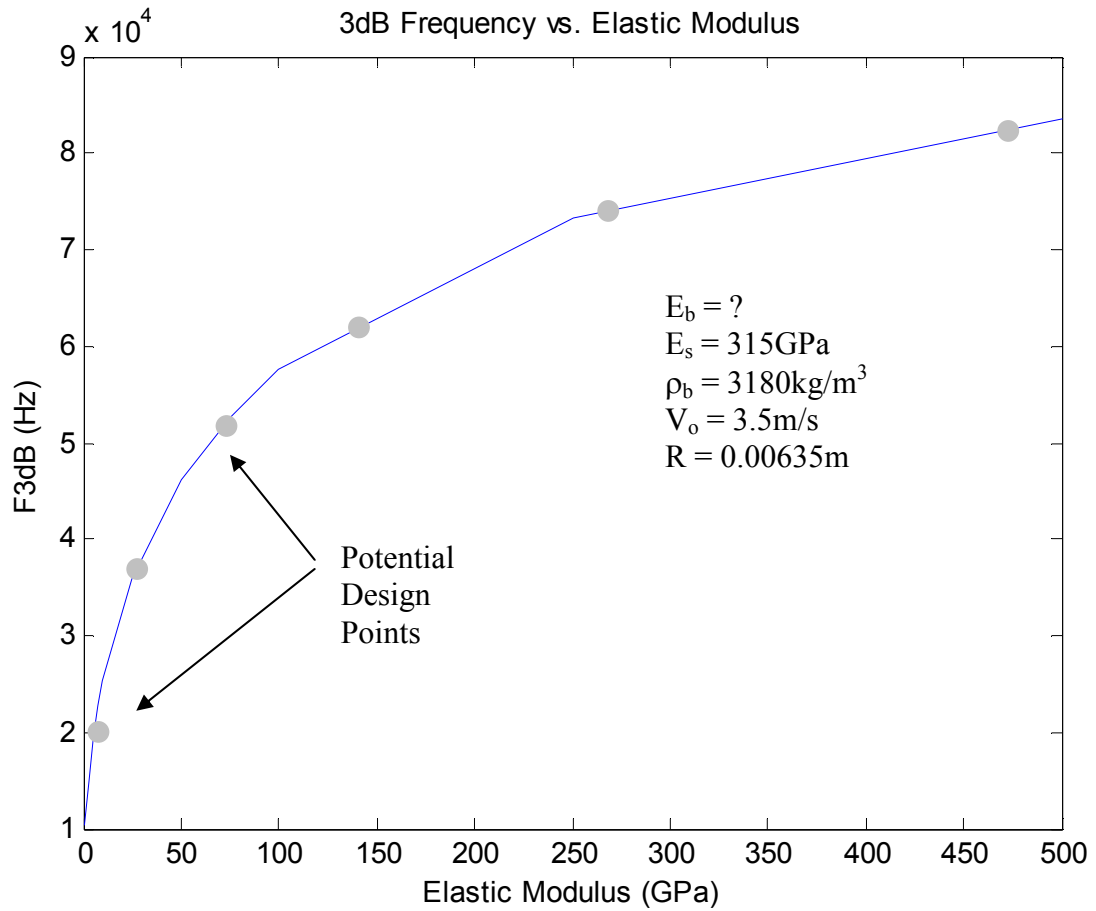
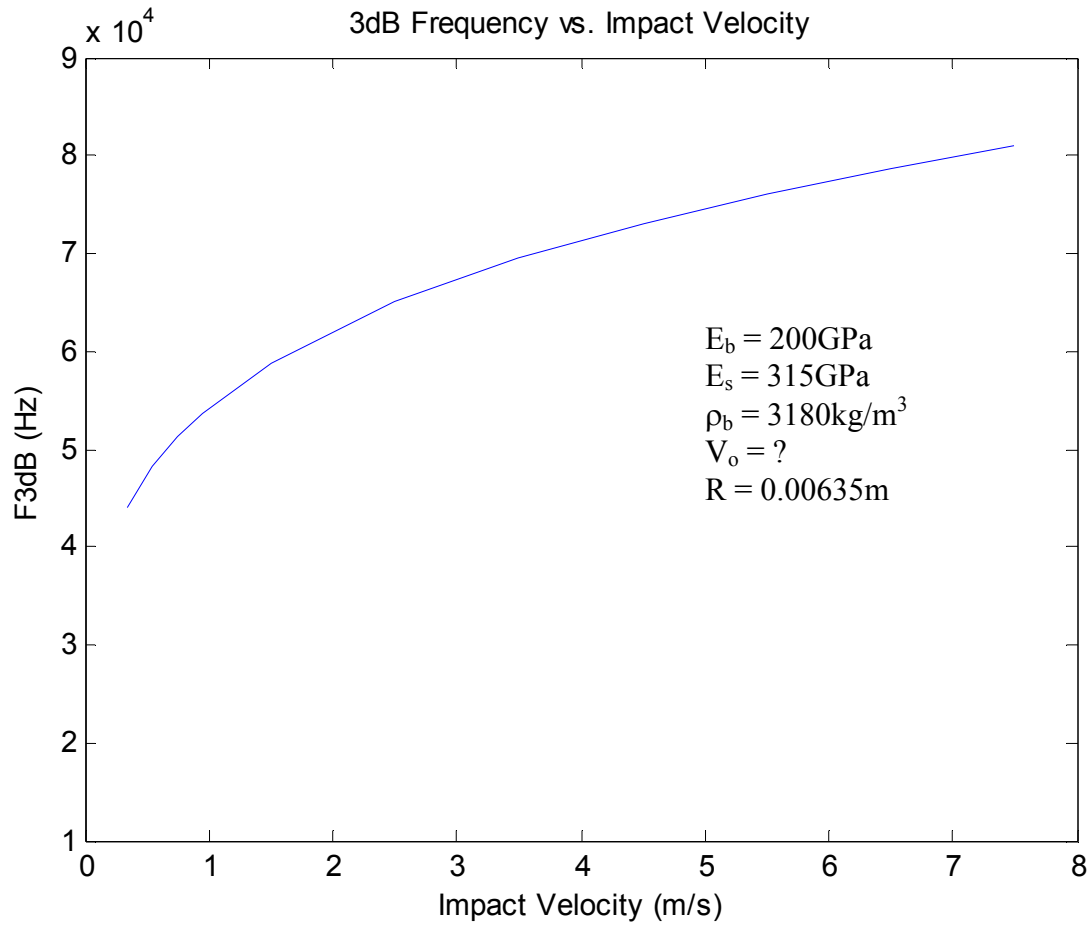


Figure 3.4: Dependence of Pulsewidth on Elastic Modulus of Ball



**Figure 3.5: Dependence of  $f_{3db}$  on Elastic Modulus of Ball**

The frequency contact in the stress pulse also has a dependence on impact velocity, although a weaker dependence, as shown in Figure 3.6 for a ball with an elastic modulus of 200GPa and a diameter of  $\frac{1}{2}$  inch.



**Figure 3.6: Dependence of  $f_{3\text{dB}}$  on Impact Velocity of Ball**

Finally, the frequency content is also dependent on the radius of curvature of both the ball and the face of the rod. Figure 3.7 shows the dependence of the 3dB frequency for a ball with different radii of curvature, and an elastic modulus of 200GPa, impacting on a flat surface at 3.5m/s.

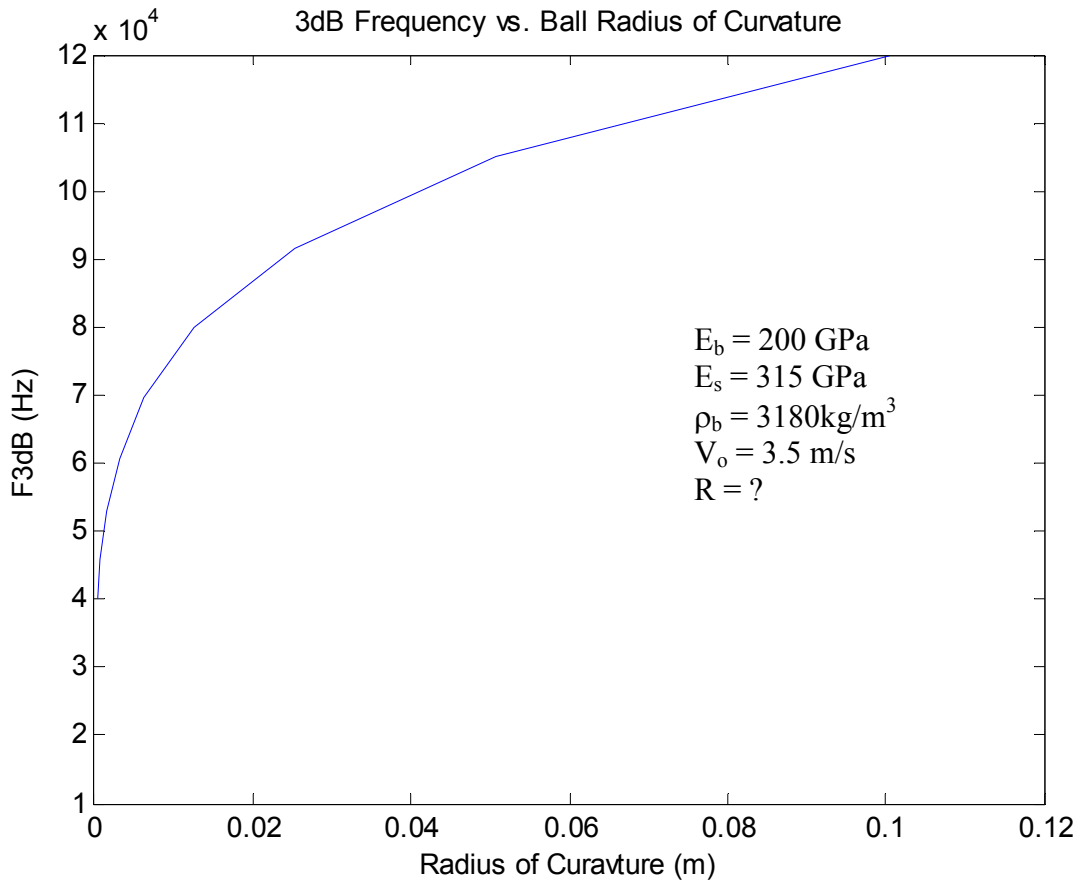


**Figure 3.7: Dependence of  $f_{3db}$  on Ball Radius of Curvature**

The frequency content in the stress pulse is therefore more dependent on the radius of curvature than the impact velocity. Fortunately, the radius of curvature is easier to control in that it is a geometrical factor set by design. Velocity of impact will be a variable in impact scenarios, and will need to be either controlled or measured.

### 3.1.2 Ball-on-Plate Impact

The analysis so far has been for a ball impact on an infinitely long rod with a flat face. However, actual sensor geometry would be a plate-like structure such as a disk or a cone, as a long rod would be impractical for many applications. The spatial length of the

acoustic pulse will be greater than the structure's thickness, and will therefore be modified by the reflections within it. A time-domain mechanical event simulation based on finite element analysis was performed in Algor Multiphysics to investigate this response and the local displacements seen by the transducer array due to different impacts on a cone with a flattened tip. The outputs from the FEA are then input into a behavioral simulation in Matlab/Simulink to predict the response of the sensor array under these different impacts

The distance over which the ball falls in normal gravity during a time period,  $t$ , is given by

$$x = \frac{1}{2}gt^2 . \quad (17)$$

The time it takes the ball to drop from height,  $x$ , is found by rearranging as

$$t = \sqrt{\frac{2x}{g}} . \quad (18)$$

Then, the velocity,  $v$ , that the ball has reached after that time, for a 2" drop, is

$$v = gt = \sqrt{2xg} = \sqrt{2(5 \times 10^{-2})9.8} = 0.99 \frac{m}{s} . \quad (19)$$

Figure 3.8 shows the finite element model of a ½ inch sphere impacting on the face of a short cone with a flat tip. The model is axisymmetric, so only the positive  $y$  portion of the model is drawn. The analysis assumes a 360° revolution of this model, significantly reducing simulation time. The cone is hardened A4620 Annealed Steel. The

sphere was either Stainless Steel or Teflon. The sphere was given an initial velocity of -1m/s, which is equivalent to a drop from about 2 inches, as calculated earlier.

In the FEA model, the sphere was placed at an initial distance of 100 $\mu$ m from the surface of the cone. This was to minimize the number of time steps required prior to actual impact. A nonlinear mechanical event simulation was then performed for a 2ms duration and a 1 $\mu$ s timestep. The duration was selected to be outside the low end of the range of interest, with 2ms corresponding to about 500Hz. The 1 $\mu$ s timestep was selected to capture signals faster than the 100 kHz maximum of interest. The simulation resulted in 2000 data points, with each data point storing a full spatial distribution of stresses, strains, and displacements. The marker in Figure 3.8 shows a particular node of interest. The stress and displacement were recorded for this nodal point.

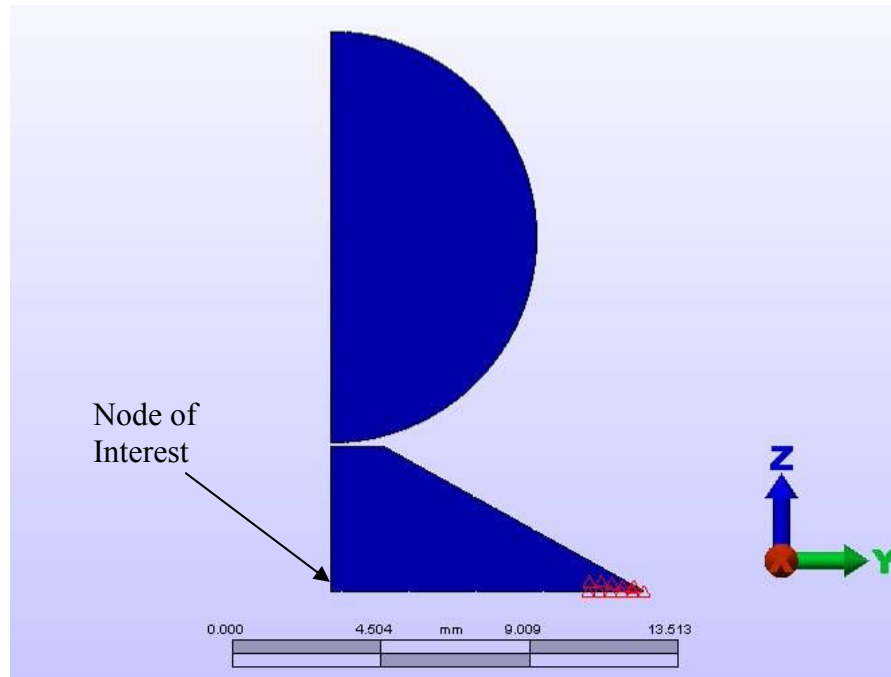


**Figure 3.8: FEA of Ball Drop**

Figure 3.9 shows the predicted displacement of the selected node as a function of time when a Teflon sphere is used to impact the cone. The overall pulsewidth is determined by the material properties, impact geometry, and impact velocity as described earlier, and matches well with the analytical model. However, upon impact, an acoustic wave is launched into the cone and another one is launched into the sphere. After the wave reaches the other side of the sphere and cone, all of the particles reach a new velocity. The acoustic wave then reflects at the interface with air. After that wave reaches the bottom of the sphere, the entire sphere has slowed down, and a portion of the cone has increased its velocity. This series of reflections occurs both in the ball and in the cone as the ball velocity is reversed and moves away from the cone. The acoustic wave reflections are seen as the ringing in waveform riding on top of the basic pulse.

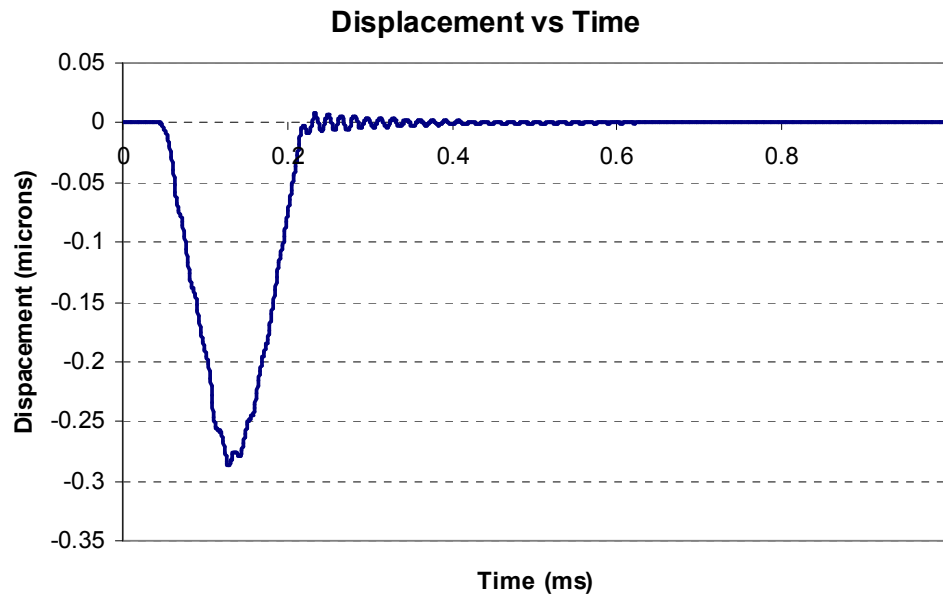


**Figure 3.9: Nodal Displacement - Teflon Ball Drop**

Figure 3.10 shows the same nodal displacement, except that the impacting sphere is now steel. The pulse width is dramatically narrower. In addition, both the pulse

amplitude and the ringing are significantly higher because of the much larger energy in this sphere.

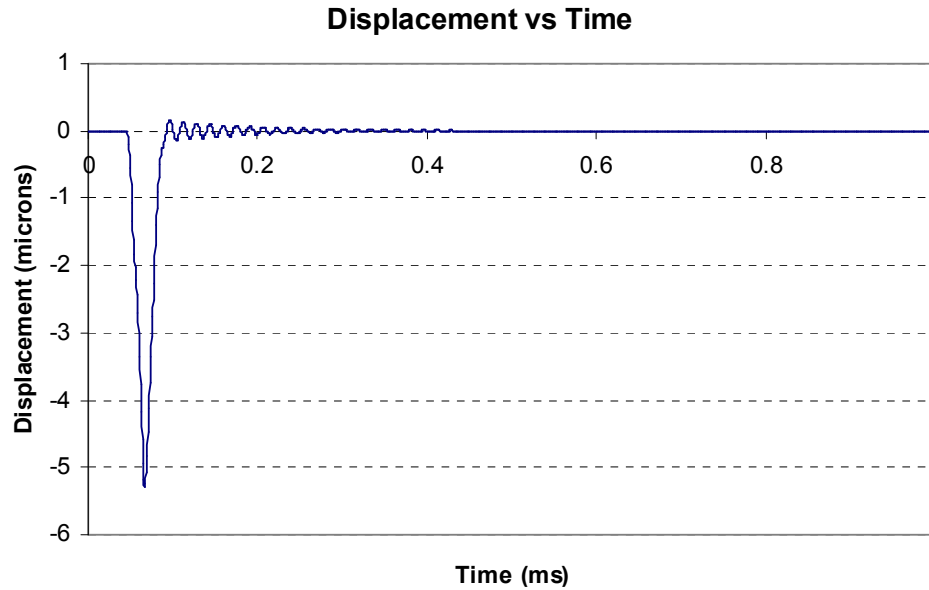


**Figure 3.10: Nodal Displacement - Steel Impact**

Both impacts show the excitation of the cone from the impact. A small amplitude ringing waveform with a frequency of about 60 kHz is seen after the primary pulse. That waveform is the excitation of the cone's fundamental mode by the impact. This is an additional signal that will be seen by a sensor array, and could alter conclusions drawn from it. Therefore, it is beneficial to have the natural modes of the structure on which the sensors are attached moved to outside the band of frequencies seen by the sensors themselves.

If these stress pulses are applied to a sensor array with elements that have different natural frequencies, each element will respond differently. In order to excite an element into damped harmonic oscillation, the pulse needs to contain frequency content (*i.e.* be a sharp enough pulse) higher than the natural frequency of the element. The

displacement pulse due to steel impact is about  $30\mu\text{s}$  wide, corresponding to 3dB frequency of greater than 33 kHz. The Teflon pulse is significantly wider. This would suggest that the steel impact would yield damped harmonic oscillation in transducers with a natural frequency around 33kHz, but that the Teflon pulse would not.

## **3.2 Impact Characterization**

Due to the importance of creating known stress pulses, a ball drop test apparatus was assembled. This section describes the apparatus and the pulses it generated.

### **3.2.1 Ball-on-Rod Impact**

Critical to the research was the ability to characterize the acoustic pulses generated by the various impacts. This was initially performed using an impact on a rod as opposed to the plate that the actual sensor array will be mounted on, as seen in Figure 3.11. The rod separates acoustic reflections in time; thereby allowing capture of single original pulses. Later characterizations were performed with a ball on a plate to more accurately parallel the actual system. Two basic impact sources were used. One was a short slug of material, and the second was a sphere of material. In order to adjust the pulsewidth achieved by impact, one approach used was to place intervening layers of tape on the surface of the flat plane. A second approach to pulsewidth adjustment was to use different materials for the slug or ball.

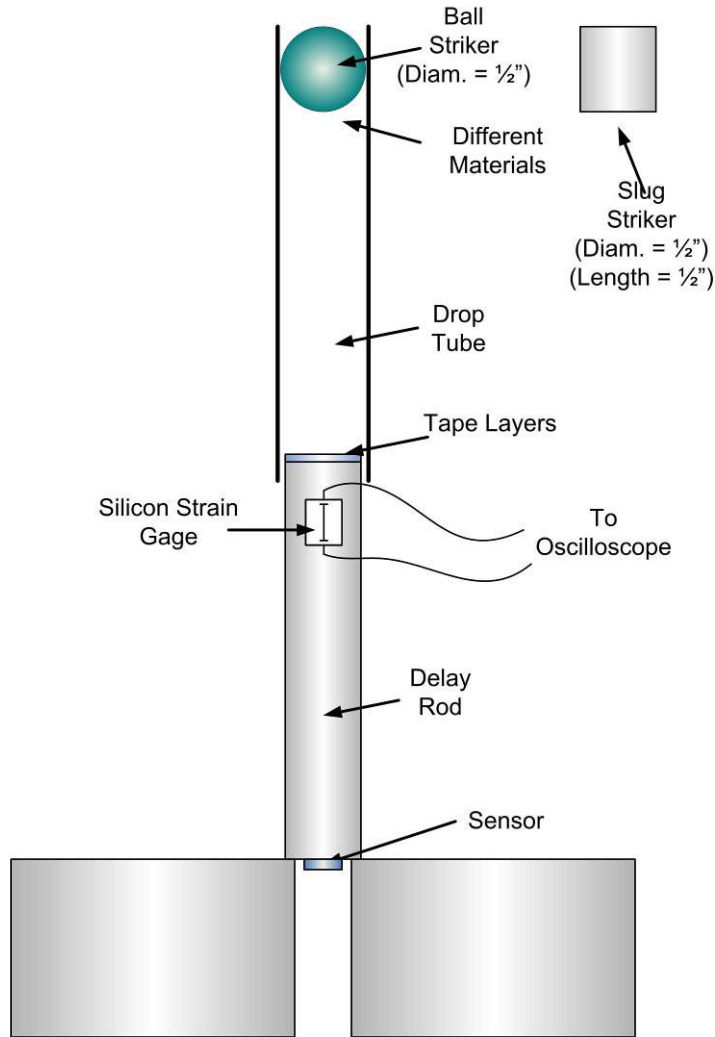


**Figure 3.11: Pulse Characterization Setup**

The rod was made of hardened A2 steel, and was 8 inches long. A strain gage was attached to the impact end of the rod. An optional sensor could be placed at the other end of the rod. An impact on the rod would send a stress pulse traveling down the rod. The pulse first passes by the silicon strain gage and the oscilloscope records the waveform. After approximately  $40\mu\text{s}$ , the pulse reflects off the back of the rod. After another  $40\mu\text{s}$ , the reflected pulse reaches the strain gage. The advantage of the rod configuration is that the reflected pulse is delayed by a total of over  $80\mu\text{s}$ . This allows clean capture of the

incident pulse without corrupting it by reflections within a plate. This approach is similar to the Hopkinson Bar [4] apparatus commonly used for high velocity impacts.

Figure 3.12 shows the stress pulses generated from a steel slug impact on zero, one, two, and three layers of 2-mil thick cellophane tape [40], with the narrowest pulse being zero layers and the longest being three layers. Poor control of the alignment of the slug face to the rod face at the time of impact led to variation in the stress pulses.

Therefore, the preferred impact source was a silicon nitride ball.

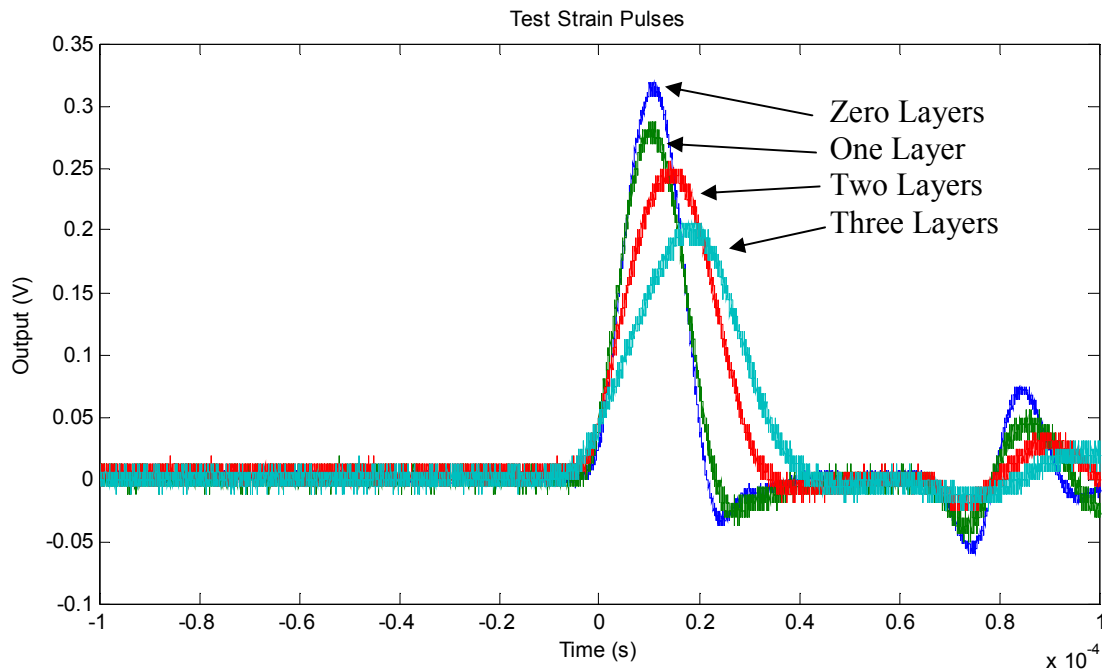


**Figure 3.12: Stress Pulses from A2 Steel on Multiple Tape Thicknesses**

The silicon nitride source had the narrowest pulse width, with the pulsewidth easily controllable in small increments through the use of intervening tape layers. Figure 3.13 shows the stress pulses derived from this set of impacts for zero to 5 tape layers. The shortest pulse is from direct ball-on-rod impact. The FWHM pulsewidth for that impact is approximately 12 microseconds, as predicted from the theoretical analysis performed earlier. The longest pulsewidth is almost 30 microseconds, which is similar to the

predicted impact of an acrylic ball of the same size. The advantage of using the tape layers is that multiple pulsewidths can be achieved between the extremes while maintaining consistent impact energy because the same ball is used for each drop.

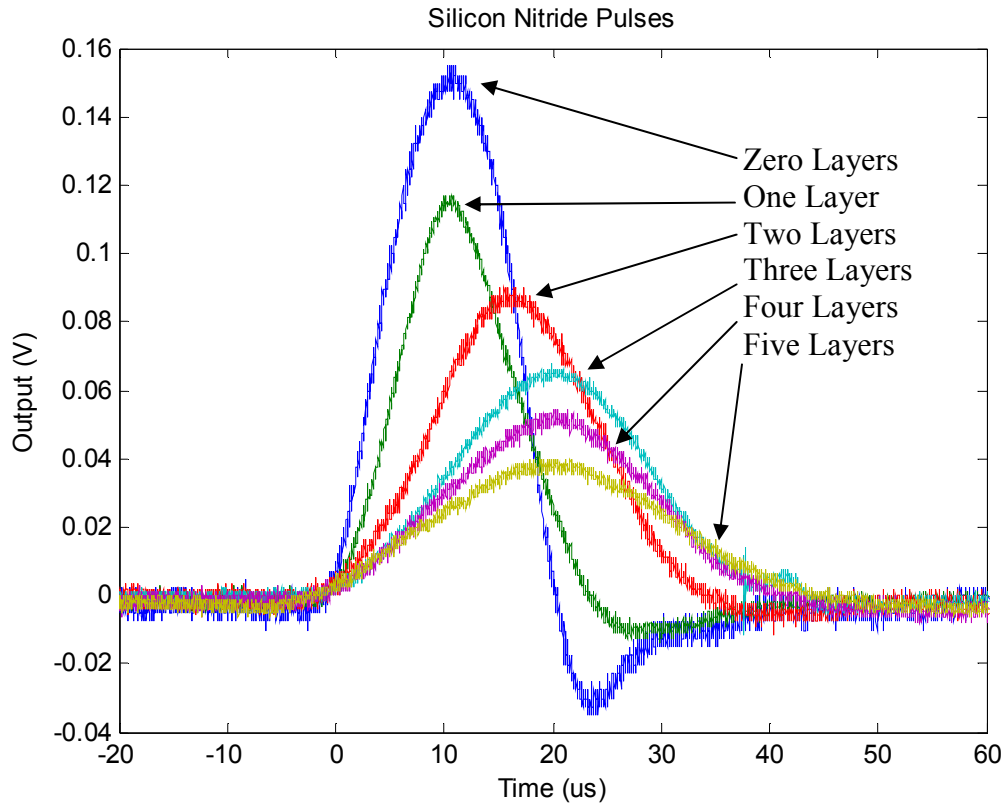
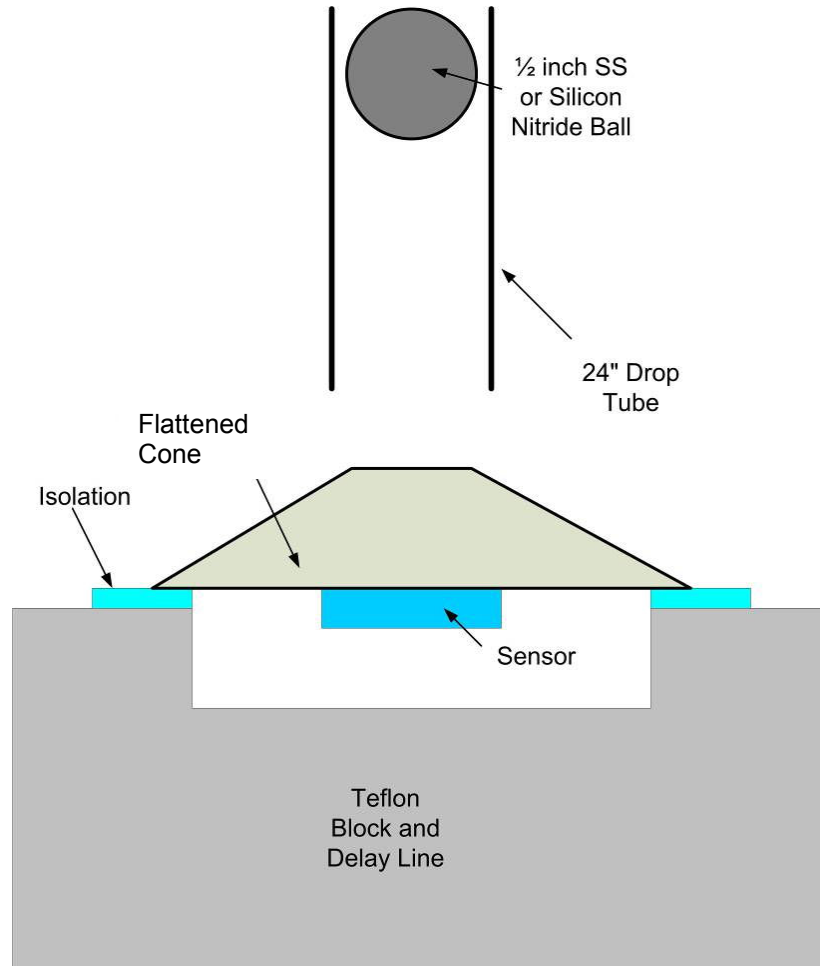


Figure 3.13: Stress Pulses from Silicon Nitride Ball on Multiple Tape Thicknesses

### 3.2.2 Ball-on-Plate Impact

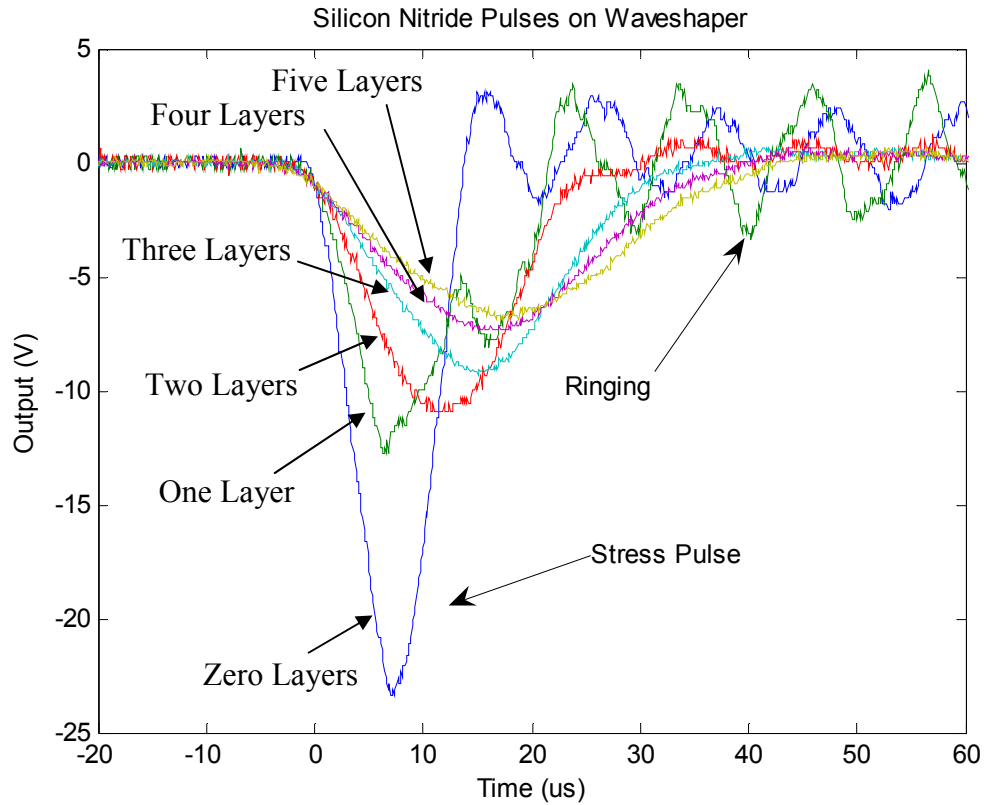
After characterizing the acoustic sources on the bar using a silicon strain gage, the pulses had to be characterized on plate structures that would be similar to what the sensor array would be mounted to. Two plate structures were employed. The first was the hardened A2 steel cone with a flattened tip described earlier. The second structure was a  $\frac{3}{4}$  inch diameter  $\frac{3}{16}$  inch thick 99.9% alumina disc. The primary excited mode of the cone and ceramic disc, as calculated using FEA, are 96 kHz and 133 kHz respectively.

Figure 3.14 shows the setup used to characterize pulses on these plate-like structures. The sensor used during characterization was a broadband PZT disc mounted to the back of the structure. An oscilloscope with a  $1\text{ M}\Omega$  input impedance captured the pulses, as will be seen in Chapter VII. This is the same setup used to capture data from the fabricated sensor array, with the array taking the place of the PZT disc transducer. Two critical components of the ball drop apparatus are the Teflon block and the isolation layer. Through successive drops measuring the amplitude of the reflected pulse seen by the transducer, the thickness of the isolation layer was optimized such that the reflected amplitude was minimized. The Teflon block serves as a time delay like the rod did in the earlier apparatus. The Teflon has a very slow speed of sound, so a one inch thick block provides enough delay to move the reflected pulse out of the timeframe of interest.



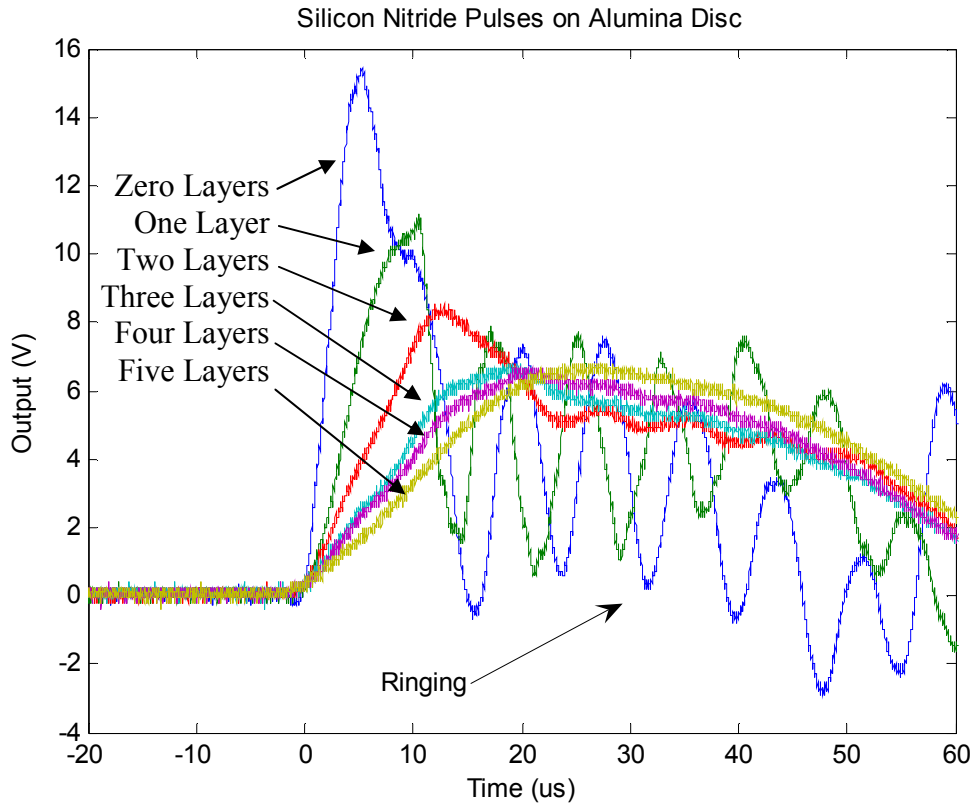
**Figure 3.14: Pulse Characterization on Plate-Like Structure**

Figure 3.15 shows the pulses captured from the Silicon Nitride ball drop on the flattened steel cone with zero to five layers of tape. The inversion is due to the polarity of the PZT sensor attached to the structure. The primary feature that can be seen in these waveforms is as approximately 95 kHz oscillations riding on the pulse. This is the excitation and damped harmonic oscillation of the primary mode of the cone.



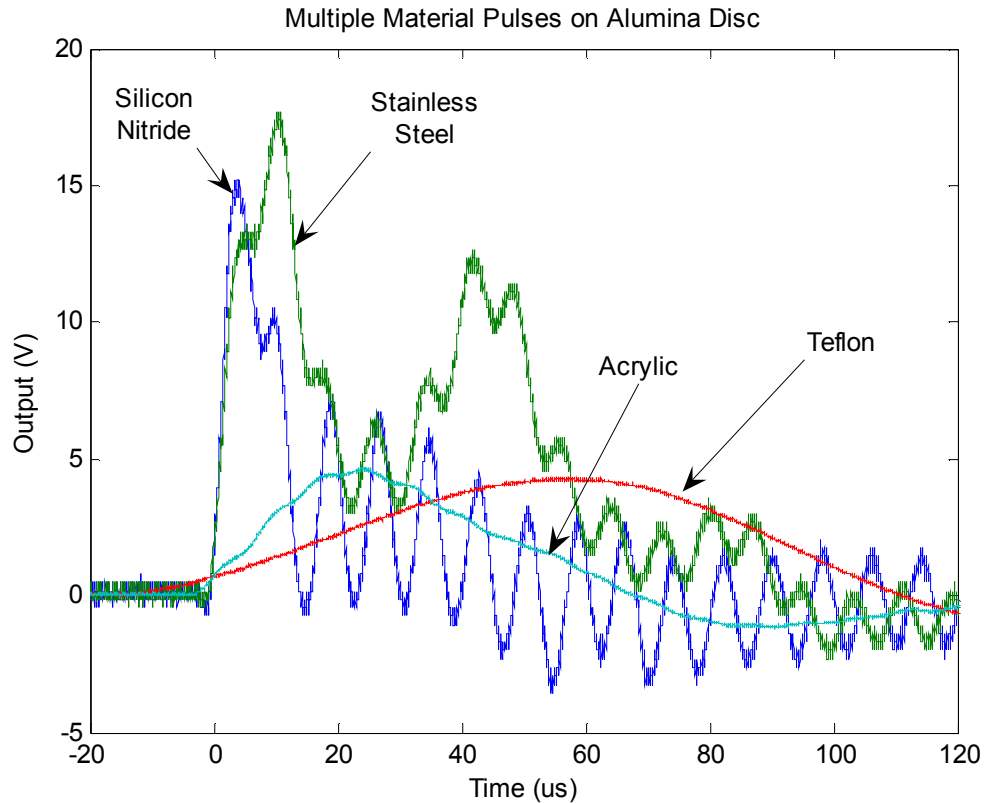
**Figure 3.15: Stress Pulses from Silicon Nitride Impact on Flattened Steel Cone**

Figure 3.16 shows the captured stress pulses from a silicon nitride ball impact on zero to five layers of tape on the alumina disc. The primary item of note is that the ring-down oscillation of the alumina disc is at approximately 130 kHz, as predicted by FEA. As will be seen in Chapter V and Chapter VII, the advantage of the alumina disc is that the ring-down frequency is outside the range of interest of sensors in the fabricated array.



**Figure 3.16: Stress Pulses from Silicon Nitride Impact on Alumina Disc**

Finally, a set of pulses was captured for ½ inch balls of different materials. This is to test the main function of the sensor array, that of determining the stiffness of the material being impacted. Figure 3.17 shows the stress pulses captured under these conditions. Silicon Nitride shows the shortest pulse, followed by stainless steel, then acrylic, then Teflon, as predicted in the theoretical analysis earlier. As will be seen in Chapter VII, these pulses will be input into a sensor array after fabrication and assembly.



**Figure 3.17: Stress Pulses Due to Impacts by ½ Inch Spheres of Different Materials**

After sensor fabrication, these same impacts and stress pulses sources will be inputs into the sensor array, as will be discussed in Chapter VII. The idealized nature of the waveforms allows calibration of the sensor array, and understanding of array operation. Furthermore, these idealized pulses have similar characteristics to realistic pulses, allowing conclusions and predictions to be drawn for sensor arrays operating in actual applications.

### 3.3 Array Response Analysis

The pulses generated from the ball-on-plate impact will travel through the structure and into a sensor array. Each element in the sensor array will respond

differently to that stress pulse according to the dynamics of its design. These elements are second order systems that sense displacement, as shown in Figure 3.18.

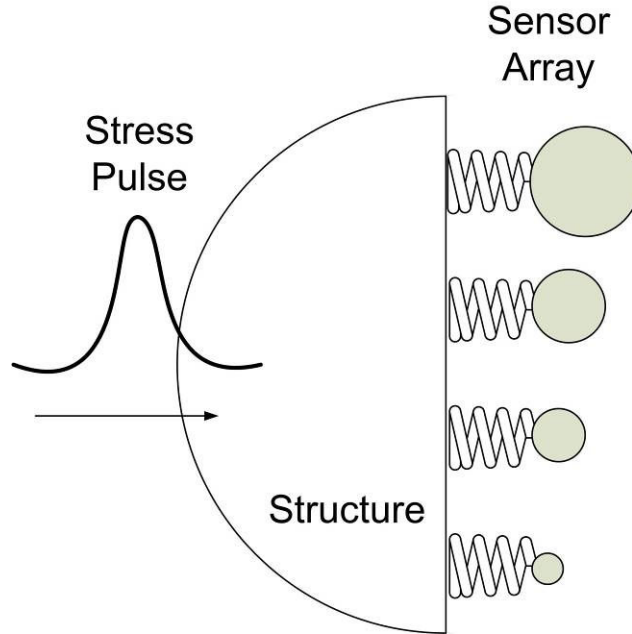


**Figure 3.18: Schematic Representation of Impact on Array**

Figure 3.19 shows a representation of the response, in the frequency domain, of a four-element acoustic sensor array,  $F_i(s)$ , as well as a set of Gaussian source functions with different pulse widths but equal energy,  $U_j(s)$ . Each element of the acoustic sensor array is modeled as an acoustic displacement sensor employing a second-order mass-spring element [41]. The output of the sensor array will be determined by the products of these various spectra,  $H_{ij}(s) = F_i(s) U_j(s)$ .

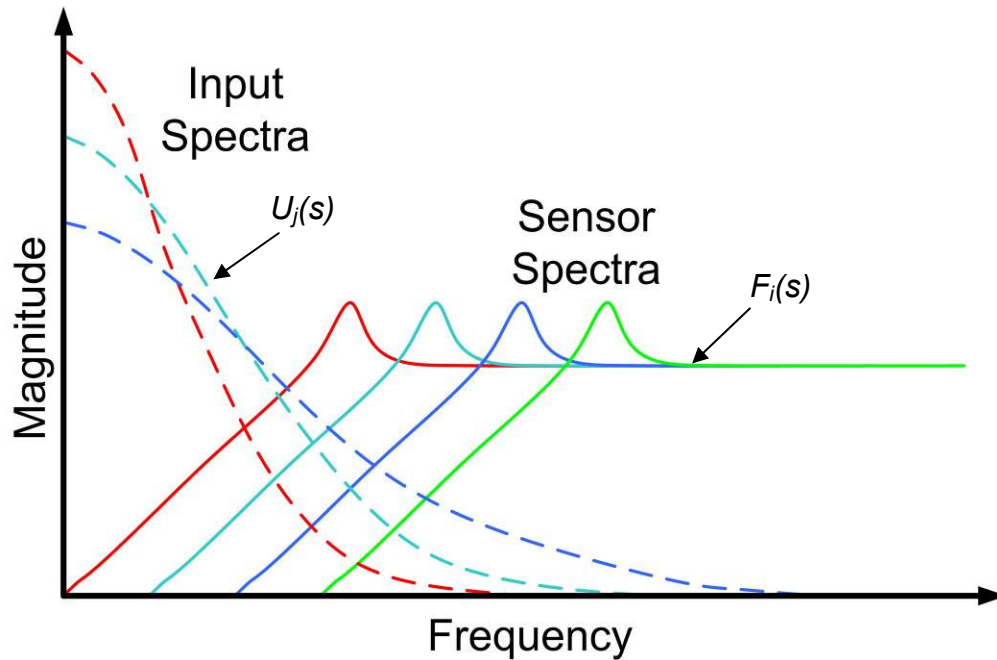


Figure 3.19: Frequency Representation of Input Functions and Sensor Response

### 3.3.1 Gaussian Pulse Frequency Content

Figure 3.20 below shows the calculated frequency response,  $U_j(s)$ , of six Gaussian pulses with varying pulsewidths corresponding to impacts from different materials, as well as the frequency response,  $F_i(s)$ , of ten resonant sensor structures equally spaced from 10 kHz to 100 kHz. The Gaussian sources do not correlate exactly to the actual materials used as impact sources later in this work, but were selected to have roll-offs that occurred within the same range. These frequency responses do not yet include any response of the structure on which the sensors are attached.

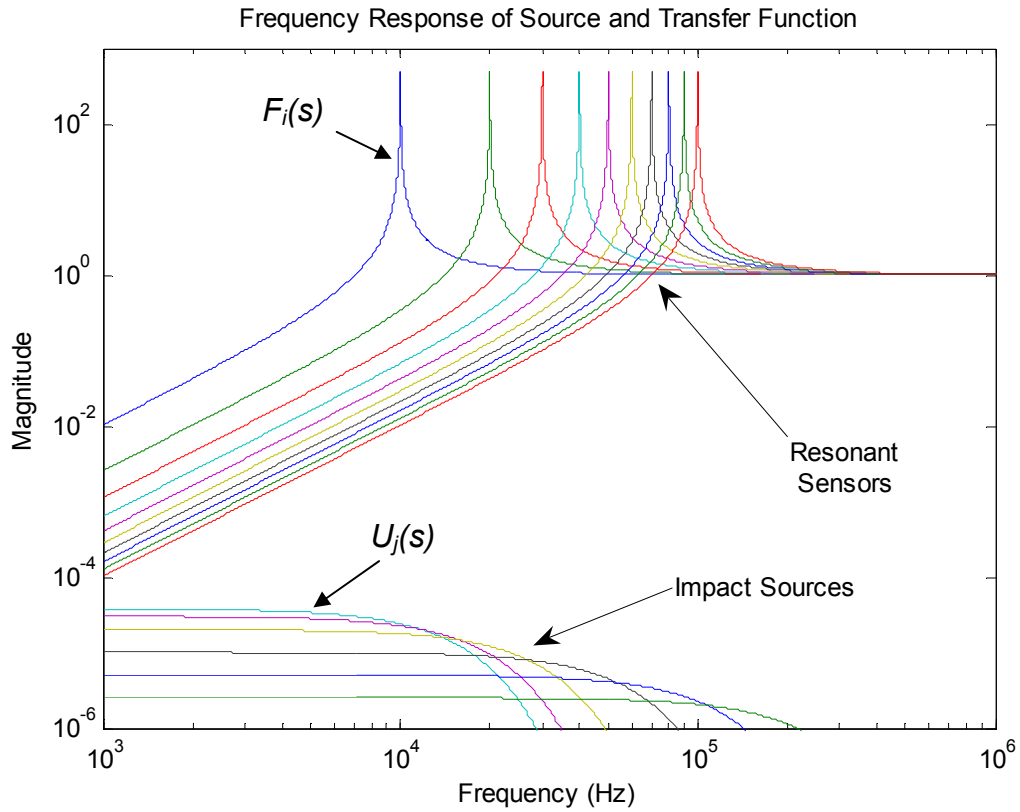


Figure 3.20: Frequency Spectrum of Impact Sources and Sensor Response

Table 3.4 lists the full-width half maximum (FWHM) pulsewidths for each impact source used in the analysis.

Table 3.4: Pulsewidth and -3dB Frequency for Stress Pulses

Pulse No.	Pulsewidth (us)	F3dB (Hz)
Teflon	74.79	
1	35.3	25,000
Acrylic	33.78	
2	28.3	31,200
3	18.8	46,900
Stainless Steel	18.14	
Silicon Nitride	11.29	
4	9.42	93,700
5	4.71	187,000
6	2.35	375,000

Figure 3.21 through Figure 3.26 show the output spectrum for each sensor with the application of the Gaussian pulse, as calculated from the product of the sensor and the input transfer functions. These figures are in order of decreasing source pulse width.

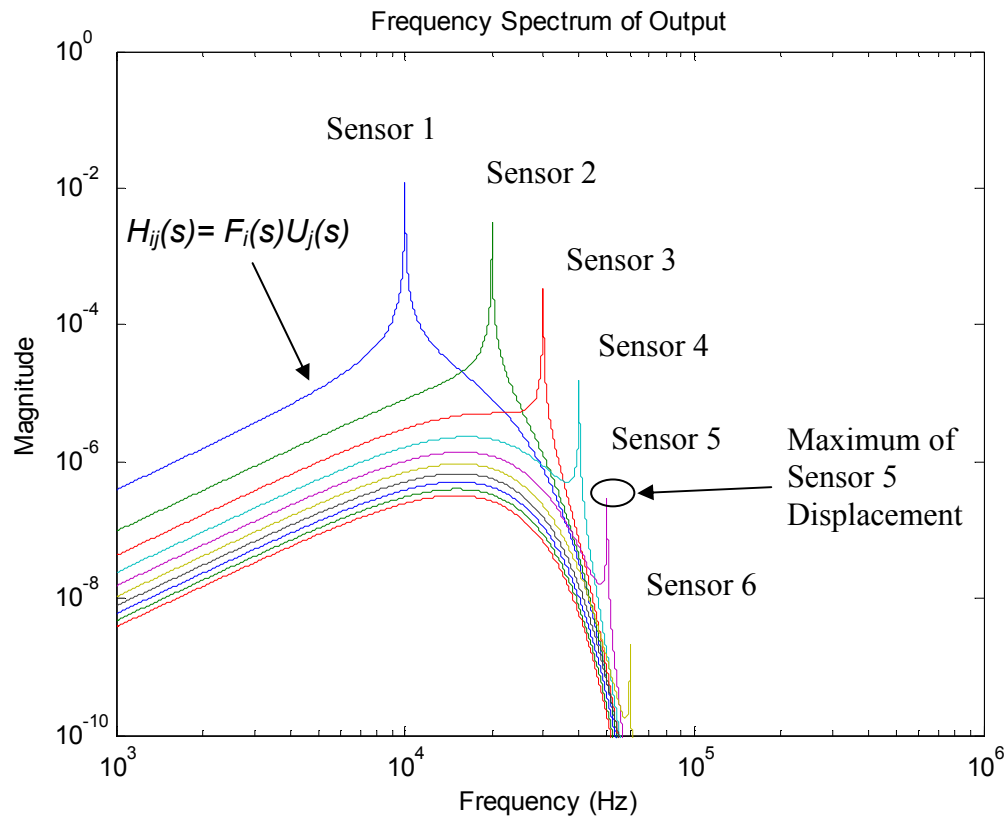
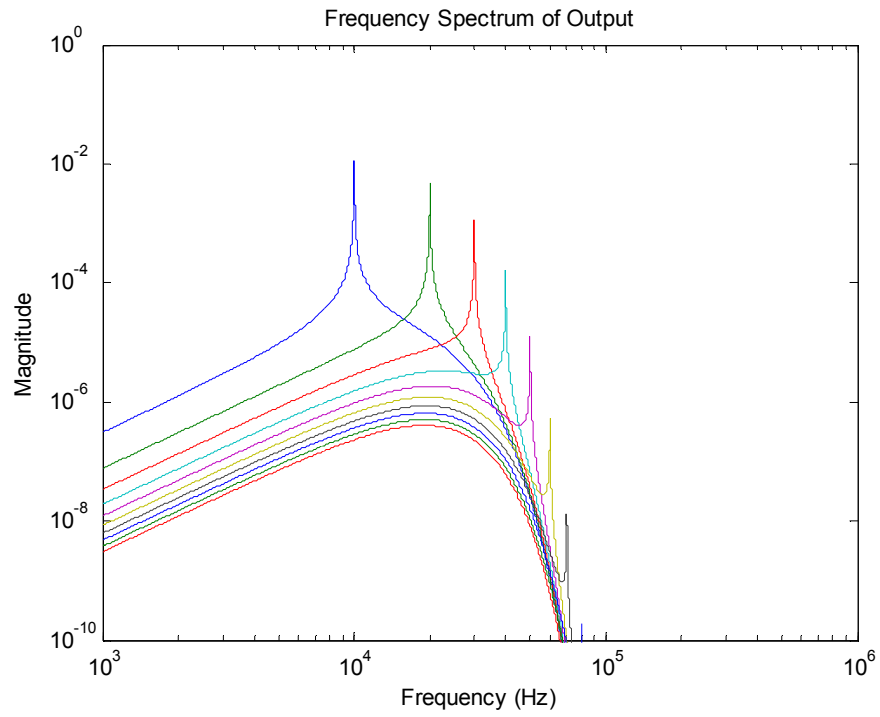
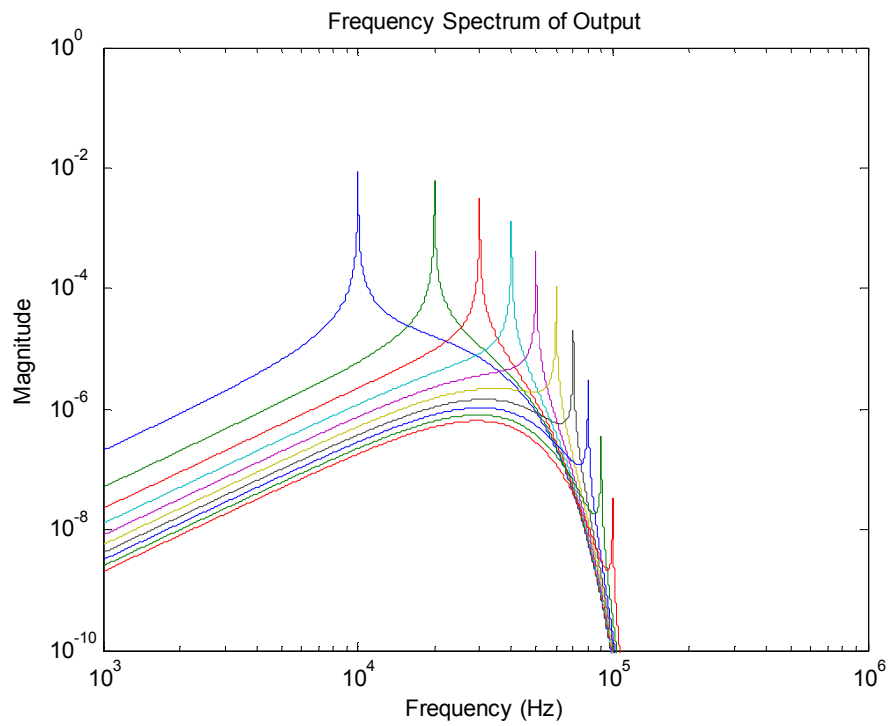


Figure 3.21: Pulse One Output Spectrum



**Figure 3.22: Pulse Two Output Spectrum**



**Figure 3.23: Pulse Three Output Spectrum**

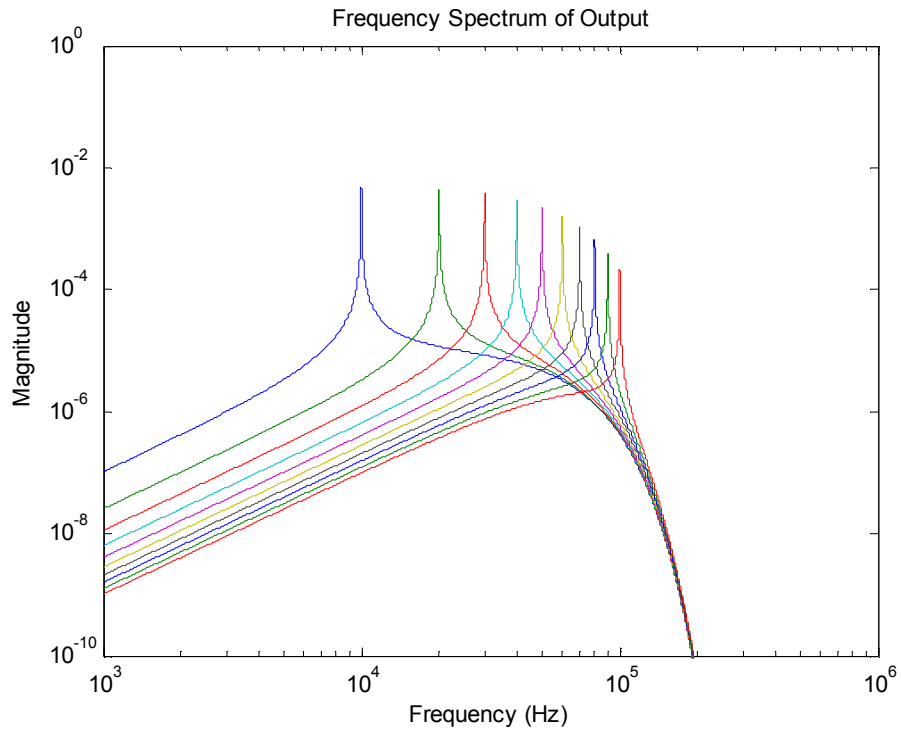


**Figure 3.24: Pulse Four Output Spectrum**

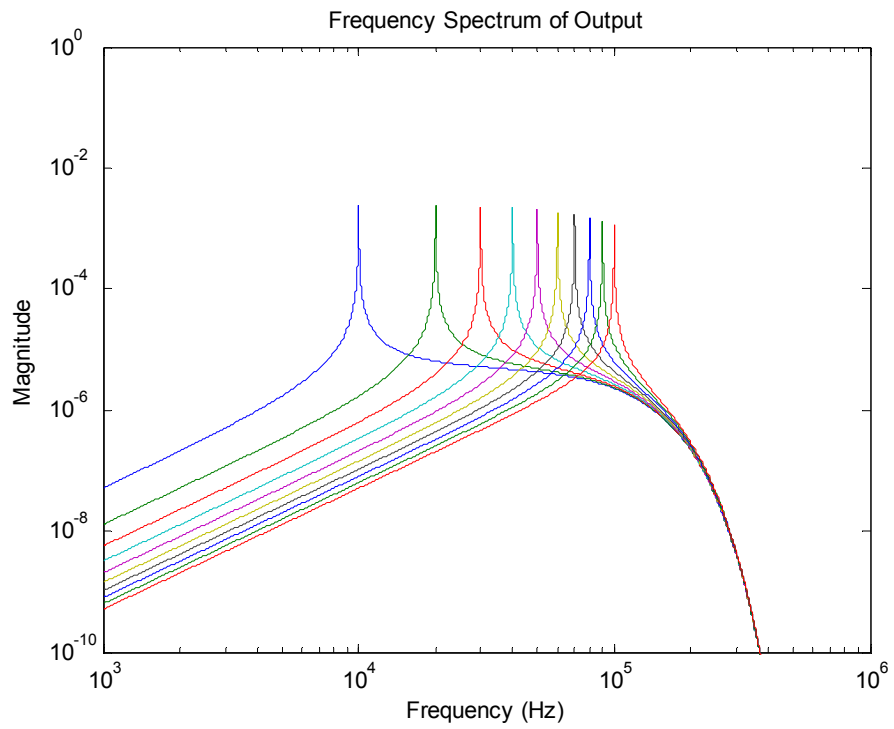


**Figure 3.25: Pulse Five Output Spectrum**

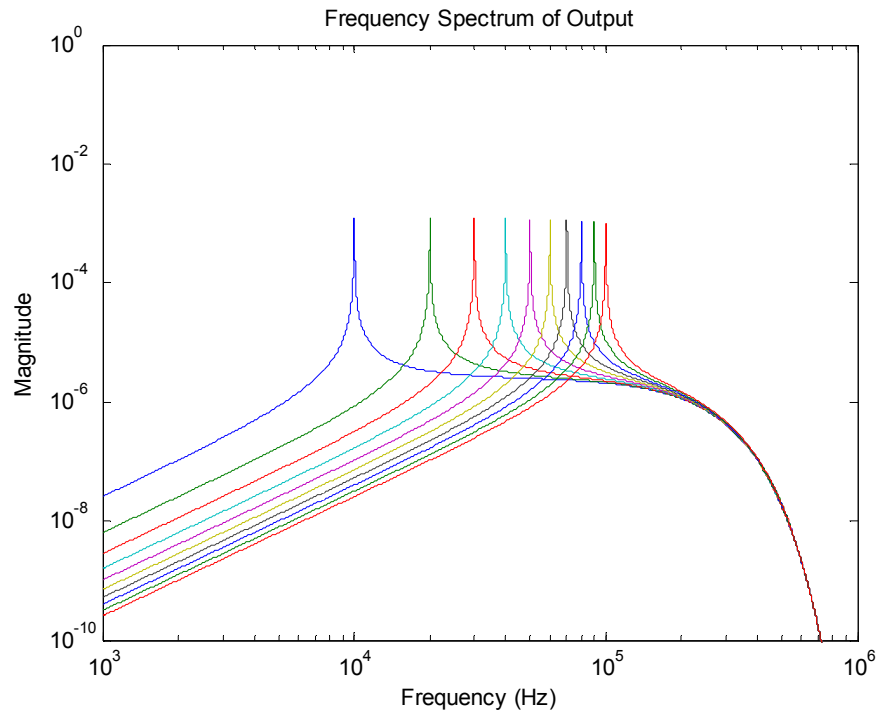


**Figure 3.26: Pulse Six Output Spectrum**

The sensor array “spectrum” is taken as the maximum of the sensor displacement after impact. This is similar to how the traditional Shock Response Spectrum is developed. Taking the maximum value of each sensor and plotting the sensor output as an array is shown in Figure 3.27 below.

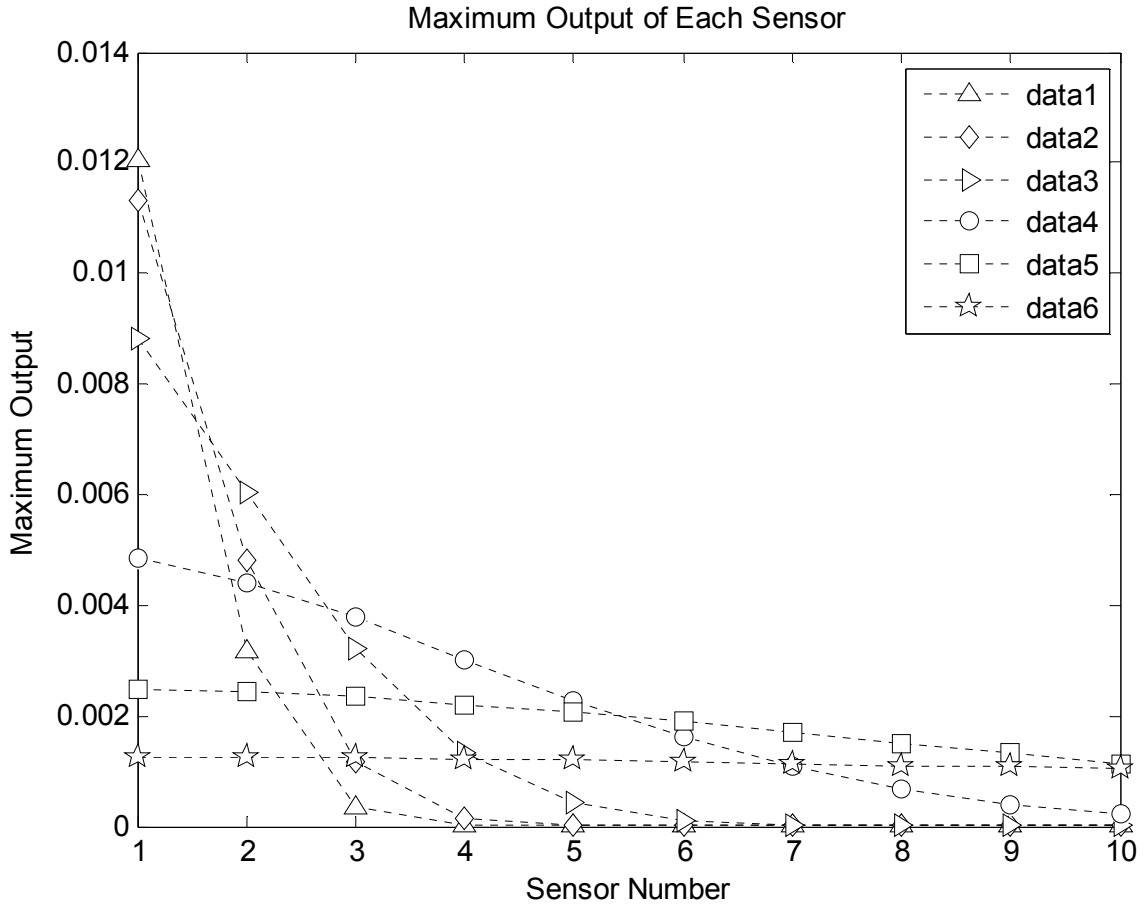


**Figure 3.27: Sensor Array Spectra (linear plot)**

When plotted this way, the longer pulsewidths correspond to the highest line slope, with the highest frequency sensors showing the least response. The shortest pulse widths are the smallest line slope, with higher levels of response from the higher frequency sensors. Since the natural frequencies of the sensors in the array are spaced linearly through the range of interest, plotting sensor output using logarithmic axes is similar to standard practice. Figure 3.28 below shows these spectra in a log-log plot.

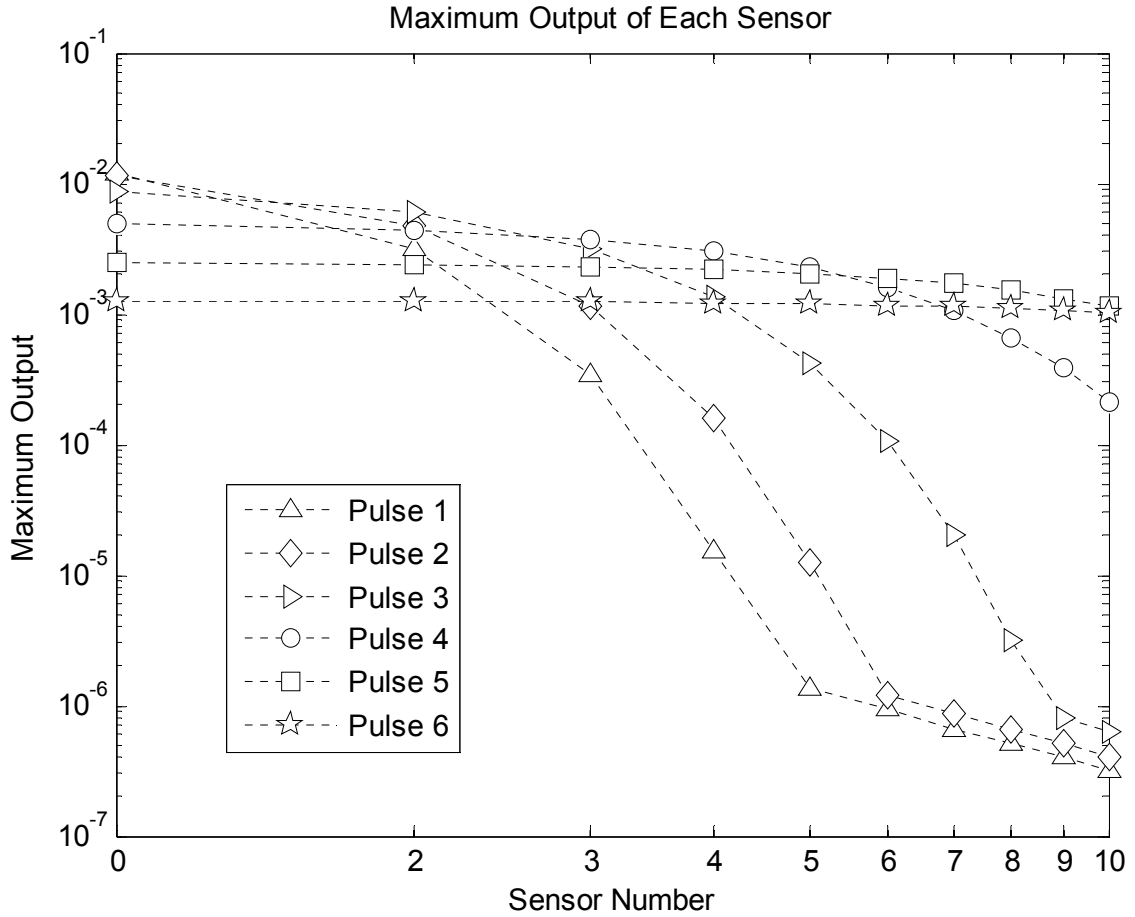


**Figure 3.28: Sensor Array Spectra (log-log plot)**

The above frequency analysis is not actually what is captured by the sensors in the array. The output of the sensors is actually a time domain waveform. A time domain simulation in Matlab/Simulink was performed of the same sensor array and same six stress pulses. Figure 3.29 shows a block diagram of a 10-element array of second-order systems corresponding to the sensor spectra shown previously.

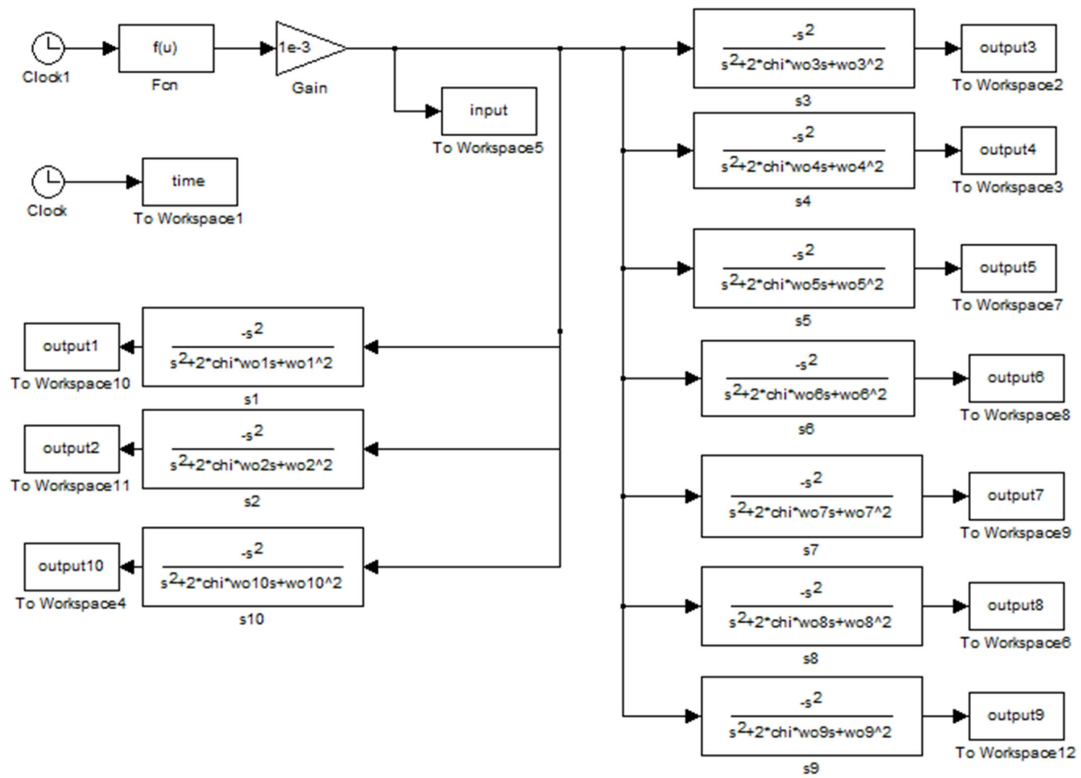


**Figure 3.29: Time Domain Simulation of 10-Element Sensor Array**

The following figures show time-domain simulations and the transient output waveforms in order of decreasing source pulsewidth. In these figures, the top plot is the input stress pulse for the sensor array. The nine plots after that are the time domain outputs of each element in order of increasing sensor resonant frequency. As the pulsewidth decreases, larger amplitudes are seen by the higher frequency sensors.

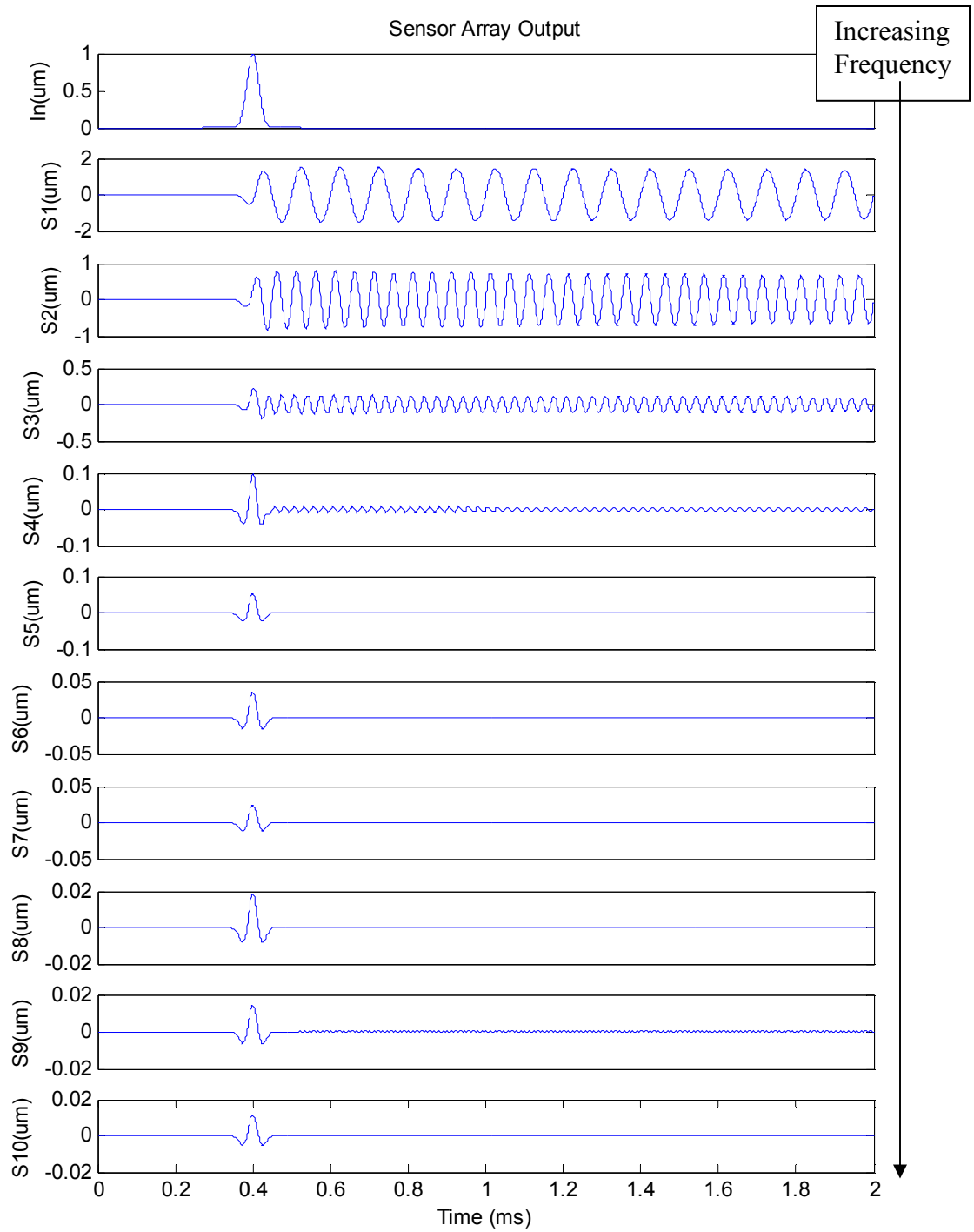


**Figure 3.30: Pulse One Output Waveform**

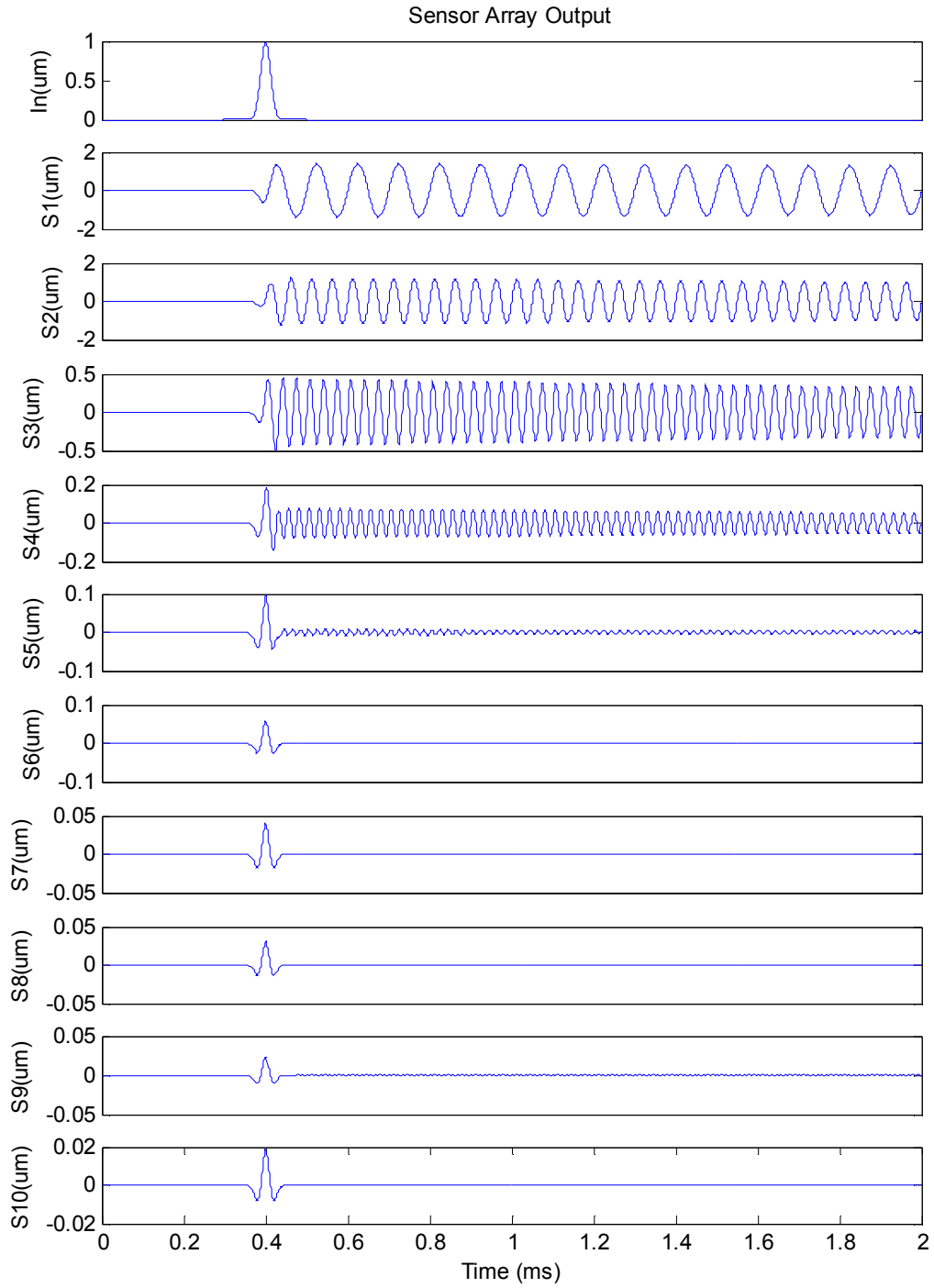
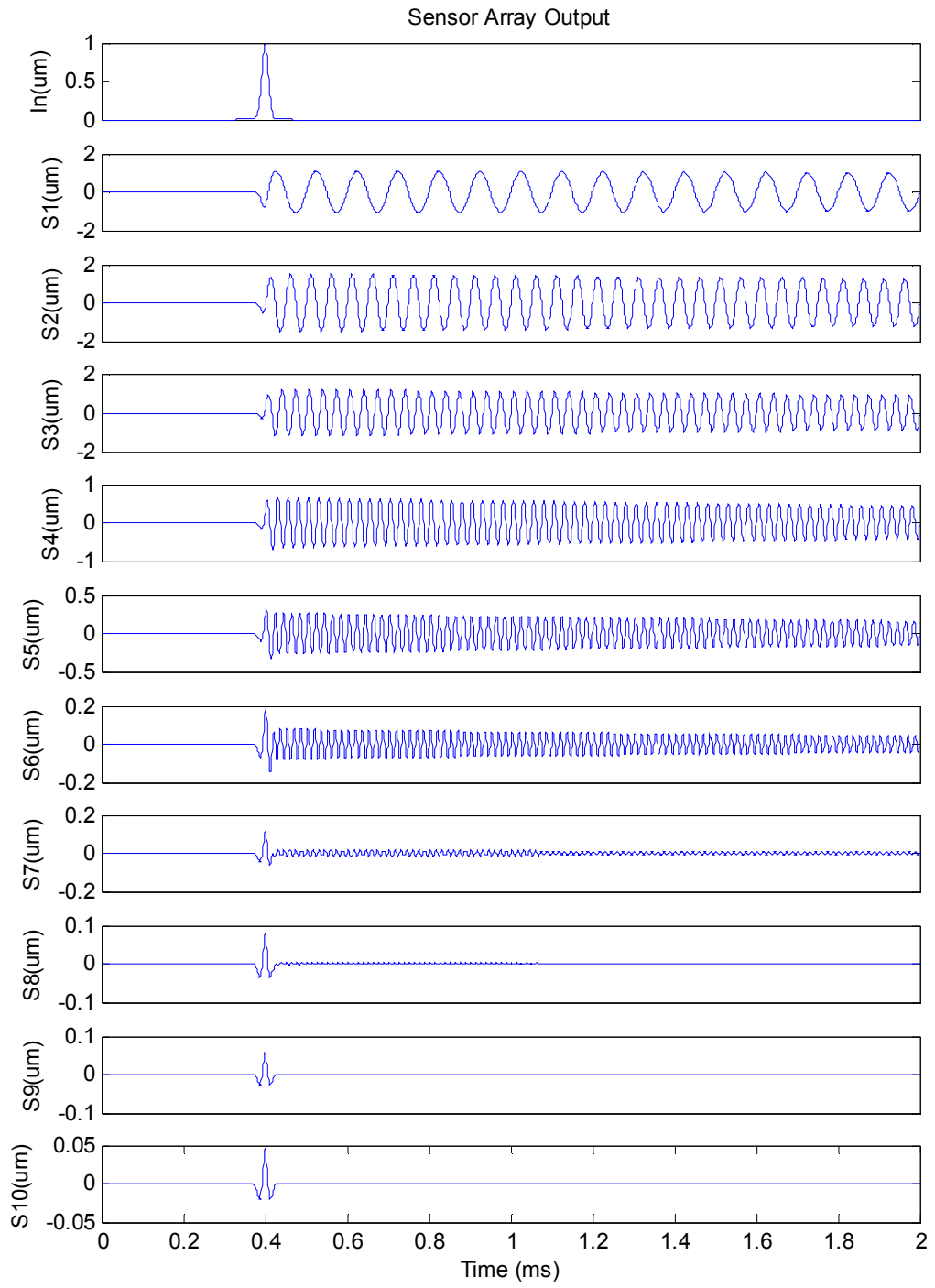


Figure 3.31: Pulse Two Output Waveform



**Figure 3.32: Pulse Three Output Waveform**

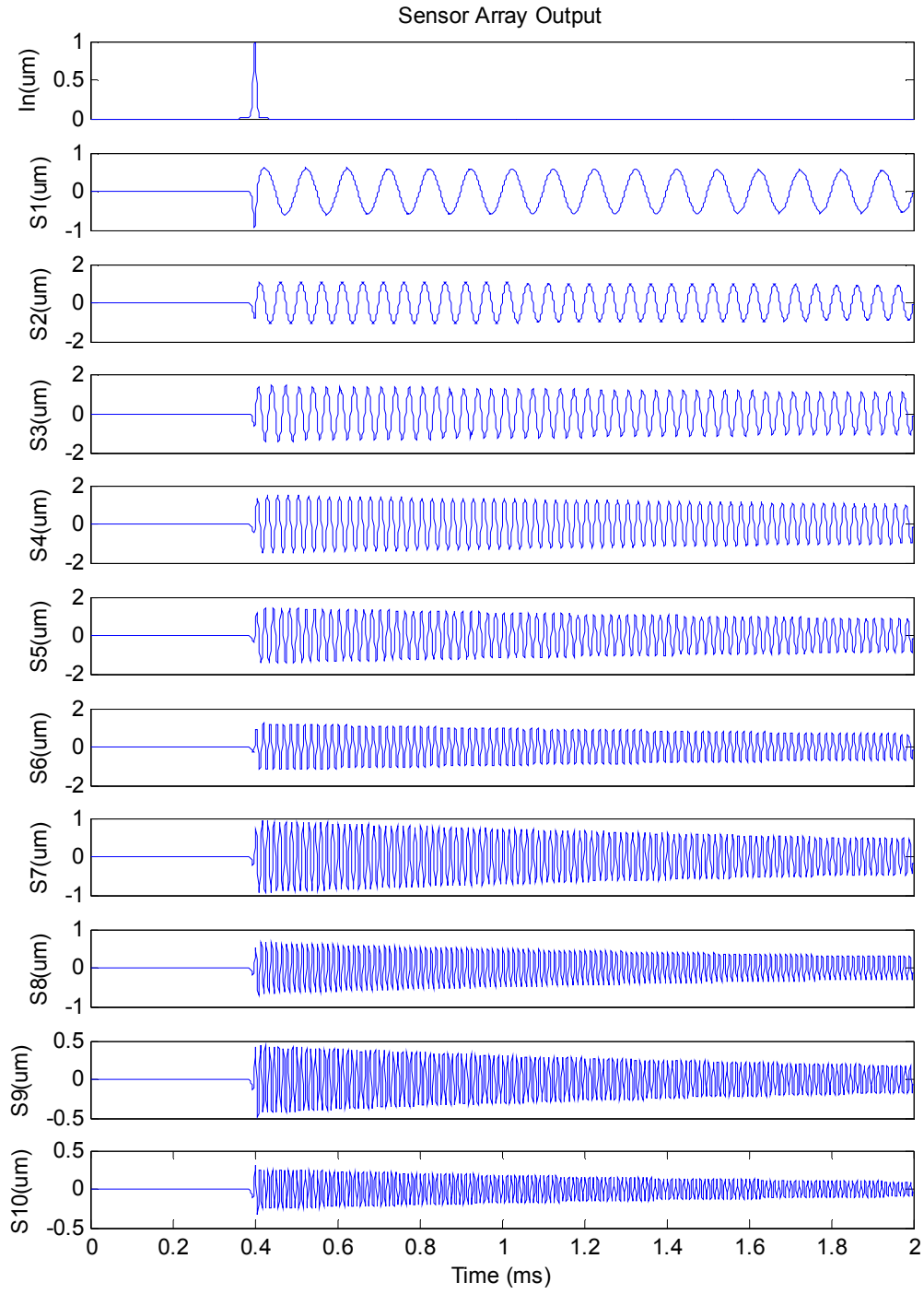


Figure 3.33: Pulse Four Output Waveform

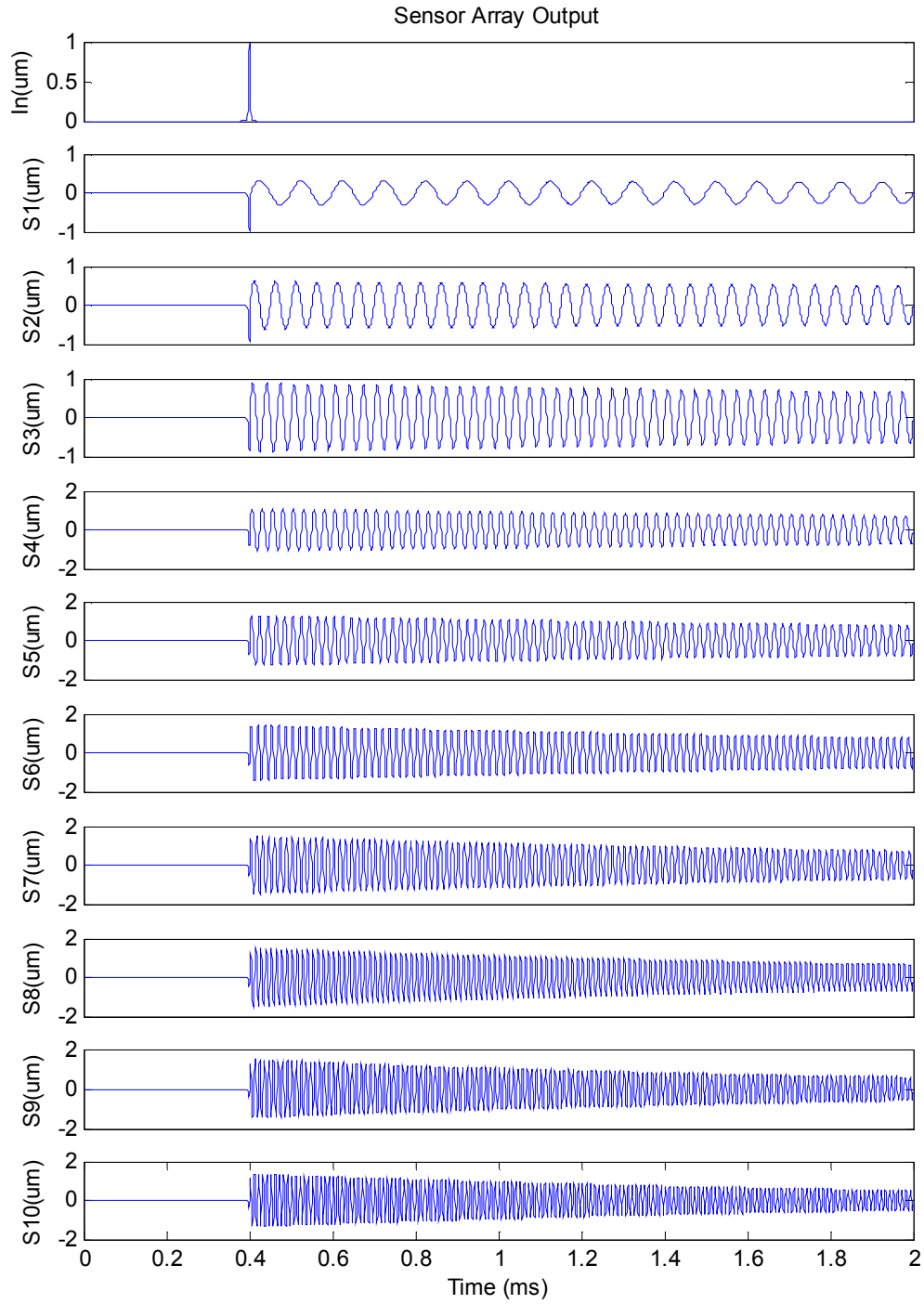
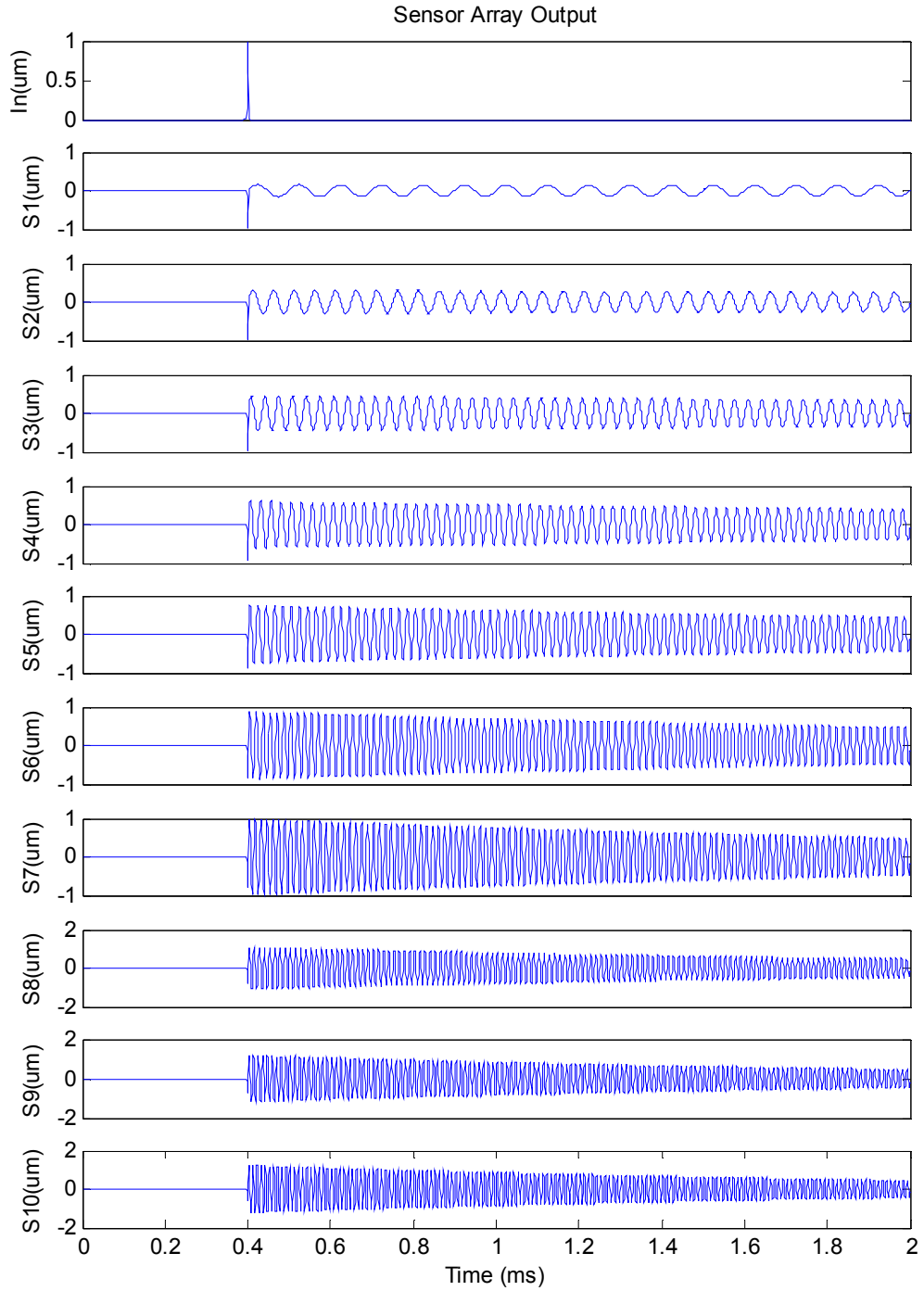


Figure 3.34: Pulse Five Output Waveform



**Figure 3.35: Pulse Six Output Waveform**

Figure 3.36 shows the maximum of each waveform plotted against the sensor number. Figure 3.37 shows the same on a Log-Log plot.

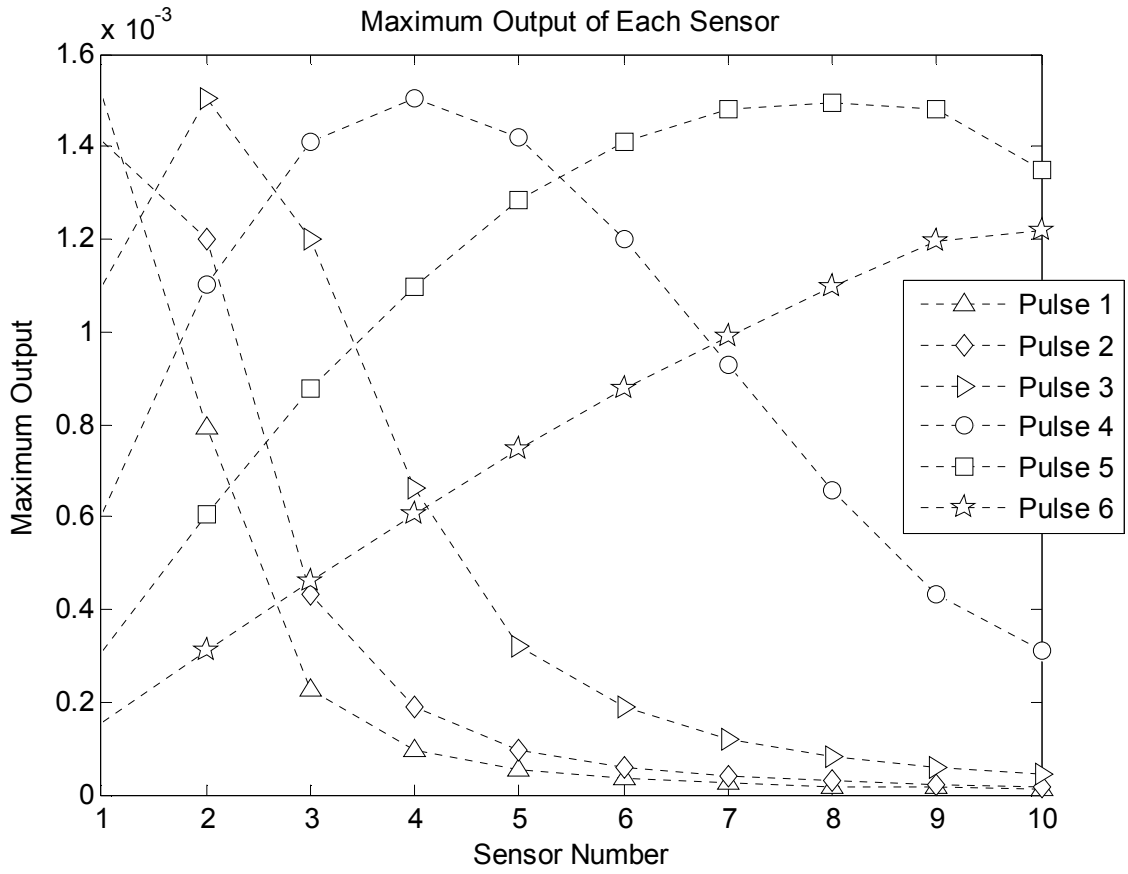


Figure 3.36: Sensor Array Output Spectra (linear plot)

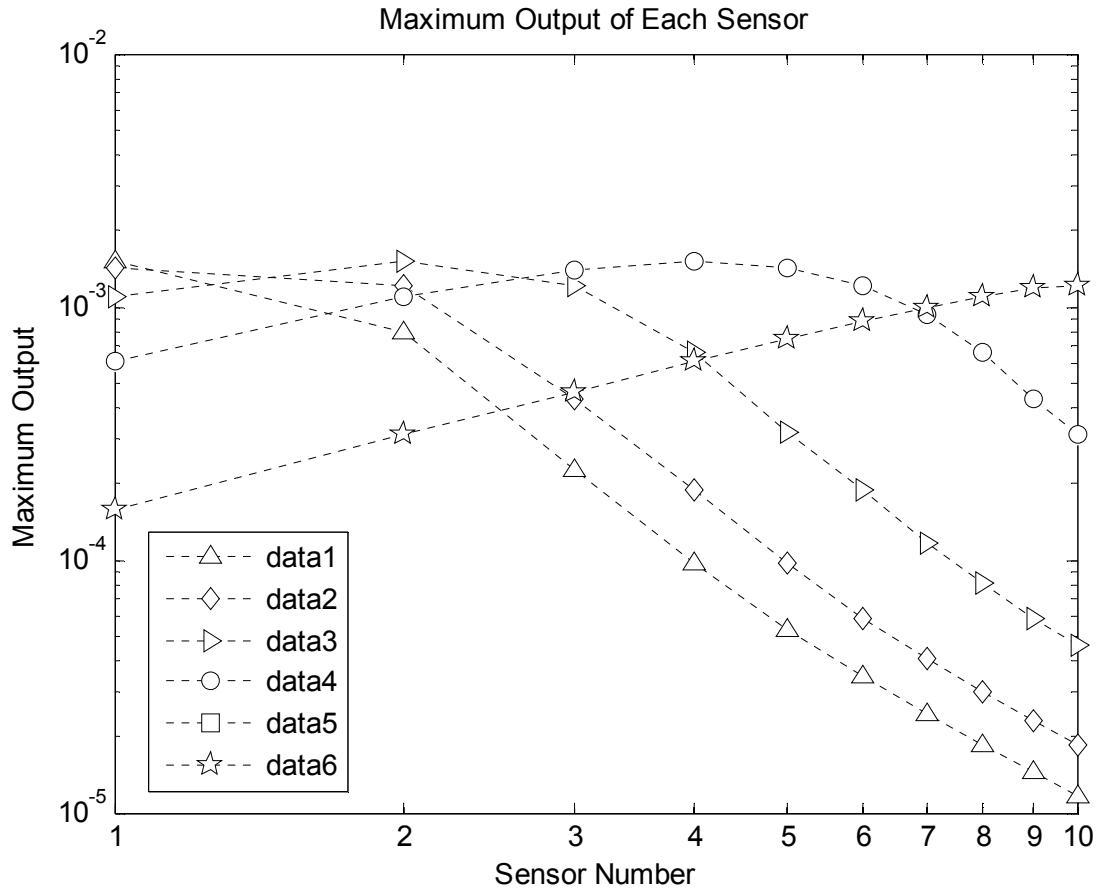
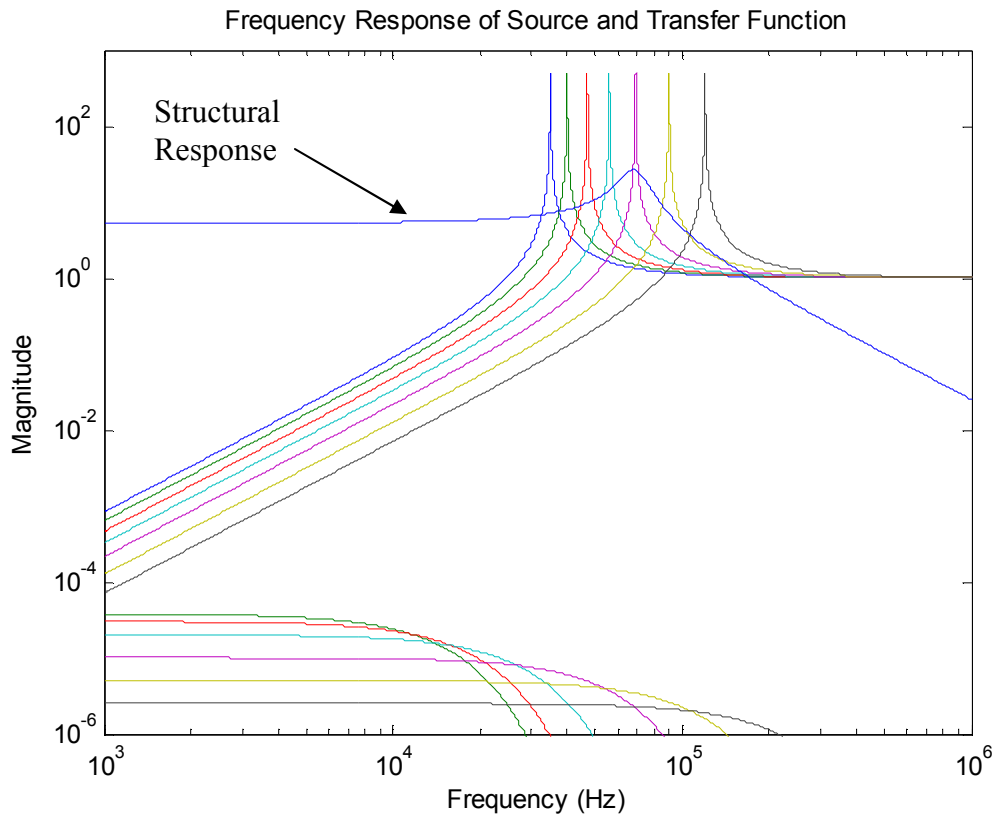


Figure 3.37: Sensor Array Output Spectra (log-log plot)

The significant difference between these plots and those generated from the frequency domain analysis is in the decreasing output of the lower frequency sensors under smaller pulsewidth inputs. This artifact is due to the use of the maximum of the output waveform rather than the minimum.

### 3.3.2 Gaussian Pulse with Plate

The structure onto which the sensor is attached, and onto which the ball actually impacts, has its own response to the impact, as well. This response will be coupled into the sensor array, and will alter the output spectrum. Figure 3.38 show the structure's response in addition to that of the sensors of the array.



**Figure 3.38: Frequency Response Representation of Source Functions, Sensor Array Response, and Plate Response**

Figure 3.39 through Figure 3.40 show the response of the sensor array including the coupling of the structure.

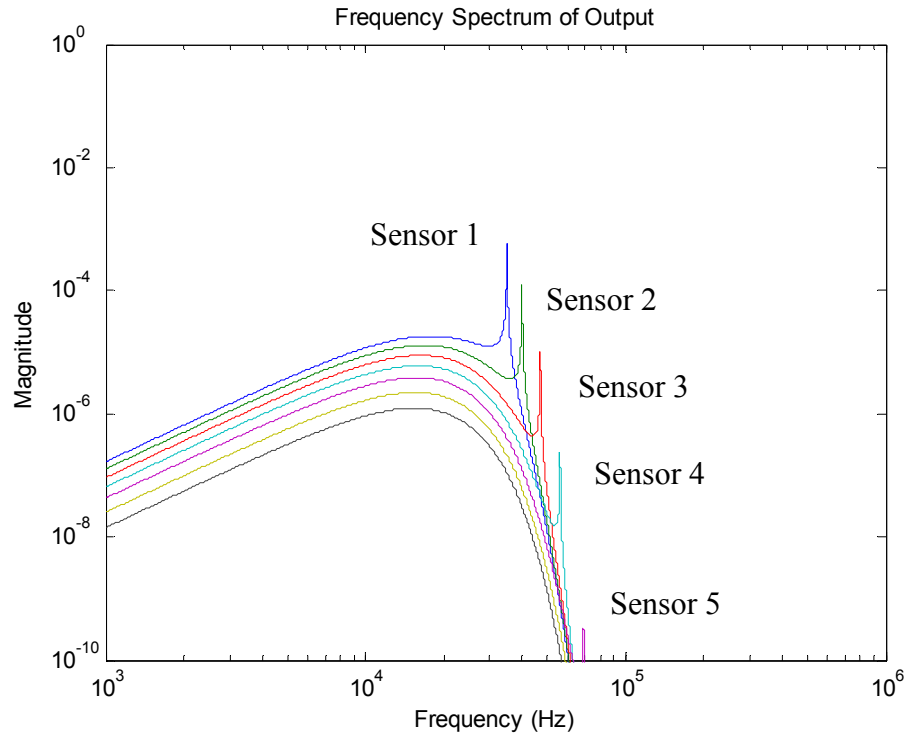


**Figure 3.39: Pulse One Output Spectrum**

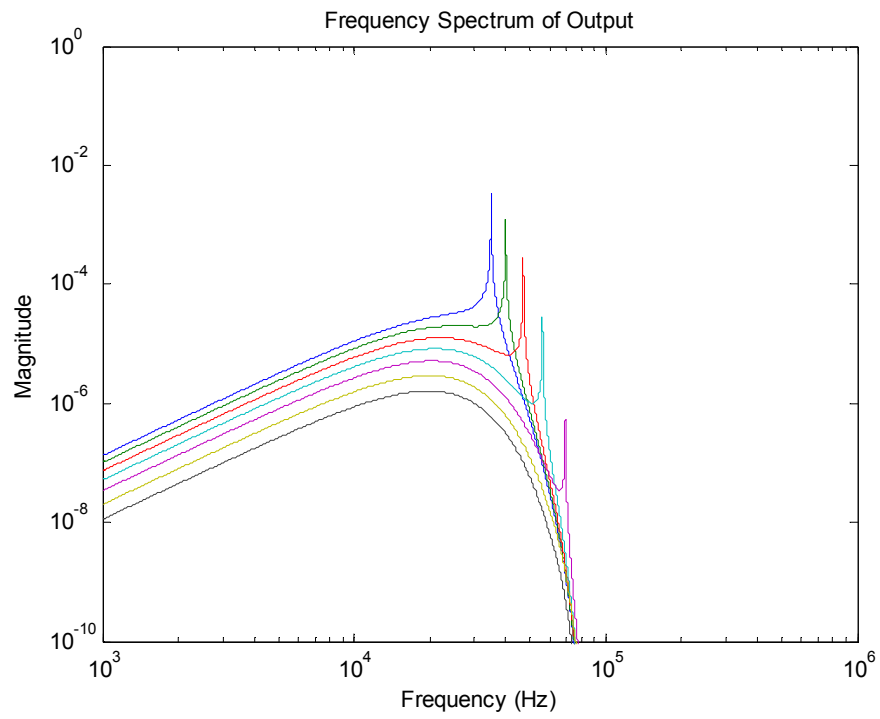


**Figure 3.40: Pulse Two Output Spectrum**

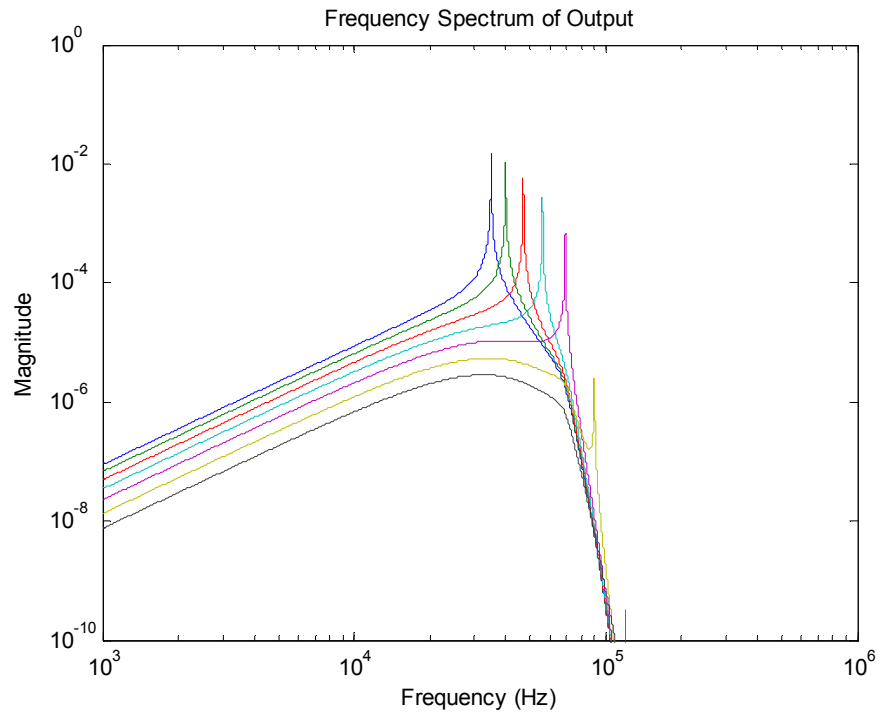


**Figure 3.41: Pulse Three Output Spectrum**

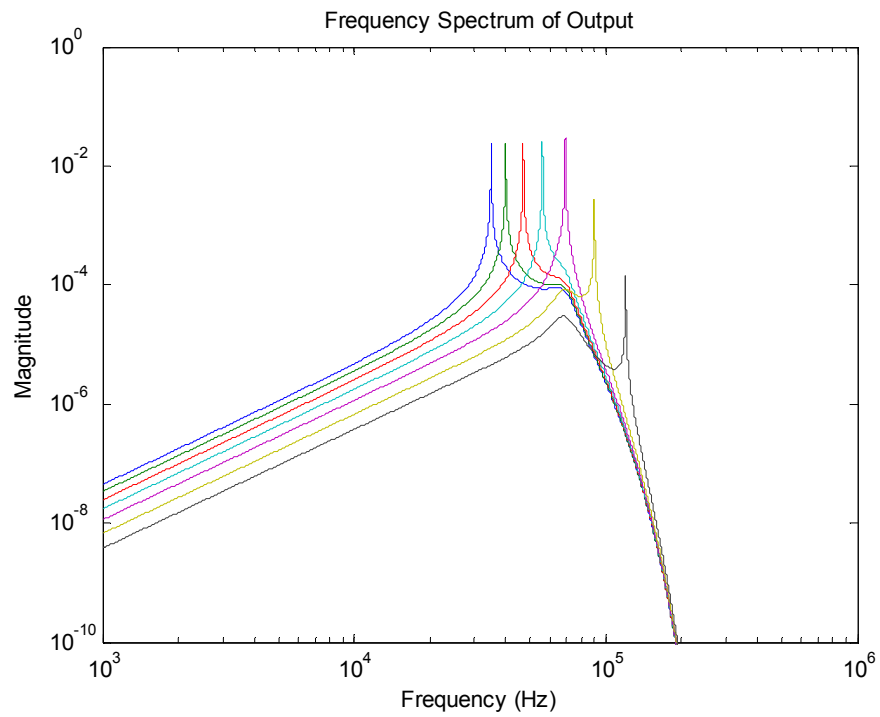


**Figure 3.42: Pulse Four Output Spectrum**

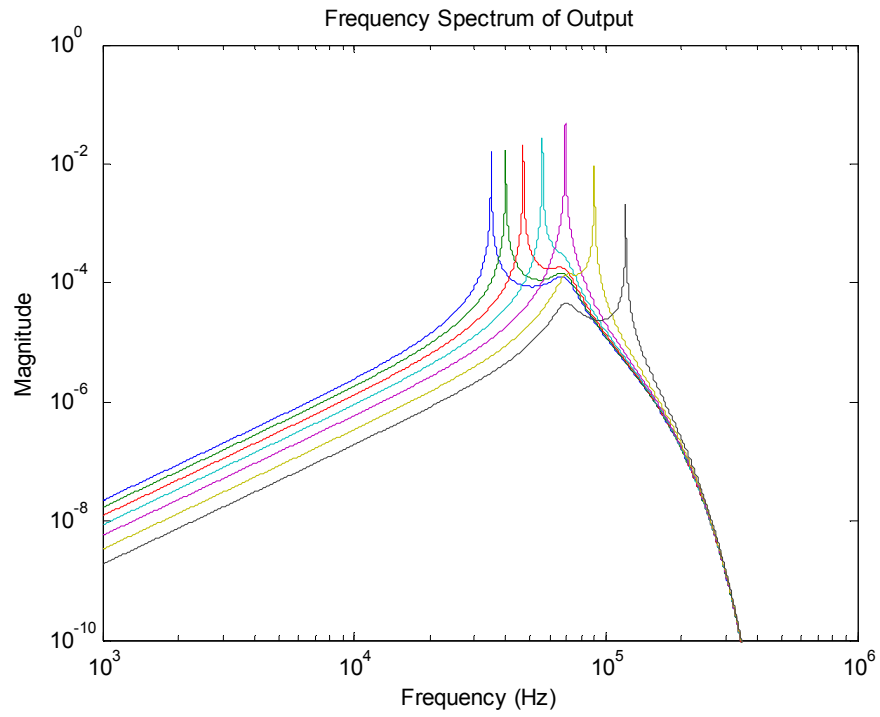


**Figure 3.43: Pulse Five Output Spectrum**

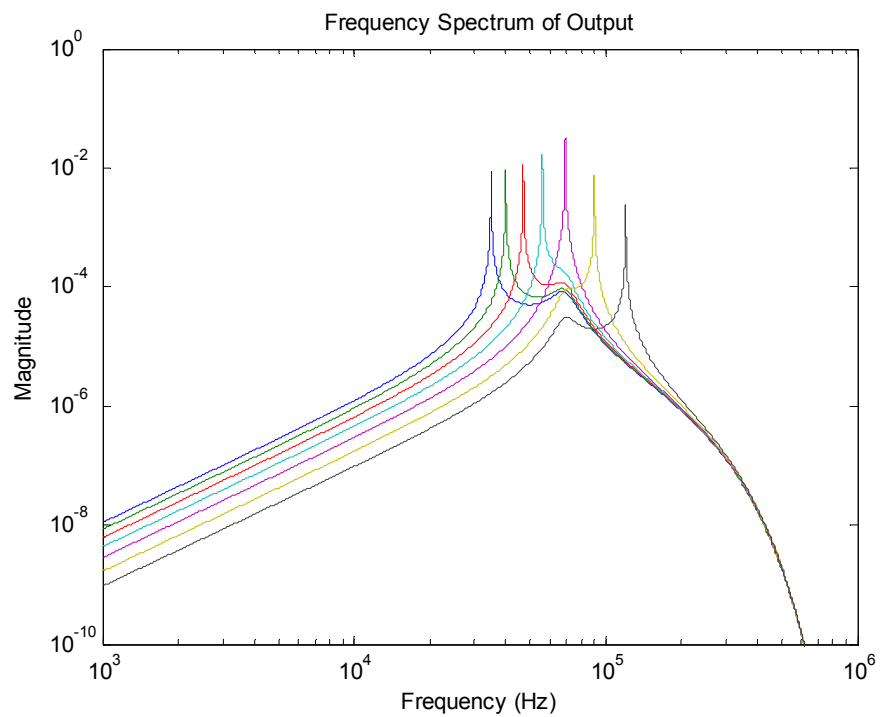


**Figure 3.44: Pulse Six Output Spectrum**

Again, taking the maximum value of each sensor and plotting the sensors as an array is shown in Figure 3.27 below.

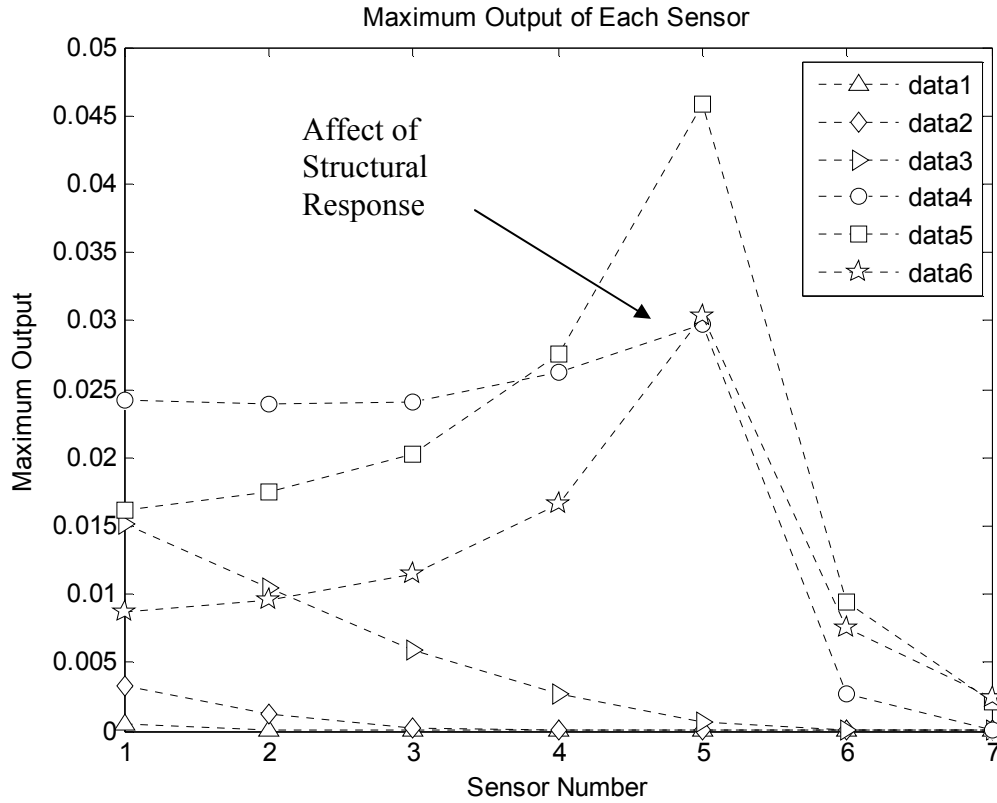
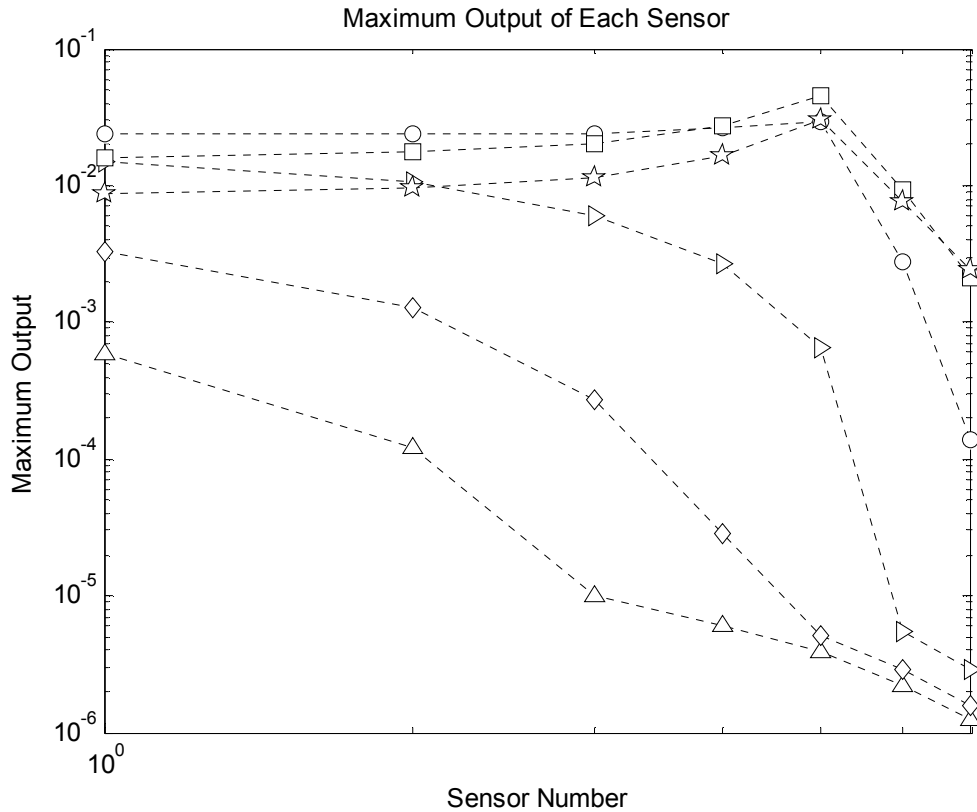


Figure 3.45: Sensor Array Spectra (linear plot)

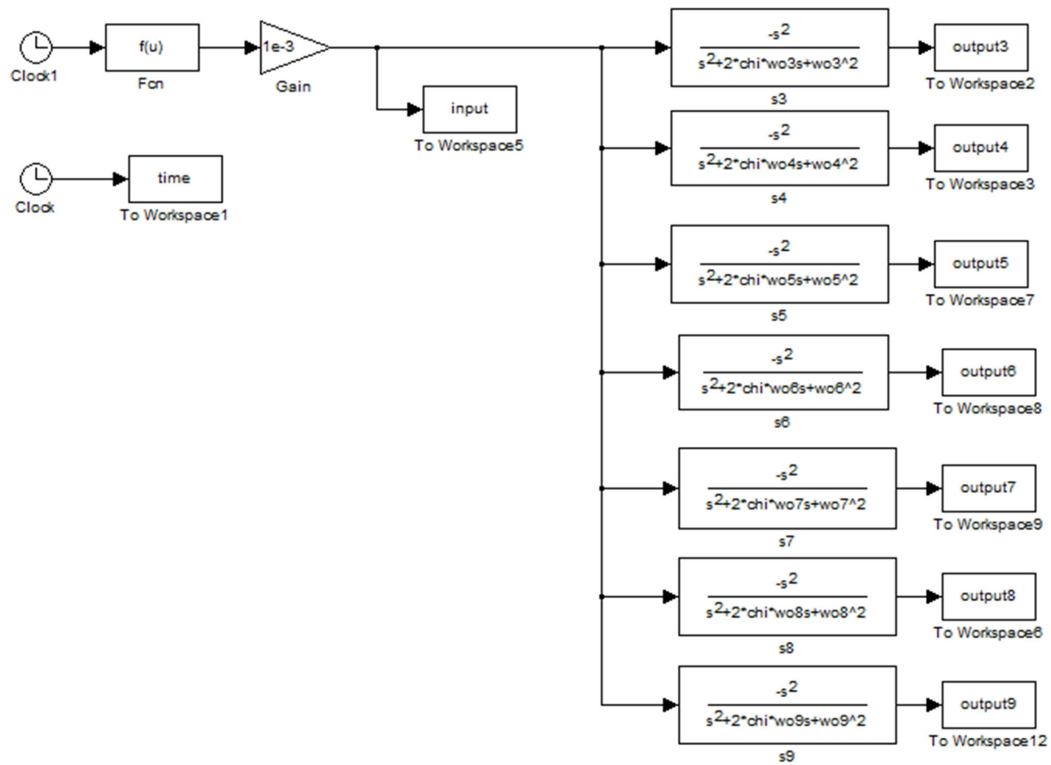
When plotted in this fashion, the longer pulsewidths again correspond to the highest line slope and smallest response from the highest frequency sensors. However, the response of the structure on which the sensor array is plotted alters the spectrum. Figure 3.28 below shows this in a log-log plot.



**Figure 3.46: Sensor Array Spectra (log-log plot)**

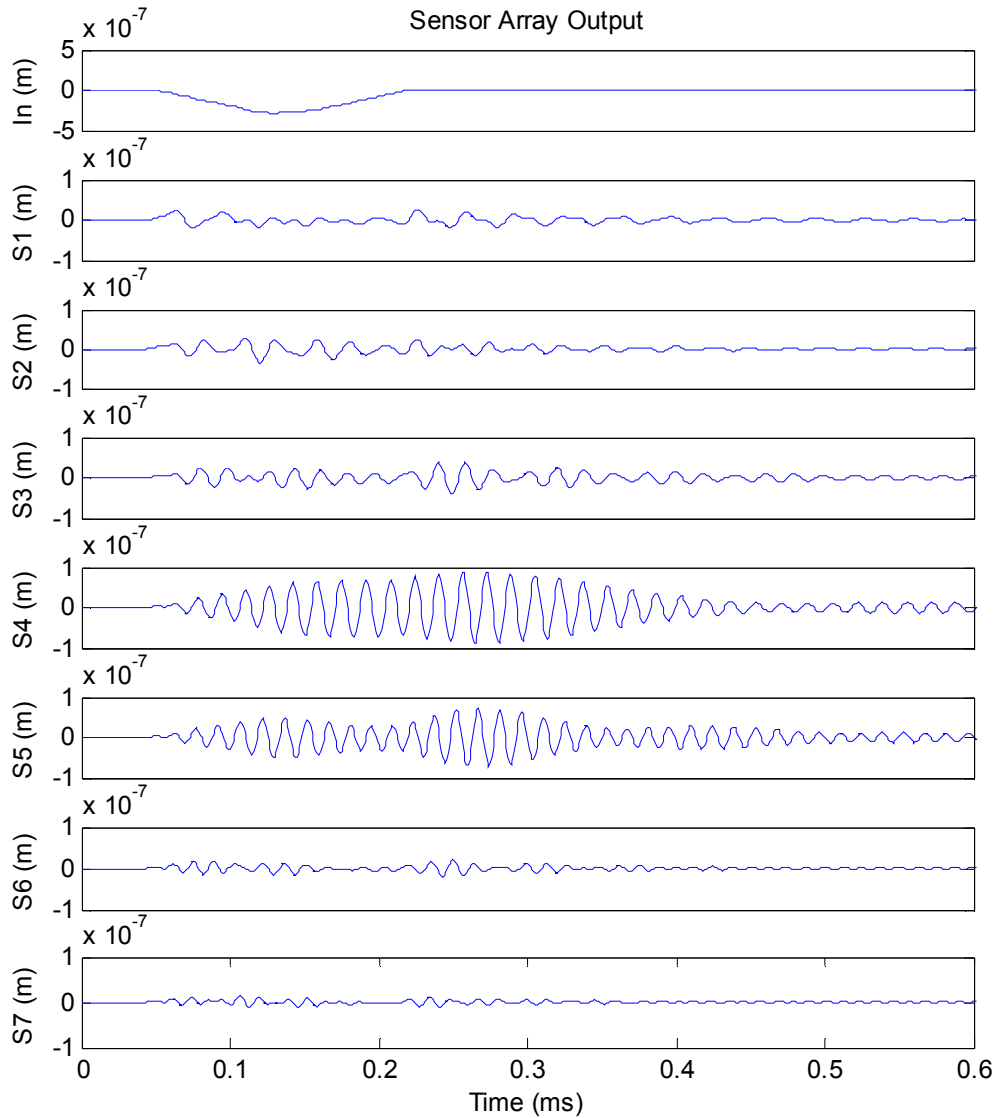
Again, time-domain simulations provide additional insight into the system response. The time domain waveforms captured from FEA analysis of ball impact on the steel flattened cone were analyzed directly in Matlab Simulink. The data from impact simulations was directly imported into Matlab and scaled. A resonator with its anchor attached to a “particle” will experience this local acceleration and respond according to its dynamics.

A simple Matlab simulation, Figure 3.47, was then assembled to predict resonator array response to these simulated impact events, and was developed to investigate the structural response using device parameters that are expected to be achieved in fabrication. This particular simulation used only seven sensors. In addition, in this case, the waveforms were only for Teflon and Stainless Steel impacts.



**Figure 3.47: Time Domain Block Diagram of Seven Element Sensor**

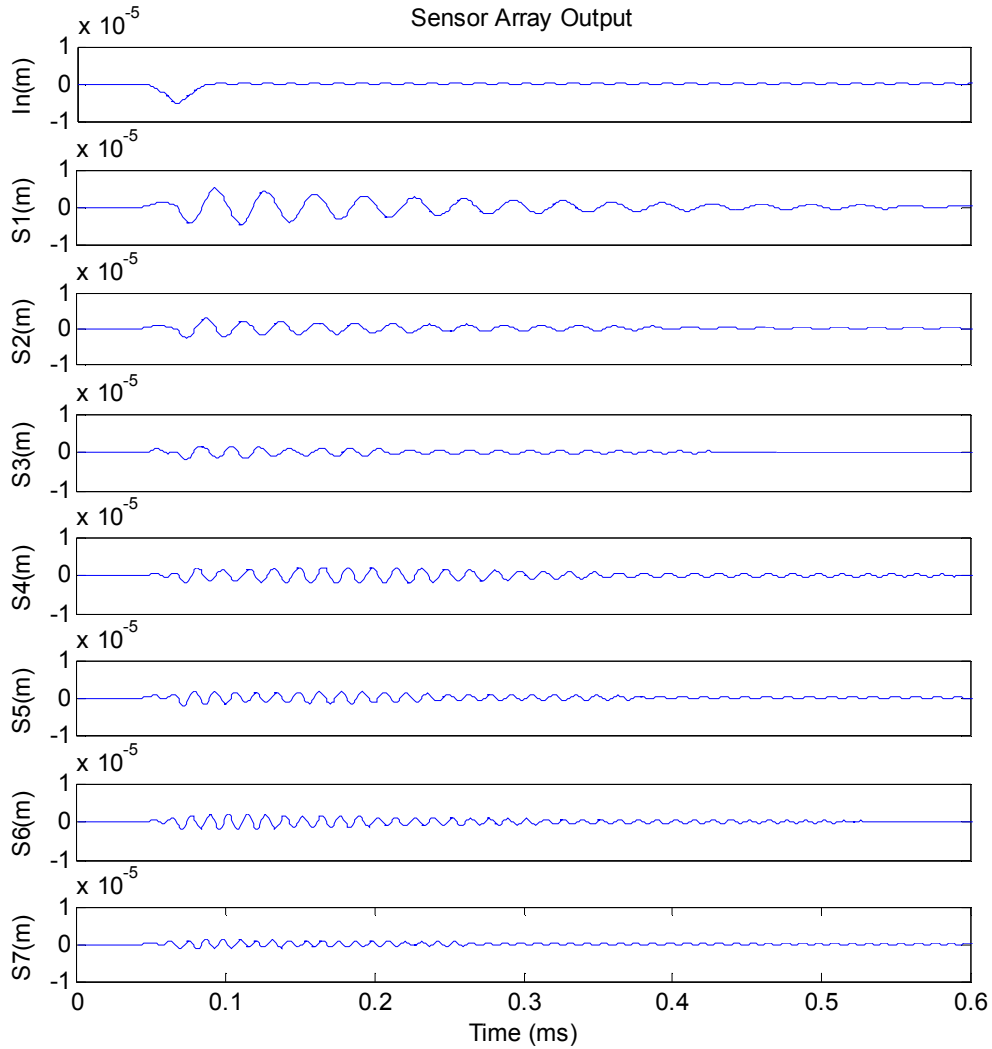
Figure 3.48 show the outputs of the model for a steel impact. The top plot shows the input displacement wave resulting from the stress data acquired from modeling activities. The next plots show the sensor displacements, ordered by resonator frequency with the highest frequency resonator being the bottom plot.



**Figure 3.48: Simulated Resonator Array Output Waveforms for Impacts on Teflon**

In these responses, sensors one, two, and three show a smaller output than sensors four and five. The Teflon impact does not have enough energy in the frequency regimes of sensors one, two, and three to create damped oscillatory motion. However, the Teflon impact does lead to excitation of the fundamental mode of the cone. That fundamental frequency is similar to the natural frequencies of sensors four and five. This manifests itself as the large output seen in those sensors. Furthermore, the largest value of that

response happens slightly after the initial impact because the oscillation of the resonant transducer builds up over time.



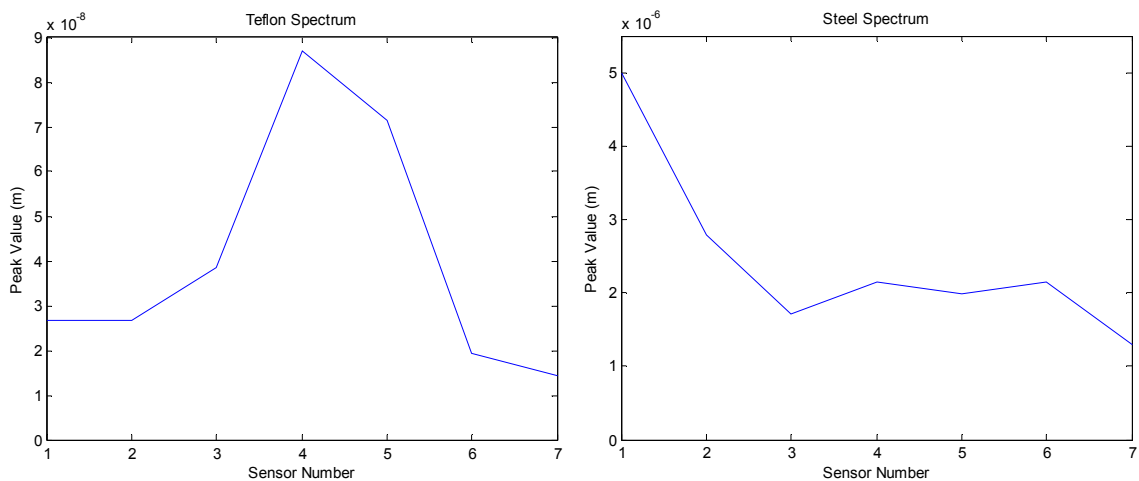
**Figure 3.49: Simulated Resonator Array Output Waveforms for Impacts on Steel**

Figure 3.49 shows the response of the same sensor array to the steel impact. Sensors four and five show a similar increasing response over time because of their match to the fundamental frequency of the cone structure itself. In this set of responses, however, sensors one and two show a relatively large output, indicating that the

frequency of the input was sufficiently high to excite the sensors into damped oscillatory motion.

These plots indicate that, given the selection of resonant frequencies in this array, it is possible to tell the difference between an impact with Teflon and an impact with steel. In order to distinguish these, a measurement technique must be applied to the resonator that can tell that the resonator is oscillating at its resonant frequency for a given amount of time.

To accomplish this, the maximum value of each waveform from each sensor was found and plotted as a spectral response. Figure 3.50 compares the spectral response from the Teflon impact (on the left) to the steel impact (on the right). There is a clear difference in the spectrum, particularly for the lower frequency sensors.



**Figure 3.50: Comparison of Teflon (left) and Steel (right) Responses**

In these simulations, however, it can be seen that the response of the structure that the sensor array is attached to couples into the array response. These signals can mask other frequencies in the impact or vibration. Therefore, moving these responses outside the band of interest is beneficial for sensor array interpretation. To accomplish this, the steel cone was replaced with an alumina disc. The natural frequency of the alumina disc

is outside the band of sensor frequencies, thereby minimizing its effect on the sensor array output. In actual application, the sensor would require mounting to a suitably high frequency structure to mitigate this issue, or the structure's response would need to be known and considered during sensor operation.

### **3.4 Resonant Processing Considerations**

Based on this analysis, multiple considerations can be addressed when contemplating the use of resonant array processing for discriminating between different impact situations. These considerations involve the dependence of the stress pulses to radius of curvature and impact velocity, nonlinear material responses under higher-energy impacts, and the coupling of the response of the sensor mounting structure into the sensor array.

The curvature of the impacting surfaces is critical to the shape of the stress pulse created during the impact, which is critical to the overall discrimination of one impact from another. The resonant array can process the pulse, but the pulse will depend not only on the stiffness of the impact materials, but also on the curvature of the surfaces. A large radius of curvature between these materials will lead to similar results from the array as impacting materials with higher elastic moduli. Therefore, the curvature of the impact needs to be controlled. This can be done by applying a curvature to the structure onto which the sensor array is attached. If the structure is then small in area, an assumption is made that the item being hit by the sensor is relatively flat compared to the sensor mounting structure.

The shape of the stress pulses is also dependent on the velocity of the impact, although to a weaker extent than it is to material properties and geometries. In many impact situations, the range of velocities that can occur is small, and therefore the resonant array processing is not negatively impacted by velocity changes. However, if the

range of velocities is large, the velocity needs to be measured and considered in the spectrum interpretation.

The structure on which the sensor is mounted also plays a critical role in the spectrum developed by the sensor array upon impact. In particular, natural frequencies of that structure couple into the sensor and create peaks in the spectrum. These peaks can either be measured and calibrated out of the spectrum, or they can be moved outside the region of interest for the impact scenarios being considered.

Finally, the analysis in this chapter was done using idealized pulses. The structural response of the system, nonlinear responses of the materials in the impact, particularly at higher strain levels, fractures, delamination, crack formation and growth, friction, and other issues lead to non-ideal pulses. These effects will lead to modifications of the array spectrum and its interpretation. Data needs to be collected from the representative impacting system to determine these characteristics and either factor them into the spectrum interpretation, or remove them from the system.

## CHAPTER 4 - INTEGRATED ELECTRETS

The basic sensor element developed in this work consists of a mass-spring system with a dynamic response designed to process the acoustic stress pulse. The motion of that mass-spring system needs to be converted into an electrical signal. Therefore, a second key portion of the work presented in this thesis is creating an electret film within a structure such as that shown in Figure 4.1. The electret in the structure creates a voltage bias for measuring the motion of the mass-spring system. A critical aspect of this is the formation of multiple electrets on a single die after device fabrication. The work explored different electret types, materials, and charging processes.

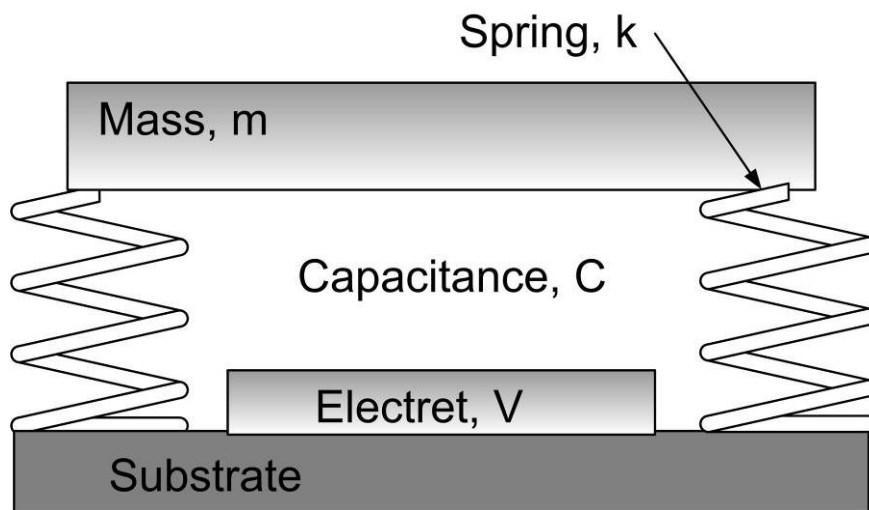


Figure 4.1: Mass-Spring System with Electret Transducer

This chapter discusses the selection and fabrication of the electret type, the materials used in electret formation, and the polarization techniques employed to realize electrets within the MEMS structure. In particular, this chapter discusses the *in situ* formation of electrets based on CYTOP, a Teflon-like spin-castable polymer, after completing device fabrication.

## **4.1 Electret Type**

Depending on the material and charging types, different classes of electret can be formed. These are characterized by the nature of the electrostatic charge distribution within the film. Both dipole and space-charge electrets were investigated in this work.

### **4.1.1 Dipole Electret**

Dipole electrets [45] are characterized by a frozen alignment of the dipoles within a polar polymer. When polarized, these electrets will exhibit a charge polarity that is opposite of the charging field. When forming a dipole electret, a polymeric material is typically first melted, or heated above its glass transition temperature, and while still in that state, a large electric field is applied. This field rotates the polymer dipoles into partial alignment. After alignment, the polymer is cooled back to a solid state and the electric field removed. The resulting electret has a polarity opposite that of the electric field applied to it, and a polarization that is highly dependent on the polar nature of the polymeric material. This is similar to the polarization of piezoelectric crystals below the Curie Point. Figure 4.2 shows a representation of this process and the resulting electret.

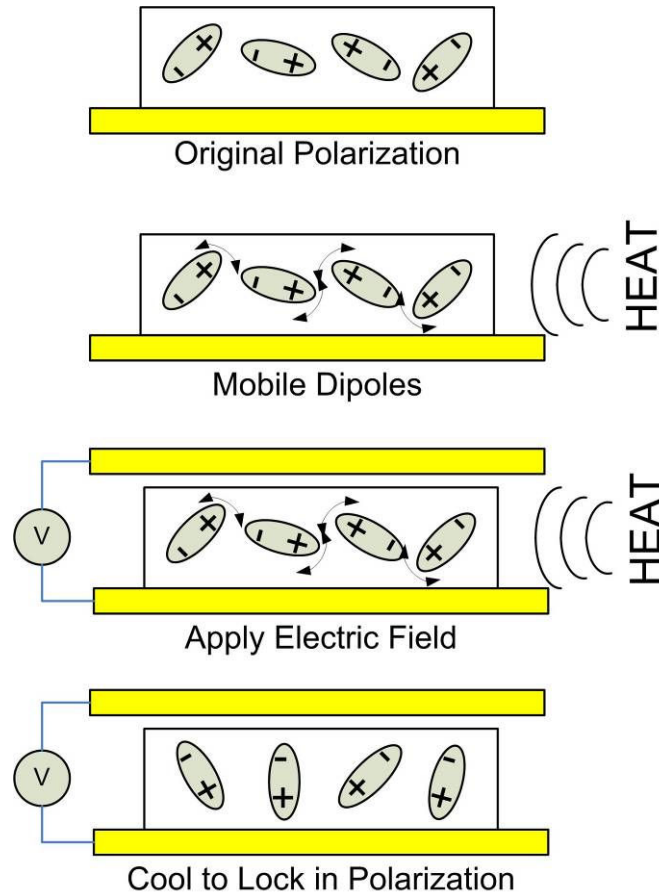


**Figure 4.2: Process for Forming a Dipole Electret**

This type of electret was not utilized in this work because of the difficulty in applying rigid, yet removable, electrodes across a melted polymer film at the microscale. Simulations were performed, however, regarding the use of high-k dielectric nanospheres within the electret material, forming a nanocomposite. The idea behind this concept is that the nanosphere matrix can provide a rigid support to the melted film during the polarization process, allowing this type of electret to be made at the microscale.

For dipole electrets that are contact charged, high-k dielectric materials were investigated. One issue with contact charging is that thermal breakdown leads to lower electric fields sustainable within the film. The use of high-k dielectrics within the film allows the entire film stack to be thicker without drastically reducing the electric field within the lower permittivity polymer.

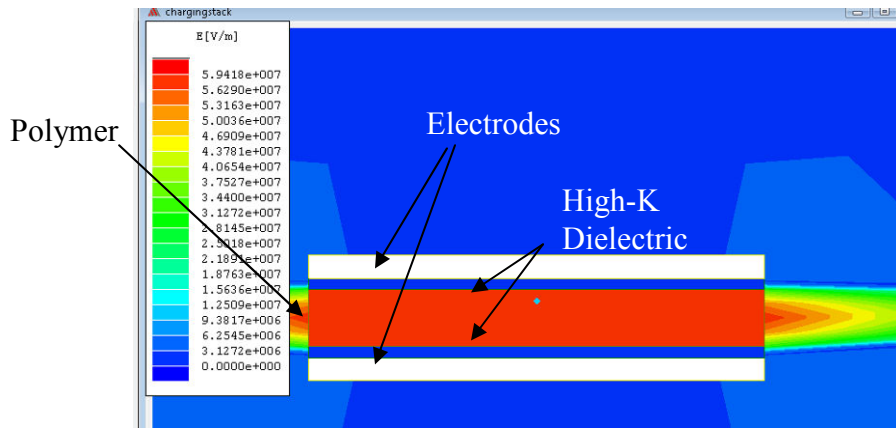


**Figure 4.3: FEA Model for High-K Dielectric Composite**

This work investigated SiC (permittivity = 10) and TiO<sub>2</sub> (permittivity = 85) as dielectrics within a Teflon-like film. Both thin film insulators and composites using dielectric nanopowders were investigated. SiC powder was mixed into Teflon in a 1:1 volumetric ratio and deposited onto an electrode. This nanocomposite was cured and coated with a top electrode. Under subsequent charging, the film sustained a higher electric field, and after charging, showed a small positive remnant charge. This process can be explored further using a polymer with a higher polarity. Teflon, with a dielectric constant of 2, is not optimal for a dipole electret. Figure 4.4 shows the geometry used in modeling the benefits of high-k dielectrics in dipole electret formation.

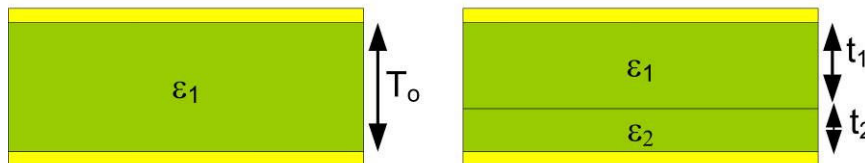


**Figure 4.4: Analytical Model for High-K Dielectric Application**

The advantage of the high-k dielectric is that it provides an insulating barrier between the contact electrodes and the electret without drastically reducing the electric

field within the electret during charging, and can also provide a thermally stable support during electret formation. For a standard parallel-plate capacitor structure, the electric field within it, as shown on the left in Figure 4.4, is

$$E_o = \frac{V_o}{T_o}. \quad (20)$$

However, the field within each material of the stack shown on the right in Figure 4.4 is different. Since the displacement fields are the same,

$$D_1 = D_2, \quad (21)$$

and therefore,

$$\varepsilon_o \varepsilon_1 E_1 = \varepsilon_o \varepsilon_2 E_2. \quad (22)$$

Simplifying this expression leads to

$$E_2 = E_1 \frac{\varepsilon_1}{\varepsilon_2}. \quad (23)$$

Therefore, if material two has a dielectric constant five times that of material one, then the field within material two is five times less. The important parameter, however, is the electric field in material one before and after converting a small portion of it to material two. That is, we want to know  $E_1$  as a function of  $E_o$ . Since we are applying the same voltage to both the left and right structures,

$$E_2 t_2 + E_1 t_1 = E_o T_o . \quad (24)$$

We also need to note that

$$t_2 + t_1 = T_o \quad (25)$$

In addition, we can define

$$k = \frac{t_1}{t_2} , \quad (26)$$

such that material two is some fraction of the thickness of material one, with a ratio of  $k$ . Through applying (23), (25), and (26) into (24), one can rearrange and simplify the expression leading to

$$E_1 = E_o \left( \frac{k+1}{k + \frac{\epsilon_1}{\epsilon_2}} \right) \quad (27)$$

The is expression, (27), states that the electric field in material one in the multilayer stack is degraded from its original level depending on the thickness of material two and the dielectric constant of material two. If the ratio of  $\epsilon_2$  to  $\epsilon_1$  is much greater than the ratio of  $t_2$  to  $t_1$ , then the insertion of material two does not drastically reduce the electric field in material one, although now there is a barrier in the structure that allows the application of higher voltage levels on the structure during the poling process. In addition, if the barrier material had a higher melting point than the dipole electret

material, the barrier material can maintain isolation of the electrodes even as the electret material melts during the poling process.

#### 4.1.2 Space-Charge Electret

Space-charge electrets, in contrast to dipole electrets, have monopole charges injected or trapped on the surface of the material or within its bulk. The resulting charge distribution yields a permanent polarization within the film, and a remnant voltage of the same polarity as the charging voltage. There are multiple techniques for forming space-charge electrets, but one of the most common is corona discharge.

The corona discharge process (Figure 4.5) forms a corona using a high-voltage point-to-plane geometry. In this geometry, a high-voltage (-7kV to -10kV) is applied between a small diameter tip (~ 2mm) and grounded plane. Between the tip and the plane is a conductive grid held at a potential of around -600 V with respect to the grounded plane. The tip to grid distance is 5mm, and the tip to grounded plane distance is 10mm.

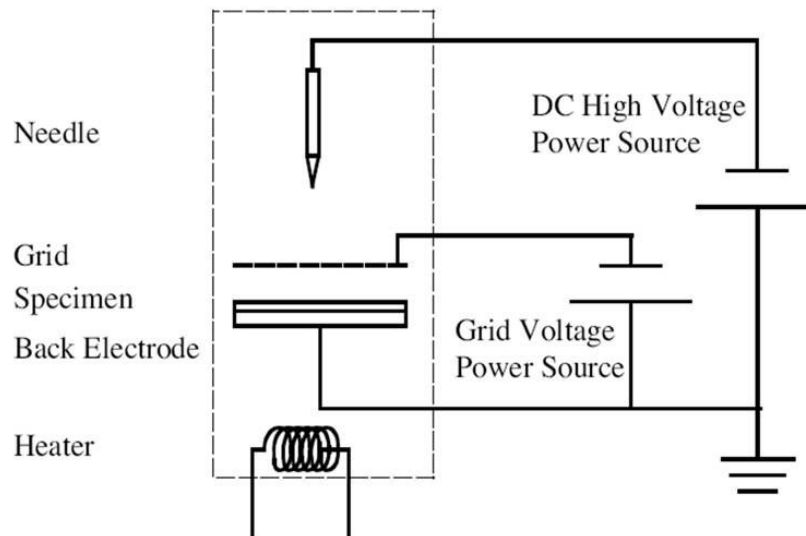


Figure 4.5: Corona Discharge Apparatus [31]

When these voltages are applied to the tip and grid, the high curvature at the tip leads to an electric field in the vicinity of the tip larger than the dielectric strength of air. A localized corona discharge forms at the tip, with the ions that are generated accelerating towards the grid, through the grid, which serves to improve charge uniformity, and towards the polymer material. These ions transfer charge to the polymer surface, increasing its potential. When the surface potential reaches that of the conductive grid, ions stop accelerating towards the polymer and the charging process stops.

The corona charging process consists of two primary currents, the current from tip to plane and the current from tip to grid. The tip-to-plane current minus the tip-to-grid current equals the charging current. As the charging process takes place, that charging current decreases. Multiple techniques have been developed to accurately measure and control these currents during the charging process [43],[46] to optimize the amount of trapped charge, maximize charge uniformity, and maximize long term charge stability.

The space-charge electret was selected for further microscale development in this work. This was done due to the ability to create fine features such as needles and wires at the microscale, and the fact that the electret film itself could remain in a structurally sound state during the polarization process. One goal of this research was then to integrate a microscale form of the corona charging process within a MEMS device so that polymer charging can occur after full device fabrication. The availability of an *in situ* charging process would significantly mitigate fabrication issues associated electret-based MEMS devices. In particular, the degradation of electret characteristics with the application of temperature narrows the process window available for subsequent MEMS processing. A post fabrication charging process removes that issue.

The physical geometry shown in Figure 4.6 is used to calculate the voltage across the space charge electret for a given surface charge density. This geometry is a standard

parallel-plate capacitor configuration [48] with charge embedded within the bulk of the dielectric.

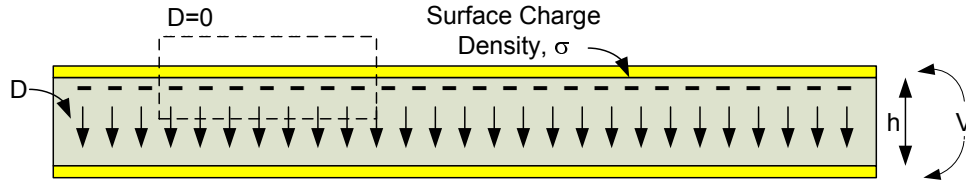


Figure 4.6: Physical Model of Space Charge Electret

In this model, there is a surface charge density,  $\sigma$ , permanently affixed to the top surface of a dielectric with thickness,  $h$ . Gauss's law in terms of free charge is

$$\int \vec{D} \cdot d\vec{a} = Q = \sigma A = DA, \quad (28)$$

where  $A$  is the area of the charge density. This leads to the classical relationship

$$D = \sigma = \epsilon E, \quad (29)$$

that yields the relationship between electric field,  $E$ , and the surface charge density,

$$E = \frac{\sigma}{\epsilon}, \quad (30)$$

where  $\epsilon$  is the permittivity of the dielectric. The voltage across the surface is then given by the relationship

$$V = Eh. \quad (31)$$

The force on a charge is given by

$$F = qE . \quad (32)$$

The typical units for charge are Coulombs, C, but an alternative set of units are found using equation (32). Since

$$q = \frac{F}{E} , \quad (33)$$

then alternative units for charge are

$$[q] = \frac{\text{meter} * \text{Newton}}{\text{Volts}} = \frac{m * N}{V} . \quad (34)$$

Therefore, alternative units for surface charge density are

$$[\sigma] = \frac{\text{Coulomb}}{\text{meter}^2} = \frac{N}{V * m} . \quad (35)$$

The surface charge density in the film is then, using alternative units,

$$\sigma = 0.68 \frac{mC}{m^2} = 6.8 \times 10^{-4} \frac{C}{m^2} = 6.8 \times 10^{-4} \frac{N}{Vm} . \quad (36)$$

Therefore, using (30) and (31), for a dielectric with a relative permittivity of 11, the electric field is

$$E = \frac{6.8 \times 10^{-4}}{(11)(8.854 \times 10^{-12})} = 6.98 \times 10^6 \frac{V}{m}, \quad (37)$$

and the voltage across the film is

$$V = Eh = (6.98 \times 10^6)(0.2 \times 10^{-3}) \approx 1400V. \quad (38)$$

Alternatively, the capacitance of the film and its total charge can be used to calculate the voltage. The capacitance of the film is given by

$$C = \frac{\epsilon A}{h}. \quad (39)$$

The total charge on the film is given by

$$Q = \sigma A, \quad (40)$$

so then the voltage across it is simply

$$V = \frac{Q}{C} \quad (41)$$

If the area of the surface charge in the structure were a 1mm by 1mm square, then the capacitance would be approximately 0.49pF. The total charge resulting from that surface charge density would be 680pC. Therefore, the resulting voltage across the film is 1387V.

The space-charge electret is well suited for MEMS applications, and has many options in terms of material type, charging techniques, and operational uses. The space-

charge electret can also easily achieve high-levels of remnant voltage, resulting in sensitive transducers. Therefore, it was selected as the type of electret employed in this work

## 4.2 Selection of Electret Materials

The materials used to form electret structures have been critical to this research effort. This section discusses analysis and modeling that went into the selection of the materials used within the final device.

### 4.2.1 Inorganic

Inorganic electrets have potential to be high temperature electret materials, but are not in common use. This work has fabricated electrets formed by Silicon Dioxide and Silicon Nitride interfaces. A silicon wafer was coated with 7000Å of silicon dioxide. After that coat, a 490Å film of silicon nitride was deposited. This formed an oxide/nitride interface. The process for this structure is shown in Table 4.1.

**Table 4.1: Inorganic Electret Deposition Process**

Process Step	Process Parameters
<b>Starting Material</b>	<b>100mm x 500um DSP Si substrate</b>
<b>SiO2 Deposition</b>	Oxidation Furnace
Measured Thickness	7000Å - 7500Å
<b>Si3N4 Deposition</b>	Sputtering Chamber
Target Thickness	500Å
Si3N4 Dep Parameters	160Watts @ 3mT with a 115.30Å/sec deposition rate
Time/Actual thickness	4min15sec, resulting in 490Å
Note:	Start @ 75Watts - ramp at rate of 25 Watts/min

Corona charging was then employed, but without the standard point-to-plane geometry. Rather, as a precursor to microcorona charging, a microneedle array was employed, separated from the material a distance of 4 mm, and raised to a potential of -2000V, as shown in Figure 4.7. A quasipermanent voltage of -470V resulted from this charging process. This voltage was nonuniform across the surface, likely due to misalignment between the plane of the electret surface and the plane of the microneedle array, leading to a higher discharge in one corner of the microneedle array. A variation on this charging approach used a fine copper mesh as the source of corona discharge, as shown in Figure 4.8.

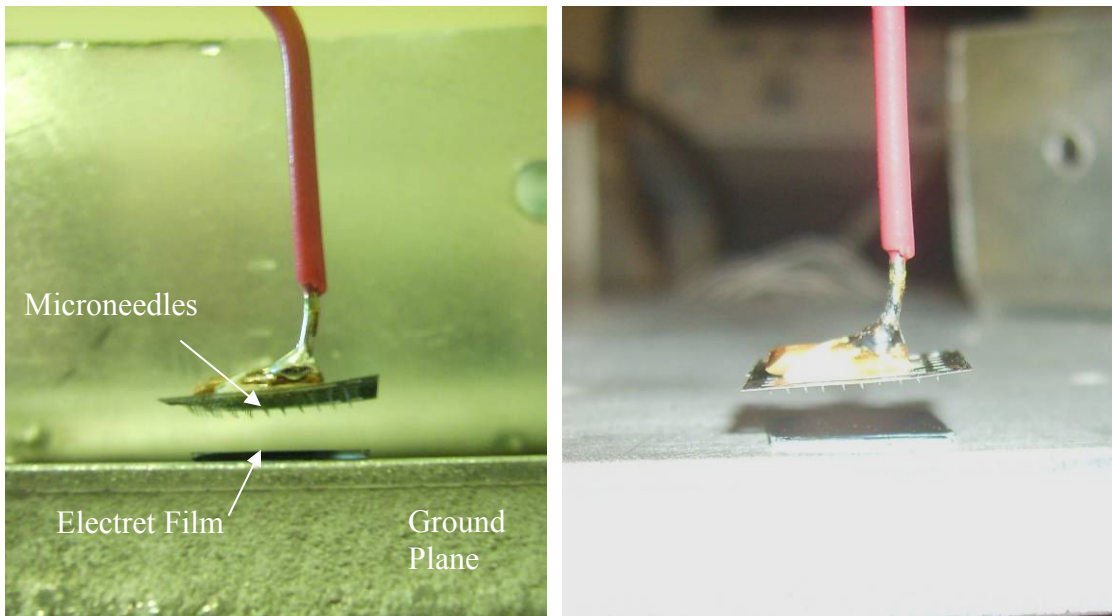


**Figure 4.7: Microneedle Array Charging Setups**

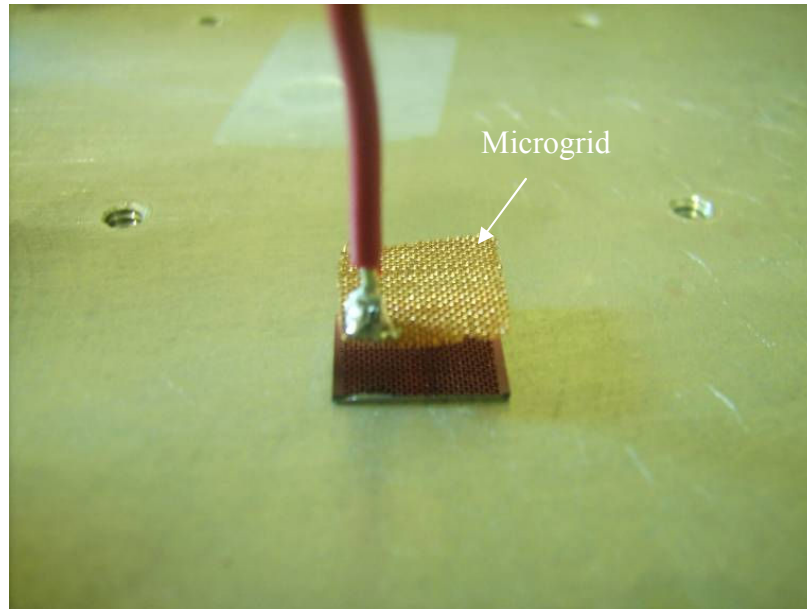


**Figure 4.8: MicroGrid Charging Setup**

The inorganic electret has potential for use in MEMS devices. The material is readily compatible with microfabrication processes, it is a common material and easily deposited, and it can potentially withstand higher operational voltages without discharging. However, the charging method and microfabrication process developed within this work was most easily applied to a polymer electret film, leaving the inorganic version to be worked in future electret charging efforts. In particular, etching posts and trenches within the polymer electret material itself, and thereby realizing a 3D electrode, was easier to implement than etching into the inorganic Nitride/Oxide interface electret, as that would destroy the charge storage interface.

#### **4.2.2 Polymer**

Polymer electrets employ a high-dielectric strength polymer, such as Teflon, to store space-charge, or a polar polymer to realize aligned dipoles, as in a dipole electret. Polymer electrets are most common, are simple to fabricate, and can be charged in multiple ways, but are more susceptible to temperature induced discharge. These

materials will typically lose polarization when approaching the glass transition temperature of the polymer film. This work selected polymer electret films because of the ease of polymer processing, the variety of charging options available, the compatibility of the uncharged polymer film with MEMS processing, and the well-understood properties of the films.

To that end, this work focused on CYTOP [47], the brand name for a perfluoropolymer similar to Teflon that is used as an encapsulant in microelectronic processes. The material can be spun coat in various thicknesses, and multiple layers can be sequentially deposited to yield films in the 10 to 20 micron range. The material has a dielectric strength of 60 V/ $\mu\text{m}$ , and has been demonstrated to hold substantial levels of space-charge for years. CYTOP electrets have been formed from both Corona discharge processes and back-lighted thyratron electron implantation [32]. These films have achieved surface charge densities of greater than 0.68mC/m<sup>2</sup> [31].

However, CYTOP has a glass transition temperature of 108°C, and temperatures above that lead to discharge within the film. Therefore, processing of charged CYTOP needs to be done at low temperatures, making it difficult to integrate directly into MEMS devices. The processes developed in this work allow CYTOP to be integrated into a device, and charged after device fabrication.

Deposition, etching, and compatibility tests were performed using this material. Corona charging was performed on cured films, leading to space-charge electrets. Corona charging processes include point-to-plane corona with and without a charging grid, microneedle array charging, and micro grid charging. Figure 4.9 shows the point-to-plane with triode grid arrangement used. Charged 10  $\mu\text{m}$  films had uniform surface potentials that were in the range of negative 500 to negative 600 volts.

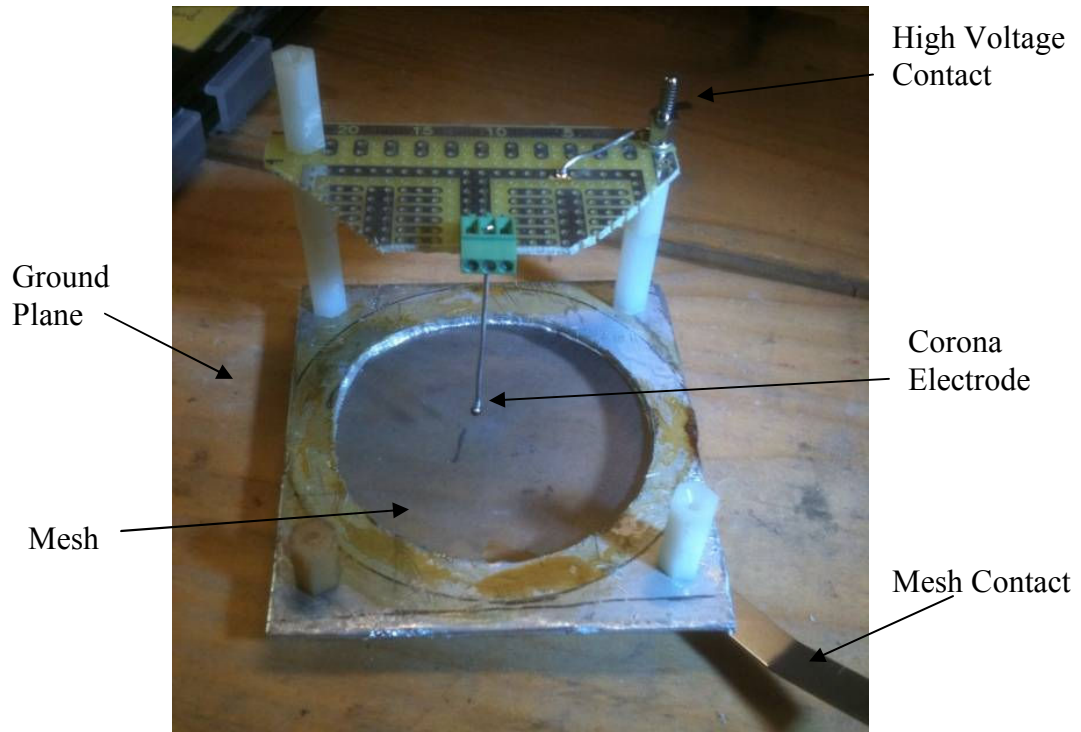


**Figure 4.9: Point-to-Plane Charging Apparatus used for Polymer Electrets**

Due to its maturity and ease of implementation, the polymer space-charge electret formed through corona discharge was selected for investigation and application in the resonant ultrasonic sensor array. Fabrication processes were then developed to integrate the material within the structure and to polarize the material after fabrication was complete.

### **4.3 Electret Integration in MEMS**

A key focus of this research has been to advance the state-of-the-art in the integration of electret structures within MEMS devices. To improve the integration of electrets into MEMS devices, a variety of techniques have been investigated. This section discusses some of the modeling and design activities that went into process selection and development.

### **4.3.1 Wafer Bonding - Localized Heating**

As discussed earlier, this research work ultimately focused on CYTOP, a Teflon-type polymer that can be spun coat, has a dielectric strength of 60 kV/mm, and a glass transition of 108°C. When charged by a corona-type discharge, CYTOP films yield a highly-stable space-charge electret. However, the film discharges at temperatures near the glass transition temperature, making it difficult to process films after charging.

One approach to electret integration that has been investigated is the use of localized heating to allow subsequent processing of charged CYTOP films. An example of a subsequent process would be some form of bonding at elevated temperatures. The conceptual process flow is shown in Figure 4.10, and employs embedded localized heating to keep the CYTOP from the high bonding temperatures during the bonding processes.

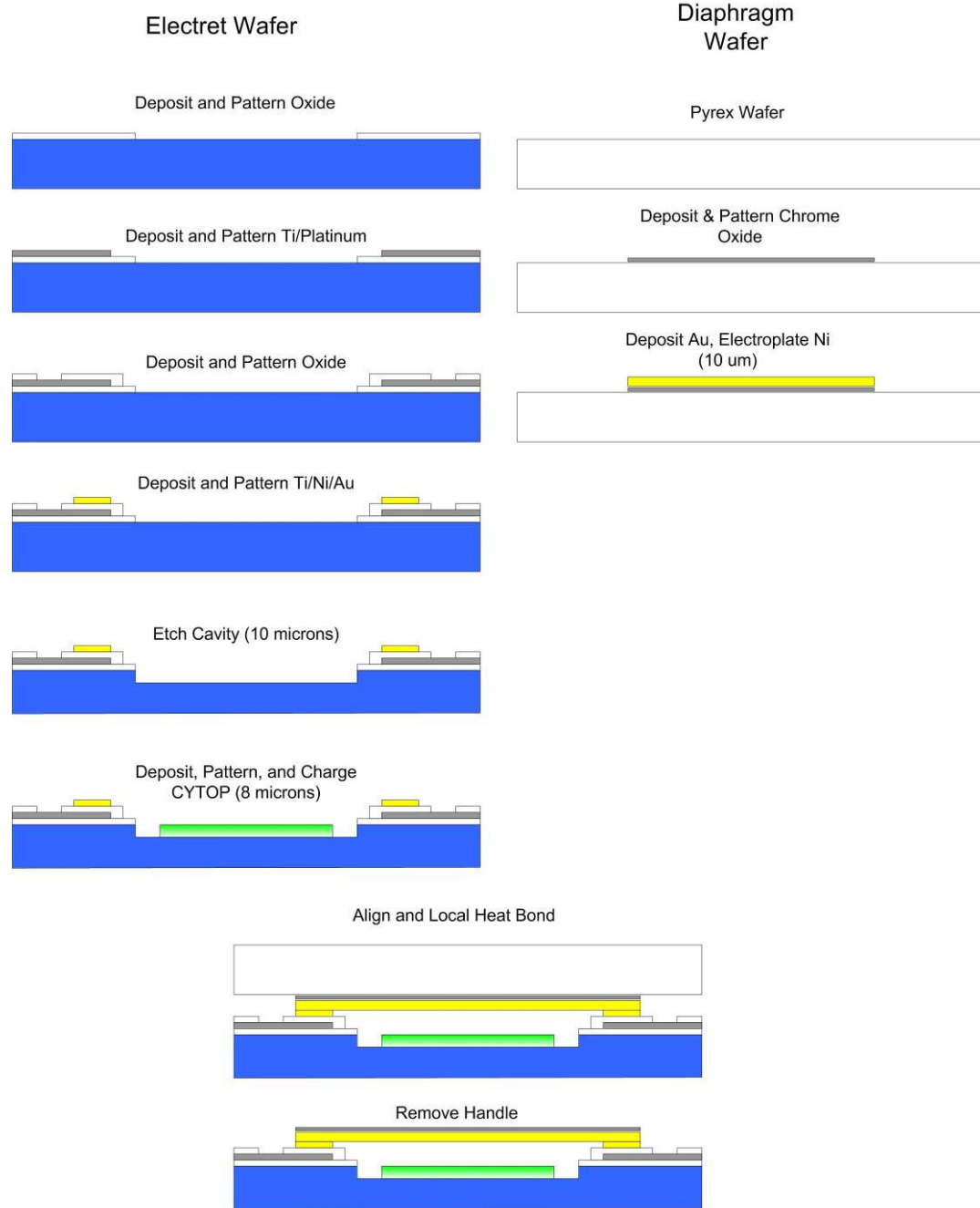


**Figure 4.10: Process Flow for Localized Heating**

The conceptual process consisted of two separate wafers; an electret wafer and a MEMS structural wafer. This process still requires wafer bonding, as many electret MEMS processes do, but this process utilizes localized heating near the bonding area to

avoid raising the temperature of the electret film, thereby allowing it to be charged prior to the bonding process, yet still surviving the bonding process.

The electret wafer was first coated with an oxide insulating film with an opening to allow the CYTOP film to be in contact with the silicon surface, which serves as the bottom electrode of the device. On top of that is deposited a Titanium adhesion layer followed by a 25 micron thick Platinum film. These films are patterned, through a liftoff process, to realize heater elements and contact pads for those elements. On top of that is deposited an insulating film to separate the bonding ring from the heater. A gold bonding ring is then deposited and patterned on top of the layer stack. Finally, a cavity is etched into the silicon to form the air gap in the device, and CYTOP film is patterned and deposited, and polarized through corona discharge.

The diaphragm wafer, on the other hand, is built on a Pyrex substrate, to allow visual alignment during bonding, and utilizes a metal transfer release mechanism that allows the fabricated metal diaphragm to be bonded to the electret wafer and then the Pyrex wafer to be subsequently removed.

The diaphragm wafer starts with a Pyrex substrate on top of which is deposited and patterned, through liftoff, a stack of chrome, chrome oxide, and gold. The metal layers are deposited in one run in an ebeam evaporator. Chrome is first deposited, followed by exposure to air, followed by a gold deposition. The interface between chrome oxide and gold has poor adhesion, and this interface will release in favor of a stronger one. On top of the gold, a thick film of nickel is plated using an electroless process. This Ni film is the structural element in the final device.

After both wafers are fabricated, they are visually aligned through the Pyrex, with an interfacial solder preform between the gold and the nickel. The localized heaters are then energized, raising the temperature of the bond ring, and hence the solder preform, to the solder melting point leading to solder reflow. After the heaters are turned off and the solder cools, the Pyrex wafer is pulled away from the stack, with the interface between

the gold on the bottom of the Ni structure “releasing” from the chrome oxide layer, finalizing the transfer of the structural element from one wafer to the other.

In this process, two key steps are required, the fabrication of local heaters, and the creation of metal structures that could be released from a carrier wafer. The local heaters are traces fabricated in a platinum thin film. To explore this process, initial process steps were performed and compared to expected results. The platinum heater elements were first designed and fabricated, and are shown in Figure 4.11.

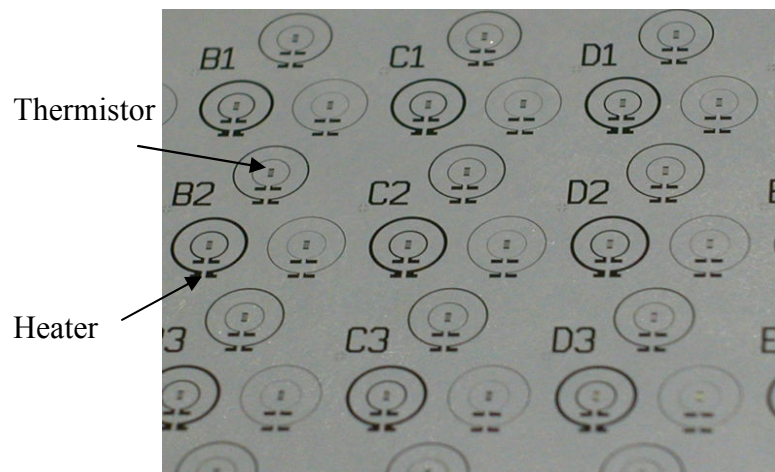


**Figure 4.11: Fabricated Local Heaters**

A single heater was coated with nitride, connected to a current controlled power supply, and operated under an IR temperature sensor. Figure 4.12 shows the temperature achieved as a function of input current. This temperature easily achieves levels necessary for a variety of bonding steps.

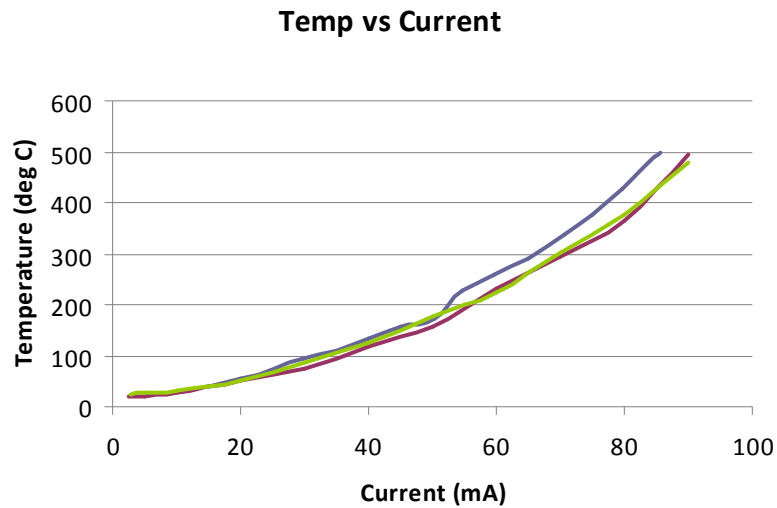


**Figure 4.12: Temperatures Achieved by Local Heaters**

The next step in the development was to verify that the temperature of the center of the heater, where the CYTOP resides, does not exceed the glass transition temperature of the CYTOP. An initial FEA model was developed to design the local heater structures. Figure 4.13 shows the temperature distribution in the substrate when operating the heater elements. This model assumes a continuous current flow through the elements. The area around the elements easily achieves over 150°C, making it useful for the performance of various bonding processes. The region where the electret would be placed, however, does not exceed 40°C. This would imply that a charged electret would not experience thermal discharge during bonding steps that would be performed using the local heating.

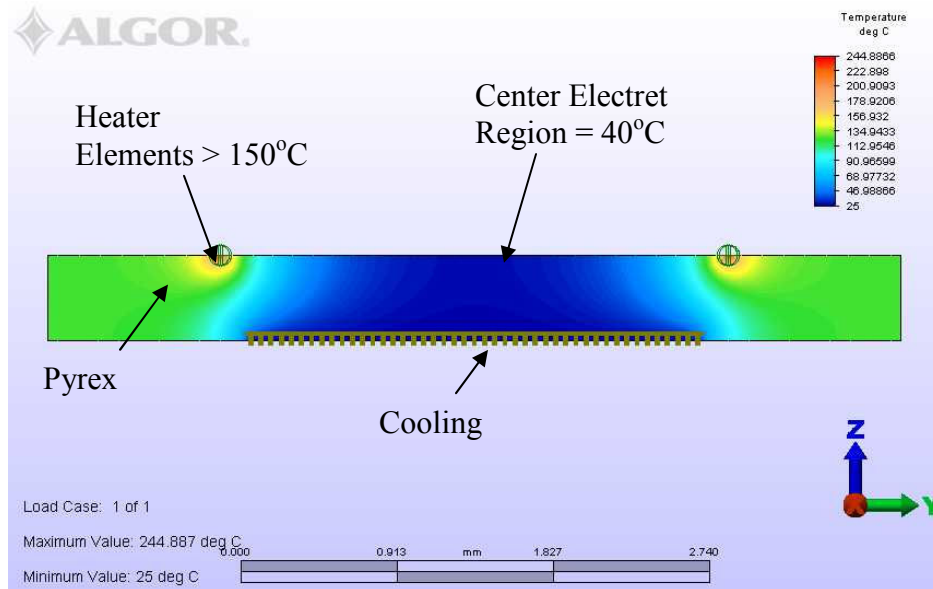


**Figure 4.13: Finite Element Model of Local Heaters**

The second piece required for the local heating process is a wafer with microstructures that can be transferred to a charged wafer and bonded using local heating. This was achieved using the poor adhesion of Gold to Chrome Oxide (CrOx). A Pyrex wafer was patterned with a CrOx/Au film using standard sputtering and liftoff process. This was followed by a standard electroless nickel plating step [49] to build up film thickness. The resulting structures are easily peeled away from the carrier wafer.

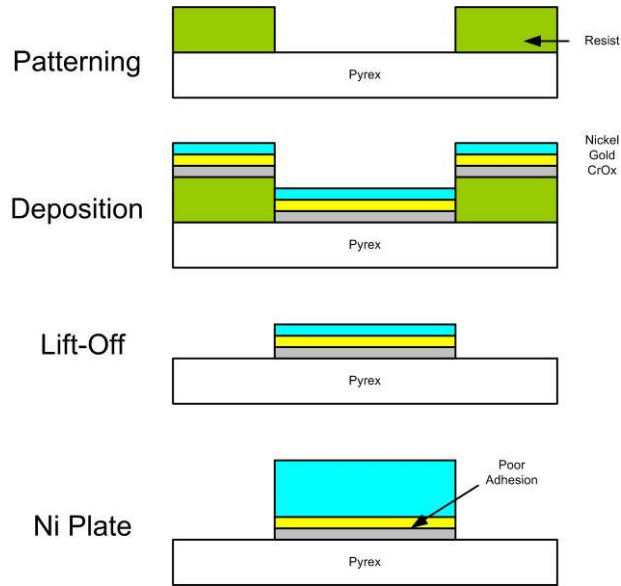


**Figure 4.14: Process Flow for Fabrication of Releasable Diaphragms**

This process has realized thick metal structures that are easily released from the substrate, as shown in Figure 4.15. The picture on the left uses side lighting, while the picture on the right uses top lighting. The plated film was relatively thick, and the stresses led to curvature and early release from the substrate. Plating began underneath the structure and added to the curvature and release. An actual device would use thinner plating; thereby mitigating this issue.

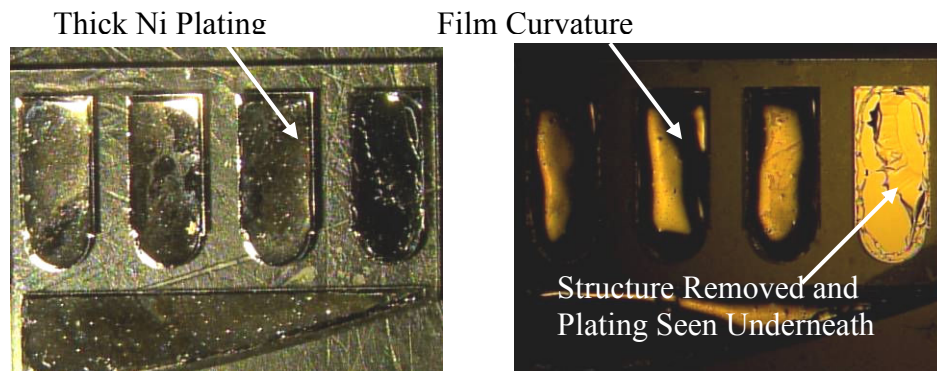


**Figure 4.15: Fabricated Releasable Diaphragms**

The local heating approach showed potential. However, due to the complexity of the bonding approaches considered for this process flow, further development ceased when *in situ* charging utilizing an embedded charging grid was performed.

#### **4.3.2 *In Situ* Charging Using MicroCorona**

Localized heating approaches still require corona charging of the electret film prior to further bonding. It is advantageous, though, to realize a process flow wherein the electret charging occurs entirely after device fabrication. This section discusses modeling and design activities associated with developing an *in situ* charging process.

The point-to-plane corona discharge is an effective technique for charging and polarizing polymer space-charge electrets. A typical point-to-plane electrode arrangement results in an electric field that is larger than the dielectric strength of the surrounding gas, leading to ionization. The ions are accelerated to the surface of the polymer and transfer their charge to charge traps, where it is retained for a long period of time.

In a conceptual *in situ* charging process flow, such as that shown in Figure 4.16, the electret film is first deposited on the substrate, followed by a charging electrode of some sort. After that, a thick release layer of material is deposited and patterned as required. Following the release layer, a structural layer is deposited. This layer is designed to meet structural requirements, but also serves to allow release of the air gap, and might also possibly serve a purpose in the charging process. After release and opening of the air gap, voltages are applied to the substrate, the middle electrode, and the top electrode, in order to charge the electret film.

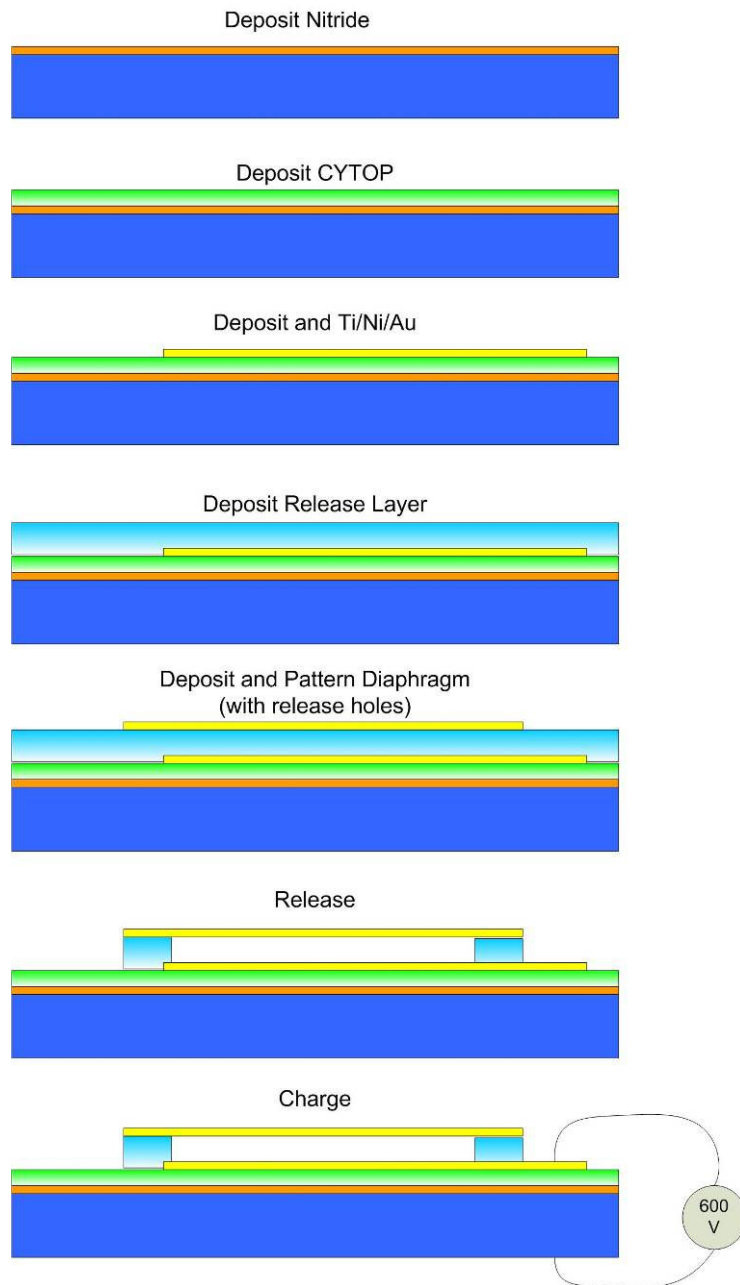


**Figure 4.16: *In Situ* Charging Process**

In a micro corona approach, the charging electrode is replaced by a microlithographically patterned grid that is specially designed to yield a corona discharge when placed at a potential of a few hundred volts, as shown in Figure 4.17.

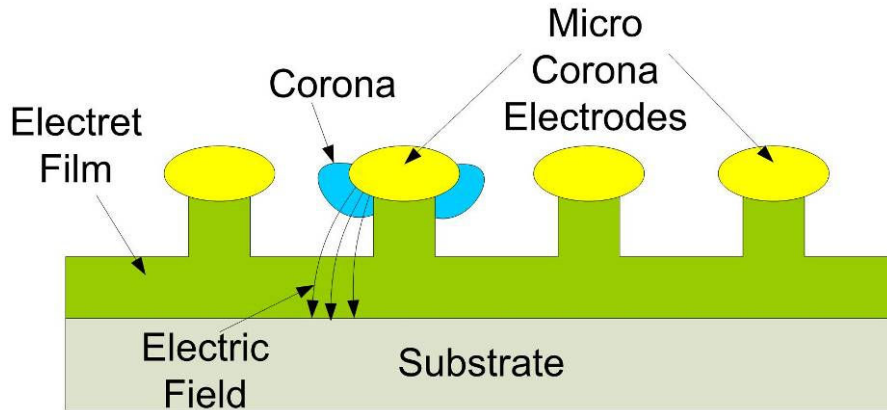


**Figure 4.17: Schematic of Microcorona Charging Approach**

Electrostatic simulations of the electric field within the air gaps of this structure were performed in ANSOFT Maxwell. Figure 4.18 shows that a thin film of metal suspended over the CYTOP can yield a small corona discharge, leading to ions that are accelerated towards the CYTOP and trapped at the surface. This approach could simplify device fabrication, although potentially at the expense of longer charging times and slightly lower voltage electrets.

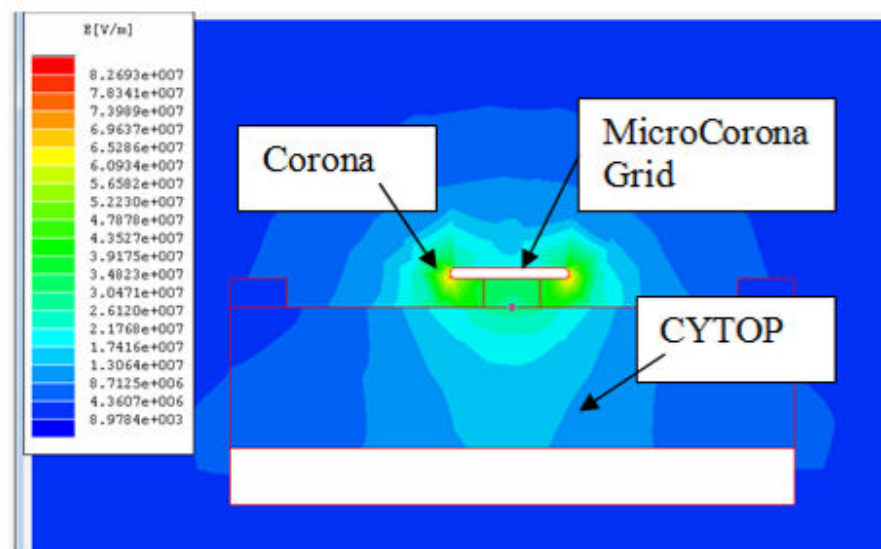


**Figure 4.18: Microplasma Electrostatic Model**

To perform a test of this concept, proof-of-principle samples were fabricated. The electret film was deposited using the process listed in Table 4.2, yielding a 10 $\mu$ m thick film [47]. Following the CYTOP deposition, metal was deposited over a hand drawn pattern of photoresist lines. The metal was deposited as listed in Table 4.3. The photoresist was then stripped and an oxygen plasma etch (Table 4.4) of the CYTOP was performed to undercut the edges of the metal by 1  $\mu$ m. Finally, the metal was placed at a potential of -600V, with the sample sitting on a grounded metal plate.

**Table 4.2: CYTOP Test Process**

Process Step	Process Parameters
Back Electrode	Cr/Au EBeam Evaporation
Adhesion Promoter	MicroChem MP90
Bake	Hotplate 95°C - 2min
Spin Coat	500rpm for 10sec then 1000rpm for 20sec
Bake	Hotplate 100°C - 30min
Spin Coat	500rpm for 10sec then 1000rpm for 20sec
Bake	Hotplate 100°C - 30min
Spin Coat	500rpm for 10sec then 1000rpm for 20sec
Bake	Hotplate 100°C - 30min
Spin Coat	500rpm for 10sec then 1000rpm for 20sec
Bake	Hotplate 100°C - 30min
Spin Coat	500rpm for 10sec then 1000rpm for 20sec
Bake	Hotplate 100°C - 30min
Bake	Hotplate 200°C - 60min
Oxygen Plasma	300W for 30sec with 12.5sccm of O <sub>2</sub> at 150mTorr

**Table 4.3: Metal Deposition Process**

<b>Process Step</b>	<b>Process Parameters</b>
Target Metal Thickness	4250Å
Machine	CHA Mark-50 E-Beam Evaporator
BP Pressure (Torr)	$7.3 \times 10^{-7}$
Cr (Dep Rate / Target Thickness)	3.0 A/sec resulting in 252Å
NiCr (Time Secs / Target Thickness)	8min resulting in 3000Å
Au (Dep Rate / Target Thickness)	2.0 A/sec resulting in 1002Å
Acetone Bath to Liffoff Metal	30 min
IPA Rinse	1 min

**Table 4.4: Oxygen Plasma Undercut Process**

<b>Process Step</b>	<b>Process Parameters</b>
Oxygen Plasma Etch	300W for 2min with 12.5sccm O <sub>2</sub> at 150mTorr

After charging, the wafers were scanned using an electrostatic voltmeter and showed high levels of static voltage (approximately -100V) near the edges of the metal lines. The static voltage may have been larger, but the resolution of the electrometer probe averages the fine charging pattern, leading to a smaller measurement.

The desire was then to create a wide area microcorona discharges at the surface of the polymer, allowing corona charging to occur within a fabricated device, as shown in Figure 4.19.

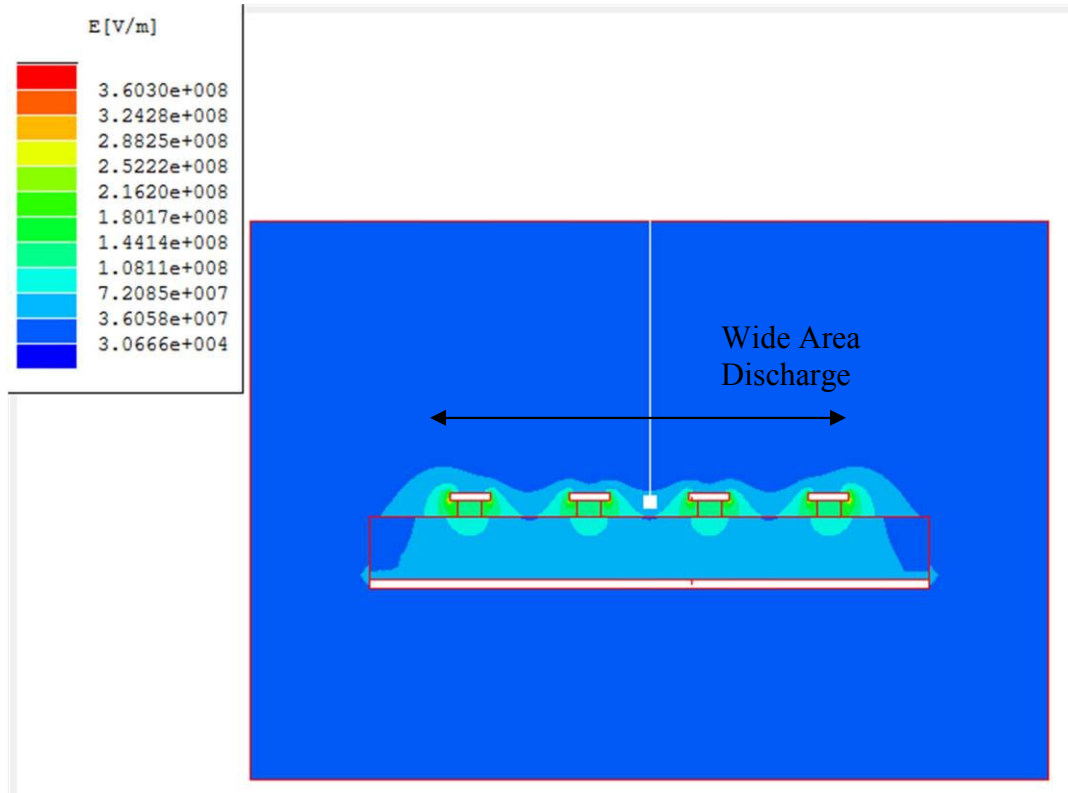


Figure 4.19: Electrostatic Simulation of MicroCorona

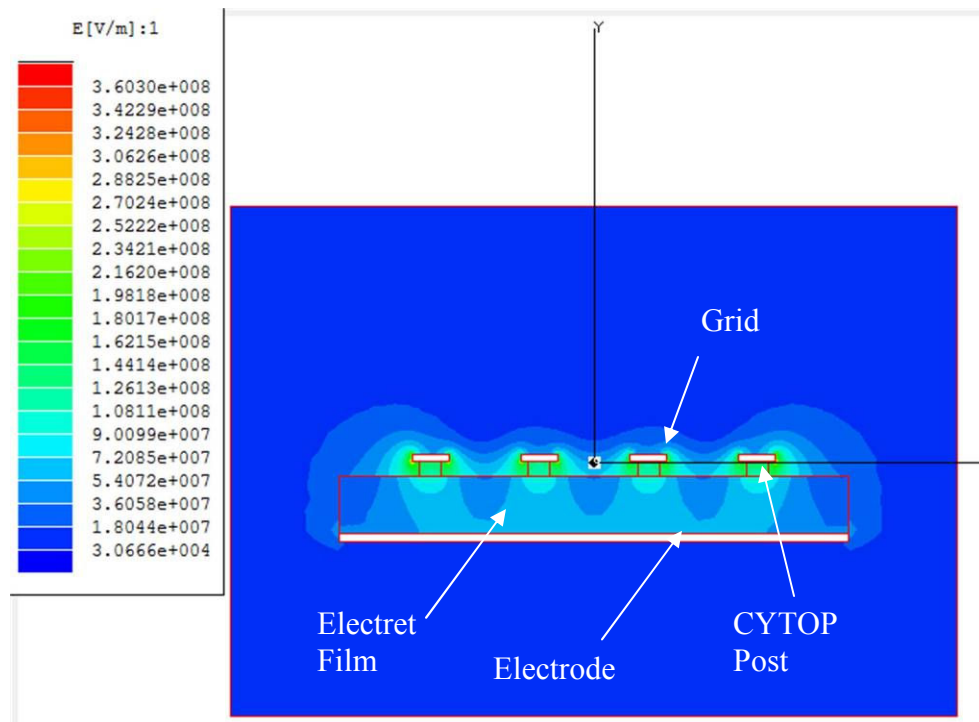
### 4.3.3 Microcorona Theoretical Analysis

This section discusses the theoretical modeling and design activities for the wide-area microcorona discharge process.

A corona discharge is a self-sustaining plasma created when the dielectric breakdown of air, or other working gas, is exceeded in a small region of high electric field. A key component of a corona discharge, however, is that the electric field is only high enough in a small portion of the region between two electrodes, not entirely throughout the region. If the electric field exceeds the dielectric strength in a continuous region between electrodes, an arc will occur. A corona discharge is the precursor to that arc. Most often, a corona is formed through the use of a highly curved electrode coupled with a planar electrode. The high electric field due to the curvature yields a corona

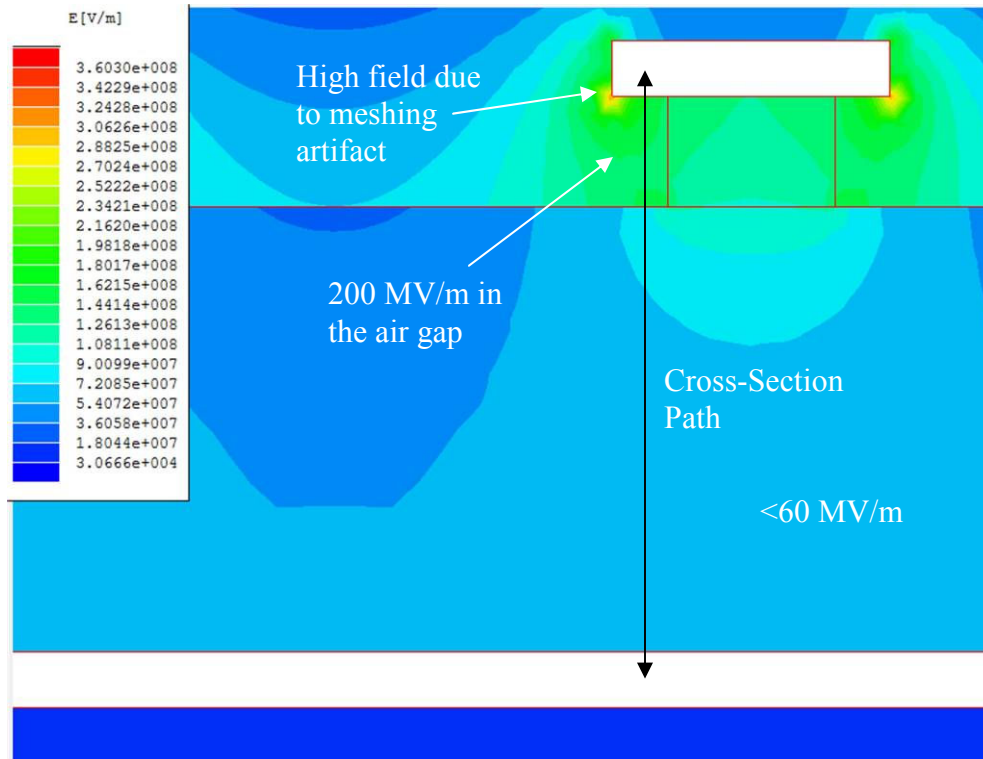
discharge in a localized region. In the microcorona described here, the high electric field is generated by a narrow metal micropatterned trace suspended above an air gap.

Figure 4.20 shows an electrostatic simulation of a microgrid with 5 micron wide metal lines, separated by 10 microns, and suspended 2 microns above the surface of a polymer electret film, in this case, CYTOP. The grid has been energized to -800V with respect to the bottom electrode. The CYTOP film is actually 8 microns thick, although a 2 micron post of CYTOP is used to suspend the grid above the surface.



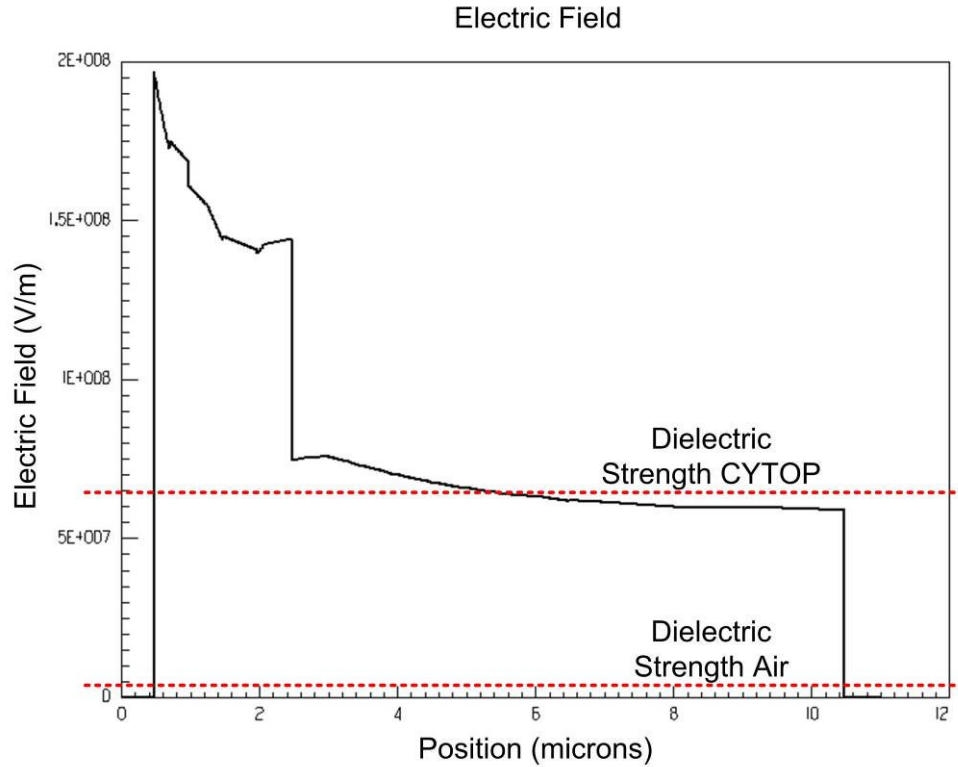
**Figure 4.20: Electrostatic Simulation of Microgrid**

Figure 4.21 shows a close-up view of the electric field magnitude near the metal line. The highest electric field is in the air gap between the metal conductor and the polymer surface.



**Figure 4.21: Electrostatic Simulation of Microgrid (Close-Up)**

Figure 4.22 shows the electric field along the cross-section path within the air gap starting from the metal grid and progressing down through the gap towards the bottom electrode. The electric field is initially at a very high value of close to 200 MV/m, and decreases exponentially to the polymer surface. This field is much larger than the breakdown of air. At the surface of the CYTOP, the field drops considerably. A short distance into the CYTOP, the electric field drops below 60MV/m. This is below the dielectric strength of CYTOP. The CYTOP does not experience breakdown. Only the air gap experiences breakdown.



**Figure 4.22: Electric Field Magnitude in Air Gap**

It is clear from these simulations that substantially less than -800V is required to achieve air breakdown conditions within the gap. A second simulation was performed to determine the minimum voltage levels required. Figure 4.23 and Figure 4.24 show the electric field within the gap at a charging grid voltage of -30V. The electric field within the gap is still slightly higher than the dielectric breakdown of air. A weak corona, with a small discharge current, may exist within this gap at this point.

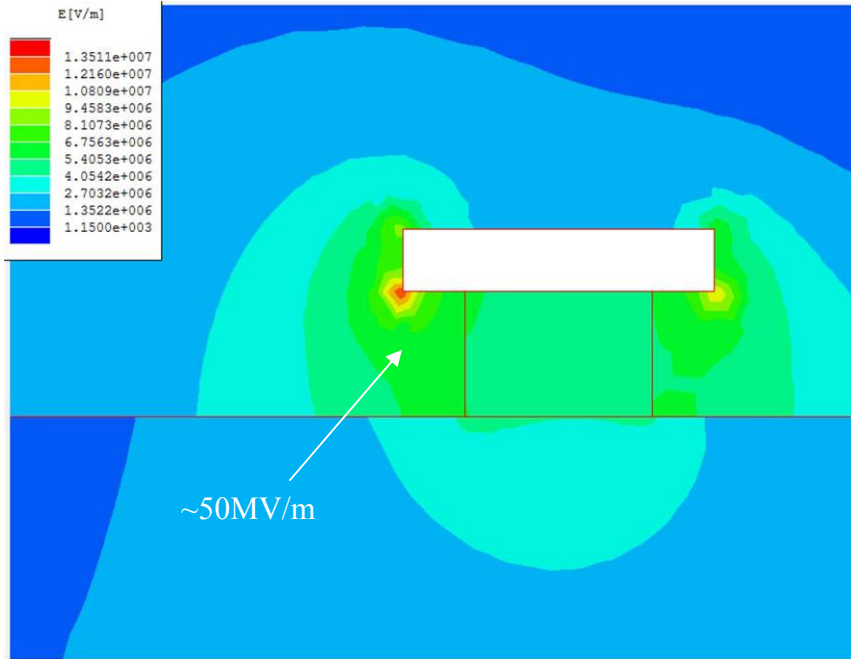


Figure 4.23: Electric Field within Gap at -30V

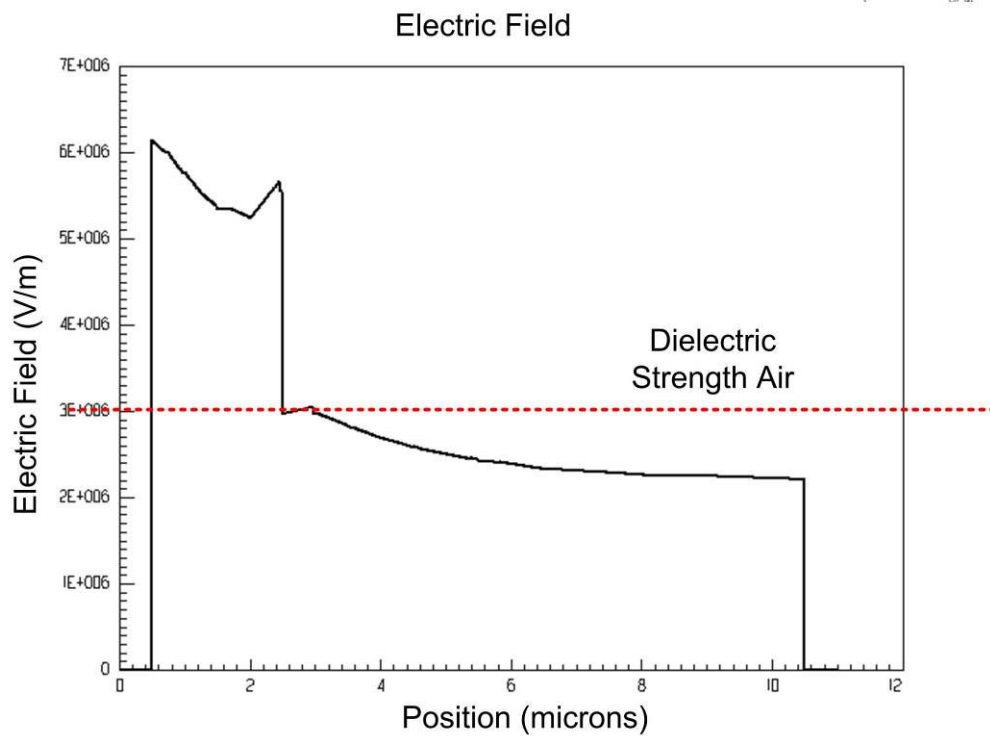


Figure 4.24: Electric Field through Gap at a -30V Grid Potential

A similar charging grid model with 45 micron spacing between metal lines is shown in Figure 4.25. The purpose of the model is to determine the impact of grid spacing on the charging process.

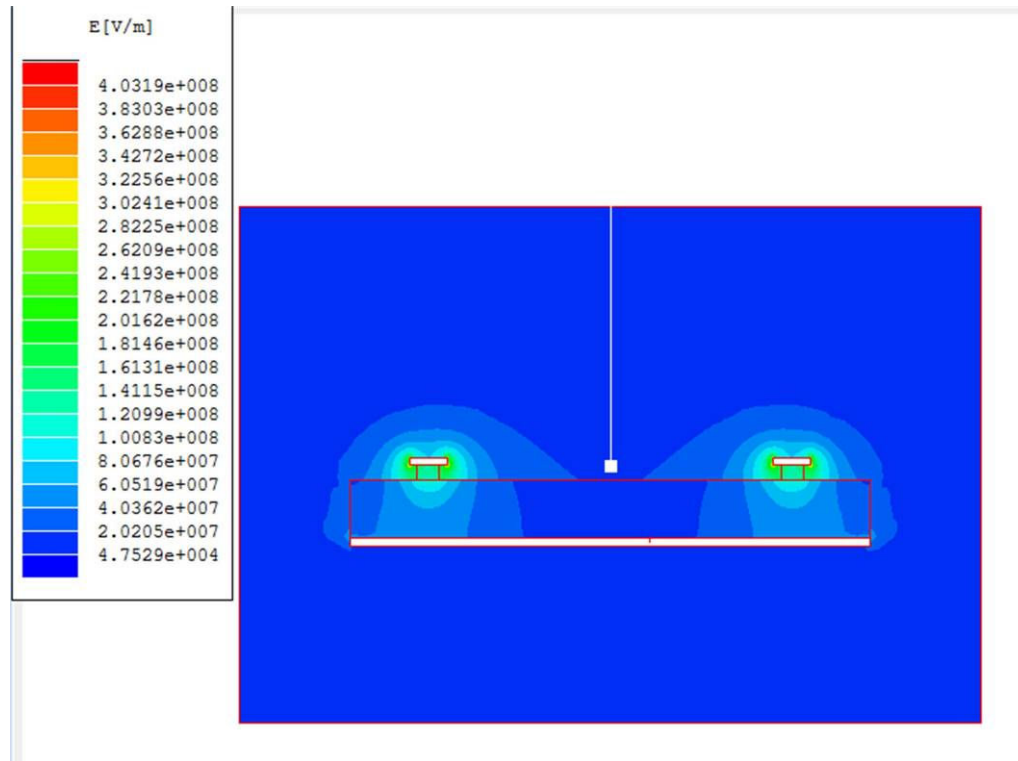
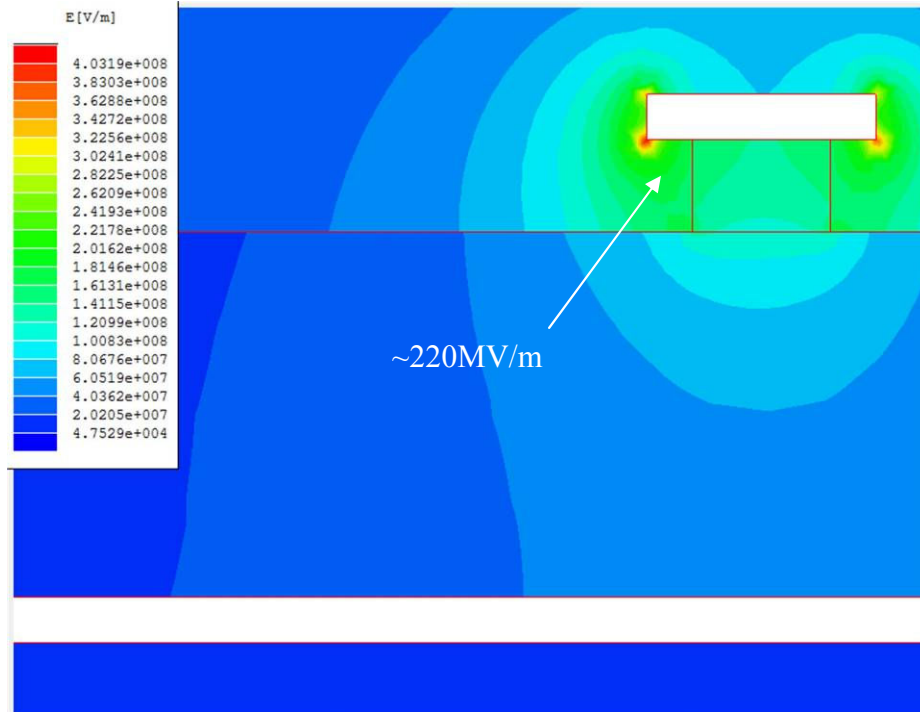


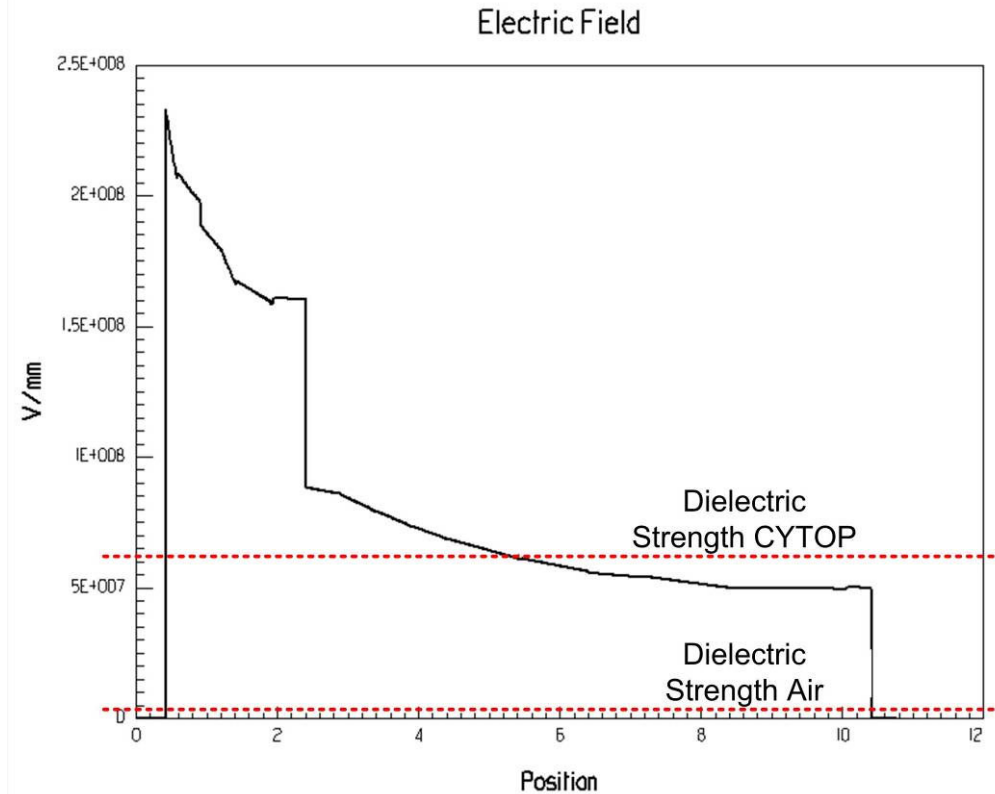
Figure 4.25: Electrostatic Simulation of Microgrid with 45 $\mu\text{m}$  Spacing

Figure 4.26 shows a close-up view of the air gap in this case. The electric field distribution looks very similar.



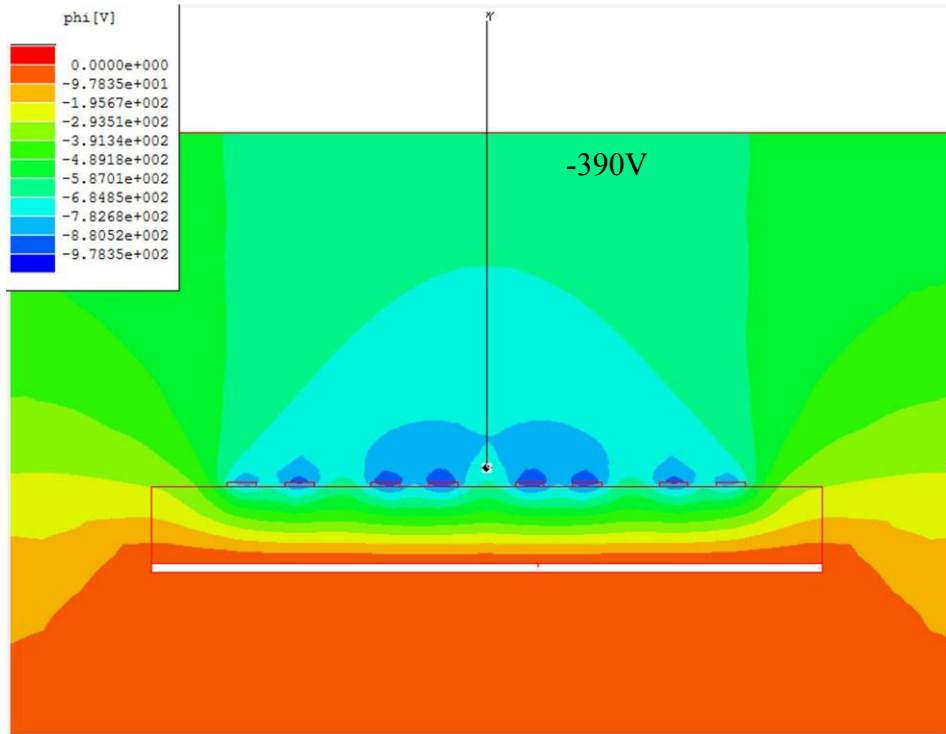
**Figure 4.26: Electrostatic Simulation of Microgrid with 45µm Spacing (Close-Up)**

Figure 4.27 shows that this charging scenario leads to a higher electric field within the air gap. This is due to the reduced coupling to nearby metal traces.



**Figure 4.27: Electric Field Magnitude through Air Gap**

It is anticipated that once the charging grid is energized and a plasma discharge occurs, it will continue as long as the potential difference between the charging grid and the surface of the electret film is large enough to maintain ionization of the gas in the gap. Therefore, it is expected that final electret voltages will be within 10's of volts of the charging grid voltage. Actual measurements show smaller remnant voltages, however. Two issues lead to this. The first is that the charge is not uniformly distributed over the surface of the film. Figure 4.28 shows the electrostatic potential distribution from a nonuniformly charged surface. The simulation shows the reduction in potential a distance from the surface due to the nonuniformity.



**Figure 4.28: Remnant Voltage from a Nonuniformly Charged Surface**

However, this nonuniformity does not account for the entire difference seen in actual measured samples. The other influential factor is the masking of the potential by the charging grid that stays in place after electret formation. The critical factor is the state of charge of that conductor. Figure 4.29 shows the potential distribution if the charging grid is simply left floating after the charging cycle is complete. This floating conductor has a net charge of zero. The potential looks very similar to the potential seen earlier if no conductive grid existed.

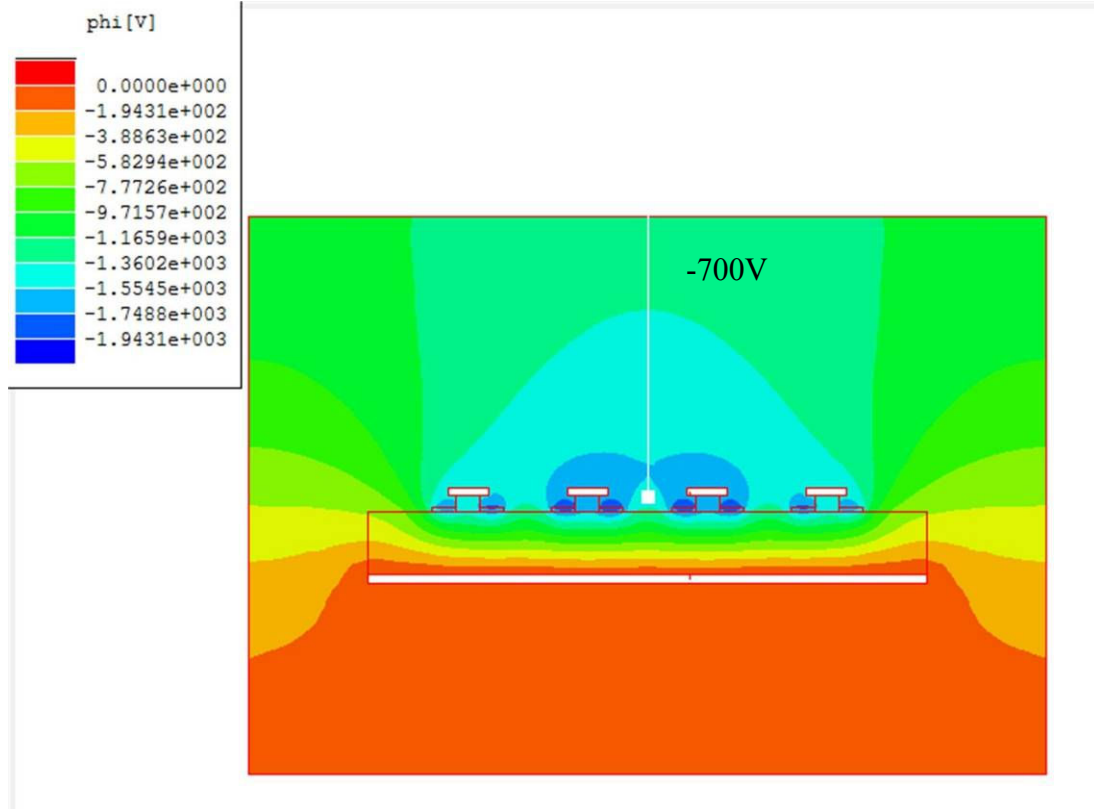


**Figure 4.29: Remnant Potential with a Floating Conductor**

Figure 4.30, however, shows the situation if the charging grid is grounded after the charging cycle takes place. In this case, the act of grounding has transferred charge to the conductor. This charge counteracts the charge from the electret and masks the voltage. A significantly smaller remnant voltage is seen at a distance, and matches actual test results, in which the charging process ends with a grounding of the charging grid prior to removal of the device from the charging apparatus.

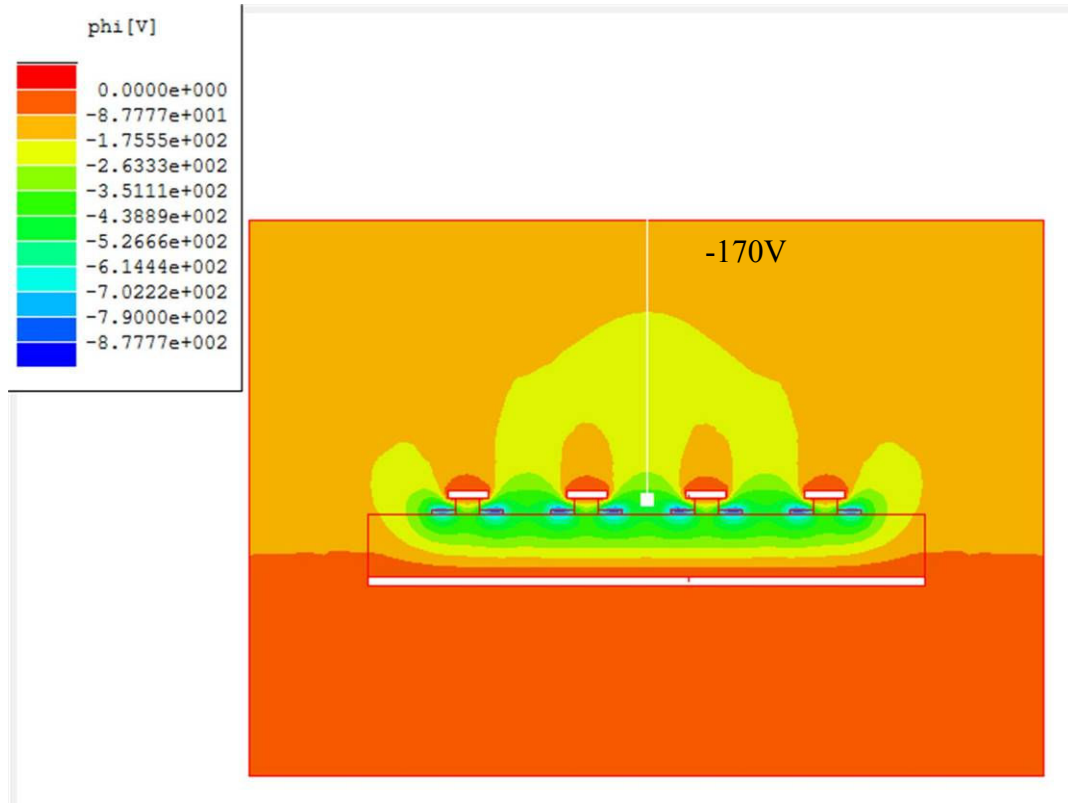


**Figure 4.30: Remnant Potential with a Grounded Conductor**

These calculations and simulations indicate that corona discharges, as well as larger arc discharges, occur in the gap between the conducting grid and the polymer surface. These discharges result in surface charging, leading to a nonuniformly charged surface. If no charging grid exists after the charging, the static voltage measured a distance from the surface would be lower than a typical corona-charged sample. If the charging grid remains floating after the charging process, almost the entire charging voltage remains. If the charging grid is grounded after the charging process, the static voltage is reduced from the charging voltage to an even larger extent. However, there is still a significant static voltage available for sensor operation.

#### 4.4 Electret Array and Charging Grid Fabrication

The process used to form the CYTOP film and charging grid is relatively simple. A ten micron thick film of CYTOP is built up using 5 sequential spin coats and soft cures of 2 micron thick CYTOP. This is followed by patterning, through a liftoff process, of the metal charging grid. Finally, a short oxygen plasma is performed to undercut the metal edges. The entire flow is shown in Figure 4.31.

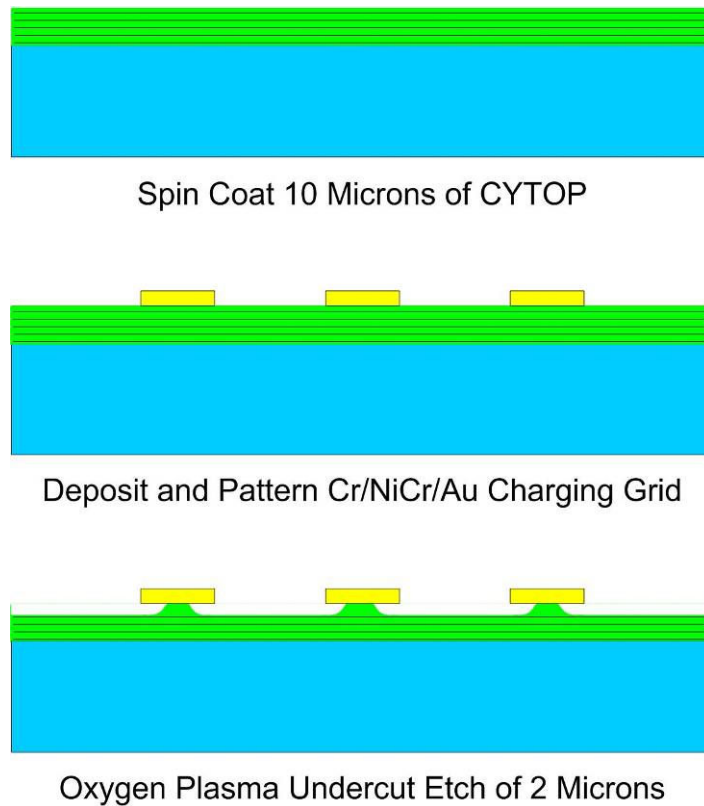


**Figure 4.31: Process Flow for Electret and Charging Grid**

The details of the process for thick CYTOP deposition are listed in Table 4.5. This is based on one of the multiple recommended processes from the manufacturer [47]. This process was selected because of the individual soft-bake step that helped stabilize the thin film during spin coating. In addition, using multiple spin coats of the material minimized bubble formation during cure.

**Table 4.5: CYTOP Deposition Process Flow**

Process Step	Process Parameters
Adhesion Promoter	MicroChem MP90
Bake	Hotplate 95°C - 2min
Spin Coat	500rpm for 10sec then 1000rpm for 20sec
Bake	Hotplate 100°C - 30min
Spin Coat	500rpm for 10sec then 1000rpm for 20sec
Bake	Hotplate 100°C - 30min
Spin Coat	500rpm for 10sec then 1000rpm for 20sec
Bake	Hotplate 100°C - 30min
Spin Coat	500rpm for 10sec then 1000rpm for 20sec
Bake	Hotplate 100°C - 30min
Spin Coat	500rpm for 10sec then 1000rpm for 20sec
Bake	Hotplate 100°C - 30min
Bake	Hotplate 200°C - 60min
Oxygen Plasma	300W for 30sec with 12.5sccm of O <sub>2</sub> at 150mTorr

Following the CYTOP deposition, a photoresist liftoff mask is deposited and patterned. Standard photoresist materials can be used for pattern transfer. Table 4.6 lists the process parameters used.

**Table 4.6: Charging Grid Patterning Process**

Process Step	Process Parameters
Adhesion Promoter	MicroChem MP-90
Bake	Hotplate 95°C for 2min
Resist/ Spin/ Time	AZ5214 at 2500rpm for 30sec
Bake	Hotplate 95°C –for 2min
Stepper	MA6
Type Alignment	No Alignment Required
Exposure Time :	10sec for 4cycles
Pre Exposure Bake	110°C for 45sec
Flood Exposure (Karl Suss)	12sec
Develop	1min30sec in MF319
DI Rinse 1	2min
Spray Rinse	10-20sec
N <sub>2</sub> dry	

After lithography is complete, the metal for the charging grid is deposited and liftoff is performed to pattern the charging grid. The process used is listed in Table 4.7.

**Table 4.7: Charging Grid Metal Deposition Process**

Process Step	Process Parameters
Target Metal Thickness	4250Å
Machine Build	CHA Mark-50 E-Beam Evaporator
BP Pressure (Torr)	$7.3 \times 10^{-7}$
Cr (Dep Rate/Target Thickness)	3.0 Å/sec for 252Å
NiCr (Time (Secs)/Target Thickness)	8min for 3000Å
Au (Dep Rate/Target Thickness)	2.0 Å/sec for 1002Å
Acetone Bath to Liftoff Metal	30 min
IPA Rinse	1 min

After liftoff, a critical step consists of isotropically etching the CYTOP so that the metal grid is suspended above the remaining CYTOP surface by short pillars. This

provides an air gap that can be ionized by the electric field. The isotropic etching process is as follows:

**Table 4.8: CYTOP Etch Process**

<b>Process Step</b>	<b>Process Parameters</b>
Oxygen Plasma Etch	300W for 2min with 12.5sccm O <sub>2</sub> at 150mTorr

To develop the *in situ* charging process, a full charging grid was fabricated in metal deposited directly on CYTOP. The design of the microcorona grid is shown in Figure 4.32. It consists of a 2.5mm by 2.5mm square mesh made up of 5 micron lines. A variety of line spacings were employed. The grid is connected by a trace to a large contact pad onto which the high voltage can be placed. The spacing between metal lines in the mesh varied from 10 microns to 45 microns in increments of 5 microns.

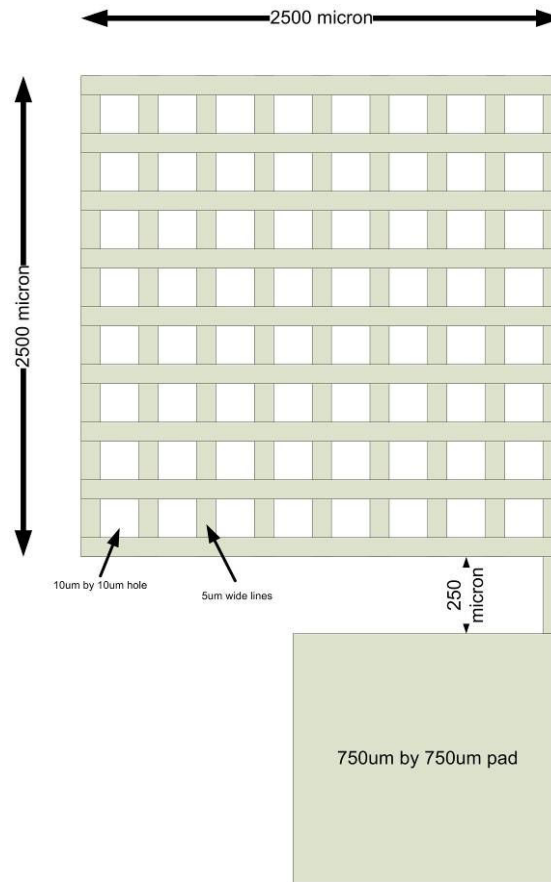


**Figure 4.32: Square Mesh MicroCorona Grid**

The test wafer was laid out as shown in Figure 4.33, and included a variety of charging grids with different metal spacings.



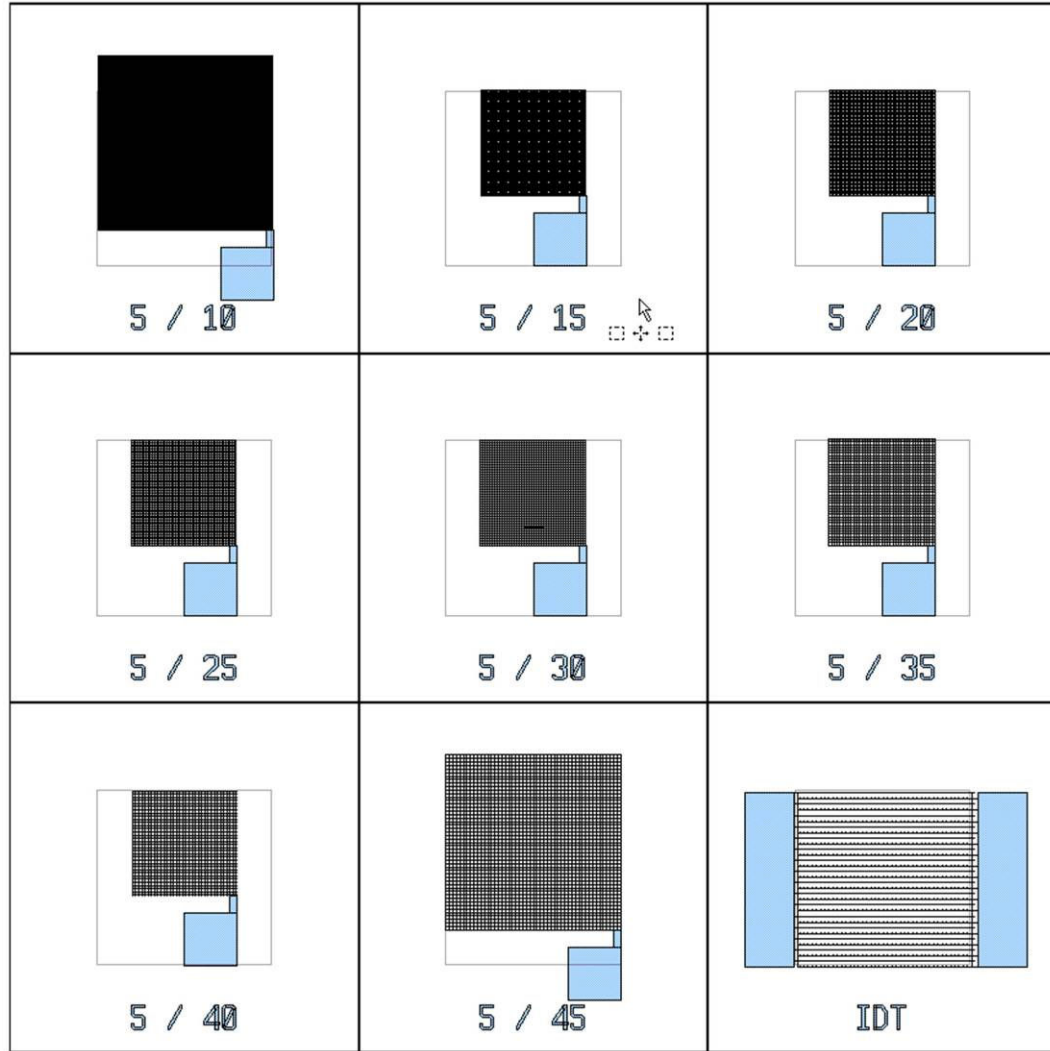
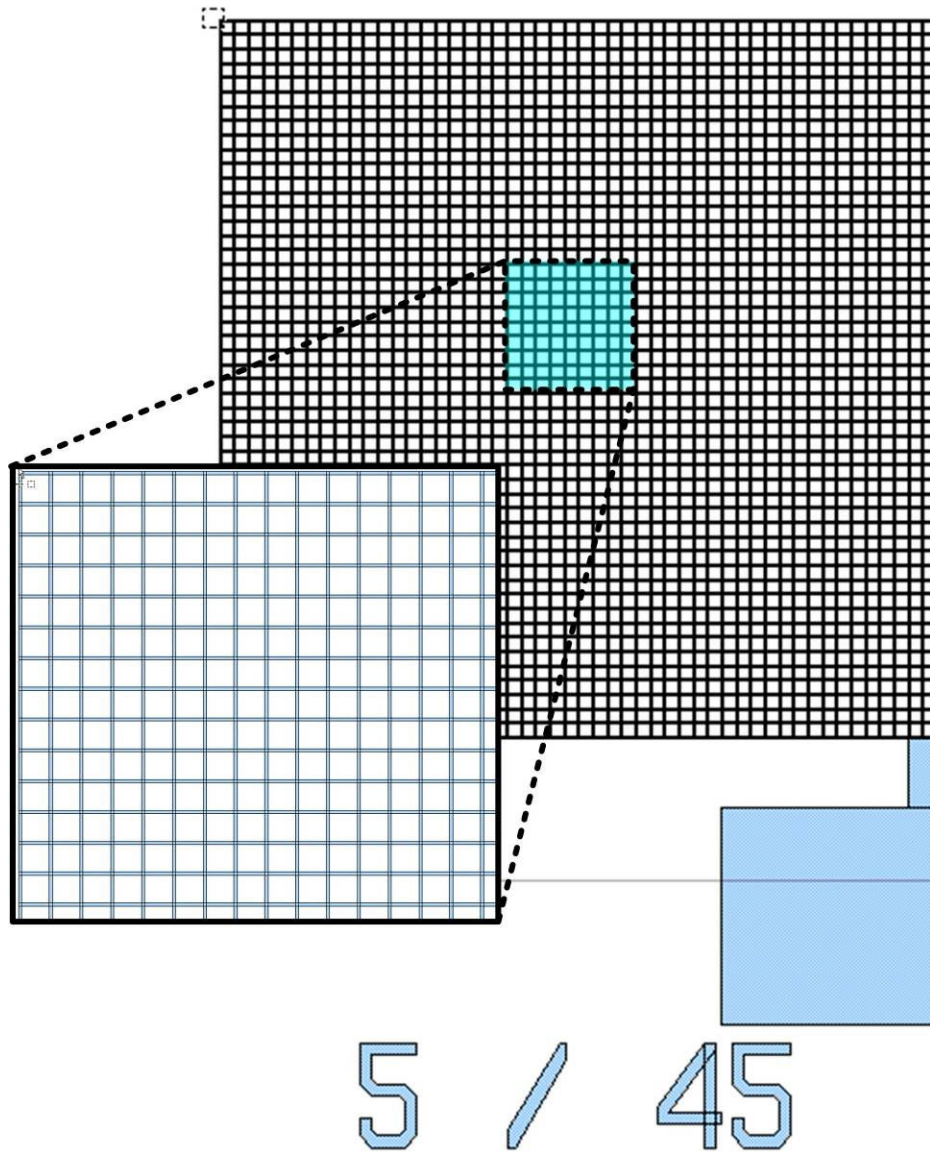


Figure 4.34: 3x3 Matrix of Test Die

A single charging grid with a metal spacing of 45 microns is shown in Figure 4.35.



**Figure 4.35: A Charging Grid with a Separation of 45 microns**

An actual fabricated charging grid with a metal spacing of 10 microns is shown in Figure 4.36, with a close-up of a 45 micron grid shown in Figure 4.37.

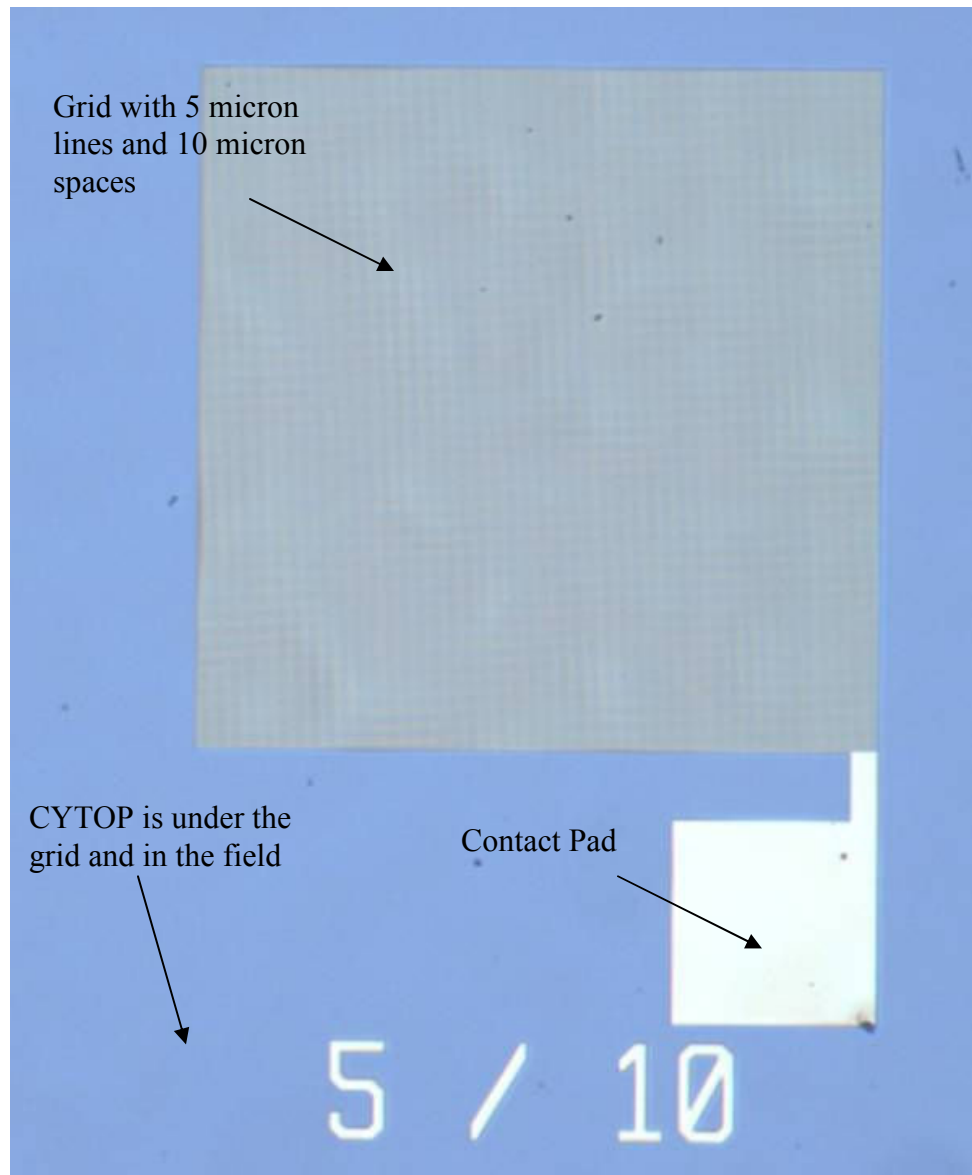


**Figure 4.36: Square Charging Grid with 10 Micron Spacing**

The metal charging grid itself has much smaller critical features than the entire charging area. A close-up is shown in Figure 4.37.

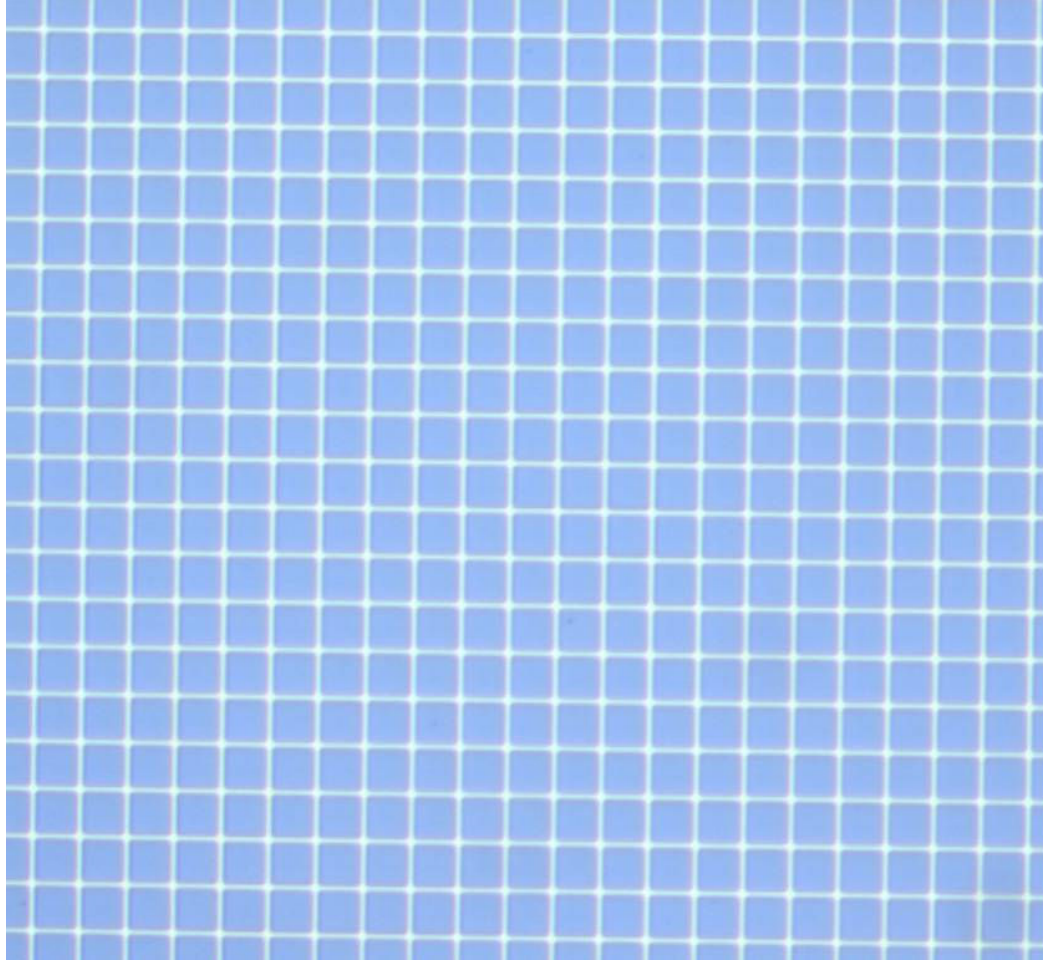


**Figure 4.37: Close-up of Charging Grid**

The actual electret formation occurs after full device fabrication and assembly. A connection is made to the metal grid through an exposed pad. The device was first heated to a temperature of 190°F and a voltage of -1000V applied to the metal grid. However, later formation processes consisted of simply applying approximately -800V to the grid. The incorporation of higher temperatures led to a substantial number of thermal breakdown failures. With the application of the high voltage, a microplasma discharge occurs at the edges of the metal grid, leading to charging of the CYTOP material. The voltage is applied for a period of 50 minutes, after which the sample is cooled for a

period of 10 minutes while the voltage remains applied. Finally, the voltage is removed and the charging process is complete.

After application of -720V to the grid, with the backside of the silicon wafer held at ground, for 1 hour at 80°C, an electrostatic voltmeter measured a stable surface voltage of -204V. These charging grids were used later to assemble single transducers for characterization purposes.

A second wafer was then fabricated that consisted of multiple die each with an array of connected circular charging areas (Figure 4.38).

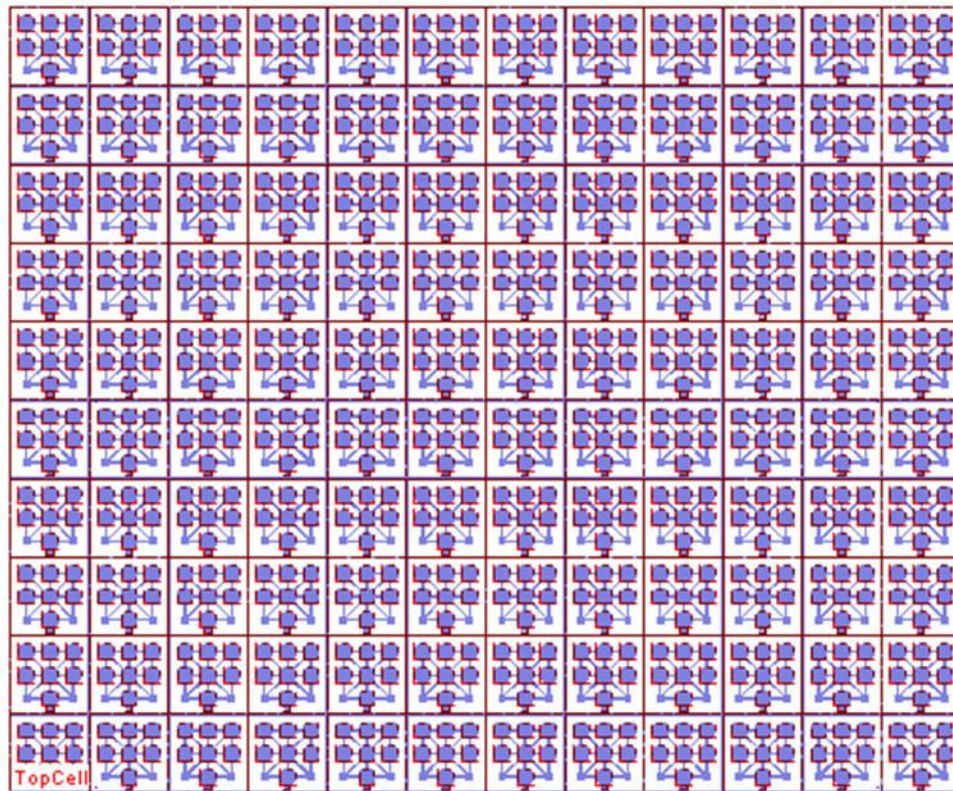


**Figure 4.38: Wafer with Circular Charging Areas**

To develop and characterize the electret formation process, independent of the rest of the sensor fabrication process, the wafer was designed with an array of microgrids

for charging multiple spots on each sensor die (Figure 4.39). Each 1 cm by 1 cm die had a general pattern of seven charging circular areas with a diameter of 2mm and separated by 1mm. The charging areas were all connected by large metal traces that also connected to two pads. These pads are where the -800V charging voltage is applied. In a fashion similar to the first wafer, this second wafer varied the spacing between metal conductors. For each type of die, the characteristic spacing between metal structures varied from 20 microns, to 30 microns, to 40 microns.

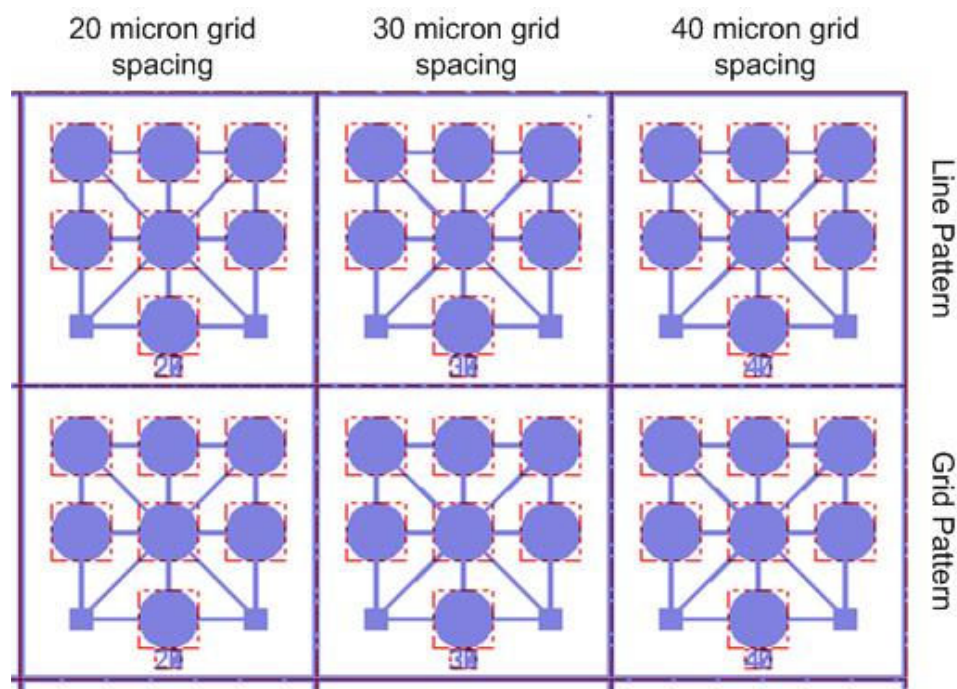


**Figure 4.39: Variations of Die on Wafer**

There are two types of charging grids on the wafer. This wafer included die with a square grid, as in a mesh, as well as die with a straight line pattern, as in an array of charging wires. The square grid, shown in Figure 4.40, was initially prototyped in the first wafer.

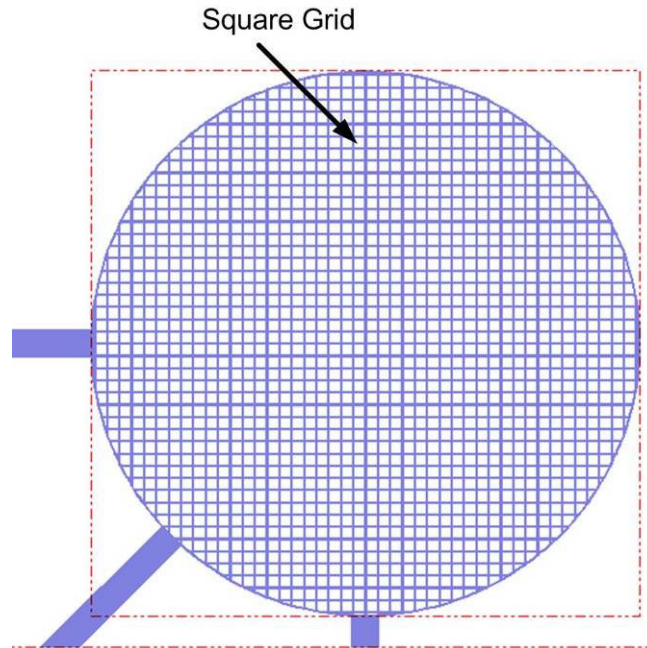


**Figure 4.40: Square Microgrid Pattern**

The second type, shown in Figure 4.41, is just a series of lines, and is similar to the corona wire devices used in laser printers and copiers.

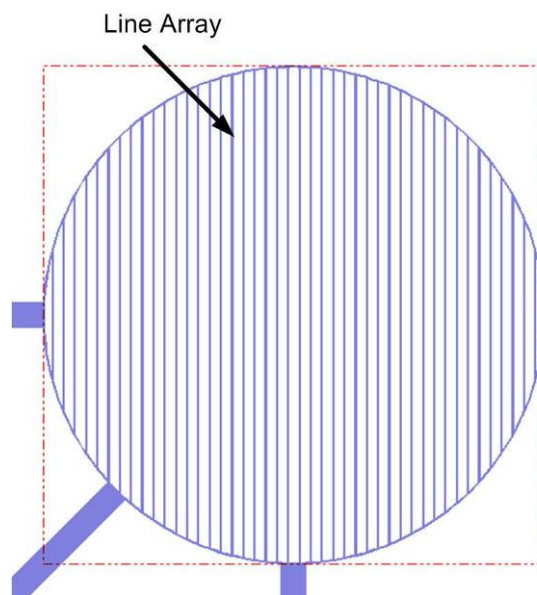


**Figure 4.41: Microline pattern**

These were fabricated in the process described earlier, with the critical step being the O<sub>2</sub> plasma undercut etch that “suspends” the metal edges above the surface of the CYTOP material. A fabricated device with a 30 micron square mesh is shown in Figure 4.42, Figure 4.43, Figure 4.44, and Figure 4.45. The SEM image clearly shows areas where the mesh was not completely cleared, leaving larger squares of metal. This will reduce overall remnant voltage after the charging process is complete.

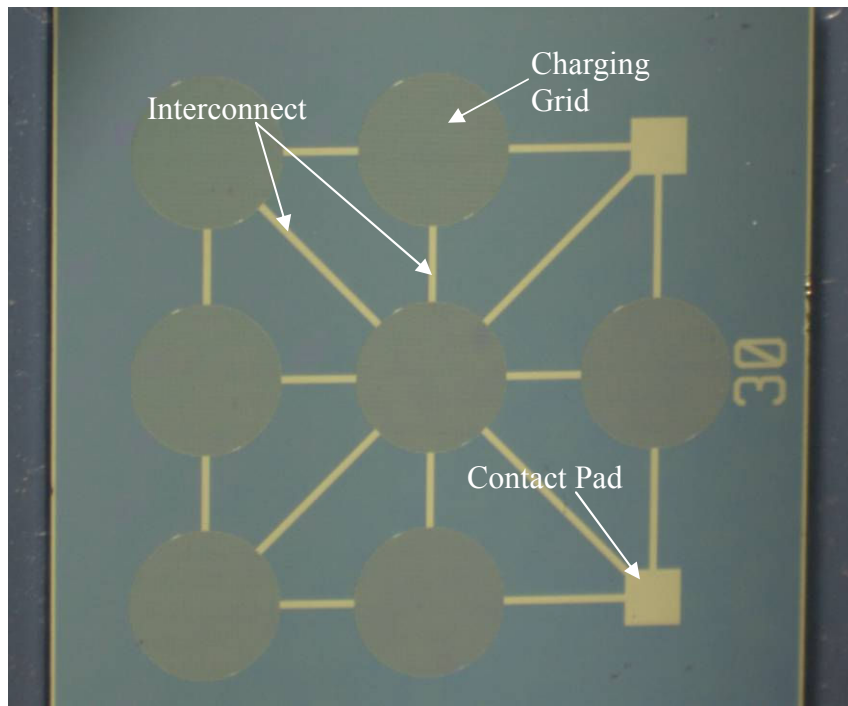


**Figure 4.42: Square Microgrid Chip with 30 Micron Spacing**

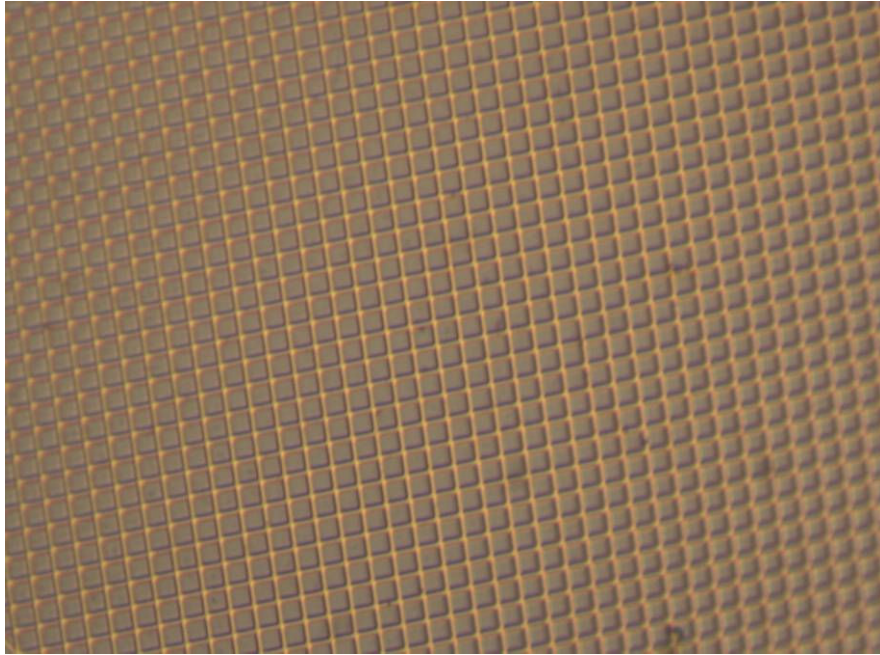


**Figure 4.43: Square Microgrid Pattern**

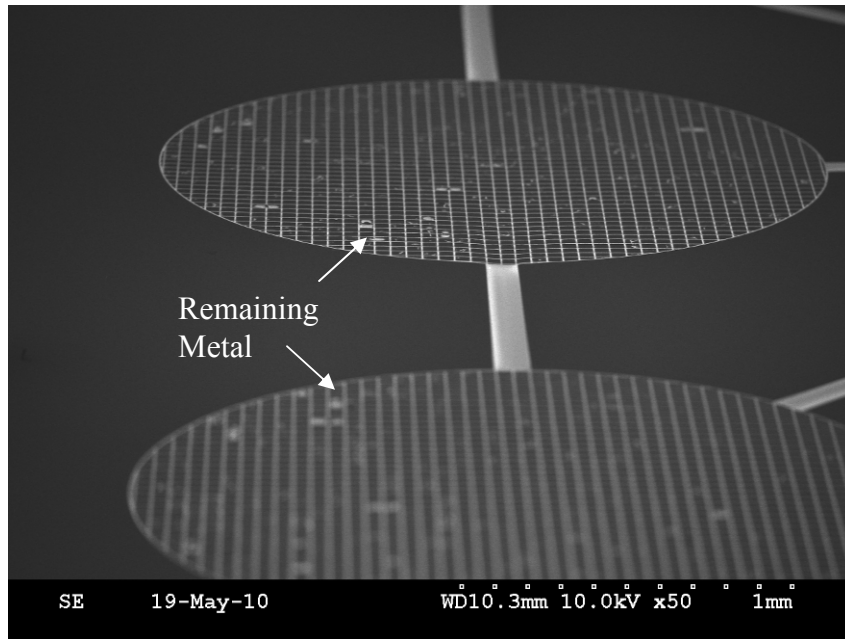


**Figure 4.44: SEM of Square Microgrid Pattern**

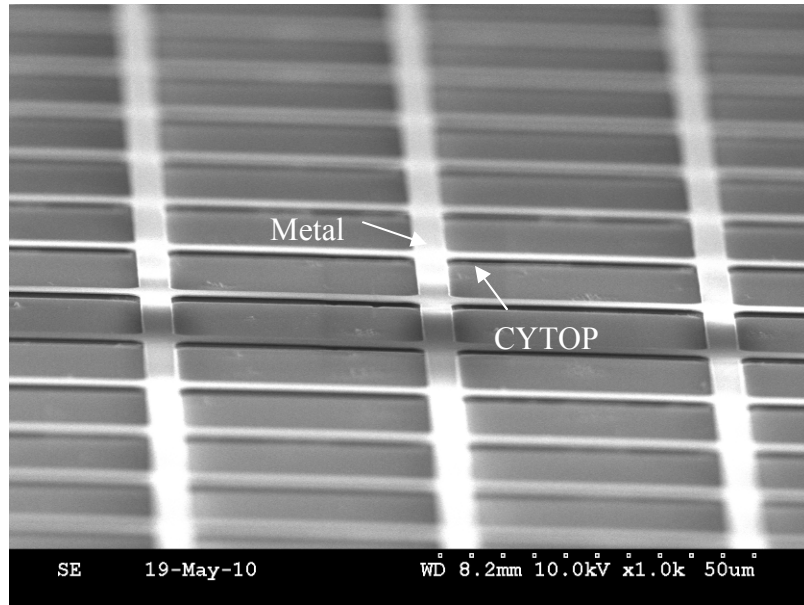


**Figure 4.45: Close-Up View of Square Microgrid Pattern**

Figure 4.46, Figure 4.47, and Figure 4.48 show images of fabricated charging areas with the microline pattern. The SEM images show the undercut of the metal grid that occurs during the oxygen plasma etch.

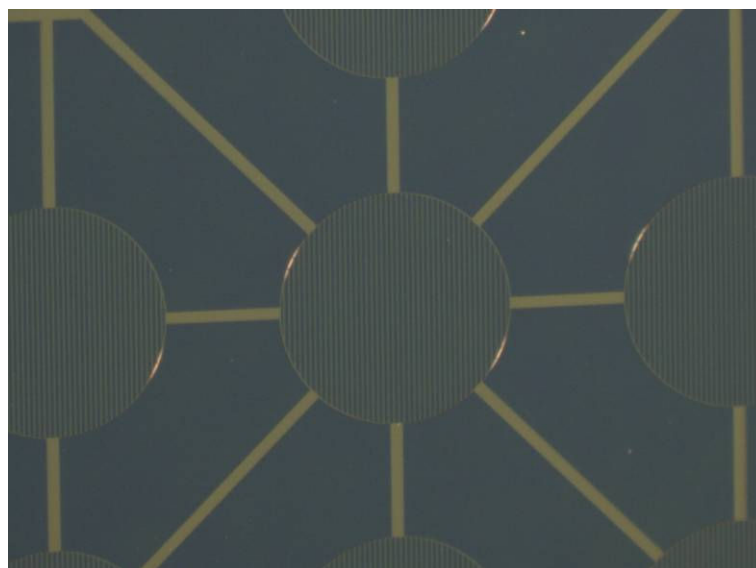


**Figure 4.46: Chip with Microline Pattern**

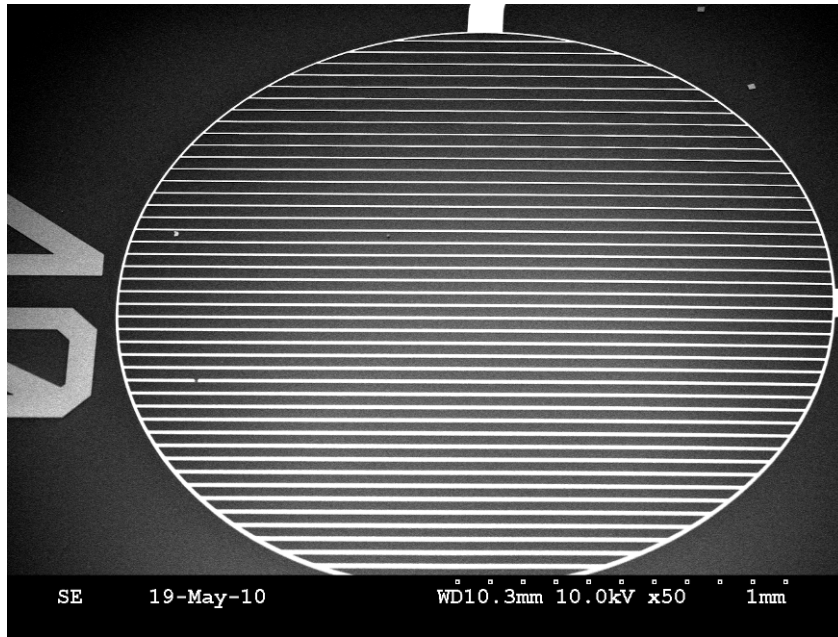


Figure 4.47: SEM of Microline Pattern

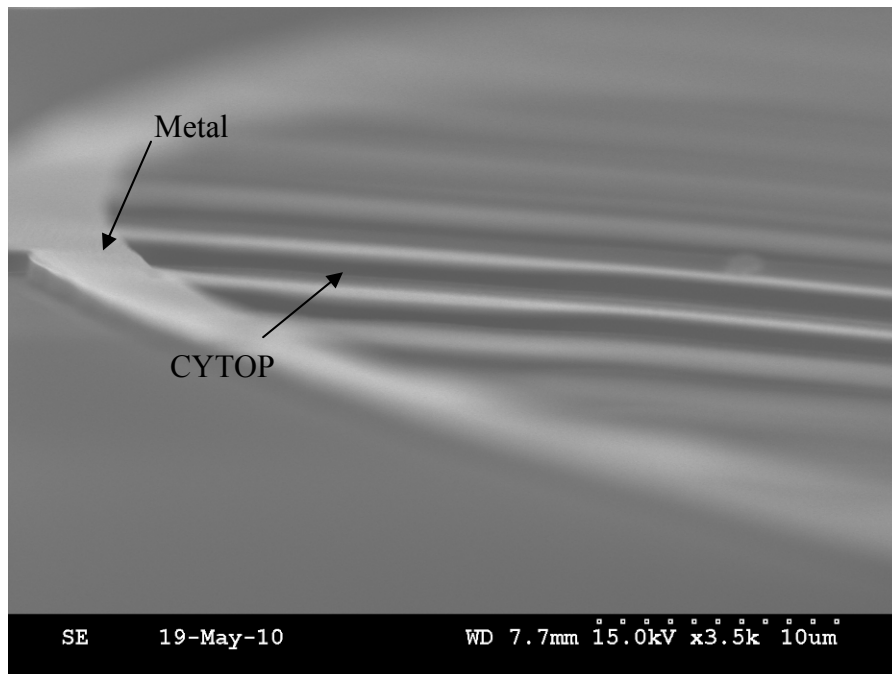


Figure 4.48: Close-up of Microline Pattern

## **4.5 Electret Measurement Techniques**

Measuring the electrostatic potential of the electret film during and after the course of fabrication, as well as the charging current flowing through the device during the charging process, was critical to this work. Electrostatic measurements are difficult to achieve because of the sensitivity of these measurements to a wide variety of parameters. Two key measurements were performed, however.

### **4.5.1 Remnant Voltage Measurement**

To measure the remnant voltage after electret charging, a high impedance voltmeter is required. This work utilized a vibrating-reed electrostatic voltmeter similar to the Monroe Electronics Model 244A Isoprobe Electrostatic Voltmeter.

A traditional contacting voltmeter is not suitable for measuring the voltage associated with the charge on an electret because it can not release the charge required to drive the input impedance of the voltmeter. An electrostatic voltmeter, with its extremely high input impedance, performs a non-contacting measurement without modifying or destroying the charge. This instrument is very useful for measuring static electrical charges, and is operated in a fashion different than that of typical voltmeters.

The electrostatic voltmeter functions by placing a field sensing probe close to the surface of interest, but without contacting the surface. The electrostatic voltmeter drives the conductive housing of the field sensing probe to a voltage necessary to null the electric field between the probe and the surface of interest. This field-nulling condition is almost always achieved when the voltage on the probe matches the unknown voltage on the surface of interest. By measuring the voltage on the probe, one determines the equal voltage on the surface of interest. This field-nulling technique is achieved with closed-loop voltage feedback using a high-voltage follower amplifier, yielding very high accuracy, excellent stability, and low drift performance for the electrostatic voltmeter.

An additional benefit of the field-nulling technique is that the probe can be placed very close to the surface of interest without fear of arc-over between the probe and the surface. This is due to the action of the electrostatic voltmeter to maintain zero electric field between these two surfaces. Furthermore, placing the probe very close to the surface of interest results in the ability to resolve very small areas ( $<1.0$  mm) on the surface of interest.

The principles behind the electrostatic voltmeter are depicted in Figure 4.49. The fundamental component of the system is the mechanically modulated electrode. That electrode vibrates at a frequency on the order of 10's of kHz. When placed in an electric field, a displacement current is generated and amplified by an integrating amplifier. Below the vibrating electrode is a counter electrode with an aperture. The bias on that counter electrode is adjusted until no displacement current is seen. That point is equivalent to nulling the electric field. The surface potential of the sample is equivalent to the bias on the counter electrode at that point.

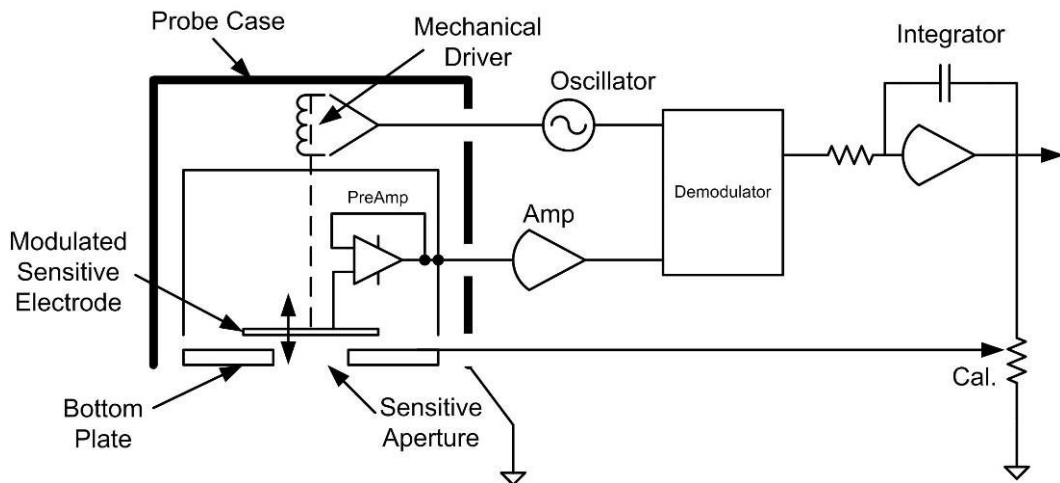


**Figure 4.49: Electrostatic Voltmeter Operation**

This measurement is very insensitive to stray electric fields and noise. In addition, for samples larger than the window for the vibrating electrode, the technique is relatively

insensitive to distance between the probe and the surface. However, to ensure this, the probe and sample are mounted in the test apparatus depicted in Figure 4.50. The test fixture attaches the probe to a stage that allows precise height position. The probe is then mounted to a grounded stage that allows x, y, and z scanning. An initial calibration step is performed wherein a known surface potential is interrogated by the probe. Calibration features of the electrostatic voltmeter are then used to minimize sensitivity to probe height. After calibration, the probe is moved to the sample under test.

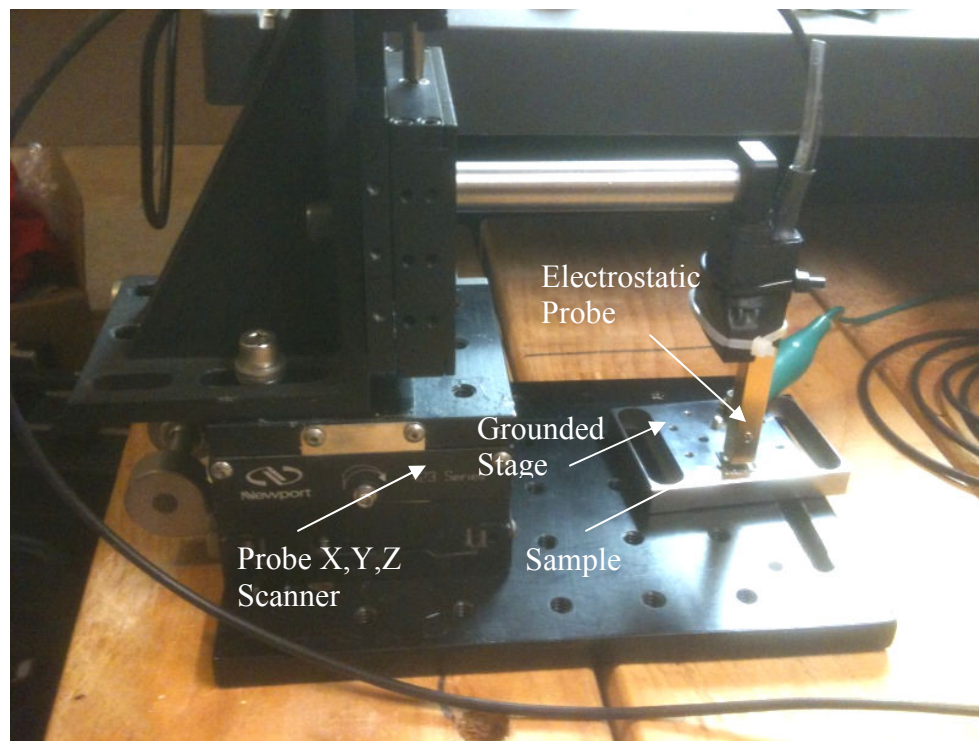


**Figure 4.50: Electrostatic Measurement Test Fixture**

With this setup, the sample under investigation can be scanned and a surface voltage profile developed. On samples with multiple charging sites, this technique highlighted where charging occurred and where it did not, at least within the resolution of the probe. For this particular probe, the resolution was on the order of 2mm.

## 4.5.2 Charging Current Measurement

The charging process that forms the electret after fabrication of the MEMS devices is critical to device operation. An electrostatic voltmeter is used after the formation process to characterize the remnant voltage. However, measurements can also be performed during the formation process. In particular, the current through the structure during charging provides characterization of the structure and the formation process. Care must be taken in measuring these currents, though, as they are in the nanoamp and picoamp range.

The square charging area die fabricated in the process described earlier were connected to a high voltage power supply and a standard picoammeter in the configuration shown in Figure 4.51. A high voltage of -800V was applied for a period of 5 minutes. The current through the device is plotted in Figure 4.52.

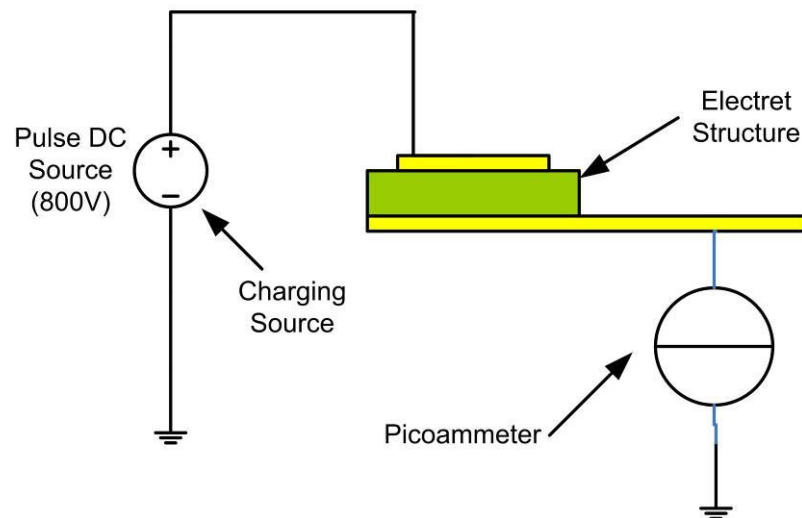
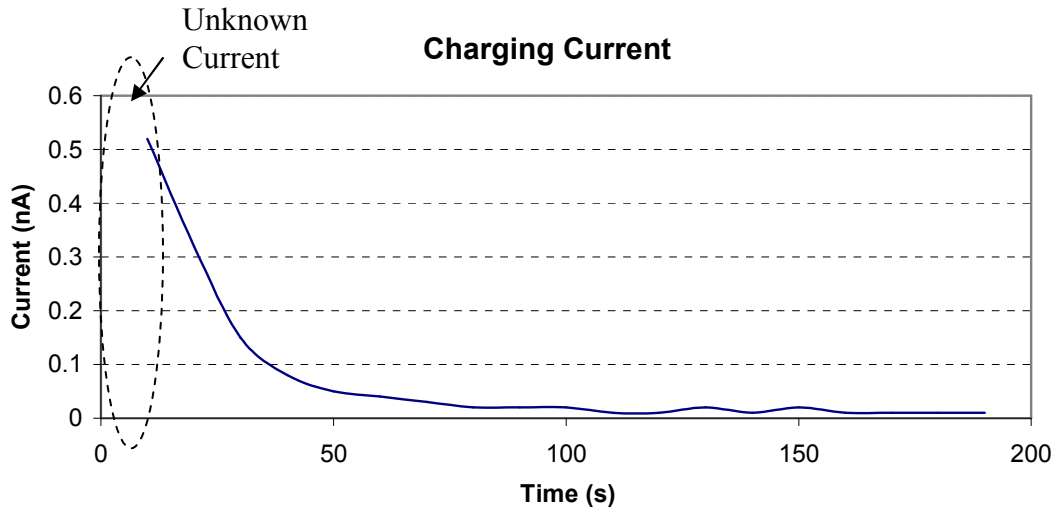


Figure 4.51: Schematic Diagram for Charging Current Measurement



**Figure 4.52: Charging Current**

The charging current has a high initial positive peak that exceeds the range of the picoammeter and occurs faster than the response time of the system. That peak represents the current that flows onto the charging grid to raise its potential with respect to ground. After that initial peak, the current decreases and the charging current is seen. This represents the microcorona current. That current consists of ions generated at the edges of the grid and travelling to the surface of the polymer. Those ions transfer charge to traps in the polymer, thereby raising the polymer surface potential. As the potential rises, the electric field in the gap between the charging grid and the surface decreases, leading to less ionization and less current. This continues until the electric field is no longer larger than the breakdown of the air in the gap. It takes less than one minute to substantially charge the polymer.

The standard picoammeter was not fast enough to fully capture the transients of the charging event. Therefore, an improved system was assembled. This system allowed capture of the entire charging event on a digital oscilloscope. The improved electrical circuit for measuring charging current is shown in Figure 4.53. The DC voltage source provides the charging current and potential. It is originally at 0V and turned on to -800V

to perform charging of the electret material. The voltage source is connected to a  $10\text{M}\Omega$  resistor that provides a voltage drop during the beginning of charging so that the input to the amplifier does not exceed the maximum limit. The resistor is then connected to the charging grid on the top of the device under test. This is accomplished through a spring-loaded probe. The bottom electrode is connected to a  $100\text{k}\Omega$  resistor to ground. This resistor serves as a current sense resistor. The voltage across the resistor is amplified by a very high impedance input instrumentation amplifier with a modest gain of 500. The output of the amplifier is sent to a digital storage oscilloscope set to perform one full scan over a 10s period.

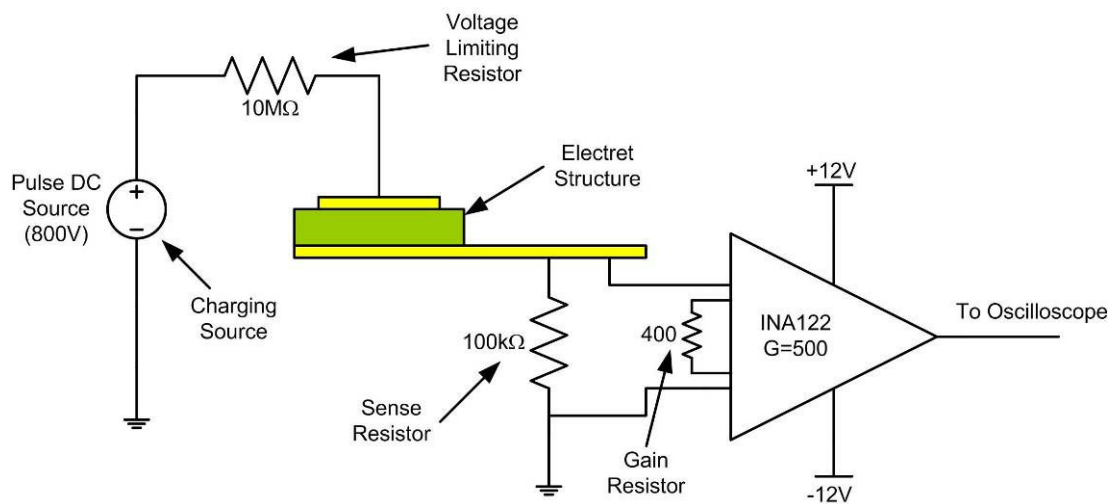


**Figure 4.53: Charging Circuit with Measurement of Charging Current**

Since this is a very high impedance circuit, significant noise sources contribute to the output signal. In particular, 60 Hz noise from power lines creates a significant signal. Two approaches were used for removing that noise. The first was a simple RC low-pass filter on the amplifier output. The issue with that approach is the relatively poor filtering, as well as that large R and C values required. The second approach was to digitally filter

the signal. The filter selected was a 6<sup>th</sup> order Butterworth low-pass with a 3dB frequency of 48Hz. The frequency response of the digital filter is shown in Figure 4.54.

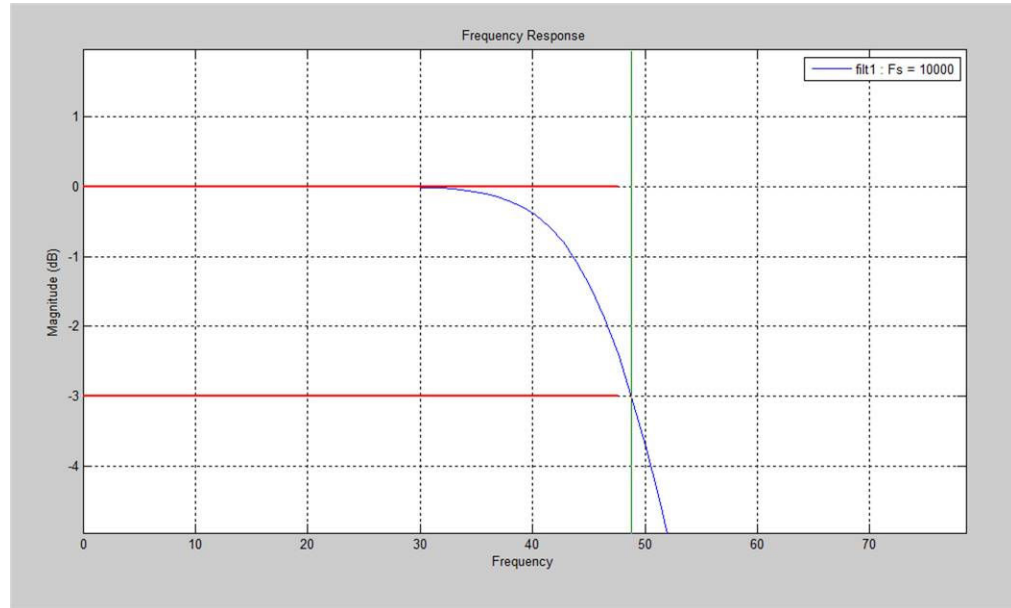


**Figure 4.54: Filter Frequency Response for 60Hz Removal**

This current measurement circuit and filtering allowed the relatively fast transient charging current to be measured and related to models for the charging process.

#### **4.6 Electret Charging Current**

A typical charging cycle would have the transient profile shown in Figure 4.55. It had peak values in the range of 0.1 microamps, but a large dynamic range, meaning that currents as low as 10pA are important. This waveform shows the charging current as a function of time following the application of -800V. This waveform is prior to any filtering that removes 60Hz noise.

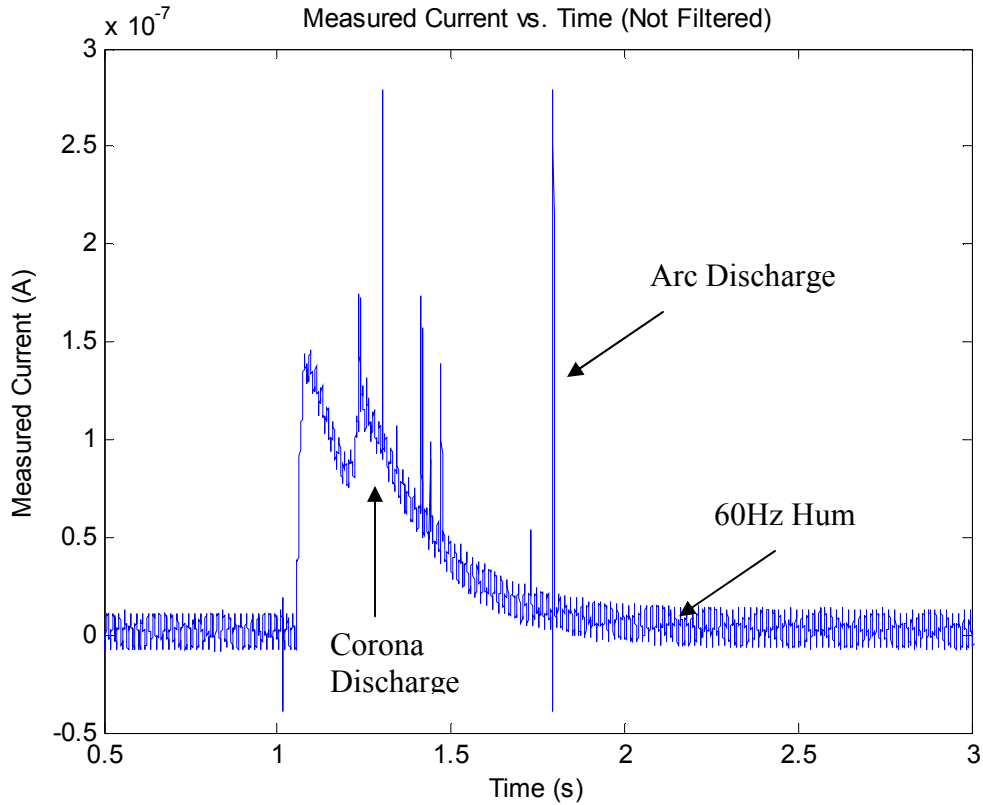


**Figure 4.55: Current vs. Time during Electret Charging Prior to Filtering**

After applying filtering, the 60Hz noise is reduced significantly, but at the expense of some fidelity in the initial rise of the waveform. Figure 4.56 shows the filtered waveforms for four consecutive charging cycles on the same electret. The first charging cycle shows a significantly different current profile than the subsequent three, which are virtually identical to one another. The difference between the first cycle and subsequent cycles represents the discharge within the structure that forms the electret.

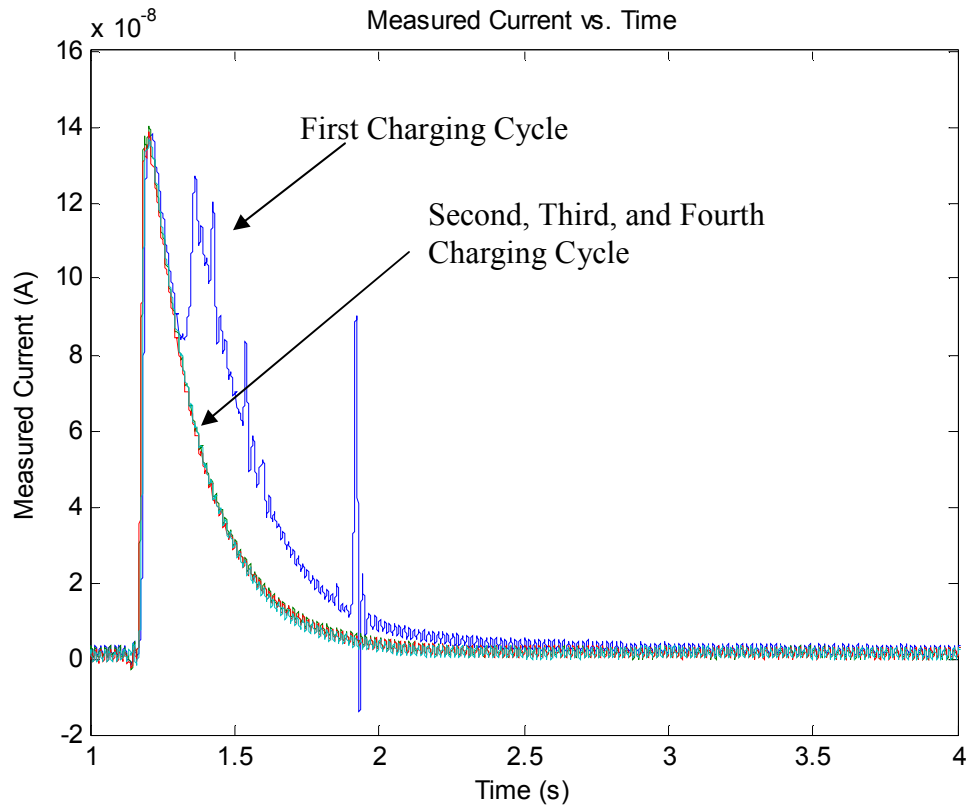


**Figure 4.56: Current vs. Time during Electret Charging With Filtering**

The difference in current between the first and subsequent charging cycles is related to the charging current applied to the electret material. Figure 4.57 shows this charging current, and it is exponential in form. This is expected because the voltage of the electret surface is increasing during the charging cycle, leading to a subsequent reduction in charging current.

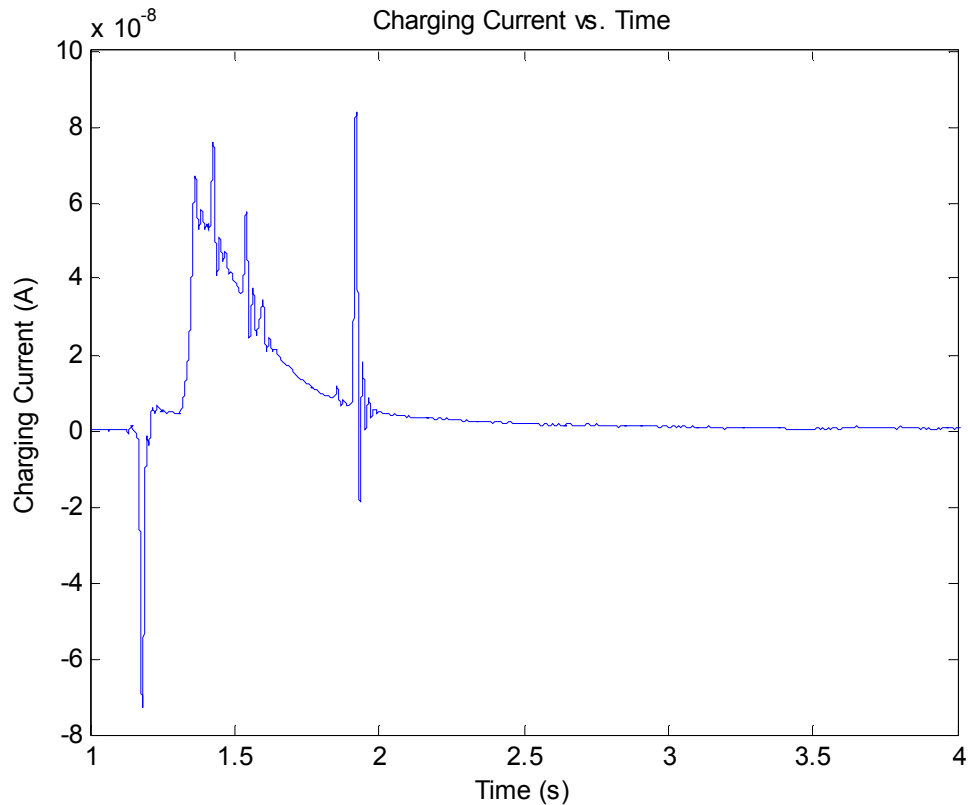


**Figure 4.57: Charging Current through Electret Film**

Integrating the area under the charging current waveform results in the total charge transfer as a function of time plot in Figure 4.58. At the end of the charging cycle, a total charge transfer of 20nC has occurred. The capacitance of the charging area to the bottom electrode was measured using a capacitance meter and a value of 54 pF was obtained. That amount of charge, if placed on that capacitance, leads to a predicted voltage of -370V. The electrostatic voltmeter was used to measure the voltage over the charging grid area and a value of -190V was obtained. The difference is attributable to the variation in voltage across the charging area and the masking of the voltage by the floating conductor of the charging grid. In the region between metal lines, the voltage drops significantly because little charging took place there. The electrostatic voltmeter averages over those areas, leading to a smaller voltage. However, the value seen by the

electrostatic voltmeter is also the value that would be seen by the metal structure that will be suspended above this charging area.

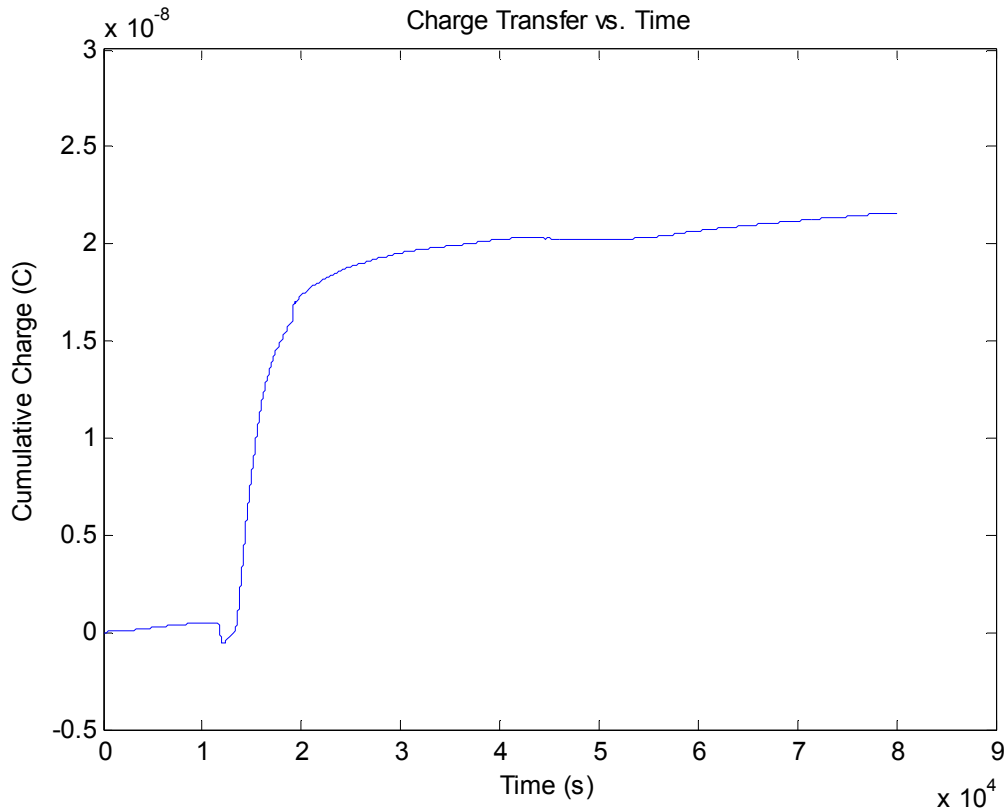


**Figure 4.58: Charge Transfer as a Function of Time**

It is interesting to note that the charging of the electret seen during the first charging cycle does not occur until noticeably after the initial turn on of the power supply. This is represented by the second peak seen in the measured current as a function of time. This second peak occurs approximately 250ms after the charging cycle starts. Figure 4.59 shows the total charge transferred as a function of time during the cycle. At the 250ms mark, approximately 22nC has been placed on the charging grid. The charging grid capacitance is approximately 50pF, meaning that electret formation doesn't start

until the charging grid reaches about -440V. At this point, the electric field is large enough to begin dielectric breakdown.

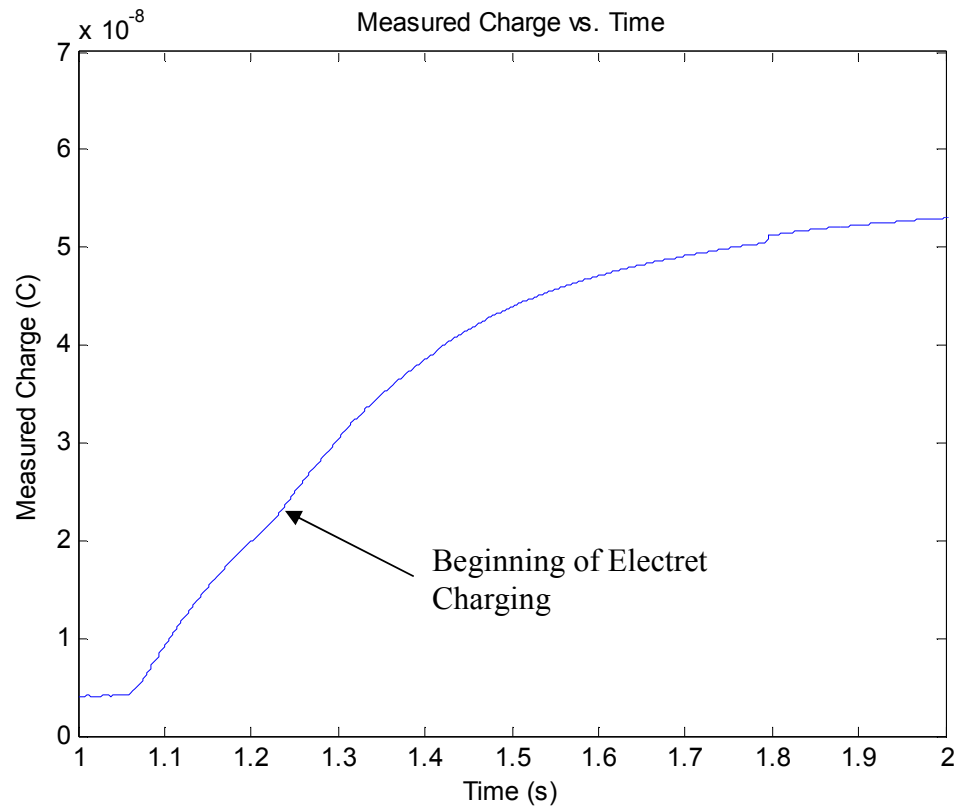


**Figure 4.59: Total Charge Transferred as a Function of Time**

These charging current results allow the creation of an electrical circuit representation of the process. To create this model, the charging power supply voltage output transient was captured on an oscilloscope, as the applied voltage is critical to the charging process. That voltage is shown in Figure 4.60.

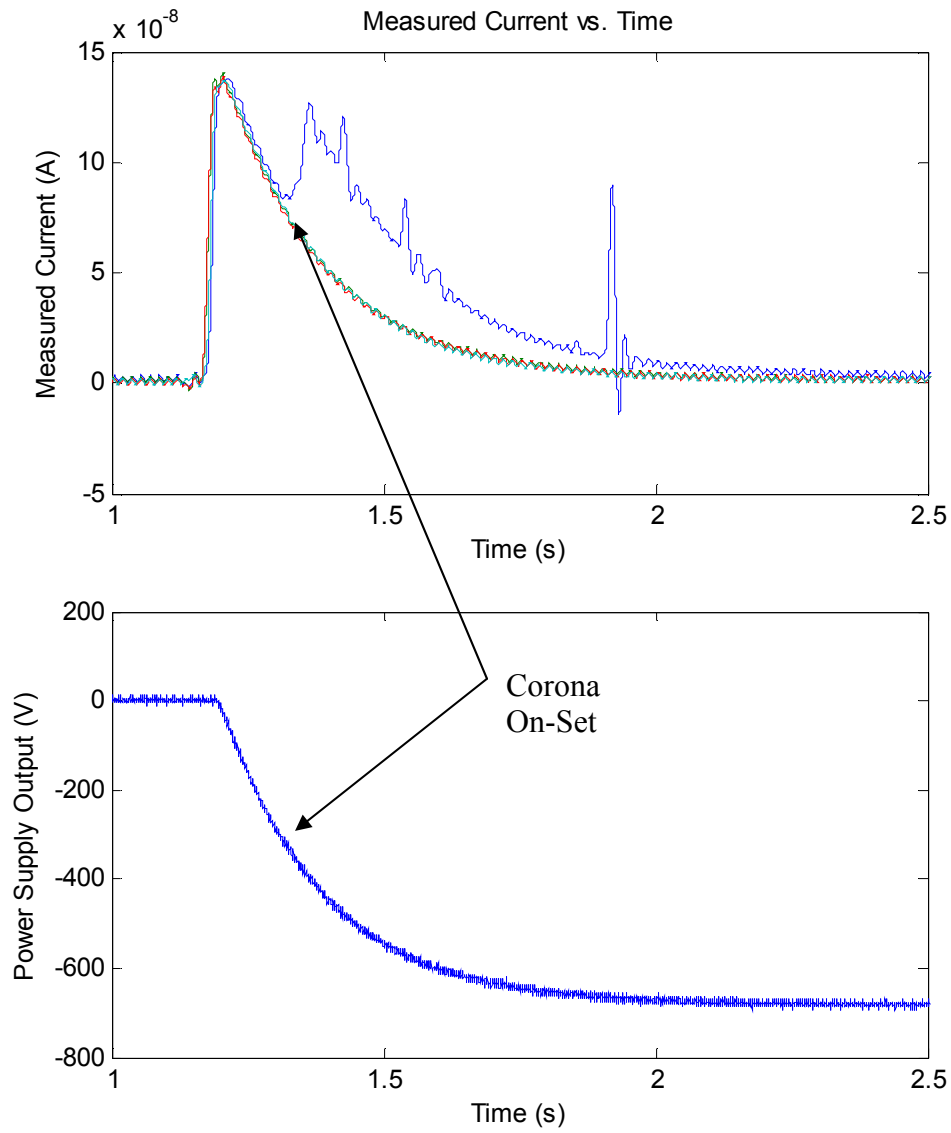


**Figure 4.60: Voltage Input Waveform during Charging Cycle**

As part of the electrical modeling of the discharge process, an equivalent circuit for the corona discharge is required. Figure 4.61 shows the various regimes encountered in an electrical discharge [50]. The corona discharge occurs just prior to electrical breakdown and is typically considered to be in the Townsend regime.

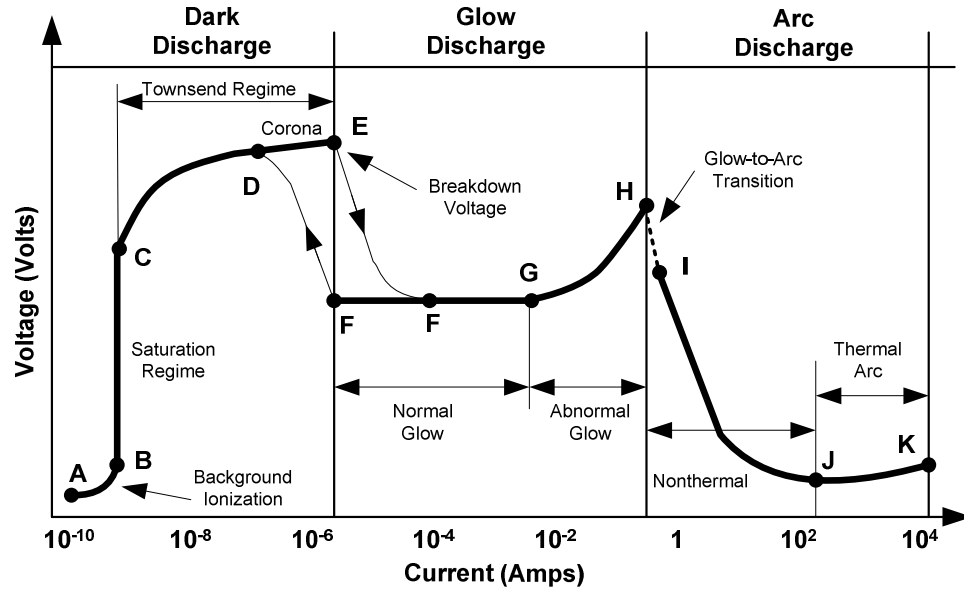


Figure 4.61: Empirical Model of Various Electrical Discharge Regimes

The Townsend regime is often utilized in systems such as avalanche detectors, radiation detectors, and other dark discharge processes. The applicability of the Townsend regime and the Townsend Relation to small gap corona discharges is currently under investigation [51]. However, the Townsend relation, an empirical relationship for the I-V characteristics of the corona discharge, is employed in the equivalent circuit model of the *in situ* charging process.

$$I = AV(V - V_o) \quad (42)$$

Where  $I$  is the current through the discharge,  $V$  is the voltage across the electrode gap,  $V_o$  is the voltage corresponding to the onset of the corona, and  $A$  is an empirical constant that takes into account items such as mean free path, collision probability, drift currents, and other complex phenomenon that occur in the discharge.

Figure 4.62 shows a SPICE model of the charging process. V1 represents the high-voltage power supply that energizes the charging grid. R4 is a large resistor that represents a leakage path and allows SPICE to derive a DC solution. R1 was placed in the circuit to ensure that the voltage seen by an instrumentation amplifier, not shown in this figure, does not exceed rated maximums. R2 is a current sensing resistor used to capture the current through the structure on an oscilloscope. C2 represents the capacitance of the charging grid to the bottom electrode of the structure. C1 represents the capacitance of the surface of the electret film to the bottom electrode. R3 represents the “resistance” of the microplasma discharge. J1 is a switch that accounts for the formation of the microplasma discharge only after a large enough electrostatic potential exists across the gap to result in dielectric breakdown of air.

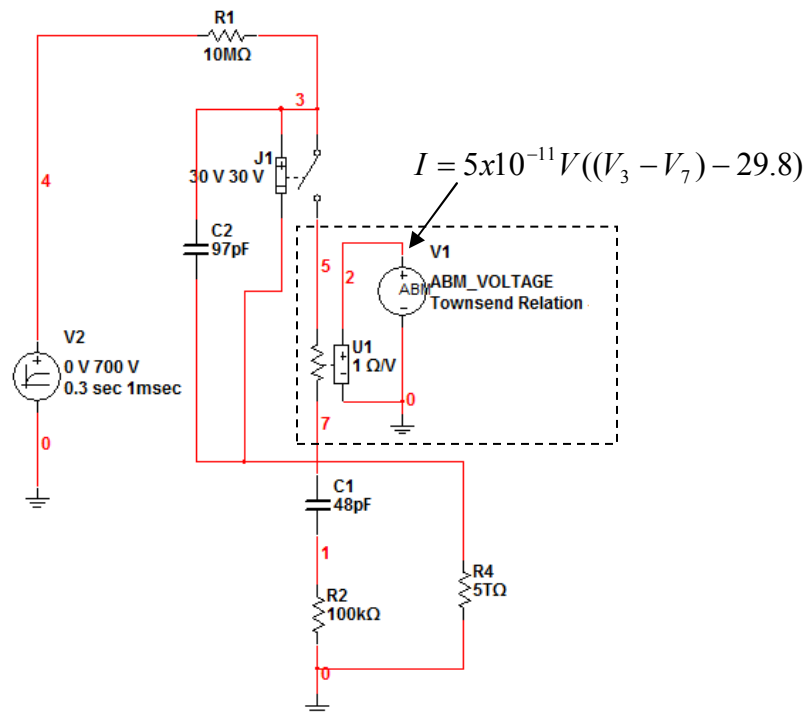
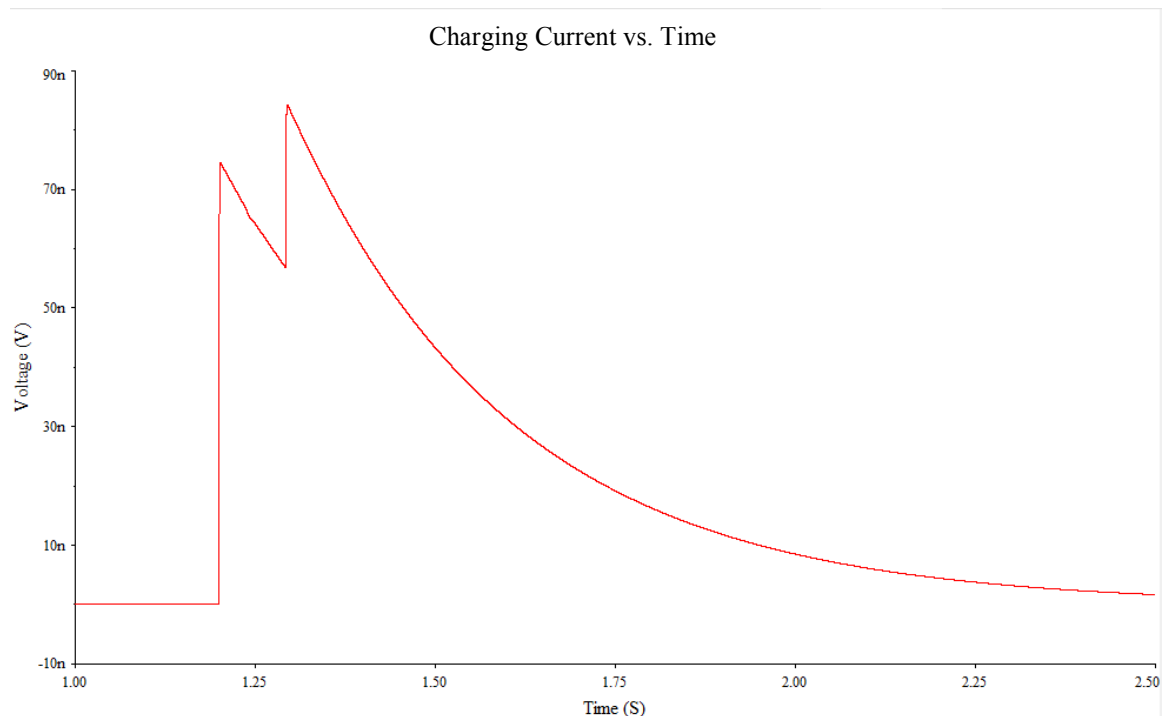


Figure 4.62: Schematic Representation of Charging Process

To account for the nonlinearity of the corona discharge, R3 is a voltage controlled resistor where the control voltage is calculated from the Townsend Relation. A SPICE transient analysis was performed using this model. Figure 4.63 shows the voltage across the sense resistor during the charging process. The two peak characteristic of the charging current is evident.



**Figure 4.63: Voltage across Sense Resistor during Charging Process**

#### **4.7 Electret Remnant Voltage**

After determining the length and I-V characteristics of the charging process (<10s), the process was applied to a series of grids with different spaces. The goal of the test was to determine the spacing that achieved the maximum final remnant voltage and compare that to the estimated value from the model. Figure 4.64 shows the remnant voltage as measured by the electrostatic voltmeter as a function of grid spacing. A characteristic increase is seen with increasing grid spacing. As the grid spacing

approaches zero, which would be the case with a single continuous electrode, the remnant voltage approaches zero. As the grid spacing increases, it is expected that the remnant voltage would it a maximum value and then start decreasing. That point was not reached on the test articles fabricated so far.

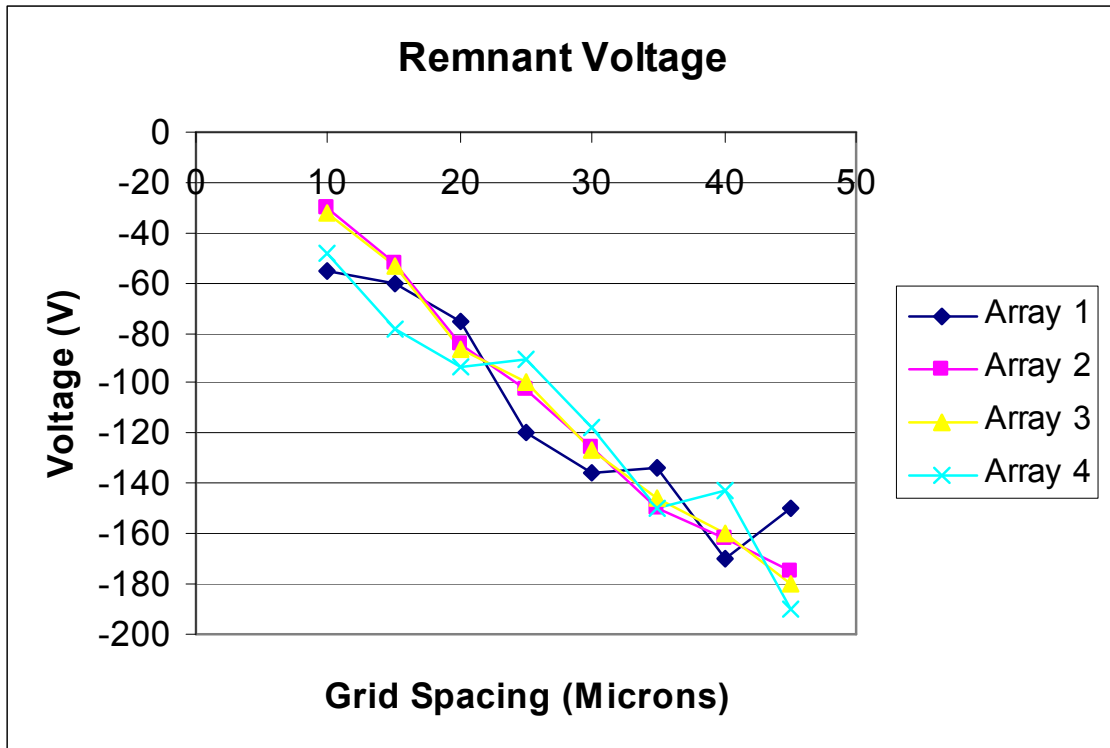


Figure 4.64: Remnant Voltage vs. Grid Spacing for Four Sets of Charging Grids

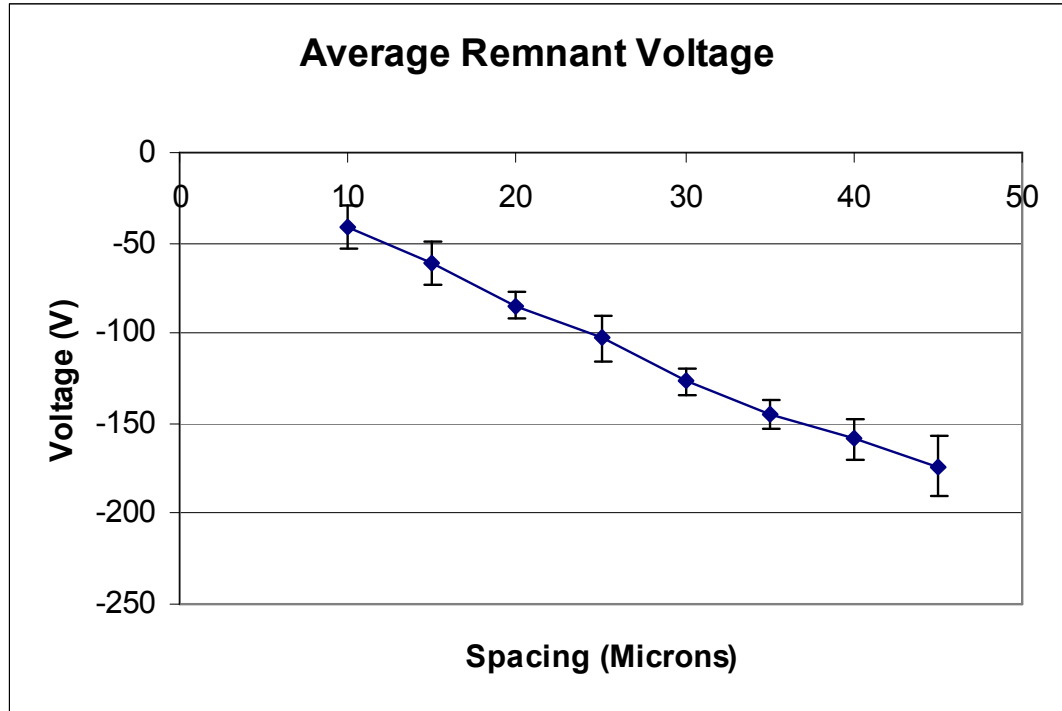


Figure 4.65: Average and Standard Deviation of Remnant Voltage

The charging protocol that developed the most consistent remnant voltage with minimum failures due to premature arcing is listed in Table 4.9. An important step in the protocol is the -200V initial voltage. When the charging was started at an initial voltage of -800V, there was a tendency to arc at various locations on and around the charging grid. This could be due to overshoot in the power supply, excessive current flow during charging of the conductor initially, or other factors. In addition, the temperature was left at ambient to avoid thermal breakdown that would occur often at elevated temperatures.

**Table 4.9: Electret Charging Protocol**

<b>Process Step</b>	<b>Process Parameters</b>
Connect	Place spring-loaded probe on contact pad
Initial Voltage	Turn on power supply set at -200V
Voltage Ramp	Linear voltage ramp from -200V to -800V in 10 seconds (60V/s)
Dwell	Hold at -800V for 1 minute
Remove	Turn off high voltage supply and remove chip

The circular charging areas on wafer B were connected to the same high voltage supply and current measurement setup. The same charging protocol was employed. However, all of the charging areas on Wafer B are connected, so one charging cycle realized seven charged sites simultaneously.

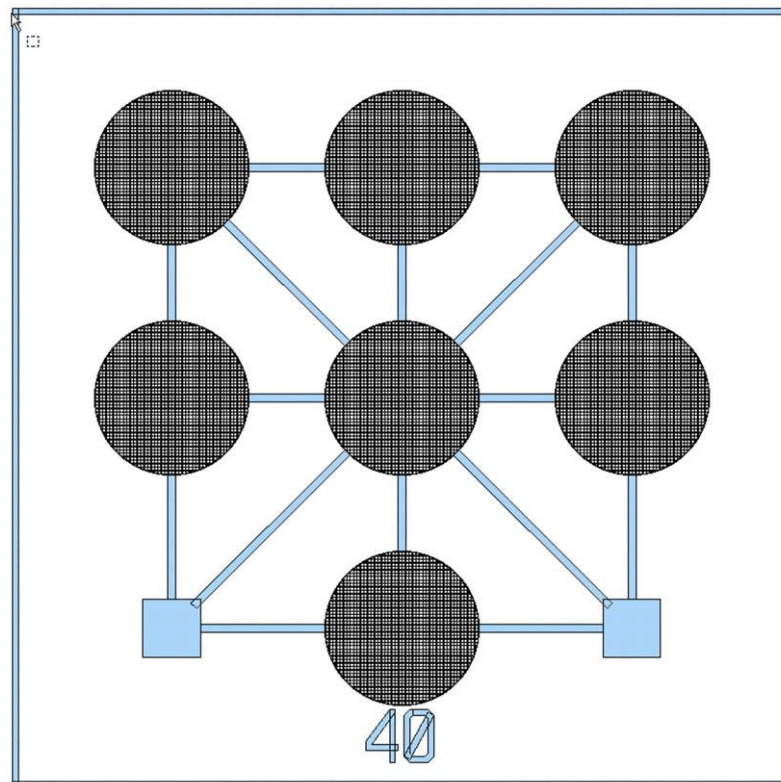


**Figure 4.66: Single Die on Electret Wafer**

Devices from this wafer underwent a series of charging experiments. When applying a -800V charging potential to the pad, the devices achieved the remnant voltages shown in Figure 4.67, Figure 4.68, Figure 4.69, and Figure 4.70.

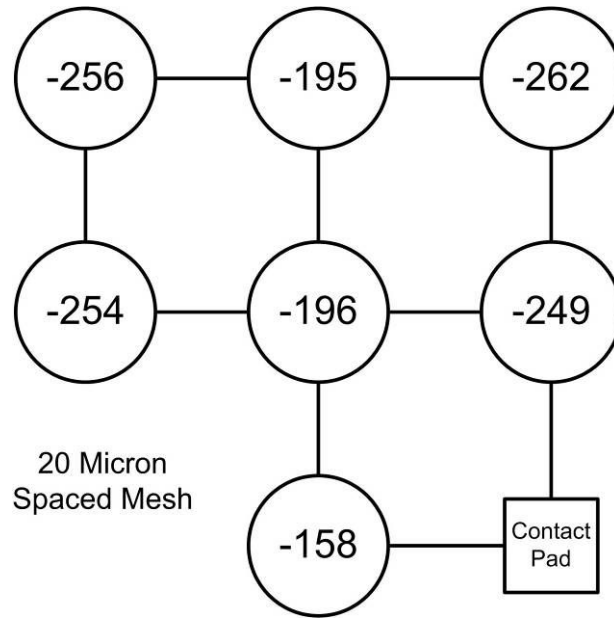


**Figure 4.67: 20 Micron Square Mesh Array**

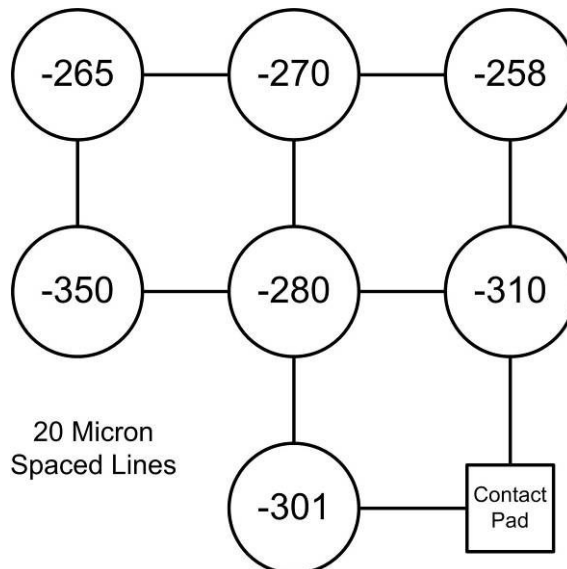


**Figure 4.68: 20 Micron Line Array**

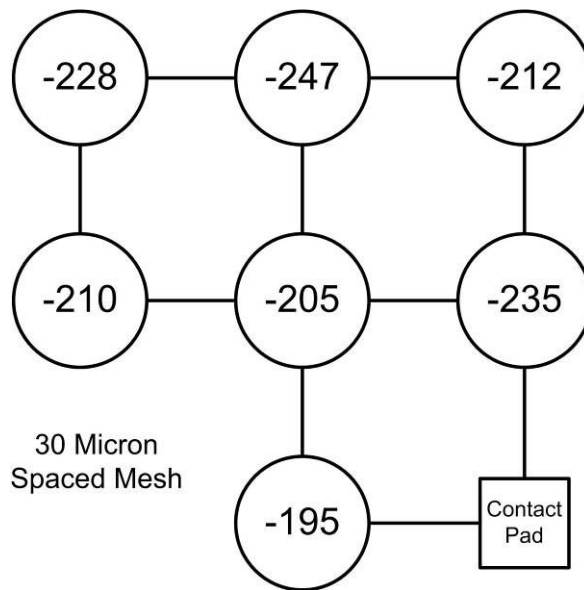


**Figure 4.69: 30 Micron Square Mesh Array**

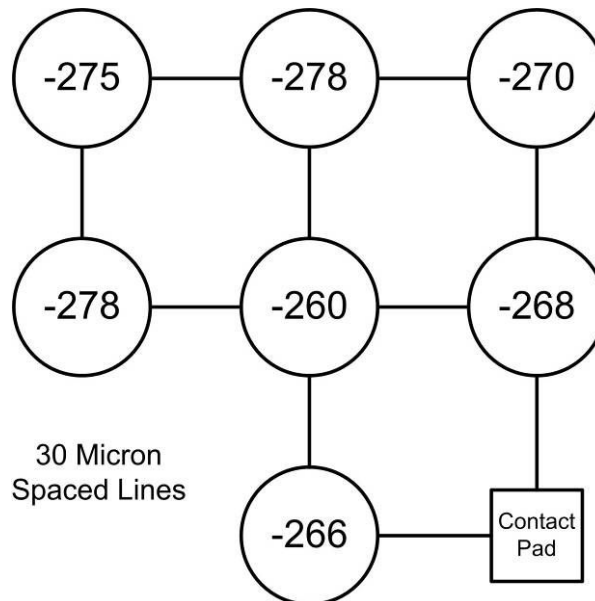


**Figure 4.70: 30 Micron Line Array**

In all of these measurements, the largest average remnant voltages were achieved using the largest spacing of metal conductors. This is due to the masking effect of the conductor on the voltage after charging. The most uniform remnant voltages were

achieved using the line arrays. It was noted that areas where substantial arcing was observed had inconsistent localized electrostatic voltage measurements that were substantially larger than the typical region. It was desirable to avoid these arcs during the rest of the study. These were avoided by reducing charging voltages and performing the charging at ambient temperatures. However, this arc discharge mechanism should be explored and exploited in future work.

#### **4.8 Integrated Electret Considerations**

The *in situ* charging method utilizing microcorona and microplasma discharge within the MEMS device was demonstrated as an effective technique for electret formation at the microscale and within a MEMS device even after full device fabrication. When compared to traditional corona-discharge, the baseline charging technique, there are a number of considerations to address. These considerations are related to the expected charging levels achieved, the process and its potential for failures, and the affect of the embedded charging structure during device operation.

The primary consideration in the application of the microcorona charging approach to electret formation is that, when compared to full corona-discharge approaches on a full film, only a portion of the potential remnant voltage is achieved. The surface charge densities achieved when utilizing the microcorona approach are comparable to standard corona discharge techniques. However, two aspects of the microcorona approach lead to less remnant voltage.

The first aspect is that the surface charge density is not uniform across the electret surface. The surface charge is confined to areas near the edges of the metal lines of the charging grid. When using the charged film, however, structures above the film see a remnant voltage that is based on the average surface charge density over a much larger area. Therefore, that voltage is significantly less than would be seen in a corona charged

device with uniform surface charge density. To increase charge uniformity, a higher density of metal lines is required.

The second aspect of the structure is the metal of the charging grid that remains after formation of the electret. That remaining metal, depending on the state of charge residing on it, alters the electric field within the structure and hence the remnant voltage seen above it by a suspended structure. Therefore, it is desirable to minimize the area of metal used by the charging grid. This is in direct opposition to the desire to maximize the density of metal edges where the corona discharges form. Using the minimum area of metal necessary to achieve the required metal density for the charge uniformity is the goal of charging grid design.

The charging process using the microcorona charging grid is quick and easy compared to normal corona charging, and is done *in situ*. However, it is difficult to measure the voltage after charging. Therefore, the actual sensitivity and uniformity of the final device is not known after device fabrication. This is a disadvantage in terms of quality control and yield measurements. Current measurement could be employed to know the level of charge placed within the structure, however, and deduce the remnant voltage.

Furthermore, to avoid microstructure snap-down during the charging process, the microstructures need to be held at the charging voltage. This can be challenging in that the structures need to be connected to this voltage during charging and then removed afterwards. This needs to be included in the packaging and assembly process of the device.

In addition, when comparing the microcorona charging to traditional corona charging, there is a greater tendency in the microcorona version for arcs and other discharges. This is due to the smaller gaps and higher electric fields. In addition, the consequences of an arc or of dielectric breakdown are greater. In most cases, an arc or dielectric breakdown event results in device failure through film breakdown. A corona-

charging process is more forgiving both in terms of the potential for an arc, as well as in terms of the consequences of an arc.

Finally, after performing an *in situ* charging cycle, the metal of the charging grid remains within the MEMS structure. In many devices and designs this would be acceptable. However, in a sensor array such as that developed in this work, the remaining metal could potentially couple multiple sensors together, leading to error and noise sources. This can be mitigated through designing switches or fuse features into the charging grid interconnect to disconnect the areas after charging, or potentially through the use of multiple disconnected charging sites. This would reduce coupling at the expense of needing to perform multiple charging processes to fully complete one device array.

## CHAPTER 5 - MEMS TRANSDUCER

This section will discuss the theoretical modeling, simulation, and design of the transducer structure based on the electret chosen, signal requirements, and processing needs. Ultimately, three different devices were designed and assembled. The first was a single transducer over one of the square charging grids. This was assembled using a simple laminated device. The second device was a laser micromachined transducer array over a circular grid array. This device was also assembled using lamination. The final device was a fully micromachined structure consisting of a transducer array suspended over an array of circular charging grids.

### 5.1 Sensor Dynamics

The sensor array used to process acoustic stress pulses from impacts was based on a resonant capacitive sensor using electret films to convert its motion to an electrical signal. The resonant sensors were fabricated in a MEMS process with *in situ* charging of the electret film. Each element in the array was designed to operate at different resonant frequency.

Figure 5.1 shows a model of a single acoustic sensor [41],[42]. The mass, in this case the mass of the diaphragm, is suspended by a spring constant of  $k$ , being the stiffness of the diaphragm. The spring connects the mass, at position  $x(t)$ , to the anchor. The anchor position is time dependent and is given by  $x_o(t)$ . A damping constant of  $b$  is applied between the mass and the anchor. A capacitance,  $C$ , exists between the mass and the anchor.

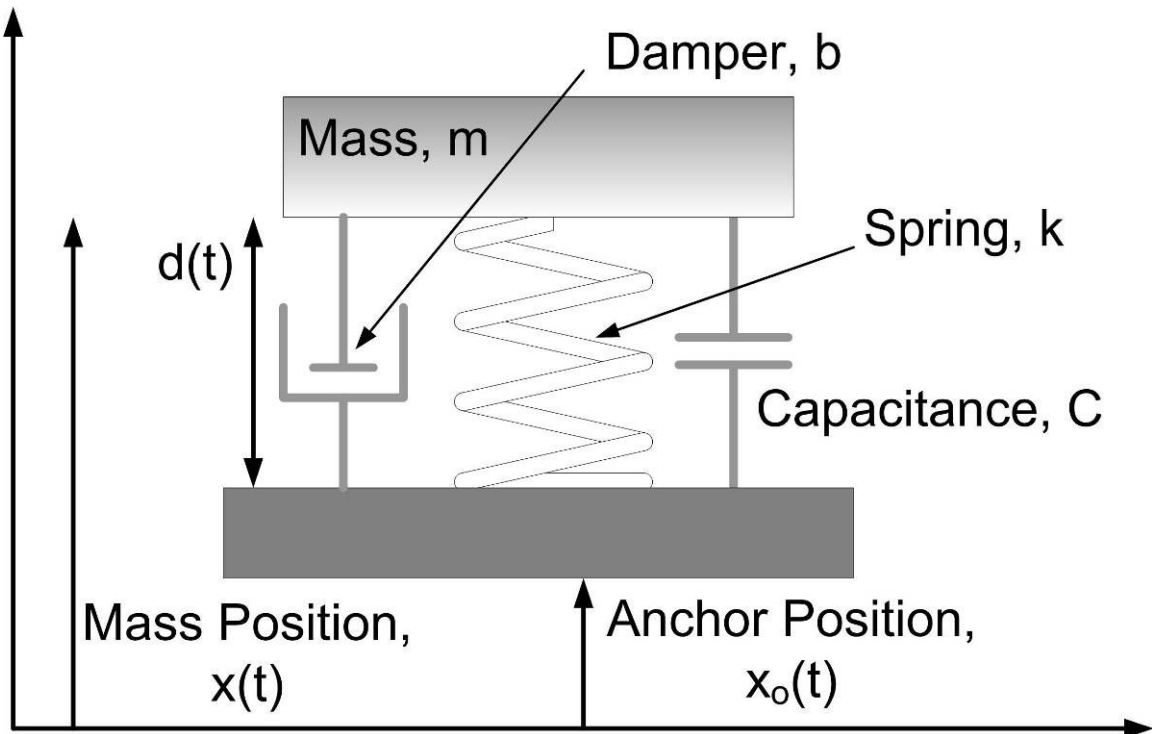


Figure 5.1: Schematic Representation of Transducer

The equation of motion (EOM) for the mass is

$$m \frac{d^2 x}{dt^2} + b \frac{d}{dt} (x - x_o) + k(x - x_o) = 0. \quad (43)$$

The variable of interest is actually  $d$ ,

$$d = x - x_o, \quad (44)$$

leading to

$$x = x_o + d. \quad (45)$$

Plugging this into the EOM yields

$$m\ddot{d} + b\dot{d} + kd = -m\ddot{x}_o, \quad (46)$$

or alternatively

$$\ddot{d} + \left(\frac{b}{m}\right)\dot{d} + \left(\frac{k}{m}\right)d = -\ddot{x}_o. \quad (47)$$

Rearranging the expression, and performing a Laplace Transform, yields

$$\frac{D(s)}{X_o(s)} = \frac{-s^2}{s^2 + \left(\frac{b}{m}\right)s + \frac{k}{m}} = F(s) \quad (48)$$

The denominator is of the form of a damped harmonic oscillator, similar to

$$\ddot{x} + 2\zeta\omega_o\dot{x} + \omega_o^2x = f(t), \quad (49)$$

with a natural frequency of

$$\omega = \omega_o \sqrt{1 - \zeta^2}. \quad (50)$$

However, the numerator of the sensor's transfer function has a second-order integrator, as well. This accounts for the fact that at very low motional frequencies, the mass simply rides on top of the anchor without deflecting towards it or away from it.

Figure 5.2 shows a plot of a typical transducer mechanical response as a function of input frequency.

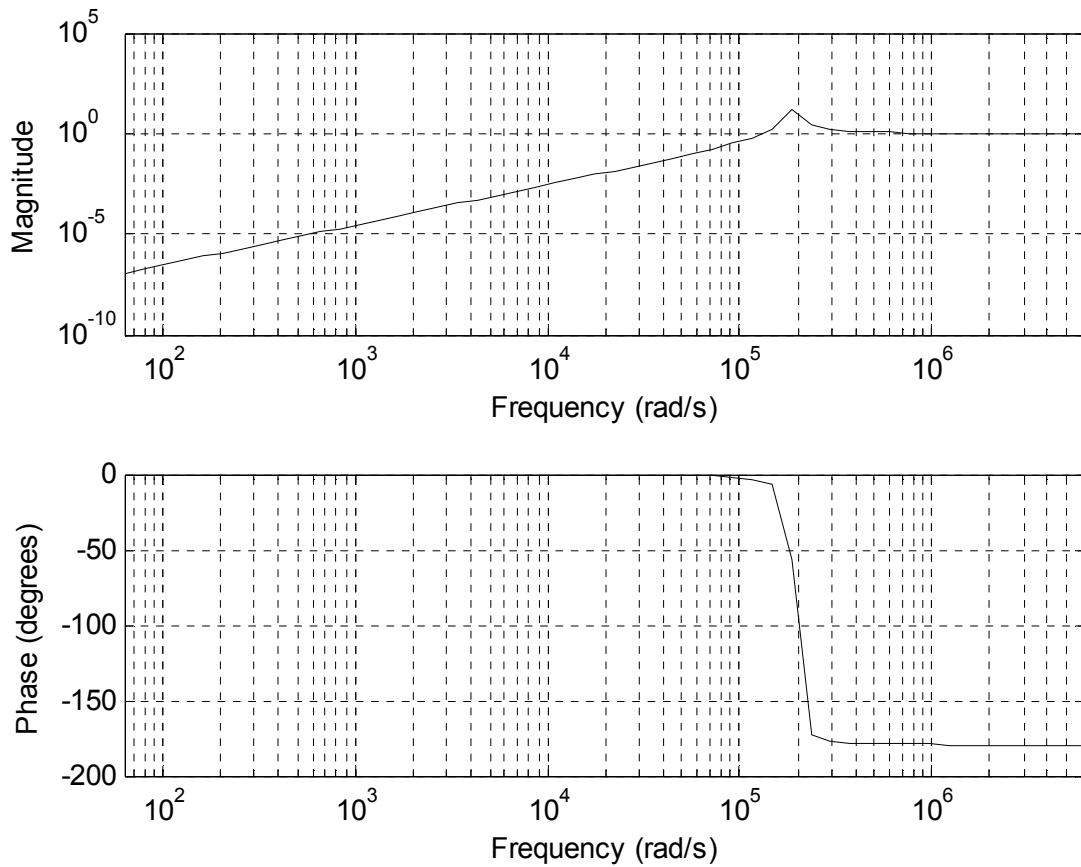


**Figure 5.2: Transducer Transfer Function**

The sensor response shows a resonance peak at the natural frequency of the harmonic oscillator. The transfer function also shows the decreasing response at low frequencies. Furthermore, the transfer function shows the response flattening and becoming unity at higher frequencies, but with the phase of the response being inverted from the acoustic signal.

## 5.2 Sensor Electrical Model

The capacitance of the sensor is given by:

$$C = \frac{\epsilon_o A}{d}, \quad (51)$$

with  $A$  being the capacitive area, and  $d$  the gap from the sensor to the surface of the electret.

In this sensor, the capacitance is nonlinear. It is helpful to linearize the equation for further analysis. The capacitance consists of a nominal capacitance plus a time-dependent change in capacitance, as given by

$$C(t) = C_o + \Delta C(t). \quad (52)$$

Given an input stress pulse function of

$$U(s) = L\{u(t)\}, \quad (53)$$

then the actual capacitor gap is given by

$$D(s) = F(s)U(s) + d_o. \quad (54)$$

Performing a Taylor Expansion of the capacitance leads to

$$C(d) \approx C(d_o) - \frac{\varepsilon_o A}{d_o^2} (d - d_o). \quad (55)$$

The Laplace Transform is given by

$$C(s) \approx C_o - \frac{C_o}{d_o} (D(s) - d_o), \quad (56)$$

and therefore,

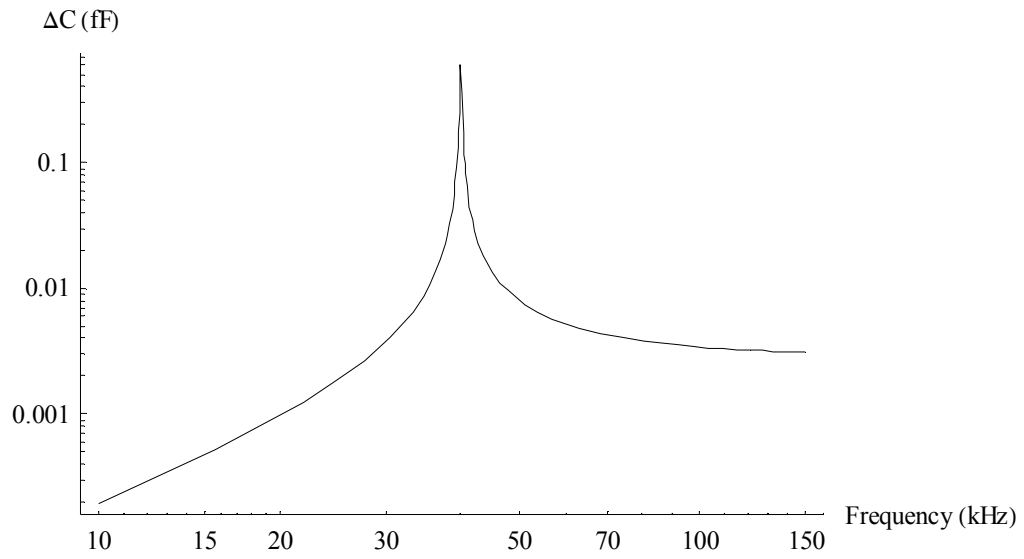
$$C(s) \approx C_o - \frac{C_o}{d_o} F(s)U(s). \quad (57)$$

The change in capacitance as a function of the input stress is then

$$\Delta C(s) \approx -\frac{C_o}{d_o} F(s)U(s), \quad (58)$$

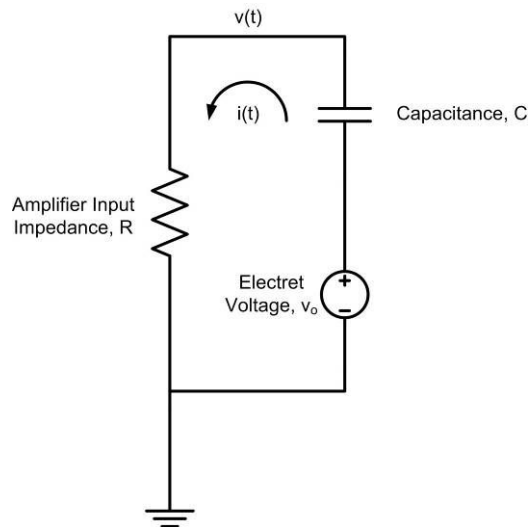
and is considered the mechanical sensitivity.

Figure 5.3 shows the change in capacitance as a function of frequency for a  $u(t)$  that is a pure sine tone with constant amplitude of 1nm. This is for a nominal capacitance,  $C_o$ , of 0.3pF, a nominal capacitor gap,  $d_o$ , of 100 $\mu$ m, a quality factor of 240, and a natural frequency of 40kHz.



**Figure 5.3: Change in Capacitance vs. Frequency**

The sensor capacitance is placed within a circuit consisting of the electret voltage bias and the input resistance of the amplifier [44]. Figure 5.4 shows an equivalent circuit diagram for the electret transducer.



**Figure 5.4: Electrical Model of Single Element of Sensor**

Applying Kirchoff's Current Law yields

$$\frac{v}{R} = C \frac{d}{dt}(v - v_o) + (v - v_o) \frac{dC}{dt}. \quad (59)$$

Again, using a linearized capacitance of

$$C(t) = C_o + \Delta C(t), \quad (60)$$

and plugging in and simplifying by noting that  $C_o$  and  $v_o$  are constant yields

$$\frac{v}{R} = C_o \frac{dv}{dt} + \Delta C(t) \frac{dv}{dt} + v \frac{d\Delta C(t)}{dt} - v_o \frac{d\Delta C(t)}{dt} \quad (61)$$

To simplify further, it is assumed that  $v$ ,  $dC(t)$ ,  $dv/dt$  and  $d\Delta C(t)/dt$  are all small quantities. Therefore, it is anticipated that the second and third terms in the above equation are much smaller than the others, leading to

$$\frac{v}{R} = C_o \dot{v} - v_o \dot{\Delta C}. \quad (62)$$

Performing a Laplace Transform yields

$$\frac{V(s)}{R} = C_o s V(s) - v_o s \Delta C(s), \quad (63)$$

and rearranging yields

$$\frac{V(s)}{\Delta C(s)} = \frac{V_o}{C_o} \frac{s}{s - \frac{1}{RC_o}}. \quad (64)$$

This is the transfer function of a high-pass filter with cut-on frequency of  $1/RC_o$ . Therefore, since the capacitance of these sensors is very small, the input impedance to the amplifier needs to be sufficiently high to allow the charge to remain on the capacitor while the voltage is measured.

From earlier,

$$\Delta C(s) \approx -\frac{C_o}{d_o} F(s)U(s), \quad (65)$$

so, the transducer transfer function is

$$\frac{V(s)}{U(s)} \approx -\frac{V_o}{d_o} F(s) \frac{s}{s - \frac{1}{RC_o}} = \frac{V_o}{d_o} \frac{s^3}{(s - \frac{1}{RC_o})(s^2 + (\frac{b}{m})s + \frac{k}{m})} \quad (66)$$

, and is the overall sensitivity.

As expected, higher sensitivities result from higher electret bias voltages and smaller capacitor gaps. Furthermore, the low capacitance of the sensor and the input impedance of the amplifier lead to a high pass filter. Figure 5.5 shows the voltage from the sensor as a function of frequency for the same input of 1nm displacement input, an electret bias voltage,  $V_o$ , of 200V, and an amplifier input impedance of 1M $\Omega$ .

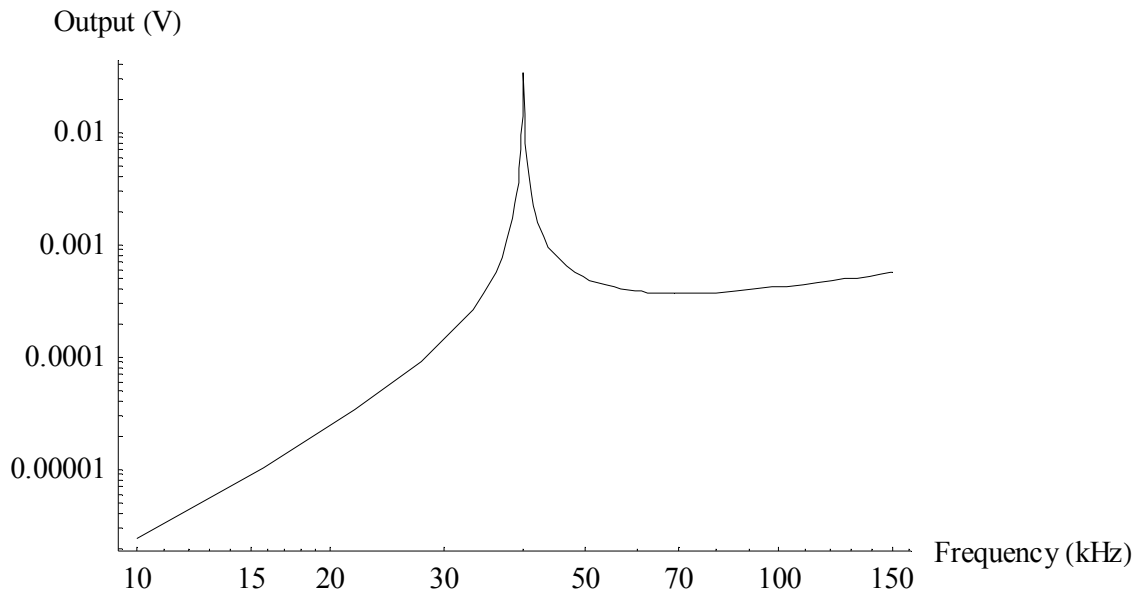


**Figure 5.5: Voltage as a Function of Frequency**

Note the portion of the response beyond resonance. That portion shows increasing response due to the high-pass filter action. This implies that the magnitude of the peak is attenuated by that same high-pass filtering action. Increasing the input impedance would therefore lead to a larger overall sensitivity.

In addition, since each sensor element in an array would have different mechanical and electrical properties, each sensor element would also have a different capacitance and mechanical sensitivity, and therefore overall sensitivity. This needs to be accounted for in signal analysis later when comparing sensor outputs in the form of a spectrum.

### **5.3 Readout Electronics**

The extremely low capacitance of the transducers requires care in buffering the signal prior to insertion into data recording instrumentation. In particular, a very high impedance input is required in order to see low frequency, on the order 10 kHz, signals as

expected in the ball and hammer drop experiments. The Texas Instruments INA122 instrumentation amplifier was selected as the fundamental component of the readout circuits. The schematic for a single channel is shown in Figure 5.6. No gain resistor is included in the circuit, leading to an overall gain of 5. At that gain, the amplifier circuit has a bandwidth of 100 kHz. A high pass output filter was added after the amplifier to remove lower frequency noises sources such as 60 Hz hum from power supplies.

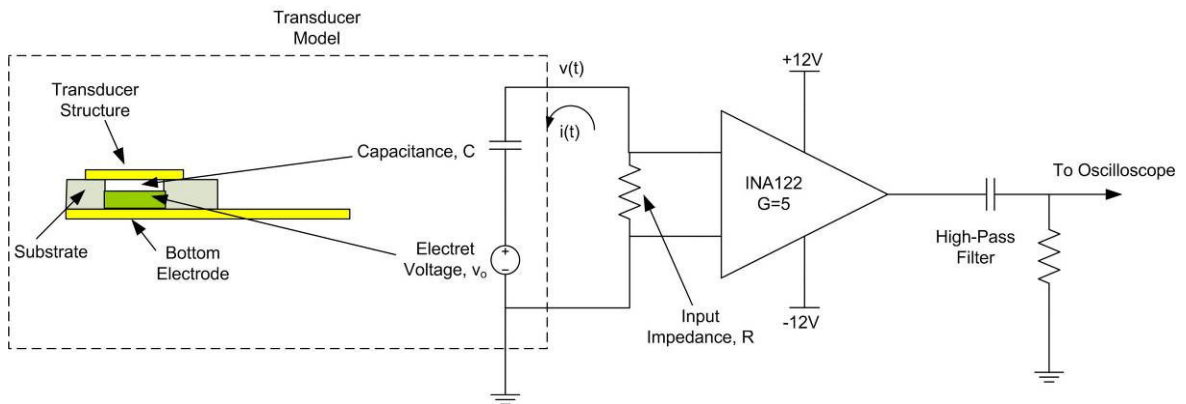


**Figure 5.6: Transducer Readout Circuits**

For most tests, four transducers were connected to four separate readout amplifier channels. The four amplifier outputs are connected to an oscilloscope using  $1\text{M}\Omega$  input impedance probes. The four-channel oscilloscope was used to acquire and store the resulting transducer waveforms.

The amplifier and output filter have a transfer function, as well, given by

$$\frac{OUT(s)}{V(s)} \approx \frac{Gw_l}{s + w_l}, \quad (67)$$

with  $G$  being the amplifier gain, and  $w_l$  being the roll-off frequency. If selected correctly, this amplifier can compensate for the high-pass filter nature of the sensor itself. With

each sensor having a different capacitance and mechanical sensitivity, the amplifier gain section may or may not be set specifically for each element, depending on how the array's spectrum is utilized.

Furthermore, during sensor characterization, the sensor is placed on a piezoelectric driver that creates ultrasonic sinusoidal waves, and allows scanning the sensor response over frequency. That piezoelectric driver also creates a signal in the amplifier due to coupling through parasitic capacitances. Furthermore, the charging grid that remains under each sensor provides a capacitive coupling between sensors during operation. These parasitic capacitances induce a current in the amplifier's input impedance, leading to a voltage of

$$V_p(s) = V_d(s) \frac{s}{s - \frac{1}{RC_p}}, \quad (68)$$

with  $R$  being the input impedance of the amplifier, and  $C_p$  being the parasitic capacitance coupling the piezoelectric drive signal into the amplifier.

During piezoelectric excitation of the sensor during characterization, the parasitic capacitance is low, but the drive voltage is high. During scans, the parasitic output is comparable to the actual signal from the resonating structure. Figure 5.7 shows the sensor output as a function of frequency for high levels of parasitic coupling. This is for a driving voltage of 10 and a parasitic capacitance of 10fF.

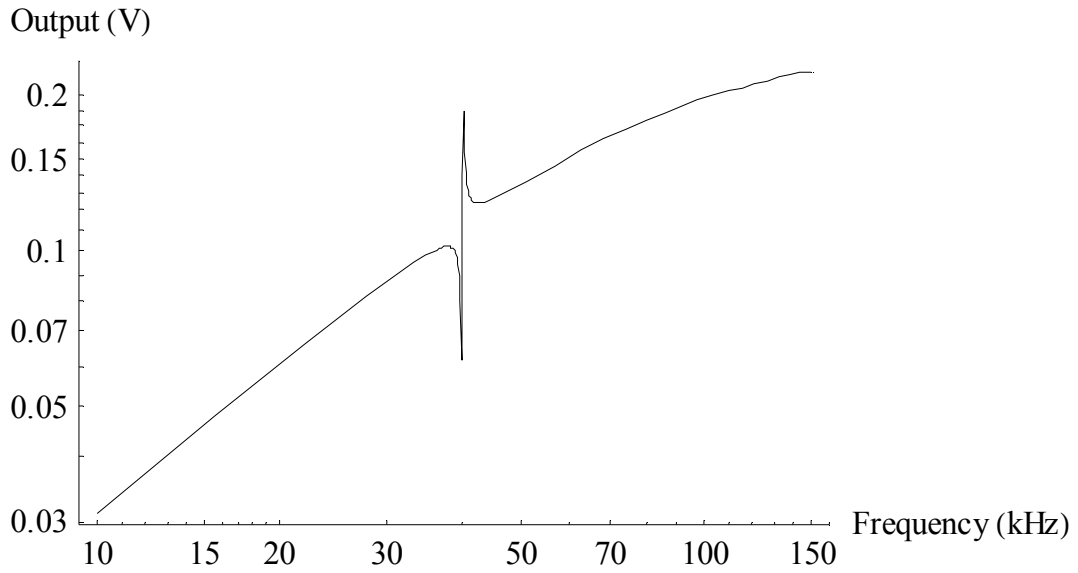


**Figure 5.7: Response from Driven Sensor Element**

A schematic representation of the sensor-to-sensor parasitic capacitance due to the charging grid is shown in Figure 5.8.

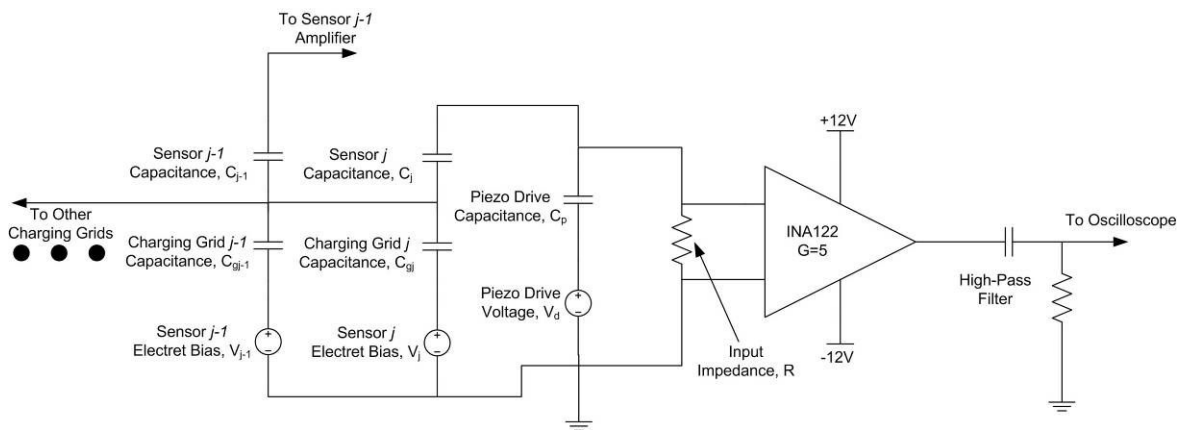


**Figure 5.8: Schematic of the Sensor including Sensor-to-Sensor Parasitic**

The capacitance from one sensor element to the charging grid is approximately the same as one element to the other electrode, on the order of 1 pF, but with much

smaller voltages being driven across it. However, these voltages are similar in magnitude across all sensors, so the coupling from sensor to sensor will result in signal levels that are approximately the same as the signal from the sensor itself. This is a drawback of the single charging grid and should be addressed in future efforts.

#### 5.4 Laser Micromachined Transducer Array

A laser micromachined sensor was assembled to test *in situ* charging. The laser micromachined transducer array consisted of a matrix of circular diaphragms suspended above the electret film as shown in Figure 5.9.

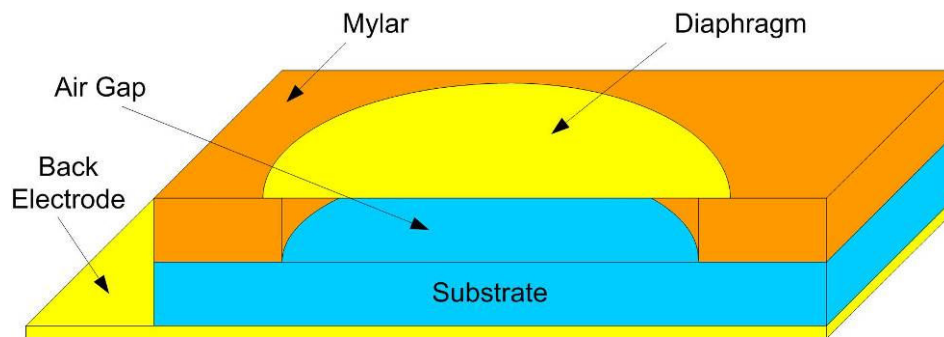


Figure 5.9: Schematic of Laser Machined Sensor

These diaphragms were laser machined and adhesively bonded on top of the charging grid arrays. These transducers were designed to have a high natural frequency so that the resonance and damped harmonic oscillations were not achieved. Finite element analysis was performed to determine the vibrational modes of the diaphragms and their natural frequencies. Figure 5.10 through Figure 5.18 show these vibrational modes.

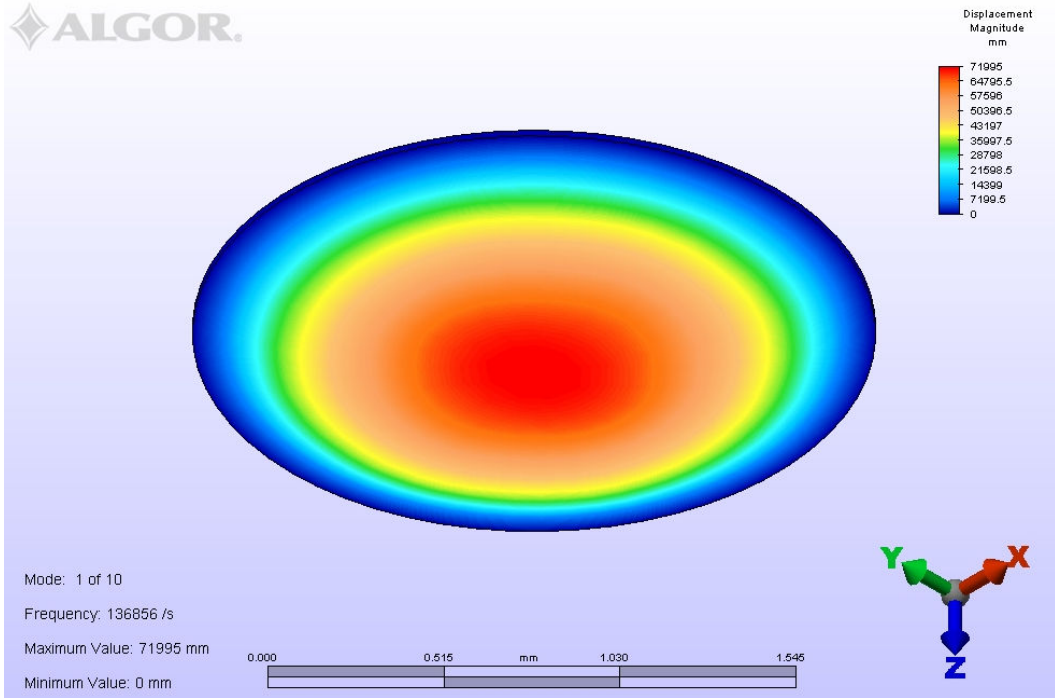


Figure 5.10: Laser Machined Sensor Mode 1

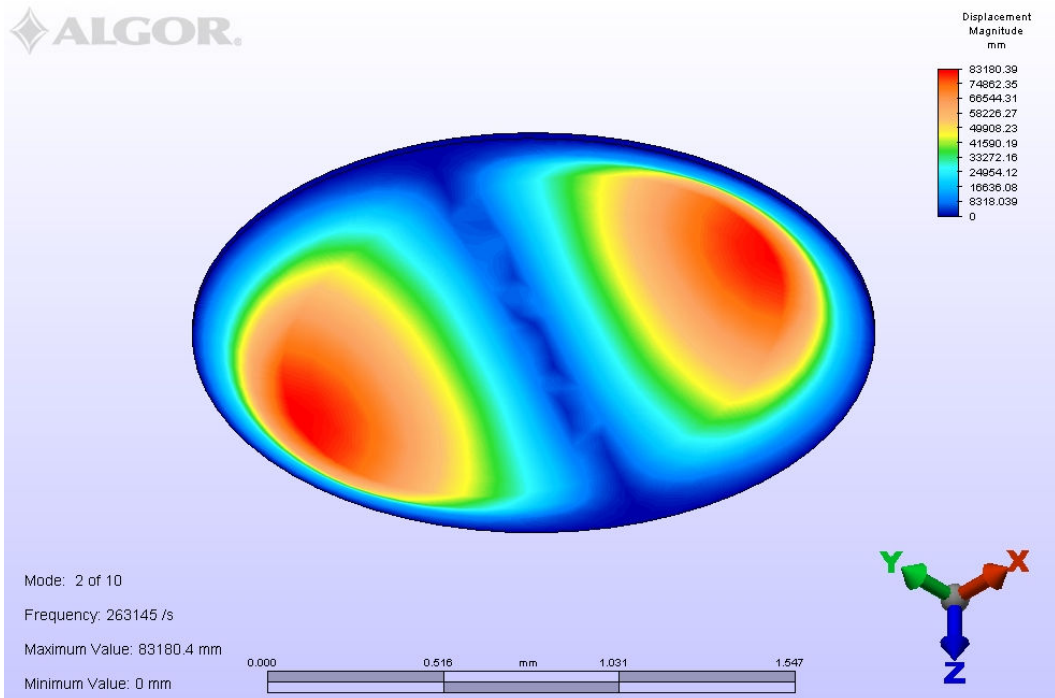


Figure 5.11: Laser Machined Sensor Mode 2

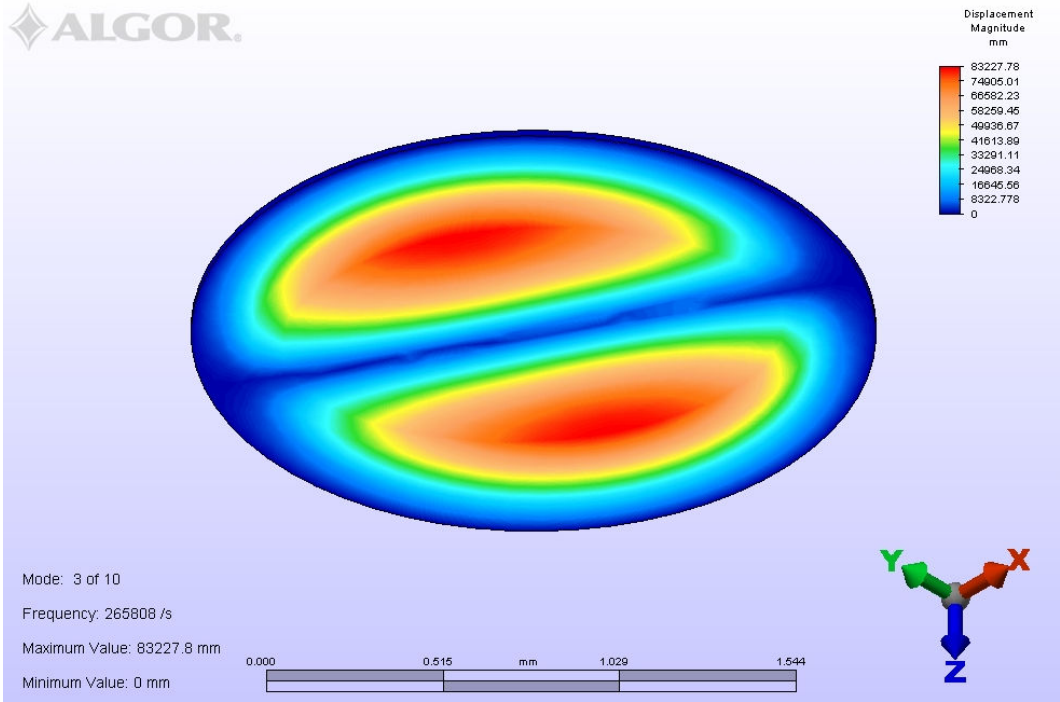


Figure 5.12: Laser Machined Sensor Mode 3

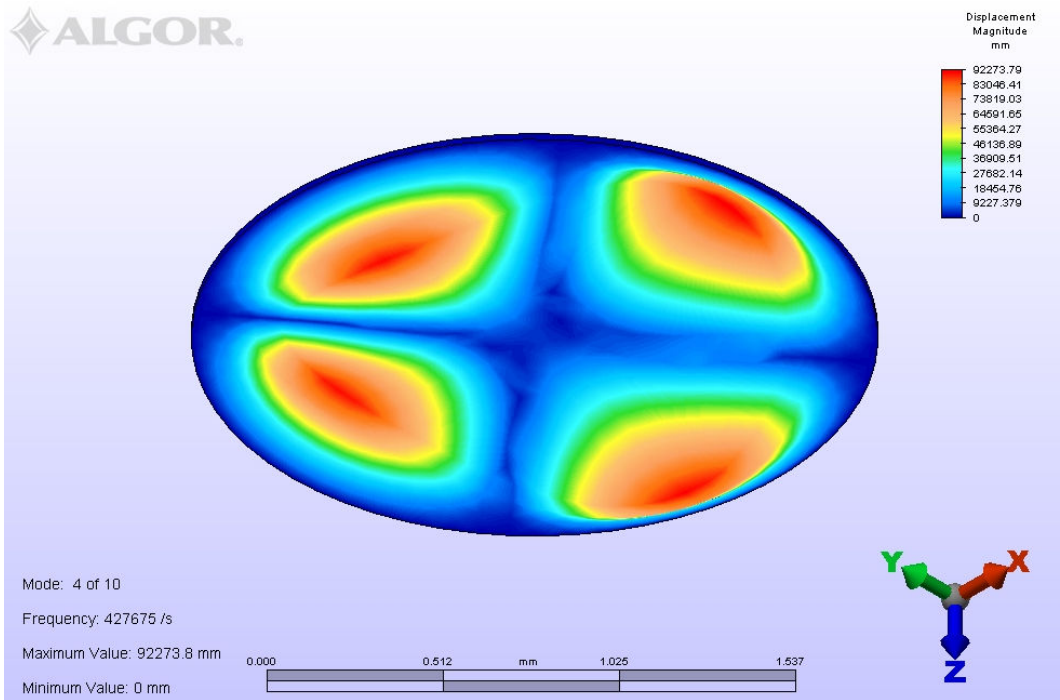


Figure 5.13: Laser Machined Sensor Mode 4

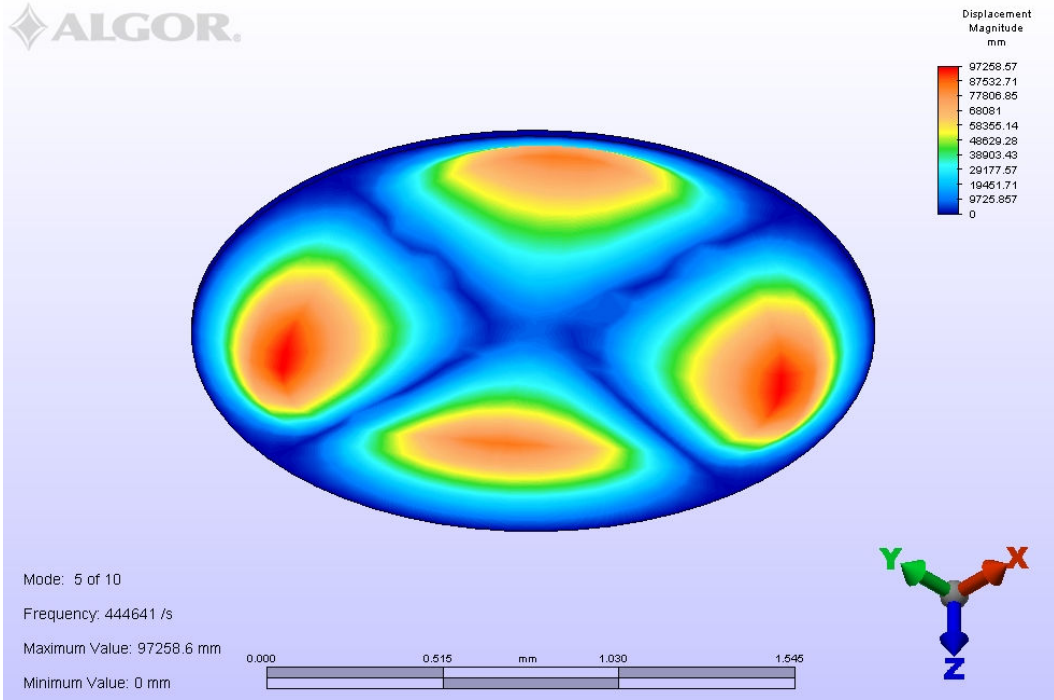


Figure 5.14: Laser Machined Sensor Mode 5

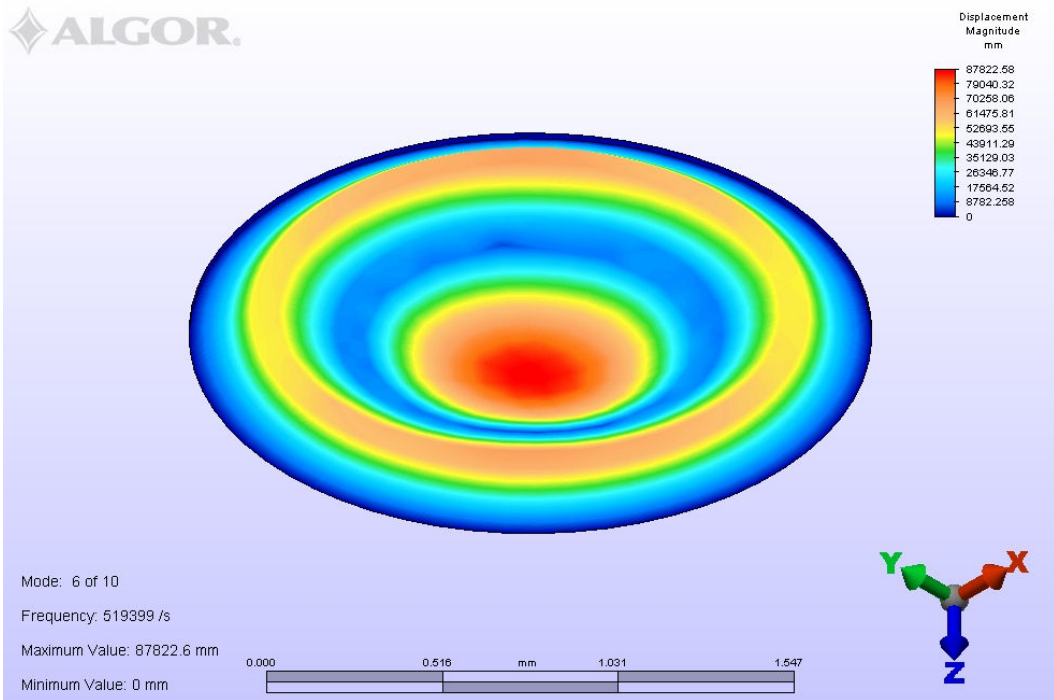


Figure 5.15: Laser Machined Sensor Mode 6

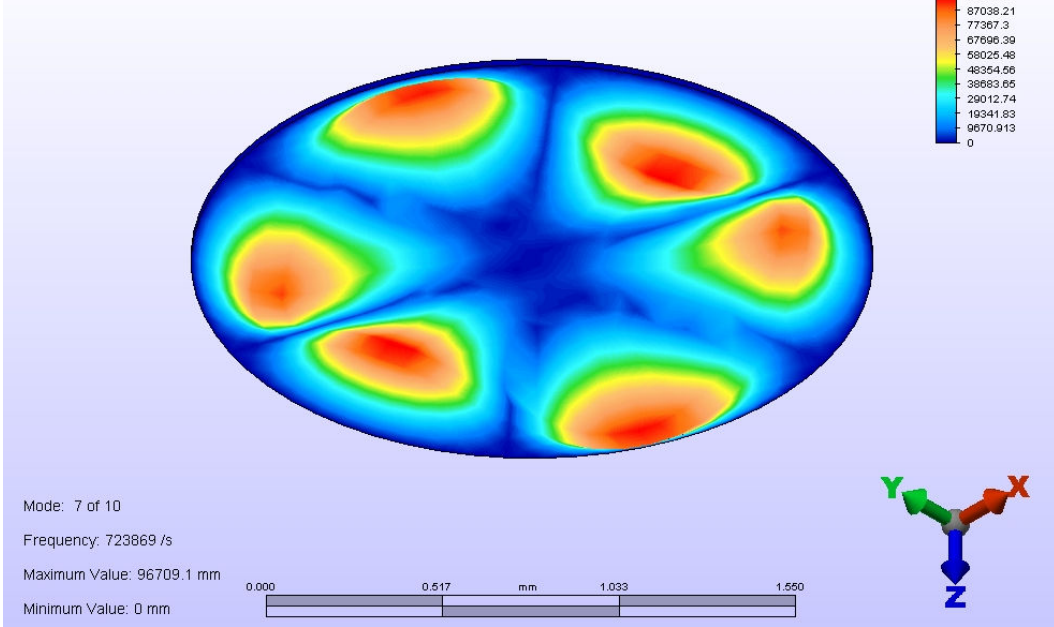


Figure 5.16: Laser Machined Sensor Mode 7

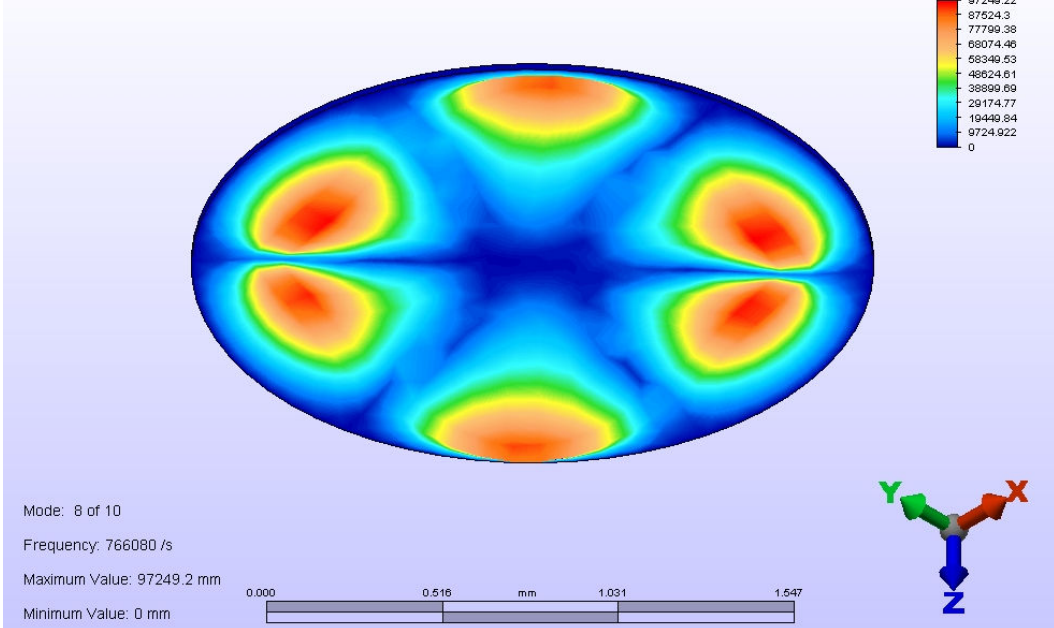
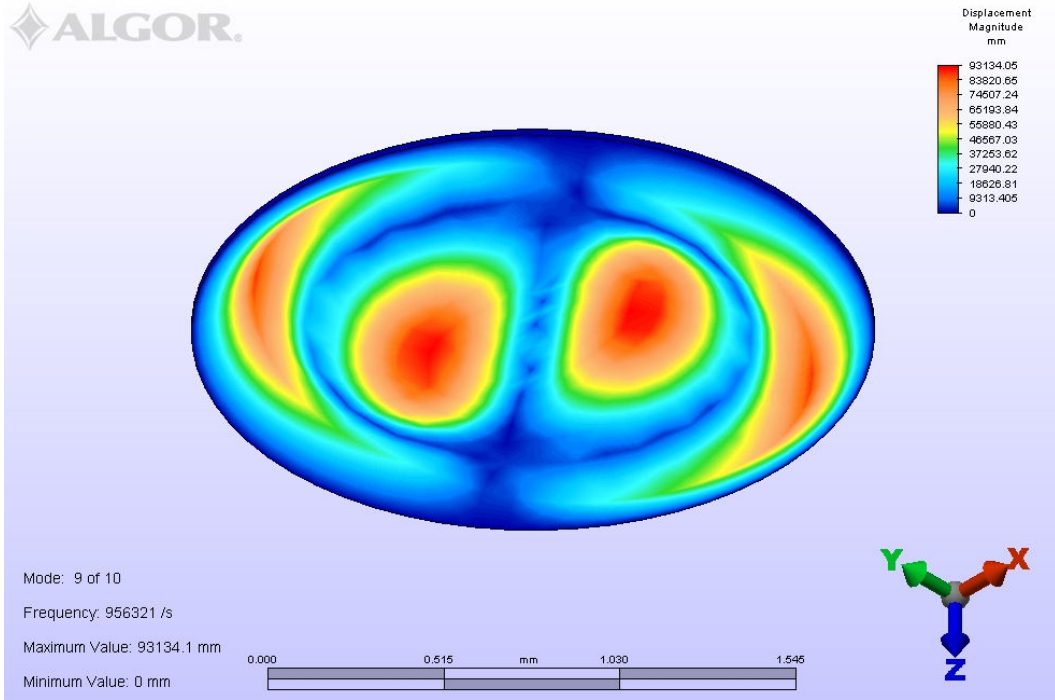


Figure 5.17: Laser Machined Sensor Mode 8



**Figure 5.18: Laser Machined Sensor Mode 9**

With only a single capacitive electrode below this diaphragm, only modes 1 and 6 are electrically active, and will result in a current running through an external circuit. Table 5.1 shows the predicted natural frequencies for the fundamental mode of each transducer.

**Table 5.1: Resonant Frequencies for Transducers in the Array**

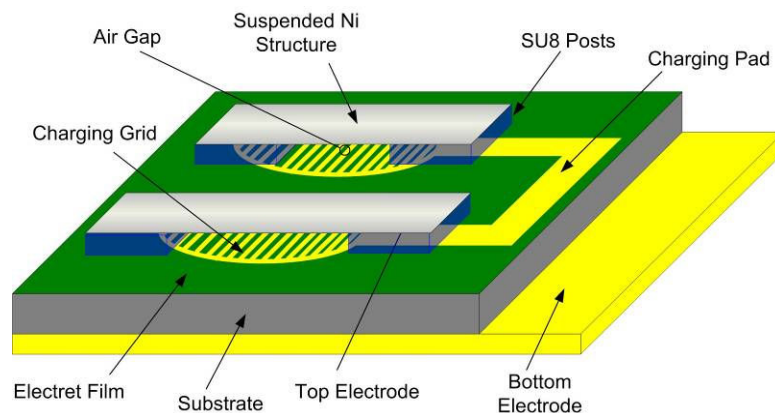
Device	Resonant Frequency
Top Left	137 kHz
Top Middle	153 kHz
Top Right	171 kHz
Bottom Left	193 kHz
Bottom Middle	229 kHz
Bottom Right	273 kHz

The laser machined devices were used to verify *in situ* electret charging and sensor operation on large structures.

## 5.5 Microfabricated Transducer Array

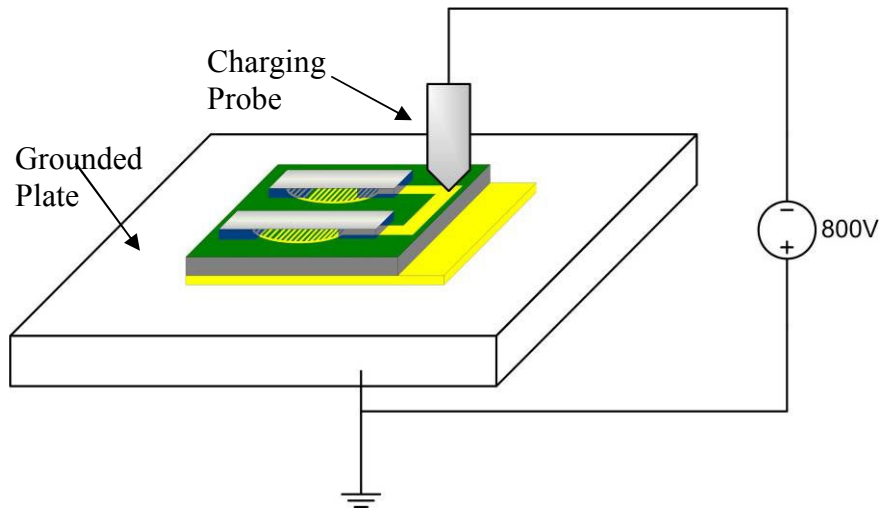
The microfabricated transducer array was intended to demonstrate the applicability of the *in situ* electret charging technique to multiple structures on a single die, as well as the use of resonant array processing to characterize impact stress pulses. The wafer consisted of multiple die with metal diaphragms suspended above the seven charging sites provided by the circular grid array. The metal bridges were designed using analytical equations for clamped-clamped beam natural frequencies.

Figure 5.19 shows a conceptual drawing of the microfabricated transducer array. It consists of a Nickel fixed-fixed beam suspended by SU8 posts above an electret film. A suspended charging grid is deposited on the electret film. This grid will actually form the electret after device fabrication. A charging pad connects to all of the charging grids to allow application of the charging voltage. The structure sits on top of a silicon substrate that has been conductively bonded to a metal foil that serves as the bottom electrode. The suspended Nickel structural layer also served to create bond pads for electrical connection to each individual bridge.



**Figure 5.19: Schematic of Microfabricated Transducer Array Device**

To perform charging, the device is placed on a grounded conductive plate, as shown in Figure 5.20. A small diameter probe is placed on the charging pad and the grid is energized to a high voltage. This initiates microplasma discharges that lead to permanent polarization of the electret film.



**Figure 5.20: Microfabricated Array Charging Setup**

During operation, the microfabricated array device would be attached to the structure under investigation and connected to readout electronics as shown in Figure 5.21.

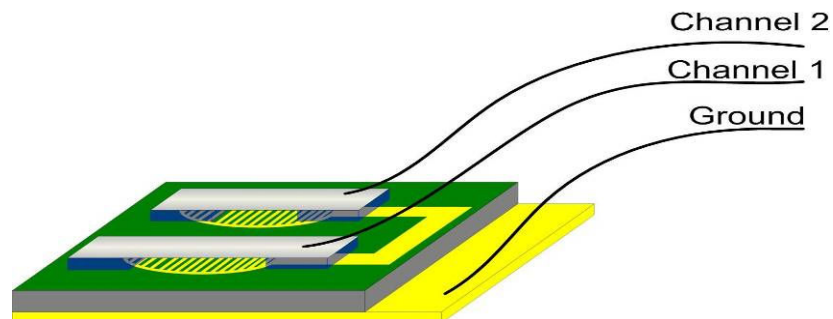


**Figure 5.21: Microfabricated Array Charging During Operation**

A single chip contains seven individual transducer elements, with each sensor suspended above its own charged electret area. The largest structure was 2mm by 2mm. Each subsequent structure was reduced in size by 200μm. The natural frequency for a clamped-clamped bridge is given by

$$f = \frac{22.37 * t}{2\pi L^2} \sqrt{\frac{E}{12\rho}}, \quad (69)$$

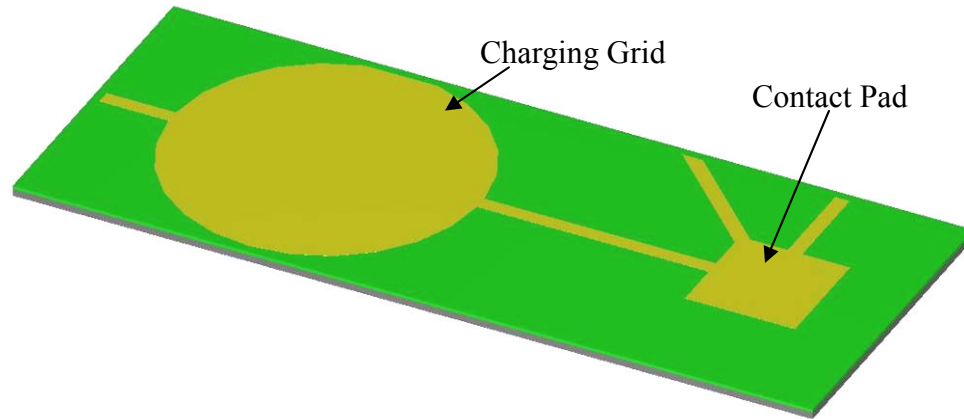
where  $t$  is the thickness of the structure,  $L$  is its length,  $E$  is the elastic modulus of the material, and  $\rho$  is the density of the material. The Nickel used in these structures was intended to be 10μm thick, had a density of 8900 kg/m<sup>3</sup> and had an elastic modulus of 221 GPa. Table 5.2 lists the expected lowest modes for each device in the array.

**Table 5.2: Natural Frequencies for Array Element Designs**

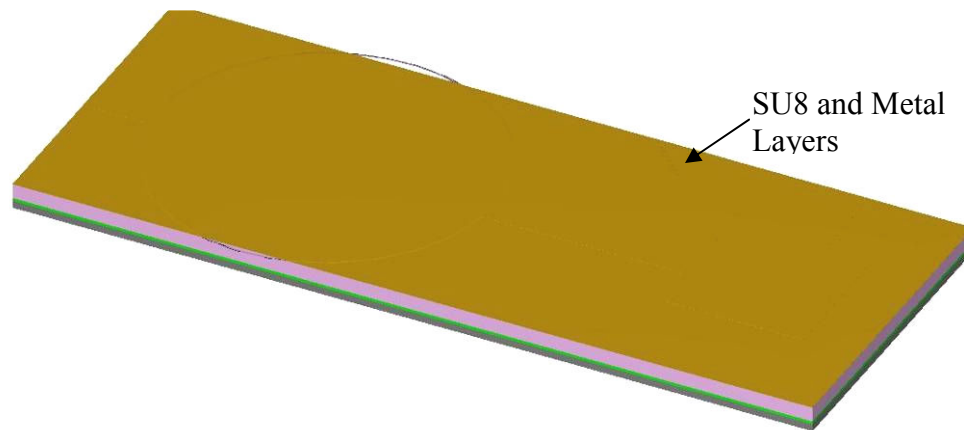
Length (mm)	Resonant Frequency
2.0	12.812 kHz
1.8	15.817 kHz
1.6	20.018 kHz
1.4	26.146 kHz
1.2	35.558 kHz
1.0	51.247 kHz
0.8	80.074 kHz

The conceptual process flow for this design starts with the fabrication of the circular charging grid as shown in Figure 5.22, using the process described in Chapter IV. A thick layer of SU8 is then deposited and exposed, but not developed. After that, a barrier layer of Chrome is deposited using low-power e-beam evaporation, followed by a thin layer of gold that serves as a seed layer for plating processes. The wafer then appears

as shown in Figure 5.23. The pattern of the unexposed SU8 is visible because the unexposed SU8 has a different surface texture.



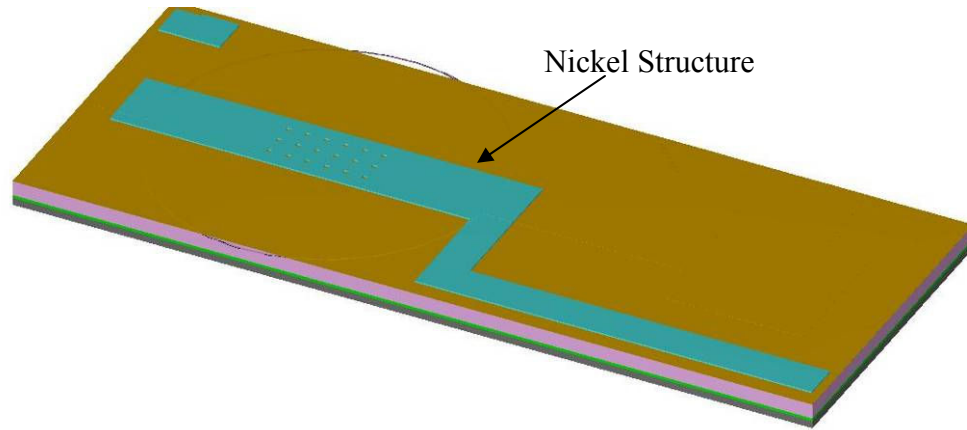
**Figure 5.22: Charging Grid Solid Model**



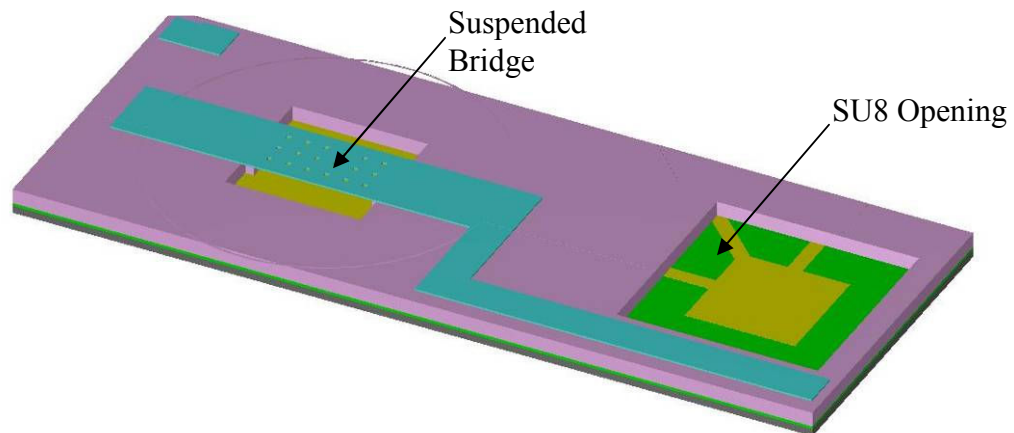
**Figure 5.23: Solid Model of Structure with SU8 and Thin Metal Layers**

Following the SU8 and barrier metal layer depositions, a photoresist plating mold model is spun coat, patterned, and baked. Electroless Nickel is then plated onto the gold seed layer, followed by a photoresist strip step. The wafer then appears as in Figure 5.24. The photoresist mold forms the suspended bridge and also had posts within it that yielded holes within the nickel structure. The gold and chrome layers are then stripped, leaving

the SU8 surface. Finally, the SU8 is developed to release the structure and expose contact pads, as shown in Figure 5.25.

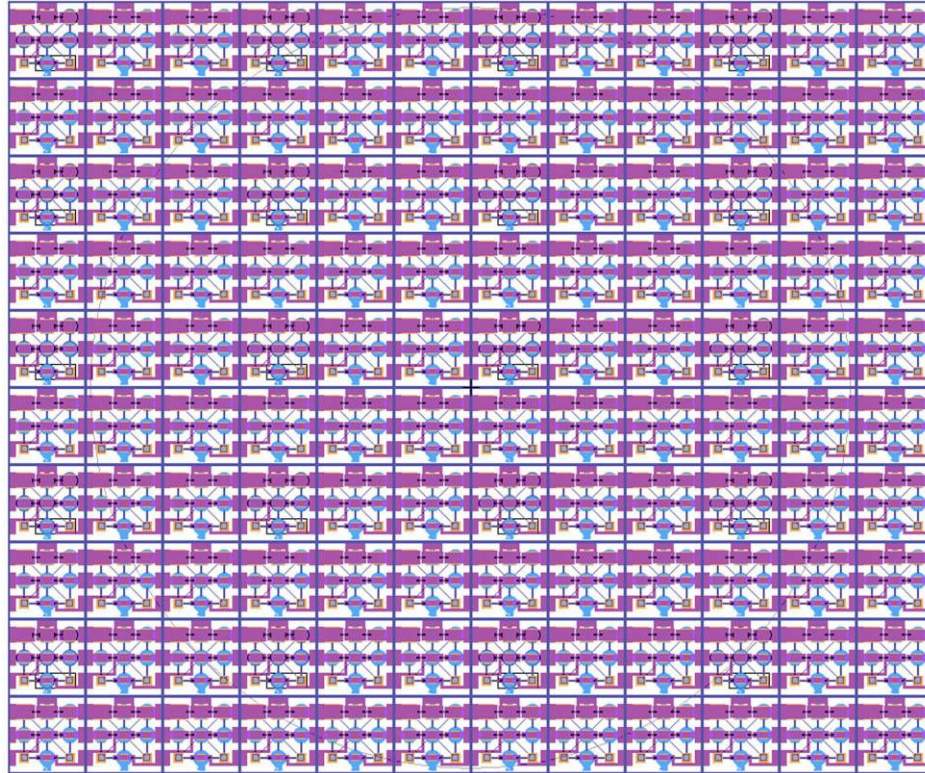


**Figure 5.24: Solid Model of Wafer after Plating and Photoresist Strip**



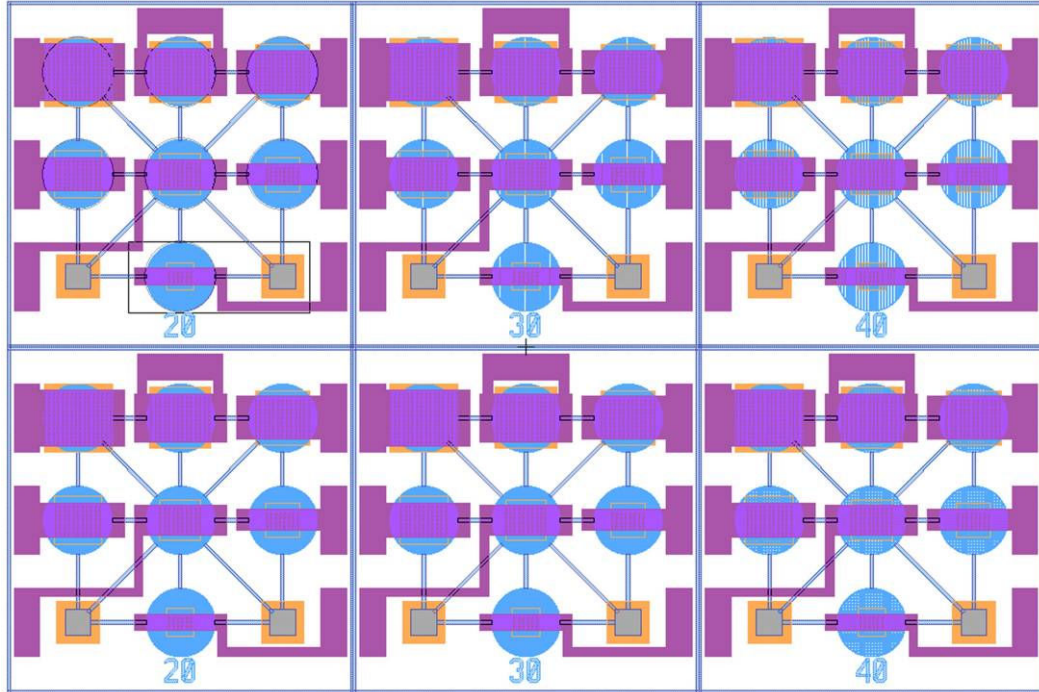
**Figure 5.25: Solid Model of Released Structure**

The wafer was laid out to include multiple copies of the same devices. The structural elements are all the same. However, they are suspended over a variety of circular charging grids. The wafer layout is shown in Figure 5.26.



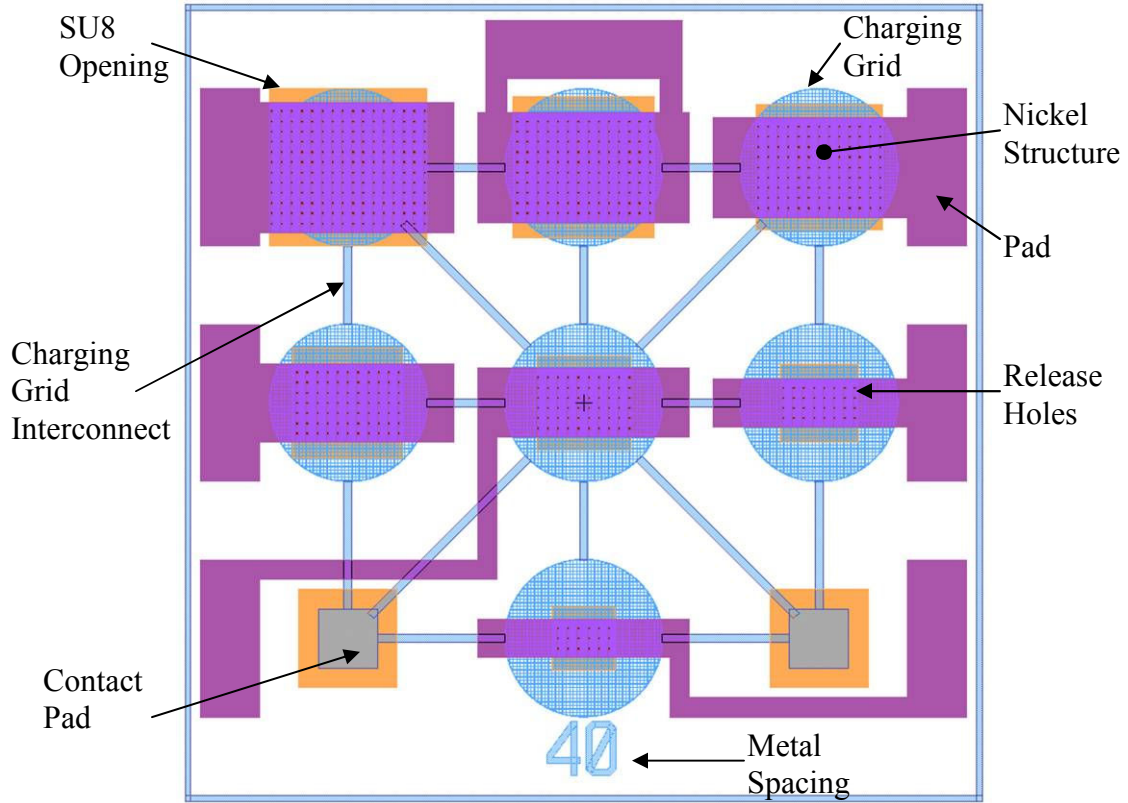
**Figure 5.26: Microfabricated Transducer Array Wafer Layout**

A test matrix was designed into the layout. This matrix included both square mesh versions of the charging grid, as well as straight line versions. There was also a variety of spacings including 20 microns, 30 microns, and 40 microns, as shown in Figure 5.27, and identified by the patterned numerical value on each chip.



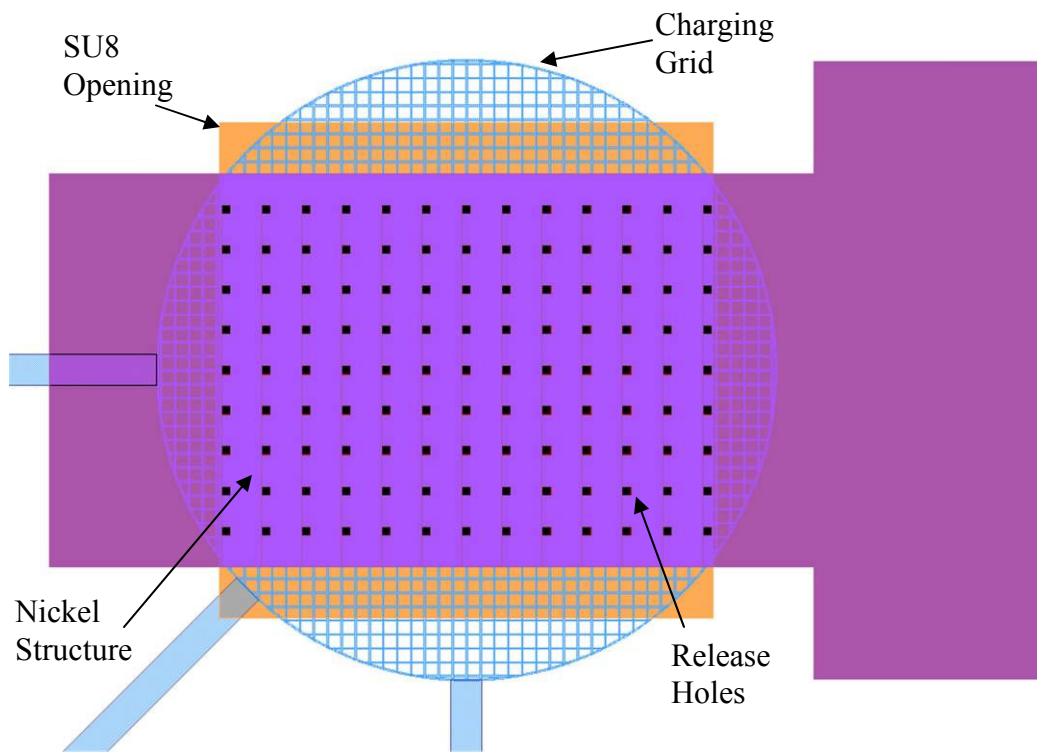
**Figure 5.27: Test Matrix Layout**

Figure 5.28 shows the layout of an actual array. The top left structure is the largest and the bottom middle structure the smallest. All of the charging areas are exactly the same in diameter and configuration. This was done to achieve as close to equal as possible remnant voltages for each transducer. Contact pads were designed into the Ni plating layer to allow wires to be soldered to the elements. Openings in the SU8 were included over the charging contact pads to allow connection to the charging grids.



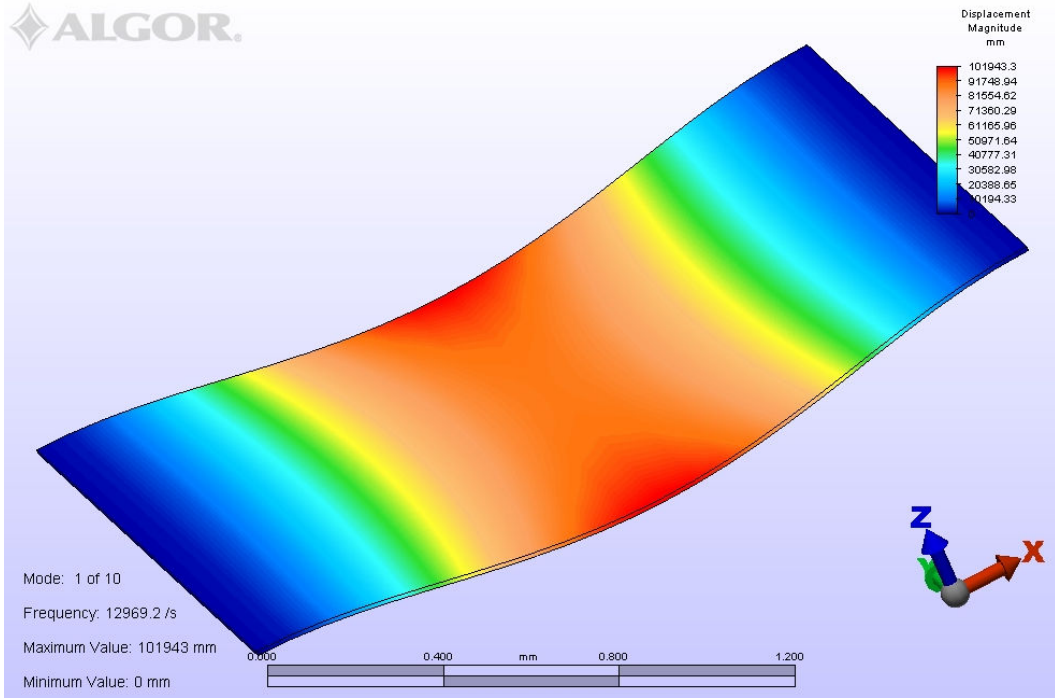
**Figure 5.28: Microfabricated Transducer Array Layout**

Figure 5.29 shows the layout of a single transducer. In the figure, the release holes are easily seen in the structure. Furthermore, the SU8 openings, shown in inverse form in the layout, are square and sized to be wider than the Ni diaphragm. This provides large open areas on either side of the Ni structure to aid in developing the SU8 in case the release holes are insufficient.



**Figure 5.29: Single Transducer in the Array**

Finite element analysis was used to examine the modes of the structure, and to compare the anticipated natural frequencies with those calculated analytically. Figure 5.30 through Figure 5.39 show these modes.



**Figure 5.30: Microfabricated Sensor Array Mode 1**

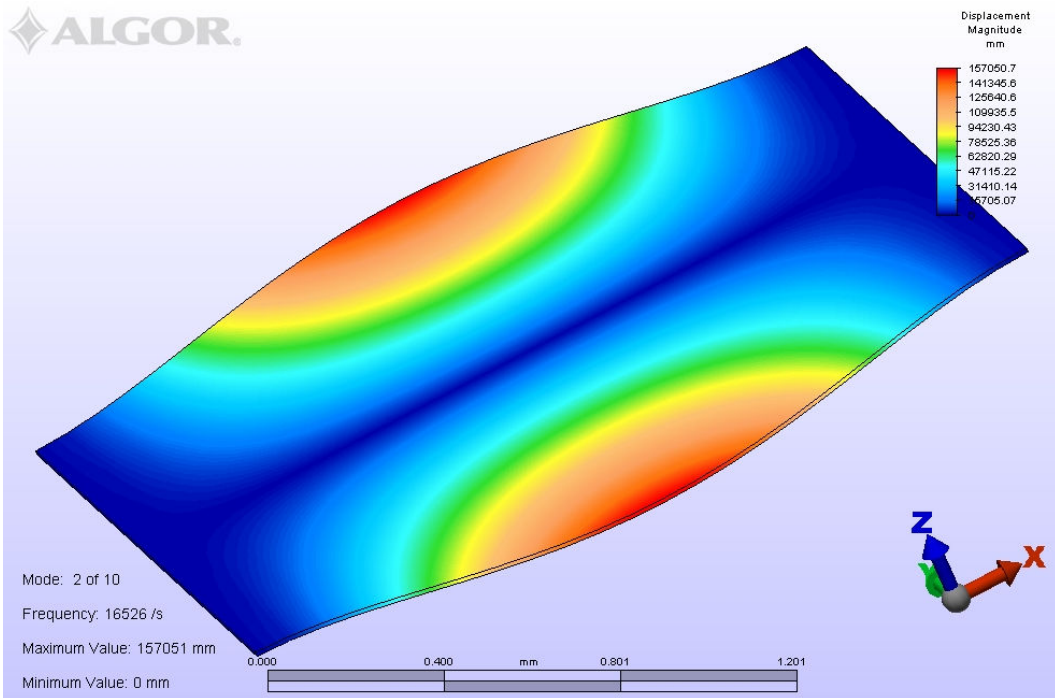


**Figure 5.31: Microfabricated Sensor Array Mode 2**

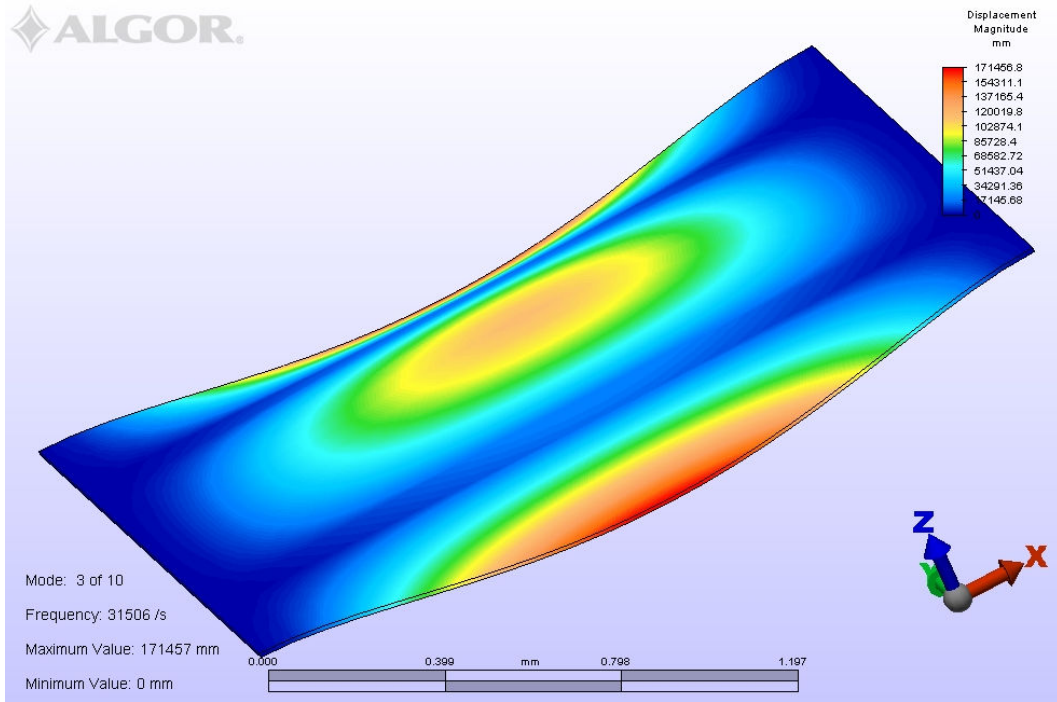


Figure 5.32: Microfabricated Sensor Array Mode 3

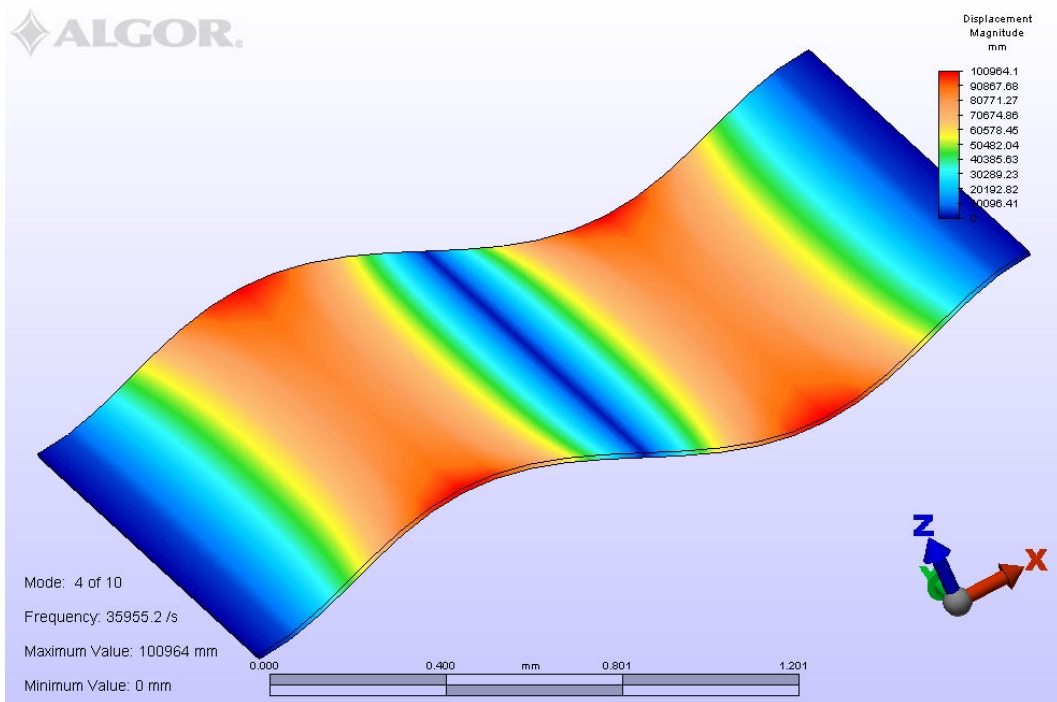


Figure 5.33: Microfabricated Sensor Array Mode 4

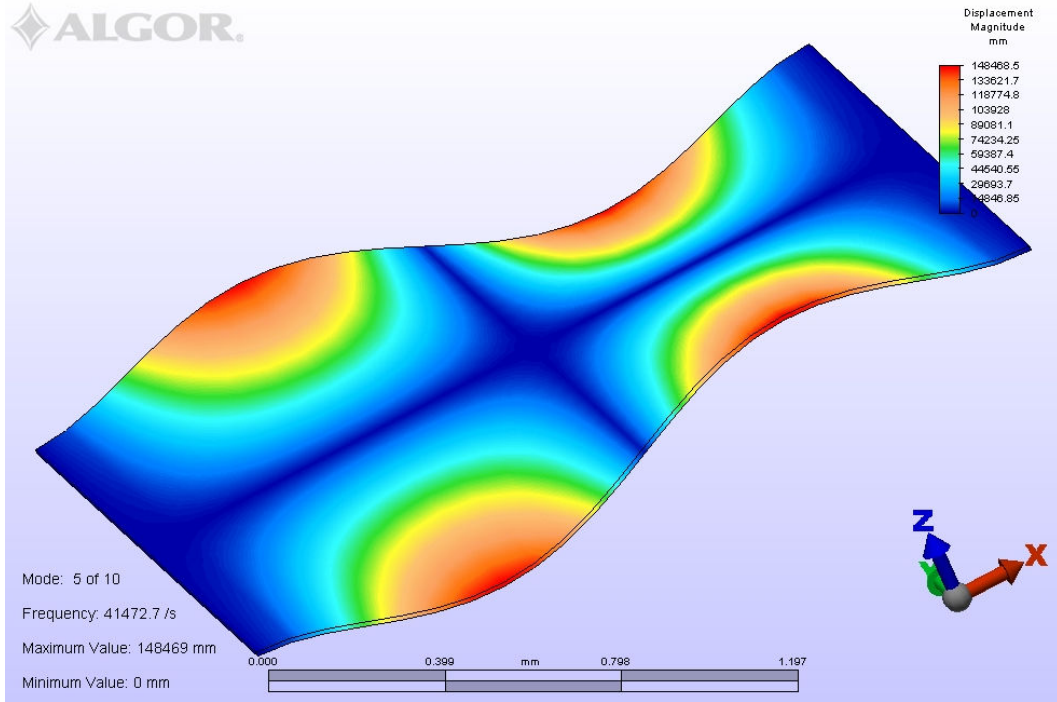


Figure 5.34: Microfabricated Sensor Array Mode 5

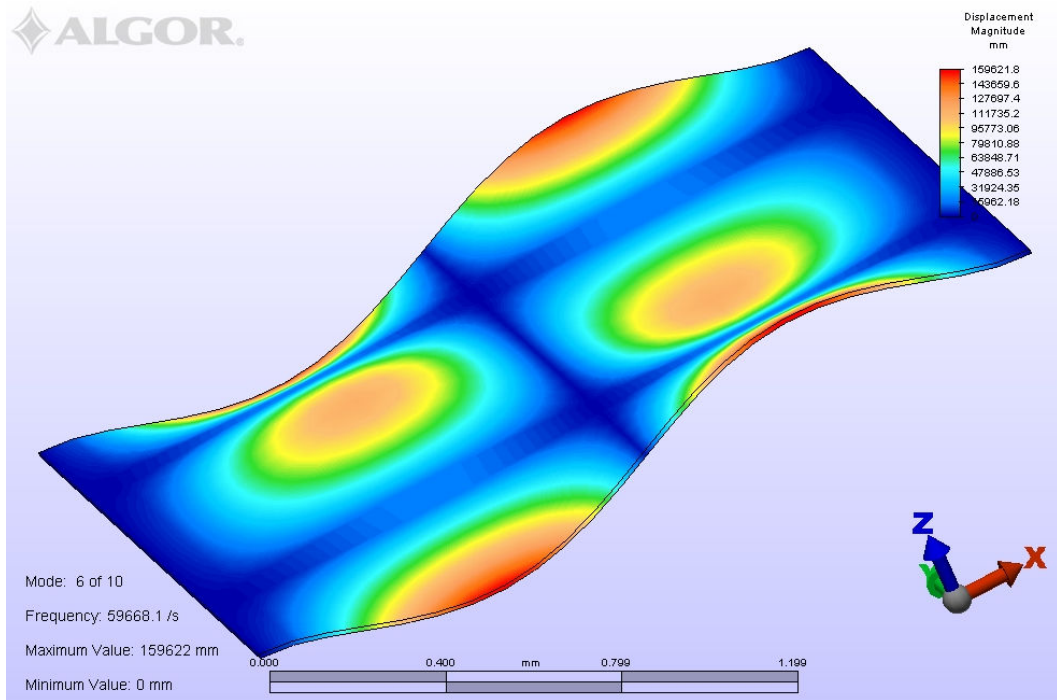


Figure 5.35: Microfabricated Sensor Array Mode 6

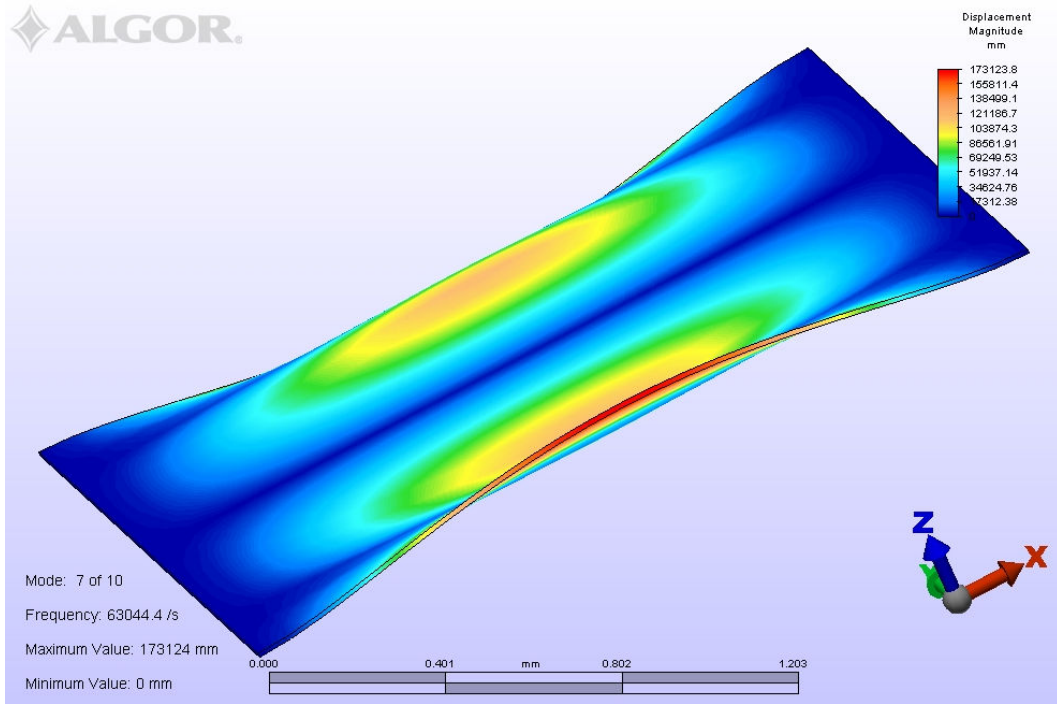


Figure 5.36: Microfabricated Sensor Array Mode 7

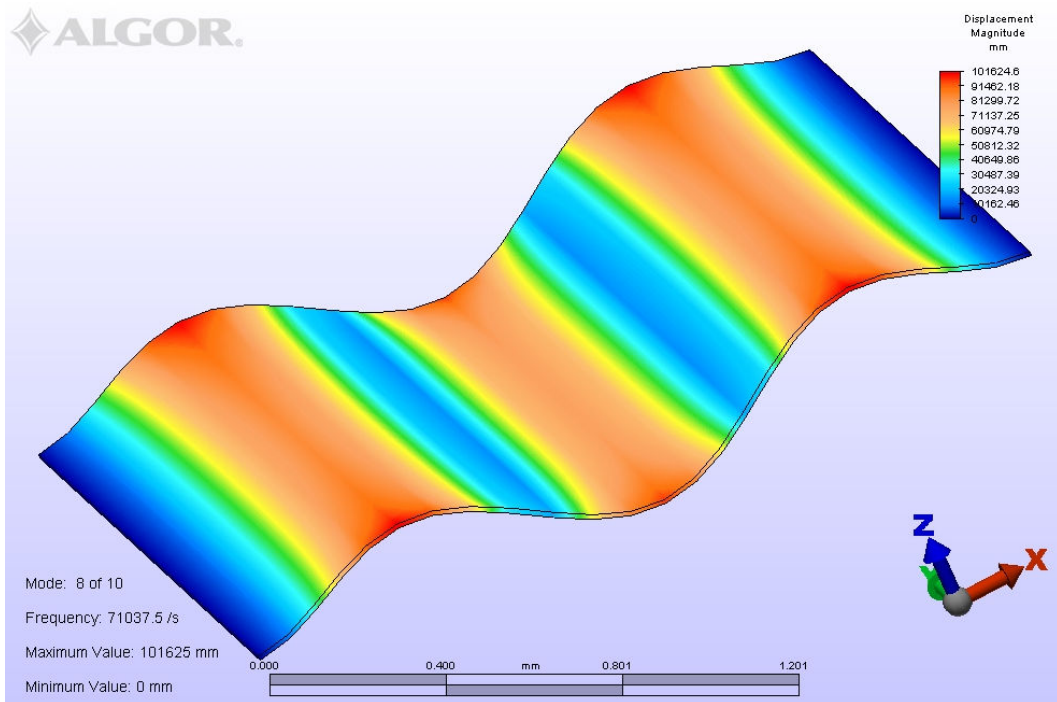


Figure 5.37: Microfabricated Sensor Array Mode 8

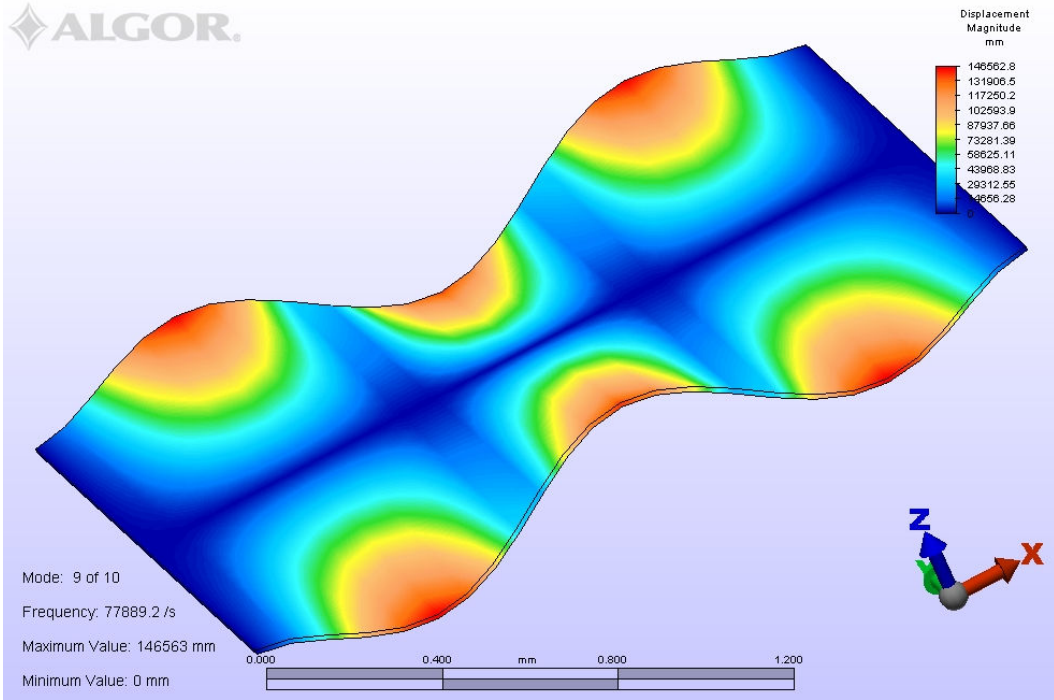


Figure 5.38: Microfabricated Sensor Array Mode 9

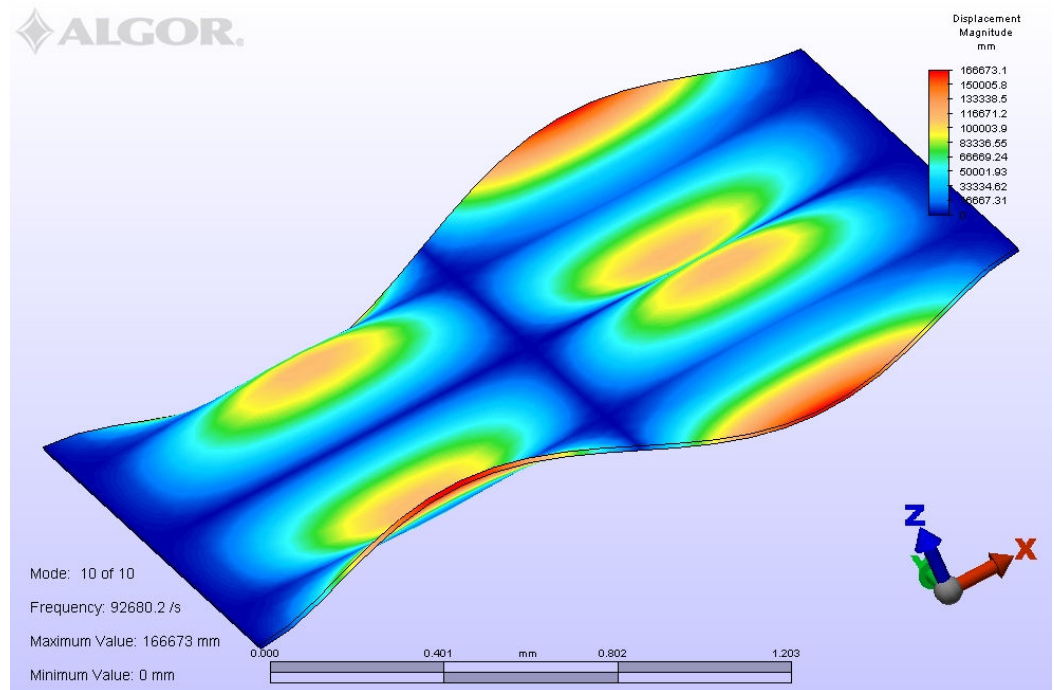


Figure 5.39: Microfabricated Sensor Array Mode 10

As in the laser machined devices, only modes 1 and 8 will lead to a signal in a capacitive electrode underneath the bridge. Table 5.3 shows the natural frequency for the fundamental mode of each device in the array as determined from FEA. These natural frequencies match well with those calculated analytically earlier.

**Table 5.3: Vibrational Frequencies for the Device Array**

Device	Resonant Frequency
Top Left	13.0 kHz
Top Middle	16.0 kHz
Top Right	20.2 kHz
Center Left	26.4 kHz
Center Middle	35.9 kHz
Center Right	51.5 kHz
Bottom Middle	80.4 kHz

From the electrical model, Table 5.4 shows the predicted capacitance, fundamental frequency, and overall sensitivity at resonance for a quality factor of 240 for each element in the array.

**Table 5.4: Electrical Model Parameters**

<b>Element</b>	<b>Fundamental Frequency</b>	<b>Capacitance (pF)</b>	<b>Overall Sensitivity</b>
One	35000	0.354	1.35
Two	40000	0.287	1.25
Three	48000	0.227	1.16
Four	56000	0.174	1.026
Five	69000	0.127	0.876
Six	90000	0.0885	0.713
Seven	120000	0.0567	0.523

The overall sensitivity is different for each sensor element in the array, and needs to be accounted for in each element during spectrum interpretation. Alternatively, the electronics gain can be adjusted to equalize overall sensitivity for each element to compensate for these differences.

### **5.6 Transducer and Electronics Considerations**

A number of considerations must be noted regarding the transducer design itself, the formation of an array of different sensors, and the design of readout electronics used to capture array output. In general, the sensor itself is a rather simple capacitive device, but when incorporated into an array, other complexities emerge. Many of these deal with the differing sensitivities of each device, the different electrical characteristics of each device when in the readout circuit, and the effect of parasitics in the array response.

Each sensor in the array is at a different position of the chip. In addition, each sensor has a different area, capacitance, and stiffness. Furthermore, the electret bias voltage under each sensor might be different based on the charging conditions and

uniformity. These factors lead to a sensor array in which the sensor output is not only different because of different natural frequencies, but also because of its basic mechanical sensitivity and spatial orientation with respect to the acoustic stress pulse. These variations in sensitivity do not hinder the array from developing a useful spectrum upon impact, but they do need to be factored into the interpretation of the spectrum. In addition, the existence of these variations leads to the requirement that each sensor element in the array needs to be calibrated. This calibration can be used to normalize the outputs of each array element and remove the variations in device performance and sensitivity.

In addition, when coupled to an array of readout amplifiers, each sensor in the array interacts differently. In particular, the capacitance of each sensor element is different, leading to a different filtering effect when connected to the high impedance of the readout amplifier. This can be either removed by calibration after fabrication, or it can be compensated for by altering the design of each amplifier to yield equivalent RC time constants and gains for each sensor in the array.

On a related note, a significant potential issue with the sensors developed in this work is the low capacitance of each individual element. In order to have a large RC time constant and to therefore see low frequency signals, the readout amplifier required high input impedance. High input impedance amplifiers are susceptible to electromagnetic noise sources. These have to be removed from the sensor array prior to spectrum interpretation.

Finally, and also related to the low capacitance of the sensor, is the effect of parasitic capacitance within the sensor array and to other structures and systems onto which the sensor is mounted. Parasitic capacitance from sensor-to-sensor, primarily from the remaining metal of the charging grid, resulted in signals from one sensor being injected into the signal processing chain of the other sensors. This adds to the overall amplitude of each sensor output and couples directly into the spectrum developed from

that sensor. This cross-talk has to be removed through either filtering, or preferably through reducing the parasitics themselves.

## CHAPTER 6 - TRANSDUCER PROCESS DEVELOPMENT

This chapter lays out the fabrication process steps and development approach related to the acoustic sensor array utilizing integrated electret biasing. The development of the sensor array began with developing processes for the polymer film deposition that would realize the final electret, as well as the processes for fabricating the microcorona charging grid and for using the charging grid to charge the electret, as were described in Chapter IV. These activities allowed the creation of charged films that could be measured. Following those activities, fabrication processes were developed to realize resonant structures suspended above the electret film and separated by an air gap. The suspended structures had to also allow placing a probe in contact with the charging grid to allow electret formation. Two types of resonant structure process flows were developed. One realized laser micromachined structures laminated with an air gap above the electret film. The second process flow realized Ni electroformed structures suspended by SU8 posts over the electret film using an SU8 release process. These fabrication processes yielded die with multiple sensor devices for additional testing and characterization.

The process flow for the transducer array started from the finished electret wafer described in Chapter IV. The electret wafer with the patterned charging grid simply continued through the rest of the fabrication processes prior to performing the charging step. Two separate transducer fabrication processes were developed. One of these built a laser micromachined array of transducers on top of the electret. The second process flow resulted in a MEMS-based micromachined sensor array on top of the electret film.

## 6.1 Laser Micromachined Transducer Array

The CYTOP and metal grid eventually form the electret within each element of the sensor die. The sensor also needs a bottom electrode, an air gap, and a suspended diaphragm connected to a top electrode. The bottom electrode and the top electrode are used to collect the current created when the sensor is excited by an acoustic wave.

The bottom electrode is simply the conductive substrate, in this case, a doped silicon wafer, on top of which the CYTOP and metal grid are fabricated. The top electrode is the same material and layer as the suspended metal diaphragm. The air gap is formed by making a cavity in the dielectric that sits on top of the CYTOP and separates the top metal from the CYTOP.

For the laser machined device, formation of the air gap and top diaphragm was performed through a simple lamination process (Figure 6.1).

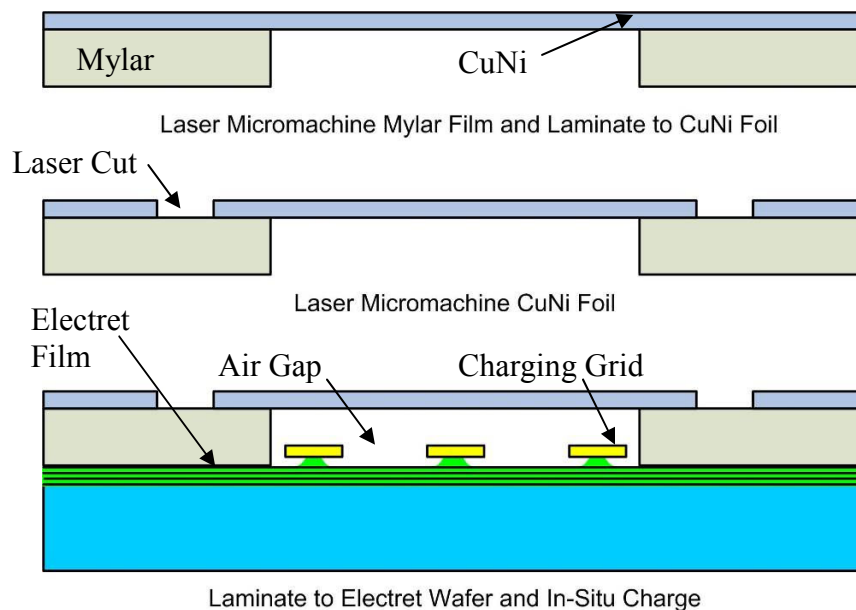


**Figure 6.1: Laser Micromachined Sensor Array Process Flow**

Mylar material of 2mil thickness, and coated on both sides with adhesive, was first laser cut to form a series of cavities (Figure 6.2). Mylar was used because of the

availability of thin sheets that are pre-coated on both sides with 10 $\mu$ m thick pressure-sensitive Densil10 adhesive [52], the ease of laser machining the material [53], and its isolative properties. These cavities defined the diameter of the suspended metal diaphragm used in the device. The diameter of the largest cavity was 2mm, with each consecutive cavity having its diameter reduced by 200 $\mu$ m. The laser was a New Hermes CO<sub>2</sub> laser with a 60W peak output, a 150 $\mu$ m beam diameter, and a wavelength of 1 $\mu$ m.

The laser-cut Mylar was then laminated at room temperature and 300kPa to 1 mil CuNi metal foil. CuNi offered ease of laser machining [53], but most importantly it is easily soldered at low temperatures. The metal foil was then laser cut to define distinct separations between the diaphragms and solder pads (Figure 6.3). The laser used was a Resonetics Impressario ND:YLF IR Laser with a peak power of 15W, a 40 $\mu$ m beam diameter, and a wavelength of 1.047 $\mu$ m.

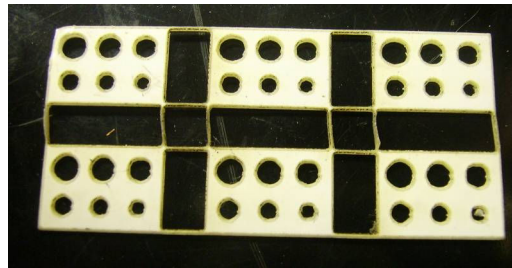


**Figure 6.2: Laser Machined Mylar Utilized to Create Circular Cavities**



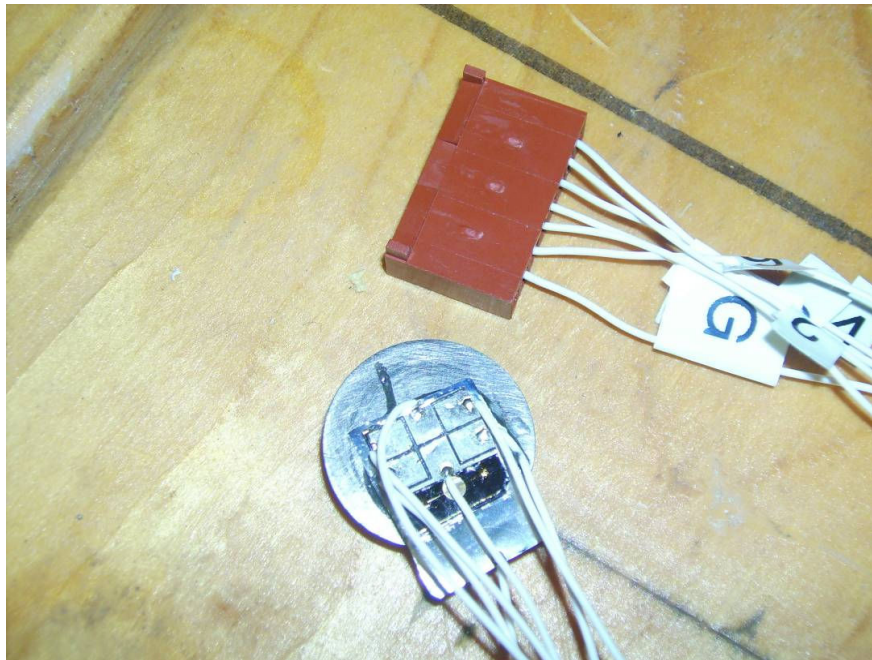
**Figure 6.3: Laser Machined Metal Diaphragms Adhered to the Mylar Surface**

Table 6.1 lists the specific process parameters for the laser cutting of the acrylic and metal.

**Table 6.1: Laser Cutting Process Parameters**

Process Step	Process Parameters
Mylar Cut	Power = 25% (15W) Speed = 50% (~10mm/s) # Passes = 4
Metal Foil Cut	Power = 20% (3W) Speed = 2mm/s # Passes = 3

After the metal foil is laminated to the Mylar, the Mylar is laminated, using the same adhesive and lamination process, to the silicon wafer onto which the CTYOP and charging grids were fabricated. The resulting completed structure could then move to the charging process.



**Figure 6.4: Laser Micromachined Transducer Array**

## 6.2 Microfabricated Transducer Array

The microfabricated version of the transducer was assembled in a SU8-based process that exploited the structural characteristics of unexposed and undeveloped SU8 film [54]. The process realized Nickel diaphragms suspended above the microcorona charging grid. The process for the Ni bridges started from a wafer with a completely fabricated CYTOP film and suspended microgrid wafer. The process flow is shown in Figure 6.5.

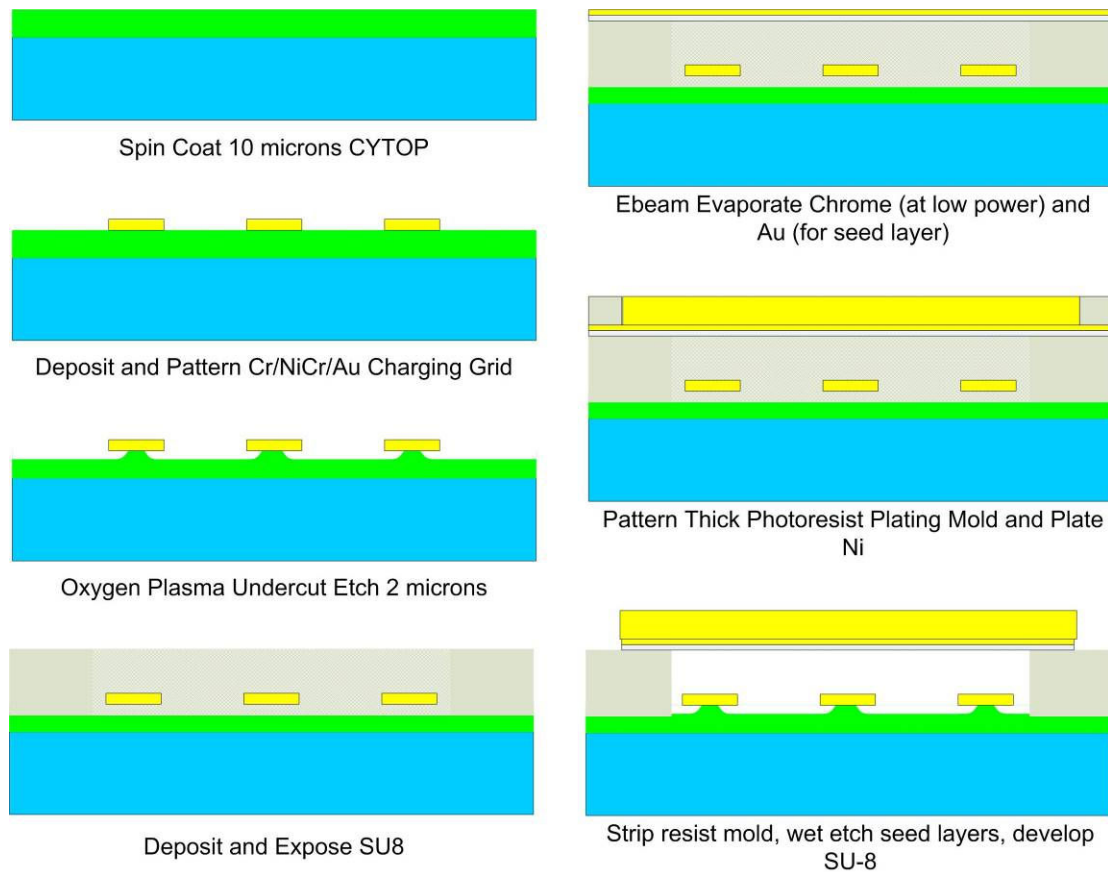


**Figure 6.5: SU8-Based Microfabrication Process for Electret Transducer Array**

The specific process steps for the SU8 spin coat are listed in Table 6.2. A key aspect of the coating process is the use of a vacuum oven to remove air bubbles within

the film prior to exposure and further baking steps. These bubbles would form along the metal edges of the charging grid, and were more prevalent on the square mesh version of the grid. The line-based grid was less susceptible to bubble formation.

**Table 6.2: SU8 Coating Process**

<b>Process Step</b>	<b>Process Parameters</b>
Adhesion Promoter	Cover wafer with VM652 adhesion promoter.
Spin Promoter	30 second puddle with 30 spin at 3000 rpm.
Bake	2 minute bake at 95 degrees C.
Cooldown	Let wafer cool for 1 minute.
Apply SU8	Puddle SU8 in the middle of the wafer.
Spin SU8	500 rpm spread for 30 seconds with 3000 rpm spin for 60 seconds.
Remove Bubbles	Place wafer in vacuum oven with no heat for 2 minutes.
Softbake	Place wafer on hotplate for 5 minutes at 65 degrees C.
Softbake (cont.)	Place wafer on hotplate for 30 minutes at 95 degrees C.
Cooldown	Remove wafer from hotplate and let rest for 1 hr.
Metrology	Measure the thickness of wafer and subtract the baseline reference for thickness of SU8.

The specific process steps for the exposure of the SU8 are listed in Table 6.3. A critical part of the process is the atypical long post-exposure bake. This step is important, however, in densifying the film enough that it survives further processing without reflow or bubbling.

**Table 6.3: SU8 Exposure Process**

<b>Process Step</b>	<b>Process Parameters</b>
Calibrate Light Source	Bulb Intensity = 8.28 mJ/cm <sup>2</sup>
Doe	30 seconds total exposure time.
Expose	Split the exposure time into 4 cycles and expose pattern. (7.5 seconds per cycle.)
Softbake	Set wafer on hotplate for 5 minutes at 65 degrees C.
Visual Inspection	Within a few minutes the pattern should be visible which indicates a good exposure dosage.
Long Post-Exposure Bake	Set wafer on hotplate for 12 hours at 100 degrees C. (This is the long post exposure bake)

After the SU8 deposition and exposure, the undeveloped film is left in place as further processing is performed. Table 6.4 lists the steps in depositing metal on the undeveloped SU8. The Chrome (Cr) deposition is a critical step. Previous work [54] demonstrated that filament evaporated Cr could be safely deposited on unexposed SU8 without exposing it. This was due to the low temperature sublimation and minimal radiation output of the filament evaporation process with Cr in particular. The work presented in this thesis showed that ebeam evaporated Cr could also be used, as long as the deposition rate, and hence ebeam power, was kept low. However, a skin did form on the SU8 surface that took extra processing to remove. A gold layer was then deposited on the chrome. The gold layer serves as the seed layer for electroless Ni plating to create the metal structures.

**Table 6.4: Barrier and Seed Layer Deposition Steps**

Process Step	Process Parameters
Chrome Barrier Layer Deposition	Chromium deposit at 1.0 angstrom per second for 250 angstrom.
Gold Seed Layer Deposition	Gold deposit at 1.0 angstrom per second for 250 angstrom
Cooldown	Let wafer cool for 1 hour

The long post exposure bake was critical to maintaining structural integrity during the metallization processes. Without sufficient baking, the SU8 would reflow and bubble. Figure 6.6 shows how the metallization should look. The image clearly shows the unexposed SU8 pattern with a smooth layer of metallization. The pattern is visible because the unexposed SU8 reflows slightly, leading to a slightly curved top surface.



**Figure 6.6: Image of Successful Metallization**

A critical step in this fabrication flow turned out to be a long post-exposure bake of the SU8 prior to ebeam evaporation of the Cr barrier metal. Without this long bake, of approximately 12 hours, the uncrosslinked SU8 can have a tendency to reflow. This leads to high levels of curvature, and even bubble formation, in the uncrosslinked SU8 regions as shown in Figure 6.7.

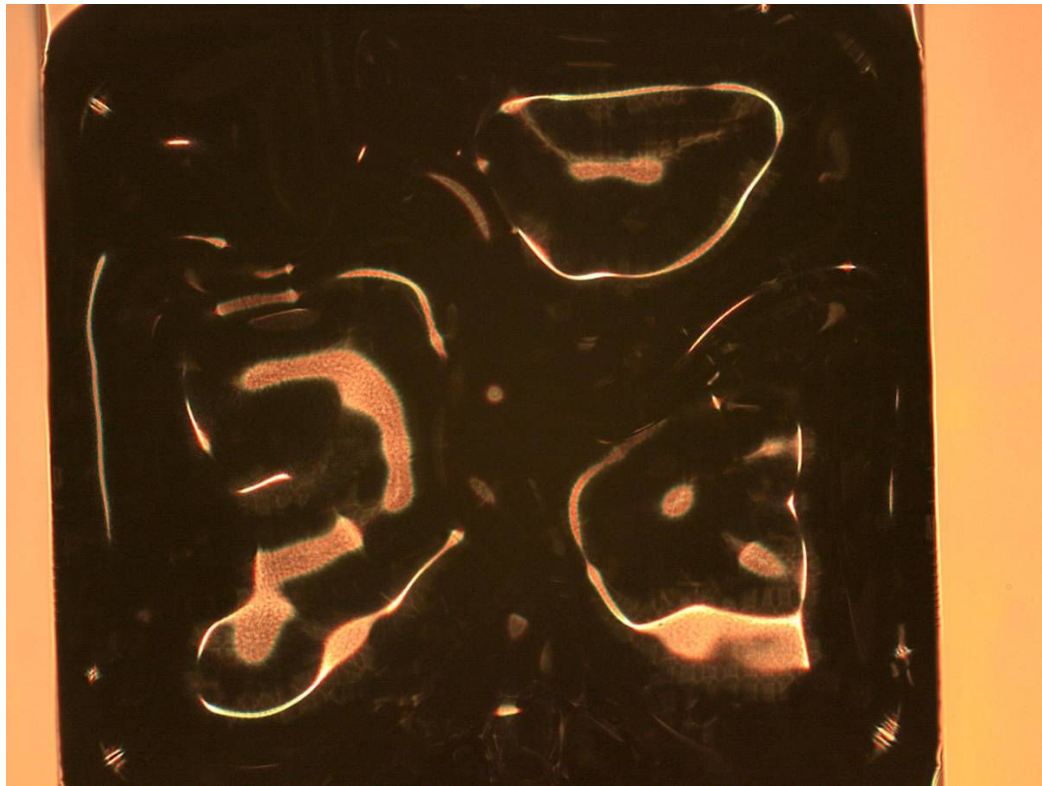


**Figure 6.7: Image of Unsuccessful Metallization Following Insufficient Post-Exposure Bake and SU8 Reflow**

After the deposition of the seed metallization layer, a thick photoresist electroplating mold is deposited and patterned. Table 6.5 lists the process flow for creation of the electroplating mold.

**Table 6.5: Thick Photoresist Mold Formation**

<b>Process Step</b>	<b>Process Parameters</b>
Deposit Resist	Puddle SPR220 in the middle of the wafer for first layer.
Spin Resist	2000 rpm spin for 30 seconds.
Softbake	Place wafer on hotplate for 5 minutes for a direct contact bake at 95 degrees C.
Exposure	Expose pattern for 30 cycles at 10 seconds per cycle.
Develop	Develop wafer in MF319 developer for 5 minutes.
Rinse	Place wafer in DI water for 1 minute.
Develop	Develop wafer in fresh MF319 developer until clear. (an additional 2 to 3 minutes.)
Hard Bake	Hard bake the wafer at 95 degrees for 30 minutes
Descum	O <sub>2</sub> descum the wafer at 300 watts for 2 minutes with 12.5 sccm of Oxygen.

The thick photoresist mold covers areas where Electroless Ni plating is not desired, including the diaphragm structures, holes within the structures, contact pads, and on-chip wiring. After forming the resist mold, Electroless Ni plating [49] fills the areas in with a 12 micron thick Nickel layer. The process is listed in Table 6.6.

**Table 6.6: Electroless Ni Plating Process**

<b>Process Step</b>	<b>Process Parameters</b>
Plating Bath	Electroless Ni bath at 90 degrees C [49]
Strike	Place steel rod on open seed layer area to initiate reaction
Plate	Plate for 30 minutes (approximately 12.5 microns of Ni)
Rinse	Remove from bath and place in 90 degree C water rinse
Cooldown	Remove and let cool for 1 hour

Figure 6.8 and Figure 6.9 show a typical electroless Ni plated structure. The surface was slightly pitted, most likely due to dilution of the bath towards the end of the plating process.

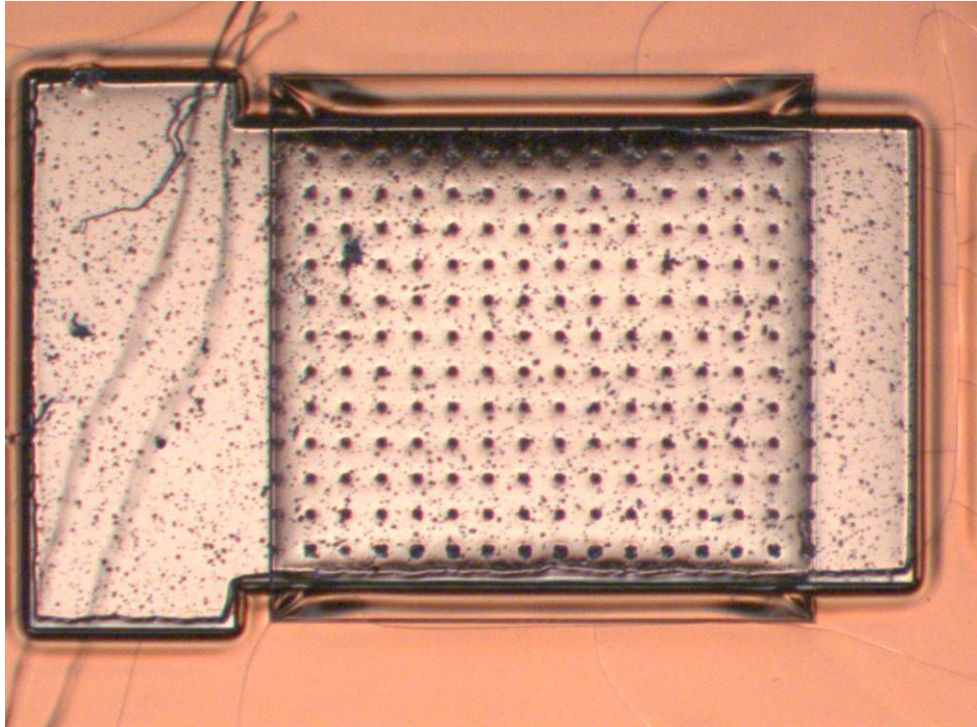


**Figure 6.8: Electroless Ni Plated Structure**

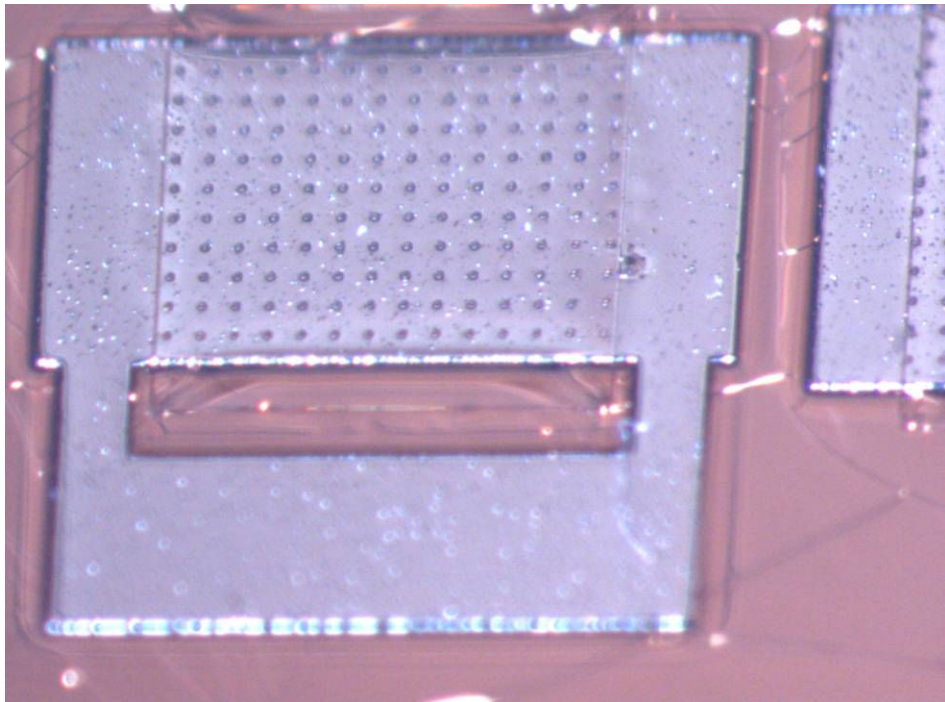


**Figure 6.9: Stereoscope Image of Plated Structure**

The electroless plating process did not completely fill the mold in some areas, as shown in Figure 6.10. This incomplete fill was most likely due to organic material that was not completely cleaned from the seed layer surface or to a remaining hydrophobic nature to the resist mold sidewalls.

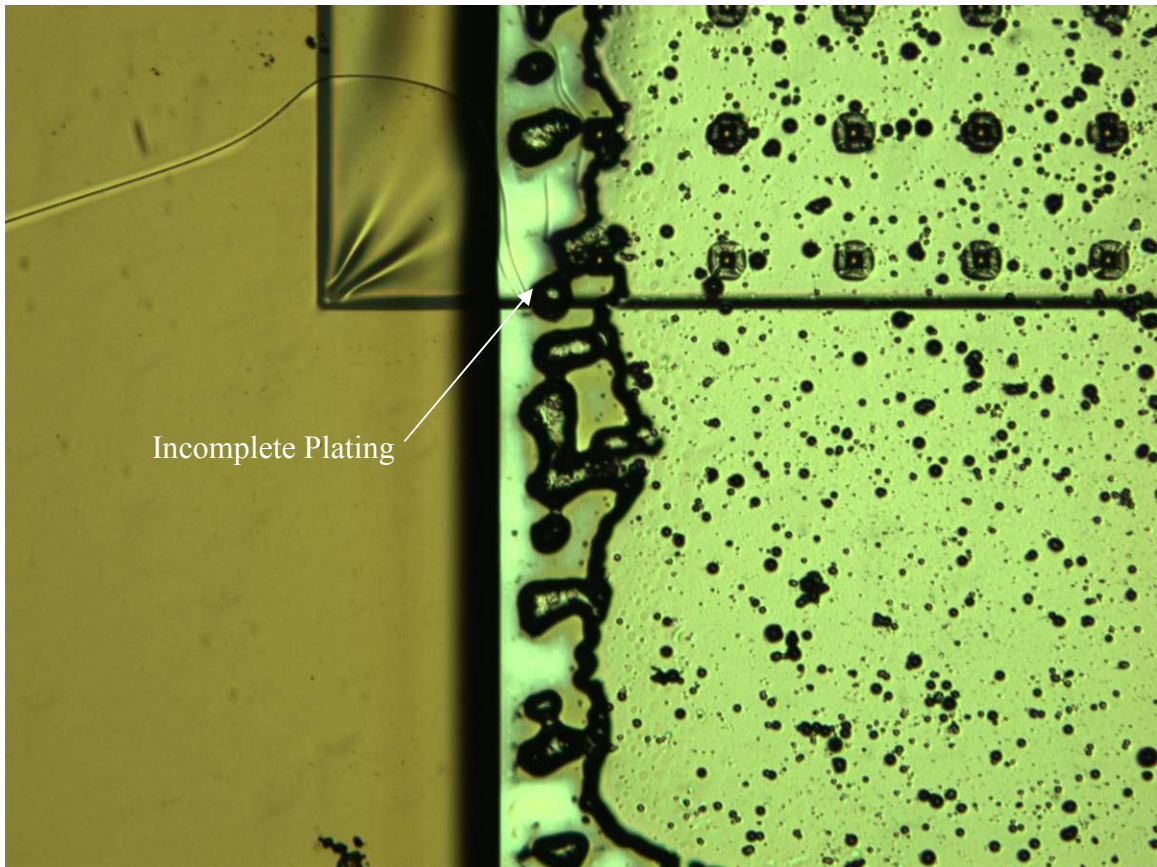


**Figure 6.10: Incomplete Fill of Electroless Plating Mold**

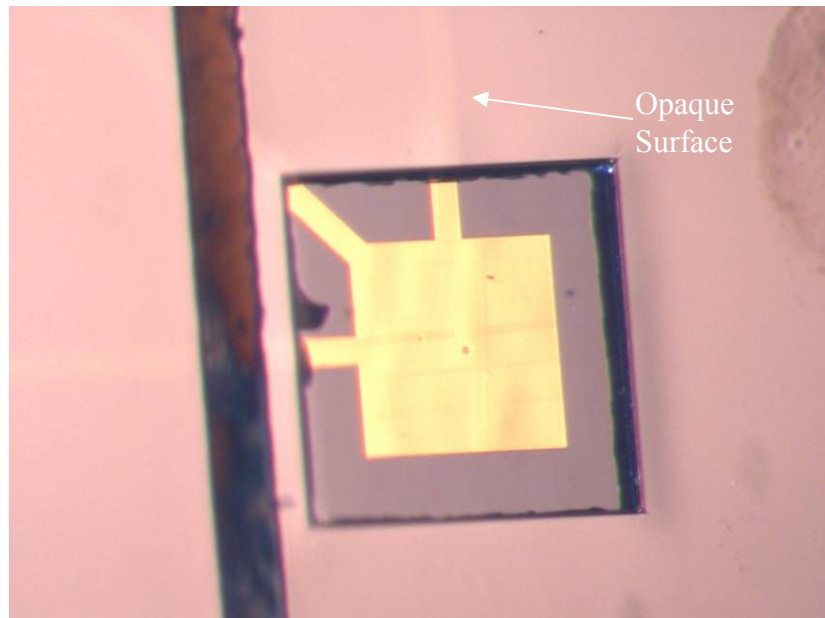
Following the electroless plating, the wafer is coated with resist and diced. Further processing, including device release, was performed at the die level. It could also be performed at the wafer level by keeping the separated die on the release tape. This was convenient because dicing was performed on robust unreleased die, making dicing yield very high. After dicing, a series of strip and develop processes were used to remove the

thick resist mold, break through and unexpected skin formed on the SU8, and develop the unexposed SU8. Table 6.7 lists the process steps.

**Table 6.7: Dice and Release Process**

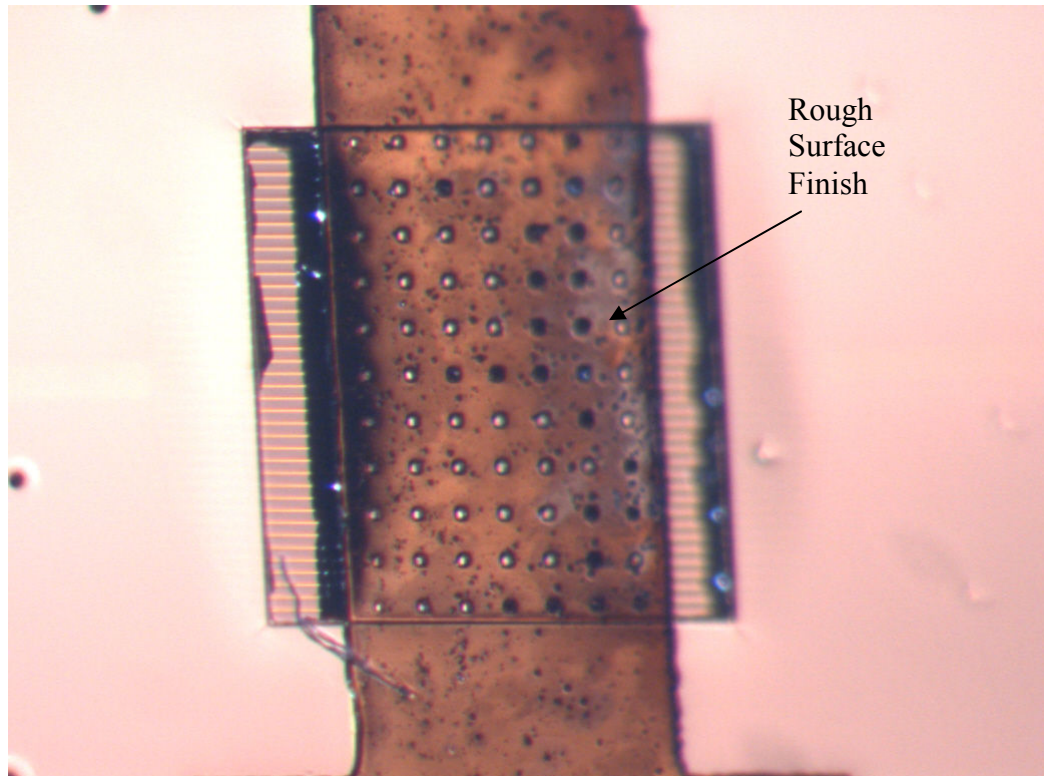
Process Step	Process Parameters
Encapsulation	Resist Coat
Dice	
Resist Strip	Acetone
Gold Etch	Transene TFA for 2 minutes
Cr Etch	Transene Cr TFD for 2 minutes
Acetone	1 minute Acetone soak in ultrasonic bath to break up skin
SU8 Develop	Developer in ultrasonic bath for 15 minutes
Rinse	IPA

Figure 6.11 shows a stereoscope image of a completely opened access hole through the SU8 to the metallization layer on which the electret charging grid resides. This hole provides access to place the corona voltage onto the microcorona grid.



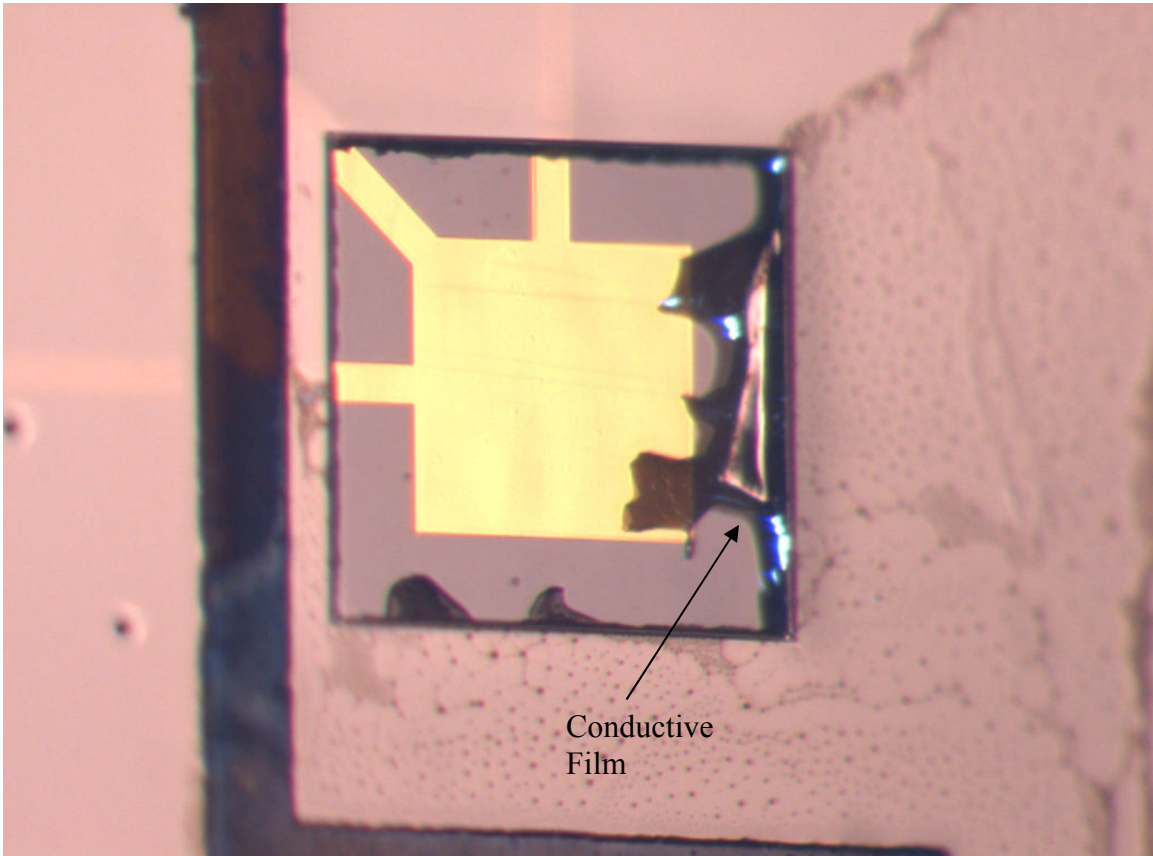
**Figure 6.11: Opened Contact Pad for the Charging Grid**

Figure 6.12 shows a stereoscope image of a suspended Nickel structure above the microcorona charging grid. The surface finish of the Ni was affected by the Cr seed layer etch, since that etchant also slightly attacks Ni. In future process flows, a different etchant may be selected.



**Figure 6.12: Fully Released Ni Structure Suspended Above Charging Grid**

Figure 6.13 shows the primary issue with the process flow. A very thin skin formed on the top surface of the unexposed regions of SU8. That skin may be a very thin layer of thermally crosslinked SU8 material formed during the ebeam metallization of the Cr barrier layer, or it may have been crosslinked from x-ray or UV radiation that did not penetrate deeply into the SU8. Agitation in the ultrasonic bath during the Acetone and Developer steps broke this film up and removed it by mechanical agitation. This is an area to be improved in future process steps, as it is unlikely that the film was removed from the release holes in the metal structure.



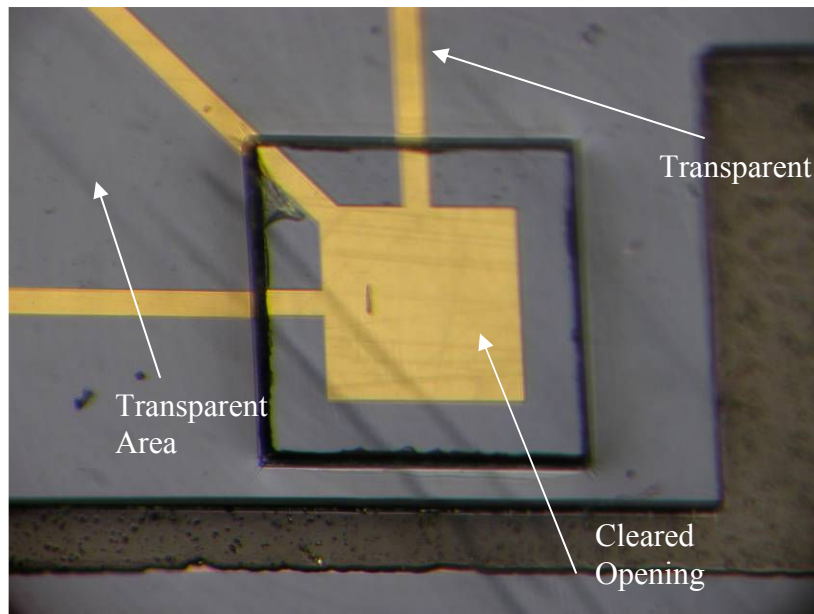
**Figure 6.13: Stereomicroscope Image of Remaining “Skin”**

After measuring surface resistivity, it was determined that at least part of this skin is conductive and consists of Cr that was not removed during the Cr etch steps. This also contributed to an abnormally difficult development process for the unexposed SU8. As such, a number of additional Cr etch recipes and processes were performed to try to remove the film. The only successful process used diluted HCl and a short touch of the Cr surface to Aluminum during the etching step. This short touch allowed a transfer of charge between the materials and initiation of Cr removal. After this process, the surface of the chip was no longer conductive. Table 6.8 lists the detailed process.

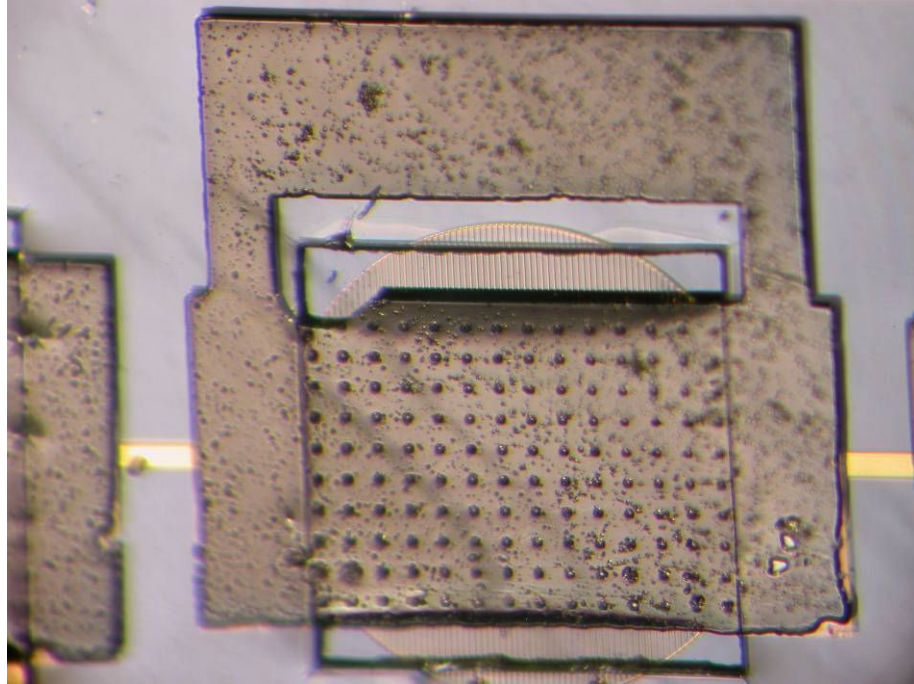
**Table 6.8: Revised Cr Etch Process**

Process Step	Process Parameters
<b>Cr etch</b>	<b>3 Minutes Total</b>
Solution	3:1 HCl: DI H <sub>2</sub> O
Immersion	Immerse die in etching solution
Initiation	Use aluminum foil to touch surface of die until the solution reacts with aluminum foil (after ~15 seconds the solution will start bubbling/fizzing aggressively)
	Remove aluminum foil
Soak	Let etch until solution is clear
Second Initiation	Touch surface with foil again until reaction
	Remove aluminum foil
Soak	At this point let the etch complete, will be able to see visual change of SU8 transparency on surface

After incorporation of the new Cr etch process, subsequent released die showed dramatic improvement in SU8 development including clearing out and release of the contact pads and diaphragms. The improved devices are shown in Figure 6.14 and Figure 6.15.

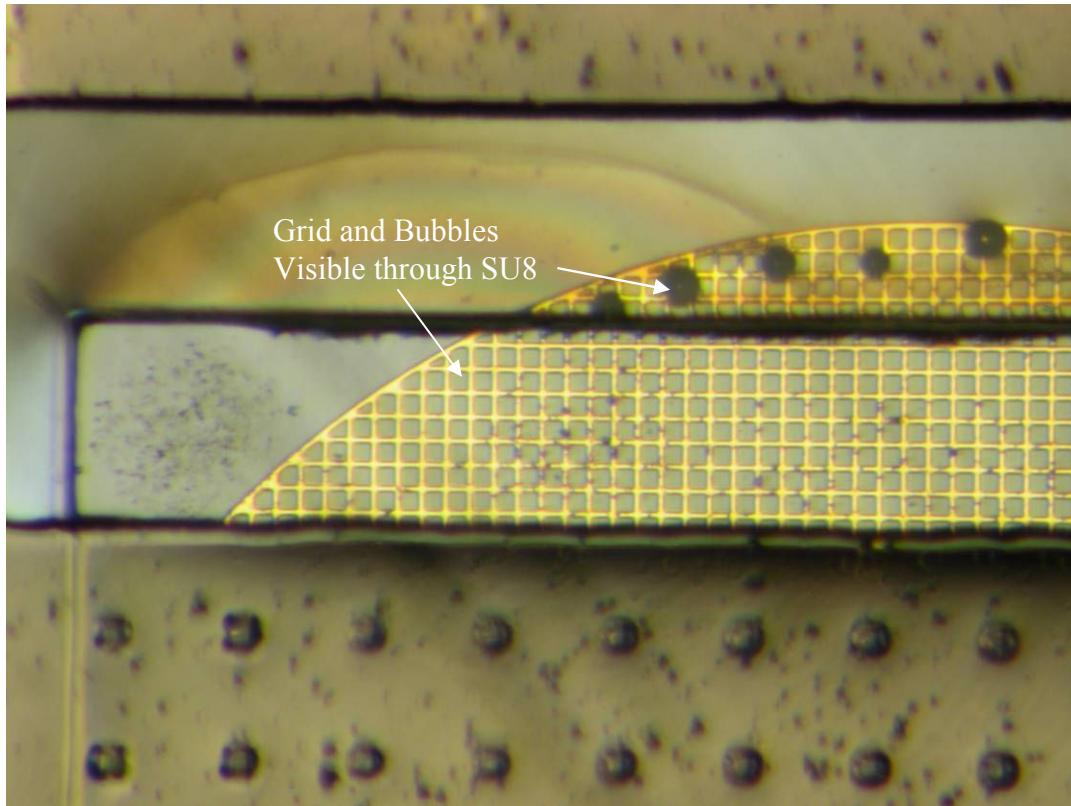


**Figure 6.14: Contact Pad Opening After Improved Cr Etch Process**



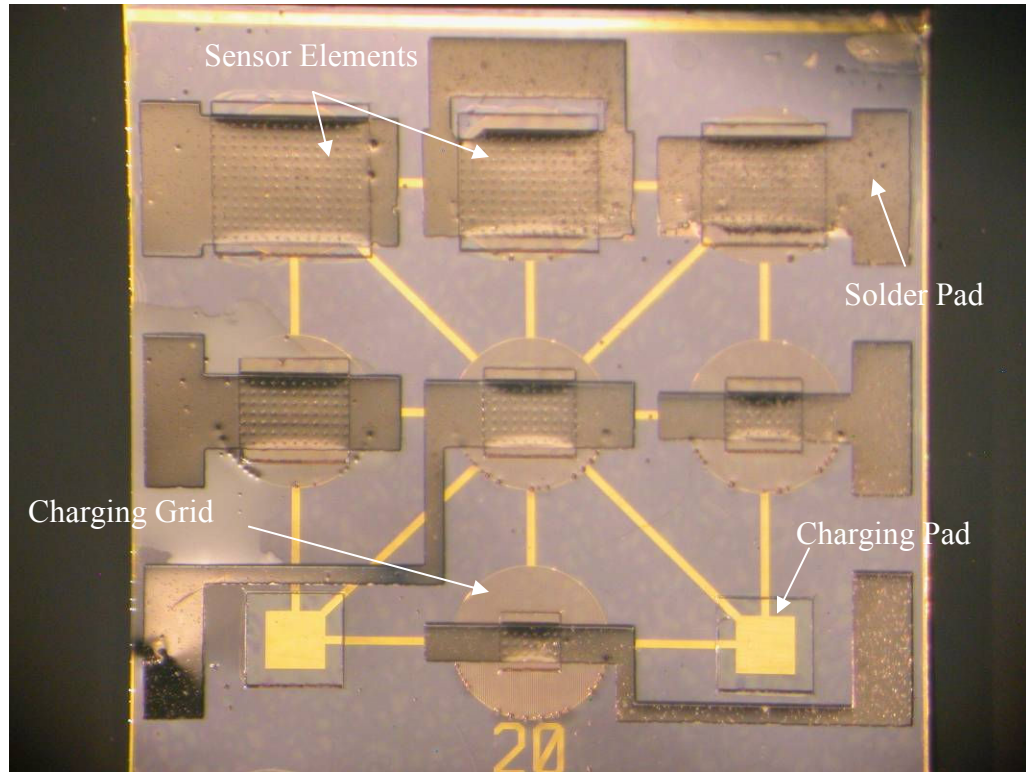
**Figure 6.15: Released Structure After Improved Cr Etch Process**

Figure 6.16 shows the charging grid as seen through the space between the structure and the edge of the air gap. It is also possible to see the grid through the clear SU8, as well as the bubbles formed in the grid region.



**Figure 6.16: Charging Grid Seen through Air Gap and the Clear SU8**

Figure 6.17 shows the entire device after fabrication and prior to soldering and assembly.



**Figure 6.17: Full Released Device**

Figure 6.18 shows an SEM of the edge portion of one of the mechanical structures. In the SEM, it is clear to see the curvature at the edge of the device that is due to shrinkage of the SU8 during processing, as well as internal stresses within the Ni film. This leads to a different natural frequency than as designed. In addition, one can also see the leftover SU8 film underneath the metal structure. Furthermore, one can see the charging grid underneath the air gap.

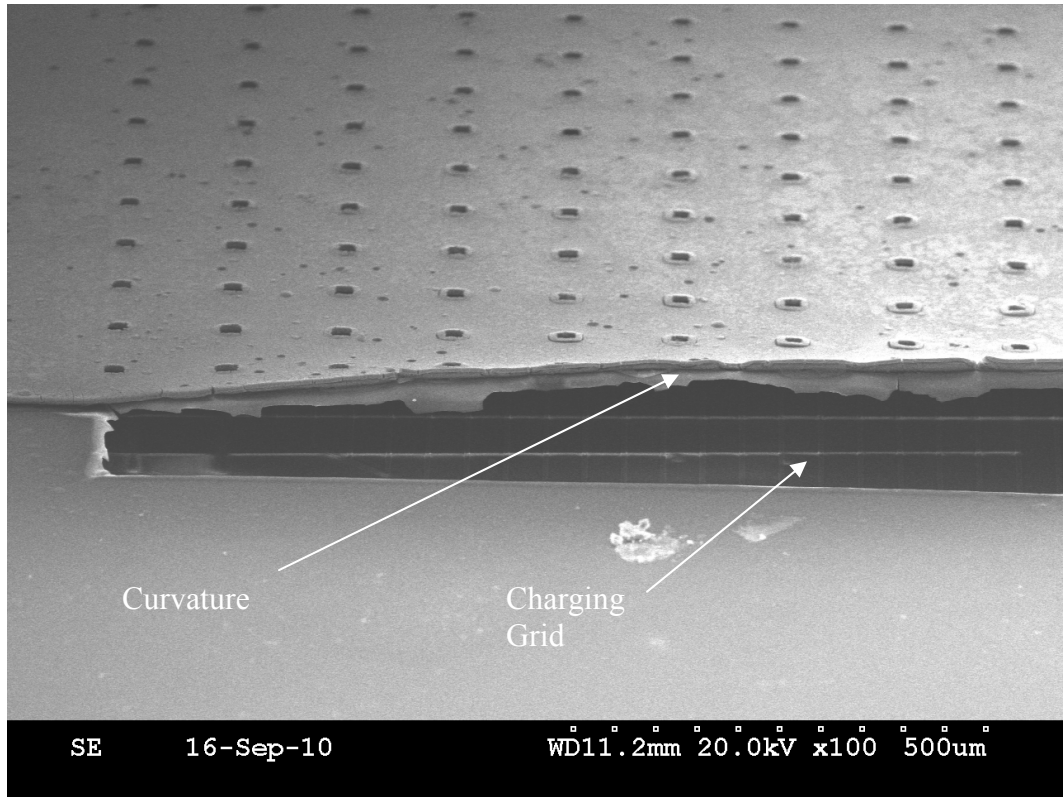


Figure 6.18: SEM of the Edge of a Released Structure

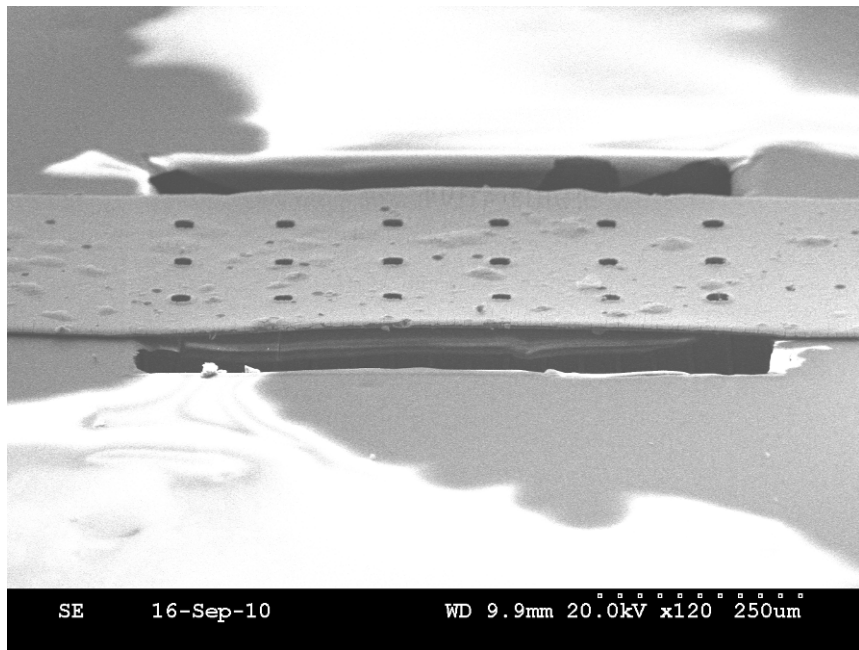


Figure 6.19: SEM of Final Smallest Structure

### 6.3 Transducer Assembly Process

After a die is fabricated, it still needs to undergo a wiring process to attach conductors to the pads, and then an assembly process to mount it to a back electrode and to test structures.

The first step was assembly of the sensor die to a back electrode. The silicon substrate in the devices was utilized as the bottom electrode for the transducer structure. However, the back surface of the silicon is difficult to connect to with an electrical conductor. Therefore, the chip was assembled to a CuNi foil. This was accomplished using LORD MD-200 Conductive Adhesive cured at 150°C for 30 minutes. This provided a reliable, rigid, and low resistivity connection to the silicon substrate. Wires could also be easily soldered to the CuNi foil, allowing connection to the back electrode.

Wires were then soldered to the solder pads patterned on the electroless Ni structural surface. This was challenging in that the pads were small and the Ni required a flux for adequate soldering. The flux used was a liquid flux specified for soldering to Ni. This same flux was used when soldering to the CuNi back electrode. Care had to be taken when placing the flux onto the pads. Only a small amount was required. If too much flux was placed on the pad, it had a tendency to flow underneath the structure. In addition, when the soldering iron was placed on the pad, an excessive amount of flux would lead to bubbling and spreading of that flux into the structures. Flux on the structures reduced the quality factor, making the resonance behavior less significant in the transducer response. Excessive flux also led to additional cross-talk between the sensor elements. Figure 6.20 shows a final wired device.

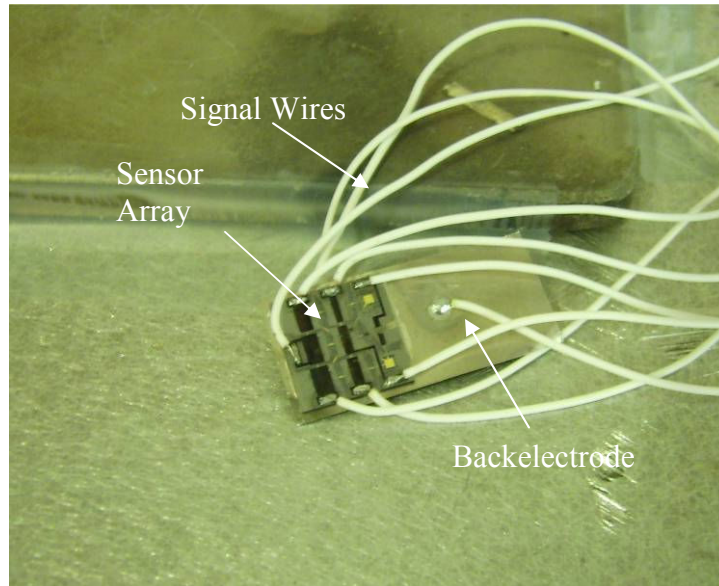


**Figure 6.20: Wired Sensor Array**

After wiring the sensors to a connector that would allow simple connection of the array to the readout circuitry, the sensor was placed in the electret charging apparatus. A spring-loaded probe was set on the charging contact pad and the high-voltage power supply switched on. The charging current was monitored during the process. The voltage was held on the pad for a total of 30 seconds for each device.

After charging, the devices were mounted to test structures. Mounting was accomplished using 5 Minute Epoxy at room temperature cure. This epoxy provided a rigid mounting, as well as a short working time. Samples were allowed to cure for over 12 hours prior to impact tests. In the mounting steps, care had to be taken that the epoxy adequately filled the entire interface between the sensor die and the structure. In addition, care was taken to ensure that epoxy did not flow over the sidewall of the device and interfere with sensor element operation. Figure 6.21 shows both a laser machined and a microfabricated sensor mounted to a large aluminum plate.

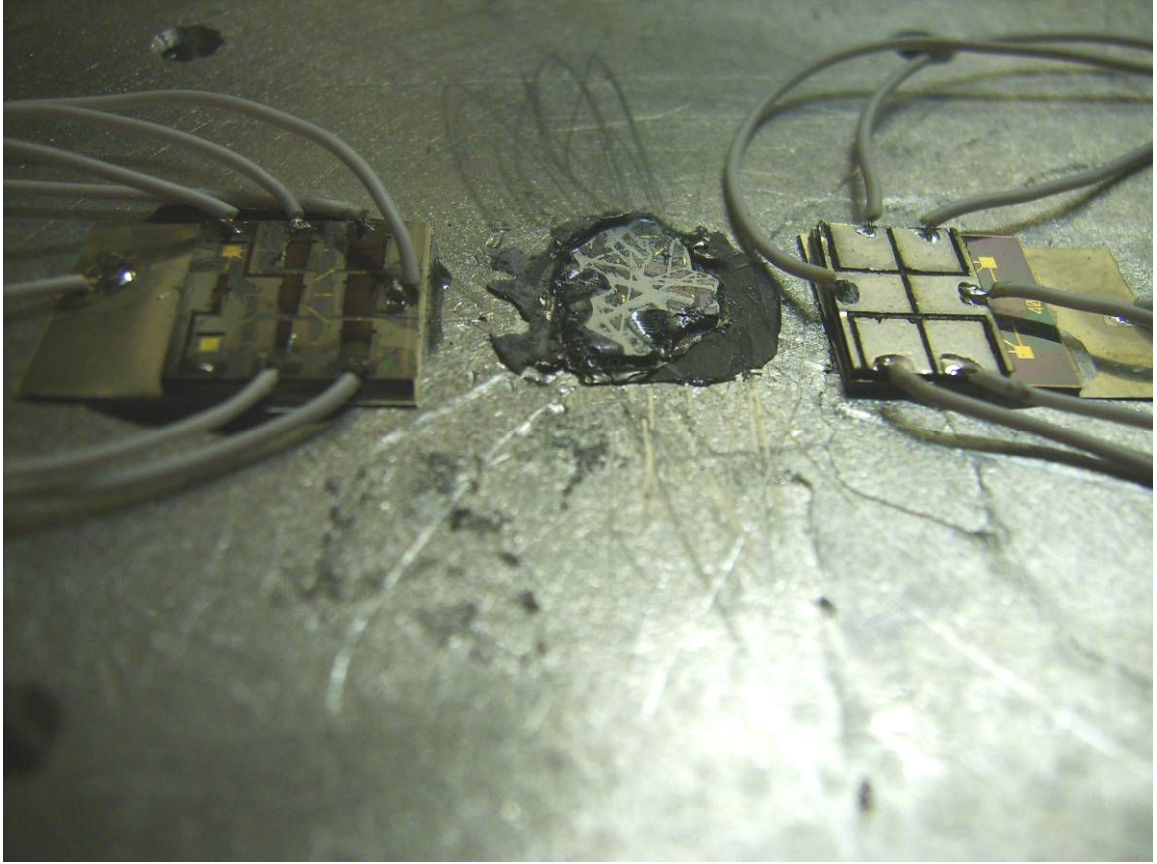


**Figure 6.21: Sensors Mounted on Large Aluminum Plate**

# CHAPTER 7 - SENSOR CHARACTERIZATION AND IMPACT TESTS

This chapter presents the results of acoustic sensor array development utilizing integrated electret biasing, and testing of the devices in impact scenarios. Transducer output waveforms are presented for a variety of impact and acoustic signal sources, including the ball drop and hammer drop. A variety of transducers, including the single laser machined transducers, the array of laser micromachined transducers, and the microfabricated transducer arrays, were subjected to these tests. Furthermore, sensors were driven by a PZT actuator to measure the frequency response of each sensor element.

## 7.1 Transducer Characterization and Frequency Scans

After fabrication, transducers were characterized using a variety of techniques that included visual, mechanical, and electrical tests.

Visual tests were performed first. These included simple inspections under a microscope to verify removal of SU8 around the contact pads and near the structure. In addition, optical inspection was used to determine whether or not film residue remained on the surface. Following inspection, devices were put under a probation to mechanically verify that the structures were released. In addition, structures were mechanically pushed and deflection observed.

Electrical tests were then performed to inspect various portions of the device. The resistance was measured across the surface of the SU-8 to verify skin removal. A thin conductive film often remained on devices. That film impaired operation and had to be removed or scratched away. In addition, the conductivity between the charging grid and substrate was measured to ensure that no short circuits existed that would impair the ability of the device to charge. Finally, the conductivity and capacitance were measured

between the transducer element and the substrate to verify that no short circuit existed there.

After visual inspection, multiple die were subjected to a mechanical actuation test to measure the natural frequencies of the structures. Transducer arrays were wired and connected to the readout circuit. On the back of the array, on the other side of the substrate, a large PZT disc transducer was bonded. This transducer had both a bottom and a top electrode. The electrodes were connected to a drive circuit that could sweep the drive frequency of the PZT transducer. Figure 7.1 shows the configuration of devices within this test.

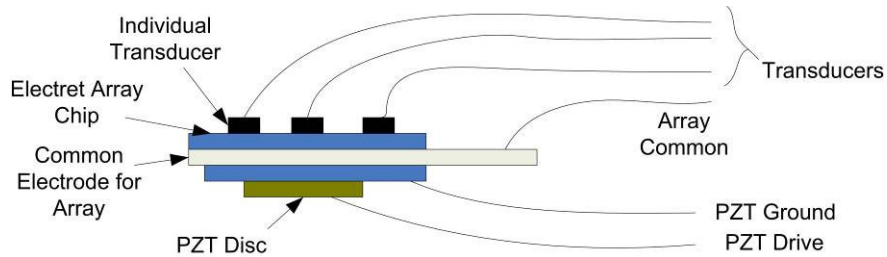


**Figure 7.1: Frequency Characterization Test**

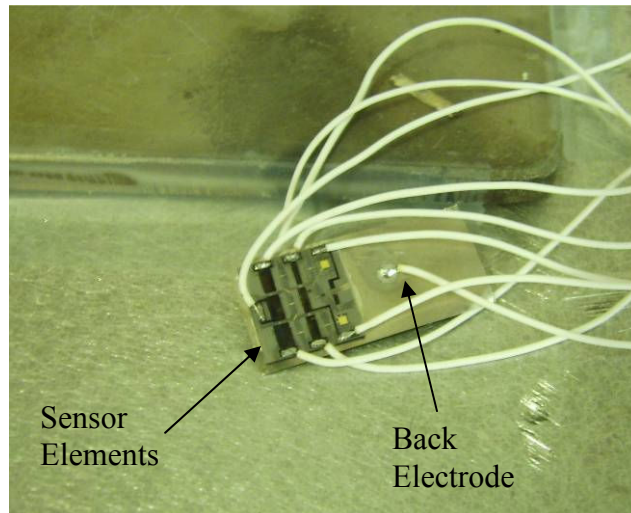


**Figure 7.2: Microfabricated Array on PZT Driver**

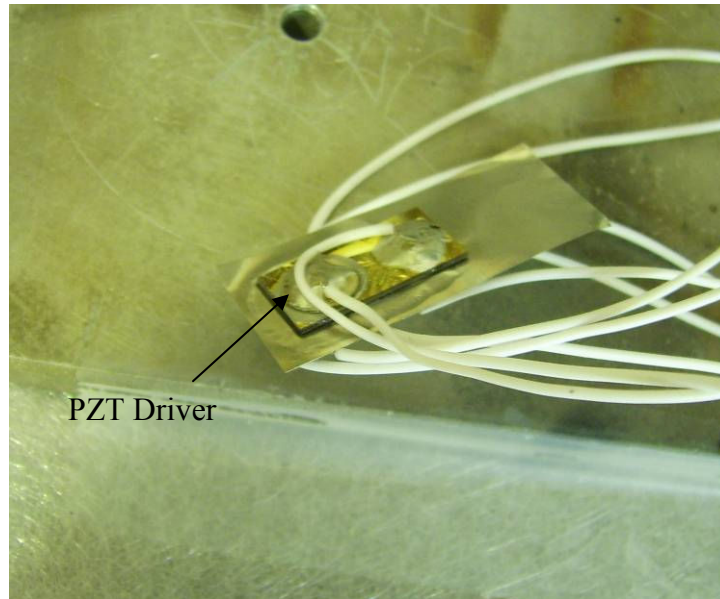


**Figure 7.3: PZT Driver**

After assembling test articles, the output of the transducer elements was captured on an oscilloscope while a function generator swept the frequency of drive voltage on the PZT disc. The PZT disc created acoustic waves that excited the electret transducers, leading to a signal generated and captured by the oscilloscope. When nearing resonant modes of the transducers, the output from the device showed amplitude peaks that were recorded. The disc was swept in frequency from 10 kHz to 100 kHz and the sensor output measured. Figure 7.4 shows the amplitude output from the largest and lowest frequency transducer during the sweep.

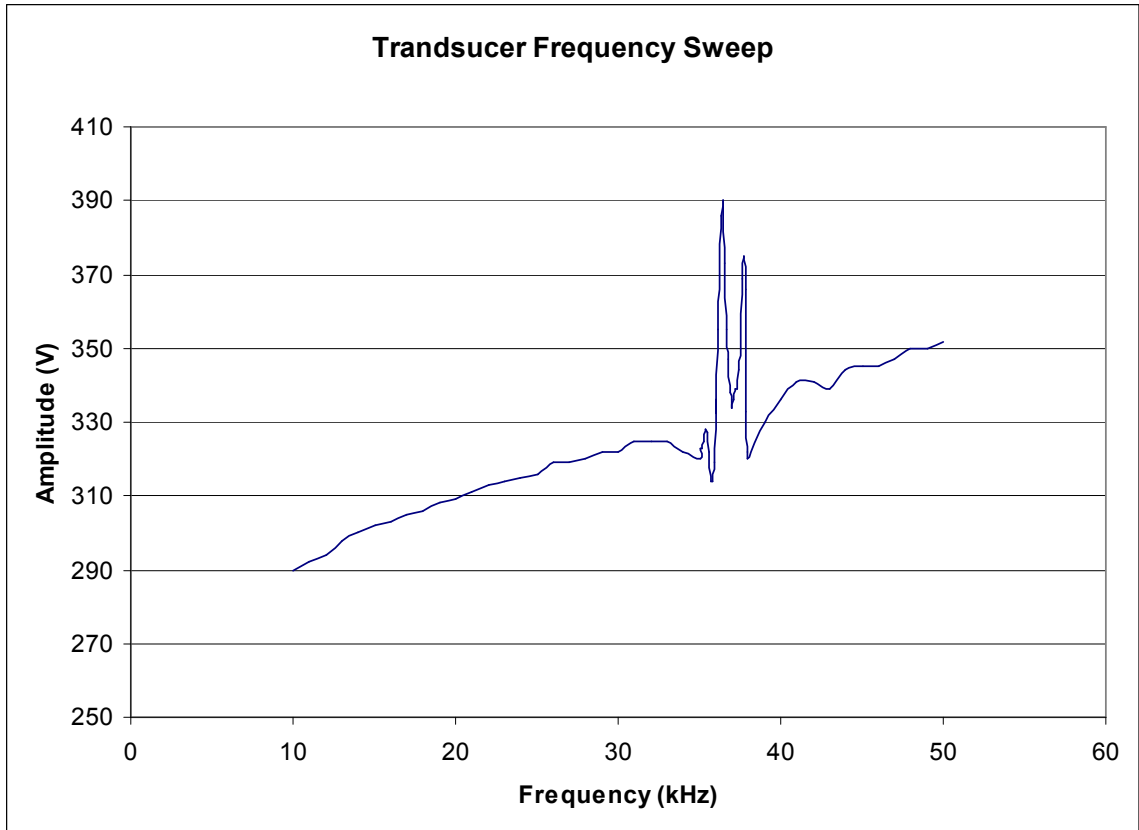


**Figure 7.4: Acoustic Frequency Sweep of Lowest Frequency Device**

This frequency sweep showed a first natural frequency at approximately 36 kHz and another at about 38 kHz. There was also a nonlinear resonance behavior evident in that the frequency sweep showed a discrete jump when increasing frequency that was at a different location than when decreasing frequency. In addition, it appeared that other frequencies were interfering with the test. Therefore, an improved test apparatus (Figure 7.5) was assembled that utilized coupling oil to hold the sensor down to a large Teflon block, and a larger piezoelectric sheet with higher piezoelectric constant to drive the sensor.

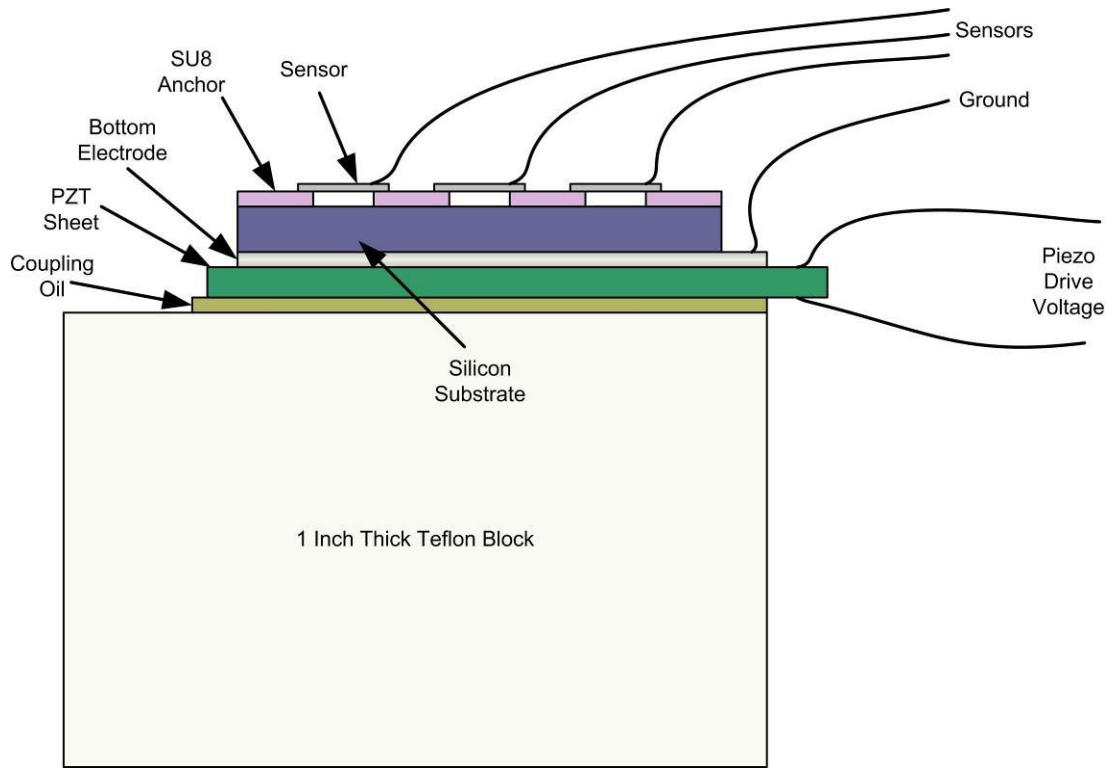


**Figure 7.5: Improved Frequency Scan Apparatus**

Figure 7.6 through Figure 7.12 show the frequency responses of the sensors.

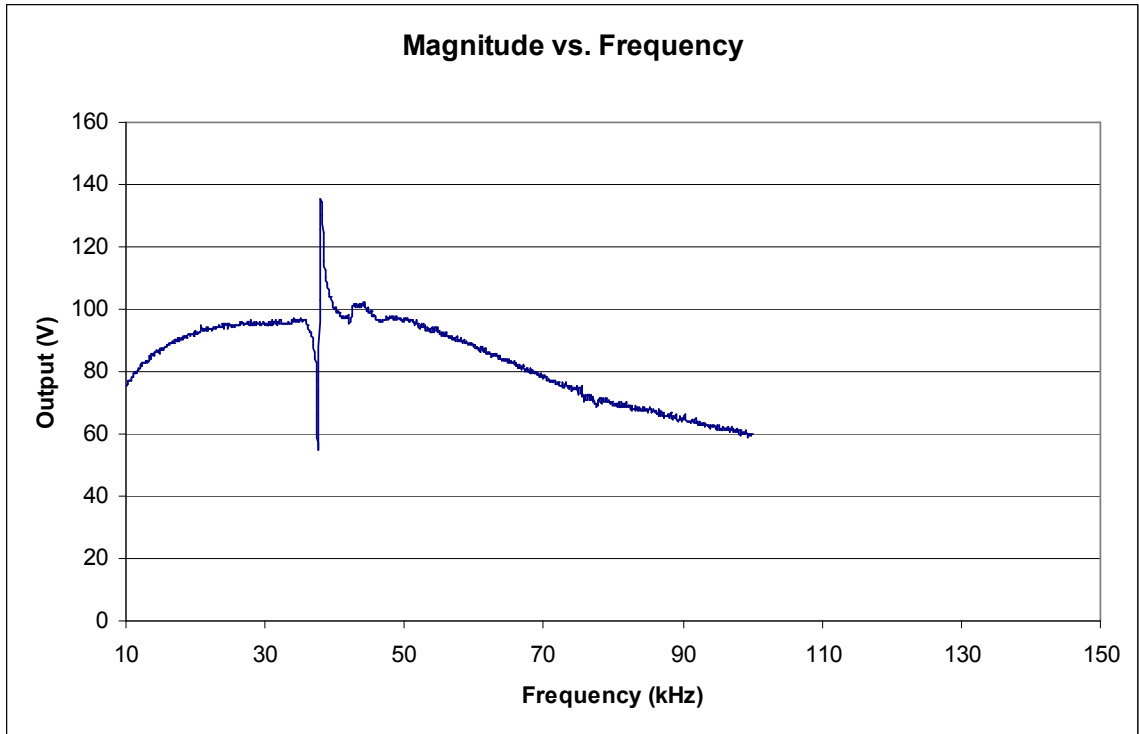


**Figure 7.6: Frequency Response Sensor One**

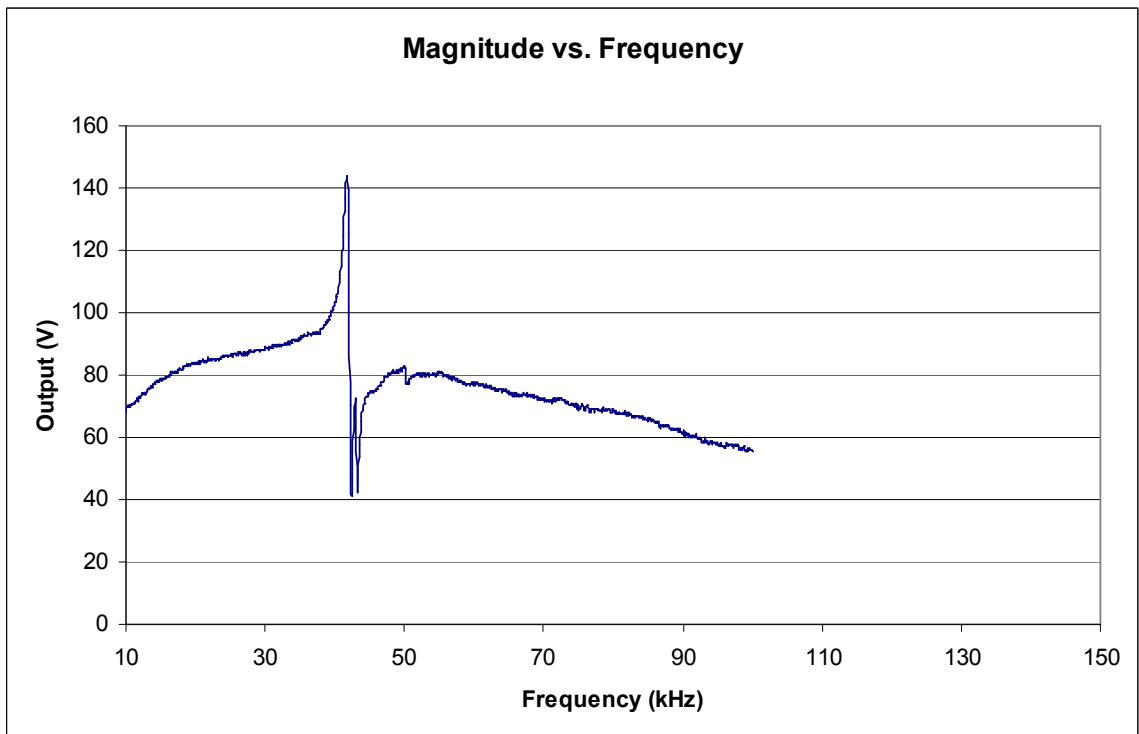


**Figure 7.7: Frequency Response Sensor Two**

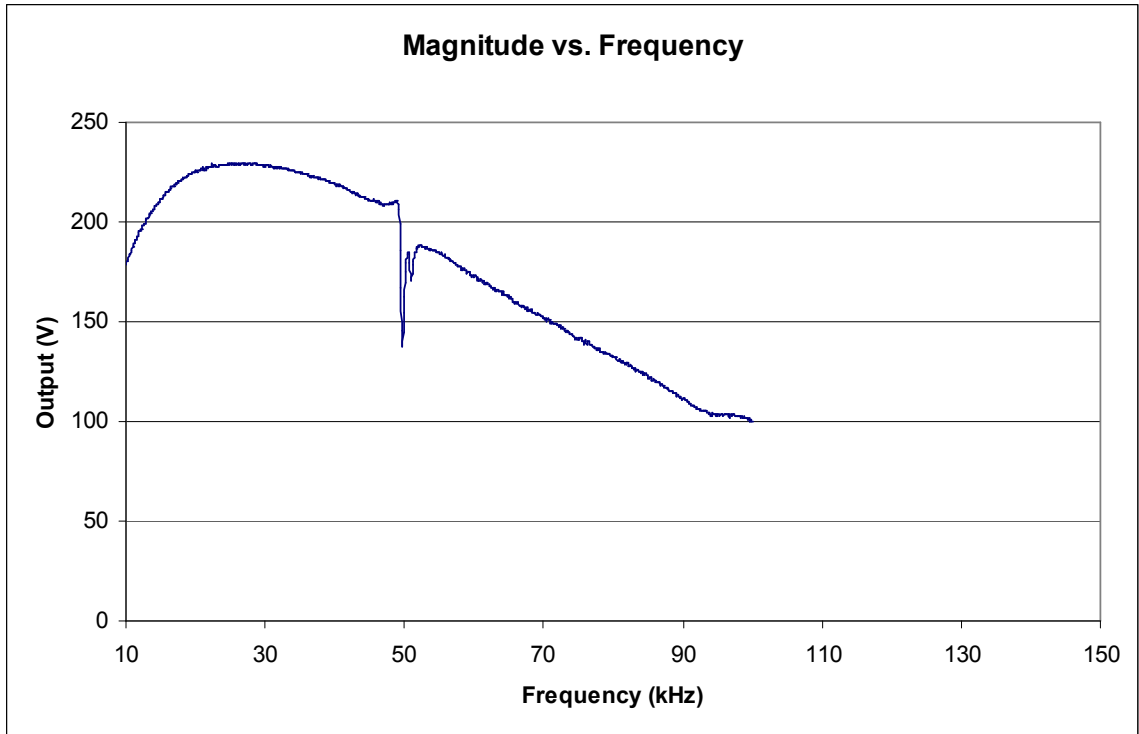


**Figure 7.8: Frequency Response Sensor Three**

The scan for sensor four on this particular device showed a double peak. It was determined from optical inspection that that particular sensor element was actually broken. It had a fracture part way across the width of the clamped-clamped beam.

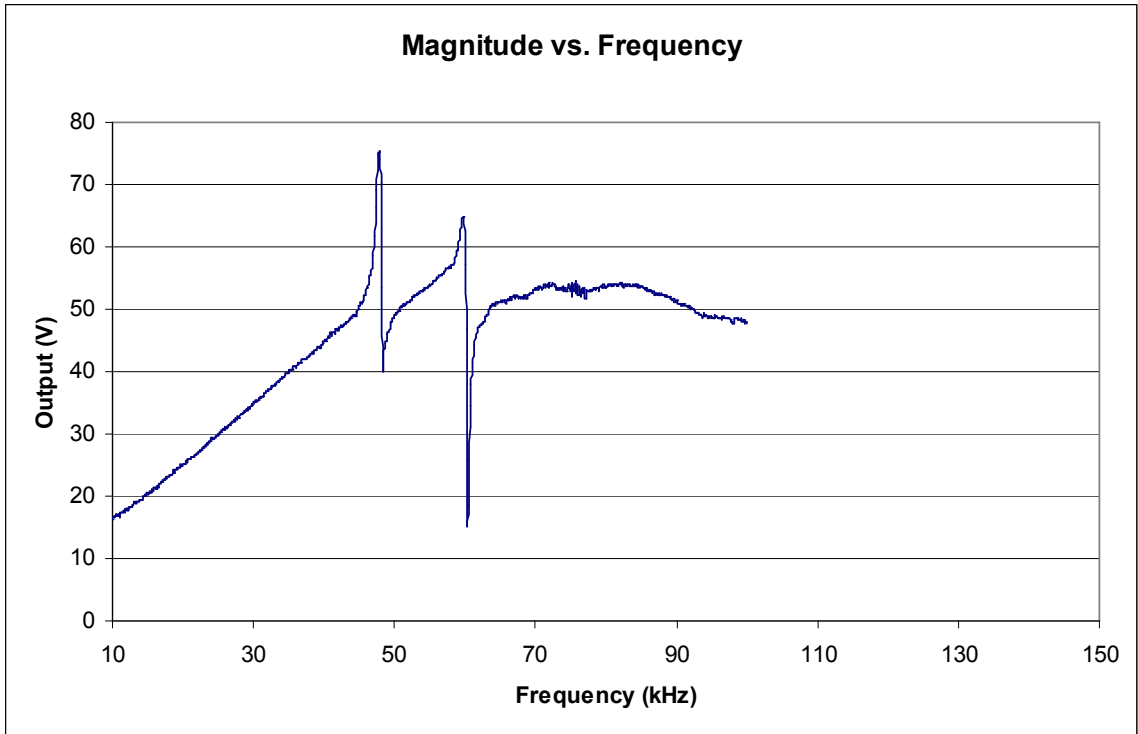


Figure 7.9: Frequency Response Sensor Four

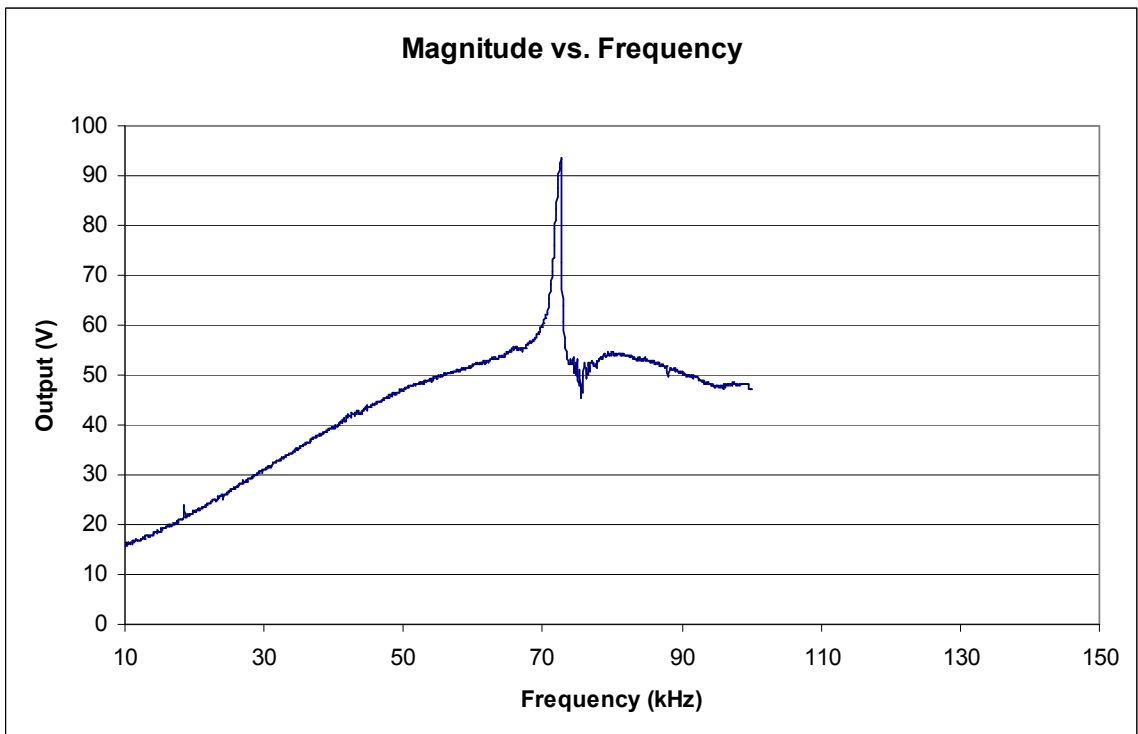
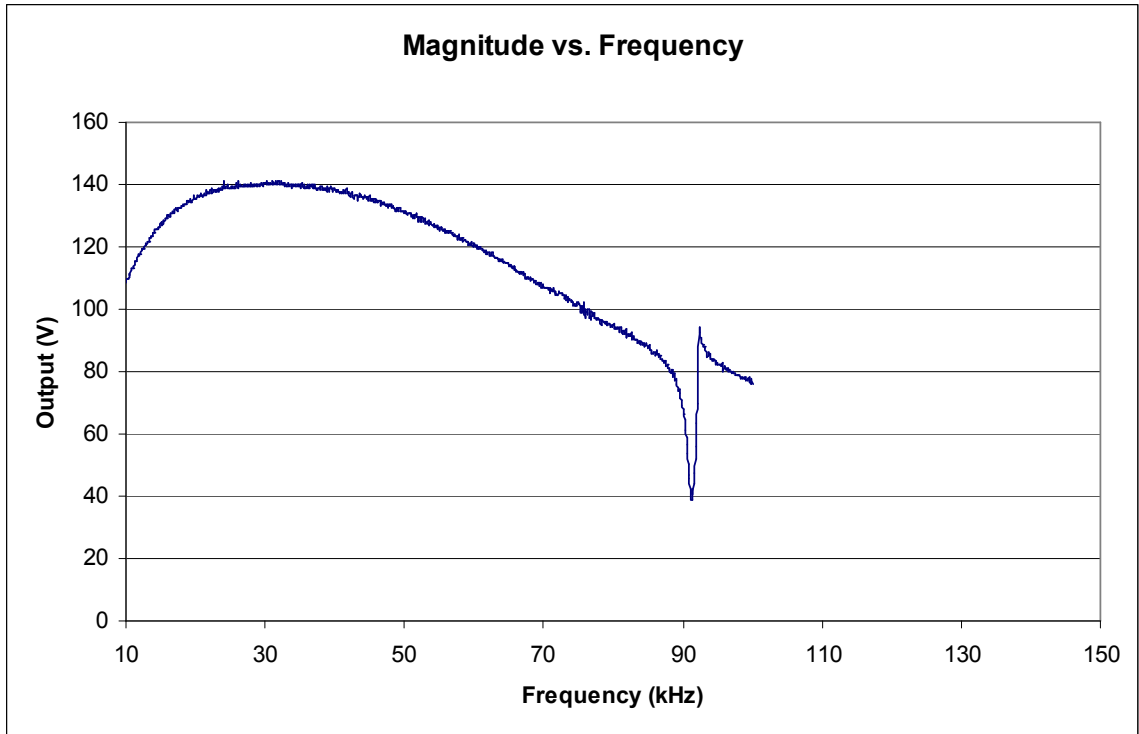
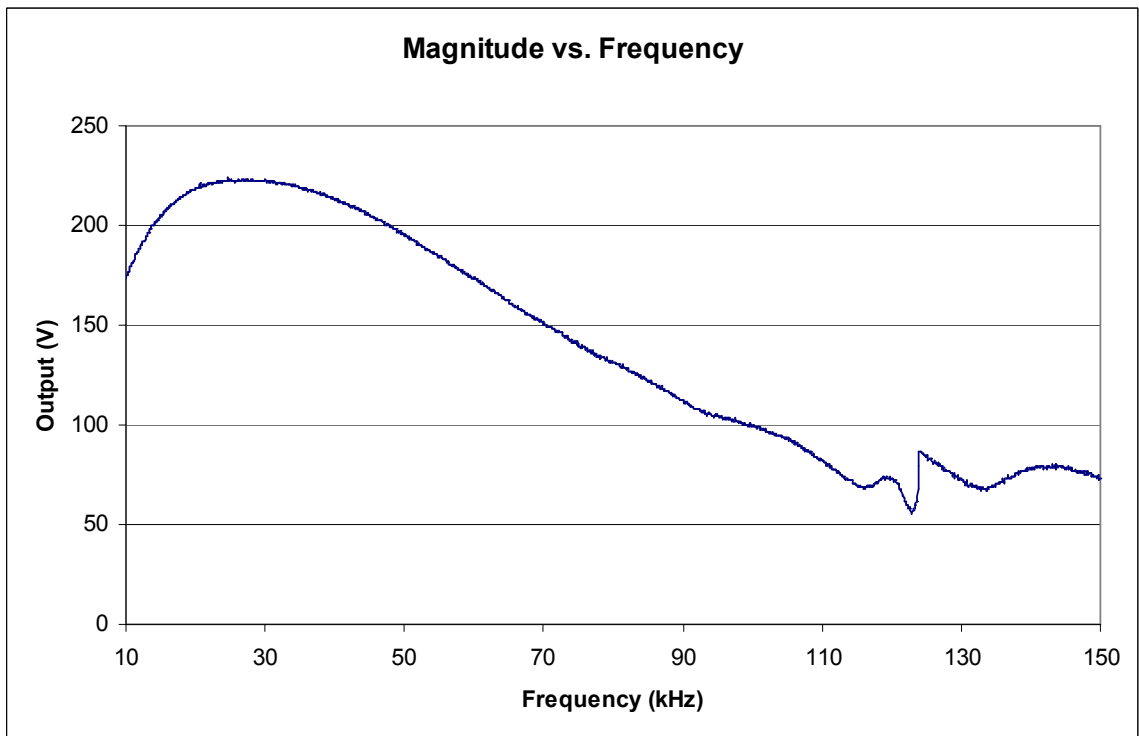


Figure 7.10: Frequency Response Sensor Five



**Figure 7.11: Frequency Response Sensor Six**



**Figure 7.12: Frequency Response Sensor Seven**

To explore the double peak response of the fourth sensor further, FEA was used to estimate natural frequencies for an intact sensor versus a fractured sensor. Figure 7.13 through Figure 7.15 show the original first three modes for a typical intact bridge.

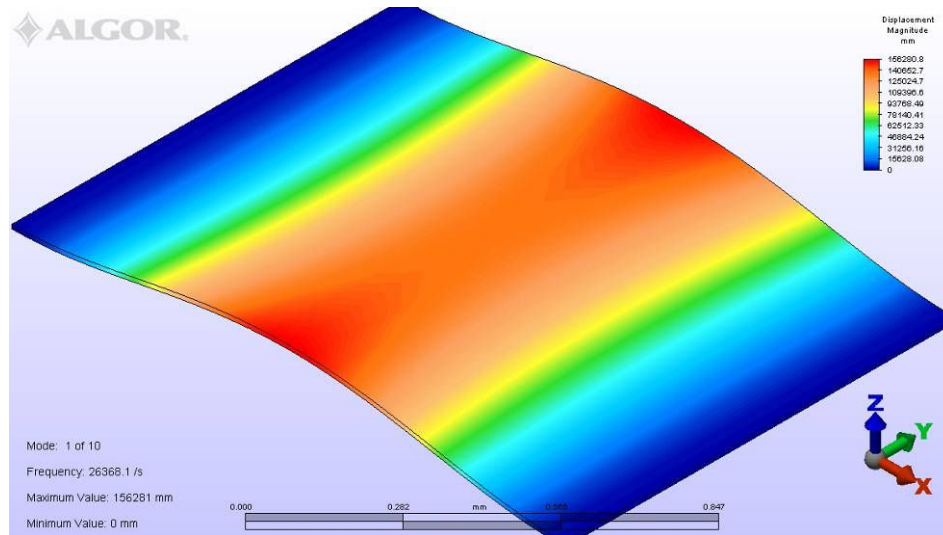


**Figure 7.13: Original First Mode Resonance**

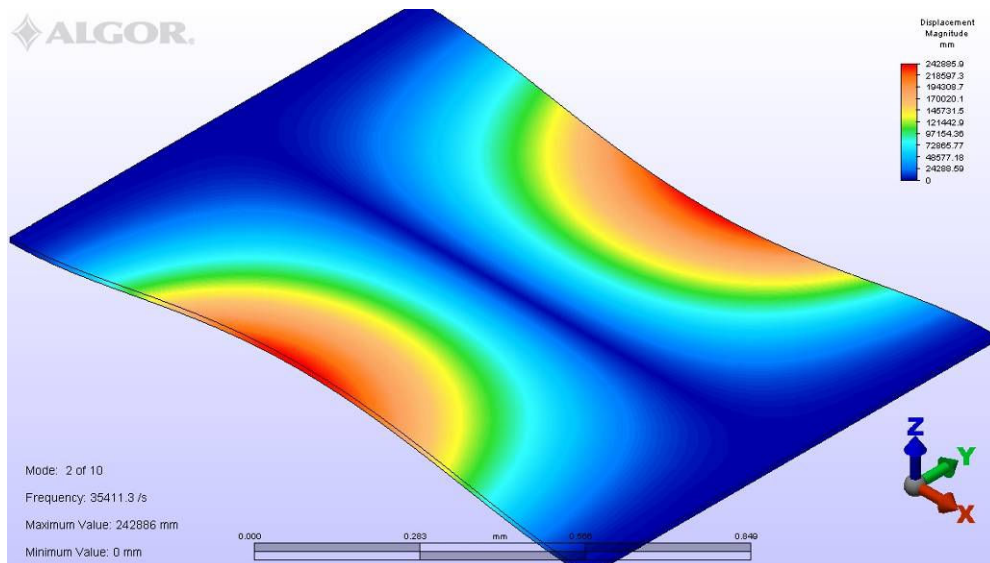


**Figure 7.14: Original Second Mode Resonance**

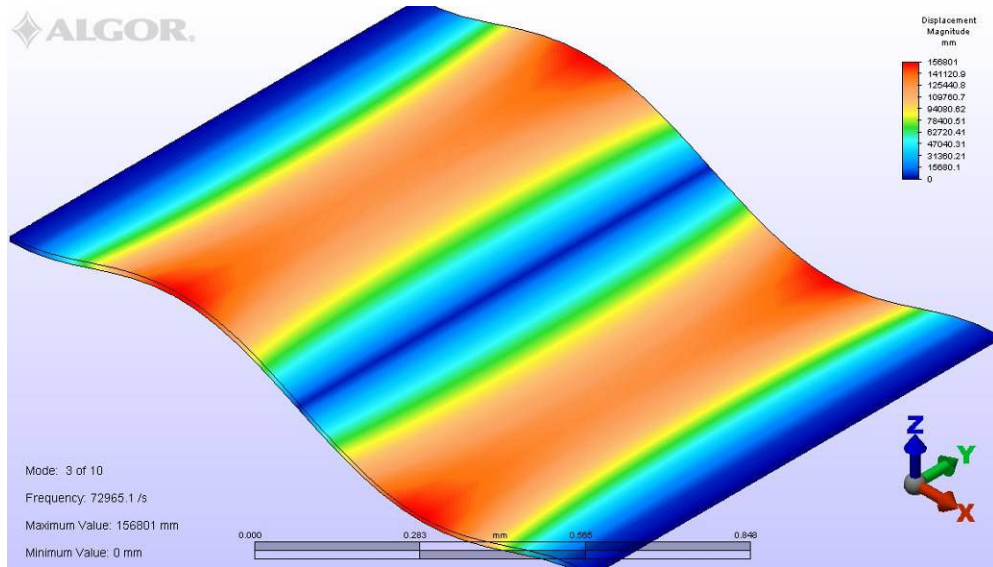


**Figure 7.15: Original Third Mode Resonance**

Figure 7.16 through Figure 7.18 show the modes of the bridge when a fracture is placed in the structure.

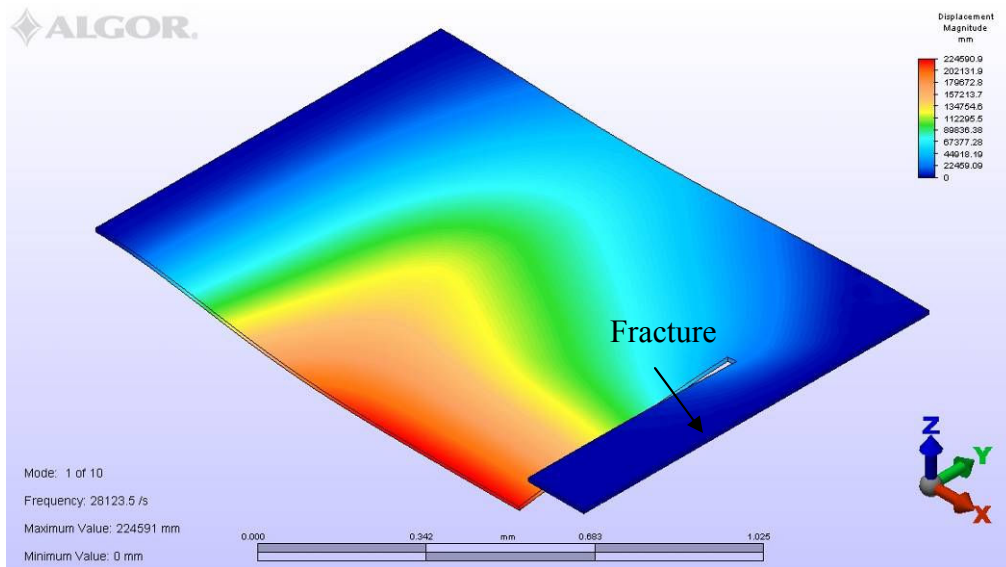


**Figure 7.16: Fractured Sensor First Mode Resonance**

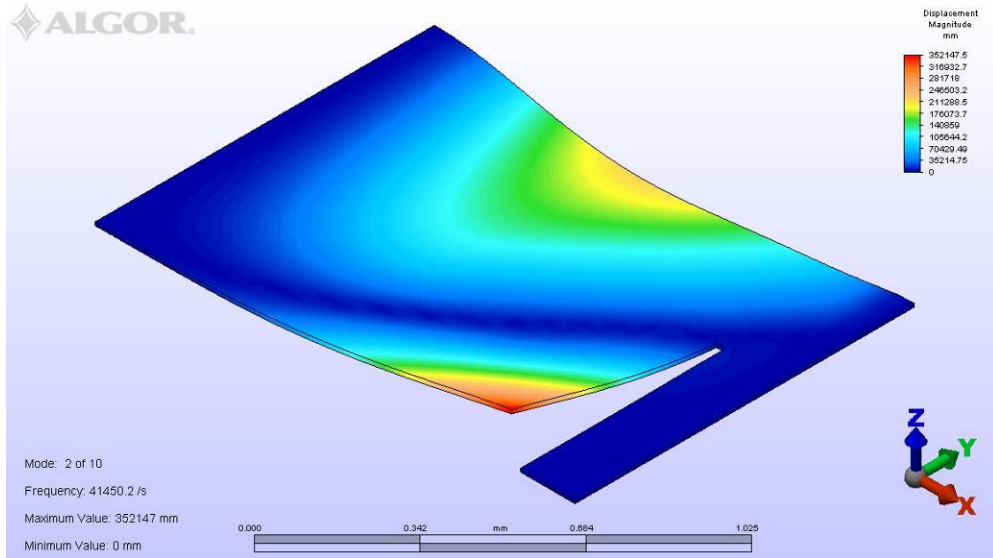


**Figure 7.17: Fractured Sensor Second Mode Resonance**

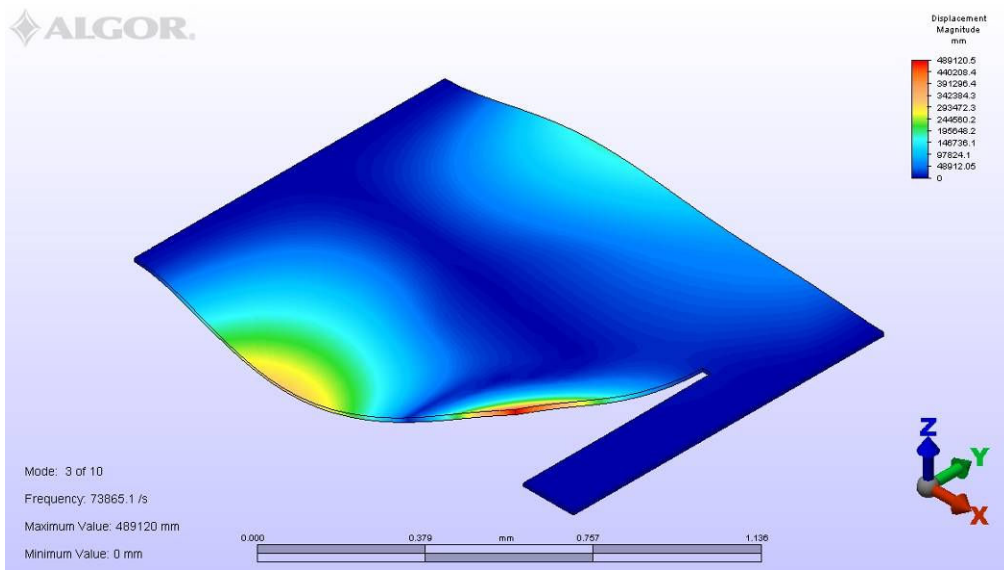


**Figure 7.18: Fractured Sensor Third Mode Resonance**

These simulations show that the original first mode resonance, and the only electrically active resonance, is split into multiple electrically-active resonance modes, as reflected in the frequency scans of this particular device (Figure 7.19).

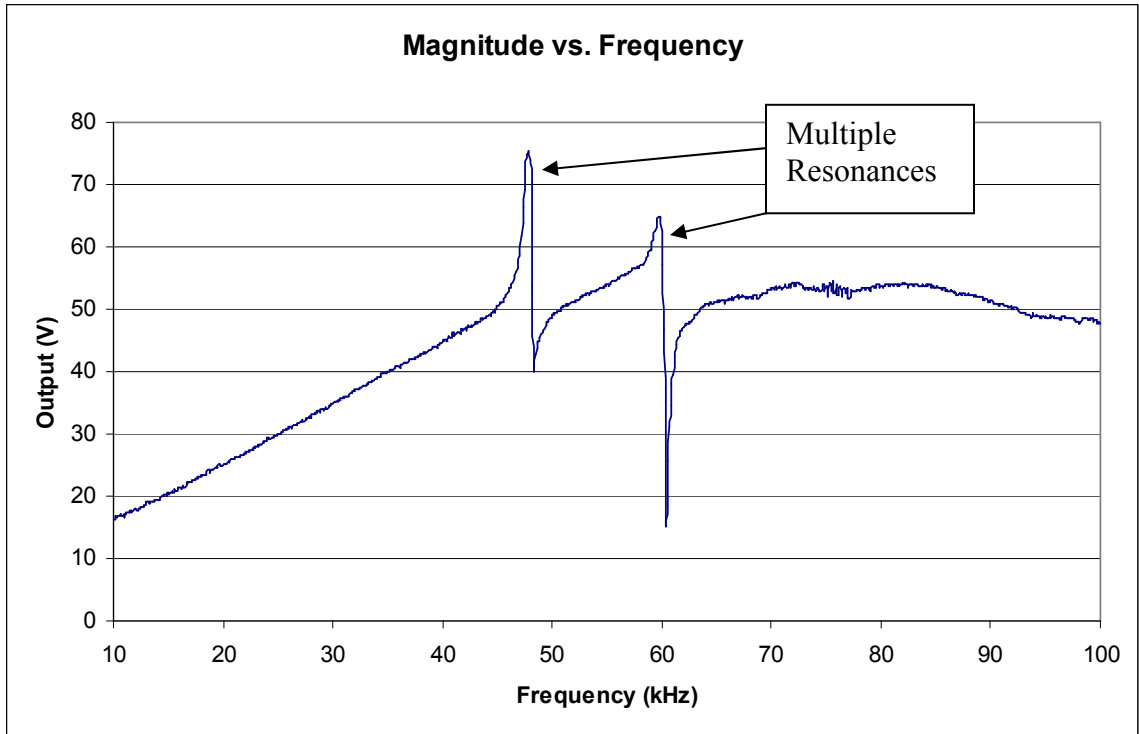


**Figure 7.19: Fractured Sensor Frequency Response**

To determine the natural frequency of an intact fourth sensor, one was selected from a different die. Figure 7.20 shows a frequency sweep from one of the intact fourth sensors in the array. This sensor displayed a more typical resonance peak.

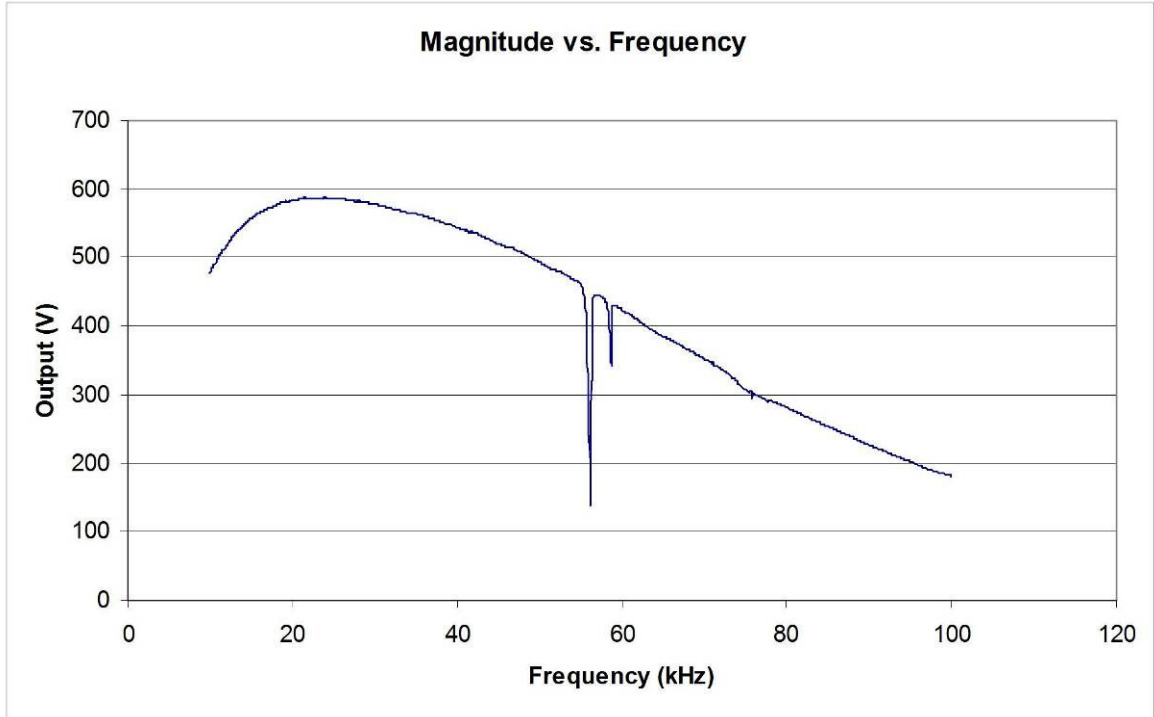


**Figure 7.20: Frequency Sweep of an Intact Fourth Sensor**

These frequency scans resulted in the following table of natural frequencies for the fabricated array.

**Table 7.1: Natural Frequencies of Fabricated Sensors**

Sensor	Frequency (kHz)
One	37.8
Two	42.2
Three	49.4
Four	56.2
Five	73.3
Six	92.1
Seven	118.4

The natural frequencies measured here are different than those expected from earlier simulations and calculations used in the sensor design. This is due to fabrication process variations. In particular, the Nickel structural film was measured to be 13 microns thick instead of the intended thickness of 10 microns. This difference in thickness changes the lowest natural frequency from 12000 Hz to close to 18000 Hz. However, this does not account for the substantially larger jump in frequency that was measured. What may account for the difference, however, is the topology of the sensor. The SU8 process included a slight shrinkage of the SU8 in unexposed areas. The shrinkage led to curvature on the surface that replicated itself in curvature of the sensor itself. Furthermore, internal stresses within the Ni film led to additional structure curvature. This curvature alters the dynamic behavior of the sensor.

To verify this, an FEA model was created based on measurements of the surface obtained with a WYCO Interferometer. The fundamental mode of the lowest frequency resonant structure is shown in Figure 7.21. The model predicts that the structure, which was original designed for a much lower frequency, has a much higher frequency of 38 kHz due to the film curvature. This effect shifts all of the resonant frequencies within the array higher.

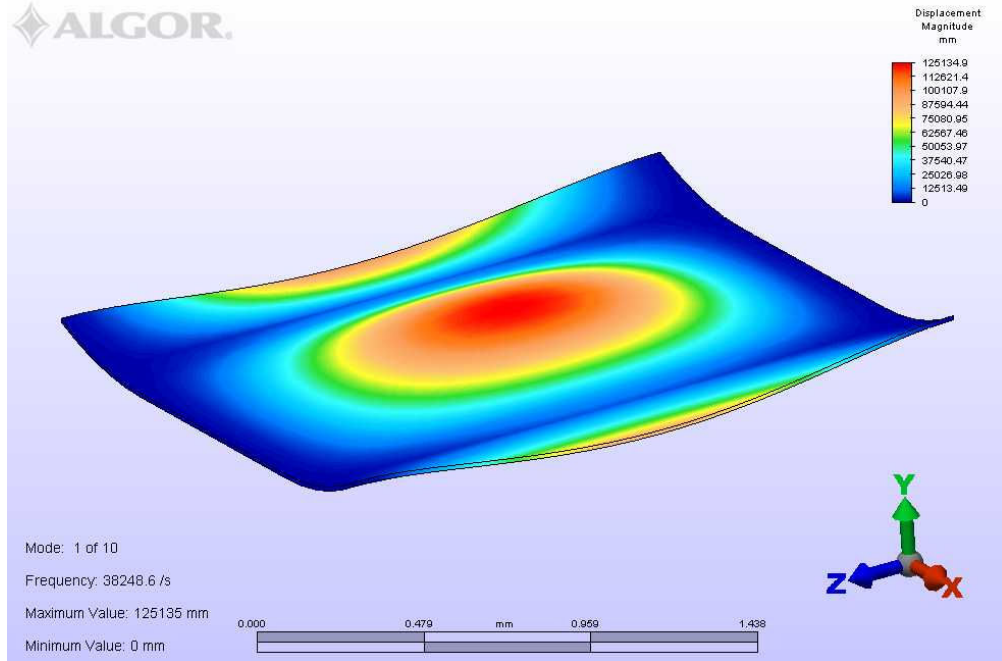


**Figure 7.21: Fundamental Mode of Curved Structure**

Even though the natural frequencies of the sensor array were all higher than originally designed, their applicability in determining an impact spectrum was still valid. The sensors still populated the frequency range of interest. In one of the final impact tests, the lowest frequency sensor was modified to reduce its frequency, thereby completely spanning the range of interest.

## **7.2 Ball and Hammer Drop Experiments**

Ball and hammer drop experiments were performed to measure the response of the sensors to consistent impacts with varying materials. Sensors were attached to four types of structures. The first type of structure was a large square aluminum plate. The second was a small aluminum plate. The third one was a hardened steel cone. The fourth was a small alumina disc.

In the hammer drop setup, Figure 7.22, a hammer is attached to a fulcrum at one end. The other end of the hammer is then aimed at the target location on the plate directly above the transducer, and raised to a consistent height. The hammer is then simply dropped and an oscilloscope captures the signals from the transducers. The advantages of the hammer drop are simple aiming of the impact and convenient variations in material. The end of the hammer is the same mass when either the steel impact occurs or the Teflon impact. Therefore, the energy of the hammer is the same, and all that is different is the boundary condition at the interface with the plate.

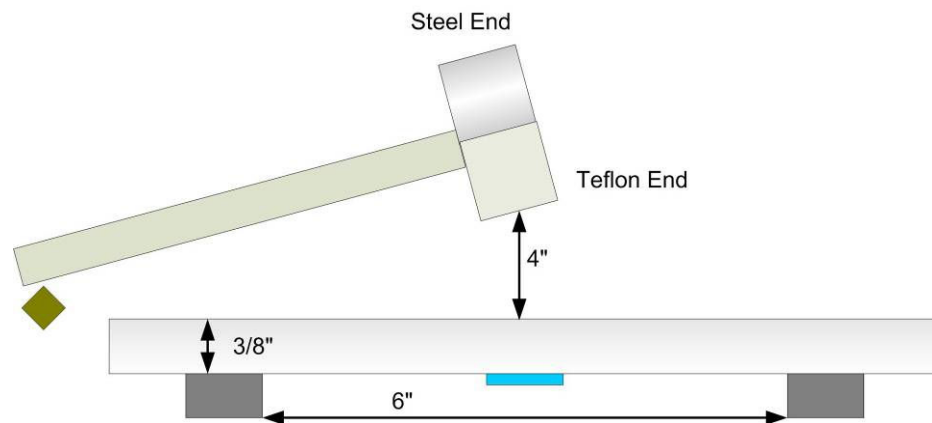


**Figure 7.22: Schematic of Hammer Drop on Square Plate**

In the ball drop experiment, a  $\frac{1}{2}$ " ball is dropped through a tube onto the article under test as shown in Figure 7.23. The ball is simply dropped from the known distance while an oscilloscope captures the signals from the transducers. The ball drop provided the most ideal pulses as described in Chapter 3.

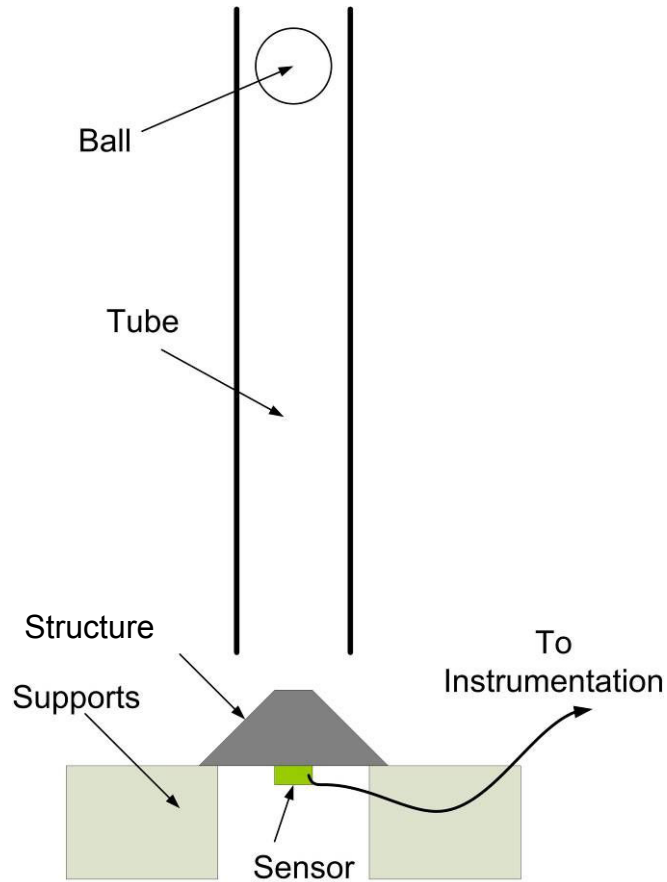


**Figure 7.23: Ball Drop Test**

A series of test articles was assembled for characterization in the ball and hammer drop tests. These articles included varieties of plates and varieties of sensor elements. Plates included a large plate, a small plate for creating higher frequency content, a flattened tip cone, and a disc. Sensor elements included both laser micromachined and fully micromachined devices. Multiple sensors were used so that comparisons and conclusions could be drawn regarding performance and operation. Figure 7.24 through Figure 7.31 show pictures of representative test articles.



**Figure 7.24: Single Laser Machined Transducer Element on a Steel Cone**

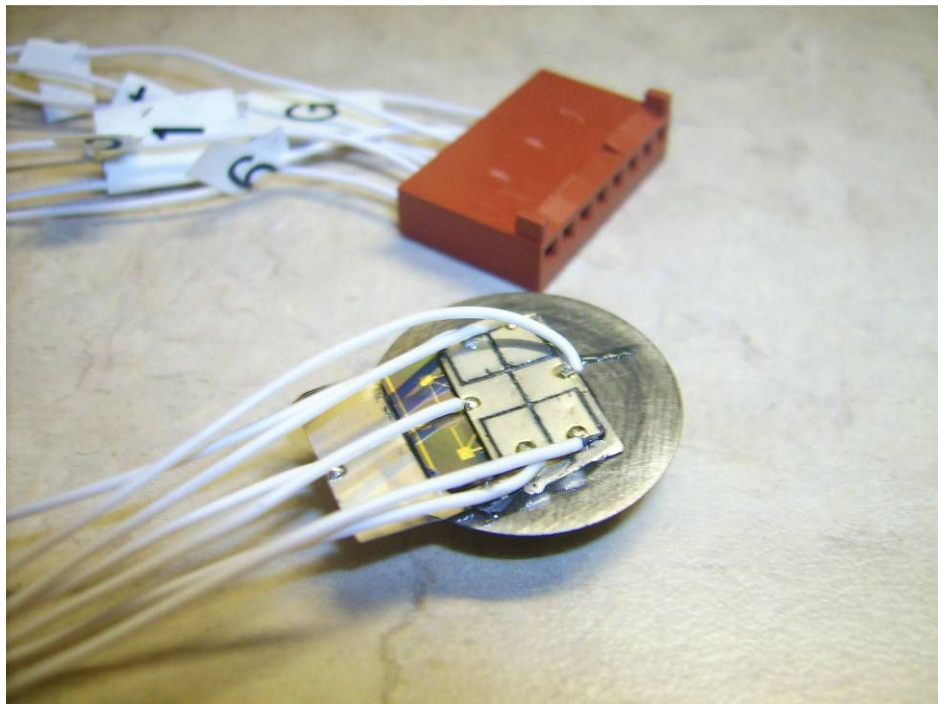


**Figure 7.25: Laser Machined Transducer Array on a Steel Cone**

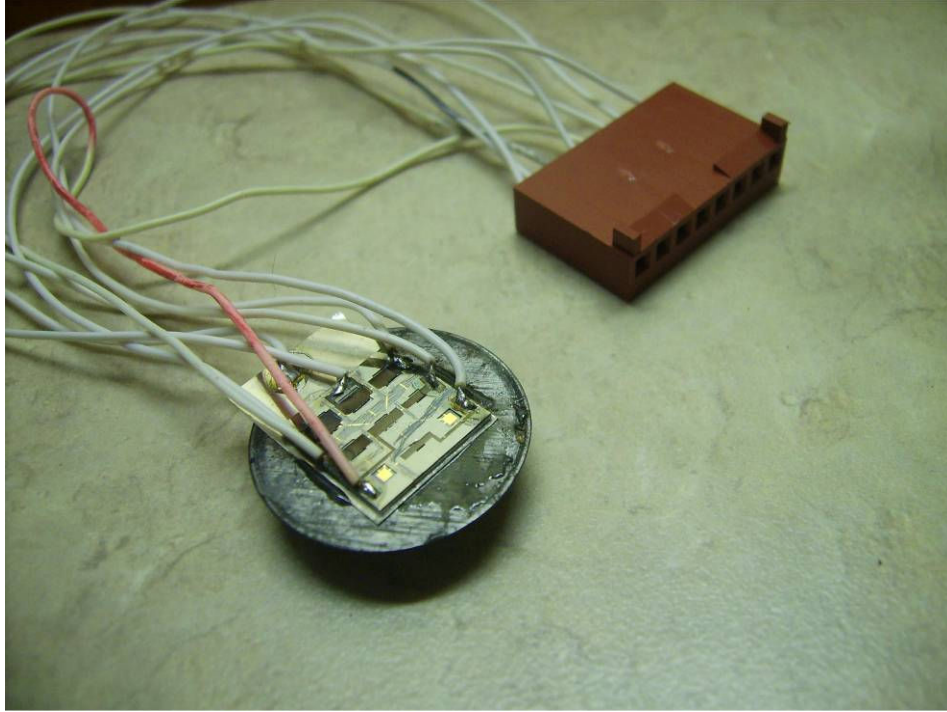


**Figure 7.26: Microfabricated Transducer Array on a Steel Cone**

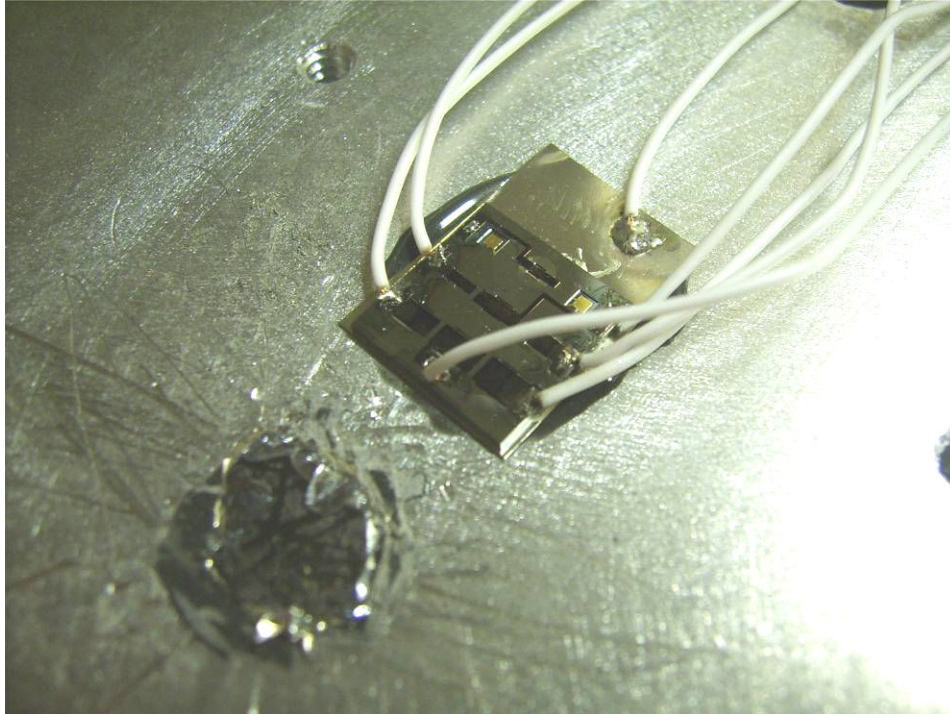


**Figure 7.27: Microfabricated Transducer Array on a Large Plate**



**Figure 7.28: Microfabricated Transducer Array on a Large Plate (Zoomed Out)**

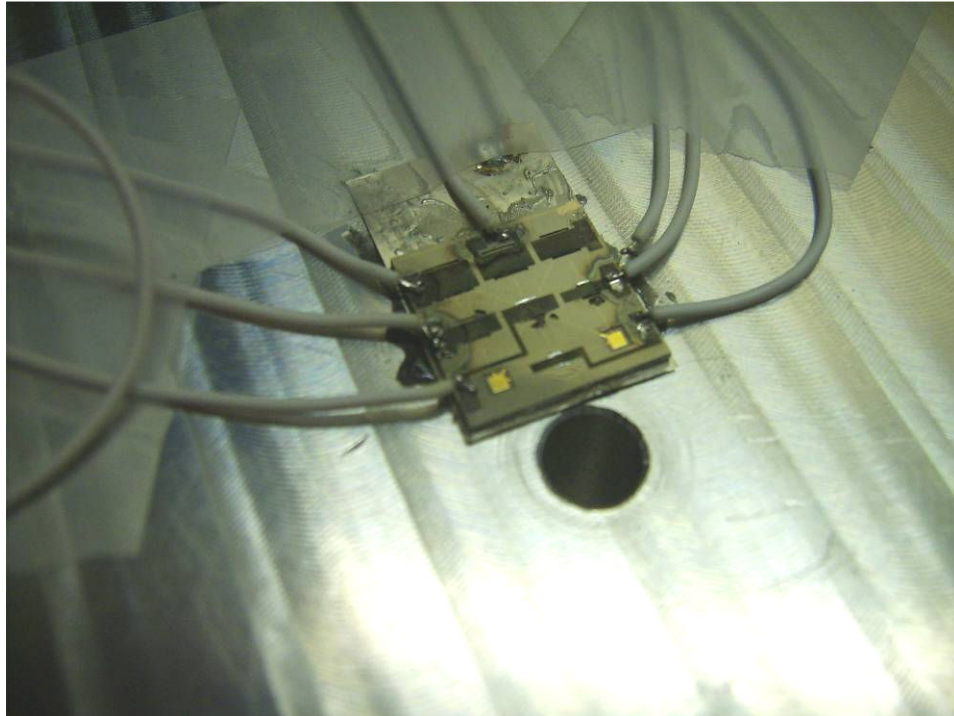


**Figure 7.29: Microfabricated Transducer Array on a Small Plate**

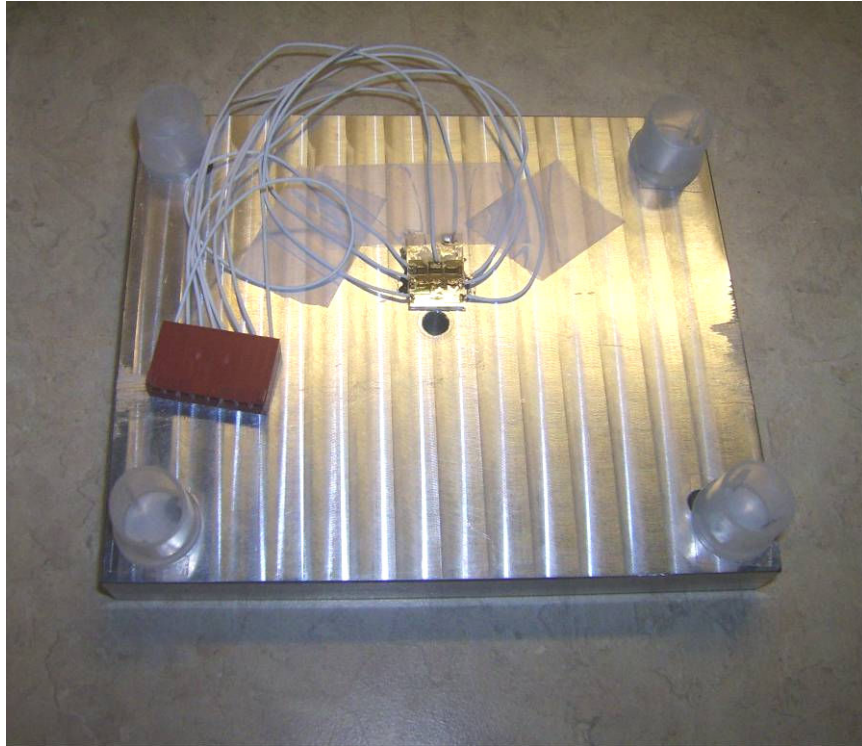


**Figure 7.30: Microfabricated Transducer Array on a Small Plate (Zoomed Out)**

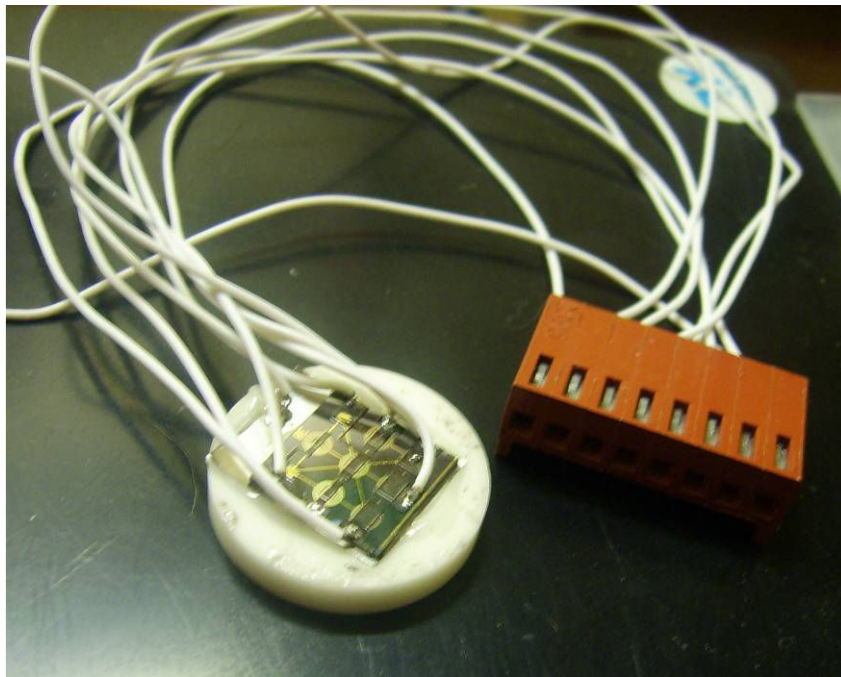


**Figure 7.31: Microfabricated Transducer Array on Small Alumina Disc**

### 7.3 Test Series

A series of tests were performed using these test articles. The purpose of the test series was to systematically look at particular aspects of the sensor operation and to deal with noise sources, error sources, and process modifications in a methodical fashion. During the course of the test series, error sources such as pulse formation, parasitic capacitance, test apparatus error sources, and other performance-affecting situations arose. The use of the test series allowed one situation to be dealt with at a time.

The test series is shown in Table 7.2. The test series used single laser machined sensors, laser machined sensor arrays, and microfabricated sensor arrays. These were placed on both large and small plates, as well as cones and discs. These items underwent impacts in both the hammer drop and the ball drop.

**Table 7.2: Test Series**

<b>Results Section</b>	<b>Structure</b>	<b>Test</b>	<b>Purpose</b>
B.1 Single Device	Steel Cone	Hammer	Verify <i>In situ</i> Charging
B.2 Large Plate	Large Al Plate	Hammer	Verify Sensor Operation
B.3 Small Plate	Small Al Plate	Hammer	Verify Structural Response
B.4 Laser Machined Array	Steel Cone	Hammer	Measure a Steel Cone Baseline Response without Sensor Ringing
B.5 First MEMS Array	Steel Cone	Hammer	- Verify Array Operation - Baseline of Cone Response with Sensor Ringing
B.6 Second MEMS Array	Steel Cone	Hammer	- Baseline of Shot-to-Shot Variation - First Tests of Different Materials - Demonstrated Filtering to Remove Test Apparatus Response
B.7 Third MEMS Array	Steel Cone	Ball	Implemented Test Apparatus with Sharper Impulse Source and Higher Repeatability
B.8 Fourth MEMS Array	Steel Cone	Ball and Slug	- Repeat for consistency - First Test of Four Different Materials
7.4 Fifth MEMS Array	Alumina disc	Ball	- Test with Tape Layers to Shape Pulse - Final Test with Four Different Material Balls

The tests (B.1 through B.8) presented in Appendix B represent a chronological progression of test, sensor, and signal processing development. The results from the final test are presented in this chapter, and incorporate the lessons learned in the previous tests.

#### 7.4 MEMS Array on Alumina Disc - Ball Drop

Through the test series presented in Appendix B, a full signal processing flow was developed for the resonant sensor arrays to remove parasitics and noise sources. These included sensor-to-sensor parasitics described in Chapter V, as well as structural and test apparatus error sources that had to be removed from the sensor waveforms. It also became evident through the test series that reducing the natural frequency of the lowest sensor would be beneficial in the processing of the input stress pulse. That first sensor and the next highest frequency sensor were very close in frequency and offered little discrimination ability. Furthermore, it became evident that parasitic coupling was occurring from sensor to sensor through the charging grid. This was a noise source that degraded the discrimination capability.

In the original array design, the lowest frequency sensor was intended to be much lower than the actual fabricated device. The lowest frequency sensor, as fabricated, had a resonant frequency of about 36 kHz. The second sensor had an as-fabricated resonance of 41 kHz. It was desirable to reduce the resonance of the first sensor. That was achieved by adding a 20mil solder ball to the structure to increase its mass. This dropped the resonance to about 25 kHz.

In addition, the ball drop setup was slightly modified as shown in Figure 7.32. The slight change was the use of the alumina disc as the structure. The alumina disc had a natural frequency of 133 kHz, which was beyond the natural frequency of the highest sensor. The Teflon block was 1 inch thick, and had a natural frequency of 15 kHz, which was below the lowest frequency sensor. The isolation layer consisted of an approximately 500 $\mu$ m thick polymer film. These modifications to the test apparatus attenuated and moved the structural response of the test apparatus outside the frequency band of interest to the sensor array.

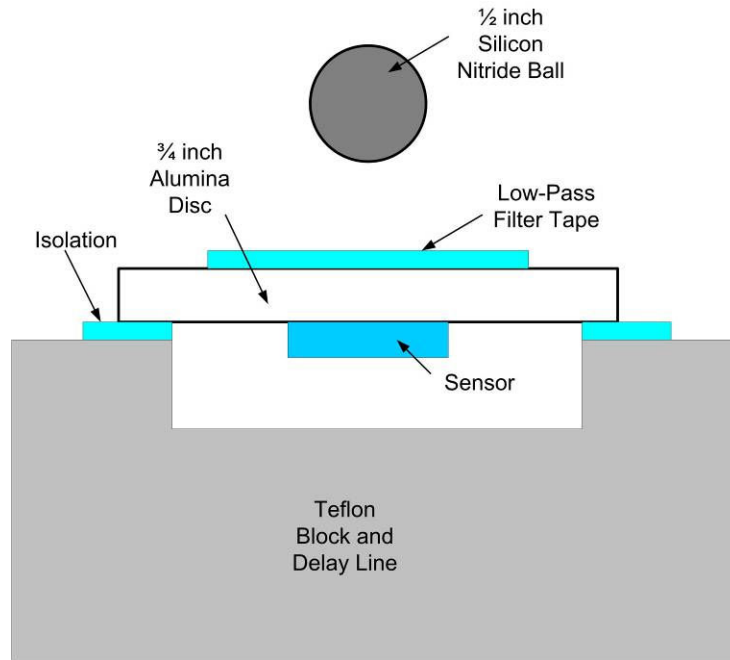


**Figure 7.32: Modified Ball Drop Apparatus**

A  $\frac{1}{2}$  inch Silicon Nitride ball was used in the drop test because the resulting Gaussian-like waveform, while using no low-pass filter tape, had a pulsewidth that fell between the fourth and fifth sensors in the array. Ten drops were performed while capturing the sensor array output. The first drop did not use low-pass filter tape. Each subsequent drop added one layer of cellophane tape, as described in Chapter III. The last drop had a total of nine layers of tape. The tape had the effect of increasing the pulsewidth of the impact waveform, as described in the Chapter 3. Figure 7.33 shows the first six stress pulses generated by this impact scenario. The sharpest pulse with a full-width at half-maximum (FWHM) value of approximately  $11\mu\text{s}$  also exhibited substantial ringing of the alumina disc at 133 kHz.

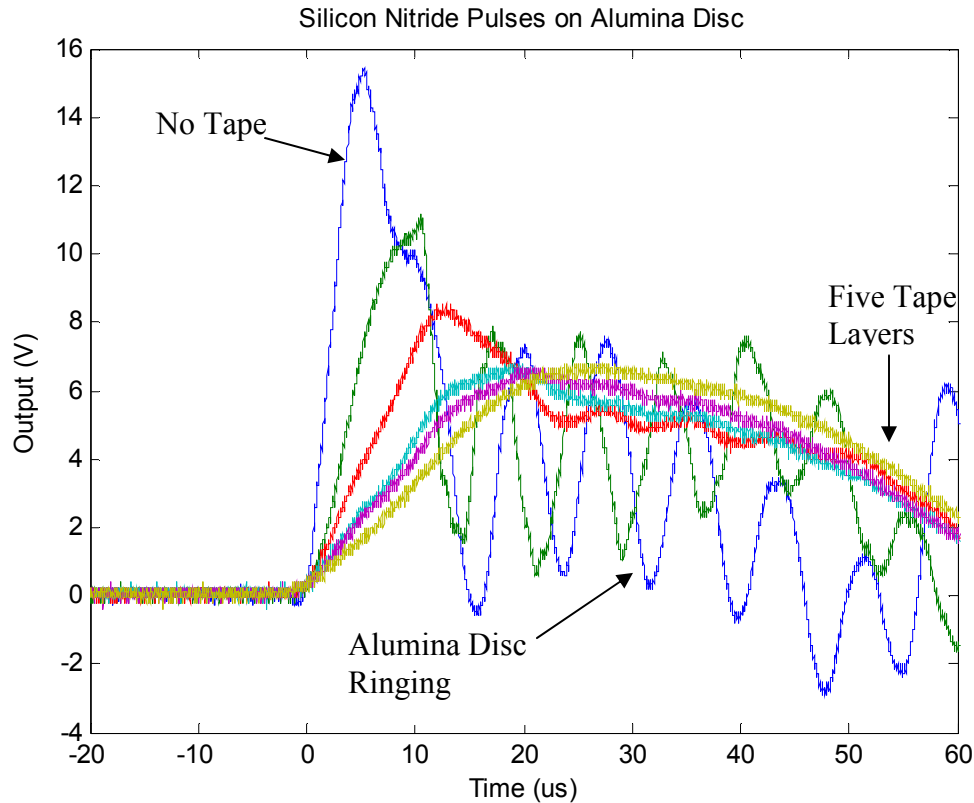


**Figure 7.33: Stress Pulses from Silicon Nitride Ball**

Figure 7.34 shows the raw output of the full seven sensor array due to the impact from the silicon nitride ball directly onto the alumina disc. Many features need to be noted regarding these waveforms. The primary feature to note is the large amount of sensor ringing, as exemplified by the damped harmonic oscillation seen in sensors one through four. This is the primary signal of interest. In addition, as most exemplified by the seventh sensor, there is also still a significant response of the test structure and test apparatus. This is a low-frequency response from the Teflon mounting block and supporting structure. Furthermore, there is a higher frequency response from the alumina disc itself, but the readout amplifier used has a low-pass cutoff frequency that substantially attenuates that signal. Finally, sensor two shows how cross-talk between

sensors can lead to one sensors output bleeding into another sensors output, leading to multiple frequencies and an incorrect amplitude measurement.

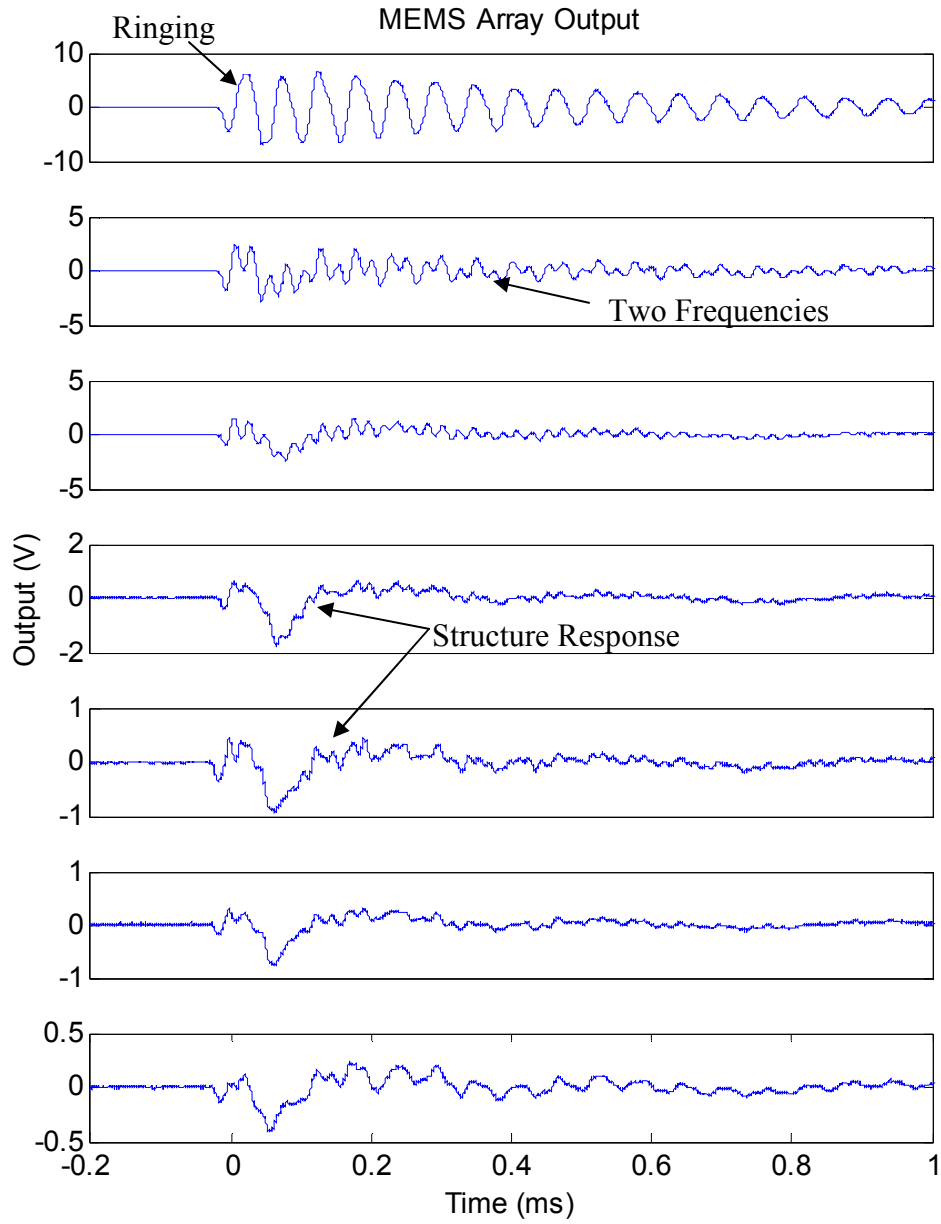


**Figure 7.34: Seven Sensor Array - Direct  $\text{Si}_3\text{N}_4$  Impact**

Figure 7.35 shows the output of the same sensor array to an impact of the silicon nitride ball on five layers of the 2 mil cellophane tape. This impact has a much wider pulse width. The primary feature to note in these waveforms is again related to the ringing of the sensor elements. Ringing can still be seen in these waveforms, but upon closer inspection, the nature of that ringing is different. In particular, while sensor two does show damped harmonic oscillation, that oscillation frequency is actually primarily the frequency of sensor one. The higher natural frequency of sensor two is not seen as it was during a direct Silicon Nitride impact. The signal seen in this low frequency impact is the crosstalk from sensor-to-sensor.

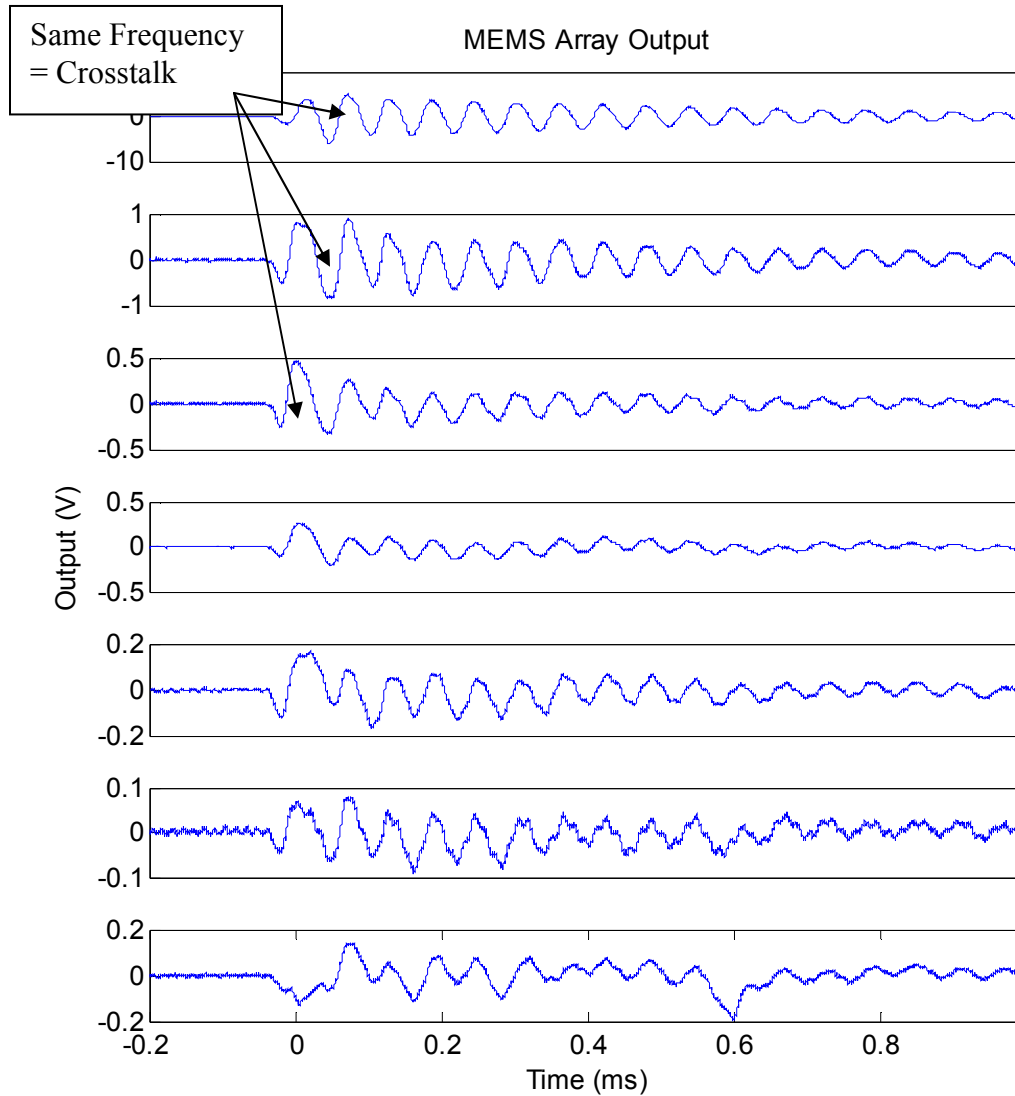
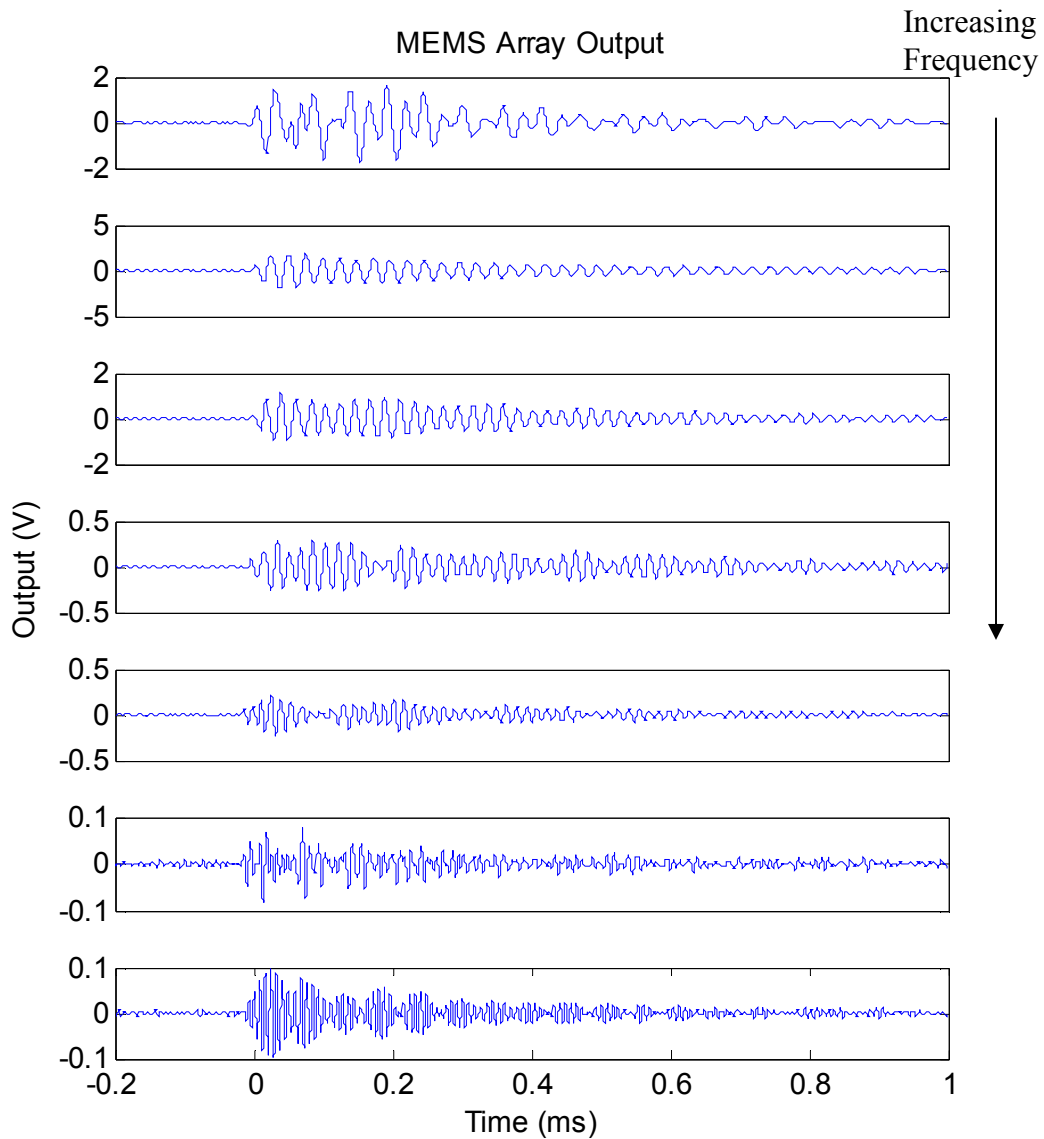


**Figure 7.35: Seven Sensor Array - Si<sub>3</sub>N<sub>4</sub> Impact - Five Tape Layers**

The errors due to the structural response of the system and the sensor-to-sensor crosstalk required post-collection band-pass filtering of the raw waveform. In particular, all sensors had frequencies above the highest frequency element (120kHz) filtered out. In addition, to remove structural noise sources, all of the sensors had frequencies below 10kHz filtered out. Furthermore, each sensor output had frequencies below its own resonance filtered out. The goal of that last filtering step was to remove sensor-to-sensor

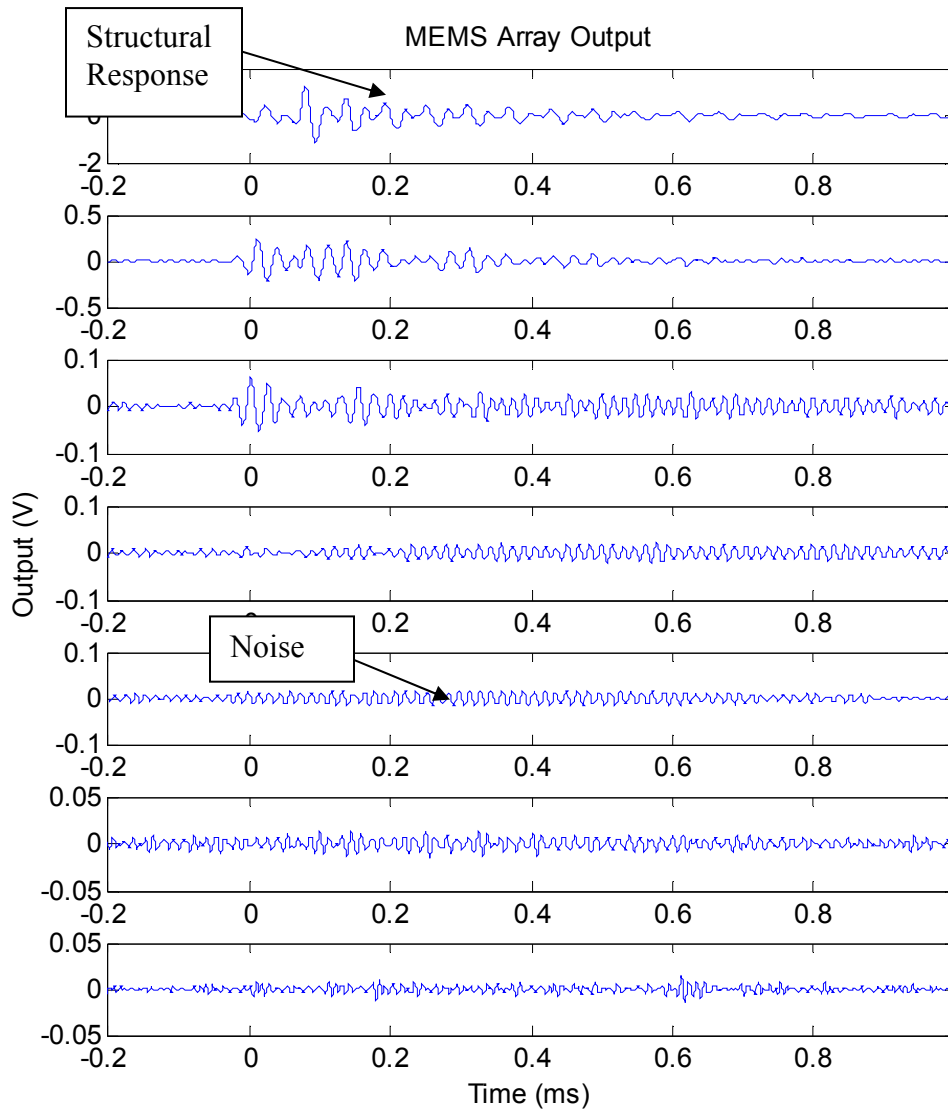
crosstalk. Ideally, the sensor array would be redesigned to remove the cross-talk at the sensor level, rather than rely on additional filtering.

Figure 7.36 shows the direct silicon nitride impact waveforms after the application of the filtering. It is clear in these waveforms that each sensor is ringing at its natural frequency. This can be seen by the fact that the ringing frequency is increasing in this series of plots.



**Figure 7.36: Filtered Seven Sensor Array - Direct  $\text{Si}_3\text{N}_4$  Impact**

Figure 7.37 shows the same for the impact of the silicon nitride on five layers of tape. In these waveforms, it is clear that the amplitude of ringing has changed for each sensor, with the higher frequency sensors exhibiting substantially less damped harmonic oscillation.



**Figure 7.37: Filtered Seven Sensor Array -  $\text{Si}_3\text{N}_4$  Impact - Five Tape Layers**

To develop a spectrum using the sensor array, the maximum value of each sensor's output is found and plotted against that of the other sensors. This is similar to the

Shock Response Spectrum technique. Figure 7.38 shows the maximum value of the waveform per sensor, per drop, for zero tape layers to nine tape layers.

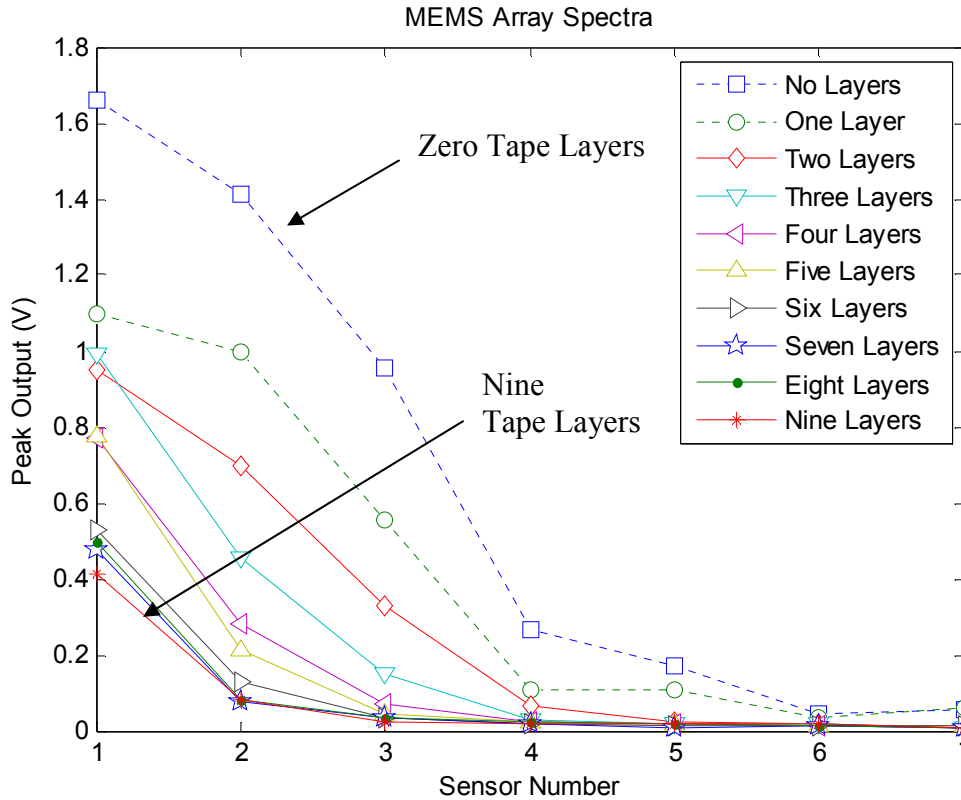
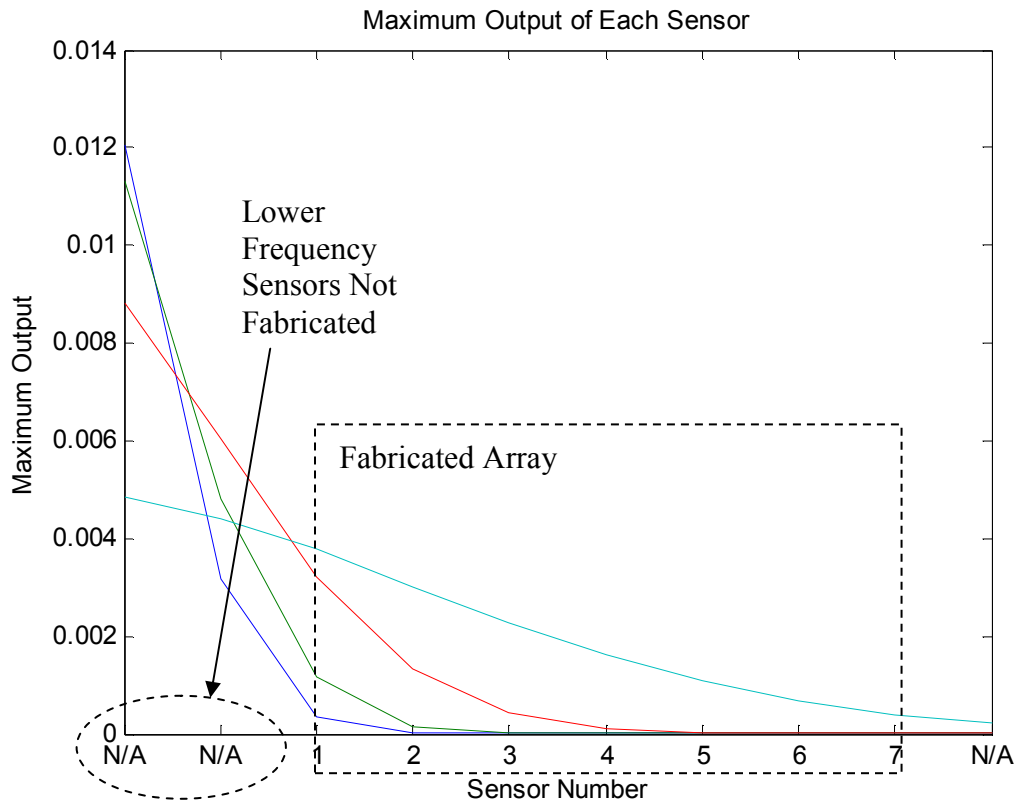


Figure 7.38: Array Output from Silicon Nitride Impact and Multiple Tape Layers

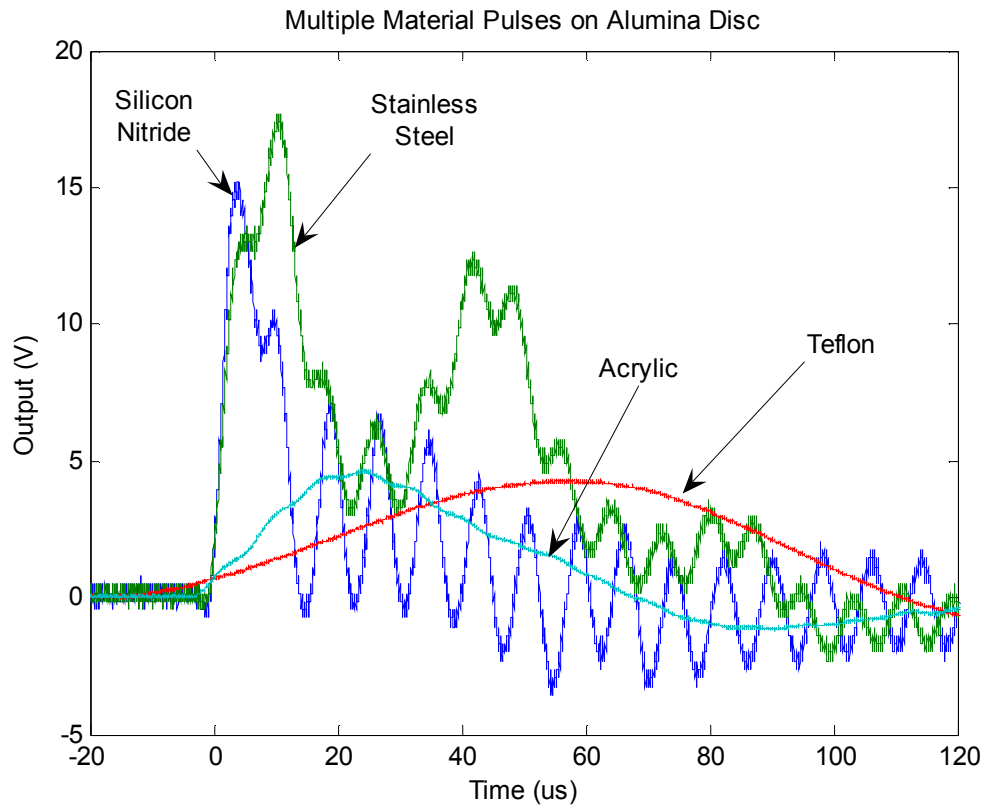
Figure 7.39 shows the predicted array response. Note that the fabricated array only includes sensors three through ten of the simulated devices. In addition, the two shortest pulsewidths in the simulated system could not be achieved by the Silicon Nitride ball. Therefore, the space within which these tests are occurring is indicated by the dotted box. An important point to repeat in these tests is that additional filtering was added to remove capacitive coupling from the lower frequency sensors into the higher frequency devices, as described in Chapter 5. The lower frequency sensors had large capacitive areas because of their larger structural area. This led to greater crosstalk effects from

those sensors. In particular, the output of sensor  $j$  had to be high-pass filtered at a frequency above all of the sensors from  $j-1$  to the lowest frequency device.



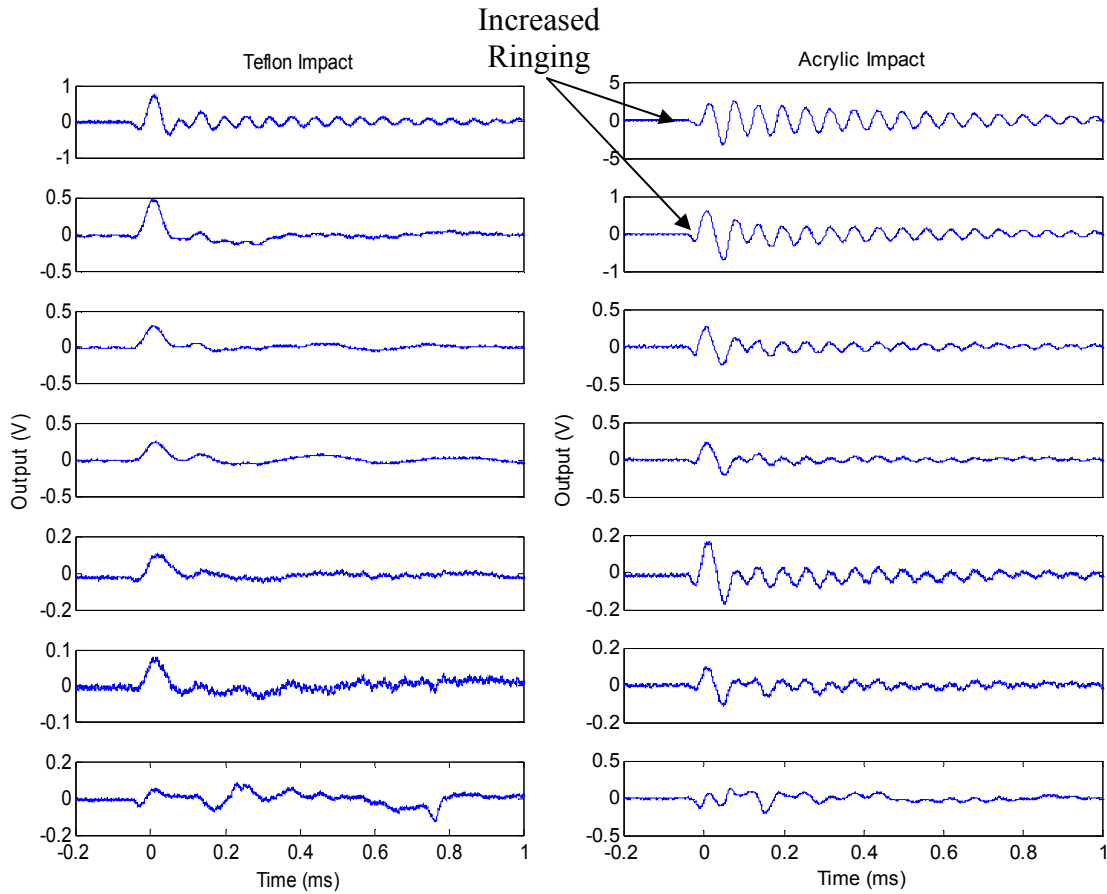
**Figure 7.39: Predicted Response for the Sensor Array**

After completing ball drop tests using a Silicon Nitride and tape layers to widen the pulse width, ball drop tests were performed that used different materials for each ball, but with the same ball diameter and dropped from the same height. Figure 7.40 shows stress pulses captured by a piezoelectric strain gage for ball drops of Silicon Nitride, Stainless Steel, Acrylic, and Teflon. Silicon Nitride has the shortest pulse width, followed by Stainless Steel, then Acrylic, then Teflon. The Teflon pulse width is substantially longer than the use of tape layers could provide when using a Silicon Nitride ball.



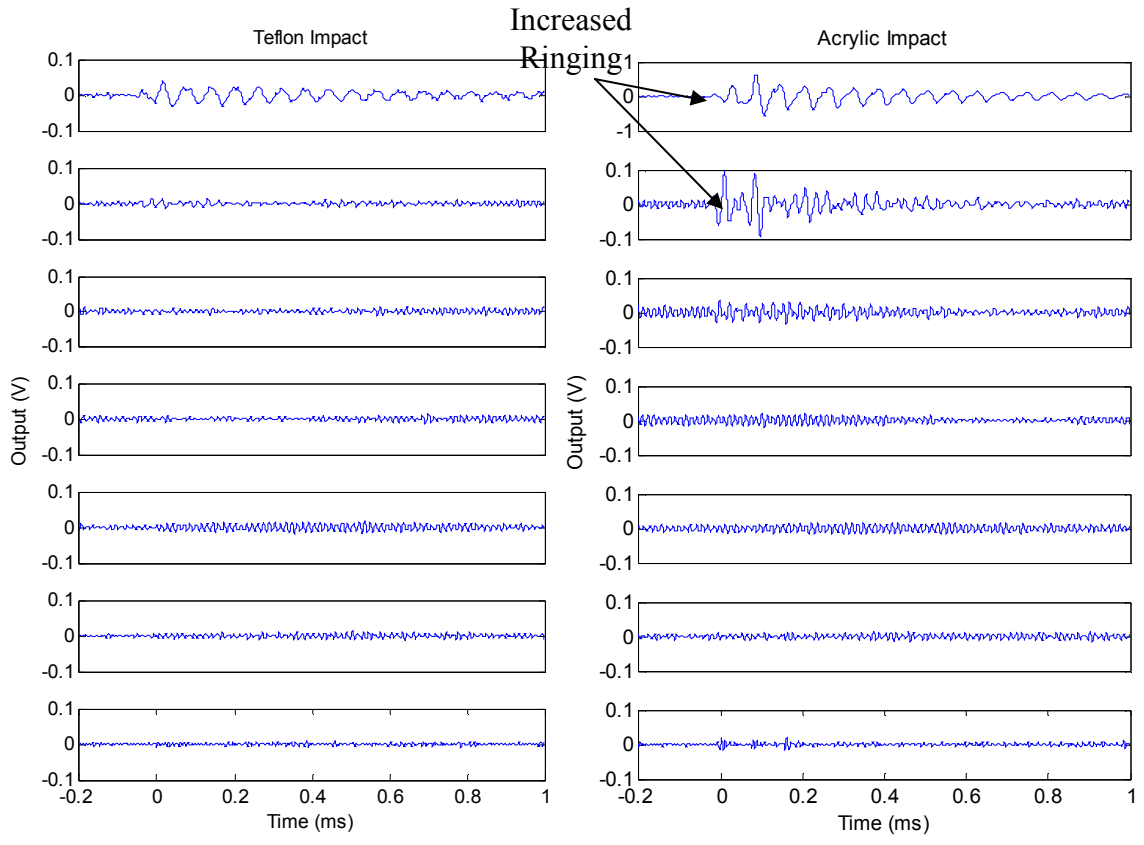
**Figure 7.40: Stress Pulses from Different Ball Materials**

Figure 7.41 shows side-by-side comparisons of the seven sensors in the array to an impact with a Teflon ball and an impact with an Acrylic ball prior to filtering.



**Figure 7.41: Seven Sensor Array Impact - Teflon (left), Acrylic (right)**

Figure 7.42 shows the same waveforms after application of the filtering. Note the removal of both structural response and sensor cross-talk. Also note the significantly smaller amount of ringing of sensors one and two due to Teflon impact, and substantial ringing of sensors one and two due to Acrylic impact. This demonstrates the affect of pulse width on the damped harmonic oscillation of the sensor element.



**Figure 7.42: Filtered Seven Sensor Array Impact - Teflon (left), Acrylic (right)**

Figure 7.43 shows the sensor array spectrum for a 1/2 inch Teflon ball versus 1/2 inch acrylic ball in the same test apparatus. Both balls were dropped from the same height. The interesting aspect of this set is that the acrylic ball has less mass than the Teflon, yet since Acrylic has a higher modulus, there is more energy in the frequency range of the sensors, leading to a larger response.

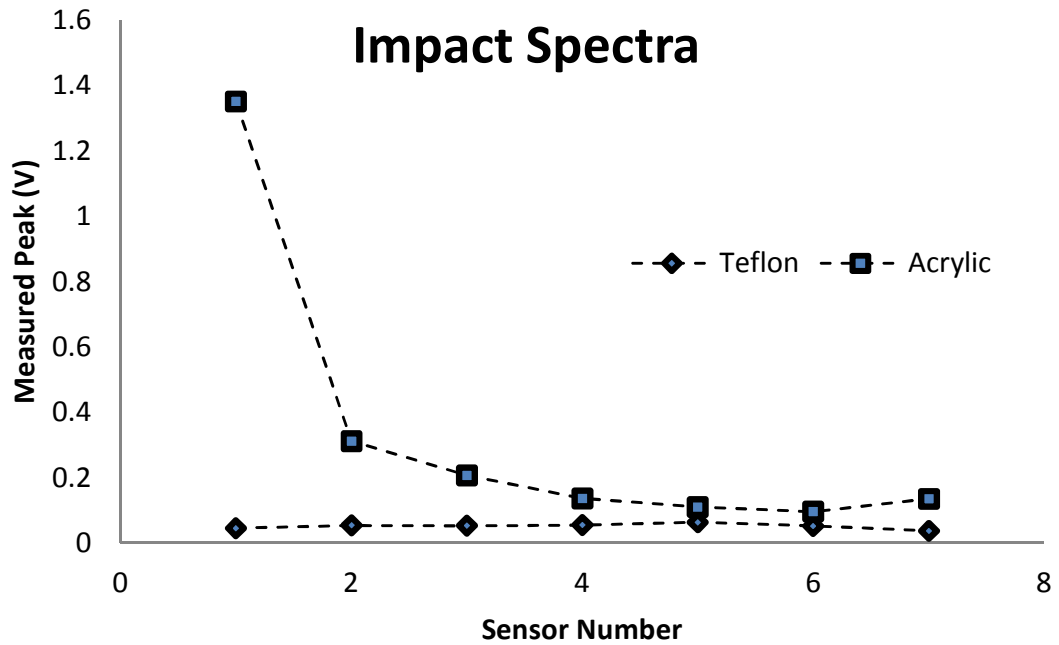
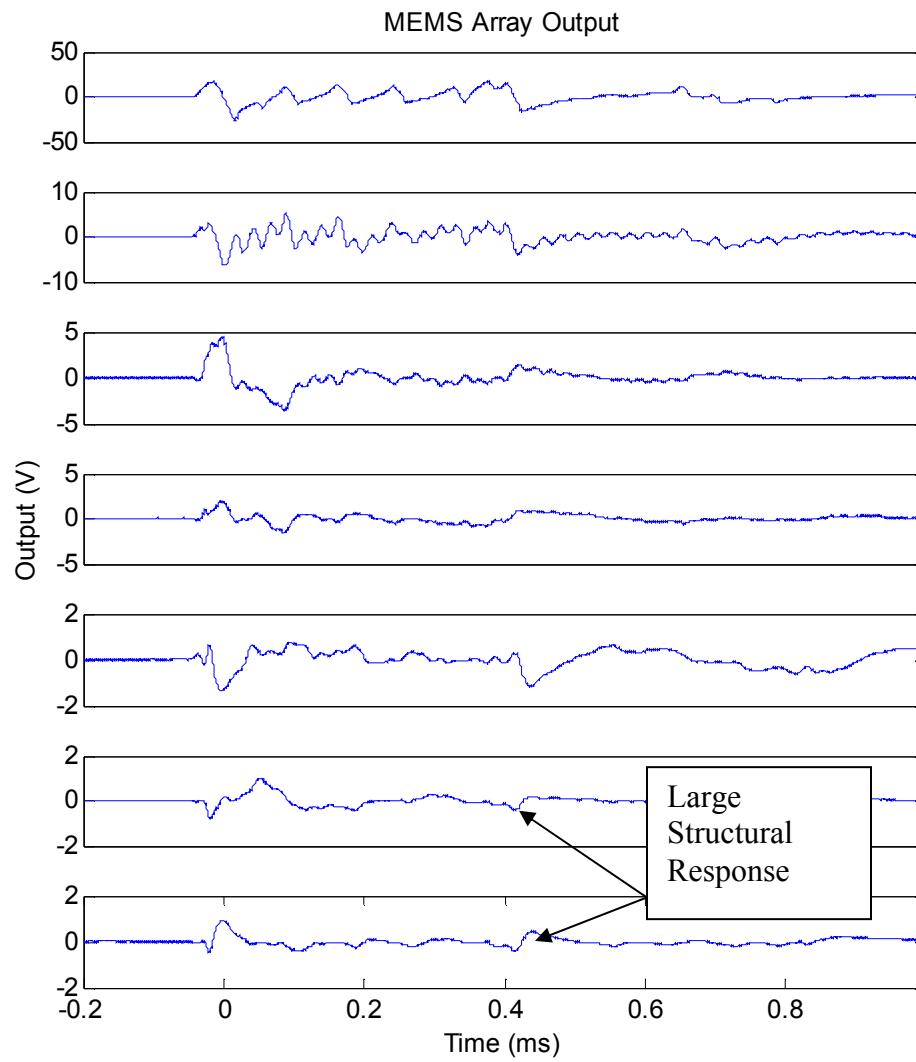


Figure 7.43: Array Spectrum from Acrylic and Teflon Ball Drops

Finally, an impact with a stainless steel ball was performed. The stainless steel had the largest amount of mass, but was not the shortest pulsewidth. Figure 7.44 shows the output of the full seven sensor array to that impact. Of particular note is the large amount of structural response seen due to the large mass of the stainless steel ball.



**Figure 7.44: Seven Sensor Array - Direct Stainless Steel Impact**

Figure 7.45 shows that same data after filtering is applied.

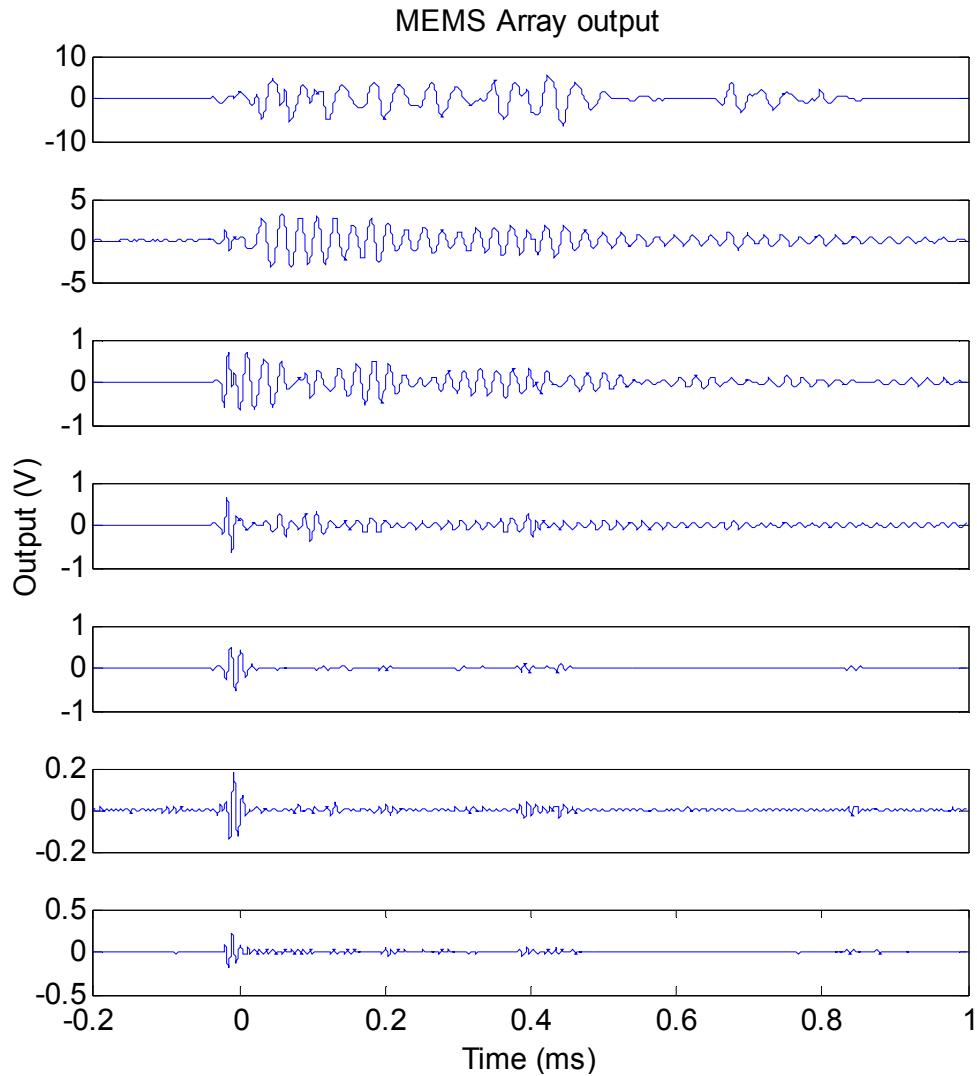


**Figure 7.45: Filtered Seven Sensor Array - Direct Stainless Steel Impact**

Figure 7.46 adds the responses from the Stainless Steel and Silicon Nitride ball drops to those of the Teflon and Acrylic drops. All of these ball drops occurred from the same height, but they all had different masses. Therefore, they all had different energies of  $E=mgh$ . This plot normalized the outputs by the mass of the ball. Teflon and Stainless Steel have the most mass. Silicon Nitride and Acrylic have the least.

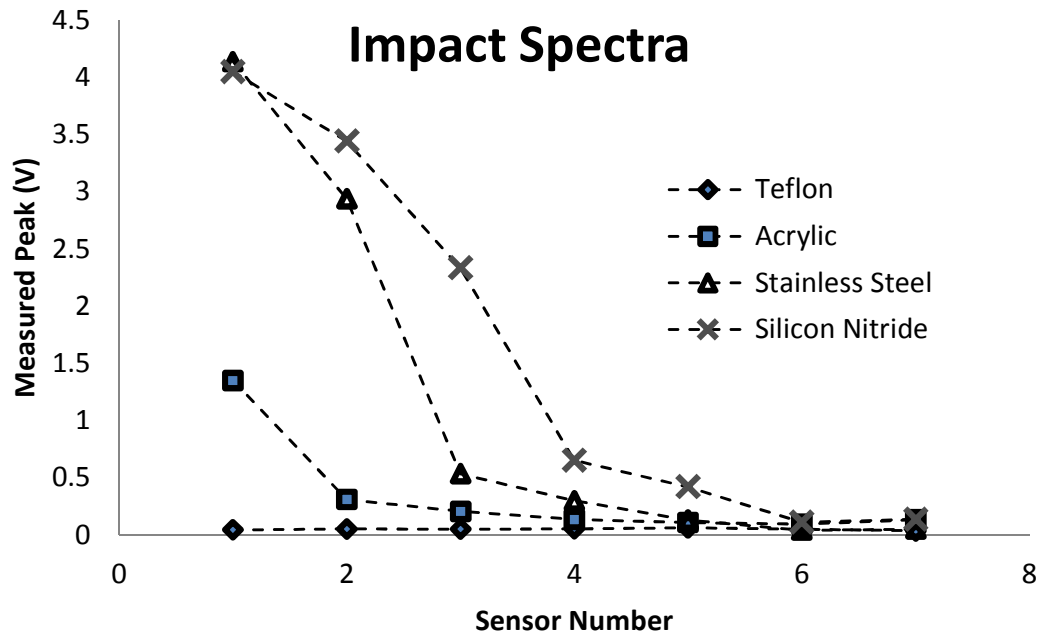


Figure 7.46: Array Spectra from Four Different Materials

Achieving this final result, which is very close to the predicted result, required mitigating a number of issues that arose in the actual fabricated devices.

1. The devices had to maintain a high quality factor throughout processing. In particular, flux residue often led to reduced quality factor and poor resonant processing performance.
2. Low-pass filtering was required to remove the larger lower frequency responses of the mounting system used in the test apparatus.
3. High-pass filtering was also required to remove higher frequency noise sources, and in particular, the resonant response of the disc onto which the sensor was mounted.
4. Low-pass filtering was also required on each sensor element in the array to remove cross-talk from the parasitic capacitance that existed between itself and the higher sensitivity, but lower-frequency sensors in the array.

5. The natural frequency of the structure on which the sensor array is mounted couples directly into the spectrum developed by the array. Using a higher natural frequency structure moved that error outside of the sensor array region.

## CHAPTER 8 - CONCLUSION

This chapter presents conclusions regarding the application of resonant sensor processing to the characterization of impacts, the integration of electrets into MEMS devices through an *in situ* process, and the design, fabrication, and application of a MEMS ultrasonic array to perform impact classification. In addition, potential directions for future work are presented and discussed.

### 8.1 Electret Comparison and Integration

The first component of this research effort was the development of new techniques for integrating electrets into MEMS structures.

Multiple electret options were explored in this work for application to an impact sensor array. Many factors were considered including performance of the material (*i.e.* dielectric properties, dipole, space-charge), type of material (*i.e.* organic vs. inorganic), material processing (*i.e.* spin coat, thin film deposition, screen print, etc.), polarization process (*i.e.* contact, corona, etc.), and compatibility with other MEMS process flows. At the end, corona charged polymer electrets were selected and *in situ* charging process developed.

The polymer space-charge electret was selected, using a fluoropolymer called CYTOP, which is similar to Teflon. CYTOP can be spun coat multiple times to achieve the desired thickness, has a high dielectric strength of 60kV/m, and is very robust to subsequent MEM processing. CYTOP has a low dielectric constant, making it unsuitable as a dipole electret, but serves well as a space-charge electret because of its high resistivity. The difficulty is that subsequent processing must not take the CYTOP near its glass transition temperature after charging has occurred or else the static charge can dissipate. Therefore, localized heating or *in situ* charging is required.

Multiple options for film charging were investigated. The use of composites with high-k dielectrics would potentially allow a more thermally-robust electret film that could survive post processing. Localized heating could be employed to apply higher temperature processes to the structure without harming the charged electret. Finally, *in situ* charging could be employed wherein electrodes within the structure apply charges post-fabrication and prior to operation.

The high-k composite material approach was promising for dipole electret films. In a dipole electret, the film is brought to its melting point, an electric field is applied, and the film is cooled. The issue is that thermal breakdown can occur when using contact electrodes. The high-k dielectric approach allows a thermally-stable film to be placed between the contact electrodes and the electret film without substantial reduction of the electric field in the material, thereby allowing a similar level of polarization. However, this effort finally selected the use of a space-charge electret, leading to no further development of the high-k dielectric composite film.

Localized heating was promising for allowing a pre-charged electret to survive post charging temperature extremes experienced in later MEMS process steps. Local heaters were achieved that could provide the necessary temperatures for a variety of bonding processes. In addition, the temperature of the electret film could be maintained below glass transition during the bonding process. However, this process option led to very complex full process flows because of the embedded heater structures, interconnect, and isolation layers. Therefore, this approach was not developed further.

The approach that was developed to the greatest extent in this work was the *in situ* charging approach. A suspended metal charging grid structure was realized just slightly suspended above the polymer film. When energizing the metal grid, a small electrical discharge occurs that results in permanent polarization of the film. Final static voltages achieved were not as high as can be achieved in standard corona charging, but much of this is due to leaving a floating metallic electrode within the structure. However, with this

process, MEMS structures could be fabricated above the electret using standard processes, and the electret charged after the full structure release. This approach was used to make a number of sensor arrays for testing and characterization.

In the *in situ* charging approach, a number of conclusions can be drawn. In the transducer array, the remnant voltage over the surface of the electret film is critical in determining the sensitivity of the device. *In situ* charging and typical corona charging both achieve comparable surface charge densities. However, microcorona charging has achieved only a portion of that remnant voltage given the same film thickness. The two primary issues are surface charge non-uniformity and metal masking of the field.

By its very nature, the *in situ* charging approach utilizing microcorona discharge at the edge of fine line features leads to a nonuniform charge distribution. The charges are localized to the area of the line edges. Therefore, a higher density of edges would yield a more uniform surface charge and an overall higher level of remnant voltage seen by the transducer.

This desire to increase edge density to improve uniformity is in direct opposition to the second issue that leads to reduced remnant voltages when compared to traditional corona-charging. That issue is the charging grid metal that remains on the electret surface after charging is complete. The state of charge of that metal geometry will alter the electric field seen at a distance. In general, the remnant voltage seen by the structure will be proportional to the area of metal used in the charging grid.

When evaluating these two issues together, the optimum charging would occur when the density of metal edges is maximized and the surface area of the metal is minimized. That naturally leads to reducing the width of the metal lines used in the charging grid. A higher density of edges can then be created while also reducing total metal area. Moving the process flow towards the creation of large area meshes with nanoscale metal lines could accomplish this, and would be performed in future research efforts.

A related impact of the *in situ* microcorona charging approach and the fact that the metal charging grid remains after charging is that that metal grid connects to other metal grids on the same die, leading to parasitic capacitance and sensor cross-talk when forming arrays of sensors simultaneously. For the sensor array developed in this work, that parasitic capacitance injected signals from other sensors into the signal of the sensor being captured. In this work, that signal was filtered out in software. Ideally, though, the parasitics would be reduced, thereby allowing removal of that signal processing step.

Removal of the parasitics could be accomplished in a number of ways. One obvious way would be to independently charge each electret area with its own charging pad, rather than having all charging sites connected to one pad. This would substantially increase process time and wiring complexity, however. A second approach would be to develop a fusing or switching mechanism that would allow the sites to be connected for the charging process, and then disconnected on the die for sensor operation. This would be another area of future research.

## **8.2 Array Processing Benefits and Challenges**

The second component of this research effort was the application of arrayed MEMS sensors to the processing of acoustic signals seen during impacts.

The first aspect of this was understating the stress pulses created by various impact geometries, material sets, and velocities. The frequency content of these stress pulses ties directly into the design of the sensor array and the interpretation of sensor spectra. Therefore, the formation of stress pulses and the characterization of those pulses in the test apparatus were both critical to calibrating and operating the sensor array.

For the impact scenarios investigated in this effort, a number of conclusions can be drawn that directly impact sensor design. First, for an impact event, there is actually little information available to discriminate one from the other. An idealized impact event

results in a simple Gaussian-like pulse with a pulsewidth and amplitude that depend on impact geometry, the materials involved in the impact, and the velocity of the impact.

Determining the materials involved in the impact is the goal of the sensor array. However, the impact geometry is critical in determining the materials in the interaction. The radius of curvature of each of the impacting materials plays a large role in the pulsewidth of the impact stress pulse. Therefore, controlling the geometry during the interaction is important. As such, the sensor needs to be on a structure with a known curved surface. In addition, the material being impacted by the sensor needs to have either a known curvature, or a radius of curvature that is much higher than the curvature of the sensor structure. Furthermore, to avoid errors in the spectrum interpretation, the curved structure that the sensor is mounted on should have a natural frequency outside the range of interest of the sensor array.

After determining the characteristics of stress pulses created by impacts, multiple sensor types were investigated. Piezoelectric discs were the baseline transducer. These discs have very high bandwidth and are commonly available. They were used to capture impact waveforms from different sized plates and structures. These waveforms identified frequencies of interest and guided the design of suspended MEMS diaphragms with filtering and natural frequency characteristics. An array of laser micromachined diaphragms was fabricated, as well. These had very high natural frequencies, but demonstrated the post-fabrication charging capability in the charging grid *in situ* process flow. Since every device in the array had very high natural frequencies, they were not useful in the array processing approach.

The microfabricated transducer array was the important test article in the array processing effort. These devices were designed to have natural frequencies in the region of interest for the plates and other structures onto which they would be attached. After fabrication and polarization, these sensors were attached to the structures, and waveforms collected and analyzed to develop the following challenges.

The first challenge was in achieving the desired frequency characteristics of all the sensors in the array. The microfabricated sensors in this effort were based on a SU8 release process that built the structures on top of uncrosslinked SU8. The uncrosslinked SU8 had the tendency to shrink, whereas crosslinked SU8 did not. Therefore, the resulting structures exhibited a curvature that increased their natural frequencies. In addition, the process led to a different change in natural frequency for each structure. To be useful in array processing, the natural frequencies would need to be more precisely controlled during fabrication.

In addition, the process variations led to a variety of mechanical sensitivities for each transducer in the array. This aspect can be easily calibrated out, however. An acoustic signal can be input into the array and the frequency swept while recording the output. The gains for the readout amplifiers can be set to equalize the mechanical sensitivity of the sensors prior to operation.

The quality factor is also critical for the array processing. The devices developed in this effort had a relatively low quality factor. This led to difficulty in discriminating the ringing of the sensor from the underlying lower frequency signal. This can also be improved by applying high pass filtering to the sensor output signal, although this would increase the size and power consumption of the array.

Finally, for impact classification, the natural frequencies of the sensors in the array need to be less than the natural frequencies of the structure on which the array is installed. If not, then the response of the structure may be more evident than the actual impact. It is possible, though, to use the natural frequencies and oscillations of the structure as the impact discriminator, though, and match the natural frequencies of the transducers to those structural oscillation modes.

With these challenges, however, the sensor array did provide impact discrimination in a substantially smaller footprint and power consumption level than the baseline system consisting of high bandwidth transducers, analog-to-digital converters,

and an FPGA. Maybe even more importantly, the sensors used were more sensitive to impacts than the piezoelectric film transducers used in the baseline system, making them strong candidates for further application.

### 8.3 Future Work

This research effort focused on initial investigations into *in situ* charging of electret films within a MEMS device, and application of that to initial sensor arrays for the analysis of acoustic signals due to impacts. Further work can be performed in both areas.

Regarding *in situ* charging of electrets, only one type was demonstrated in this effort, the polymer space-charge electret. The method could also be applied to inorganic electrets, as well as other polymeric materials. In addition, the high-k dielectric composite approach is also applicable to *in situ* charging, but needs to be demonstrated on a suitable polar polymer.

Further work in the microcorona charging grid development would include developing advanced models for the process that would allow optimization of the static voltage achieved. Metal spacing, air gap to polymer surface, and charging gas are all variables that need to be further explored. Furthermore, the impact of the floating metal grid that remains within the structure needs to be quantified.

In terms of the transducer array, future work would include refining the process flow to achieve more precise control of the post-fabrication frequencies, mechanical sensitivities, and quality factor. In particular, increasing the quality factor would significantly aid in the application of the sensor array to spectral measurements. Furthermore, developing processes that would result in lower resonant frequencies with similar device size would be beneficial for acoustic emission events. The sensors designed so far were slightly too high.

Finally, for many applications, the high energy impacts lead to acoustic signals that are very large. The sensors developed in this effort need to be demonstrated using other material sets, and in particular, through the use of different substrates than silicon. Silicon's brittleness is detrimental in high-energy impacts. Fabricating the sensor array in a process that used only nonfrangible materials would be significantly useful in these impact scenarios.

## APPENDIX A. COUPLED RESONANCE TESTS

When performing array characterization through driving the sensor elements into resonance using a piezoelectric actuator, the technique described in Chapter VII yielded the accurate frequency scans of only the sensor elements. However, other mounting scenarios were employed with a driven sensor configuration. This appendix presents these additional mounting scenarios. Some of these mounting scenarios suggested potential applications for a resonant sensor array combined with a piezoelectric actuator.

Figure A.1 shows sensor one's output when the unit was not oil coupled to a large Teflon block, but simply resting on the table. This frequency scan showed additional resonance peaks, and led to further exploration of mounting arrangements.

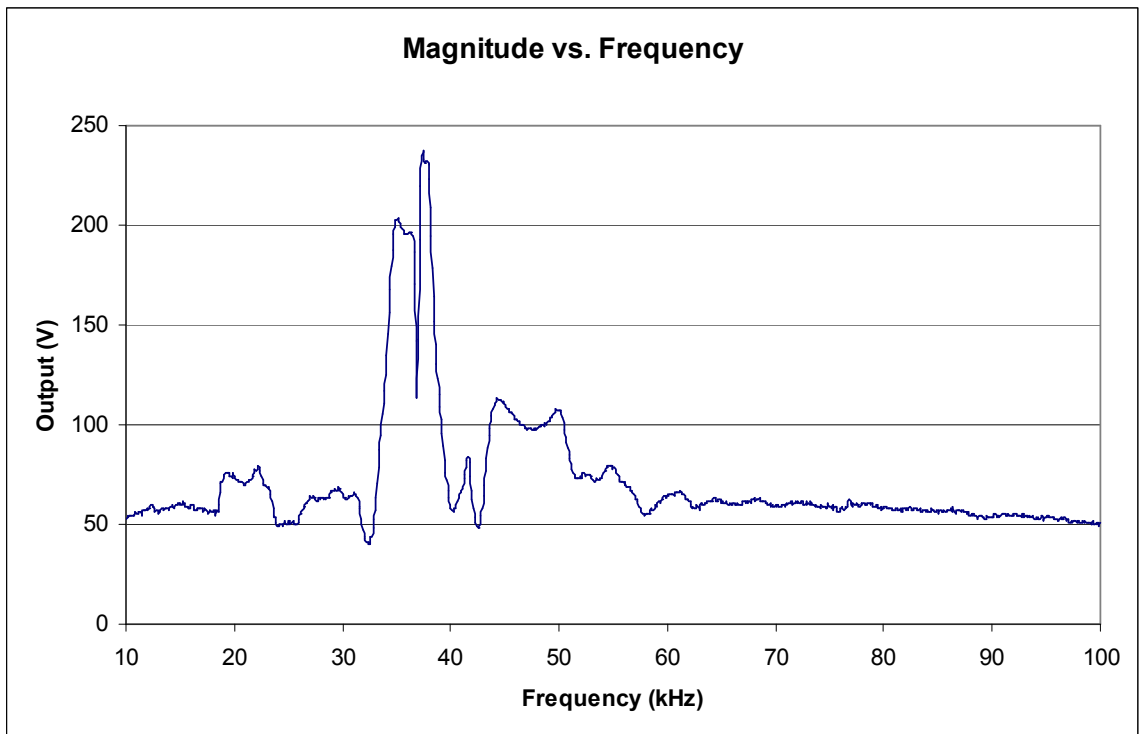
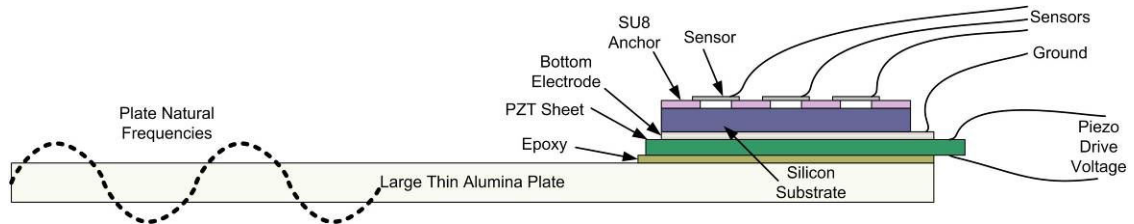


Figure A.1: Frequency Response of Sensor One when Resting on A Table

The sensor element and piezoelectric driver were epoxy attached to a large thin alumina plate as shown in Figure A.2.



**Figure A.2: Driven Sensor Array Attached to Large Thin Plate**

Figure A.3 through Figure A.8 show the output of the sensor die during scanning the drive frequency of the piezoelectric actuator. The plate had multiple resonant modes that interact with the resonant modes of the sensor array. The interesting feature is that the phase difference between the sensor modes and the plate modes leads to a very strong coupling between the two. This is potentially useful in monitoring the structural properties of the alumina plate.

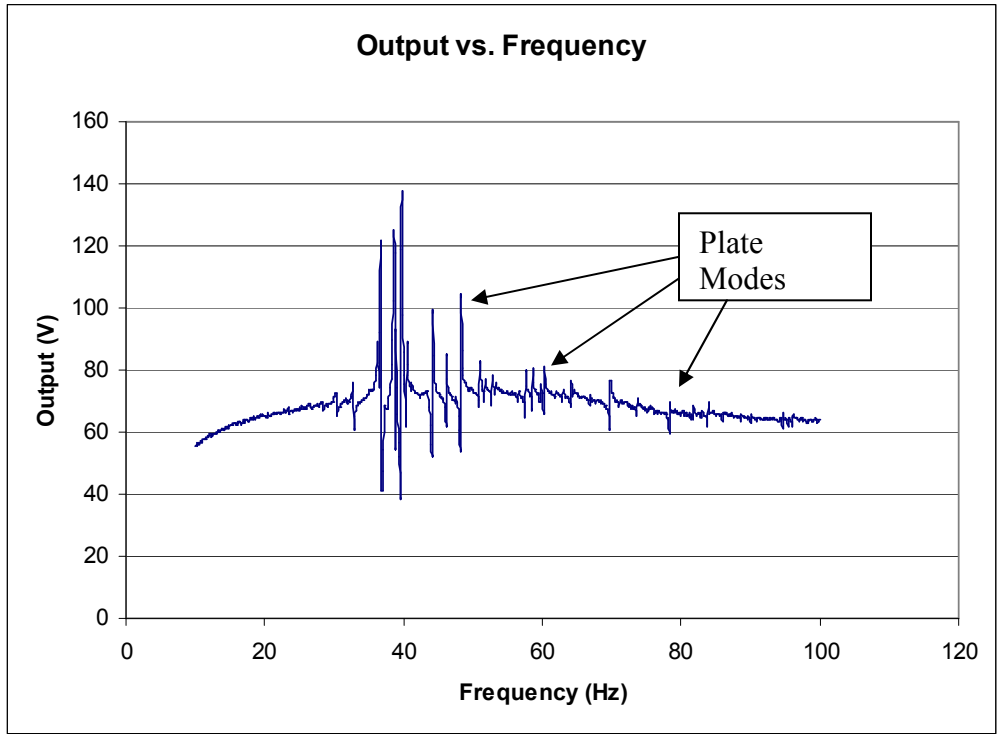


**Figure A.3: Sensor One Frequency Response on Large Alumina Plate**

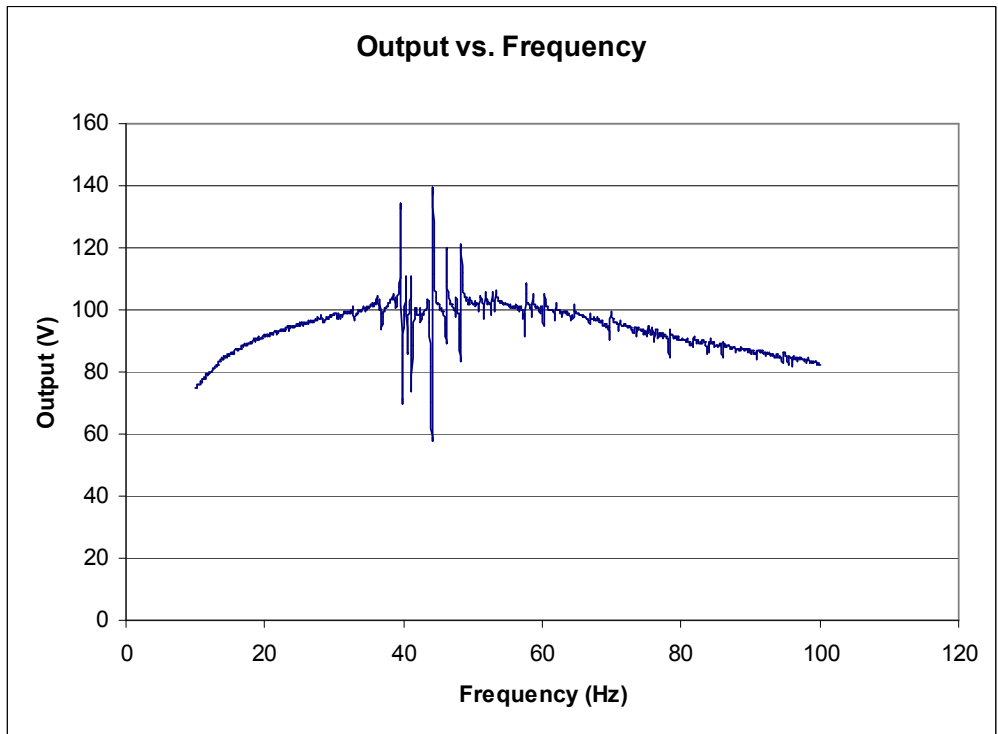


**Figure A.4: Sensor Two Frequency Response on Large Alumina Plate**

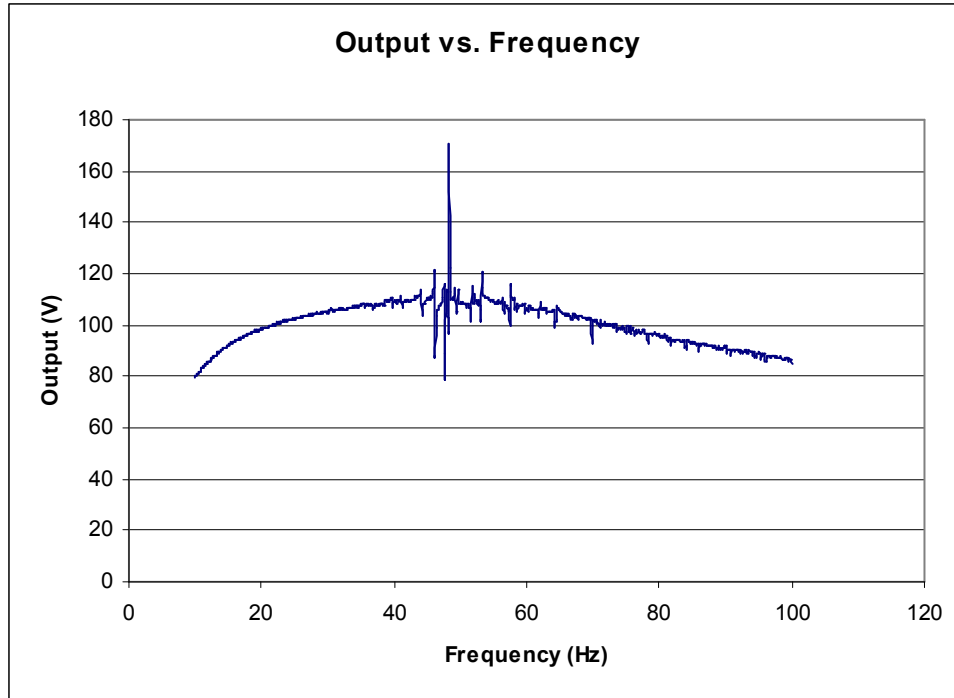


Figure A.5: Sensor Three Frequency Response on Large Alumina Plate

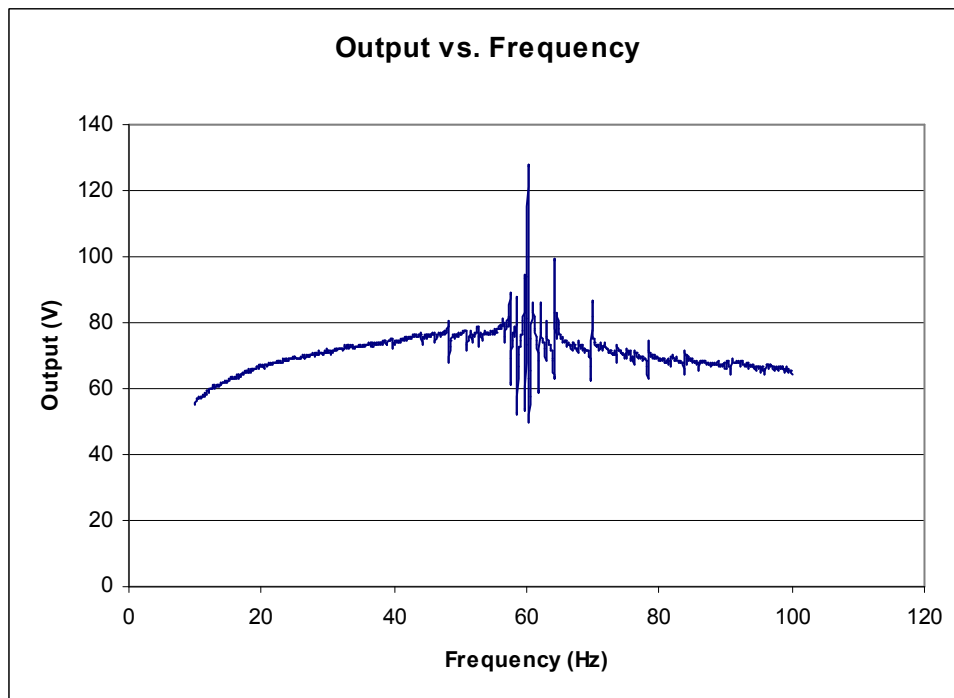
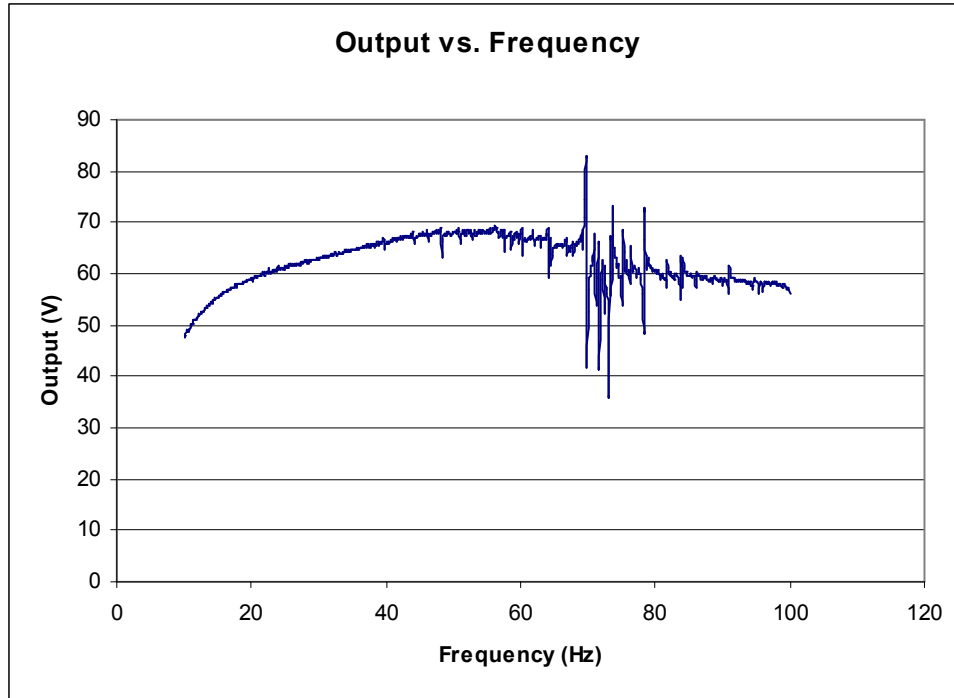
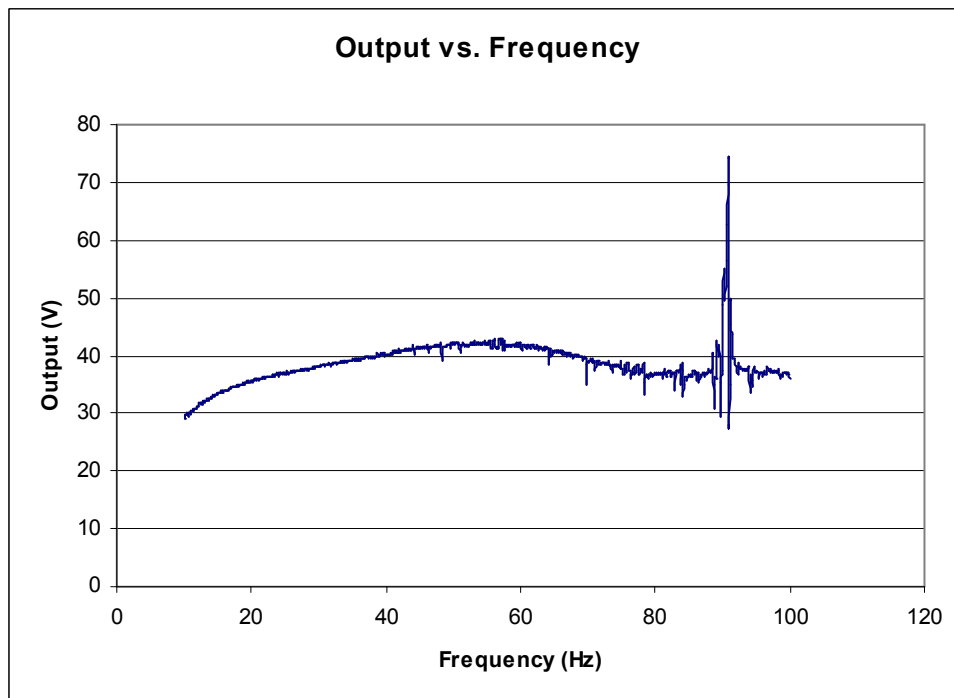


Figure A.6: Sensor Four Frequency Response on Large Alumina Plate



**Figure A.7: Sensor Five Frequency Response on Large Alumina Plate**



**Figure A.8: Sensor Six Frequency Response on Large Alumina Plate**

This strong coupling between the natural modes of the plate and the resonant frequency of the elements in the sensor array suggests an application of the array combined with the piezoelectric driver operating in an active arrangement. In many structural health monitoring applications, it is desirable to determine whether or not the properties or geometry of a structure have been altered or affected by the environment, by operational fatigue, or by accidental damage. The high quality factor of the sensor array elements, tuned to specific resonance modes of the structure can provide a highly sensitive indicator of changes to that natural frequency when the system is excited by an actuator similar to the piezoelectric device used in the above frequency scans. This could provide an efficient and low-power sensor for detecting potential structural issues quickly and with high levels of sensitivity.

## APPENDIX B. TEST SERIES RESULTS

This appendix presents test results from the chronological development test series described in Chapter VII. Multiple array versions, mounting structures, and impact scenarios were employed as described in Chapter VII. This appendix presents results from that test series that led to the final results that were presented in that chapter.

### B.1 Single Laser Micromachined Device

A simple electret sensor was fabricated by laminating a metal diaphragm over a charging grid region, as shown in Figure B.1, and then performing a post-lamination charging process.

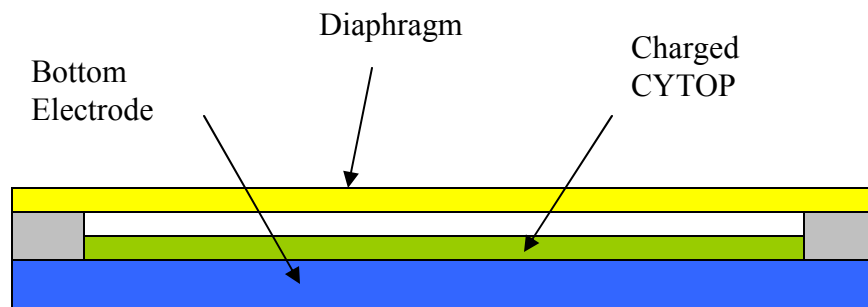
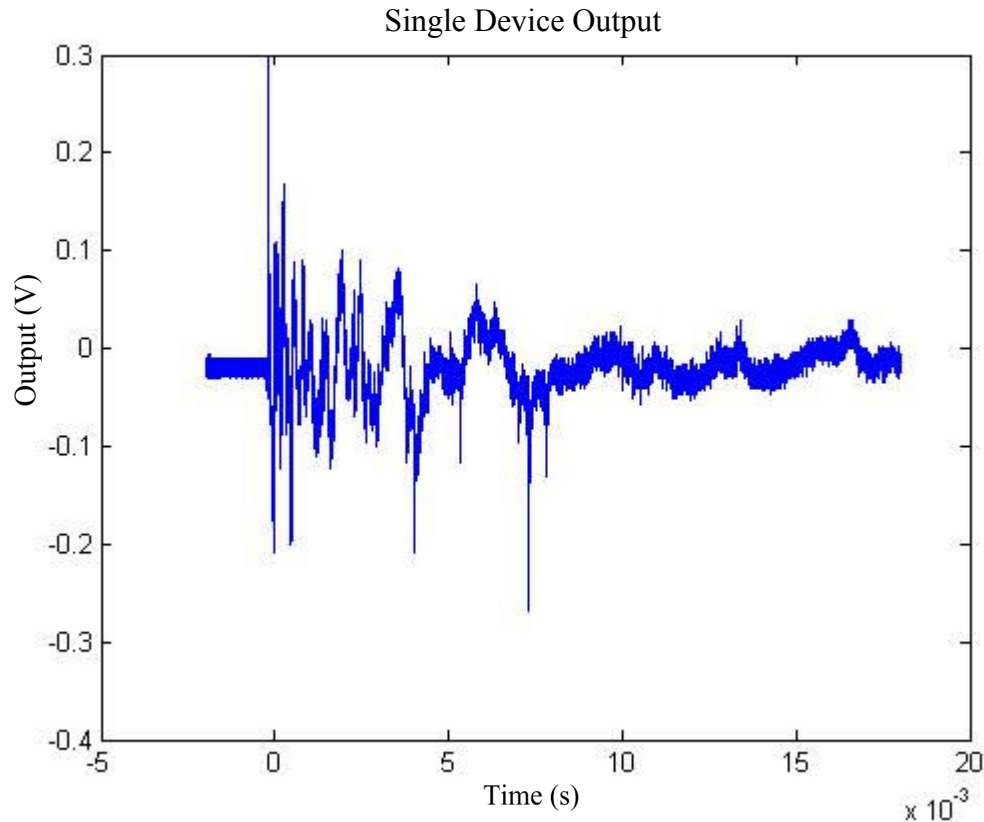


Figure B.1: Cross-section of Single Laser Machined Transducer

This sensor was placed on a steel cone. The cone is placed in the ball drop apparatus that allows spheres composed of different materials to be dropped onto the structure from a repeatable height and the sensor output recorded in Figure B.2. The x-axis is time, and the y-axis is output voltage recorded on a standard oscilloscope without amplification.



**Figure B.2: Single Transducer Output**

This test simply demonstrated that *in situ* charging could be performed, and that a reasonable output voltage could be achieved. Further tests determined performance capabilities, error and noise sources, and signal processing requirements for the sensor arrays.

### **B.2 Large Plate Results**

A large aluminum plate was instrumented with a laser machined array transducer, and a microfabricated array transducer. The plate has important modes at anticipated frequencies of 1600 Hz, 4000Hz, and 7600 Hz as determined from FEA (Figure B.3 and Figure B.4). The natural frequencies for all of the attached sensors were higher than these modes, so it was not anticipated that transducer characteristics would impact the

waveforms to a large degree. This test was used to simply verify accurate operation of the sensors.

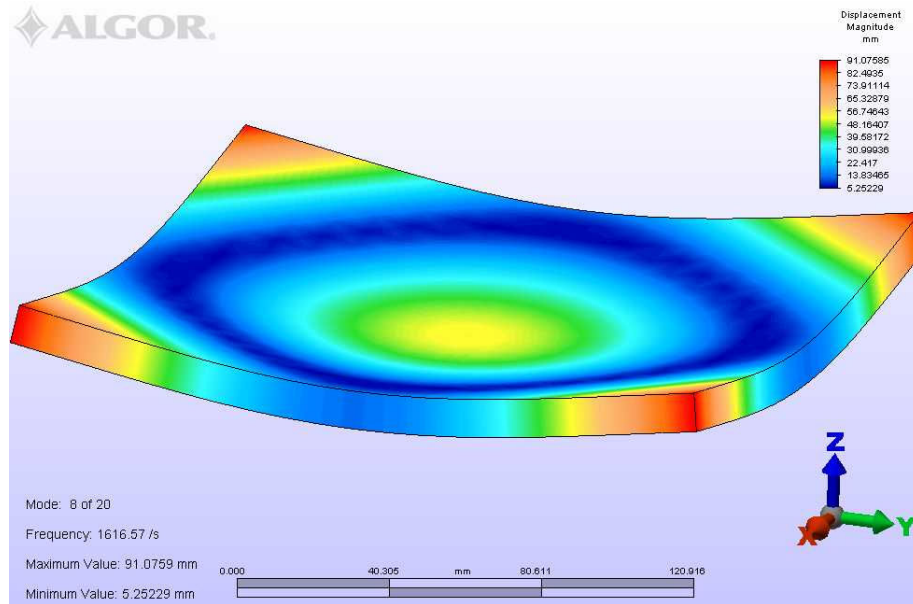


**Figure B.3: First Mode of Large Plate**

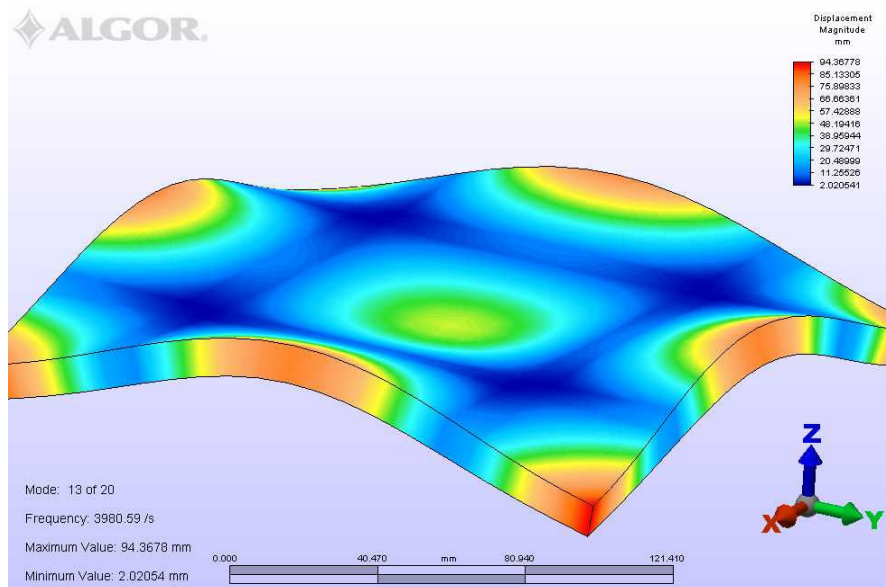


**Figure B.4: Second Mode of Large Plate**

The following four figures show the response of the laser and microfabricated array sensors to a Teflon impact on the plate.

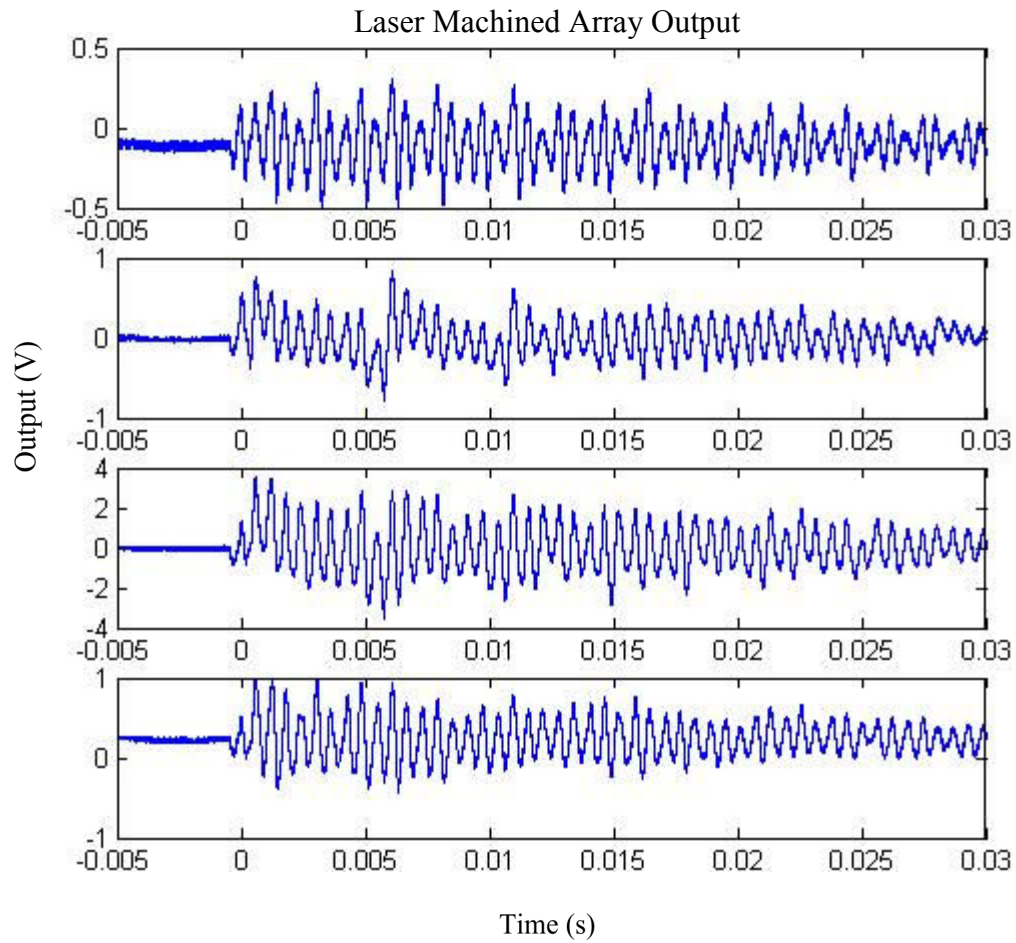


**Figure B.5: Laser Fabricated Array - Teflon Hammer on Large Plate**

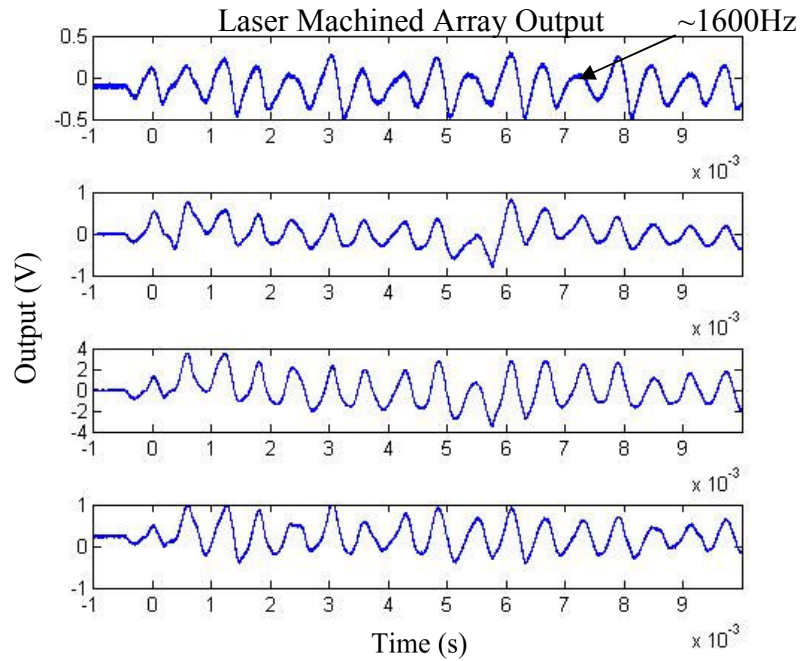


**Figure B.6: Laser Fabricated Array - Teflon Hammer on Large Plate (Close-Up)**

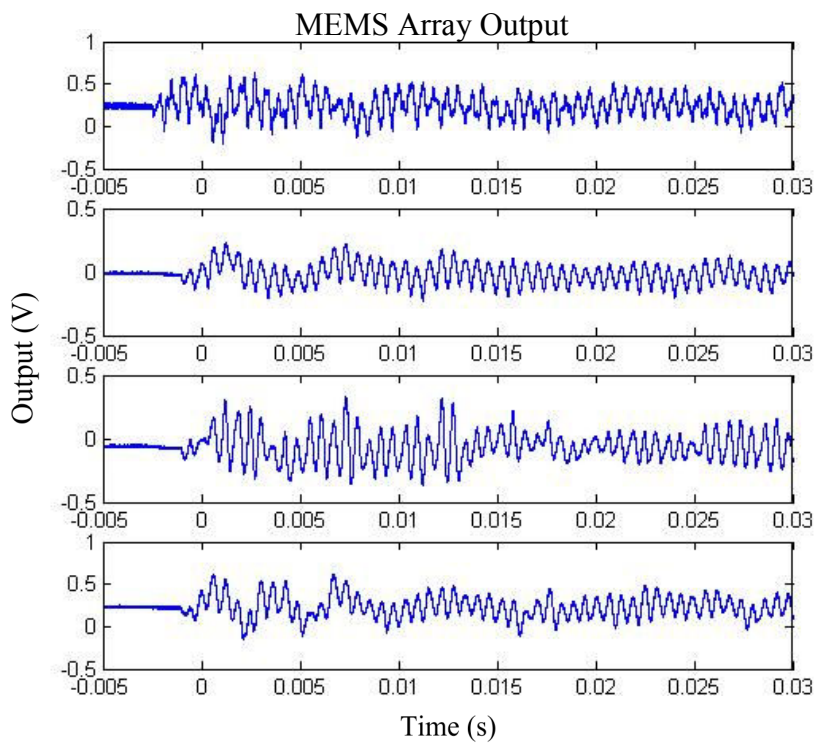


**Figure B.7: Microfabricated Array - Teflon Hammer on Large Plate**

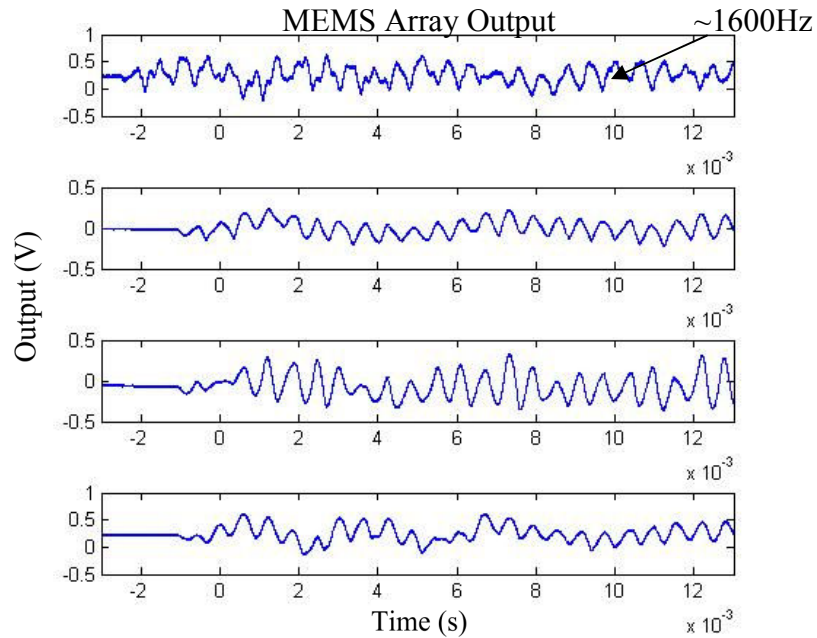


**Figure B.8: Microfabricated Array - Teflon Hammer on Large Plate (Close-Up)**

All of these waveforms show a primary natural oscillation with a frequency on the order of 1600 Hz, as expected. These sensors are primarily responding to the lowest natural frequency of the plate and its natural oscillation after impact.

The next set of four figures shows the response of the laser and the microfabricated sensor arrays to a steel impact on the same plate.

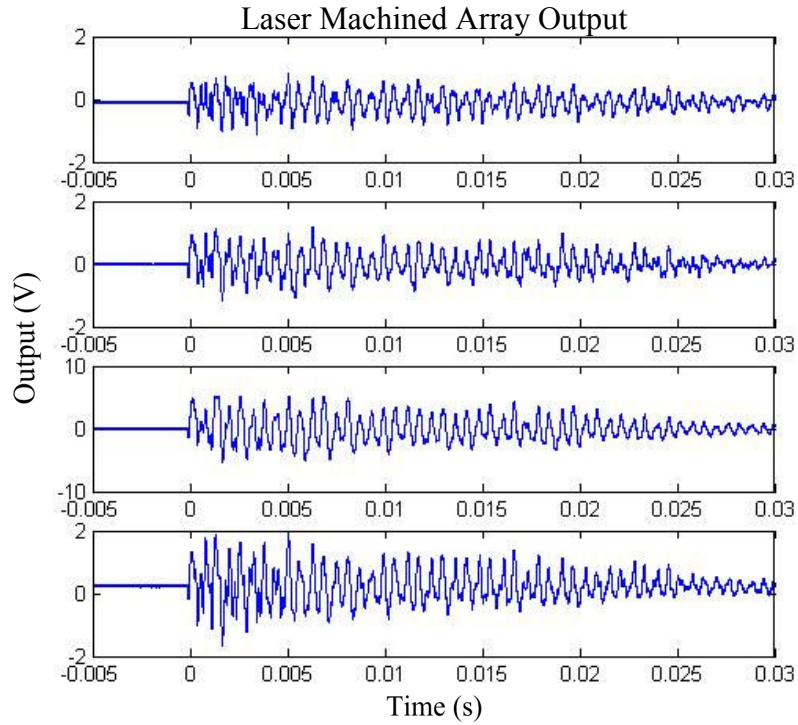


Figure B.9: Laser Fabricated Array - Steel Hammer on Large Plate

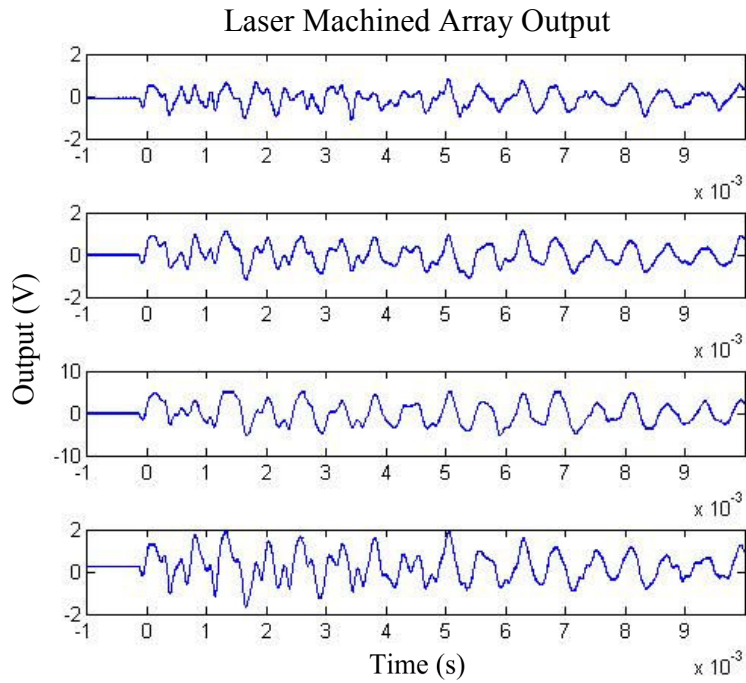


Figure B.10: Laser Fabricated Array - Steel Hammer on Large Plate (Zoomed In)

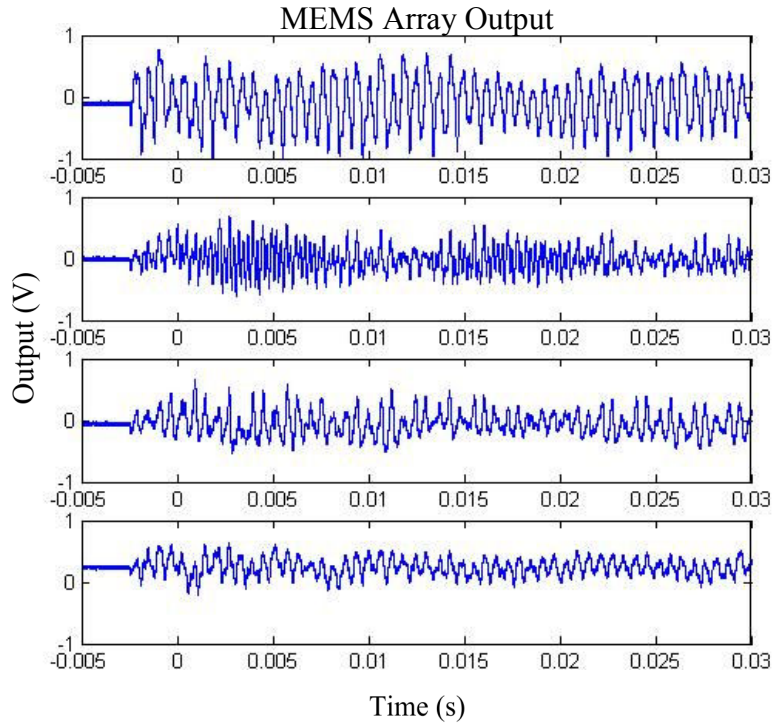


Figure B.11: Microfabricated Array - Steel Hammer on Large Plate

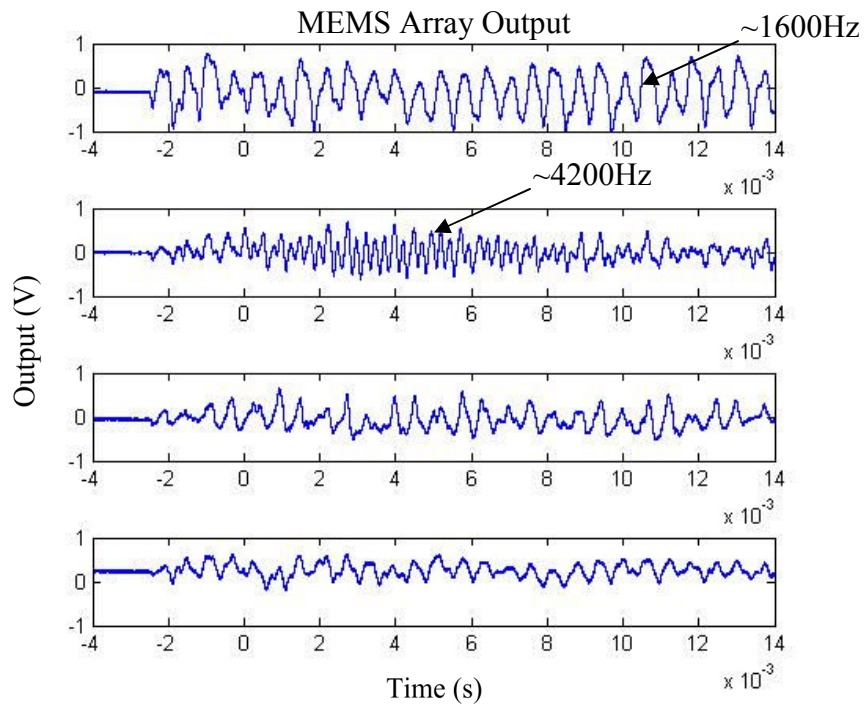
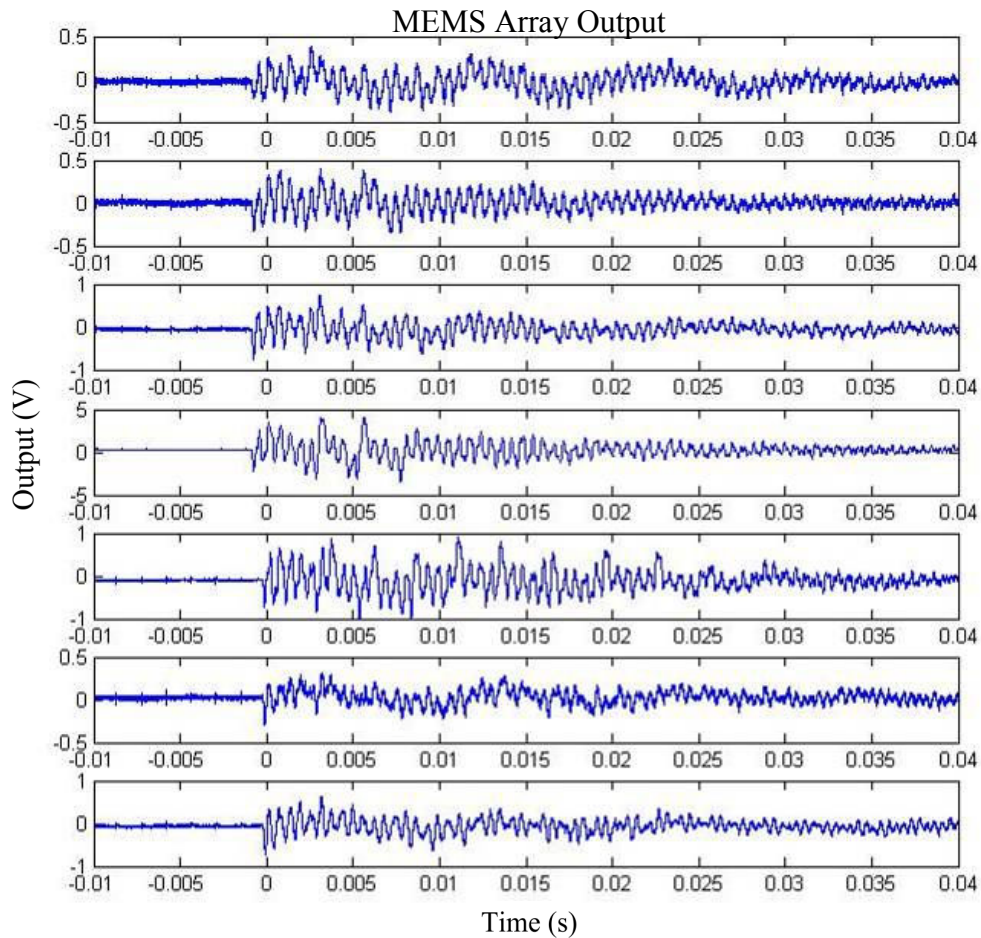


Figure B.12: Microfabricated Array - Steel Hammer on Large Plate (Close-Up)

Again, the primary frequency seen in these tests is the fundamental 1600Hz of the plate itself. However, the second transducer in the microfabricated array picked up a substantial amount of an approximately 4200 Hz oscillation. This is very likely due to the second natural frequency of the plate itself.

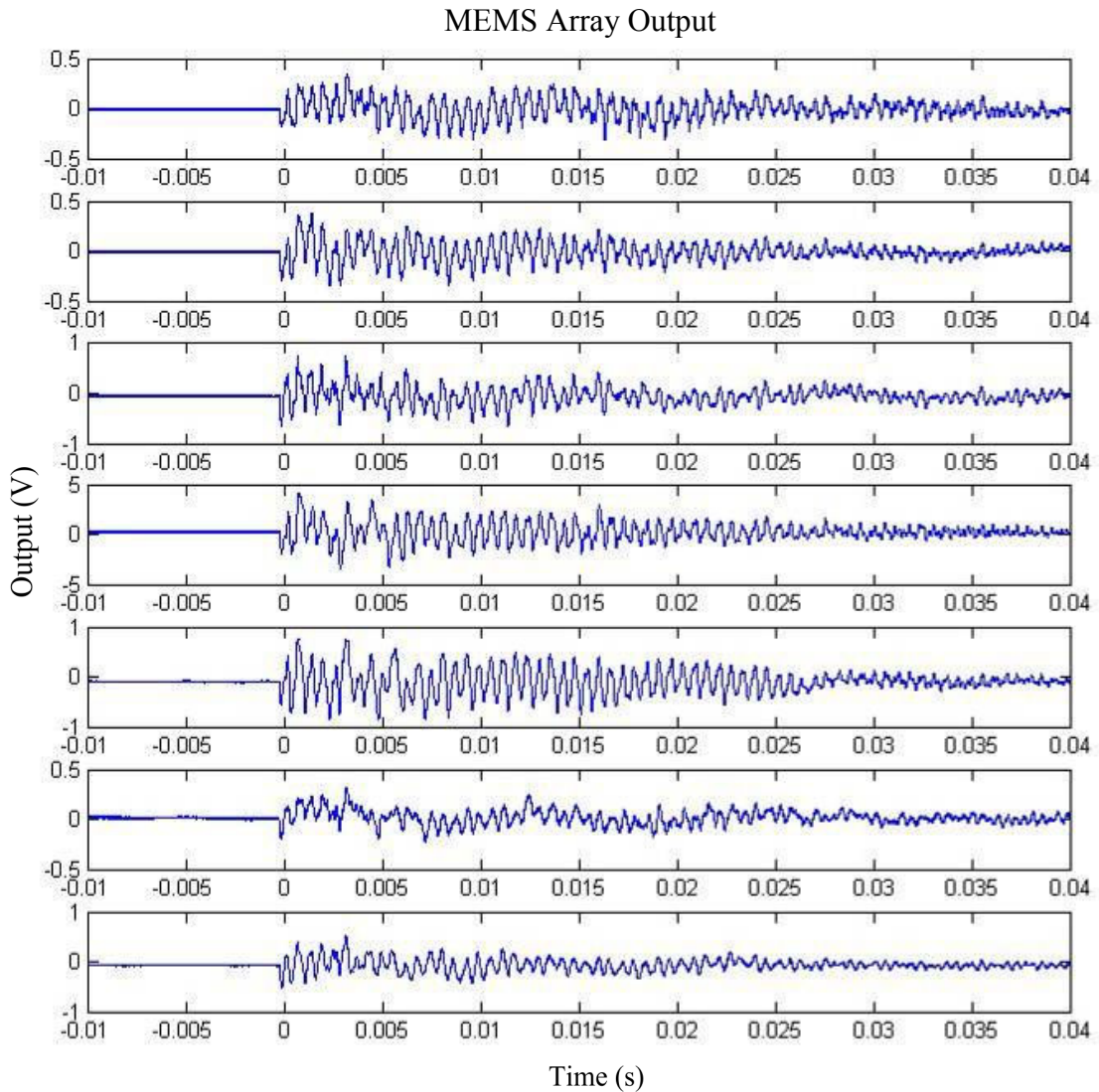
To demonstrate and characterize consistency from sensor to sensor and drop to drop, a second microfabricated array was attached to the large plate. Figure B.13 shows the output of all seven sensors.



**Figure B.13: Seven Sensor Array - Steel Impact on Large Plate**

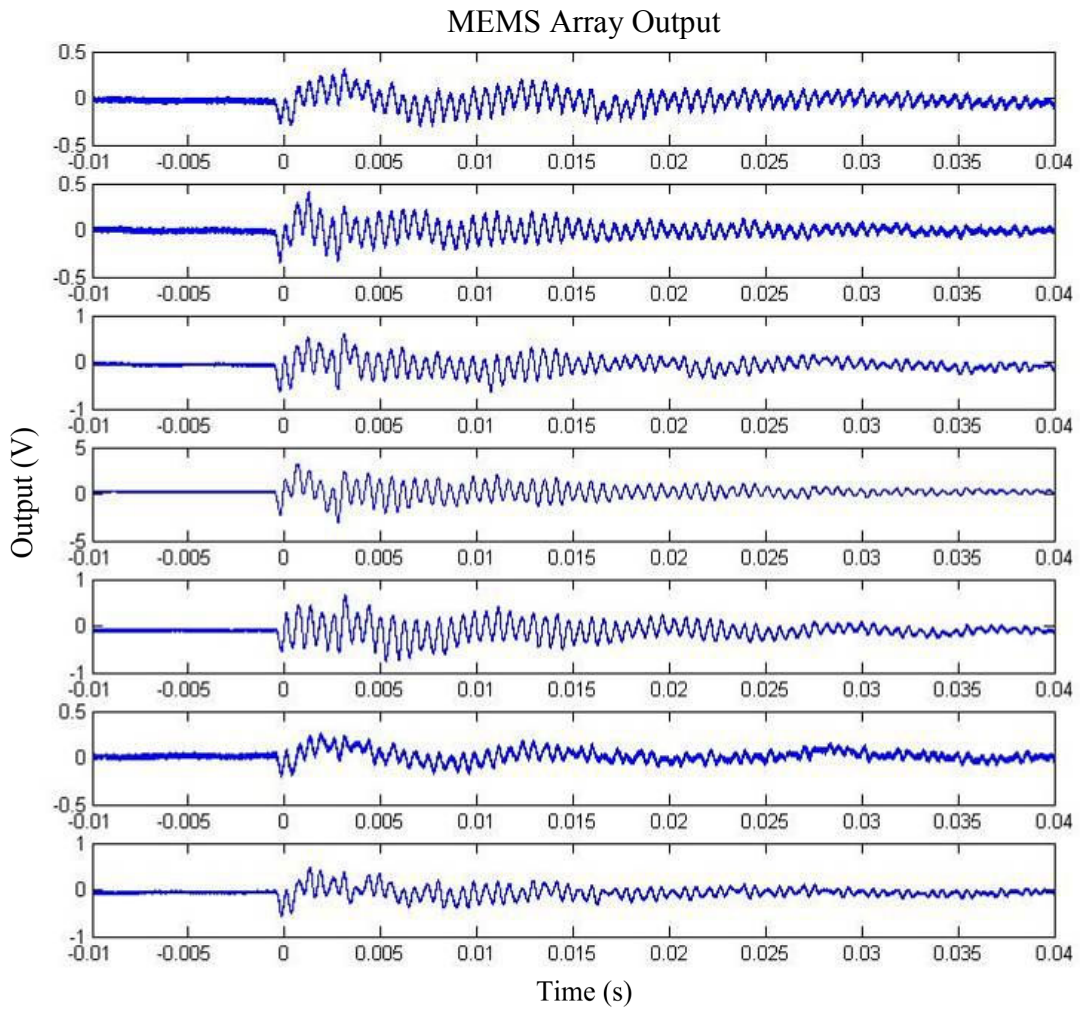
A second impact was captured using the same sensor set, and it is shown in Figure

B.14.



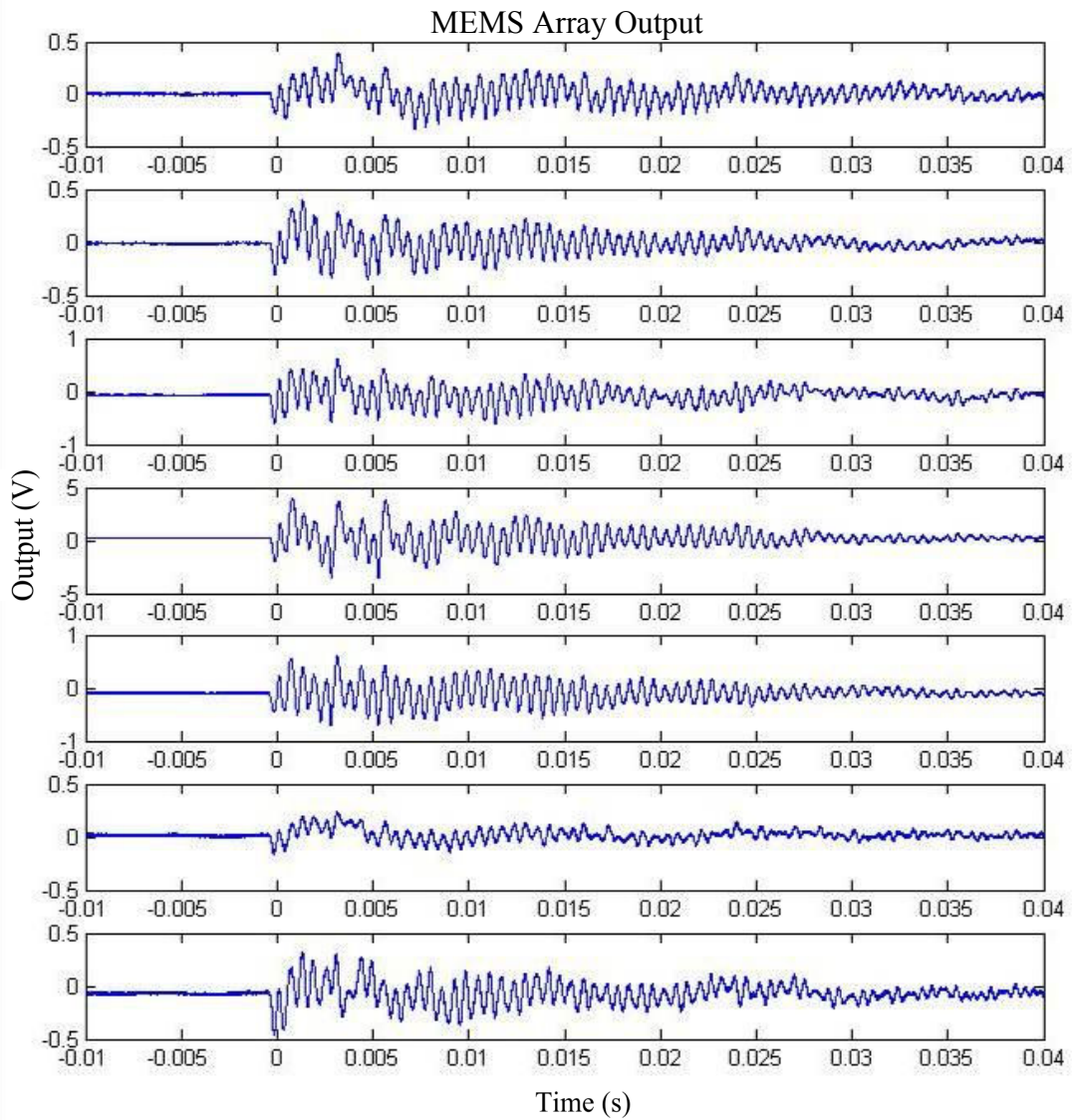
**Figure B.14: Seven Sensor Array - Steel Impact on Large Plate (second shot)**

Similarly, two impacts with Teflon hammer were performed using this second seven transducer array. Figure B.15 shows the waveforms collected from the first of these two impacts.



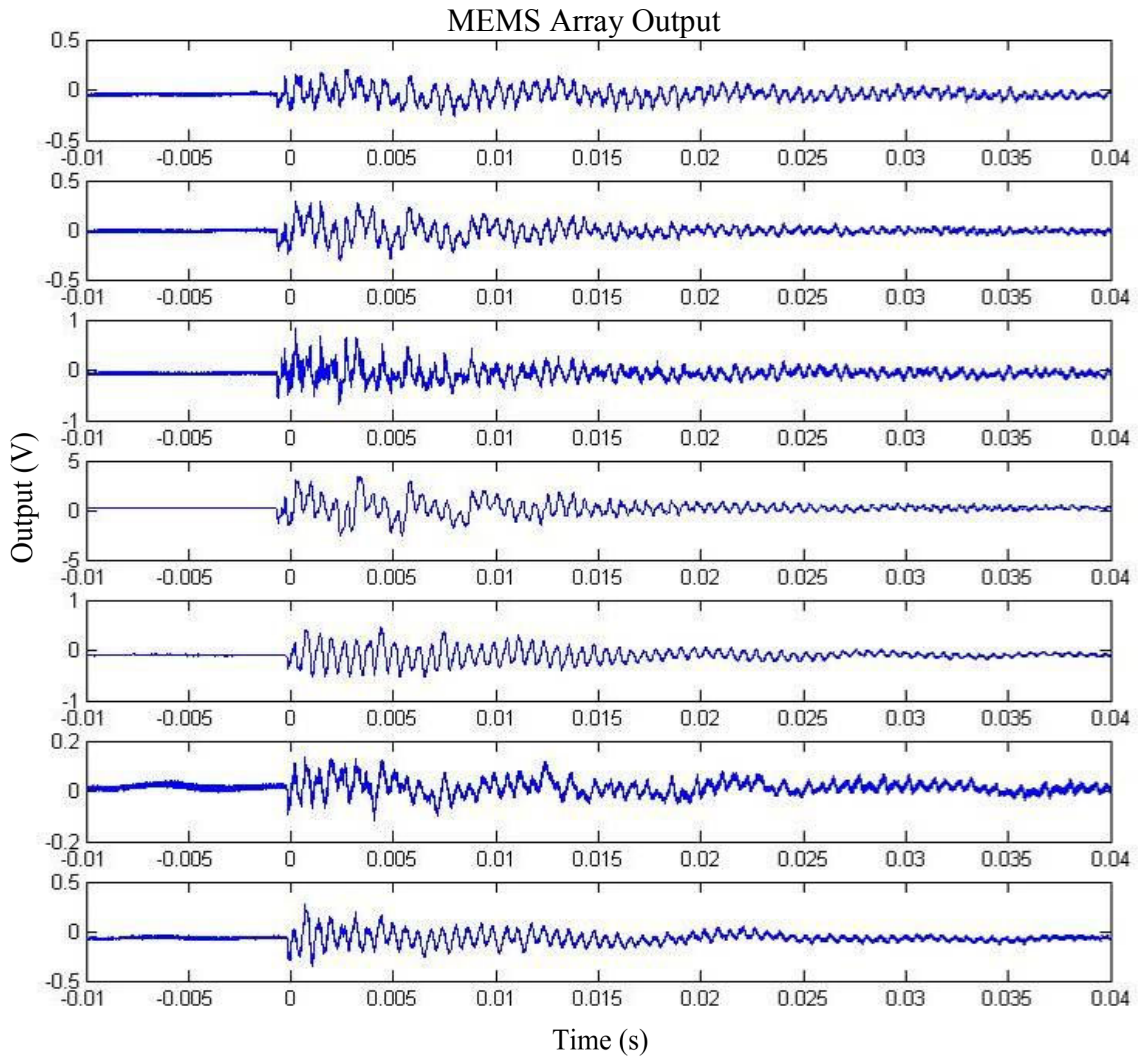
**Figure B.15: Seven Sensor Array - Teflon Impact on Large Plate**

Figure B.16 shows the data from the second impact.



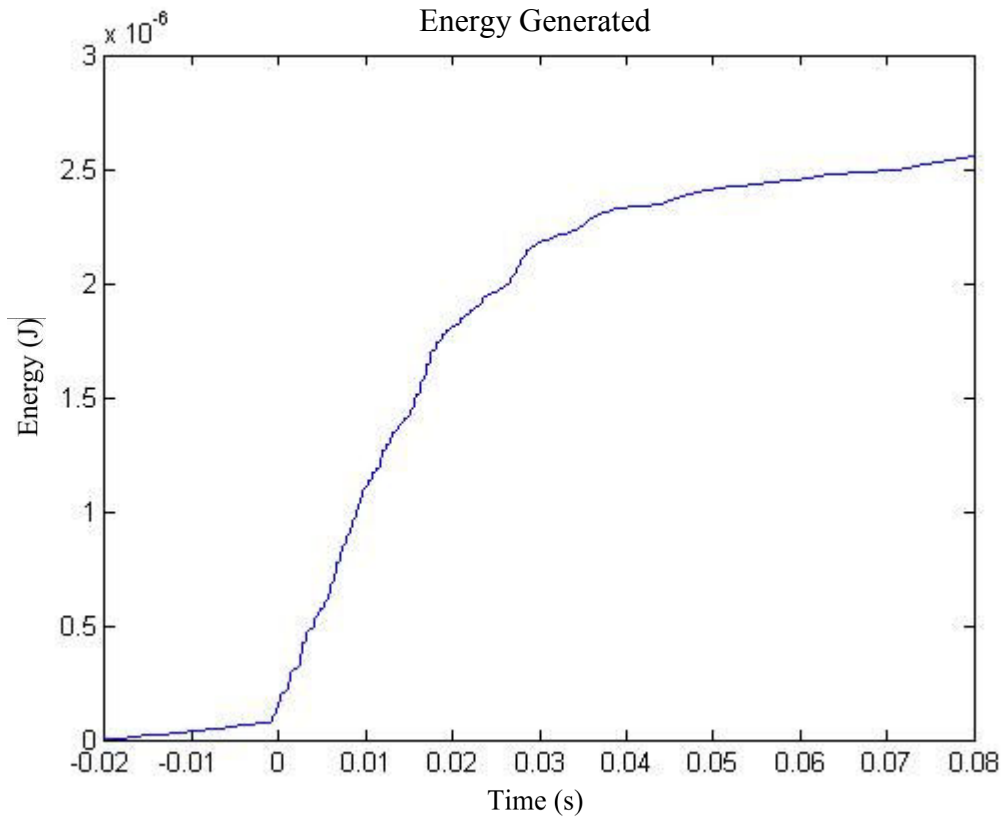
**Figure B.16: Seven Sensor Array - Teflon Impact on Large Plate (second shot)**

Figure B.17 shows the output from the same array to a stainless steel ball drop.



**Figure B.17: Seven Sensor Array - Impact from a Stainless Steel Ball**

On a related note, the energy scavenged by the device from an impact was also calculated when impacting a large plate. Figure B.18 shows the amount of energy scavenged from the same impact. A total of 2.5 micro Joule was collected over a period of 50ms, equivalent to a power output of 50microWatts.



**Figure B.18: Scavenged Energy from Large Plate Impact**

### **B.3 Small Plate Results**

A smaller aluminum plate was also instrumented with a laser machined array transducer and a microfabricated array transducer. The plate has important modes at frequencies of 4750Hz and 7220Hz, as determined from FEA (Figure B.19 and Figure B.20). The bandwidths for all of the attached sensors were still higher than these modes, so it was not anticipated that transducer characteristics would substantially affect the waveforms.

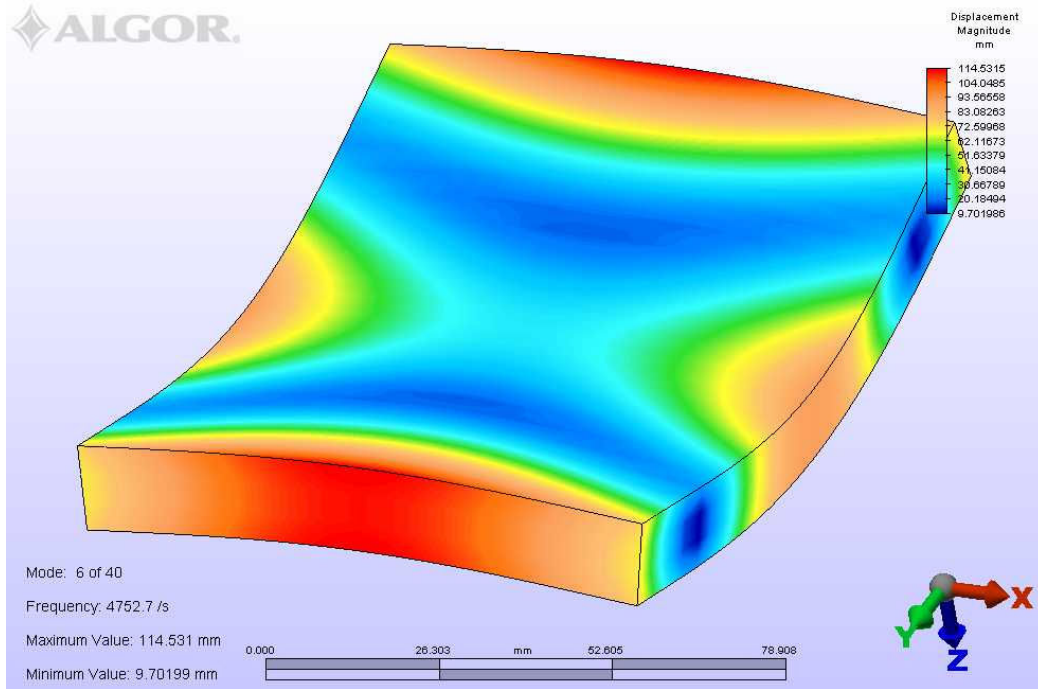


**Figure B.19: First Excited Mode of Small Plate**

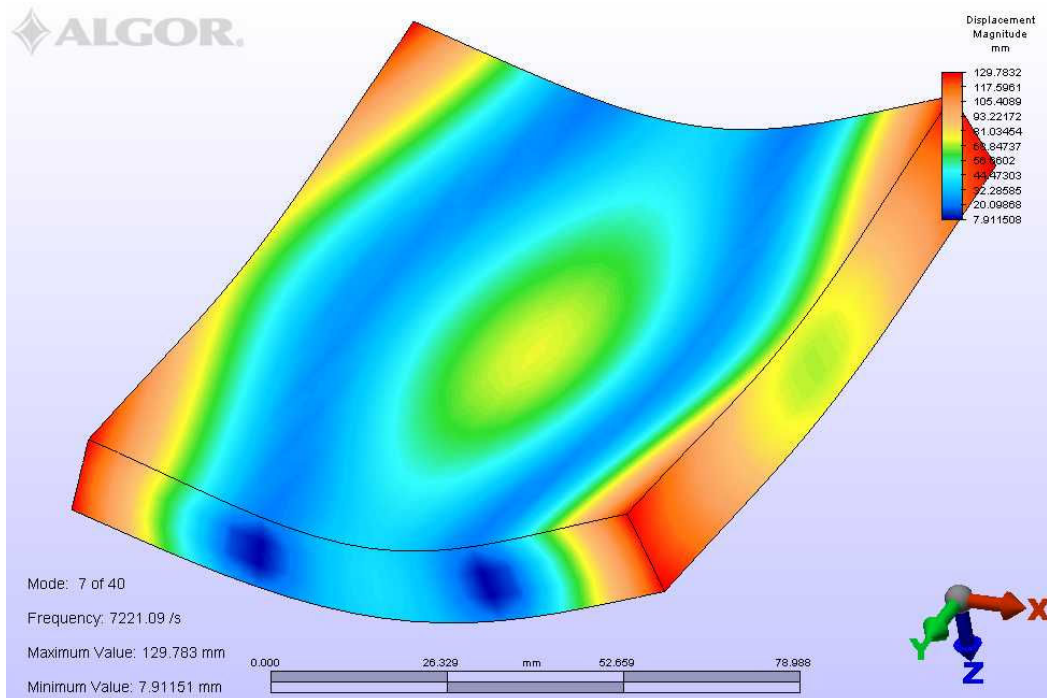


**Figure B.20: Second Excited Mode of Small Plate**

The following four figures show the response of the laser and microfabricated sensor arrays to a Teflon impact on the plate. Rigid plate motion is seen in these waveforms. This signal is from the flexibility of the mounting supports on which the plate is held during impact.

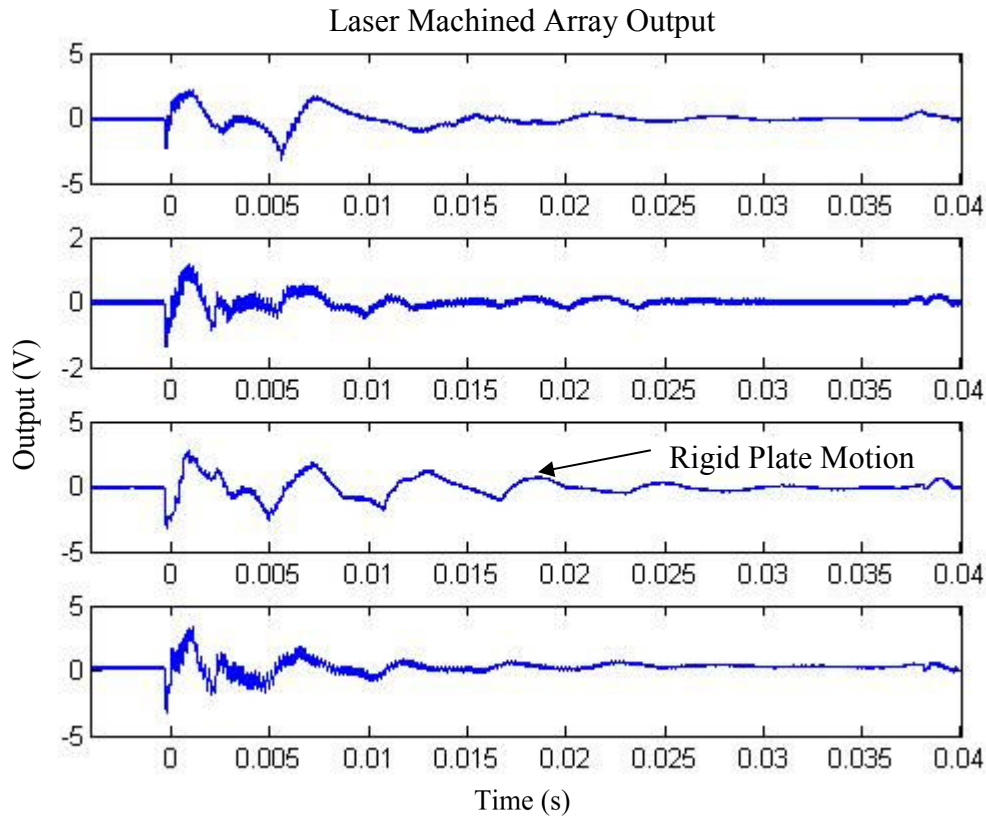


**Figure B.21: Laser Fabricated Array - Teflon Hammer on Small Plate**

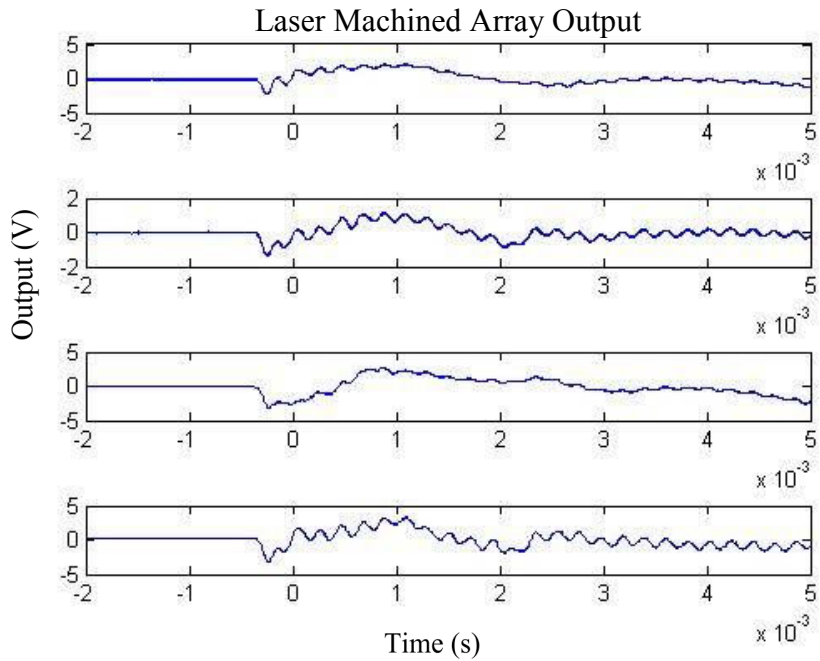


**Figure B.22: Laser Fabricated Array - Teflon Hammer on Small Plate (Close-Up)**

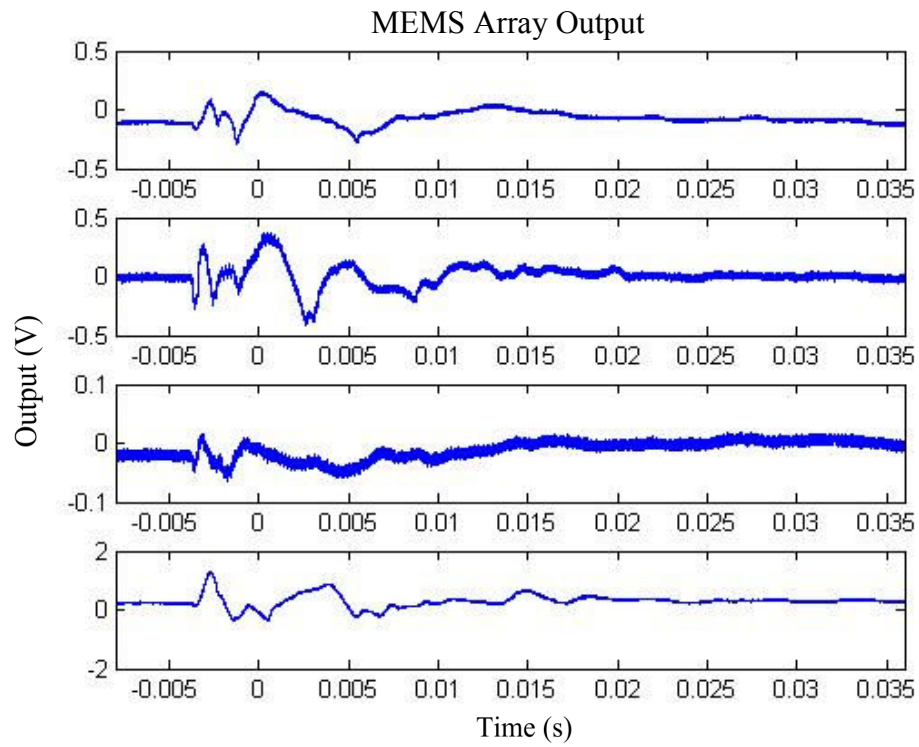


**Figure B.23: Microfabricated Array - Teflon Hammer on Small Plate**

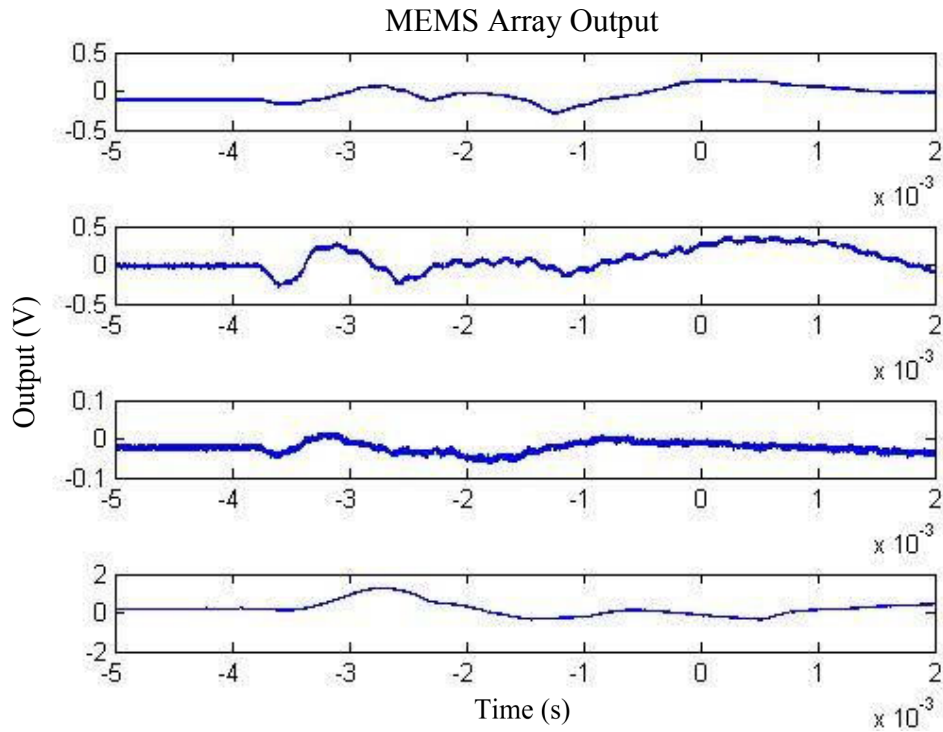


**Figure B.24: Microfabricated Array - Teflon Hammer on Small Plate (Close-Up)**

All of these waveforms show a primary natural oscillation with a frequency on the order of 4800 Hz, as expected. These sensors are primarily responding to the lowest natural frequency of the plate and its natural oscillation after impact.

The next set of four figures shows the response of the laser and microfabricated sensor arrays to a steel impact on the plate.

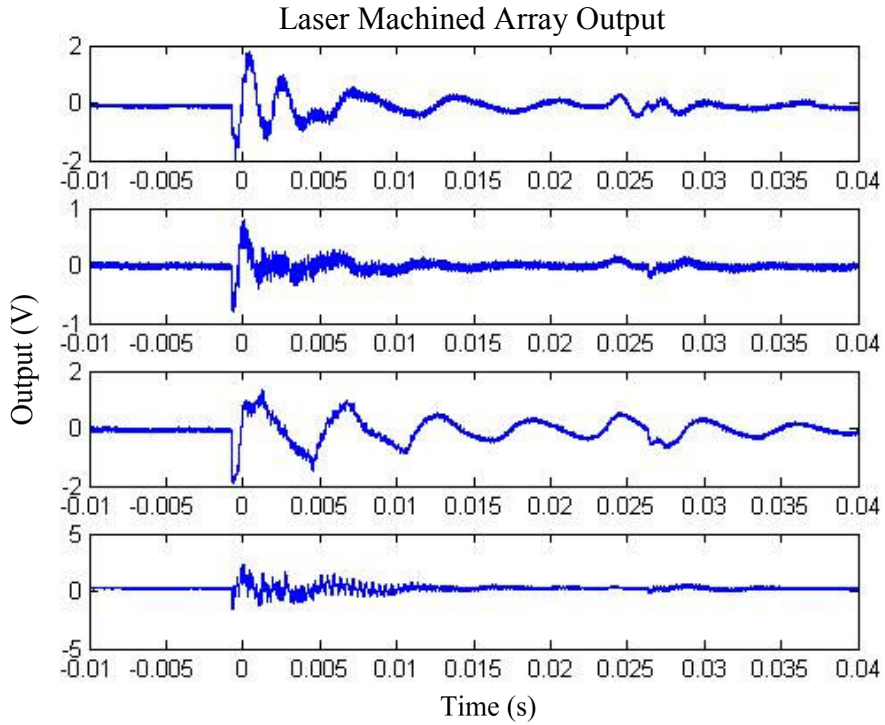


**Figure B.25: Laser Fabricated Array - Steel Hammer on Small Plate**

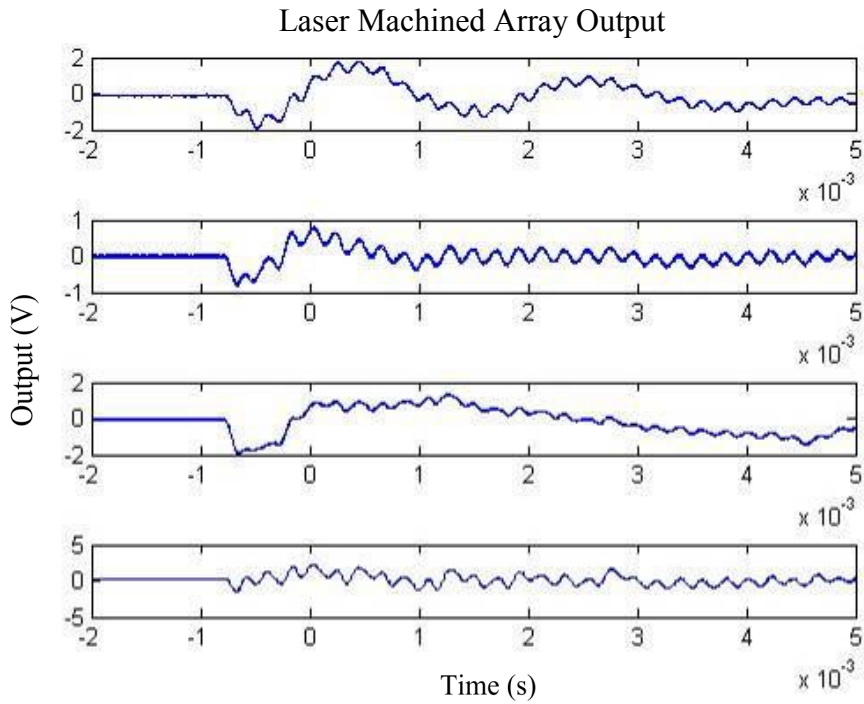


**Figure B.26: Laser Fabricated Array - Steel Hammer on Small Plate (Close-Up)**

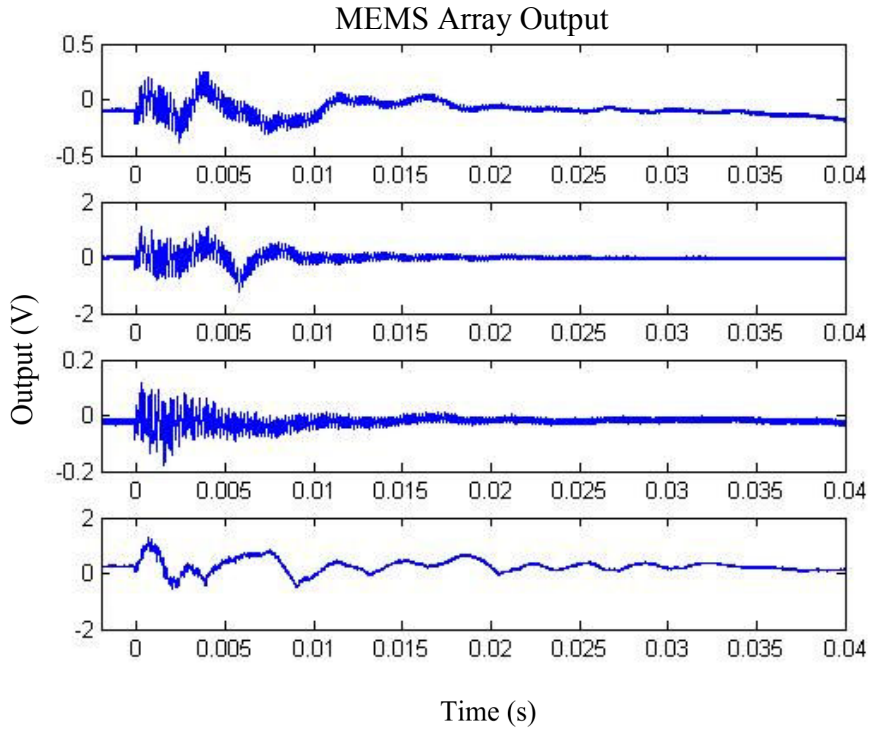


Figure B.27: Microfabricated Array - Steel Hammer on Small Plate

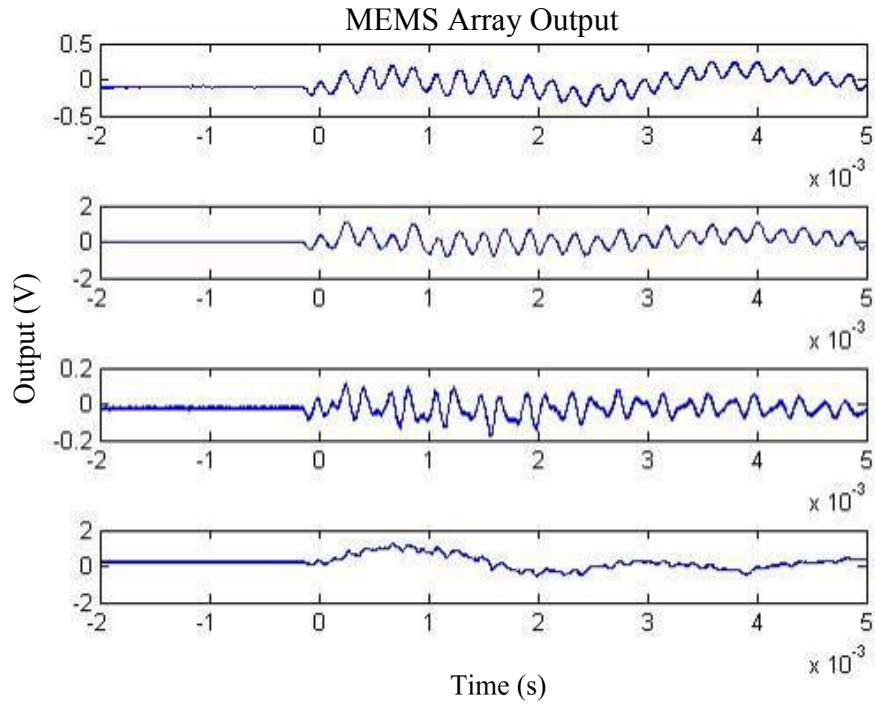
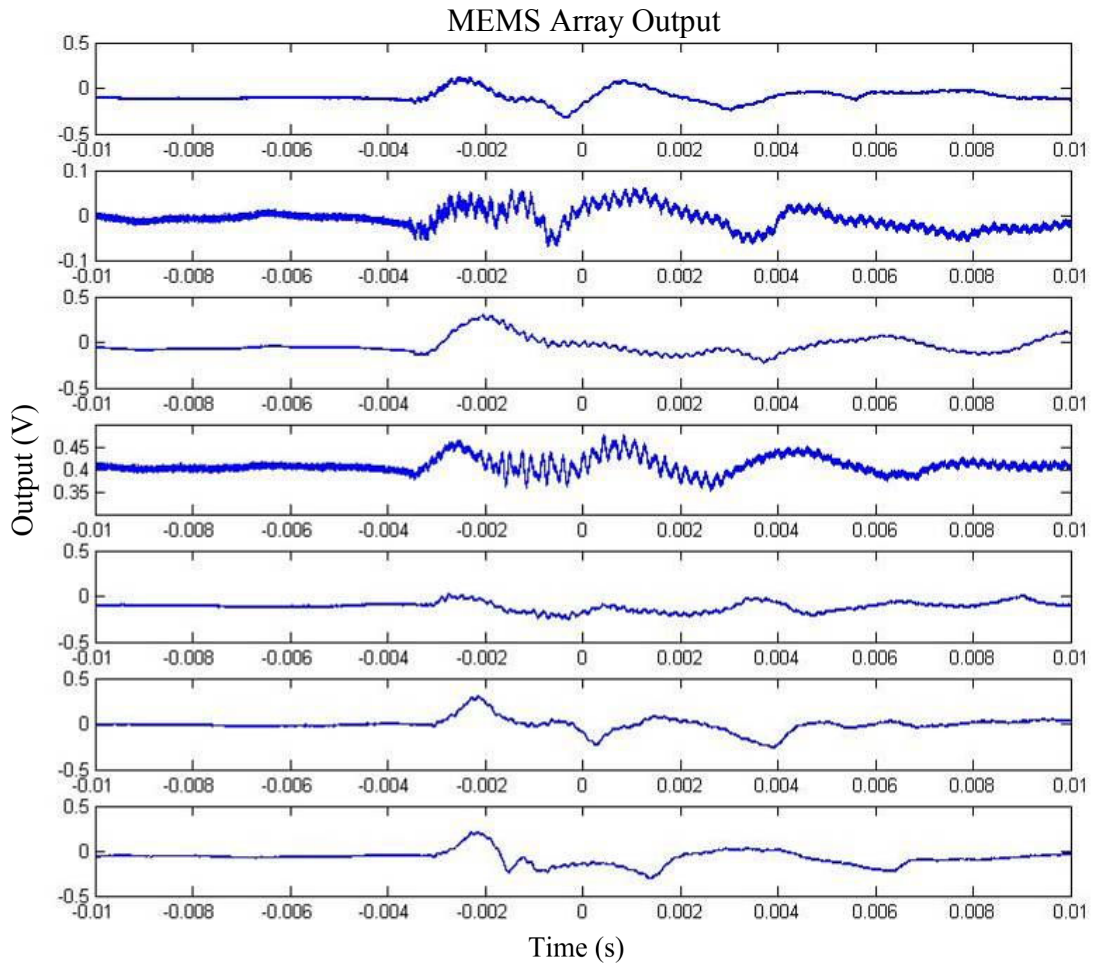


Figure B.28: Microfabricated Array - Steel Hammer on Small Plate (Close-Up)

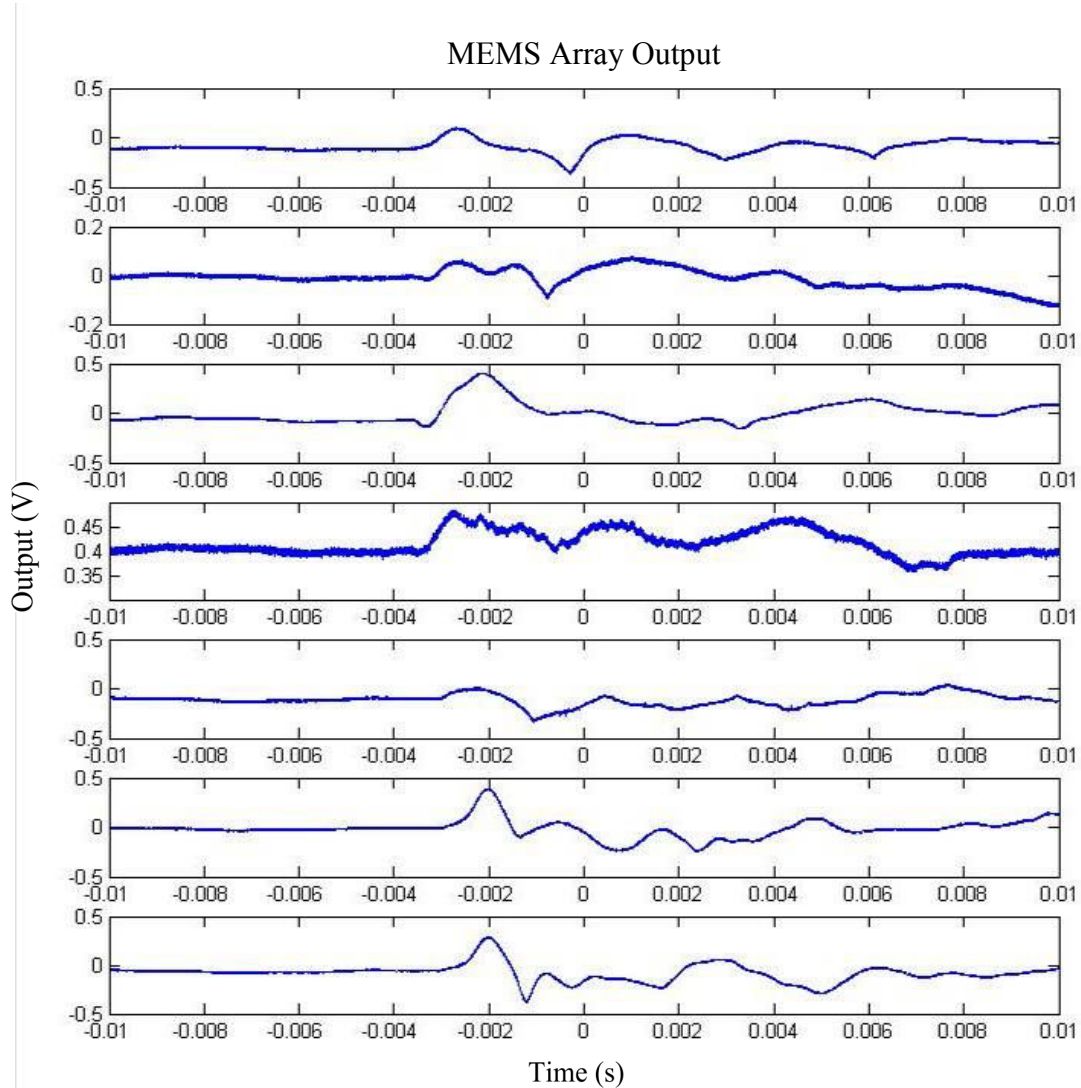
Again, the primary frequency seen in these tests is the fundamental 4800Hz of the plate itself. However, in this particular test, the amount of 4800 Hz in the signal with respect to lower frequency content is substantially higher in the steel impact. This is the spectral discrimination inherent in the smaller plate.

As was done with the large plate tests, a second microfabricated transducer array was attached to the small plate, and a series of impacts performed. Figure B.29 shows the response of a full seven sensor array to steel impact on the small plate.



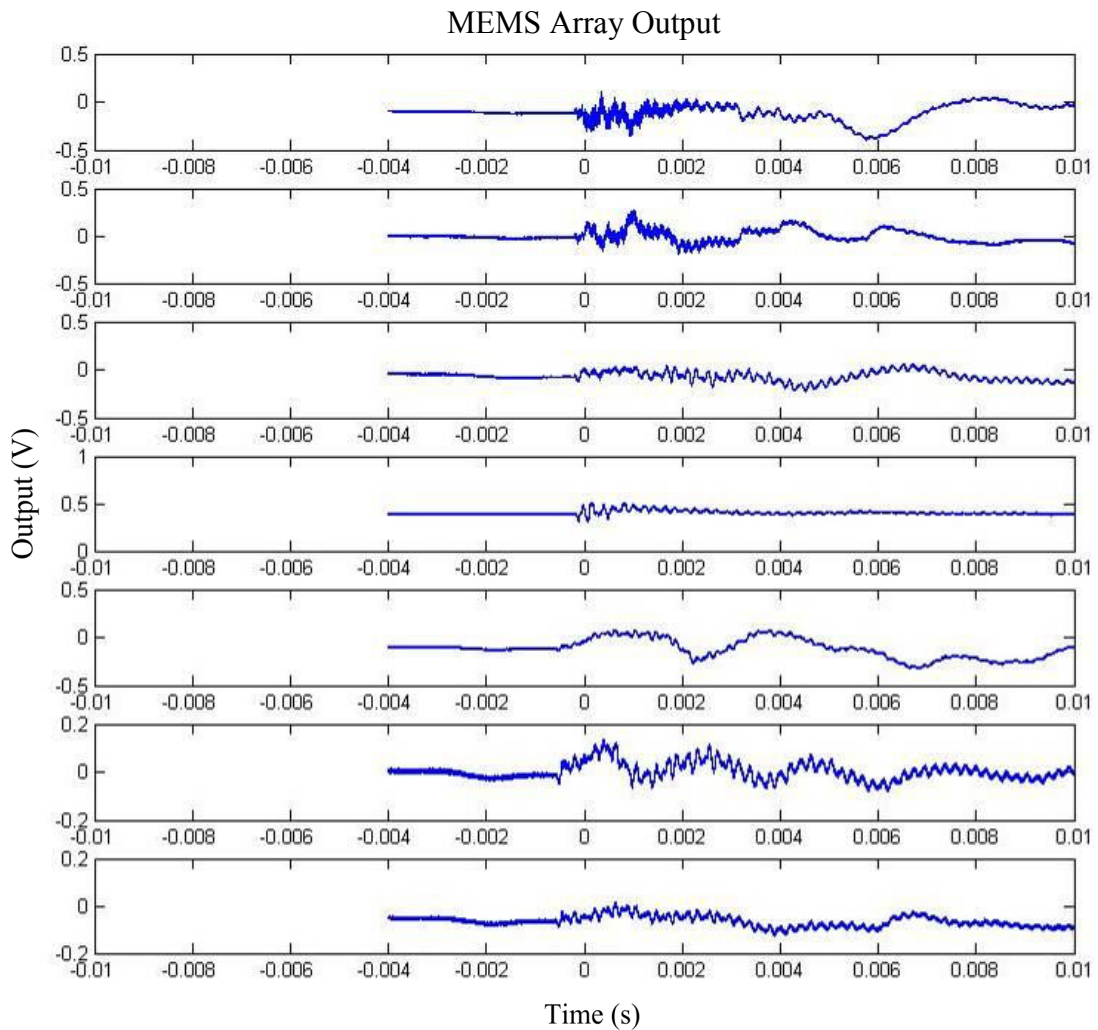
**Figure B.29: Seven Sensor Array - Steel Impact on Small Plate**

Figure B.30 shows the response of the same plate and sensor array to the impact with the Teflon hammer.



**Figure B.30: Seven Sensor Array - Teflon Impact on Small Plate**

It is again evident in these responses that the steel impact excites a higher level of the fundamental mode of the plate, whereas the Teflon impact simply excites the rigid body motion of the plate on its support stands. Figure B.31 shows a similar result when the impact is with a stainless steel ball



**Figure B.31: Seven Sensor Array - Impact of Stainless Steel Ball**

These tests showed the consistency of the impact tests. They also highlighted the effect on the signal due to the mounting supports for the test article. The lower frequency component common to all of these plots correlates to the rigid body motion of the plate if placed on compliant mounts. A Finite Element Analysis was performed to verify this situation. In the model, the small plate was placed on top of plastic supports. The rigid body modes had a frequency of approximately 180Hz.

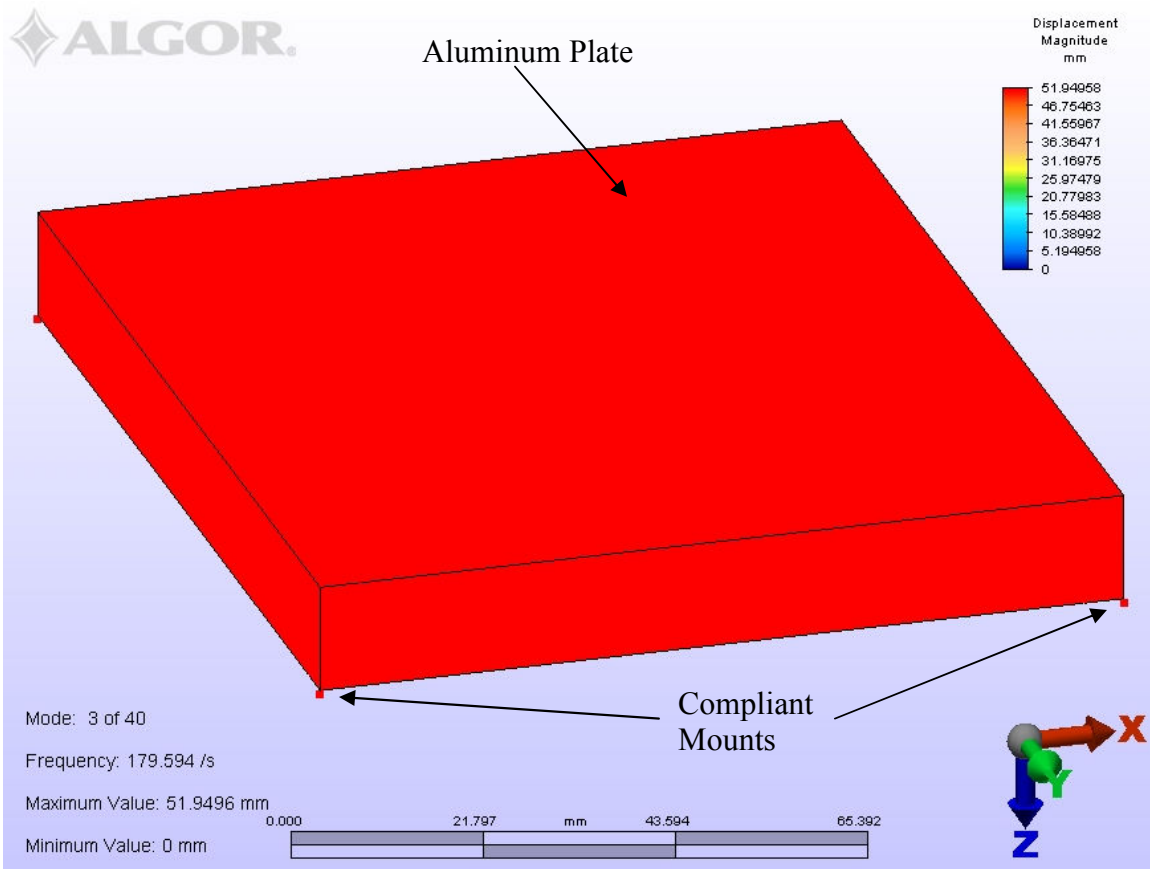


**Figure B.32: Finite Element Analysis of Small Plate on Compliant Mounts**

#### **B.4 Laser Micromachined Array on Steel Cone**

The laser micromachined array theoretically had a higher natural frequency than the microfabricated device. Therefore, the laser microfabricated device was used to capture representative waveforms that did not include sensor ringing. A laser fabricated array was attached to a steel cone and placed in the hammer drop apparatus. Multiple drops were performed on both the steel end of the hammer and the Teflon end, and waveforms captured from the four lowest frequency devices in the array. Figure B.33 shows the response of the array to a drop of the steel end. Figure B.34 shows the same response, but zoomed in to the first 2ms of the response.

### Laser Machined Array Output

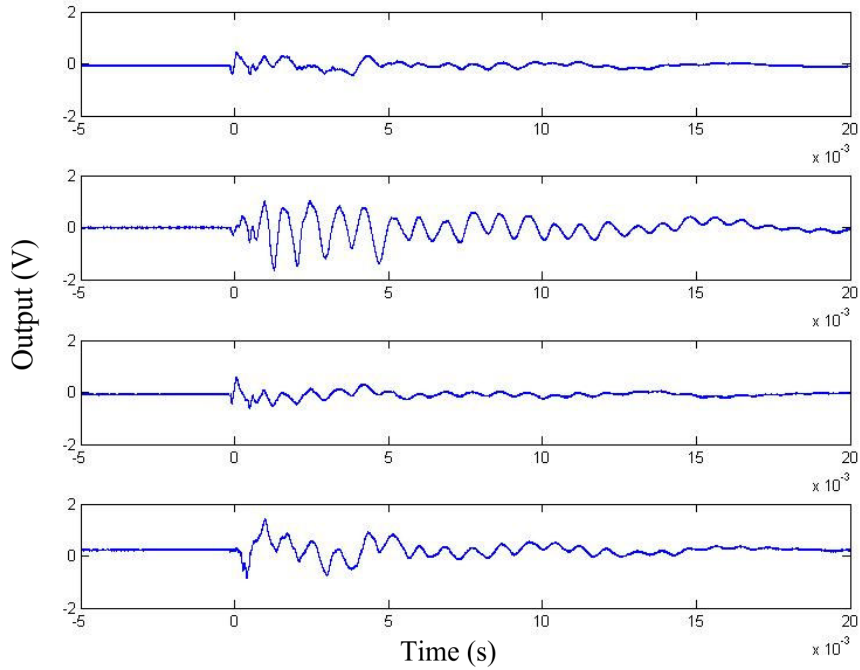


**Figure B.33: Laser Machined Array with Steel Hammer Drop**

### Laser Machined Array Output

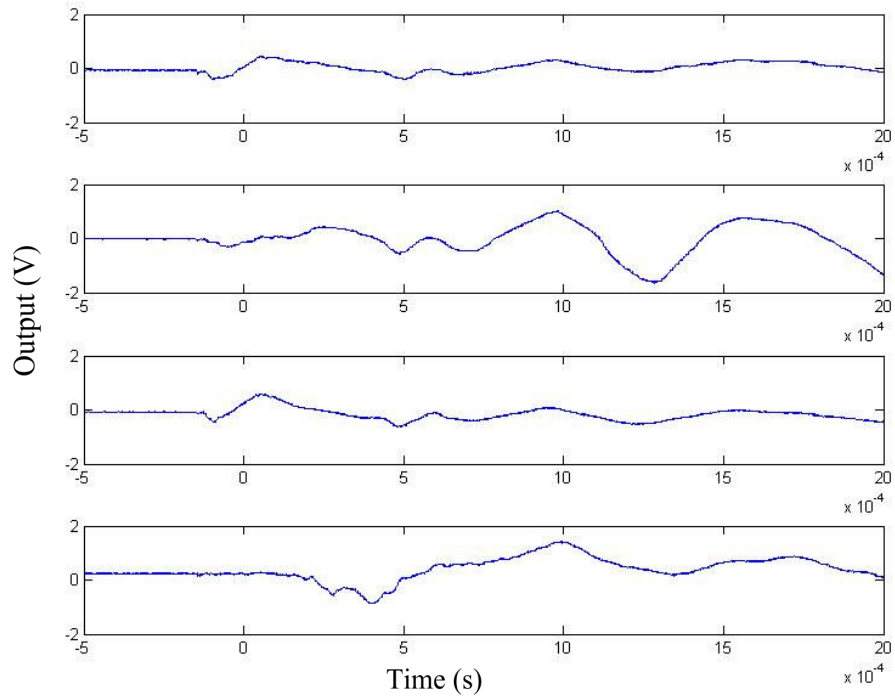


**Figure B.34: Laser Machined Array with Steel Hammer Drop (Close-Up)**

Figure B.35 and Figure B.36 show the response of the same sensor array to an impact with the Teflon end of the hammer. The second figure is zoomed in to the first 2ms of the waveform.

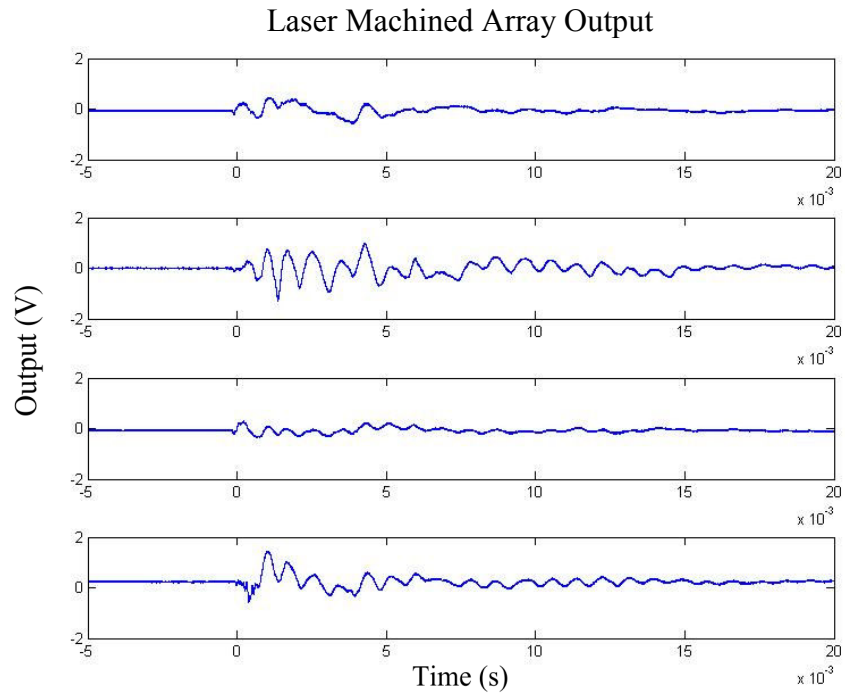


**Figure B.35: Laser Machined Array with Teflon Hammer Drop**

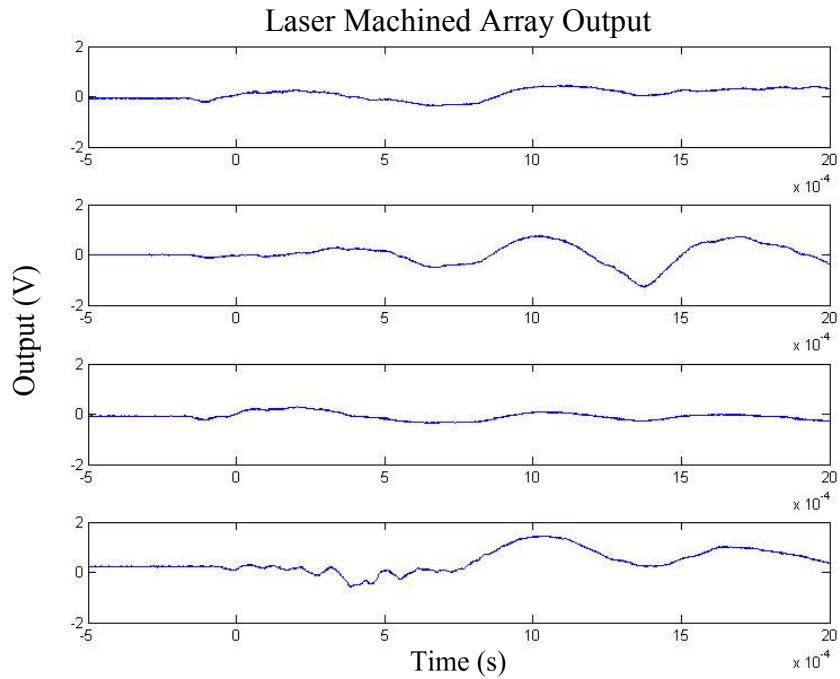


**Figure B.36: Laser Machined Array with Teflon Hammer Drop**

The critical feature of these waveforms is the lack of ringing at the beginning when the impact occurs. The high frequency response of the transducers captures the input acoustic signals without overshoot or ringing. This will be compared and contrasted with the same impact scenario using the microfabricated transducers that possess a lower natural frequency.

### **B.5 1<sup>st</sup> MEMS Array on Steel Cone - Hammer Drop**

After verifying suitable operation, microfabricated arrays were placed on small cones and discs. The microfabricated arrays were first attached to the cone structure to capture waveforms comparable to those captured by piezoelectric sensors and the higher frequency laser machined arrays. Figure B.37 and Figure B.38 show the waveforms captured during an impact with the steel end of the hammer.

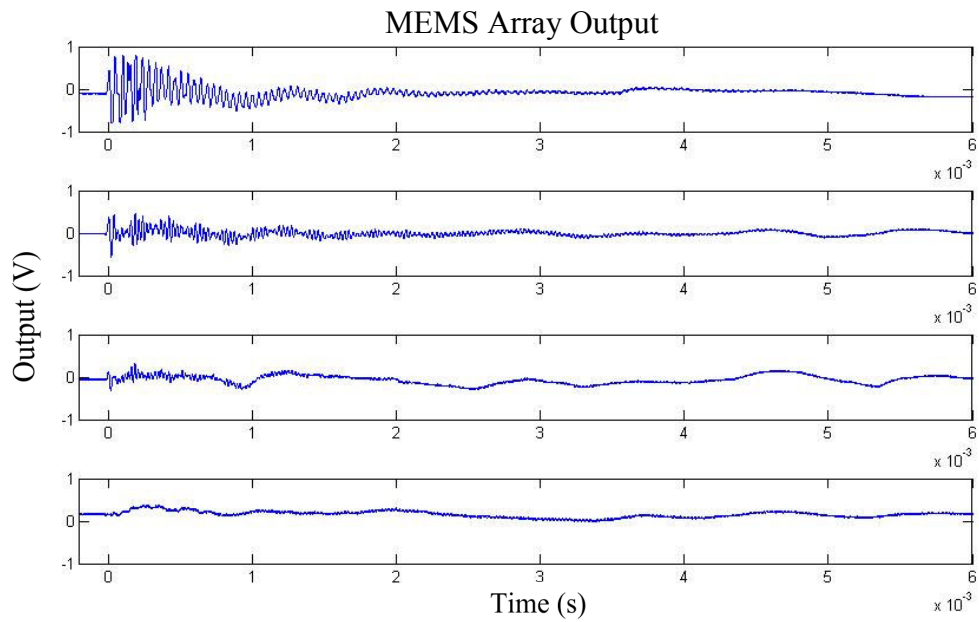


**Figure B.37: Steel Hammer Impact on MEMS Array**

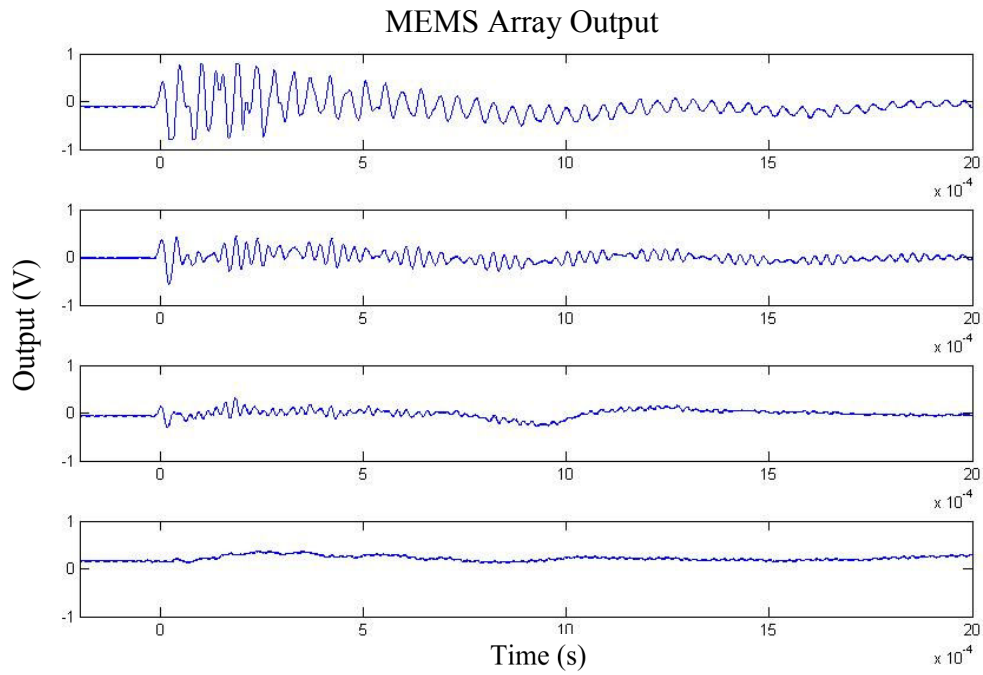


**Figure B.38: Steel Hammer Impact on MEMS Array (Close-Up)**

Figure B.39 and Figure B.40 show the response from the same test apparatus to an impact from the Teflon end of the hammer.

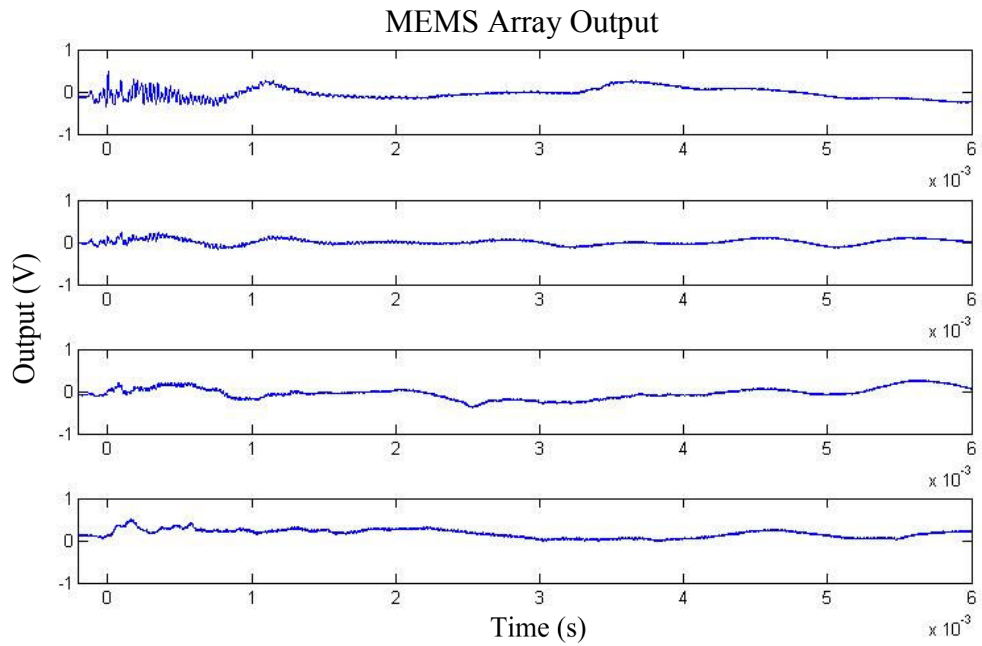


**Figure B.39: Teflon Hammer Impact on MEMS Array**

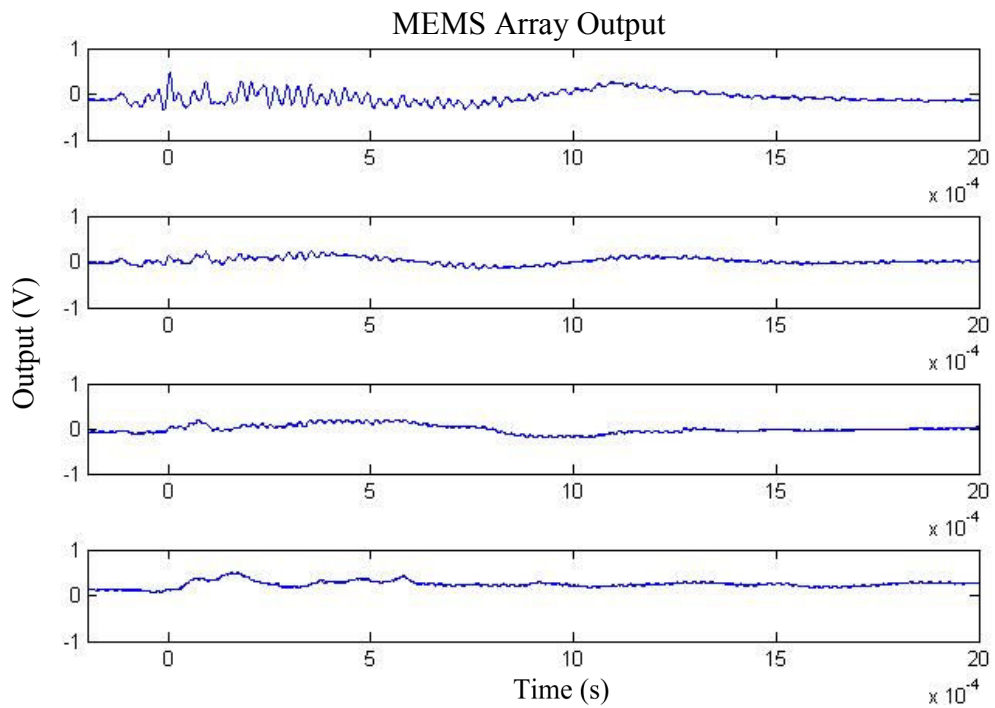
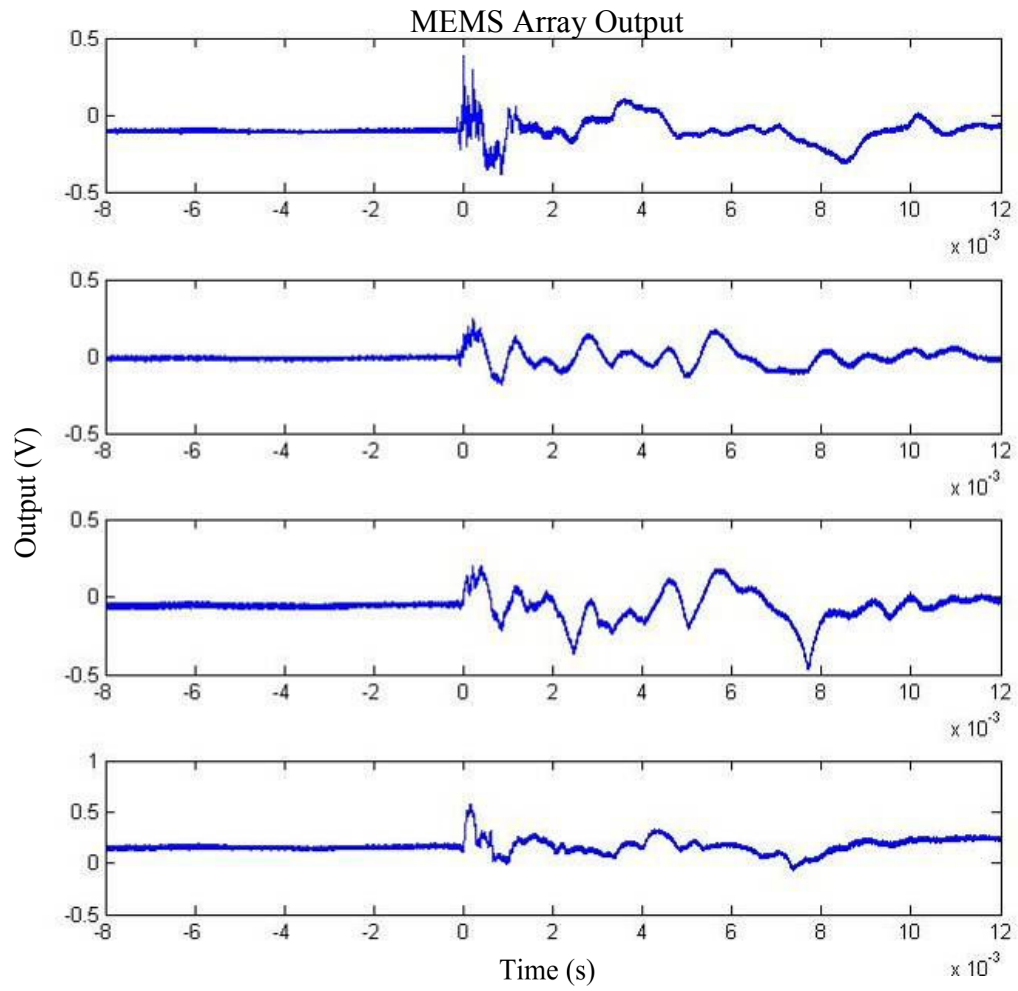


**Figure B.40: Teflon Hammer Impact on MEMS Array (Close-Up)**

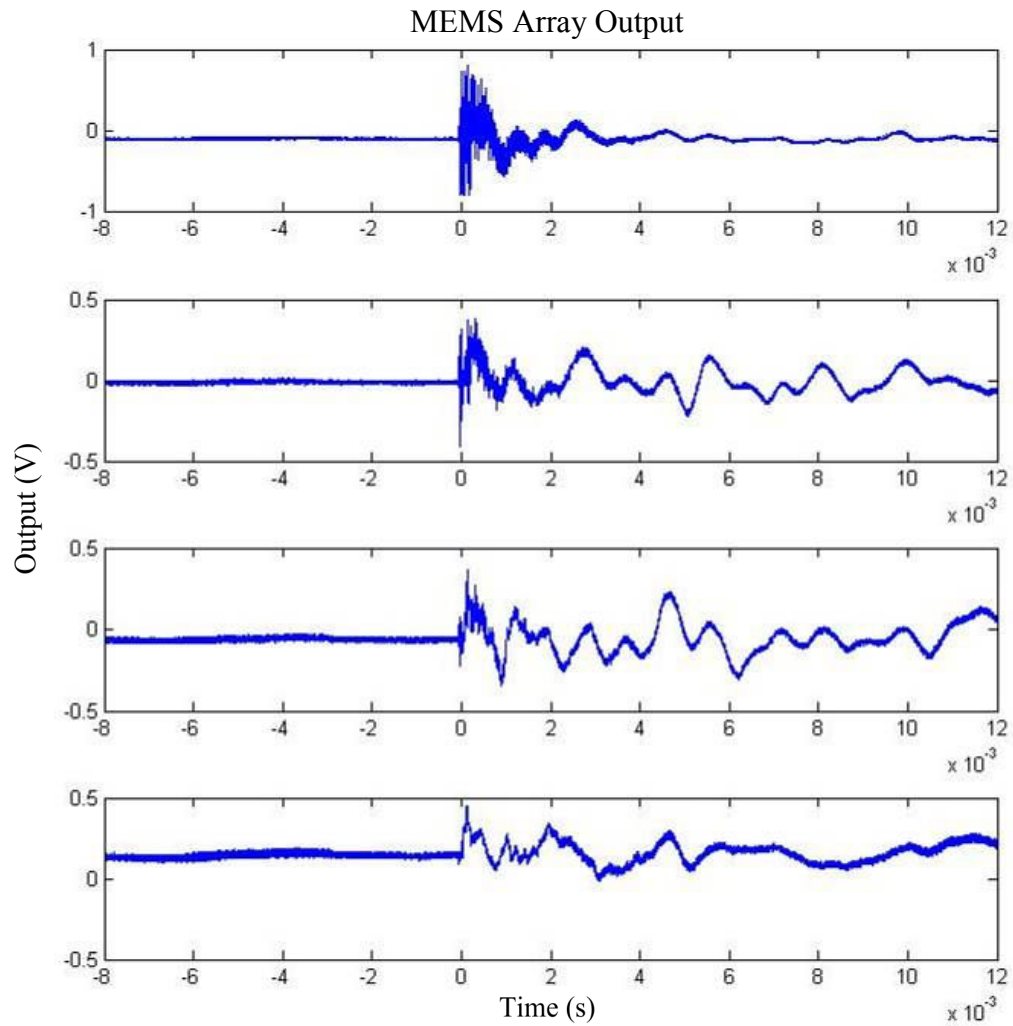
The important feature to note in these waveforms that wasn't present in the laser machined sensor responses is the ringing at the front end of the waveform during steel impacts. As in simulations presented earlier, the ringing is due to the frequency response of the transducers in the array. The higher frequency content of the steel impact results in damped harmonic oscillation of the resonant structures at their natural frequency. The important parameter is the ratio of ringing amplitude to normal signal amplitude. Also of note is that in the Teflon impact, there is still some ringing seen in the largest and lowest frequency device, indicating that the impact created frequency content near that of the natural frequency of the largest transducer in the array, but not in the others. The steel impact had high enough frequency content to induce oscillations in the higher frequency sensors, as evidenced by the ringing seen in those devices.

### **B.6 2<sup>nd</sup> MEMS Array on Steel Cone - Hammer Drop**

To characterize the consistency of these waveforms, a second set of transducers were applied to the same cone structure and another set of impacts performed.

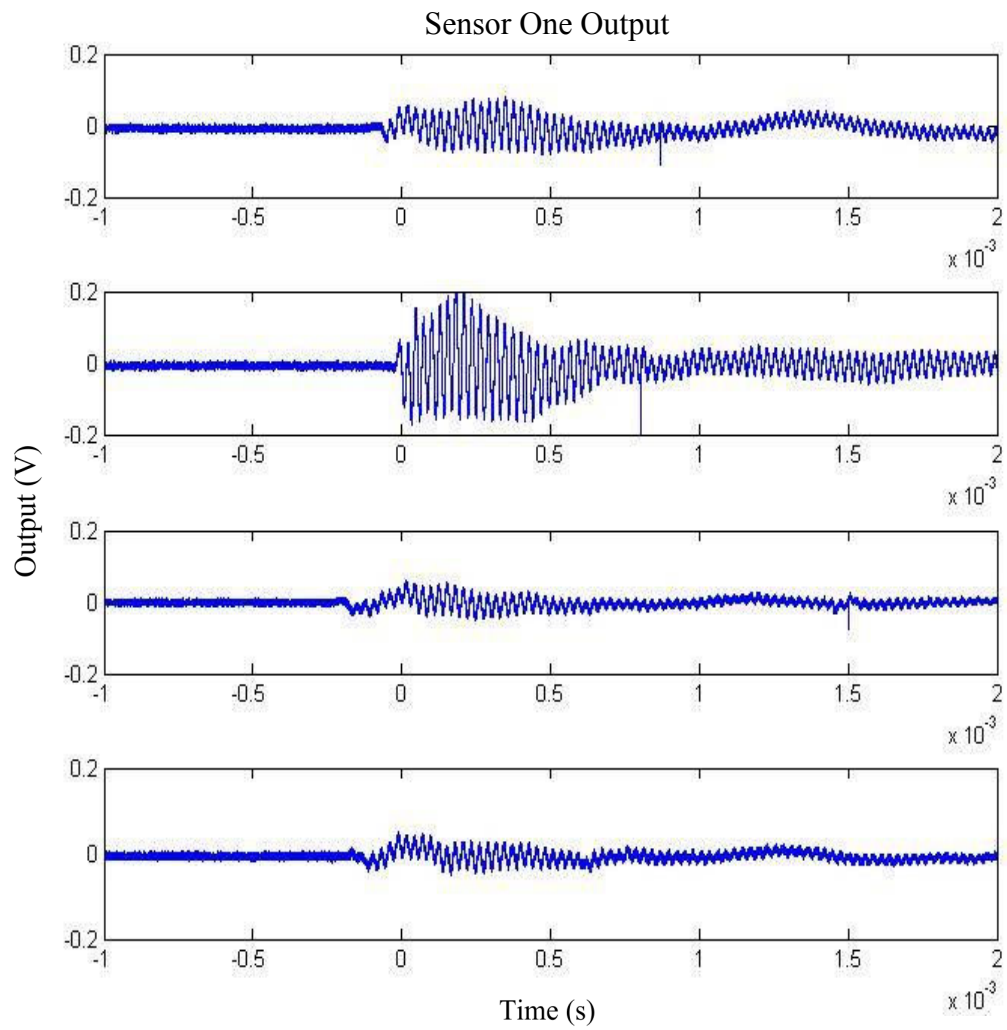


**Figure B.41: Waveforms from Second Array with Teflon Impact**

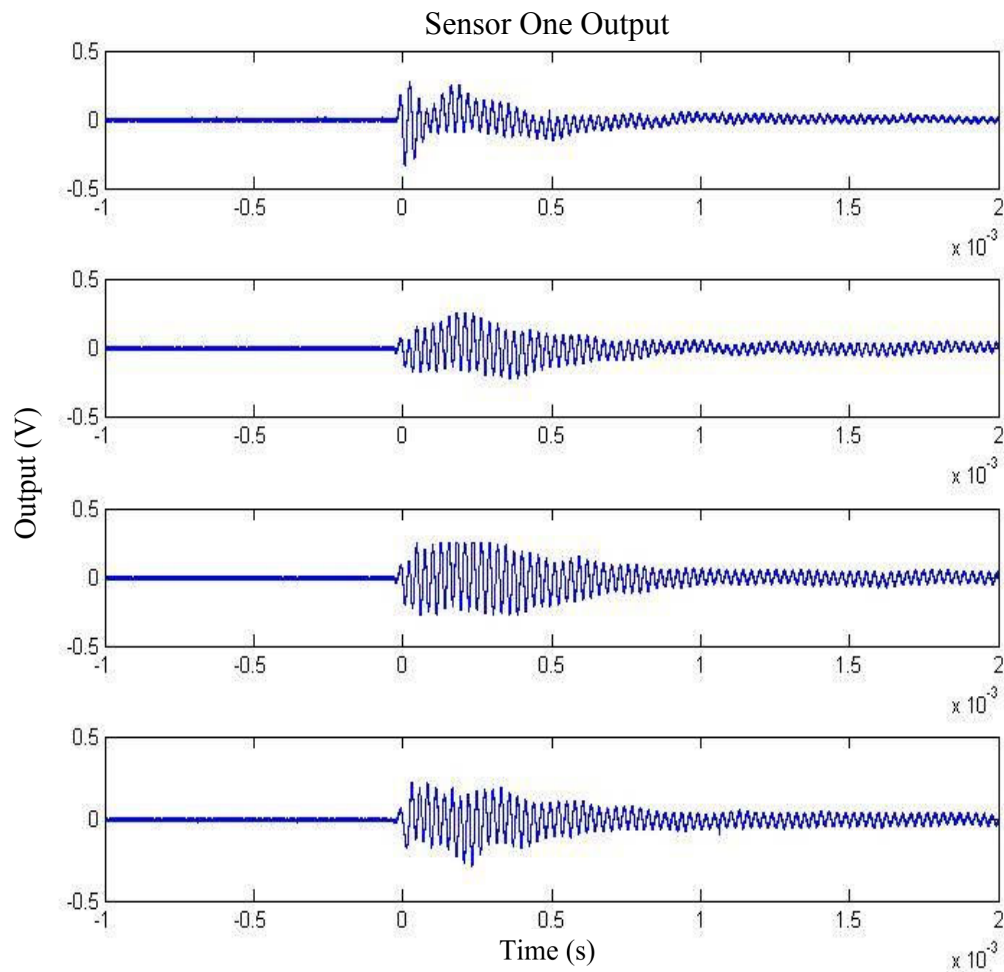


**Figure B.42: Waveforms from Second Array with Steel Impact**

Again, in these impacts with steel, sensors three and four show additional ringing at their natural frequency compared to the response of the same sensor to Teflon impacts. This indicates that the steel impacts were “sharper” in time, *i.e.* had high frequency component in their transient response. A series of four impacts were then performed. Figure B.43 and Figure B.44 show the response of sensor one to those four impacts with Teflon and four impacts with steel. The responses and the amount of ringing are very similar.

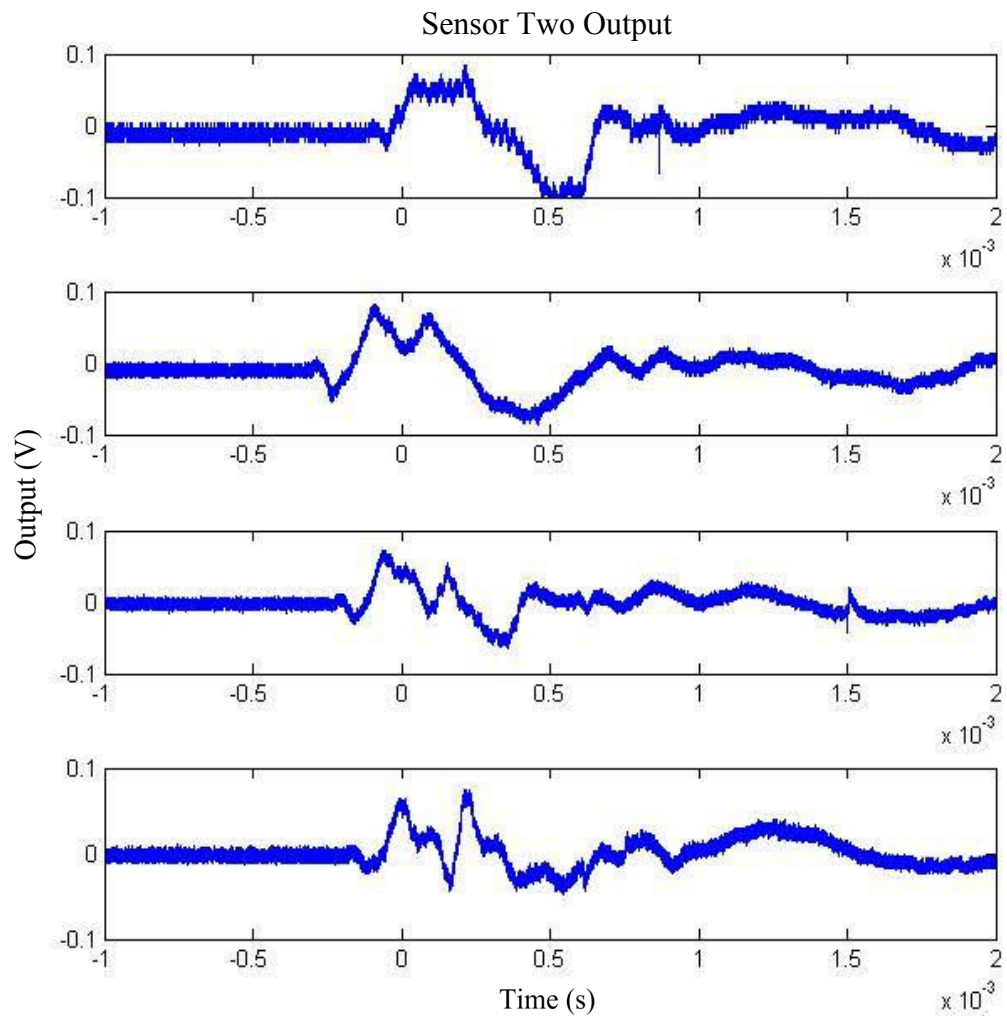


**Figure B.43: Sensor One Response to Four Impacts with Teflon**

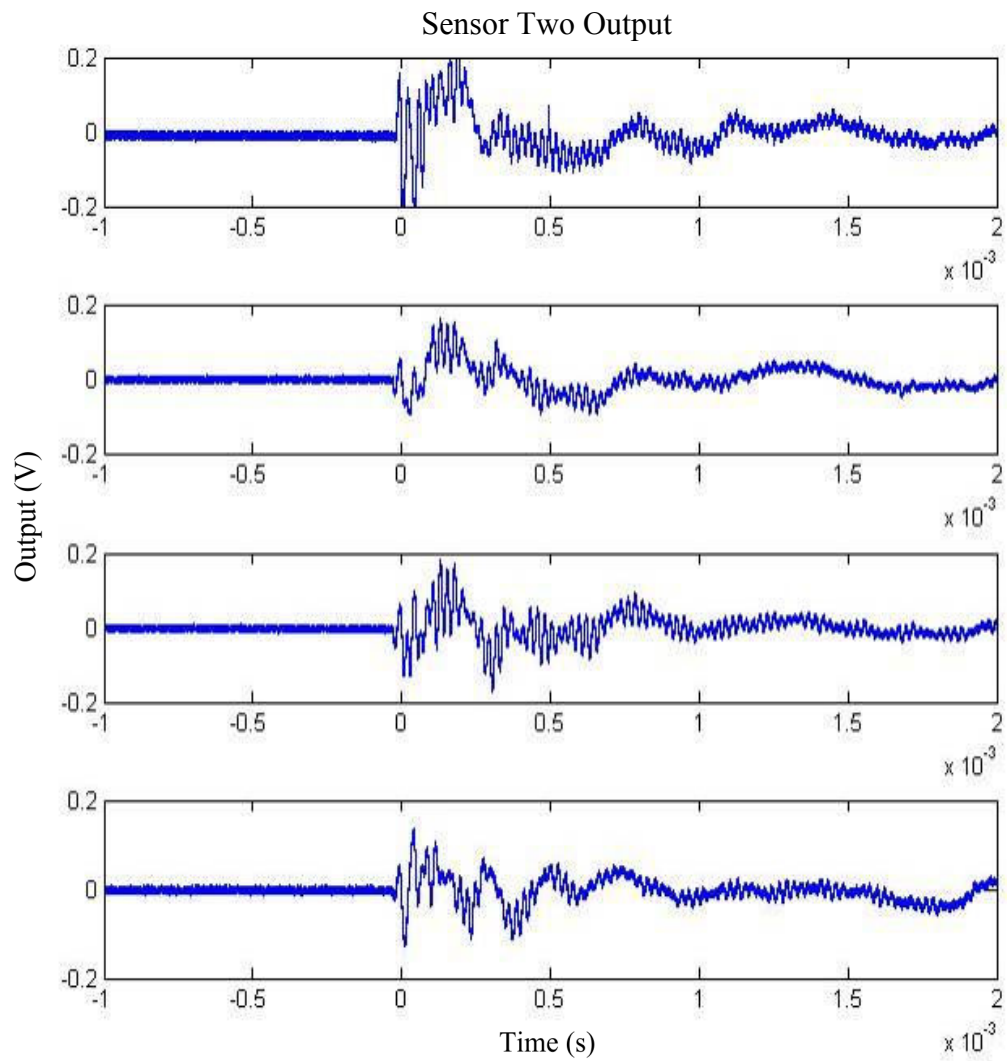


**Figure B.44: Sensor One Response to Four Impacts with Steel**

As shown in Figure B.45 and Figure B.46, it is with sensor two that the differences in response begin to show. Under the steel impact, the amount of sensor ringing is significantly larger than in the Teflon impact. This is indicative of the sharper acoustic pulse created by the impact.

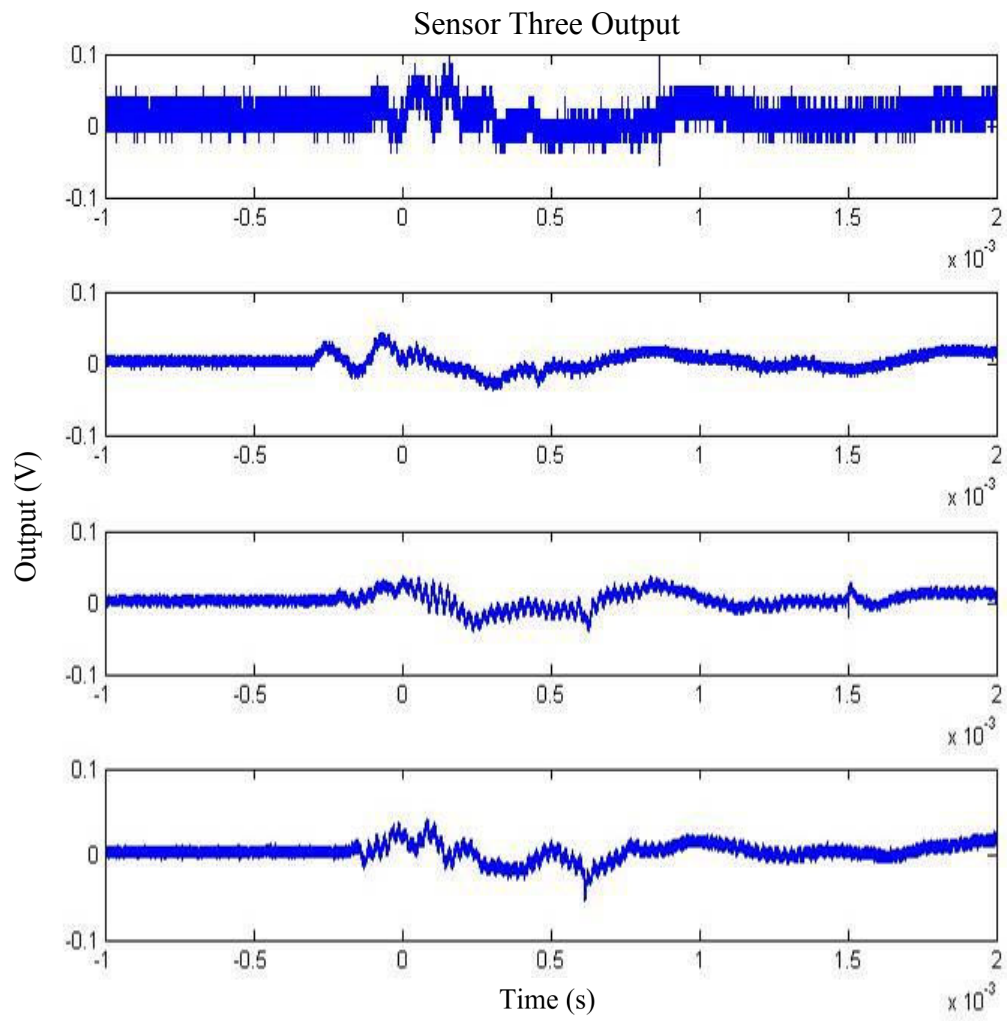


**Figure B.45: Sensor Two Response to Four Impacts with Teflon**

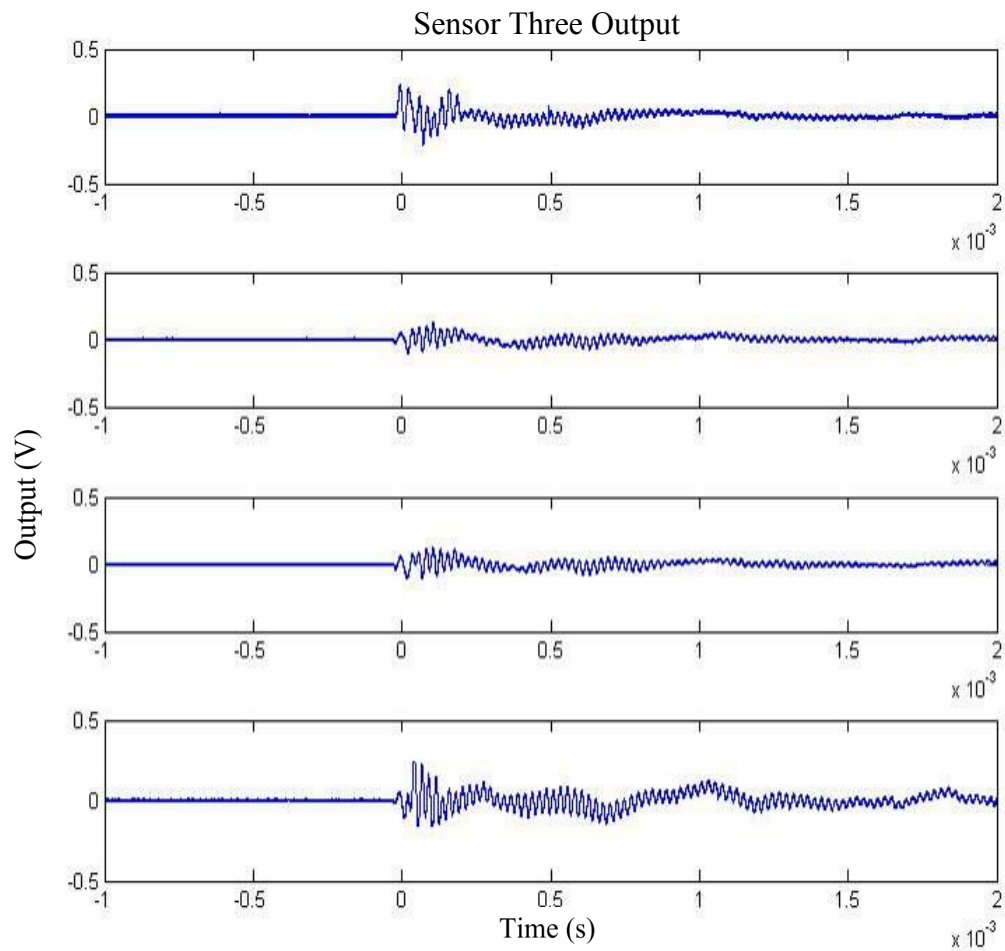


**Figure B.46: Sensor Two Response to Four Impacts with Steel**

Figure B.47 and Figure B.48 show that similar differences existed in sensor three for the different impacts.

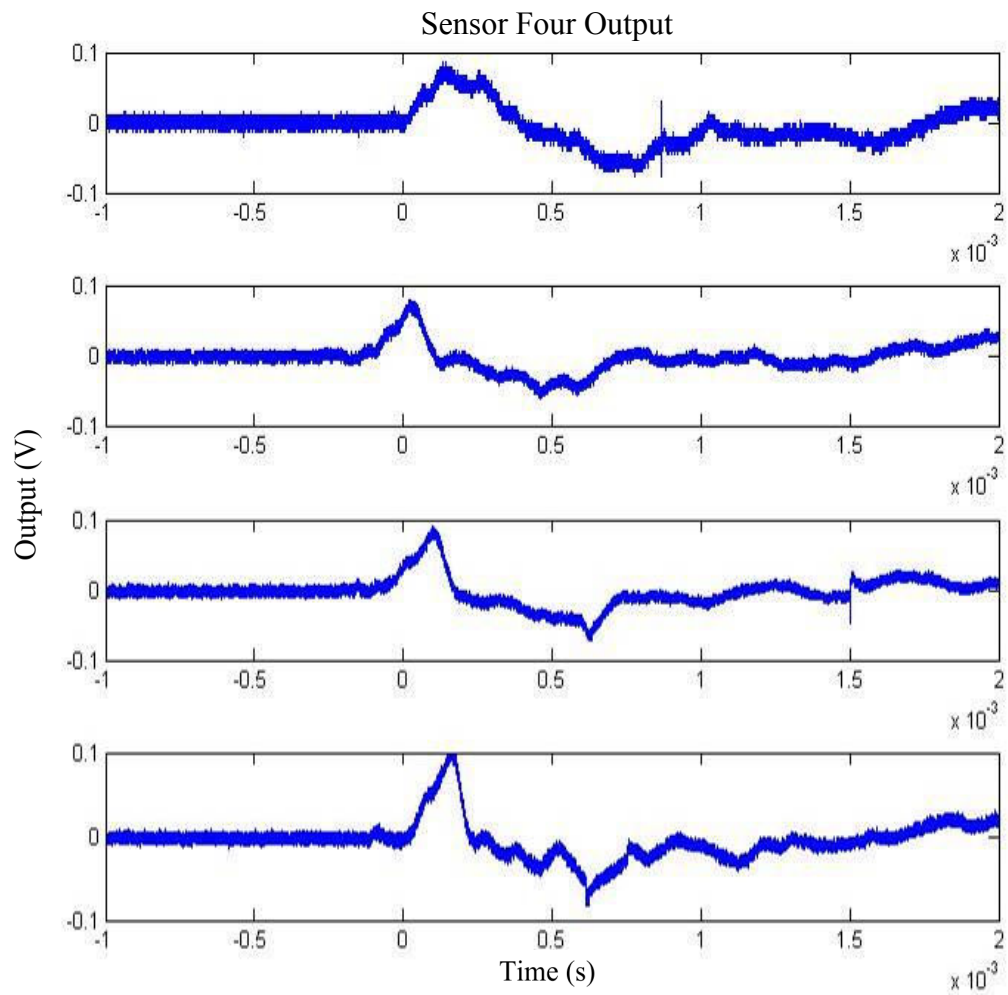


**Figure B.47: Sensor Three Response to Four Impacts with Teflon**

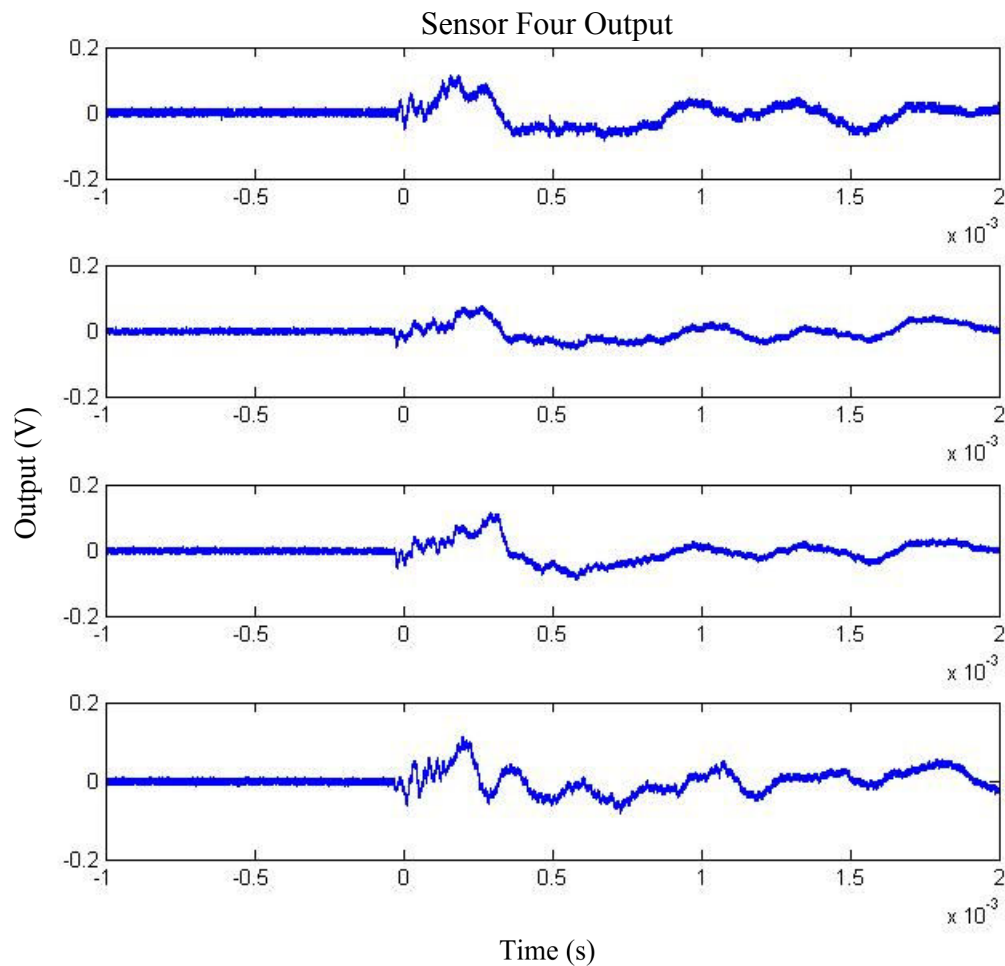


**Figure B.48: Sensor Three Response to Four Impacts with Steel**

Figure B.49 and Figure B.50 show that sensor four showed similar responses for the two types of impacts, and did not exhibit sensor ringing under either steel or Teflon impact, suggesting that the acoustic waveform was not sharp enough to induce ringing in that sensor.

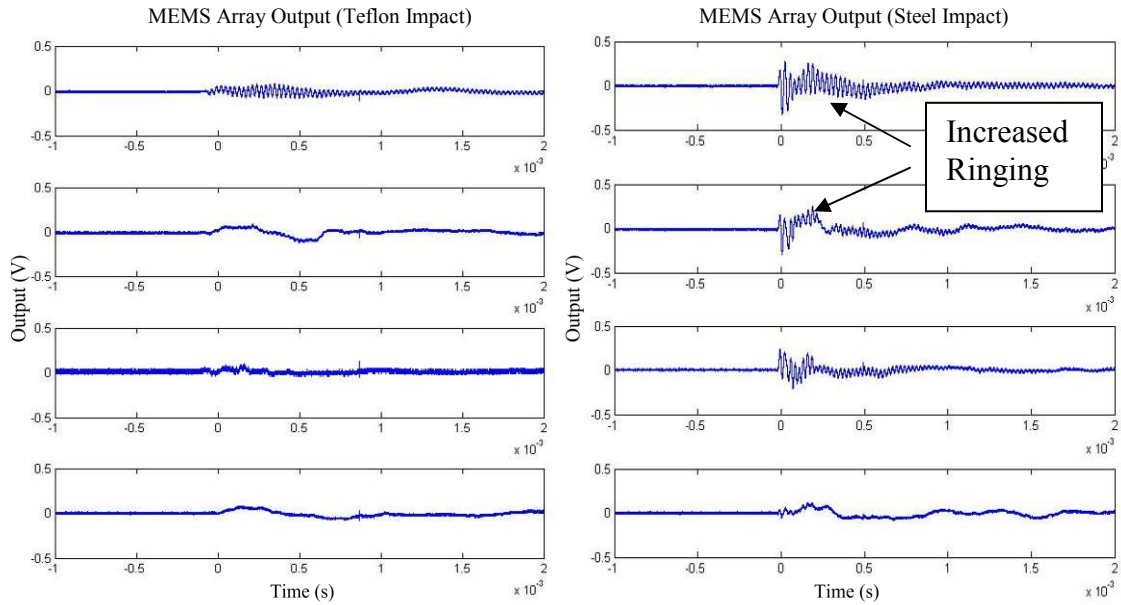


**Figure B.49: Sensor Four Response to Four Impacts with Teflon**

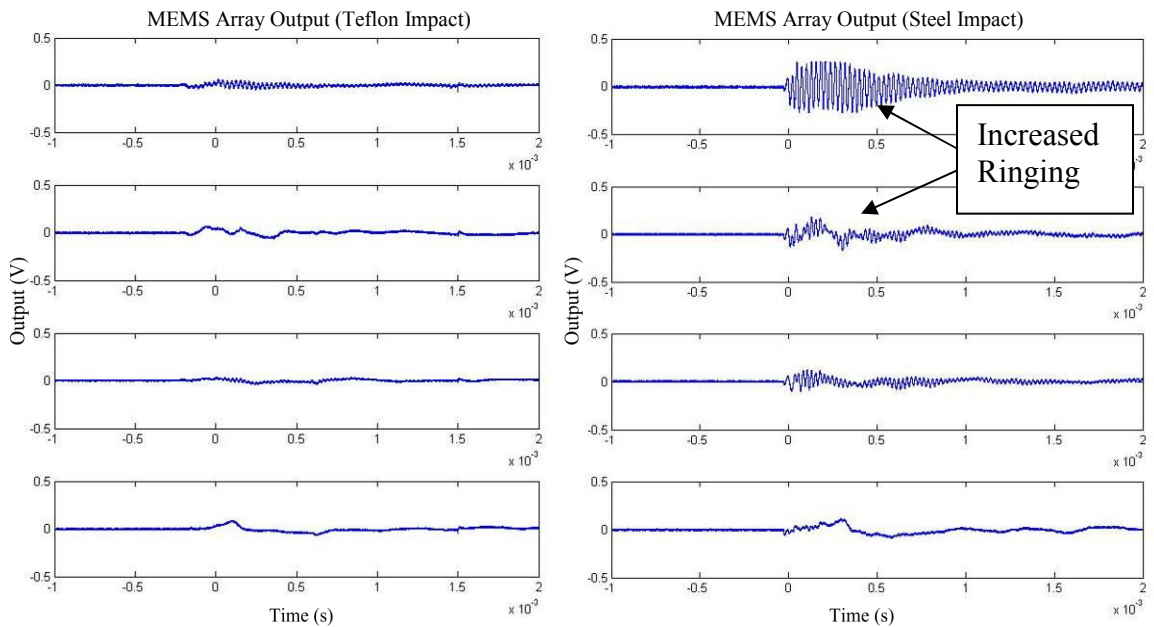


**Figure B.50: Sensor Four Response to Four Impacts with Steel**

Figure B.51 and Figure B.52 show side-by-side comparisons for two sets of Teflon versus steel impacts. The substantially higher levels of sensor ringing and amplitude are clearly seen in the steel impacts. This indicates that the frequency content of the impact waveforms is higher in the steel impacts, and extends somewhere between sensor three and sensor four.



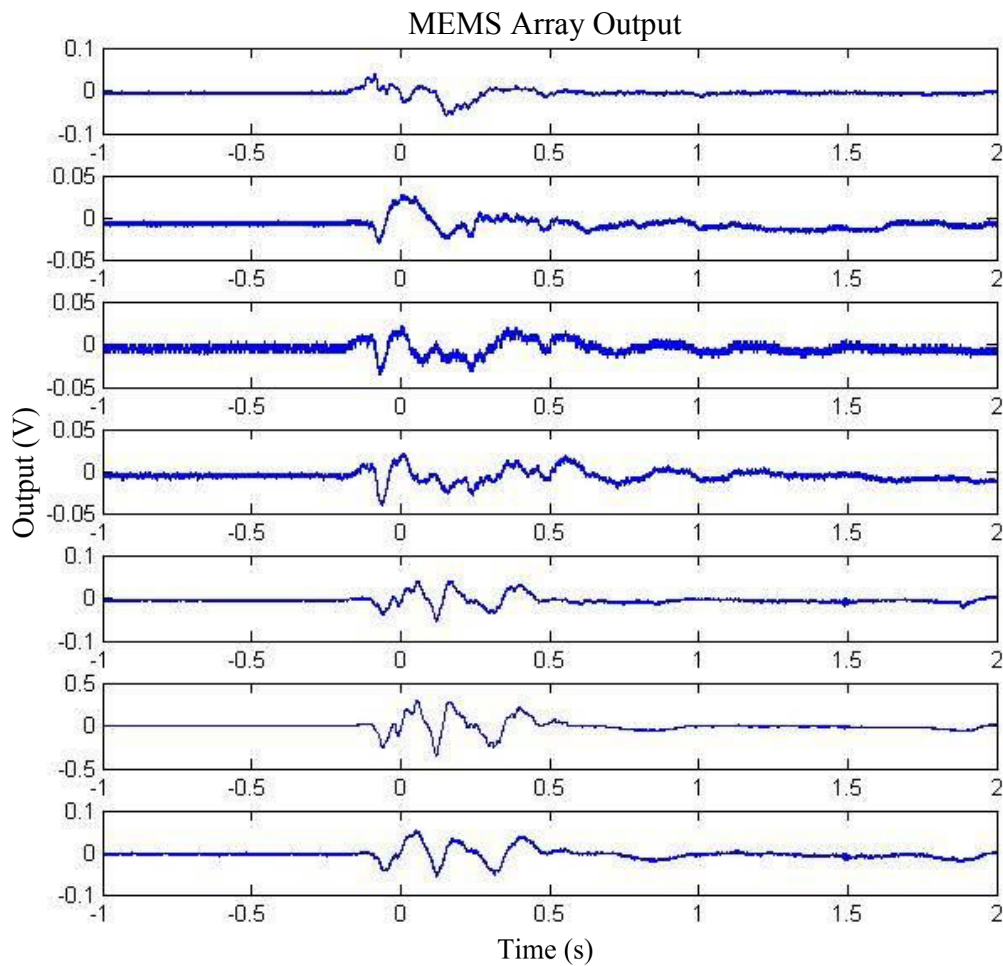
**Figure B.51: Side-by-Side Comparison of Sensor Response for Teflon Impact (left) and Steel Impact (right) - Shot One**



**Figure B.52: Side-by-Side Comparison of Sensor Response for Teflon Impact (left) and Steel Impact (right) - Shot Two**

Even though the waveforms show characteristic differences, it was difficult to use these captured waveforms to discriminate a steel impact from a Teflon impact. In

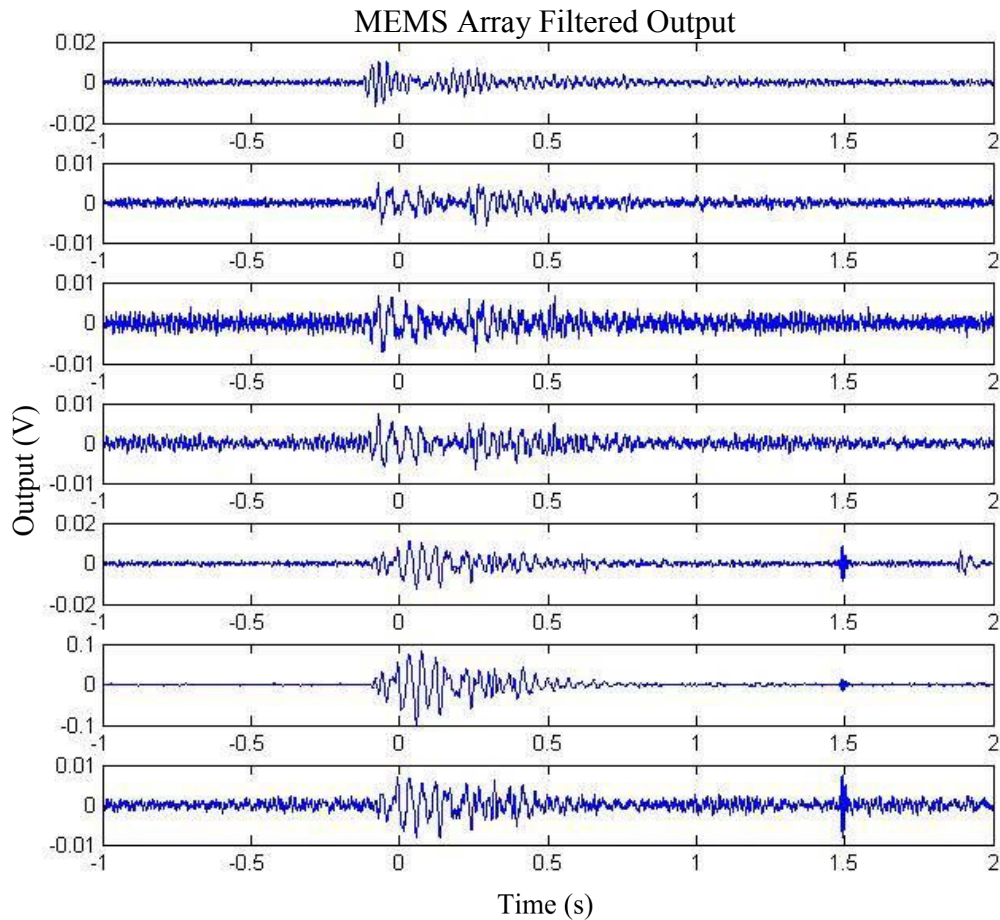
particular, sources of error such as test apparatus and mounting structure response, and parasitic crosstalk between sensor elements, had to be removed from the waveforms. Therefore, some additional processing of the waveforms was performed to yield a spectrum similar to those simulated in Chapter III. Figure B.53 shows the response of a full sensor array to impact with the Teflon hammer.



**Figure B.53: Seven Sensor Output - Teflon Hammer Impact**

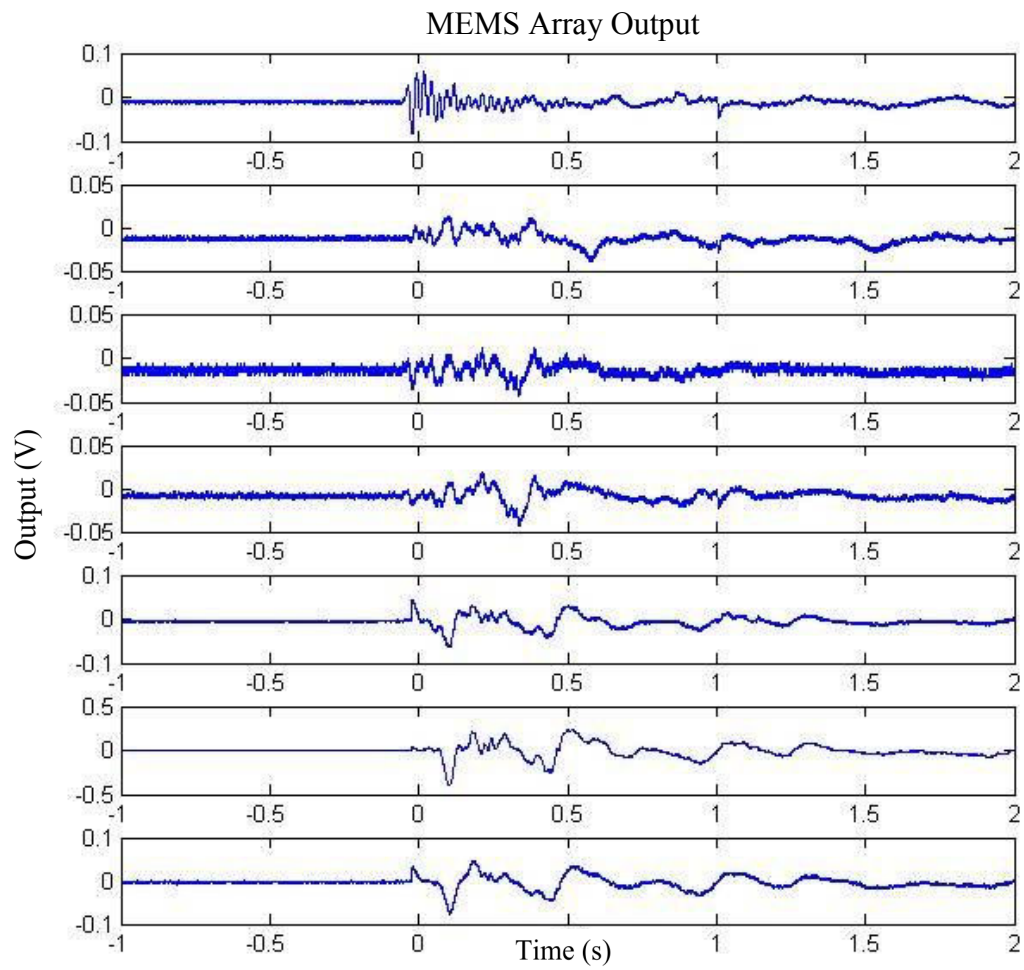
In further processing of this signal, the large amount of lower frequency content, most of it being attributable to the test setup being used, and in particular the hammer length and plate mounting feet, hindered achieving the desired discrimination. Therefore,

a 4<sup>th</sup> order high-pass Butterworth filter was applied to the data. The high-pass cut-on frequency was set to 10 kHz. In addition, to reduce noise levels, a 4<sup>th</sup>-order low-pass Butterworth filter with a cut-off frequency of 100 kHz was applied to each waveform. The filtered response is shown in Figure B.54.

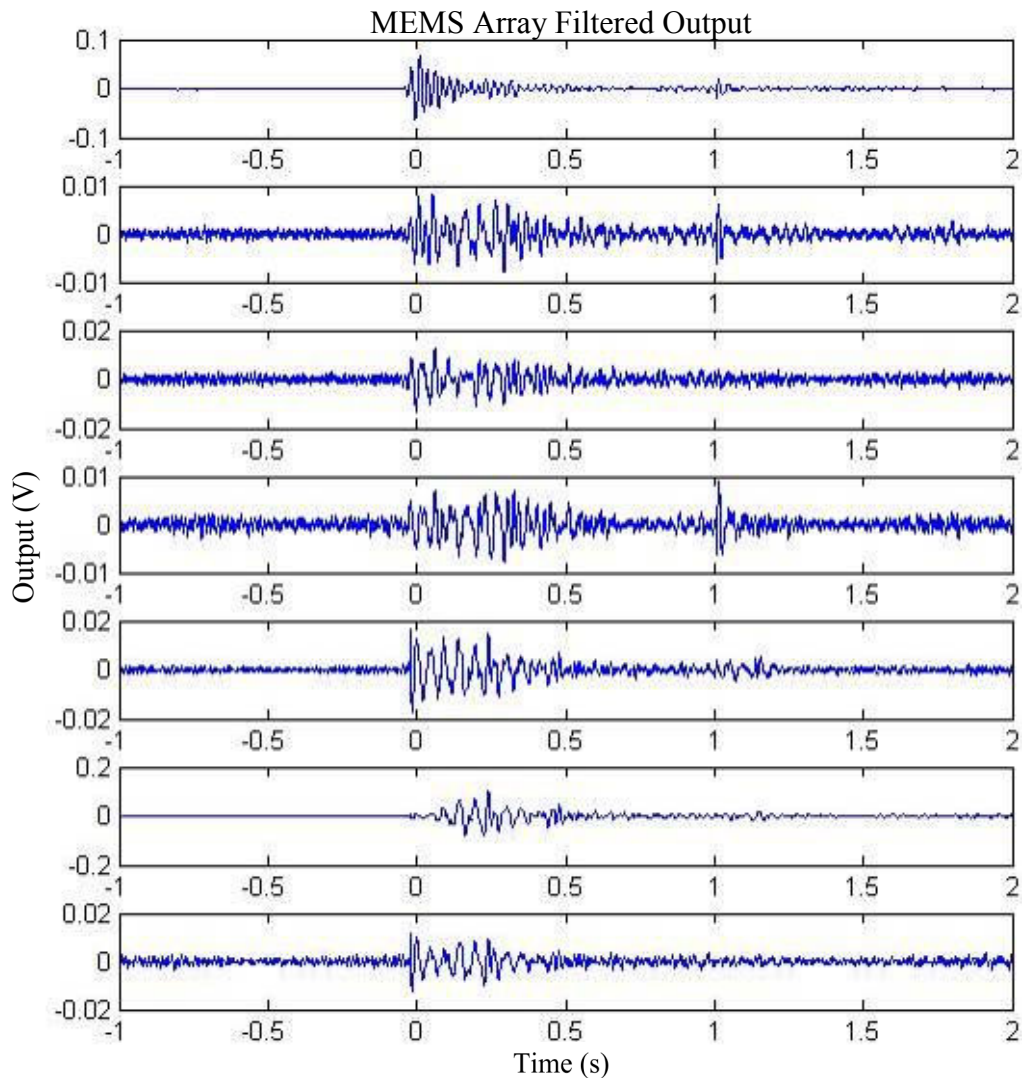


**Figure B.54: Band-Pass Filtered Response to Teflon Hammer Impact**

Similarly, Figure B.55 shows the response of the array to an impact with the Steel Hammer. Again, a large amount of low-frequency content is evident in the signal. Applying the same filtering to the signal led to the waveform shown in Figure B.56.

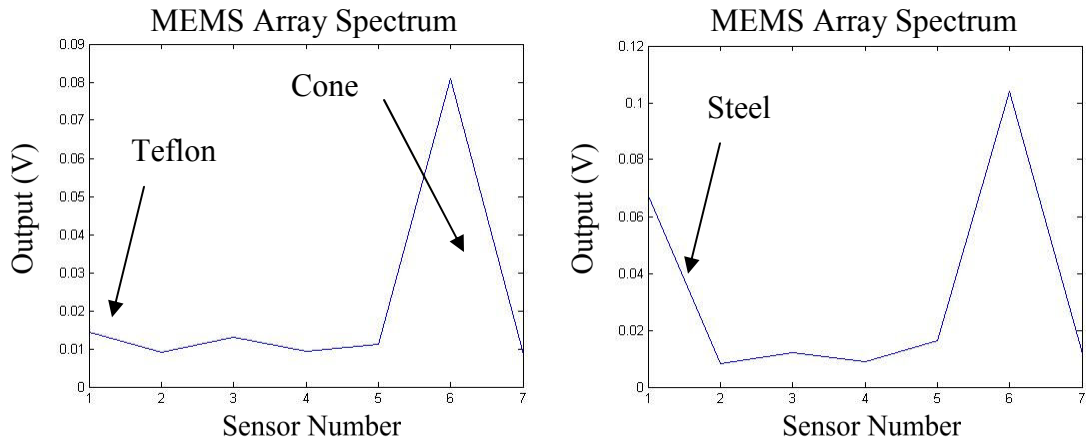


**Figure B.55: Seven Sensor Output - Steel Hammer Impact**



**Figure B.56: Band-Pass Filtered Response - Steel Hammer Impact**

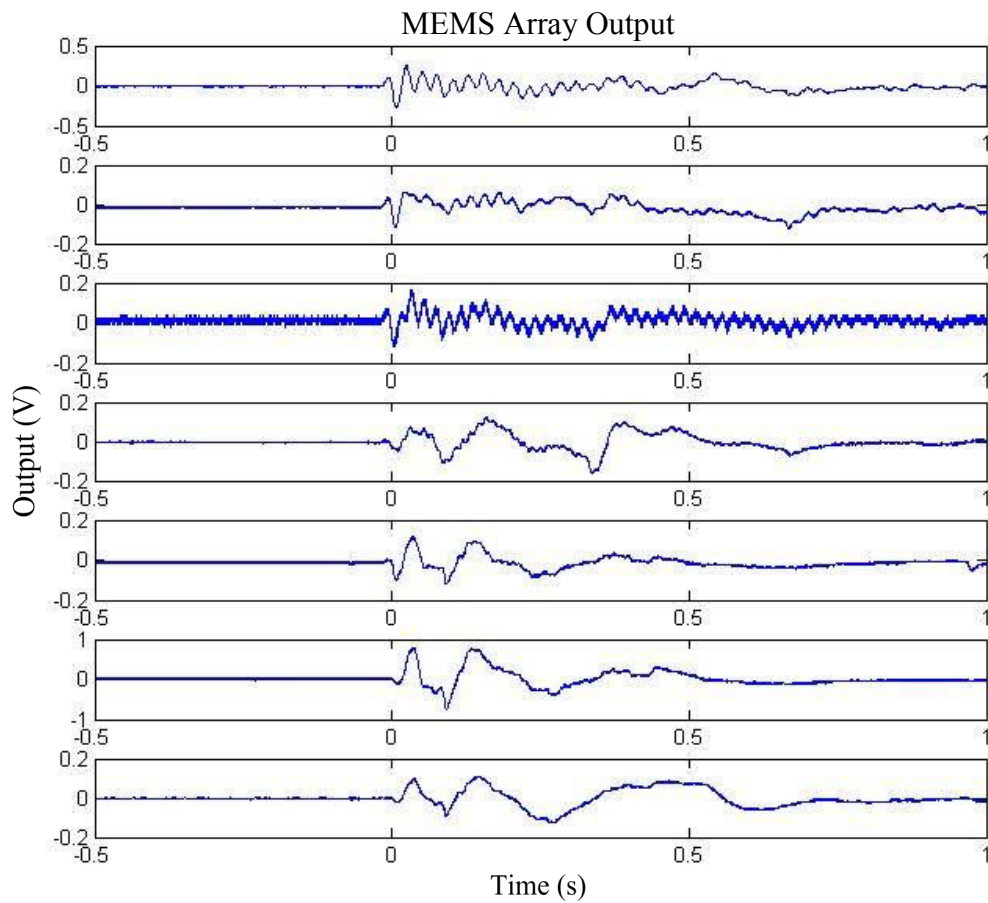
The maximum level of each of these waveforms is then found to yield the shock response spectrum. The spectra for the impact with Teflon and the impact with steel are shown in Figure B.57. The primary difference between these two spectra is related to the response of sensor 1. It shows significantly larger output during the steel impact, making it a discriminator for steel events.



**Figure B.57: Spectra from Teflon Impact (left) and Steel Impact (right)**

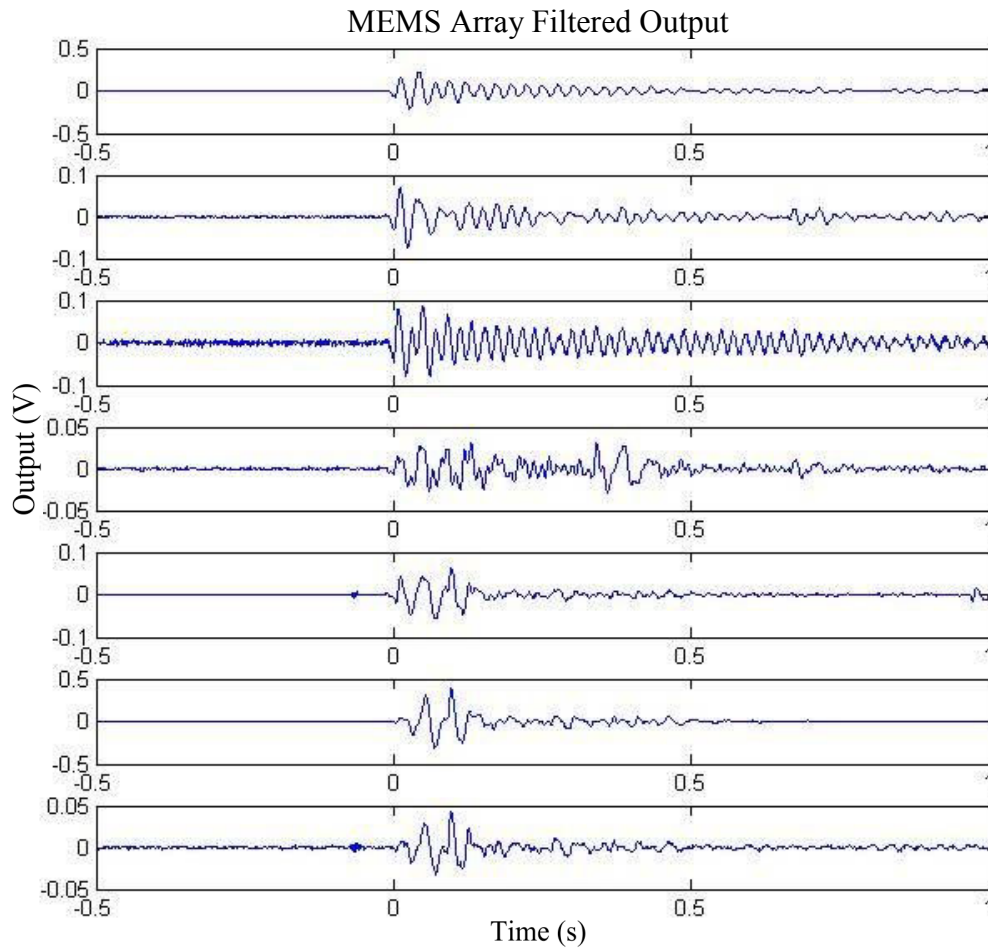
### **B.7 3<sup>rd</sup> MEMS Array on Steel Cone - Ball Drop**

Part of the response of the hammer setup is due to the length of the hammer, and the fact that the acoustic waveform takes a significant amount of time to travel from one end of it to the other. Therefore, further testing was performed using the ball drop apparatus. The small diameter of the ball leads to a higher frequency output. Figure B.58 shows the response of the array to the stainless steel ball drop.



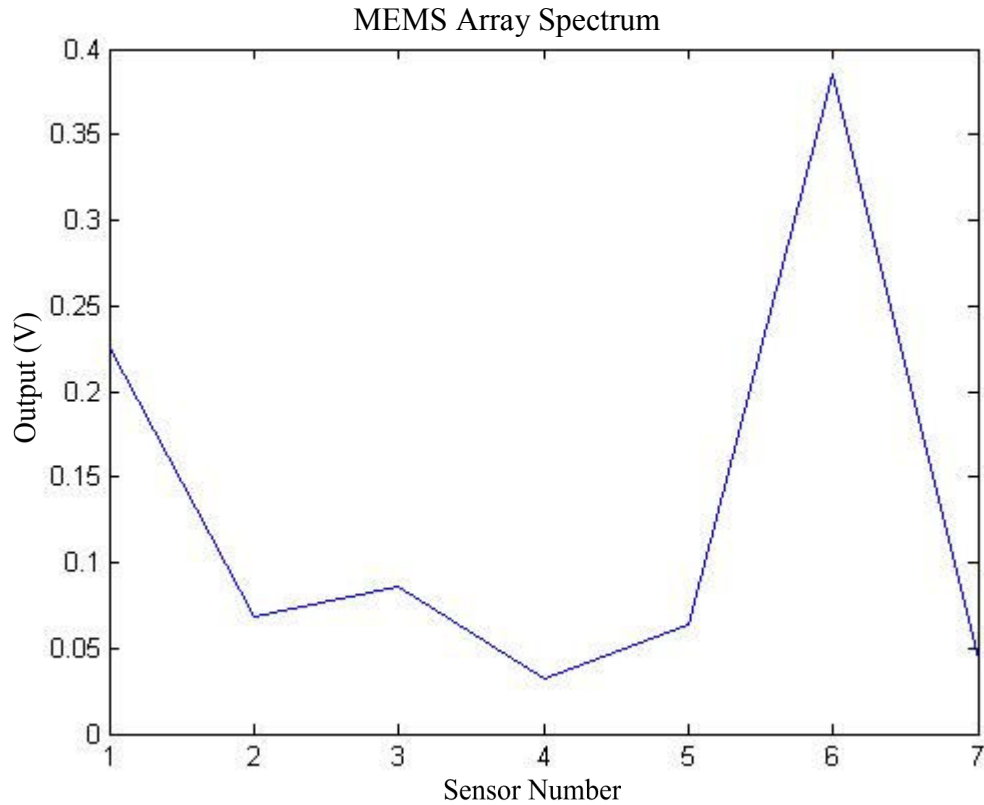
**Figure B.58: Seven Sensor Array Output - Stainless Steel Ball Impact**

Figure B.59 shows the response after applying the same filtering that was applied to the previous hammer drop tests. This filtering reduces the level of low frequency content in the signal.



**Figure B.59: Band-Pass Filtered Response - Stainless Steel Ball Impact**

Again, Figure B.60 shows the spectrum of the impact as determined by capturing the maximum output of the waveform as done in the shock response spectrum technique. Comparing this spectrum to the steel and Teflon hammer impacts, one can see the relatively larger output from sensors 2 and 3. This is indicative of slightly higher frequency content in the impact, due to both the smaller size of the ball and the slightly higher speed of sound in the material.



**Figure B.60: Spectrum Acquired from Stainless Steel Ball Impact**

A similar sized Teflon ball was not available, and even then, the lower density of Teflon would lead to a substantially smaller amplitude signal. Therefore, a custom test article was fabricated. It consisted of a steel tube 1/2inch long that was filled with Teflon. The revised ball drop setup is shown in Figure B.61. This provided a Teflon material to interface with the cone, as well as provided mass to increase the signal amplitude. This Teflon “slug” was dropped in the same apparatus as the ball drop experiment. Figure B.62 shows the waveform captured from that test.

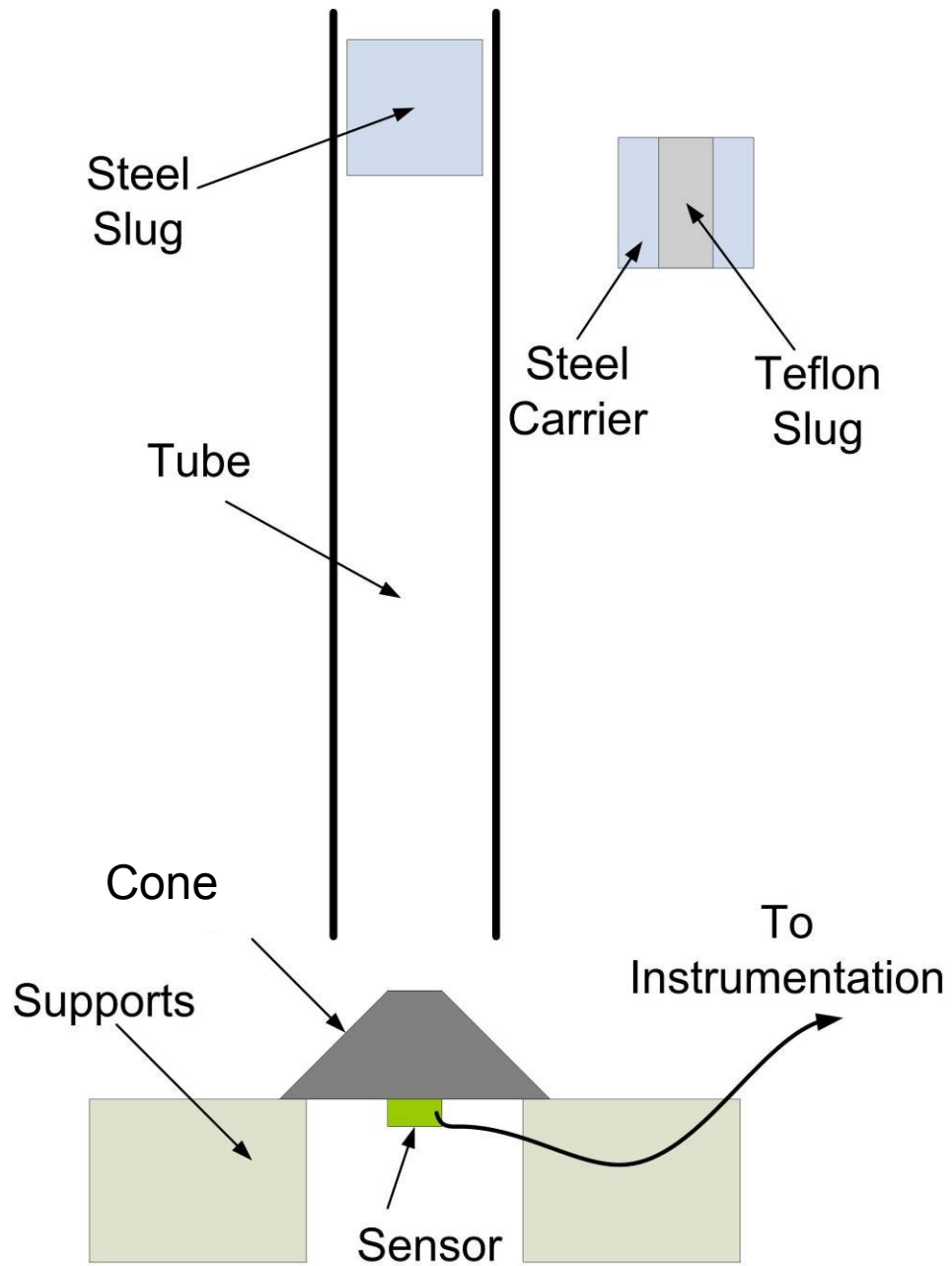
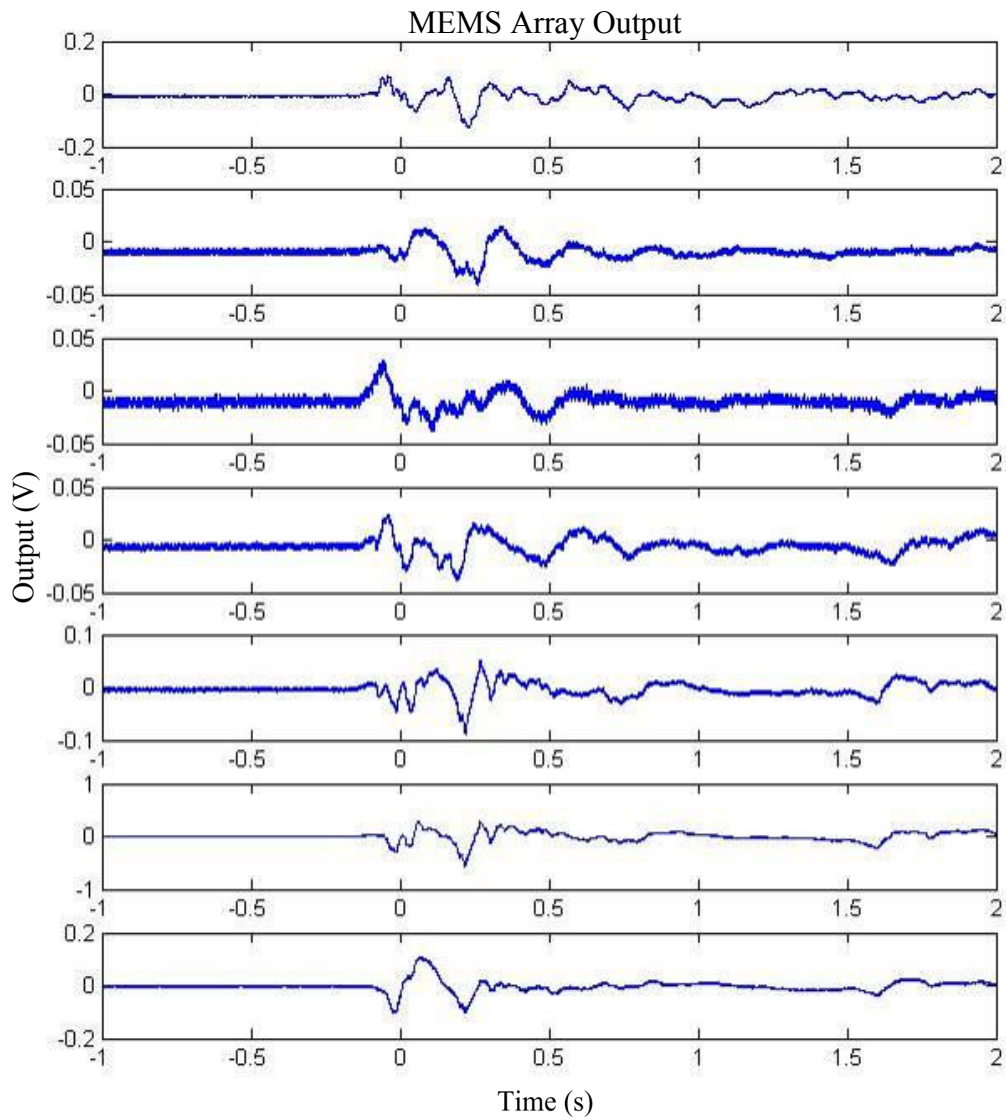
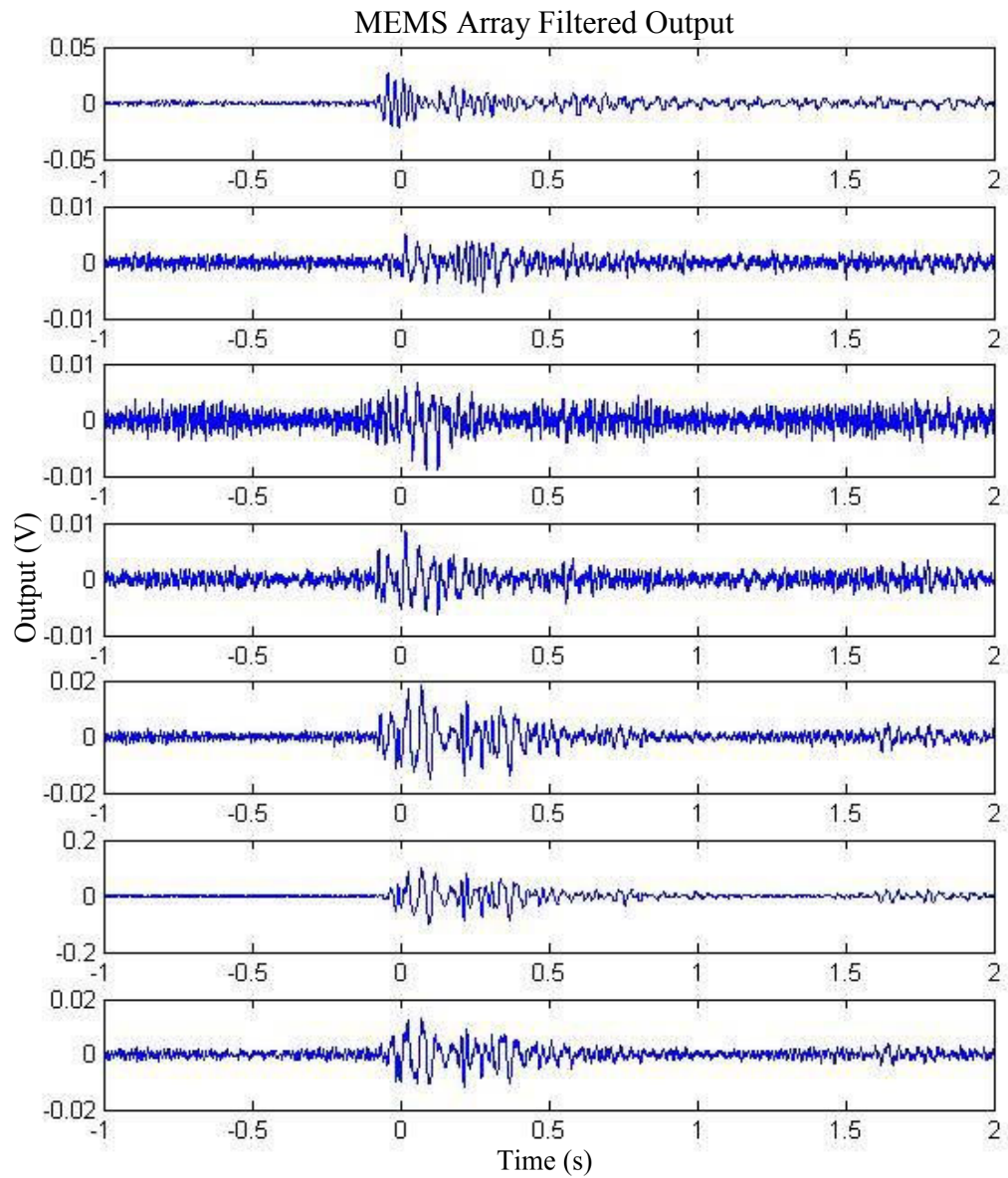


Figure B.61: Modified Ball Drop Setup



**Figure B.62: Seven Sensor Array Output - Teflon Slug Impact**

Again, the signal was band-pass filtered to remove the lower frequency portions of the signal. Figure B.63 shows this filtered response.



**Figure B.63: Band-Pass Filtered Response - Teflon Slug Impact**

A slug that was fully steel was then dropped in the same apparatus. This provided a test with the same amount of drop energy, but with a different material interface. Figure B.64 shows the filtered waveform from this impact.

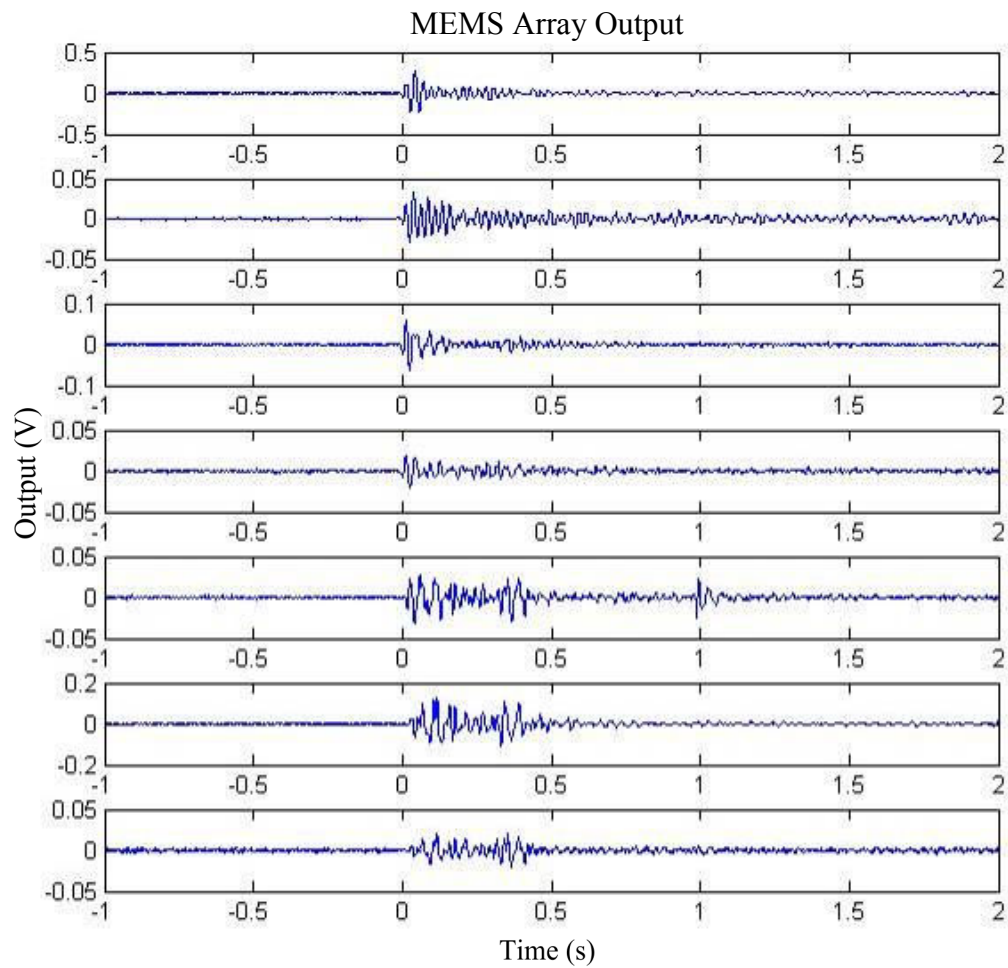


**Figure B.64: Band-Pass Filtered Response to Teflon Slug Impact**

As before, the maxima of these waveforms were determined and combined into a spectrum, as done in a shock response spectrum.

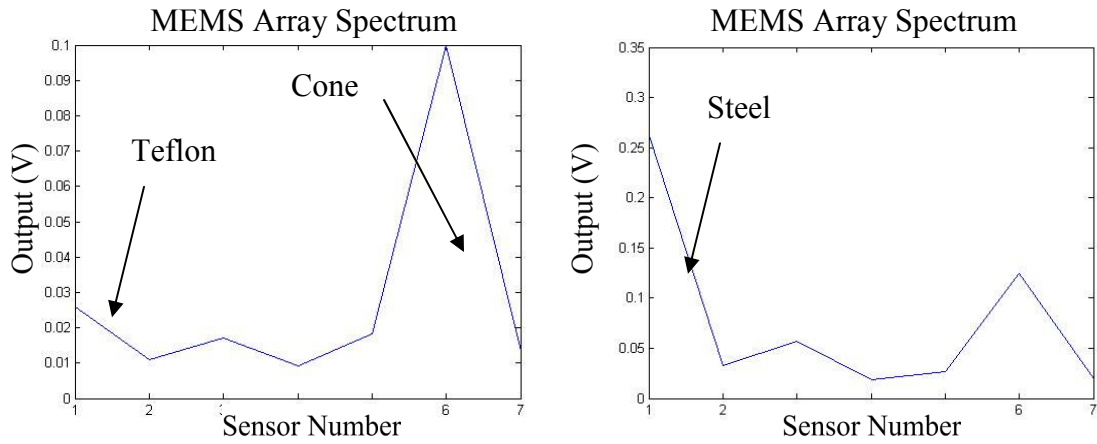


**Figure B.65: Spectra from Teflon Impact (left) and Steel Impact (right)**

Comparing these two spectra, it is clear that the sensors one, two, three, and four were excited to a larger extent by the steel impact, as would be expected.

### **B.8 4<sup>th</sup> MEMS Array on Steel Cone - Ball and Slug Drop**

A second series of tests were performed on a second die. The following figures show the captured waveforms and spectra.

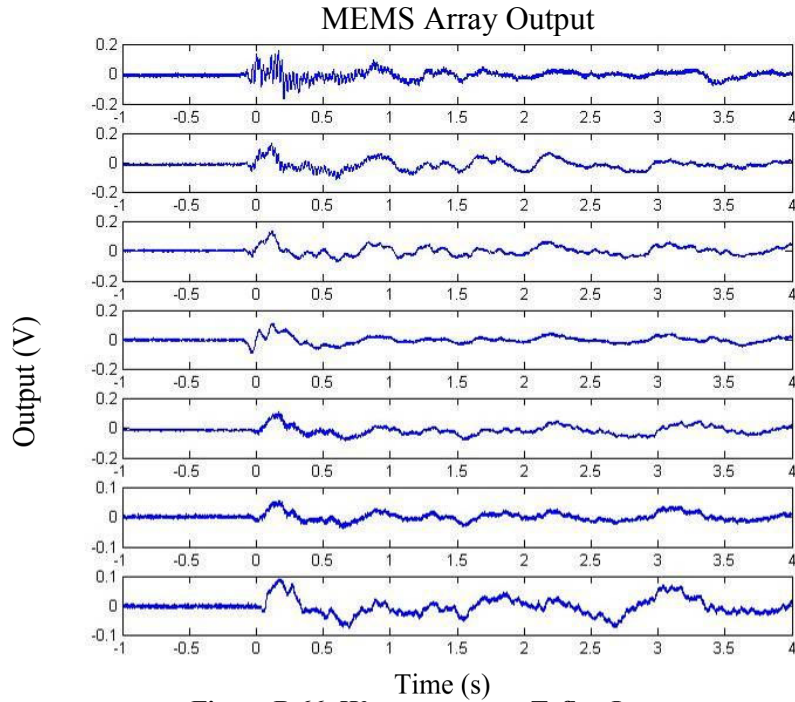


**Figure B.66: Waveform from Teflon Impact**

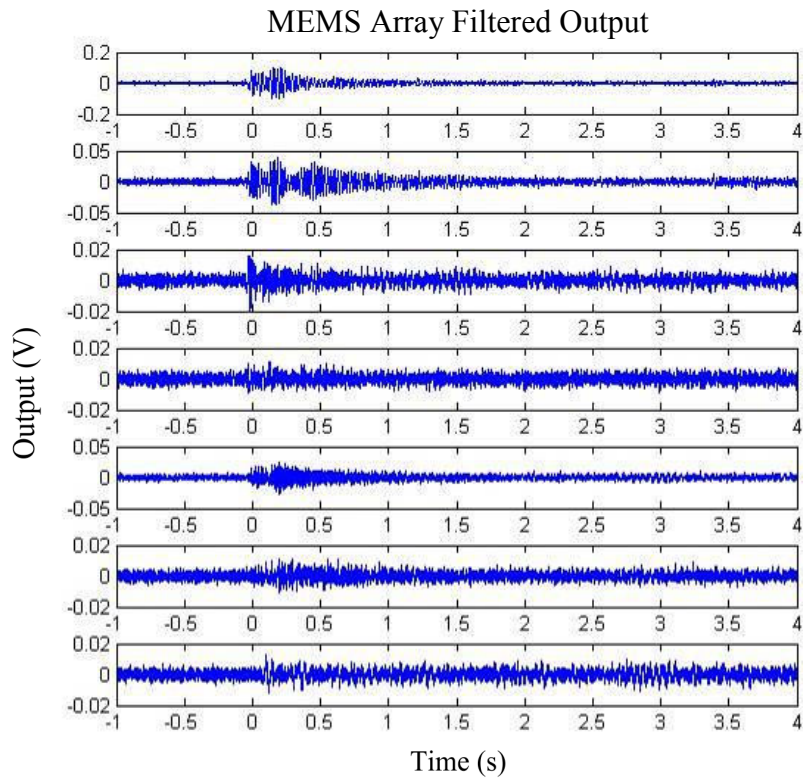


**Figure B.67: Filtered Waveform from Teflon Impact**

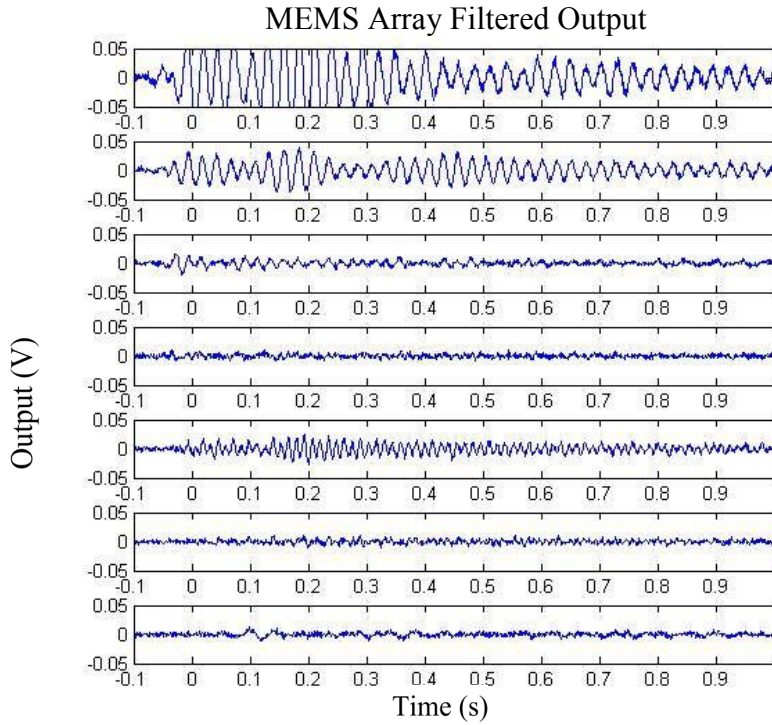


**Figure B.68: Filtered Waveform from Teflon Impact (Close-Up)**

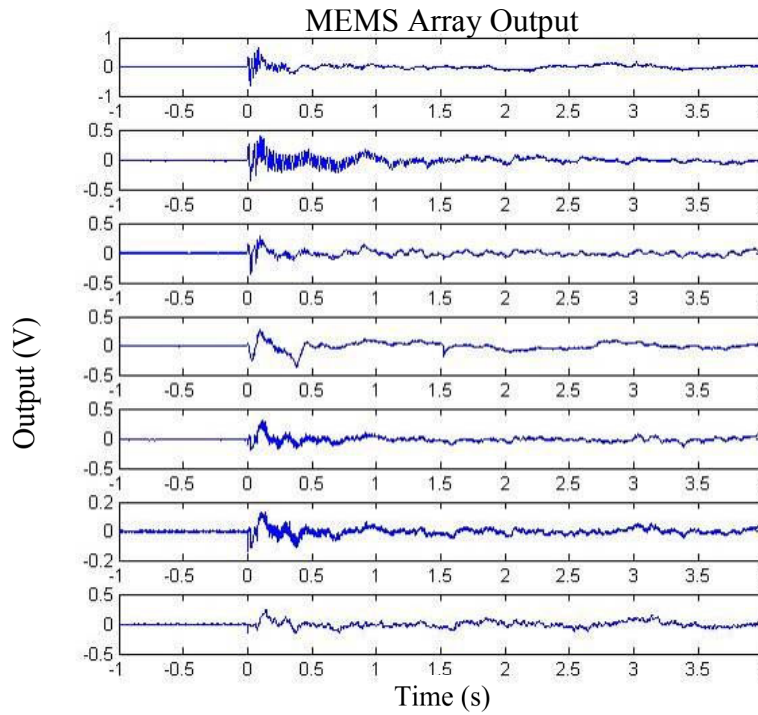


**Figure B.69: Waveform from Steel Impact**

### MEMS Array Filtered Output

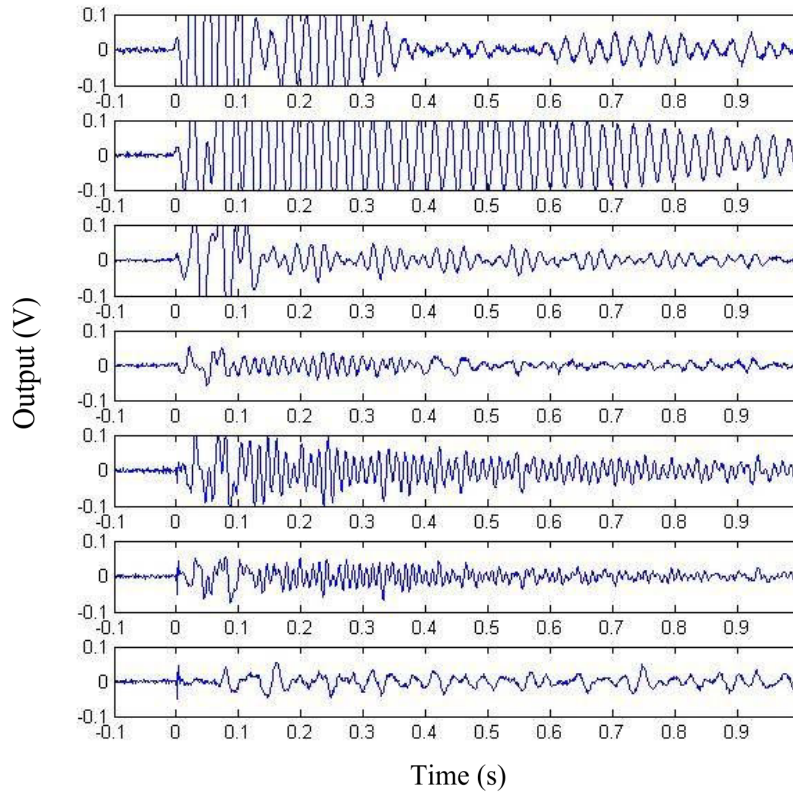


**Figure B.70: Filtered Waveform from Steel Impact (Close-Up)**

### MEMS Array Spectrum

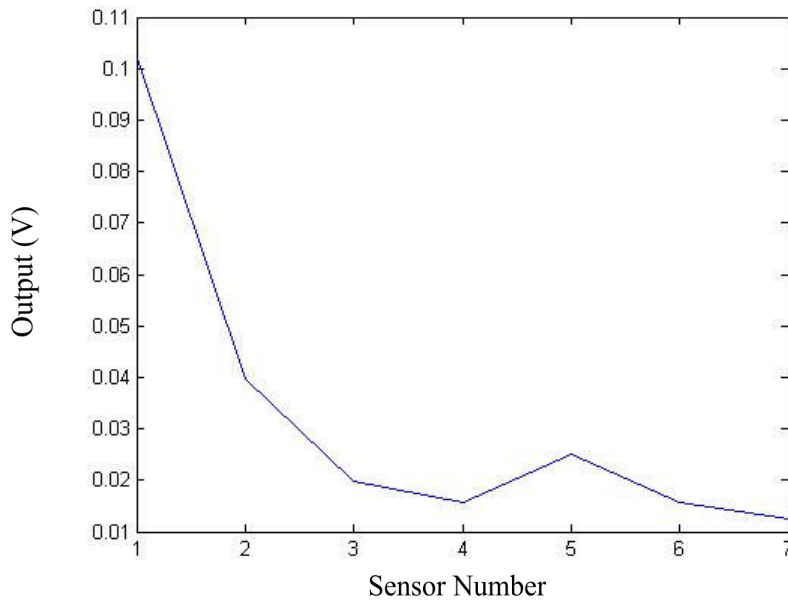


**Figure B.71: Teflon Spectra**

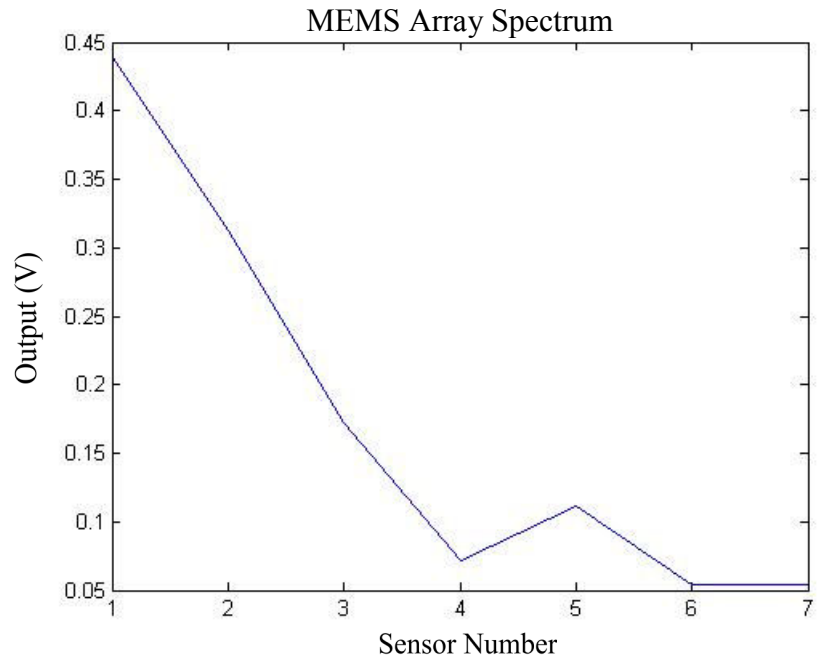


**Figure B.72: Steel Spectra**

To further investigate actual array response and compare to the model, a series of tests were performed with projectiles of various length and material. These included steel, stainless steel, aluminum, and Teflon. The various lengths and materials were selected to approximate the variety of source impulse functions used previously to simulate device output. The following figures show the filtered array responses in the time domain.

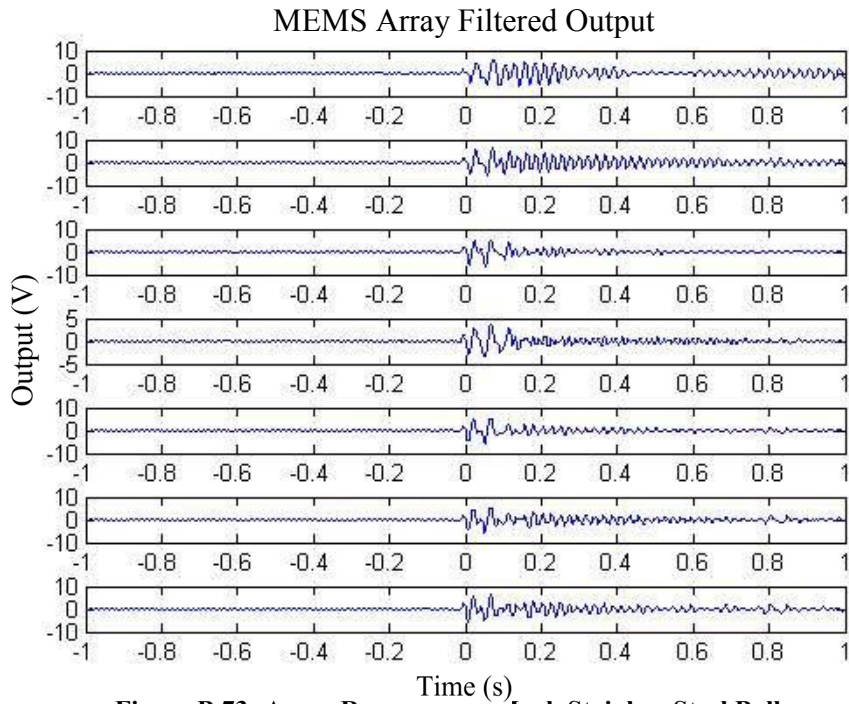


**Figure B.73: Array Response to 1/2 Inch Stainless Steel Ball**

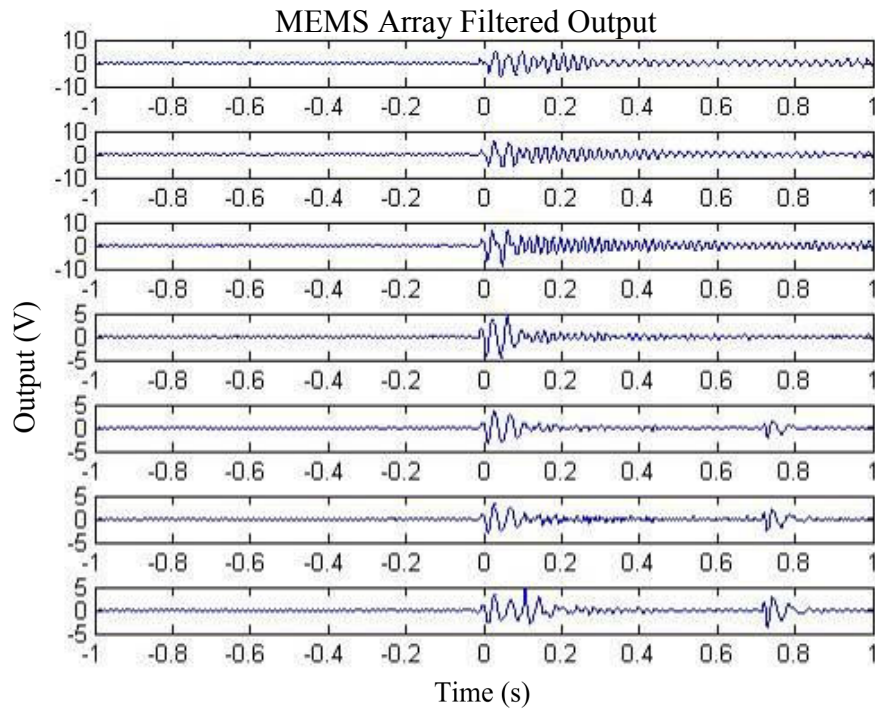


**Figure B.74: Array Response to 1/2 Inch Steel Rod**

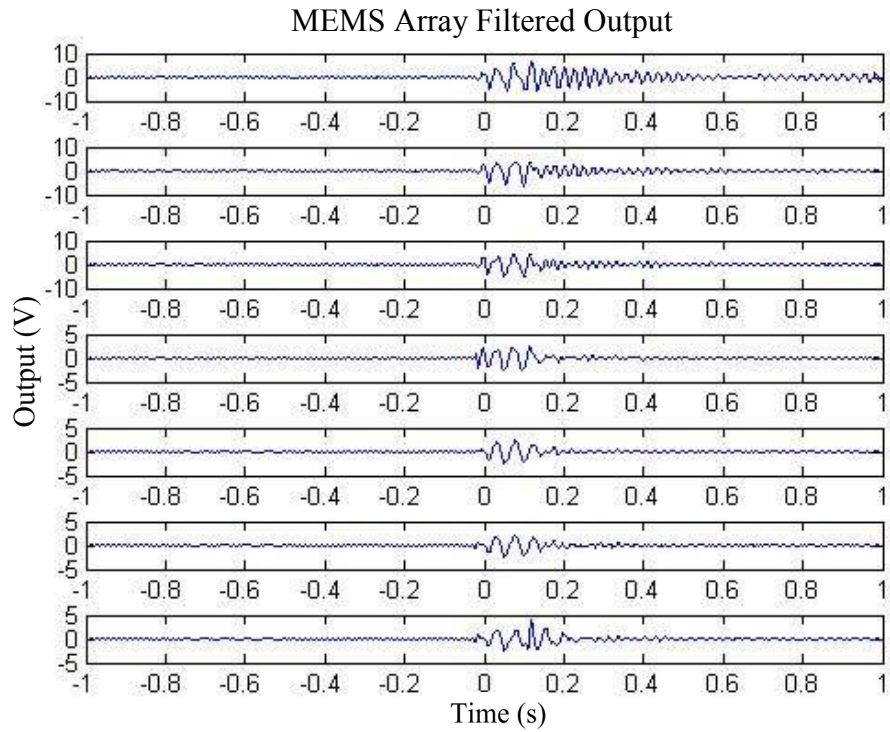


**Figure B.75: Array Response to 2½ Inch Aluminum Rod**

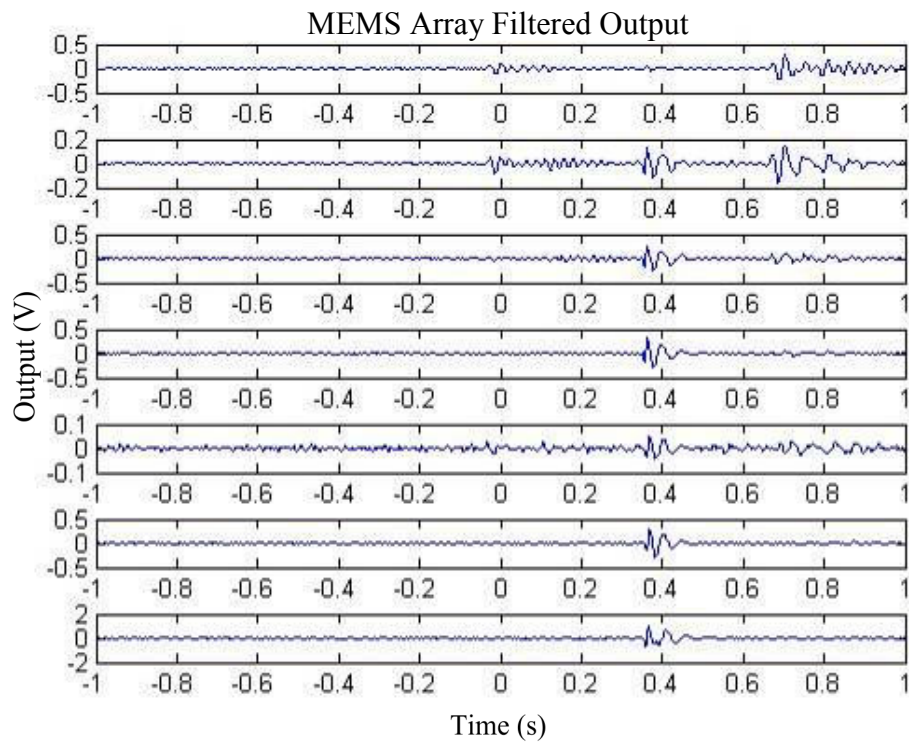


**Figure B.76: Array Response to 2 Inch Teflon Rod**

Figure B.77 shows the array spectra for each of these impact scenarios. The output data shows the same increase in slope as harder and smaller length impact sources, equivalent to high frequency content pulses, are used in the test apparatus.

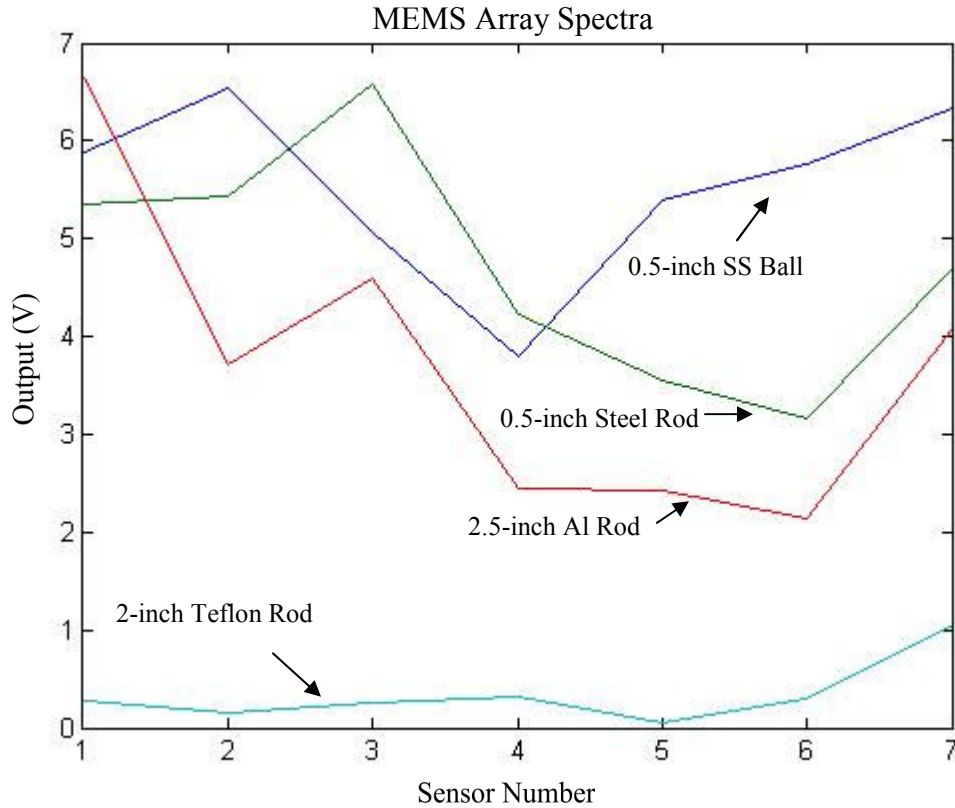


**Figure B.77: Array Spectra from Multiple Impact Sources**

This series of tests laid the groundwork for the final test series that is described in Chapter VII. That series included the signal processing developed in this historical set of data. This included the filtering of lower frequency signals from structural mounting and sensor-to-sensor crosstalk. In addition, a number of refinements to the test apparatus were developed and applied during the final tests series.

## REFERENCES

1. S.P. Beeby, M.J. Tudor, and N.M. White, "Energy Harvesting Vibration Sources for Microsystems Applications," *Measurement Science and Technology*, 17, R175-R195, 2006.
2. E. Pierazzo, G. Collins, "A Brief Introduction to Hydrocode Modeling of Impact Cratering," *Cratering in marine environments and on ice*, New York, Springer, 2004, Pages: 323 - 340.
3. James Cazamias, Stephen Schraml, "Modeling of Non-Eroding Penetration Using ALE3D and Zapotec," 15th APS Topical Conference on Shock Compression of Condensed Matter, 2007
4. G. T. Gray III, "Classic Split-Hopkinson Pressure Bar Testing," in *ASM Handbook*, Vol.8, Mechanical Testing and Evaluation, pp. 462-476, ASM International, 2000.
5. S. Burgett, M. Kranz, U.S. Patent #7267005
6. M. A. Lemkin, M. A. Ortiz, N. Wongkomet, B. E. Boser, and J. H. Smith, "A 3-axis surface micromachined  $\Sigma\Delta$  accelerometer," *Solid-State Circuits Conference*, pp. 202-203, 457, 1997.
7. Roger de Rez, *et. al.*, "Fabrication and Characterization of a Piezoelectric Accelerometer," *Journal of Micromechanics and Microengineering*, 9, pp.123-126, 1999.
8. <http://www.endevco.com/product/>, Model 2262.
9. Michael Whitley, Michael Kranz, "Latching Shock Sensors for Health Monitoring and Quality Control," *SPIE Photonics West*, 2005.
10. Heinrich Kuttruff, *Ultrasonics Fundamentals and Applications*, Elsevier Applied Science, New York, 1991.
11. [www.ferroc ceramic.com](http://www.ferroc ceramic.com)
12. [www.dupont.com](http://www.dupont.com)
13. E. Cretu, L.A. Rocha, and R.F. WolffenButtel, "Electro-Mechanical Feedback for Realization of a Mechanical Spectrum Analyzer," *Transducers '03*, 3E60.P, 2003.
14. M.H-Bao, "Micro Mechanical Transducers, Pressure Sensors, Accelerometers, and Gyroscopes," Elsevier, 2000.
15. Helmut Seidel, U.S. Patent #4885,781, "Frequency-Selective Sound Transducer," December, 1989.
16. D. W. Greve, I. J. Oppenheim, W. Wu, and A. P. Wright, "Development of a MEMS Acoustic Emission Sensor System," SPIE Smart Structures/NDE Joint Conf., 2007.
17. Huang, *et. al.* "Using Acoustic Emission in Fatigue and Fracture Materials Research," *Journal of Minerals, Metals, and Materials*, vol. 50, no. 11, November 1998.
18. [www.acousticemission.com](http://www.acousticemission.com)

19. J.E. Michaels, T. E. Michaels, and W. Sachse, "Applications of Deconvolution to Acoustic Emission Signal Analysis," *Materials Evaluation*, Vol. 39, No. 11, pp. 1032-1036.
20. D. J. Buttle and C. B. Scruby, "Characterization of Fatigue of Aluminum Alloys by Acoustic Emission, Part 1-Identification of Source Mechanism," *Journal of Acoustic Emission*, 9, No. 4, 1990a, 243-254.
21. H. Suzuki, T. Kinjo, Y. Hayashi, M. Takemoto and K. Ono, "Wavelet Transform of Acoustic Emission Signals." *Journal of Acoustic Emission*, 14, No. 2, 1996, 69-84.
22. D.J. Buttle and C.B. Scruby, "Characterization of particle impact by quantitative acoustic emission," *WEAR*, 137, pp63-90, 1990.
23. Gachagan, A., Mulholland, A. J., Hayward, G., Tramontana, M., Nordon, A., Carson, G. "Particle Sizing in the Process Industry using Hertz-Zener Impact Theory and Acoustic Emission Spectra," *Ultrasonics Symposium*, 2006, Oct. 2006 Page(s):1406 - 1409.
24. C.B. Williams, *et. al.*, "Development of an Electromagnetic Microgenerator," *IEEE Proceedings Circuits Devices Systems*, 148 (6), pp. 337-342, December 2001.
25. M. Umeda, K. Nakamura, and S. Ueha, "Analysis of the Transformation of Mechanical Impact Energy to Electrical Energy Using a Piezoelectric Vibrator," *Japanese Journal of Applied Physics*, Vol. 35, Part 1, No. 5B, pp. 3267-3273, May 1996.
26. S. Roundy, P.K. Wright, K.S.J. Pister, "MicroElectrostatic Vibration-to-Electricity Converters," *Proceedings of IMECE2002*, 1-10, 2002.
27. B. Cavallier, *et. al.*, "Energy Harvesting Using Vibrating Structures Excited by Shock," *2005 IEEE Ultrasonics Symposium*, pp. 943-945, 2005.
28. Sprenkels, A.J., *et. al.*, "The Use of Silicon Technology for an Electret Microphone Construction," *Proceedings of 6<sup>th</sup> International Symposium on Electrets*, 1988, pp. 593-597.
29. US Patent#3,944,756, "Electret Microphone," Electro-Voice Incorporated, March 16, 1976.
30. Hsu, *et. al.*, "A Thin-Film Teflon Electret Technology for Microphone Applications," *Tech. Dig. Solid-State Sensors and Actuators Workshop*, 1996.
31. Tsutsumino, *et. al.*, "High-Performance Polymer Electret for Micro Seismic Generator," *The Fifth International Workshop on Micro and Nanotechnology for Power Generation and Energy Conversion Applications, PowerMEMS2005*, November 28-30, 2005, Tokyo, Japan.
32. Y. Arakawa, *et. al.*, "Micro Seismic Power Generator Using Electret Power Film," *PowerMEMS 2004*, pp. 187-190, November 2004.
33. Sterken T, Baert K, Puers R, Borghs S (2002) "Power extraction from ambient vibration," *Proceedings of SeSens (Workshop on Semiconductor Sensors)*, November 29, 2002 - Veldhoven, the Netherlands, p. 680-683.M.
34. Sanghoon Lee, *et. al.*, "A Micro Corona Motor," *Sensors and Actuators A 118*, 2005, pp. 226-232.

35. Chester G. Wilson and Yogesh B. Gianchandani, "Silicon Micromachining Using *In Situ* DC Microplasmas," *Journal of Microelectromechanical Systems*, Vol. 10, No. 1, March 2001.
36. Makoto Honzumi, *et. al.*, "Soft-X-Ray-Charged Vertical Electrets and Its Application to Electrostatic Transducers," *23<sup>rd</sup> IEEE International Conference on MEMS (MEMS 2010)*, Hong Kong, January 2010.
37. Gregory C. McLaskey and Steven D. Glaser, "Hertzian Impact: Experimental Study of the Force Pulse and Resulting Stress Waves," *Journal of the Acoustical Society of America*, Vol. 128, pp. 1087 - 1096, September 2010.
38. Gregory C. McLaskey and Steven D. Glaser, "High-Fidelity Conical Piezoelectric Transducers and Finite Element Models Utilized to Quantify Elastic Waves Generated from Ball Collisions," *Sensors and Smart Structures Technologies for Civil, Mechanical, and Aerospace Systems 2009*, March 2009.
39. K.F. Graff, *Wave Motion in Elastic Solids*, Dover Publications, Inc., New York, 1975.
40. [www.scotchbrand.com](http://www.scotchbrand.com)
41. D. Ozevin, D. W. Greve, I. J. Oppenheim, and S. P. Pessiki, "Resonant capacitive MEMS acoustic emission transducer," *Smart Mater. Struct.*, **15**, 2006, 1863-1871.
42. J. B. Griffiths, "Classical Dynamics," Benjamin Cummings, 3<sup>rd</sup> Edition, 1999.
43. Malti Goel, "Electret Sensors, Filters, and MEMS Devices: New Challenges in Materials Research," *Current Science*, Vol. 85, No. 24, August 2003.
44. I. Kuehne, A. Frey, D. Marinkovic, G. Eckstein, H. Seidel., "Power MEMS—A capacitive vibration-to-electrical energy converter with built-in voltage," *Sensors and Actuators A*, 142 (2008) 263–269.
45. G. M. Sessler, *Electrets*, Laplacian Press, 1980.
46. Jose A. Giacometti, *et. al.*, "Corona Charging of Polymers: Recent Advances on Constant Current Charging," *Brazilian Journal of Physics*, vol. 29, no. 2, June 1999.
47. <http://www.bellexinternational.com/products/cytop/>
48. David J. Griffiths, "Introduction to Electrodynamics," Cambridge University Press, August, 1985.
49. <http://www.caswellplating.com/kits/electroless.htm>
50. Alexander A. Fridman, Lawrence A. Kennedy, *Plasma Physics and Engineering*, Taylor & Francis Books, Inc., New York, NY, 2004.
51. R. Tirumala, *et. al.*, "Corona Discharges in Sub-Millimeter Electrode Gaps," *Journal of Electrostatics*, November 2010.
52. Flexcon, "Product construction sheet: Densil 10 78k," p. 2, June 3, 2005.
53. Brian English, "Laminated Gas Generator Actuator Arrays," Ph.D. Thesis, Georgia Institute of Technology, December, 2006.
54. Charles Chung and Mark Allen, "Uncrosslinked SU-8 as a Sacrificial Material," *Journal of Micromechanics and Microengineering*, 15, 2005, pp. N1-N5.

## **VITA**

### **Michael S. Kranz**

Michael Kranz was born in Clymer, NY. He attended public schools in Clymer, NY, received a B.S. in Engineering Physics from Cornell University, Ithaca, NY in 1996 and a M.S. in Electrical and Computer Engineering from Carnegie Mellon University, Pittsburgh, PA in 1998 before coming to Georgia Tech to pursue a doctorate in Electrical and Computer Engineering. When he is not working on his research, Mr. Kranz enjoys horseback riding, martial arts, motorcycles, and camaros.